



# Finite element simulation of multi-layer repair welding and experimental investigation of the residual stress fields in steel welded components

Ardeshir Sarmast<sup>1</sup> · Jan Schubnell<sup>1</sup> · Majid Farajian<sup>2</sup>

Received: 1 June 2021 / Accepted: 21 February 2022 / Published online: 14 April 2022  
© International Institute of Welding 2022

## Abstract

In this work, the effect of multi-pass repair welding for removing a fatigue crack on the residual stress fields of GMA-welded S355J2+N and S960QL structural steel T-joints was investigated. Two scenarios were considered, a fatigue crack smaller than half of the plate thickness, and a fatigue crack larger than half of the plate thickness. Samples were first welded in a T-joint structure; then, cracks were created on their weld toes by cyclic loading; after that, the cracks were machined at one or two sides of the plate, depending on the crack length, and finally, the sample was repaired by two-pass welding on each machined area. Longitudinal and transverse residual stresses were measured by the X-ray diffraction method. A 2D thermo-metallurgical-mechanical finite element model was developed for each sample to estimate the residual stress fields through the weldments. The results show that, regardless of the alloy or repairing in one or two sides, the repair welding increases the magnitude of the residual stresses compared to the initial weld, but the alloys show different behaviors during the process. In S960QL samples, during repair welding of one weld toe, the residual stress evolutions in previously welded areas that are not subjected to the repair welding occur due to the morphological changes in the phases and expansions and contractions, while for S355J2N samples, the expansions and contractions are mainly responsible for these changes.

**Keywords** Repair welding · Residual stress · Structural steel · Thermo-metallurgical-mechanical simulation · Finite element method

## 1 Introduction

Repair welding is widely used in various industries to either remove imperfections or increase the endurance of welded components when they reach their final service life. During arc repair welding processes, as the arc passes on the specimen, the material melts and solidifies. The transient thermal history of the weldment causes microstructural evolutions and thermal expansions and contractions [1]. These expansions and contractions during repair welding cause strains,

which lead to the formation of residual stress in the component. The resulting residual stress could be more detrimental than the welding residual stress, because of higher levels of constraint on the repair welded specimens [1, 2]. Song and Dong [3] stated that the dominance of residual stresses in repair welds is so high that the initial welding-induced residual stresses could be neglected during the repair welding simulation. Owing to the wide variety of welding processes, these residual stresses could be different in different components, even when the geometry is the same [4]. These residual stresses could be added to the pre-existing residual stresses in the material and also to the service loads and negatively affect its integrity and performance [5]. Therefore, understanding the residual stress evolutions during repair welding turned to be a key factor for an accurate, successful design. Several researchers have worked on the subject in recent years. For instance, Charkhi and Akbari [6] developed a three-dimensional finite element thermo-mechanical model to study the effect of pre-heating on the residual stress modification of repair welded A106-B carbon steel and S304

---

Recommended for publication by Commission XIII—Fatigue of Welded Components and Structures

✉ Majid Farajian  
Farajian@slv-duisburg.de

<sup>1</sup> Fraunhofer Institute for Mechanics of Materials IWM,  
Freiburg, Germany

<sup>2</sup> GSI Gesellschaft Für Schweißtechnik International mbH,  
Duisburg, Germany

stainless steel pipes. They found the effect of preheating significant in controlling the residual stresses in the component. In another work, Elcoate et al. [7] investigated the effect of short and long multi-layer repair welding and also inter-pass temperature on the residual stress of a stainless steel pipe utilizing a thermo-mechanical model. They concluded that the inter-pass temperature has a dominant effect on the magnitude of the residual stresses. They also observed high magnitude tensile residual stress in the axial direction close to the welded area in short repair samples. Salerno et al. [8] validated a 3D FE model to predict the residual stress fields in a repair welded titanium plate. They highlighted that the interaction between the pre-existing residual stresses in the component and repair welding-induced residual stresses is still unclear. Jiang et al. [9] investigated the effect of repair welding depth on the longitudinal and transverse residual stress distribution in various sections of a 316L stainless steel component by neutron diffraction and finite element methods. They developed a 3D sequentially coupled thermo-mechanical model utilizing a double ellipsoid heat source and isotropic and kinematic strain hardening models. They concluded that, due to the increase in the number of repair passes, the deeper the repair welding is, the higher the residual stress in the specimen will be.

Despite the widespread application of the repair welding and its dominant effect on the lifetime of the component, the subject is barely investigated. Because of this reason and the complex nature of residual stresses during repair welding, the effect of repair welding on the residual stress redistribution through the welded components is not completely clear yet. The fact that the residual stresses in various weldments could be different depending on the welding process parameters such as welding current, voltage and speed, the alloy and molten material behavior, clamping method, and level makes the situation even more complicated [10]. One important case is the repair welding of the structural steels due to the fatigue crack formation. This happens, especially in the structures like cranes or bridges that reach their lifetime. Repair welding these structures could make higher levels of the residual stresses that could be added to the service loads and cause early failure of the structure, which in the case of bridges and cranes can cause irreparable damages.

Therefore, this study aims towards investigating the effect of repair welding on residual stress and distortion of steel

structures that are subjected to repair welding due to the formation of the fatigue cracks. In this regard, two commonly used structural steel, S355J2+N in normalized condition and quenched and tempered S960QL alloy, were welded in a T-joint structure by gas metal arc welding (GMAW) process. Two cases of fatigue crack formation were considered, one with the crack length smaller and another with the crack length larger than the plate thickness. Then depending on the crack length, the samples were repaired on one and two sides. X-Ray diffraction method was employed to measure the residual stresses through the components. Also, the cross-section of the weldments was observed under the optical microscope, and the hardness of the weld material and surrounding area was measured. To study the residual stress distribution in the whole sample and not only in one section, 2D finite element thermomechanical-mechanical models were also developed utilizing SYSWELD software to calculate the thermal contours, phase transformations, and residual stresses of the weldments. The models were validated with the experiments. JMatPro v10 software was deployed to develop the material model for the simulation. The material model also was calibrated with the tensile tests at room and elevated temperatures.

## 2 Experimental procedure

Two stiffeners with the dimensions of  $170 \times 50 \times 10 \text{ mm}^3$  were welded in a T-joint structure on both sides of a plate with dimensions of  $170 \times 370 \times 10 \text{ mm}^3$  by the gas metal arc welding (GMAW) process. Two different steel, one, structural steel S355J2+N in the normalized condition and the other, high strength quenched and tempered S960QL were deployed as the base material. Both the stiffener and plate were from the same material. G4Si1 filler material with 1.2-mm diameter was utilized for welding of S355J2+N samples, and X90-IG ( $\text{Mn}_2\text{NiCrMo}$ ) wire with 1-mm diameter was used for S960QL samples, according to DIN EN 757. The chemical composition of the alloys and filler materials is presented in Table 1. The chemical composition of the base materials was measured by spectral analysis and the chemical composition of the filler materials was taken from the manufacturer datasheet. During welding of all samples, M21-ArC-18 was used as the shielding gas with a flow rate of 15–18 l/min to protect the hot area from reacting with the air. S960QL samples are susceptible

**Table 1** Chemical composition of the alloys and filler metals

Material	C	Al	Cr	Cu	Mn	Mo	Nb	Ni	Si	Ti	V	P	S	Fe
S355J2+N	0.16	0.032	0.04	0.015	1.46	0.007	0.014	0.035	0.168	0.0123	0.008	0.0106	0.0051	Bal
G4Si1	0.08	0	0	0	1.65	0	0	0	1	0	0	0	0	Bal
S960QL	0.156	0.057	0.196	0.013	1.24	0.608	0.013	0.083	0.206	0.0003	0.0465	0.0096	0.0018	Bal
X90-IG	0.1	0	0.35	0	1.8	0.6	0	2.3	0.8	0	0	0	0	Bal

to hot cracking; therefore, they were locally preheated before welding to temperatures between 80 and 150°C, according to SEW088 guideline [11] by a flame torch. The hot cracking is not the case for the S355J2+N samples, and they were welded without preheating.

Two possible scenarios were considered for the fatigue crack formation. First, the crack length is lower than half of the plate thickness, which could be repaired by one side machining and repair welding. Second, the length of the crack is larger than half of the plate thickness. In this case, the material removal shall be performed by three fourth of the plate thickness from one side, repair welding on this side, and machining of the plate on the opposite side of the crack and repair welding. To create cracks with different sizes for the study, the specimens were loaded on a resonance-frequency machine RUMUL 150 K (Russenberger Prüfmaschinen AG, Neuhausen am Rheinfall, Switzerland). A sinusoidal 4-point bending load was imposed on the sample. To analyze the  $\Delta f$ , a-correlation for different load levels, a beach mark test was carried out utilizing four specimens. Shutdown criterion of  $\Delta f = 0.2$  was used for crack generation on one-side repair samples ( $a < t/2$ ), and  $\Delta f = 1.2$  was used as the criterion for the double-side repair samples ( $a > t/2$ ). Figure 1 shows

the setup used for the creation of the cracks. To be sure the crack only initiates on one weld, the other three welds were mechanically treated by high-frequency mechanical impact (HFMI). The samples were tested by penetrant testing (PT) and magnetic-particle testing (MT) to make sure the crack with the desired depth was created. More details about the NDT tests and fatigue crack removal from weldments can be found in another publication of ours [12].

After crack creation, they were removed by manual machining. PT and MT were utilized to be sure that the crack was completely removed. The GMAW process was also used for the repair welding. The lag time between welding and repairing of S960QL samples was selected as the temperature of samples was 100°C. Table 2 shows the welding parameters of initial and repair welding. For all welds, the quality class B according to DIN EN ISO 5817:2014–6 was reached. During the whole welding process, type K NiCr-Ni class 1 thermocouples with a wire diameter of 0.1 mm were employed, according to EN 60,584, to record the temperature history of the weldments. Figure 2 shows the location of the thermocouples and the sequence of the process. Five thermocouples were used in total for recording the temperature history of each sample with a 1-mm distance from one another (Fig. 3).

**Fig. 1** Setup for the crack creation

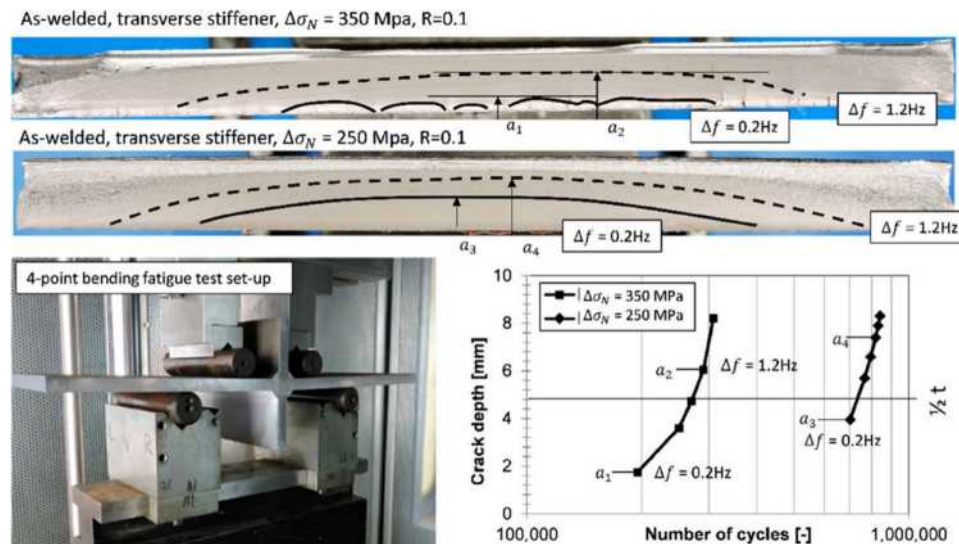


**Table 2** Welding parameters

Sample	Current (A)	Voltage (V)	Speed (mm/s)	Heat input (J/mm)	Efficiency
S355J2+N — initial weld	247	29.4	6.65	1092.22	0.9
S355J2+N — repair, root pass	212	42	7.69	1157.52	0.6*
S355J2+N — repair, cover pass	222	42	6.45	1445.22	0.6
S960QL — initial weld	216	29.4	5	1270.08	0.7
S960QL — repair, root pass	215	42	7.69	1173.9	0.9
S960QL — repair, cover pass	220	42	5.56	1663.2	0.7

\*For the double-side repair welded sample, the arc (thermal) efficiency of the root pass on the first side is considered to be 0.9

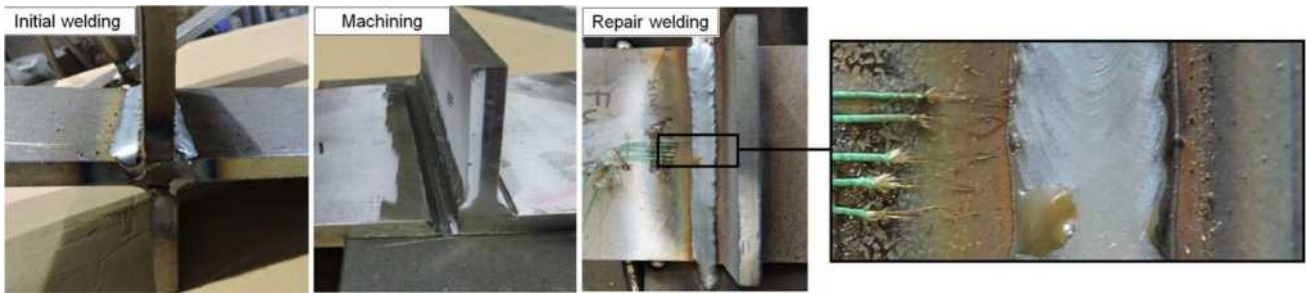


**Fig. 2** The sequence of initial welding, machining and repair welding

To study the residual stresses, an X-ray diffraction instrument with a mobile diffractometer type XSTRESS G3 was deployed. The measurements were carried out from the weld toe through the base material in longitudinal and transverse directions by Cr-K $\alpha$  radiation at the ferritic (211) lattice plane. The penetration of the X-ray was around 5  $\mu\text{m}$ . In the transverse direction, the stiffeners restricted the tilt angle of the diffractometer; thus, the measurements were done only in one tilt direction with 7 tilt angles, from 0 to 45°. In the longitudinal direction, which was free for the movement of the goniometer, 15 tilt angles were deployed to do the measurement, from -45 to 45°. Figure 4 shows the configuration of the diffractometer against the sample. The  $\sin \psi^2$ -method [13] was used for the residual stress measurement, assuming an even residual stress state for the transverse direction. For the calculation of the residual stresses from the diffraction results, the elastic constants of  $E=210$  GPa and  $v=0.3$  were used, where  $E$  is Young's modulus, and  $v$  is Poisson's ratio.

### 3 Modeling

To calculate the thermal contours and the residual stress fields, six different two-dimensional thermo-metallurgical-mechanical models for initial weld and one-side and double-side repair welded S355J2+N and S960QL components were developed in the SYSWELD software. Due to the negligible effect of the mechanical stresses on the temperature fields and solid-state phase transformations [14], the thermal and metallurgical models were fully coupled to each other and sequentially coupled to the mechanical models.

#### 3.1 Thermal modeling

To handle the thermal calculations, the conduction equation was used as the governing equation and convection and radiation were considered the boundary conditions [14]:

$$\rho C_p \frac{\partial T}{\partial t} = \nabla(k\nabla T) + Q \quad (1)$$

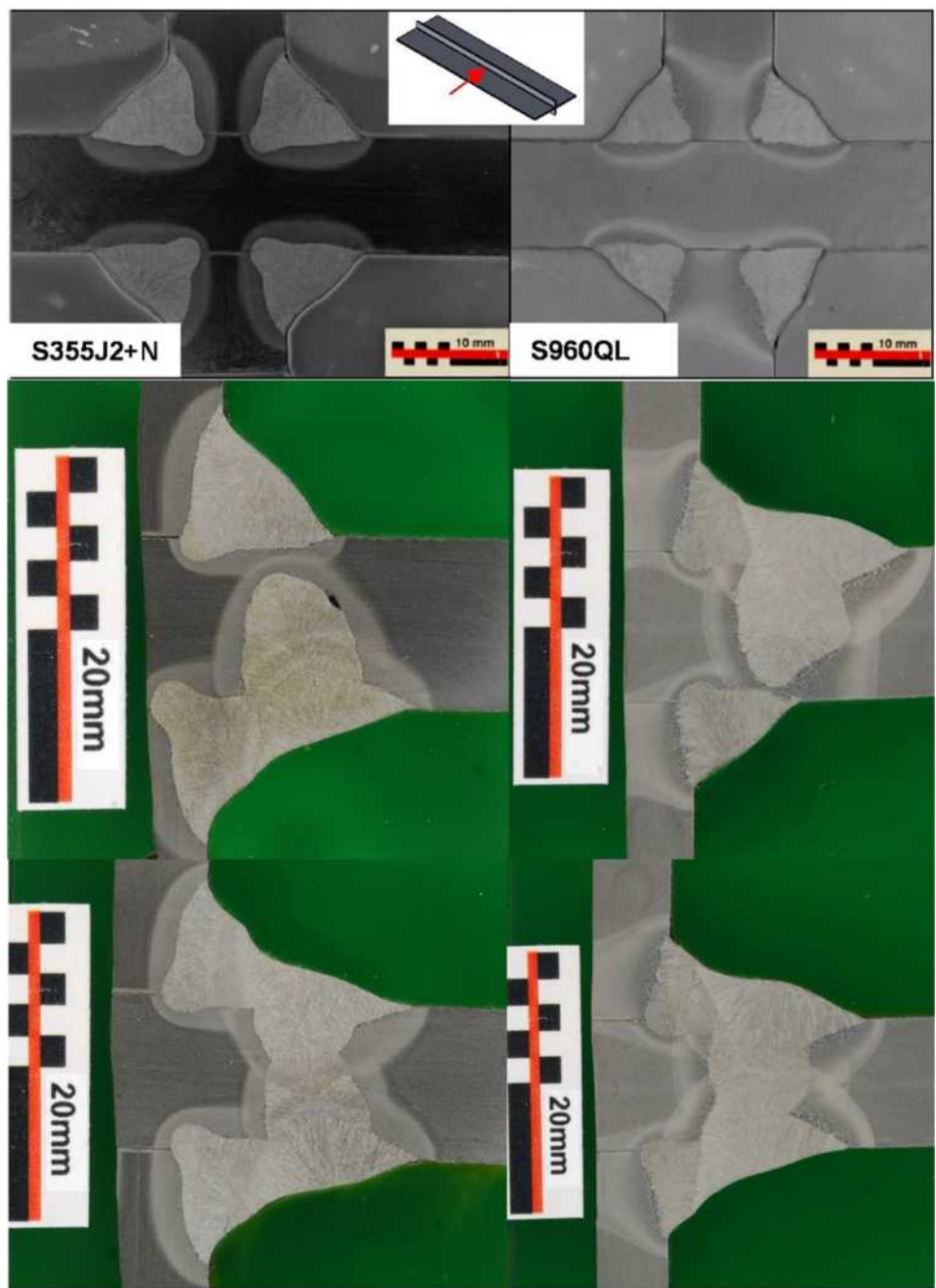
$$k \frac{\partial T}{\partial t} = -h(T - T_a) - \sigma \epsilon (T^4 - T_a^4) \quad (2)$$

where  $\rho$  is the density,  $C_p$  is the specific heat,  $T$  is the temperature,  $t$  is time,  $k$  is the thermal conductivity,  $Q$  represents the heat input from the heat source,  $h$  is the heat conduction coefficient,  $T_a$  is the ambient temperature,  $\sigma$  is Stefan-Boltzmann constant, and  $\epsilon$  is the emissivity. To increase the accuracy of the calculations, the density, thermal conductivity, and specific heat of the alloys were considered to be temperature- and phase-dependent. Figure 5 shows the material properties used in the thermo-metallurgical-mechanical simulations. The properties of the base materials and filler metals of S960QL samples were modeled by the JMatPro-v10 software. SYSWELD database was used for the material properties of S355J2+N base material, and the relevant filler material properties were modeled by JMatPro v10. The calculated material properties were calibrated with the tensile tests on the base material at various temperatures. Due to the fluid flow characteristics of the weld pool, its thermal conductivity is significantly higher than that of the liquid material under quasi-static conditions [15]. To consider the stirring effects of the weld pool, the thermal conductivity of the liquid material was considered to be a characteristic of the welding process and assumed three times higher than that of the base material at room temperature. In all models, the emissivity and the heat transfer coefficient were taken as 0.3 and 8 W/m<sup>2</sup>K, respectively.

Another boundary condition of the thermal model is the heat input from the welding torch. According to the observed melt pool, the double ellipsoid equation developed by Goldak et al. [16] was deployed to simulate the imposed heat from the heat source. To estimate the weld pool shape and thermal history of the weldments more precisely, conical distribution along the weld pool depth was taken with double ellipsoid distribution on the surface.

$$q(x, y, z) = \frac{6\sqrt{3}f_f Q}{ab_f c\pi\sqrt{\pi}} \exp\left(\frac{-3x^2}{a^2} + \frac{-3[y + v(\tau - t)]^2}{b_f^2} + \frac{-3z^2}{c^2}\right) \quad (3)$$

**Fig. 3** Residual stress measurement by XRD



$$q(x, y, z) = \frac{6\sqrt{3}f_r Q}{ab_r c \pi \sqrt{\pi}} \exp\left(-\frac{-3x^2}{a^2} + \frac{-3[y + v(\tau - t)]^2}{b_r^2} + \frac{-3z^2}{c^2}\right) \quad (4)$$

In these equations,  $f_f$  and  $f_r$  are the heat fractions of the front and rear portions of the heat source;  $a$ ,  $b_f$ ,  $b_r$ , and  $c$  are the geometrical parameters of the double ellipsoid function;  $x$ ,  $y$ , and  $z$  are the coordinates;  $\tau$  is the lag factor;  $t$  is the time;  $Q$  represents the welding heat input which is defined as  $\eta VI$  in arc welding processes, where  $\eta$  is the arc efficiency,  $V$  is the welding voltage, and  $I$  is the arc current. The arc

efficiency of an arc welding process depends on many factors such as the shielding gas, the current polarity, and the arc length [17, 18]. According to reported values for the arc efficiency of the GMAW process in literature [19–22], values shown in Table 2 were taken as the arc efficiency in the models. The geometrical parameters of the double ellipsoid equation, arc efficiency, convection coefficient, emissivity, and melt pool conductance were considered variables. The values of the variables were determined through the validation process of the thermal model with the temperature recorded by thermocouples and the melt pool dimensions.



**Fig. 4** Residual stress measurement by XRD

### 3.2 Metallurgical modeling

Metallurgical models are responsible for the calculation of microstructural evolutions. Microstructural evolutions consist of grain growth, solidification, solid-state phase transformations, precipitation evolution, etc. [23]. In the employed alloys in this study, the controlling microstructural feature, which defines the mechanical properties of the specimen, is the solid-state phase transformation. The fraction of the final phases and their morphology define the final material properties that determine the performance of the product. Steel alloys undergo a series of diffusion-controlled and diffusionless transformations during the heating and cooling cycles of welding. Austenite is the key phase during the metallurgical simulation of steels. All phase transformations go toward or out of this phase. The equilibrium phase fraction of the austenite phase determines whether this phase forms or dissolves. During heating of the alloy, as the temperature rises, the

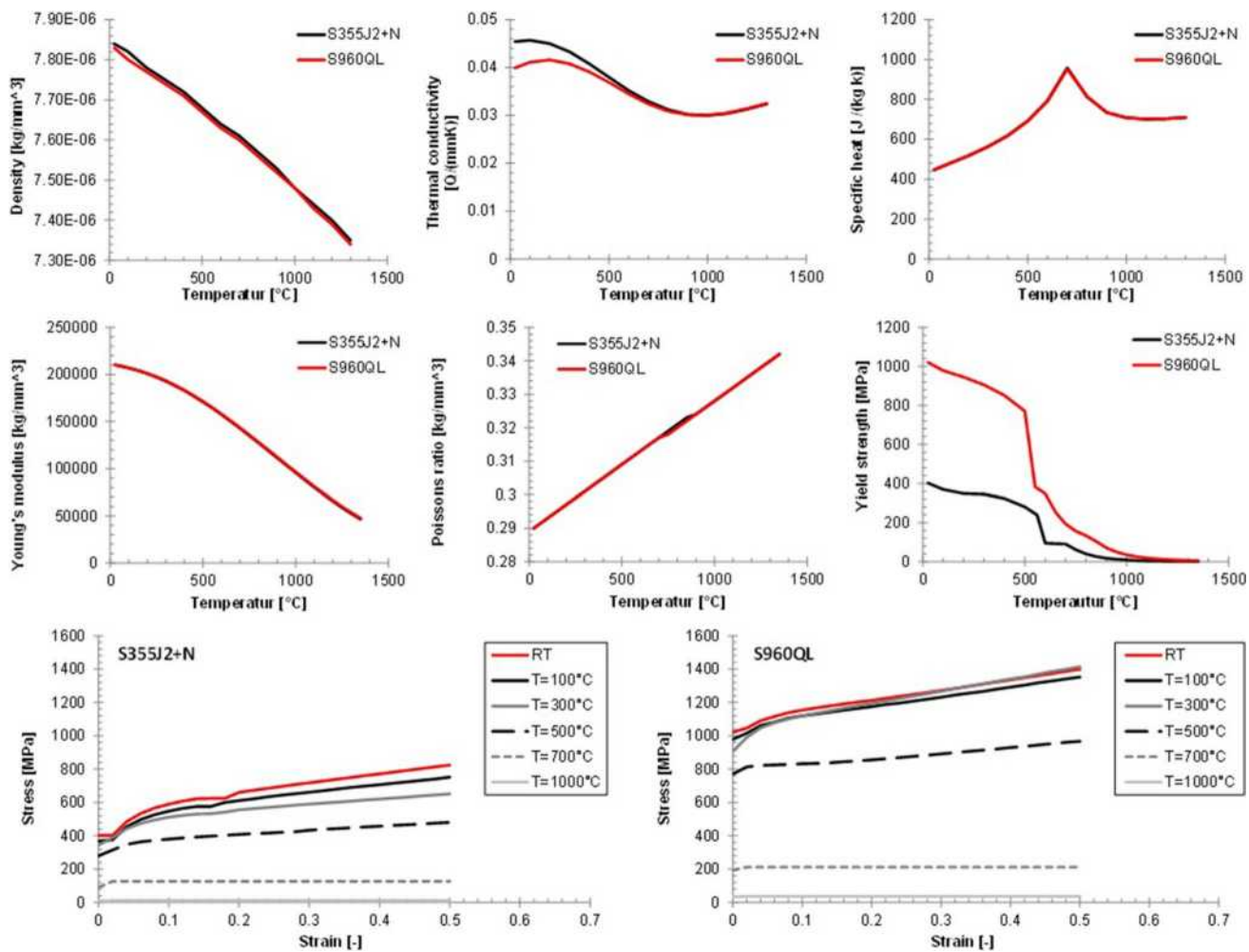


**Fig. 5** Thermo-physical and mechanical properties of S355J2+N and S960QL alloys employed in the models

equilibrium austenite phase fraction gradually increases and pre-existing phases transform to the austenite. During the cooling, on the other hand, the equilibrium austenite phase fraction decreases by decreasing the temperature and depending on the cooling rate the austenite phase dissolves to ferrite ( $\alpha$ ), pearlite (P), bainite (B), martensite (M), or a combination of them. Figure 6 shows the flowchart of the phase transformation used in this study.

The formation of the austenite phase from all these phases is diffusion-controlled and so are the transformations of austenite to ferrite, pearlite, and bainite phases. The austenite to martensite transformation, however, is a diffusionless phenomenon. To estimate the diffusion-controlled phase formations, the equation developed by Leblond and Devaux [24] was utilized:

$$\dot{X} = \frac{X_{eq}(T) - X}{\tau(T)} \quad (5)$$

where  $X$  is the phase proportion,  $X_{eq}$  is the equilibrium phase proportion,  $\tau$  represents the time after that  $X$  reaches 1, and  $T$  is the temperature. The equation contains two functions of the temperature,  $X_{eq}(T)$  and  $\tau(T)$ . The former changes between 0 and 1 and the latter is always positive; otherwise,  $X$  would not tend towards  $X_{eq}$ . For the diffusionless austenite to martensite transformation, Koistinen-Marburger equation [25] was utilized:

$$X_M = (1 - \exp(-b_{KM}(T_{ms} - T)))X_\gamma \quad T < T_{ms} \quad (6)$$

where  $X_\gamma$  is the austenite phase proportion available at the start of the martensite transformation,  $T$  is the temperature to reach,  $T_{ms}$  is the martensite start temperature, and  $b_{KM}$  is a material-dependent coefficient.

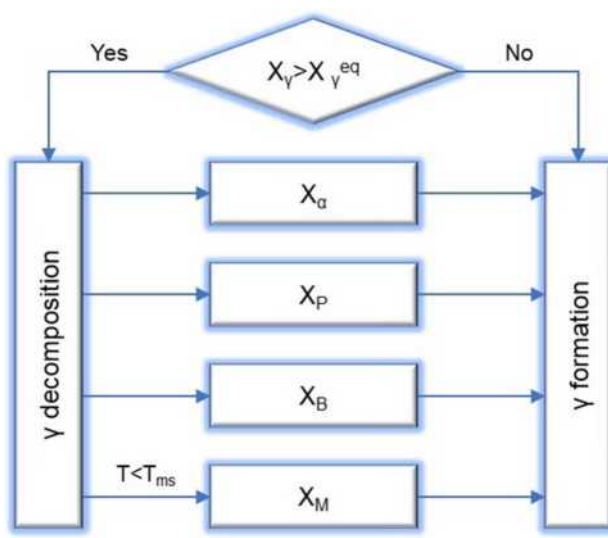


**Fig. 6** Schematic of metallurgical simulation

The constant values of the abovementioned equations were extracted from the continuous cooling transformation (CCT) diagram of the alloys, which was calculated by JMatPro software (Version 10) based on the interpolation from the Thermtech Database [26]. The Austenitization temperature (AC3) and the initial grain size are the input of the calculation. The AC3 was estimated according to the empirical formulation proposed by Trzaska [27] based on the chemical composition of the base materials, given in Table 1. The average grain size was estimated according to ASTM E112 – 13 (2017) that was 20  $\mu\text{m}$  for S355J2+N, and 9  $\mu\text{m}$  for S960QL samples. Figure 7 shows the calculated CCT diagram of the alloys calculated by JMatPro compared to the data taken from ZTU-Atlas [28].

The parameters of Leblond and Koistinen-Marburger equations were also calibrated with the JMatPro software package. For S355J2+N alloy, the martensite start temperature was 420 °C, and  $b_{KM}$  was 0.01428. These values for the S960QL alloy were 404 °C and 0.0208, respectively. Leblond parameters were selected according to the CCT diagrams (Fig. 7).

### 3.3 Mechanical modeling

By having the thermal contours and phase proportions of the samples in hand, stress fields can be calculated. The principle of minimum potential energy on an elastic–plastic material can be used [29]:

$$\delta\pi = \int (d\sigma)^T \delta d\epsilon dV - \int (dF)^T \delta du fS = 0 \quad (7)$$

Here,  $d\sigma$  and  $d\epsilon$  are the vectors of the stress and strain increments, respectively;  $dF$  is the surface traction vector, and  $du$  is the displacement vector. Also, the constitutive equation was deployed during the mechanical simulation [30]:

$$\sigma = D\epsilon^e \quad (8)$$

where  $D$  is the stiffness matrix of the material. The strain vector in welding can be decomposed to several elements including elastic strain tensor ( $\epsilon^e$ ), plastic strain tensor ( $\epsilon^p$ ), thermal strain tensor ( $\epsilon^{th}$ ), visco-plastic strain tensor ( $\epsilon^{vp}$ ), creep strain tensor ( $\epsilon^c$ ), metallurgical strain tensor ( $\epsilon^{tr}$ ), and transformation plasticity strain tensor ( $\epsilon^{tp}$ ). In the mechanical simulation of welding, in addition to the elastic and thermal strain tensors, at least one plastic strain tensor must be considered to calculate the residual stress fields [31]. Because of the negligible effect of creep and visco-plastic strains during welding, they were removed from the total strain equation [32]:

$$\epsilon = \epsilon^e + \epsilon^p + \epsilon^{th} + \epsilon^{tr} + \epsilon^{tp} \quad (9)$$

Thermal and metallurgical strains are briefly known as thermal strain and were calculated by [33]:

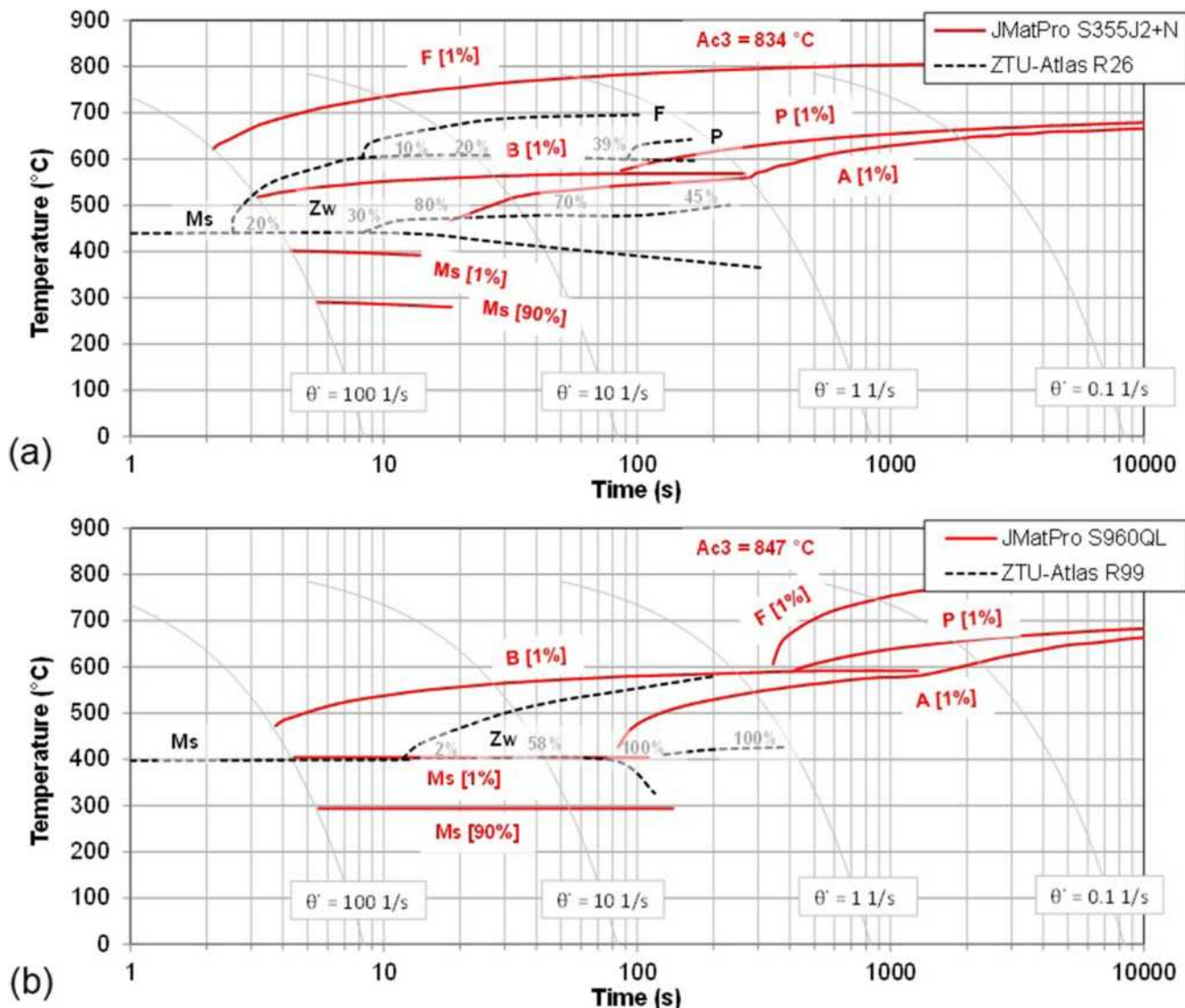


**Fig. 7** CCT diagram of a S355J2+N and b S960QL sample calculated by JMatPro and reference values from ZTU-Atlas [28]

$$\varepsilon^{th} = \sum X_i \varepsilon_i^{th}(T) \quad (10)$$

where  $X_i$  is the fraction of phase  $i$ , and  $\varepsilon_i^{th}(T)$  is the thermal strain of phase  $i$  at temperature  $T$ . The transformation plasticity strain was calculated by [33]:

$$\dot{\varepsilon}^{tp} = -\frac{3}{2} k \times h \left( \frac{\bar{\sigma}}{\sigma_y} \right) \times S \times \ln(x) \times \dot{x} \quad (11)$$

where  $k$  is the coefficient of the transformation plasticity,  $h$  is a non-linear function for the applied stress,  $x$  is the fraction of the hardener phase,  $S$  is the strain deviator,  $\bar{\sigma}$  is the equivalent stress, and  $\sigma_y$  is the yield stress of the material.

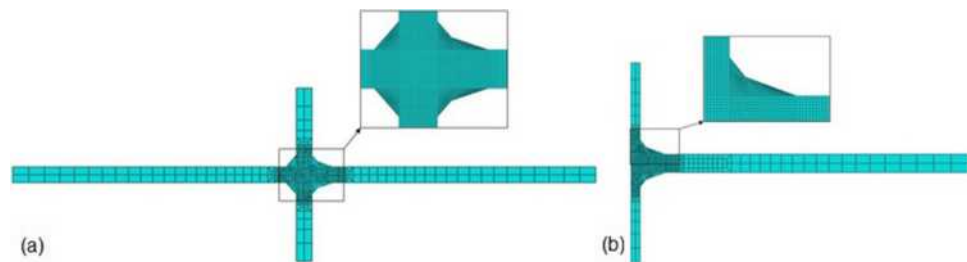
Since the welds on both sides of the stiffener in S960QL samples were deposited simultaneously, half of the sample was considered in the modeling. The implemented meshing

system for both thermo-metallurgical and mechanical models is presented in Fig. 8. Non-uniform meshing system was employed to reduce the calculation time. To make sure of the calculation accuracy, a mesh sensitivity analysis was carried out. Also, to consider machining and depositing of the filler material, the elements activation and deactivation method were implemented.

## 4 Results and discussion

Figure 9 shows the cross-section of the initial weld, one-side repair welded, and double-side repair welded S355J2+N samples, also the temperature history of a point on the surface in the HAZ 2-mm away from the weld toe during the initial welding and the complete thermal cycle of repair

**Fig. 8** The meshing system used in thermo-metallurgical-mechanical model of a S355J2+N and b S960QL sample



welding of S355J2+N sample. Owing to the conical heat distribution in the weld pool depth, the predicted weld pool shape and dimensions are in good agreement with the measured values. As can be seen, the actual cooling rate of the weldment is lower than the estimated value. One reason is that during 2D modeling the heating of the sample in farther cross-sections due to welding is not being considered. The convection through the cooler material causes higher heat sinks which result in faster cooling of the specimen. The model was validated using the thermocouple measurements and weld pool dimensions of the base weld and then used for the simulation of the repair welds.

Figure 10 shows the measured and estimated cross-sections and also the temperature-time curve for initial welding and repair welding of the S960QL sample. In this sample, however, the modeled and measured cooling rates are almost the same. During the welding of S960QL alloy, the sample was preheated to 100°C locally at the weld location by a torch. While during the modeling of the process, the initial temperature of the whole sample was considered to be 100°C. It means that, in practice, there was a temperature gradient in the transverse direction of the sample, which

causes higher heat sinks in the weldments compared to the model. Considering this fact and the effect of neglecting the heating of the farther sections in 2D modeling, the estimated and measured values are closer to one another compared to the S355J2+N sample. It should be noted that, in the repair welding thermal history of both alloys, the side that temperature was measured is the second repair weld, and therefore, the last temperature peaks show the melting at the vicinity of the measurement area.

Fatigue crack usually initiates at the weld toe of a T-joint, therefore, this study focuses on the residual stress evolution at the weld toe of the weldments. To validate the mechanical models, estimated values were compared to the measured ones for the initial welding. Since only half of the tilt angles were used for the transverse residual stress measurement, only measured longitudinal residual stresses were used for the model validation. Figure 11 shows the distribution of the longitudinal residual stresses from 1.5 mm away from the weld toe to the base material of the initial welds. The predicted and measured residual stress profiles are almost the same, but there is a slight difference between their magnitudes. During the production of the specimens, samples

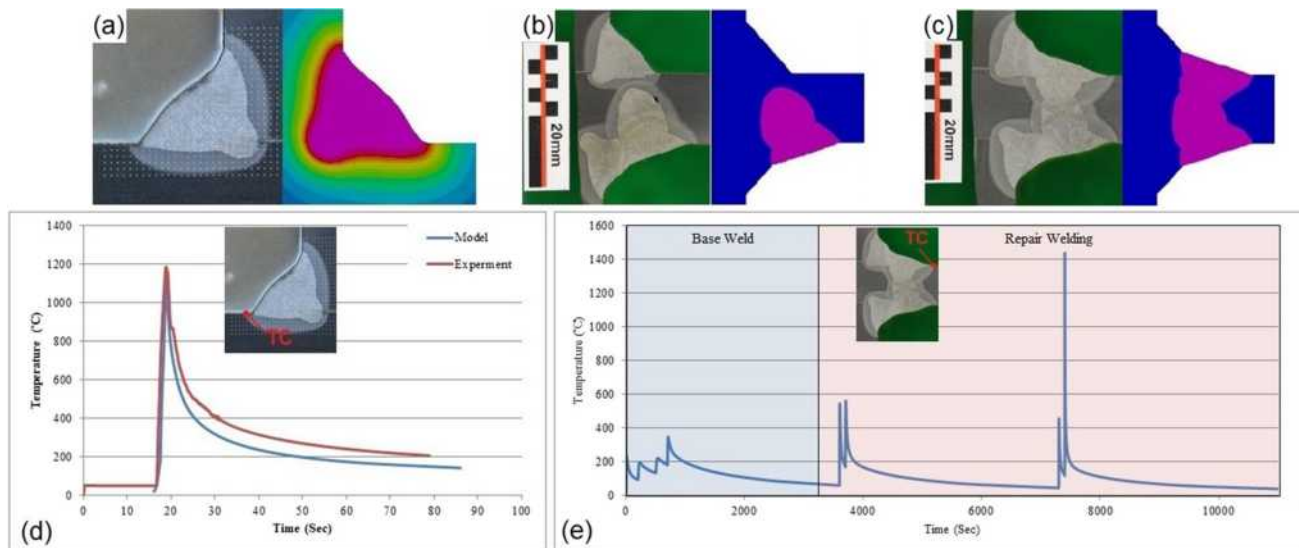


**Fig. 9** a Weld pool cross-section of initial weld, b weld pool cross-section of one-side repair welded, c weld pool cross-section of double-side repair welded, d temperature history of the initial weld, and e temperature history of double-side repair welded of S355J2+N sample

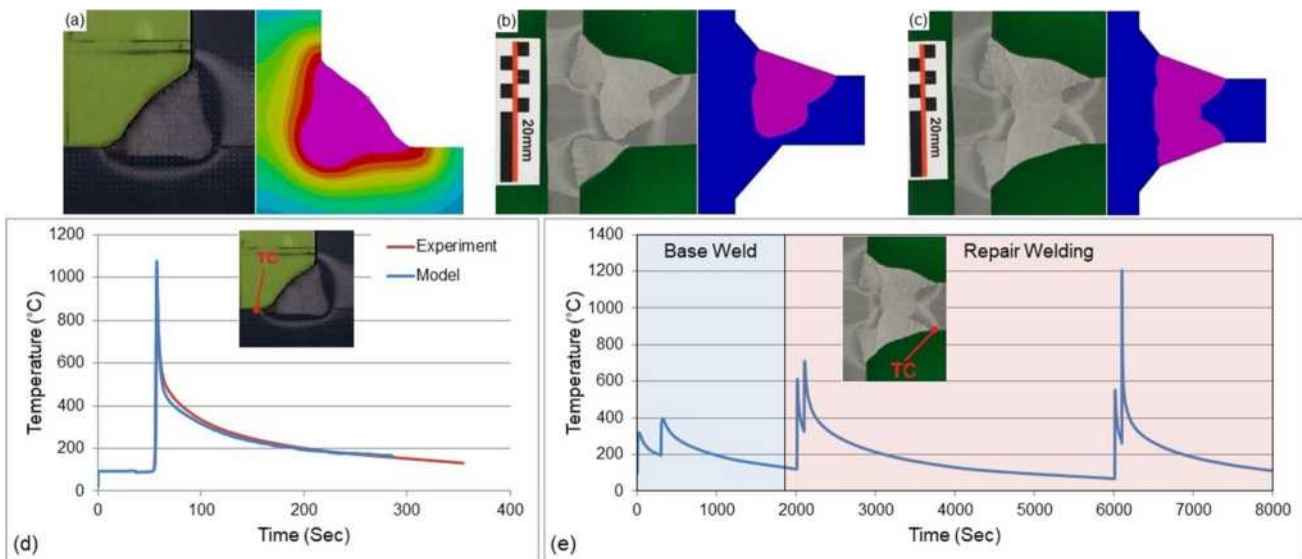


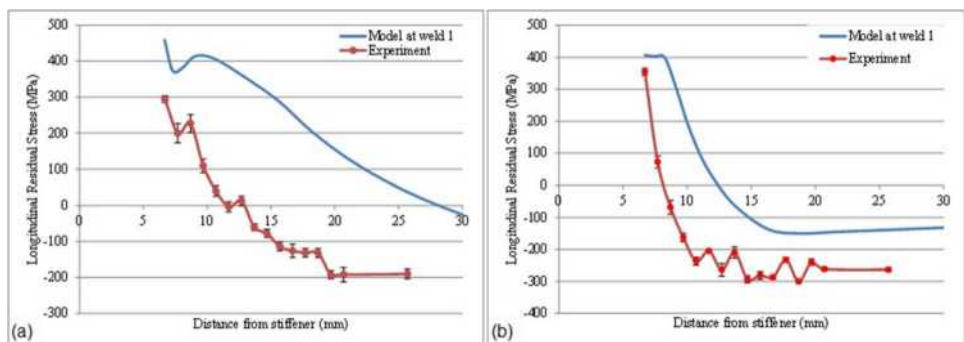
**Fig. 10** **a** Weld pool cross-section of initial weld, **b** weld pool cross-section of one-side repair welded, **c** weld pool cross-section of double-side repair welded, **d** temperature history of the initial weld, and **e** temperature history of double-side repair welded S960QL sample

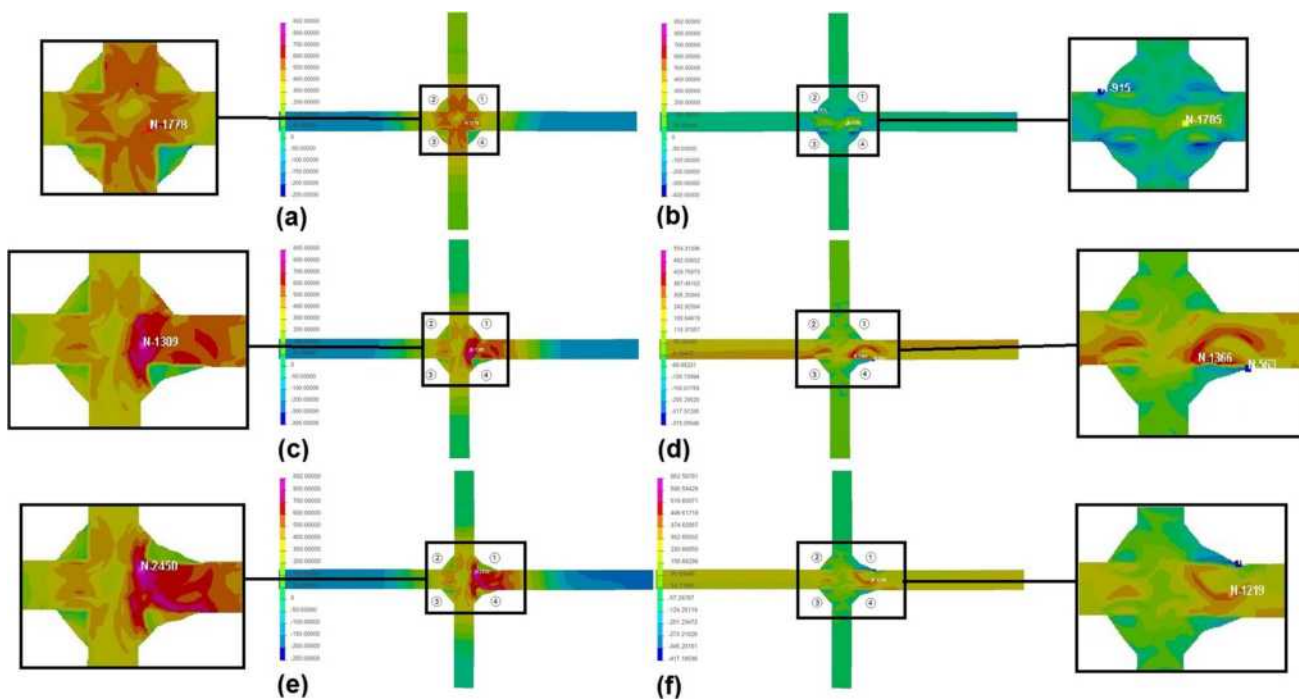
were blasted after welding. Blasting of the samples introduces compressive residual stresses on the surface of the specimens. As mentioned in the experimental procedure, the XRD measurement focuses on a few micrometers underneath the surface. Therefore, the actual residual stress of the as-welded samples should be higher than the measured values. As can be seen in this figure, despite the higher strength of the S960QL alloy, its weldments show a smaller area of tensile stresses. The thermal conductivities of the materials are very close, and the welding parameters of both samples are almost the same. This difference is the effect of the preheating of the S960QL sample. Due to preheating of S960QL weldments, the temperature gradient is smaller and lower levels of tensile stresses are observed.

Figure 12 illustrates the residual stress evolution through the whole sample during initial welding and repair welding of the S355J2 + N sample in longitudinal and transverse directions. The numbers show the sequence of welding. In the double-side repair welded sample, repair welding was first carried out in weld toe of weld 4 and

then weld 1. Residual stress in both directions significantly increased by repairing the components. At the weld toe of the initial weld, one-side repair weld, and double-side repair weld of S355J2 + N, the longitudinal residual stresses are 460 MPa, 586 MPa, and 719 MPa, respectively. The maximum transverse residual stresses on the surface of the initial weld, one-side repair welded, and double-side repair welded samples are 74 MPa, 389 MPa, and 324 MPa, respectively. Initial welding creates compressive transverse residual stress at all weld toes, while repair welding transforms it to the tensile residual stress. Although the longitudinal residual stress increases by proceeding with the repair welding, the transverse residual stress reduces a little after repair welding on two sides of the plate. To look at the evolution of residual stress of the alloy at the weld toe of each weld more precisely, Fig. 13 shows the residual stress distribution from the weld toe to the base metal of S355J2 + N. It is worth mentioning that the locations of the weld toe of weld 1 and 4 changes after repair welding and corresponding residual stresses were

**Fig. 11** Numerical and experimental longitudinal residual stresses from 1.5 mm from the weld toe to the base material of **a** S355J2 + N and **b** S960QL sample





**Fig. 12** **a** Residual stress distribution in a longitudinal direction of initial weld, **b** transverse direction of initial weld, **c** longitudinal direction of one-side repair welding, **d** transverse direction of one-

side repair welding, **e** longitudinal direction of double-side repair welding, and **f** transverse direction of double-side repair welding of S355J2+N sample

measured at the new weld toes. As can be seen, after initial welding, the residual stresses of welds are not the same. Welding on the back of the plate (weld 3 and 4) increases the residual stress on the top side of the plate (weld 1 and 2), which has already been welded. *T-t* diagrams of the weldments (Fig. 9), show that welding on the back of the

plate increases the temperature of the weld toes on the top of the plate to temperatures lower than 600 °C. These temperatures are not high enough to accelerate the stress relief of the specimen. In contrast, it causes higher temperature gradients in the component, which contribute to the formation of higher residual stress. Due to the same

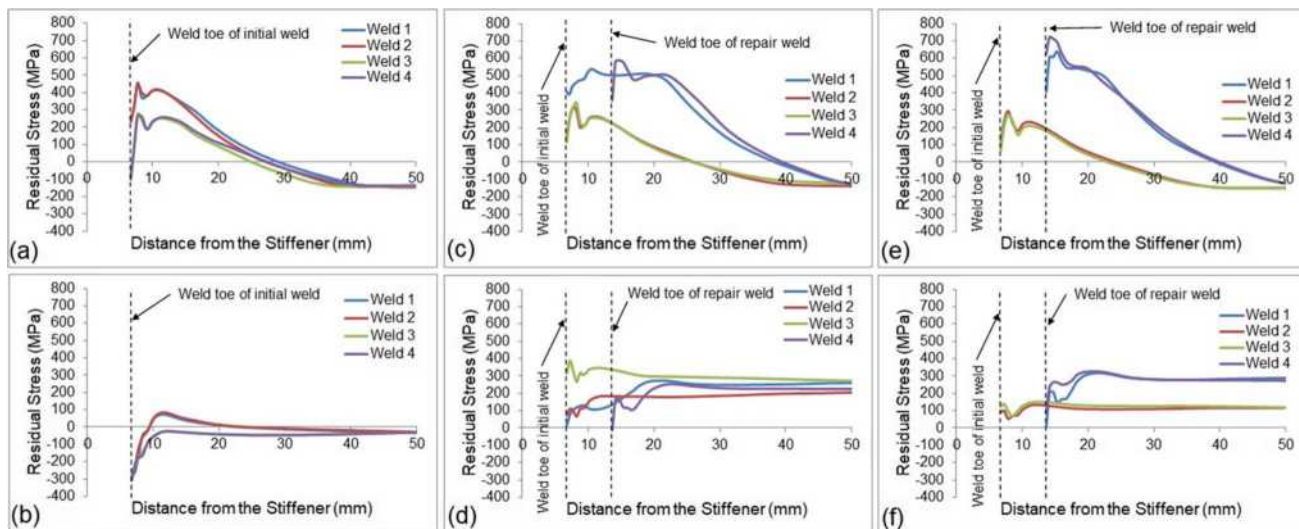


**Fig. 13** **a** The surface residual stress distribution from weld toe through base material of S355J2+N sample in a longitudinal direction of initial weld, **b** transverse direction of initial weld, **c** longitu-

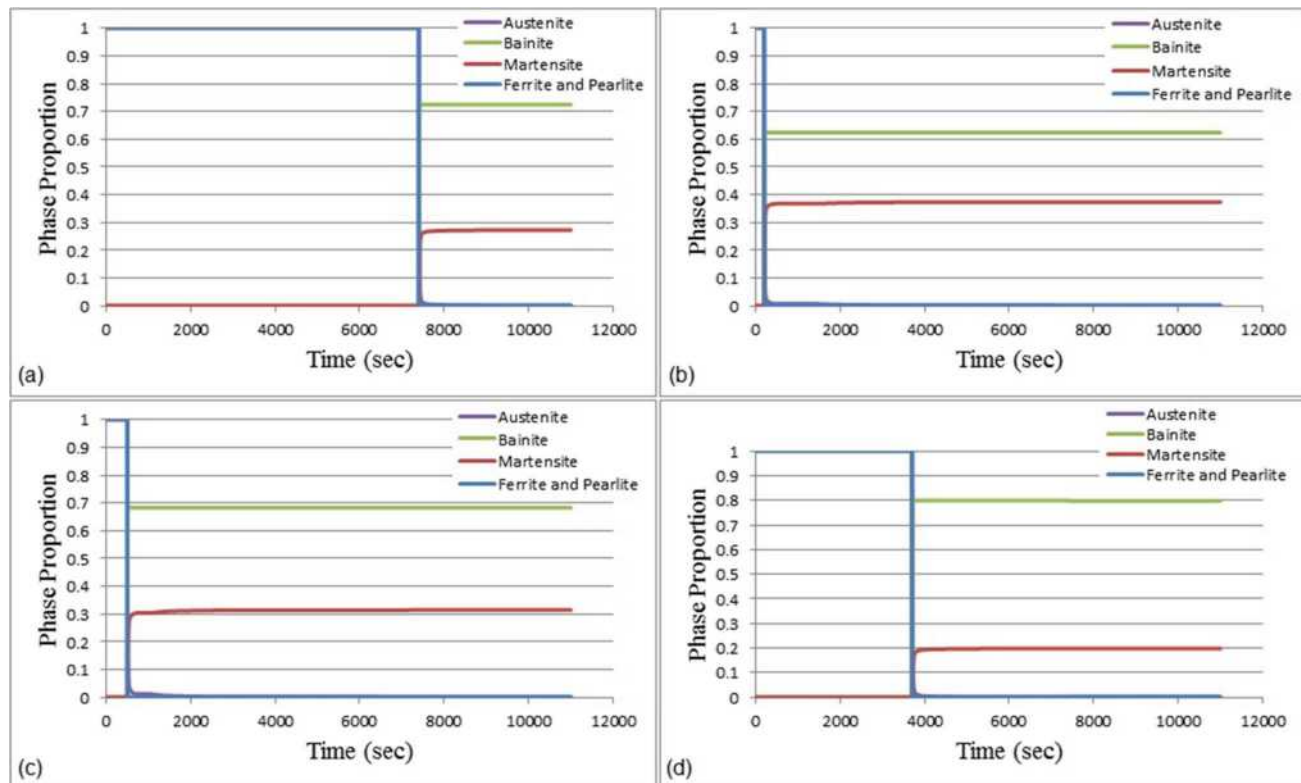
dinal direction of one-side repair welded, **d** transverse direction of one-side repair welded, **e** longitudinal direction of double-side repair welded, and **f** transverse direction of double-side repair welded

reason, repair welding on one side of the plate (weld 4) increases the residual stress of that side and the other side of the plate (weld 1). Continuation of the repair process on the second side of the plate (weld 1) increases the residual stress on both repaired weld toes to higher magnitudes. Looking at the other side of the stiffener (welds 2 and 3), which were not subjected to the repair welding, reveals that first repair welding (weld 4) decreases the longitudinal residual stress of weld 2, while increasing the transverse residual stress of weld 3. The second repair welding (weld 1) likewise decreases the residual stress of weld 3, but more slightly, and does not increase the residual stress of weld 2 significantly. The temperature changes on the weld toes of welds 2 and 3 are not high enough to either activate the solid-state phase transformations or release the residual stresses. The only reason for these changes is the balance of the residual stresses at these weld toes due to the changes in the residual stress of the surrounding area.

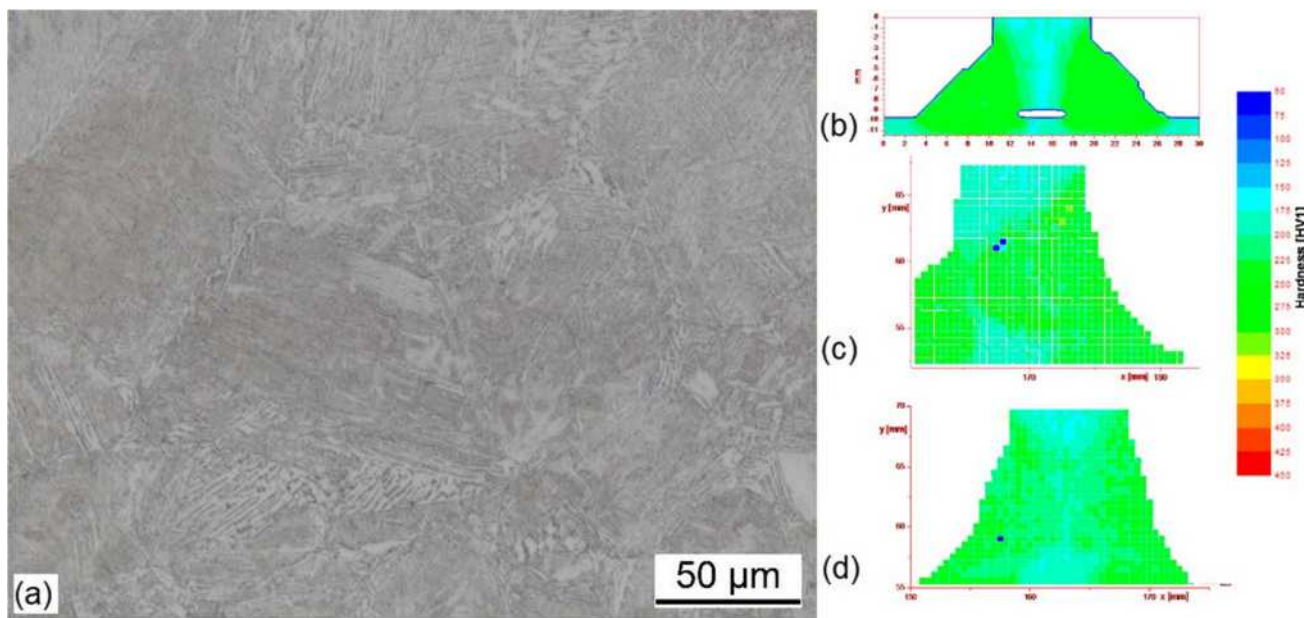
It is evident in Fig. 13 that the maximum value of the longitudinal residual stress almost in all welds happens in the close vicinity of the weld toe. But for the transverse direction, the maximum value is normally away from the weld toe. Nonetheless, the residual stress values at all weld toes are high, and taking the stress concentration effect at the weld toe into account, they could contribute to an early failure of the component.

Figure 14 shows the proportion of the phases at the weld toes of all the welds after double-side repair welding of the S355J2+N sample. It should be noted that the weld toes of welds 1 and 4 belong to the repair welds; thus, the phase transformation for the initial welds at these corners is not evident. No phase transformation happens in a given weld toe due to welding of the other corners of the T-joint. It was also expected considering the fact that the maximum temperature of a given weld toe is lower than the critical temperature for the solid-state transformations during welding of the other corners. The model suggests that the microstructure of all weld toes consists of Bainite and Martensite, although the proportion of the phases is different at different weld toes. Figure 15 shows the microstructure of the specimen in this region, which consists of bainite and martensite. According to the figure, the hardness of the weld toe of the other side of the plate did not change significantly during repair welding of the opposite side, showing that there was no considerable change in the phase morphologies. All these results prove that the changes in the residual stress of other weld toes during repair welding of one weld toe are due to expansions and contractions at these areas.

Figures 16 and 17 show the residual stress evolution in the longitudinal and transverse directions during initial welding, one-side, and double-side repair welding of the S960QL sample. As can be seen, the magnitude of the



**Fig. 14** Phase proportions at weld toe of **a** weld 1, **b** weld 2, **c** weld 3, and **d** weld 4 of S355J2+N sample



**Fig. 15** **a** Microstructure of the weld toe, **b** hardness of the sample after initial welding, **c** hardness of the sample after one-side repair welding, and **d** hardness of the sample after double-side repair welding of S355J2+N sample

residual stress in both directions increases after repair welding compared to the initial weld, regardless of repairing on one or two sides. But after double-side repair welding, longitudinal and transverse residual stresses are reduced compared to one-side repair welding. As can be seen in the results of the metallurgical simulation (Fig. 18), there is no phase transformation on the other weld toes during repair welding. Checking the temperature contours of the specimens approves that the temperature of the other welds does not reach the austenitization temperature of the alloy. Therefore, during repair welding, the phase transformations are limited to the repaired area and its adjacent material. Looking at the microstructure and hardness of the specimen at the weld toe (Fig. 19) reveals that the microstructure of the weld toe consists of bainite phase only, which is in agreement with the model. But a closer look at the hardness values after repair welding shows that, although there was no phase transformation in the area, the temperature was high enough to change the morphology of the phases. The change in the morphology of the bainite phase reduced its hardness that contributes to decreasing the yield strength of the material and deformation in lower stresses. Furthermore, by moving from the weld toe to the base material, the hardness first decreases then increases. The same happens to the residual stresses of the regions. The region with lower strength yields sooner and shows lower residual stress magnitude. With the same logic, the region with higher strength yields at higher stresses and shows higher levels of residual stress. As can be seen in Fig. 17, the maximum longitudinal residual stress happens away from the weld toe, while

the maximum value in the transverse direction is at or in the direct vicinity of the weld toe. The magnitude of the residual stress in both directions at the weld toe is almost the same. Considering the stress concentration at the weld toe, these values could be even more critical than the higher values in HAZ far away from the weld toe. In conclusion, the morphological changes in the phases and contractions and expansions together are responsible for the residual stress evolutions in the repair welded S960QL sample. It is worth mentioning that the highest residual stress values are inside the components, but since the fatigue crack initiates from the surface of the specimen, they are not studied here.

## 5 Conclusion

Residual stress evolutions during repair welding of a fatigue crack in S355J2N and S960QL structural steel T-joints have been studied through experimentation and numerical models. The results show that repair welding increases the magnitude of residual stress in the components in transverse and longitudinal directions compared to the initial weld. The residual stress at the weld toe of all initial welds increased regardless of the location of welding. The alloys show different responses to the repair welding on the opposite side of the plate. Double-side repair welding of the S355J2+N component reduced the level of transverse residual stress at weld toes while the longitudinal residual stress increased at all weld toes. In the S960QL sample, on the other hand, the magnitude of

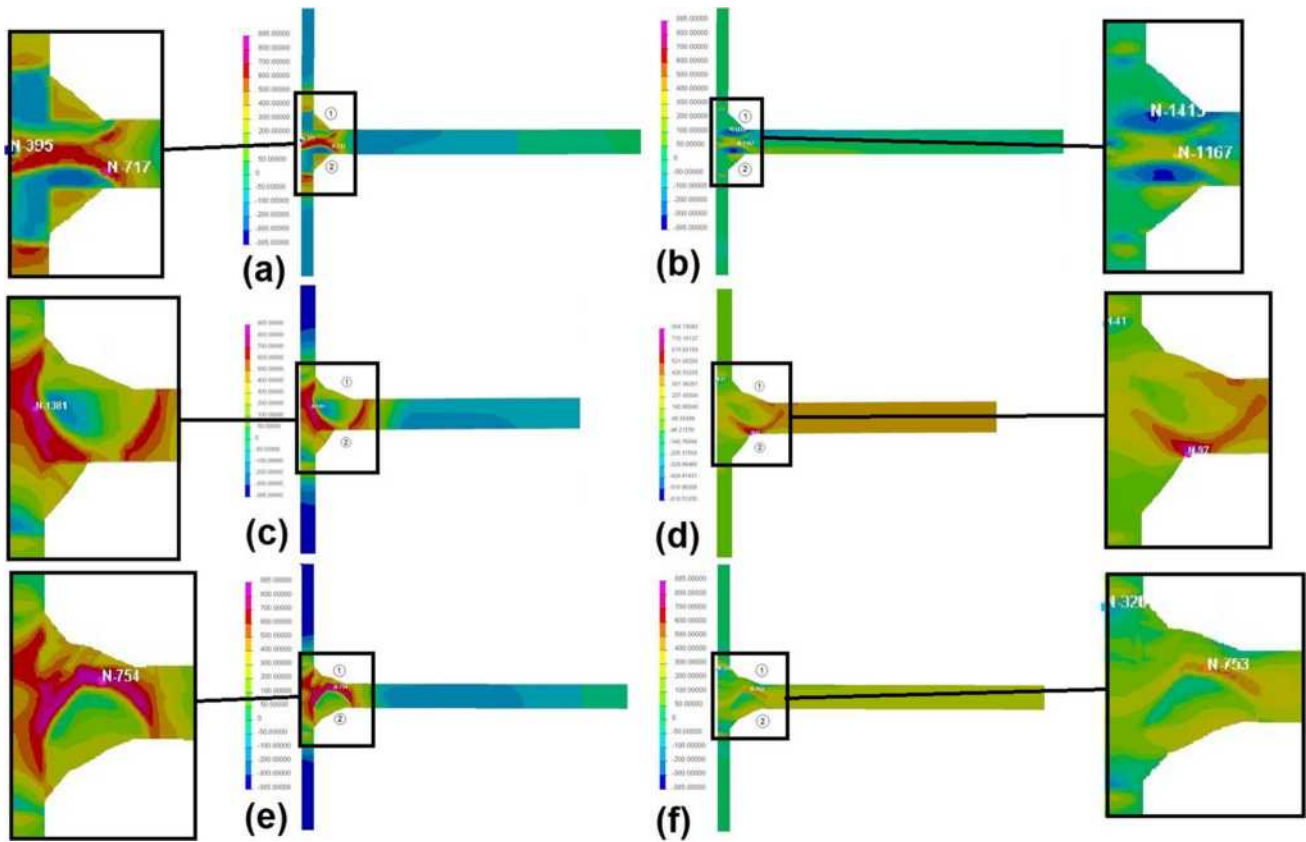


**Fig. 16** Residual stress distribution in **a** longitudinal direction of initial weld, **b** transverse direction of initial weld, **c** longitudinal direction of one-side repair welding, **d** transverse direction of one-side

repair weld, **e** longitudinal direction of two-side repair weld, and **f** transverse direction of two-side repair weld of S960QL sample

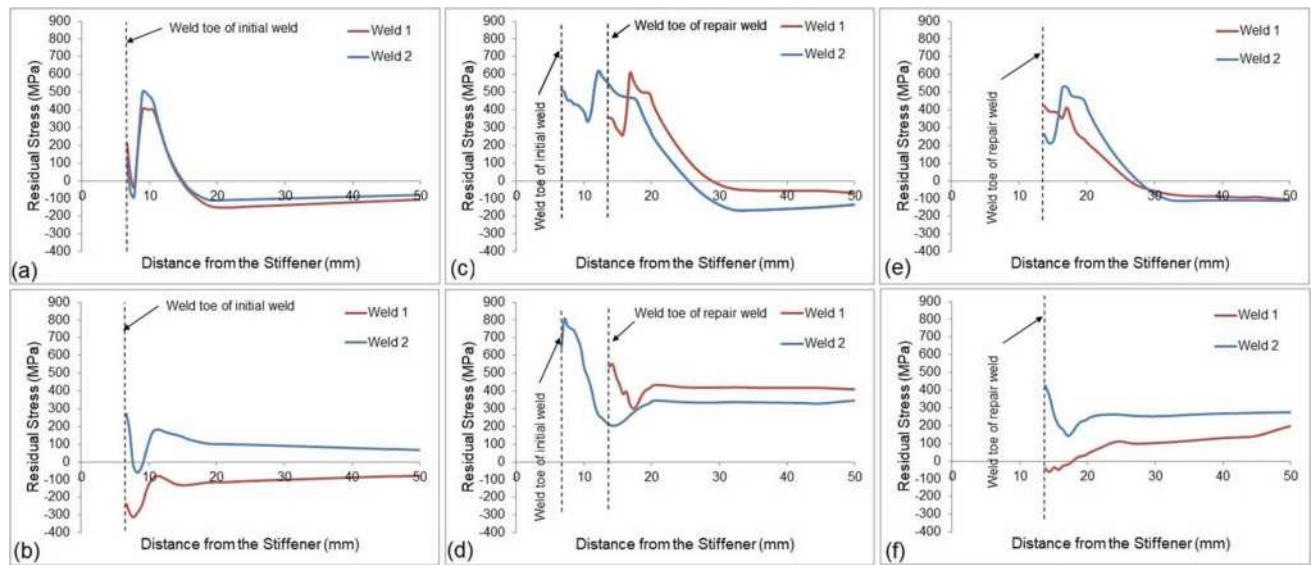


**Fig. 17** The surface residual stress distribution from weld toe through base material of S960QL sample in **a** longitudinal direction of initial weld, **b** transverse direction of initial weld, **c** longitudinal direction

of one-side repair welding, **d** transverse direction of one-side repair welding, **e** longitudinal direction of two-side repair weld, and **f** transverse direction of two-side repair weld

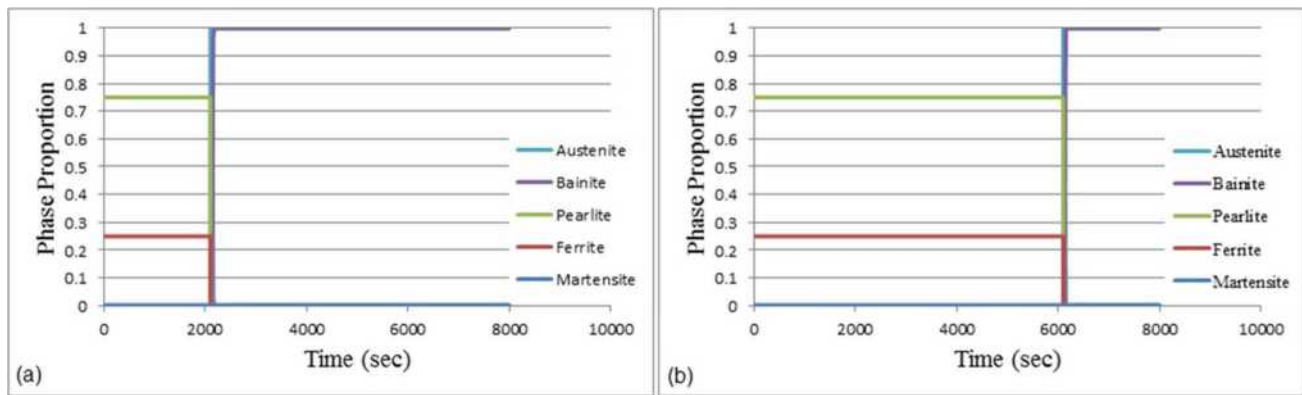


**Fig. 18** Phase proportions at weld toe of **a** weld 1 and **b** weld 2 of S960QL sample

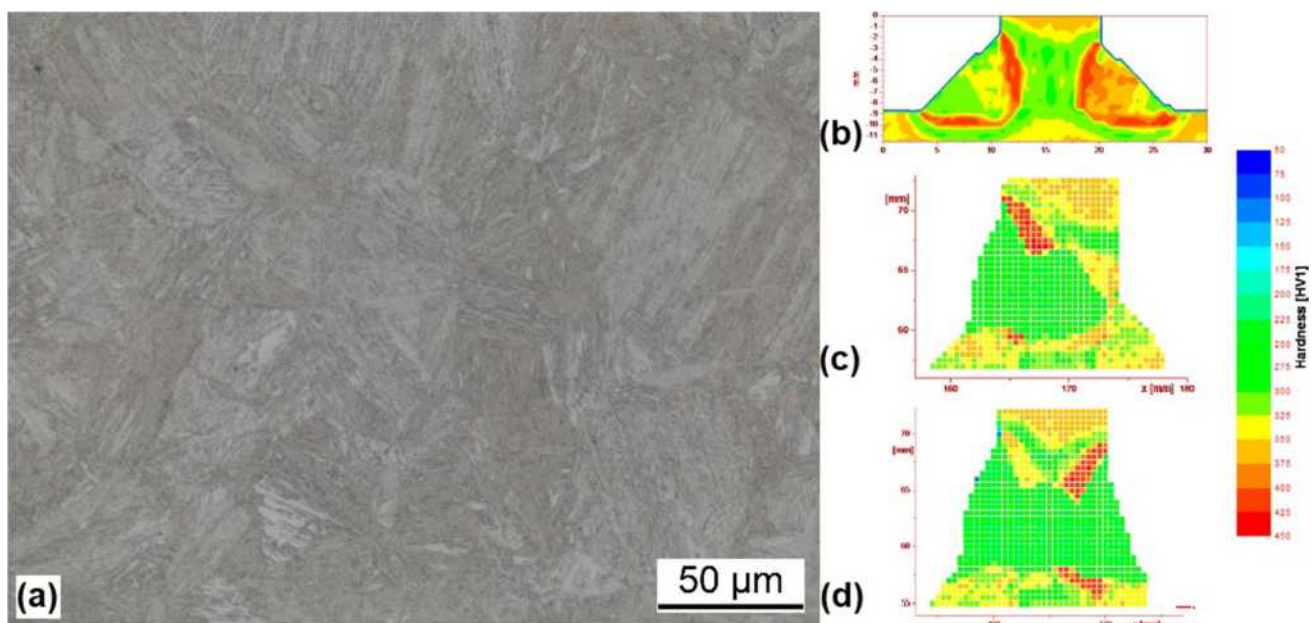


**Fig. 19** **a** Microstructure close to the weld toe, **b** hardness of the sample after initial welding, **c** hardness of the sample after one-side repair welding, and **d** hardness of the sample after double-side repair welding of S355J2+N sample

residual stresses in both directions decreased after double-side repair welding compared to the residual stress of the one-side repair welding. Furthermore, repair welding does not necessarily cause maximum residual stresses in the repaired area. The results show that the magnitude of the residual stresses in both directions of the S355J2+N sample is higher on the weld toe of the weld on the opposite side of the stiffener. Repair welding causes phase transformations only at and in the vicinity of the repaired area but changes the distribution and magnitude of the residual stresses through the whole component. Although, there are morphological changes in the Bainite phase in the HAZ of the S960QL sample after double-side repair welding compared to the one-side repair welding. These

morphological changes are not evident in the S355J2+N sample. The reason for the evolution of the residual stresses in the locations far from the repaired area in the S355J2+N sample, therefore, is the expansion and contraction leading to an inhomogeneous plastic deformation of the material through the weldment. While in the S960QL sample, the morphological changes also contribute to the residual stress evolution in addition to the expansion and contraction.

## Declarations

**Conflict of interest** The authors declare no competing interest.

## References

1. Goldak J, Asadi M (2014) Challenges in validation of computational weld mechanics code to compute residual stress and distortion in welds. *J Press Vessel Technol Trans ASME* 136:1–8. <https://doi.org/10.1115/1.4024458>
2. Dong P (2018) On repair weld residual stresses and significance to structural integrity. *Weld World* 62:351–362. <https://doi.org/10.1007/s40194-018-0554-1>
3. Song S, Dong P (2017) Residual stresses at weld repairs and effects of repair geometry. *Sci Technol Weld Join* 22:265–277. <https://doi.org/10.1080/13621718.2016.1224544>
4. Unsworth D, Driver RG, Li L (2020) Measurement and prediction of residual stresses in welded girders. *J Constr Steel Res* 169:106007. <https://doi.org/10.1016/j.jcsr.2020.106007>
5. Farajian M, Nitschke-Pagel T, Siegela D (2014) Welding residual stress behavior in tubular steel joints under multiaxial loading. *HTM J Heat Treat Mater* 69:6–13. <https://doi.org/10.3139/105.110208>
6. Charkhi M, Akbari D (2019) Experimental and numerical investigation of the effects of the pre-heating in the modification of residual stresses in the repair welding process. *Int J Press Vessel Pip* 171:79–91. <https://doi.org/10.1016/j.ijpvp.2019.02.006>
7. Elcoate CD, Dennis RJ, Bouchard PJ, Smith MC (2005) Three dimensional multi-pass repair weld simulations. *Int J Press Vessel Pip* 82:244–257. <https://doi.org/10.1016/j.ijpvp.2004.08.003>
8. Salerno G, Bennett CJ, Sun W, Becker AA (2017) Residual stress analysis and finite element modelling of repair-welded titanium sheets. *Weld World* 61:1211–1223. <https://doi.org/10.1007/s40194-017-0506-1>
9. Jiang W, Luo Y, Wang BY et al (2015) Neutron diffraction measurement and numerical simulation to study the effect of repair depth on residual stress in 316L stainless steel repair weld. *J Press Vessel Technol Trans ASME* 137:1–12. <https://doi.org/10.1115/1.4028515>
10. Withers PJ (2007) Residual stress and its role in failure. *Reports Prog Phys* 70:2211–2264. <https://doi.org/10.1088/0034-4885/70/12/R04>
11. SEW 088 Guidline (2017) Supplementary Sheet 1 to SEW 088: Weldable Fine Grain Steels: Guidelines for Processing, Particular for Fusion Welding, Cold Cracking During Welding, Determining Appropriate Minimum Preheating, DIN German Institute for Standardization. Berlin, Germany
12. Schubnell J, Ladendorf P, Sarmast A et al (2021) Fatigue performance of high- and low-strength repaired welded steel joints. *Metals (Basel)* 11:293
13. Macherauch E, Müller P (1961) Das  $\sin^2\psi$  Verfahren von Röntgenographische Eigenspannungen. *Z angew Phys* 13:305–312
14. Goldak JA, Akhlaghi M (2005) Computational welding mechanics. Springer Science+Business Media, Inc., 233 Spring Street, New York
15. De A, DebRoy T (2004) A smart model to estimate effective thermal conductivity and viscosity in the weld pool. *J Appl Phys* 95:5230–5240. <https://doi.org/10.1063/1.1695593>
16. Goldak J, Chakravarti A, Bibby M (1984) A new finite element model for welding heat sources. *Metall Trans B* 15:299–305
17. Grong ØY (1997) Metallurgical modelling of welding, 2nd edn. The Institute of Materials, London
18. Gourd LM (1995) Principles of welding technology, 3rd edn. Edward Arnold, London
19. Aarbogh HM, Hamide M, Fjær HG et al (2010) Experimental validation of finite element codes for welding deformations. *J Mater Process Technol* 210:1681–1689. <https://doi.org/10.1016/j.jmatprotoc.2010.05.014>
20. Bajpe T, Chelladurai H, Ansari MZ (2016) Mitigation of residual stresses and distortions in thin aluminium alloy GMAW plates using different heat sink models. *J Manuf Process* 22:199–210. <https://doi.org/10.1016/j.jmapro.2016.03.011>
21. Goyal VK, Ghosh PK, Saini JS (2009) Analytical studies on thermal behaviour and geometry of weld pool in pulsed current gas metal arc welding. *J Mater Process Technol* 209:1318–1336. <https://doi.org/10.1016/j.jmatprotoc.2008.03.035>
22. Schenk T, Richardson IM, Kraska M, Ohnimus S (2009) Modeling buckling distortion of DP600 overlap joints due to gas metal arc welding and the influence of the mesh density. *Comput Mater Sci* 46:977–986. <https://doi.org/10.1016/j.commatsci.2009.05.003>
23. Lindgren L-E (2007) Computational welding mechanics: thermo-mechanical and microstructural simulations. Woodhead Publishing, Cambridge, London
24. Leblond JB, Devaux J (1984) A new kinetic model for anisothermal metallurgical transformations in steels including effect of austenite grain size. *Acta Metall* 32:137–146. [https://doi.org/10.1016/0001-6160\(84\)90211-6](https://doi.org/10.1016/0001-6160(84)90211-6)
25. Koistinen DP (1959) A general equation prescribing the extent of the austenite-martensite transformation in pure iron-carbon alloys and plain carbon steels. *Acta Metall* 7:59–60
26. Saunders N, Miodownik P (1998) CALPHAD (Calculation of Phase Diagrams): A Comprehensive Guide, 1st ed. Elsevier Science Ltd, Langford Lane, Kidlington, Oxford
27. Trzaska J (2016) Calculation of critical temperatures by empirical formulae. *Arch Metall Mater* 61:981–986. <https://doi.org/10.1515/am-2016-0167>
28. Seyffarth P, Meyer B, Scharff A (2018) Großer Atlas Schweiß-ZTU-Schaubilder, 2nd ed. DVS Media GmbH, Dusseldorf
29. Belytschko T, Liu WK, Moran B, Elkhodary KI (2014) Nonlinear finite elements for continua and structures, 2nd ed. John Wiley & Sons, Ltd, Hoboken
30. Sarmast A, Serajzadeh S (2019) The influence of welding polarity on mechanical properties, microstructure and residual stresses of gas tungsten arc welded AA5052. *Int J Adv Manuf Technol* 105:3397–3409. <https://doi.org/10.1007/s00170-019-04580-7>
31. Lindgren LE (2001) Finite element modeling and simulation of welding. part 2: Improved material modeling. *J Therm Stress* 24:195–231. <https://doi.org/10.1080/014957301300006380>
32. Hamelin CJ, Muránsky O, Smith MC et al (2014) Validation of a numerical model used to predict phase distribution and residual stress in ferritic steel weldments. *Acta Mater* 75:1–19. <https://doi.org/10.1016/j.actamat.2014.04.045>
33. Hemmesi K, Farajian M, Boin M (2017) Numerical studies of welding residual stresses in tubular joints and experimental validations by means of x-ray and neutron diffraction analysis. *Mater Des* 126:339–350. <https://doi.org/10.1016/j.matdes.2017.03.088>

**Publisher's note** Springer Nature remains neutral with regard to jurisdictional claims in published maps and institutional affiliations.



## Fracture and fatigue crack growth analyses on a weld-repaired railway rail



Hyun-Kyu Jun <sup>a</sup>, Jung-Won Seo <sup>a</sup>, Il-Sik Jeon <sup>b</sup>, Sang-Hwan Lee <sup>c</sup>, Yoon-Suk Chang <sup>c,\*</sup>

<sup>a</sup> Korea Railroad Research Institute, Uiwang, Gyeonggi-do 437-755, Republic of Korea

<sup>b</sup> Korea Railroad Corporation, Cheongju, Chungcheongbuk-do 363-951, Republic of Korea

<sup>c</sup> Dept. of Nuclear Engineering, Kyung Hee Univ., Yongin, Kyonggi-do 446-701, Republic of Korea

### ARTICLE INFO

**Article history:**

Received 9 July 2015

Received in revised form 12 October 2015

Accepted 4 November 2015

Available online 5 November 2015

**Keywords:**

Failure analysis

Fatigue crack growth

Residual stress

Rolling contact fatigue

Welding technology

### ABSTRACT

Although repair by arc welding is a well-known method for damaged rail surface recovery due to its ease of application, the method is vulnerable to the creation of cracks. In this study, a series of failure analyses and crack growth analyses were carried out on a fractured weld-repaired rail to determine the cause of the rail failure and the effect of residual stress on the crack growth rate. For this purpose, the residual stress profiles of rails under various conditions were obtained by both sectioning the physical rail and simulating the weld-repair process of the rail using the finite element method. Subsequently, the fatigue crack growth in the weld-repaired rail was simulated by assuming that a semi-elliptical crack was initiated at the boundary between the weld pool and heat-affected zone. From these analyses, it was found that weld defects, such as porosity, lamella line cracks, and quick transitions in material hardness and microstructure, especially at the boundaries, could be the causes of the crack initiation. The crack growth rate was strongly influenced by the magnitude of the residual stress, while it was significantly increased in the presence of high tensile residual stress at the rail head due to the weld repair. Therefore, reducing the tensile stress magnitude and increasing the compressive stress magnitude in the rail head is crucial to solving this problem in railway rail weld repair.

© 2015 Elsevier Ltd. All rights reserved.

### 1. Introduction

A rail head surface is continuously exposed to repetitive wheel rail contact fatigue [1], wheel burns due to slips [2], and flying ballast imprinting during the railway operating service, all of which cause damage to the head surface of the rail. The damaged rail head surface should be repaired immediately to secure good riding comfort and to prevent the failure of the rail by implementing a proper repair method. When the surface damage is light, it can be corrected by the simple grinding of the entire damaged area. Grinding of the damaged area [3] is a well-known rail surface maintenance method in the railway industry that is used because of its ease of immediate application over a large area. However, this method requires a long grinding area to minimize the impact from vertical winding, even though it offers the elimination of point defects. In the case of a high-speed rail, sometimes the length of the grinding area needs to be 2000 times the damage depth in both directions of the rail. When the surface damage is moderate and it is too difficult to repair by using only grinding, the damaged region needs to be removed and built up with a new material. An overlay weld-repair method has been frequently used as a build-up method in conventional railway networks in many countries [4–7]. When the damage is severe, it is necessary to cut out the entire damaged section and replace it with a new section [8–13]. Each repair method has advantages and disadvantages, so it is difficult to determine a single method that

\* Corresponding author.

E-mail address: [yschang@khu.ac.kr](mailto:yschang@khu.ac.kr) (Y.-S. Chang).

is best in all cases. In this context, the railway operator needs to carefully choose the proper repair method by considering various factors such as the risk of poor quality of repair, cost and time, and required the availability of the rail network.

The method of repairing the surface has many advantages because of its ease of implementation and its freedom from the risks associated with restructuring existing rail constructions. Because the method only requires cutting out a small portion of the rail, even in a worst-case scenario, the rail can still maintain its strength. However, although this method has significant potential, it has not been extensively utilized in high-speed railways for safety reasons because it is vulnerable to the creation of cracks. These cracks are difficult to detect because the weld boundary reflects the echo signal of ultra sound, preventing it from penetrating the boundary. Many studies [14–19] have shown that a welded rail is more vulnerable to defects than a parent rail. It is extremely important to fully understand the method of surface repair by welding for the application to high-speed rails, because inclusions, porosity, lack of fusion, and high residual stresses, are possible causes of crack initiation. However, few studies on this topic have been [5–10] published.

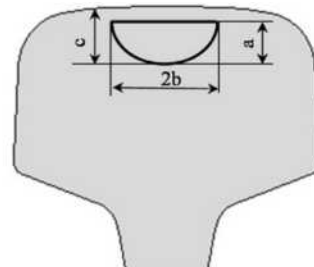
The objectives of this study are to find the causes of failure in a weld-repaired rail and to calculate the growth speed on a crack created at the weld boundary to assist in the development of a cost-effective and enhanced-durability weld-repair method. For this purpose, a series of failure analyses were performed on cracked weld-repaired rails. The residual stresses along the depth of the weld were obtained by both sectioning the physical rails and simulating the weld-repair process of the rail using finite element (FE) analysis. Finally, the crack growths were calculated based on fracture mechanics analyses by assuming that a crack is initiated at the boundary between the weld pool and the heat-affected zone (HAZ).

## 2. Failure analyses of a cracked weld-repaired rail

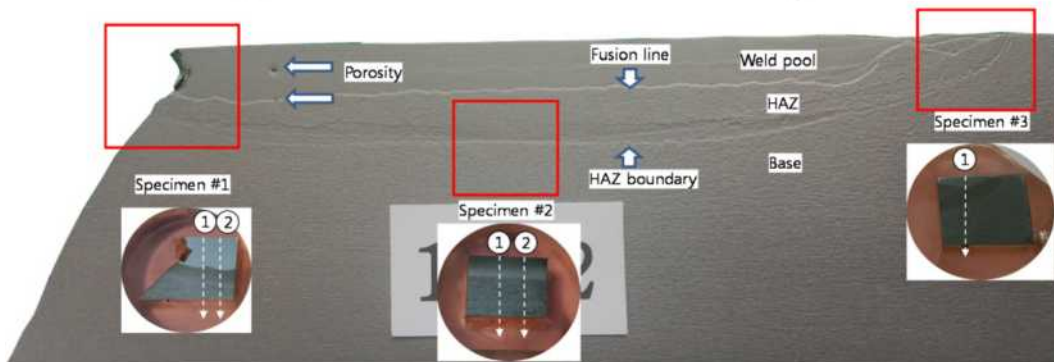
A series of failure analyses on a cracked weld-repaired rail were carried out to determine the cause of weld failure and to further study crack growth. The analyses consist of a macroscopic visual inspection of the failure surface, a chemical content analysis, a material microhardness analysis, and a microstructure analysis on the weld.

### 2.1. Macroscopic visual inspection

Macroscopic visual inspection on the failure surface of the weld-repaired rail was performed to determine the cause of crack initiation. Fig. 1(a) shows the vertical cross-section of the rail. A dark and smooth fractured surface at the rail head, which is thought to be formed by fatigue crack propagation, can be clearly observed, and is clearly distinguished by the rough gray surface formed by the cleavage fracture. The physical crack was idealized as a semi-elliptical shape, which is 57 mm wide ( $2b$ ) and 28 mm deep ( $a$ ). The crack area ( $A = \pi \times a \times 2b / 2$ ) was  $1254 \text{ mm}^2$  corresponding to approximately 41% of the total rail



(a) Cross-section of a crack and its idealized shape



(b) Longitudinal cross-section

**Fig. 1.** Fracture morphology of the fractured weld-repaired rail.

head area ( $3092 \text{ mm}^2$ ) of UIC 60 rail. From the shape and surface roughness of the crack, it is thought to be initiated at the border between the fusion zone, which is defined as the weld pool, and the base. Subsequently, it propagated to the top and bottom directions of the rail. Fig. 1(b) shows the longitudinal cross-section of the rail. The depth of the weld repair is measured to be approximately 7 mm from the rail top surface. The inclination angle of the crack is measured to be approximately  $20^\circ$  against the vertical axis of the rail, which shows that the crack growth is influenced by the shear stress that is induced when a train passes over the crack. A fusion line between the weld pool and the HAZ can be clearly observed, and it is also clearly distinguished by the color difference of the specimens that were cut out of the sectioned rail and etched to microscopically inspect the material. The boundary between the HAZ and the base of the material can also be clearly observed. Small and fine-size porosities were observed in the weld pool and the fusion zone.

## 2.2. Chemical analysis

Chemical analyses were carried out on the weld along its depth, for which specimen #3, shown in Fig. 1(b), was used. The rail material analyzed was UIC60 Gr.260 rail steel, which is often used for high-speed rail networks, and the filler material was MF-1-GF-300, manufactured by TRANSLARAIL. Table 1 presents the chemical compositions of the parent rail and filler materials. The carbon, phosphorus, and sulfur contents of the filler material are very low compared with those of the rail material. In contrast, the content of manganese is high. Fig. 2 shows a total of 8 points for the chemical analysis along the depth of weld. The point denoted by (a) is the point in the middle of the weld pool, 0.6 mm from the surface. Point (b) is at the fusion line between the weld pool and the HAZ, 2.8 mm from the surface. Point (c) is at the HAZ and is 3.8 mm from the surface, while point (d) is also at the HAZ and is 5.0 mm from the surface. Point (e) is at the boundary between the HAZ and the base material and is 6.6 mm from the surface. Point (f) is in the middle of the base material and is 7.6 mm from the surface.

Inductively coupled plasma (ICP) by PerkinElmer and scanning electron microscopy (SEM) with energy dispersive X-ray spectroscopy (EDS) were utilized to conduct the analyses. The weld pool denoted as (a) was analyzed with the ICP (which has a higher resolution for the study of the chemical composition) instead of the HAZ, and the base materials denoted as (b)–(f) were analyzed using SEM to study the variation of the chemical compositions along the depth of the weld. Fig. 3 depicts the spectrum of the chemical compositions at point (b), and Table 2 shows the variation of the chemical compositions obtained along the depth of the weld. The carbon content in the weld pool is slightly increased from 0.11 wt.% to 0.24 wt.%, which is thought to be caused by the mixtures of filler and rail materials. In addition, the carbon content increases to 1.00–1.50 wt.% in the HAZ and base material. A variation of the silicon content is not found in the weld pool but it increases in other areas from 0.40 wt.% to 0.60–0.80 wt.%. A variation of the manganese content is not found but slightly increases in other areas from 1.50 wt.% to 1.80–2.10 wt.%.

## 2.3. Vickers microhardness of the weld

The material microhardness of the weld-repaired rail along the depth of the weld was investigated. Three specimens were prepared by cutting in three different weld locations, as shown in Fig. 1(b). A  $50 \times$  Vickers microhardness tester was used to obtain more accurate measurement results. The specimens were measured along the depth of the weld from the rail surface to the rail bottom every 0.2 mm. The hardness of the filler material is 320 Hv, and that of the UIC60 Gr.260 rail steel is 310 Hv. Fig. 4 shows the measured hardness values along the depth of the weld. The hardness values measured near the surface of the rail are slightly higher than those of the parent filler material, and they gradually increase with the depth of the weld pool until the fusion zone to a peak value over 400 Hv. However, the hardness values rapidly decrease after the fusion zone until they reach the boundary between the HAZ and the base material. The lowest hardness value is approximately 210 Hv, and it gradually increases to the hardness level of the parent rail material.

## 2.4. Microstructural characteristics of the weld

The microstructure of the weld-repaired rail along the depth of the weld was also investigated on the three specimens, as shown in Fig. 1(b), but only the result from specimen #3 is shown in this paper due to the limited space. The specimens were polished and etched with 2% Nital for 150 s after finishing the Vickers hardness testing to easily measure the depth from the surface by counting the number of marks for the hardness test. The HAZ and base materials were well etched, as shown in the shaded area, while the weld pool remained in the white area. Fig. 2(a) shows the microstructure of the weld pool, where it is 0.6 mm from the rail surface of specimen #3. Although, it is not clearly distinguished because of its white color, we can see the dendrite in the microstructure, which mostly consists of a ferrite area and a light cementite stem. Because the carbon content of the weld pool is low compared with that of the rail material, most of the area is thought to consist of ferrite material. The diamond-shaped mark at the center is a mark indicating the Vickers hardness test. Many fine pores were found in the entire area of the

**Table 1**

Chemical compositions of the rail and filler material.

	[Unit: wt.%]										
	C	Si	Mn	P	S	Cr	Ni	Al	N	Mo	H
Rail	0.65–0.82	0.13–0.60	0.65–1.25	~0.030	0.008–0.030			~0.004	0.010		~2.5 ppm
Filler	0.11	0.40	1.50	0.005	0.002	0.30	2.8	1.40	0.5		

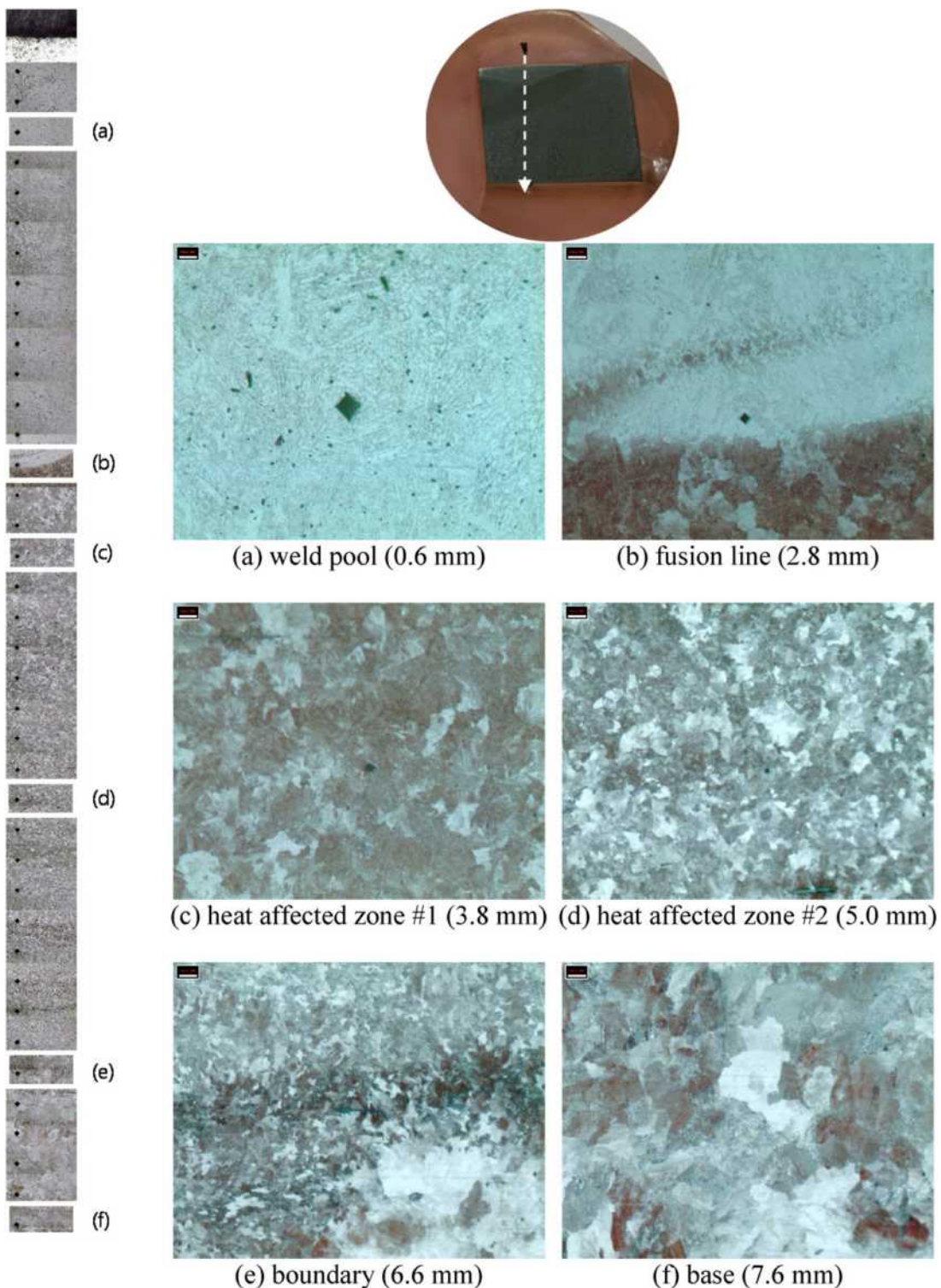


**Fig. 2.** Schematic of the chemical composition analysis location and the microstructure of the material.

weld pool. Fig. 2(b) shows the microstructure of the fusion zone, where the microstructure is 2.8 mm from the rail surface. The boundary between the weld pool and the HAZ is clearly distinguished by the difference in color and grain size. The color transforms into a mixture of black and white due to the increment of the carbon content and because the grain size of the HAZ is much

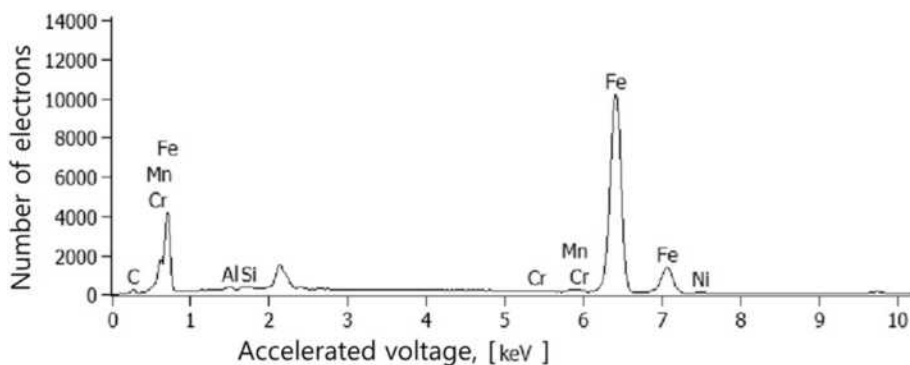


**Fig. 3.** Spectrum of the chemical compositions at point (b).

larger than that of the weld pool. Fig. 2(c) and (d) shows the microstructure of the boundary between the HAZ and the base material, which are 3.8 mm and 5.0 mm from the rail surface, respectively. The grain sizes are small compared with those of the base material, and the microstructure shows a mixture of ferrite and cementite. Fig. 2(e) shows the microstructure of the boundary between the HAZ and the base. The grain sizes are clearly distinguished bordering the boundary. Fig. 2(f) shows the microstructure of the base material, where it is 7.6 mm from the surface of the rail. It consists of large grains made up of ferrite and pearlite, and the grain sizes are much larger than those of HAZ. The diamond shape of the Vickers hardness test mark is not found, and the mark is thought to have been worn out during polishing.

## 2.5. Discussion

To understand the cause of rail failure in the weld-repaired rail, systematic analyses of the weld were performed. From the visual inspection, the crack is found to be initiated at the boundary between the weld pool and the HAZ, and the boundary is thought to be vulnerable compared with other areas such as the weld pool, the HAZ, and the base material. Repeated fatigue stresses in the normal and shear directions are thought to accelerate the crack growth from the beach-marked fracture surface of the rail and the inclination of the crack angle. The crack can be idealized as a semi-elliptical shape for the crack growth analysis. From the chemical composition analysis, it is found that the variation of the carbon content at the weld pool is low, but that it changes quickly bordering the fusion zone, which is thought to derive from measurement error due to the low resolution of SEM-EDS. The difference in the chemical composition between the filler material and the weld pool is thought to be minimal, and the mixture of the filler and the rail material seems to not be a concern. From the hardness test on the weld, it is found that the hardness of the fusion zone between the weld pool and the HAZ changes considerably, and the hardness value of the HAZ is very low compared with that of the parent rail material, which can negatively affect the rail strength. From the microstructure analysis of the weld, it is found that the materials between the weld pool and the HAZ differ significantly and that the grain sizes also differ, while many fine pores and small lamella-type cracks are found as shown in Fig. 5. The weld-repair environment of the rail in the field is not as conducive as one that is indoors, and various welding defects can therefore be produced. These welding defects are thought to be triggers of crack initiation, and the crack growths along the boundary are found in other specimens. Therefore, maintaining a good quality of welding is crucial, especially in harsh environments of the field.

## 3. Residual stress analysis of the weld-repaired rail

When a train passes over a cracked rail, the crack undergoes dynamic global bending and experiences local contact stresses in addition to static residual and thermal stresses. Among these, the residual and contact stress components are known to have a significant effect on fatigue crack initiation and propagation due to their higher stress magnitude than other forms of stress. The global bending stress, local contact stress, and thermal stress can be calculated from previous research [20]. However, because

**Table 2**

Variations of the chemical composition along the depth of rail from the surface.

Description	[Unit: wt.%]							Method
	C	Si	Mn	Cr	Ni	Al	Fe	
(a) Weld pool (0.6 mm)	0.24	0.38	1.54	0.31	2.07	1.2	94.26	ICP-OES
(b) Fusion line (2.8 mm)	1.00	0.70	1.80	0.10	0.80	0.30	95.30	SEM-EDS
(c) HAZ (3.4 mm)	1.50		1.90				95.60	
(d) HAZ (5.0 mm)	1.30		2.00				96.70	
(e) Boundary (6.6 mm)	1.30		1.90				96.80	
(f) Base (7.6 mm)	1.20	0.60	1.90				96.30	

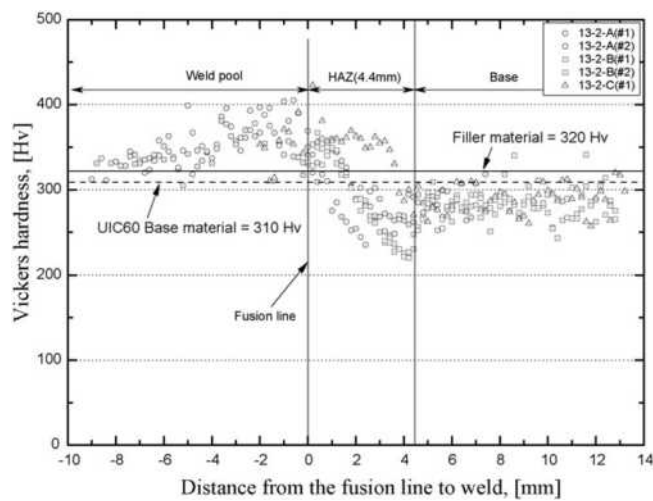


**Fig. 4.** Hardness variation along the depth of the weld.

the residual stress in the rail changes considerably depending on the rail operating condition, the distribution and magnitude first need to be quantified to calculate the crack growth in the weld-repaired rail.

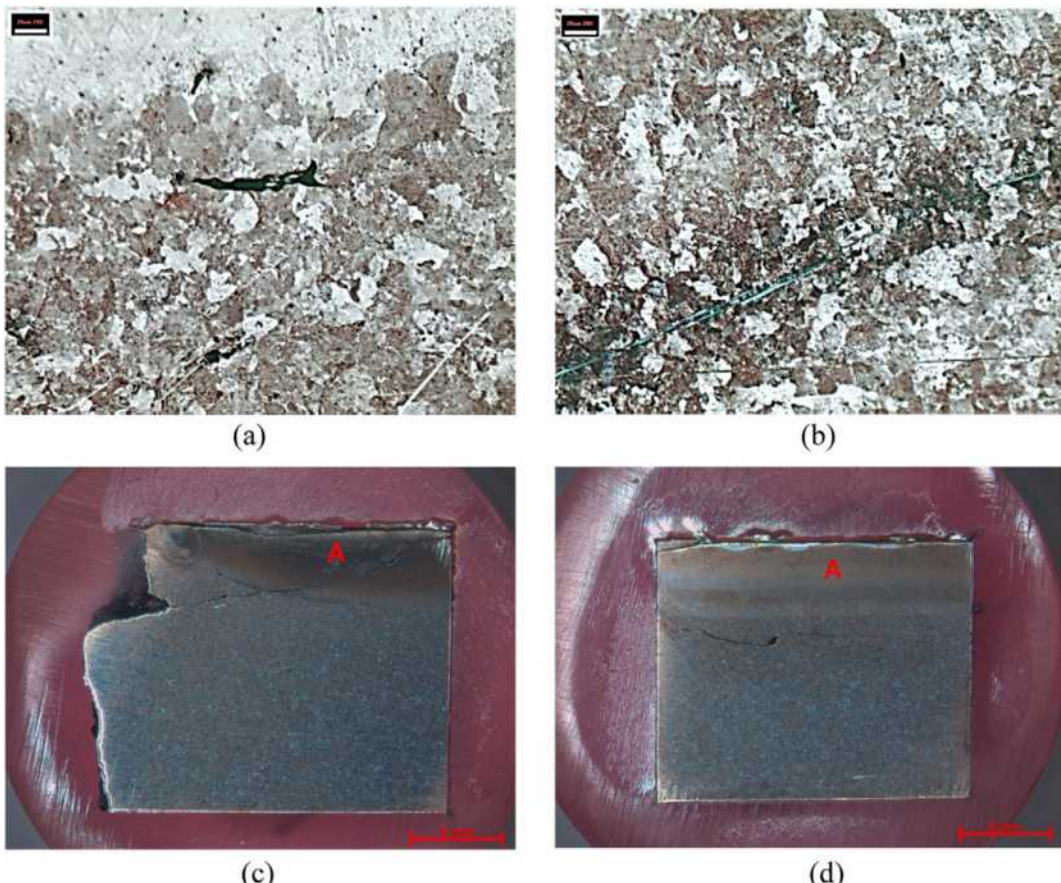
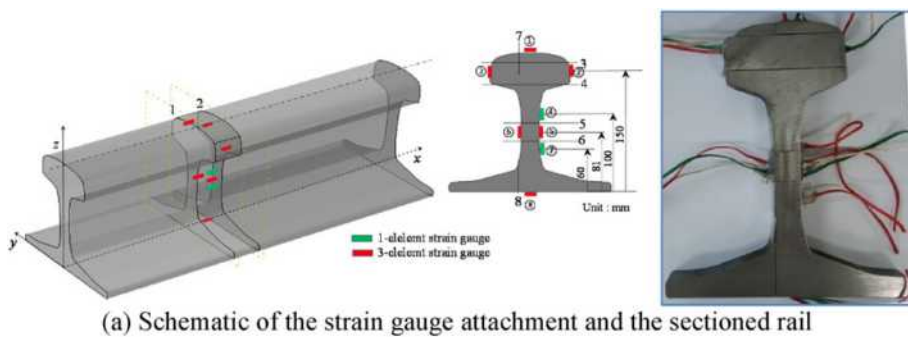
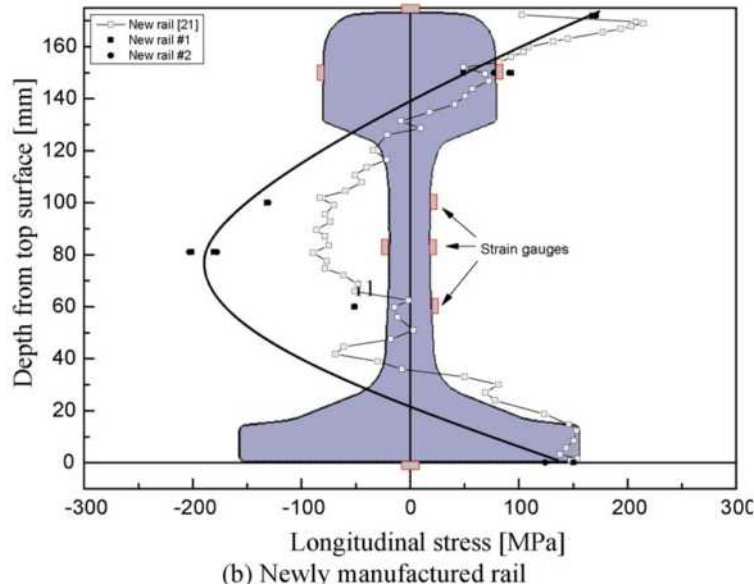


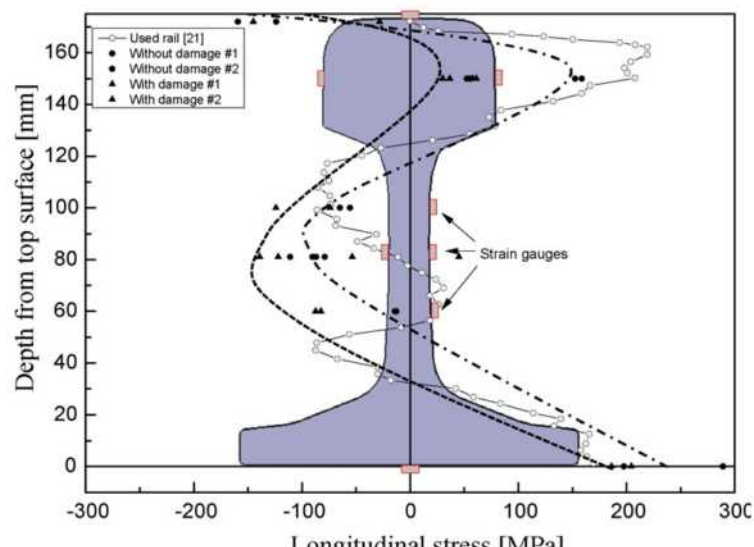
**Fig. 5.** Welding defect found in the fusion line in a lamellar crack shape (a, b) and an example of crack growth along the boundary in the other fractured rail (c, d).



(a) Schematic of the strain gauge attachment and the sectioned rail



(b) Newly manufactured rail



(c) Used rail

**Fig. 6.** Residual stress measurement and distribution of the UIC60 rails [21].

### 3.1. Residual stress measurement

The residual stresses, in the non-weld repaired new and used rails as well as the weld-repaired rail were measured through their partial sectioning. Fig. 6(a) shows the schematic of the residual stress measurement by applying the strain gauges in the rail head, web, and bottom. The residual strains were measured at two points on the rail head surface, at two points on each side of the rail head, at three points on one side of the web and one point on the other side of the web, and two points on the bottom of the rail. Both sides of the rail, apart from approximately 10 mm from the center of the strain gauge, were cut into sections with a mechanical band saw to achieve fully relieved residual stress on every strain gauge. Enough coolant was applied to avoid a temperature increment during the sectioning. Fig. 6(b) and (c) shows a comparison of the residual stress in the longitudinal direction of the rail with that from a previous study [21]. For the new rails, very high tensile stresses are observed in the rail head compared with those of the previous study, and they become compressive stresses in the web of the rail and tensile stresses in the base of the rail. For the rails used, very high compressive residual stresses, with a magnitude of approximately 150 MPa, compared with those of the previous study are observed, but they soon become tensile stresses and show a similar trend to the case of the new rail. For the weld-repaired rails, that were cut from the rail network after several years of service following the repair, high (150 MPa) and low (30 MPa) compressive residual stresses are observed.

### 3.2. Residual stress analysis of weld-repaired rail

A FE simulation in accordance with the weld-repair process was performed to determine the residual stress distribution of the rail. The commercial software ABAQUS was utilized to perform the elastic–plastic FE analysis by using 8-node linear heat transfer and reduced integration elements (element types DC3D8 and C3D8R in the ABAQUS element library) through sensitivity analyses. To calculate the residual stresses according to welding processes, the isotropic strain hardening law and the incremental plasticity option were employed. The details of the FE model are shown in Fig. 7, and relevant information can be found in a previously published paper [10]. A moving point heat, which is defined as a step by step heat input process for the arc welding simulation, was applied in this study at three different defect depths of 2, 5 and 10 mm; to build up a 2 mm deep defect, it was necessary to model one welding layer that consists of 6 welding passes. Two welding layers that consist of 12 welding passes were needed to build up a 5-mm deep defect. Finally, to build up a 10-mm depth of defect, three welding layers that consist of 18 welding passes were needed. Because each welding pass consists of 20 analysis steps, 123 steps of analysis related to the pre-heating and post-cooling were required for one-layered welding, and 363 steps of analysis were necessary to build up a three-layered weld. All of the analyses required a considerably long simulation time and extensive computation resources.

Fig. 8 shows the temperature distributions along the depth from the fusion line to the rail bottom during the welding process. The temperatures were obtained at points along the depth in the middle of the weld. The temperature distributions consist of peaks and valleys according to the degree of closeness of the welder to the point. Fig. 8(a) shows the temperature distribution of a weld repair with a 2-mm depth. As the welder approaches the point, the temperature increases rapidly and reaches a peak value of 931 °C, before dropping rapidly to 749 °C at the end of the welding pass as the welder moves further away from the point. Therefore, if we calculate the phase transformation of the weld based on only the temperature, which is higher than the eutectoid temperature (723 °C), a phase transformation is expected to occur from the 3rd passage to the 5th passage and to continue for approximately 20 s at each pass. The phase transformation is thought to be induced at approximately 7-mm depth from the fusion line. Fig. 8(b) shows the temperature distribution of a weld repair of with a 5-mm depth, in which we can see the two ridges consisting of peaks and valleys. The first ridge indicates the weld repair of the 1st layer, and the second indicates the weld repair of the 2nd layer. The peak of the second ridge is very low compared with the peak of the first ridge when we weld the second layer because the distance from the fusion line is greater than that of the first layer. Because the phase transformation at the second layer is induced at a depth of only approximately 3.5 mm, it seems that the weld repair of the first layer is more dominant than the weld repair of the second layer. Fig. 8(c) shows the temperature distribution of a weld repair with a 10-mm depth. We can see the three ridges consisting of peaks and valleys. The peaks of the second and third ridges gradually decrease. The phase transformation at the third layer is not expected to be induced because the peak

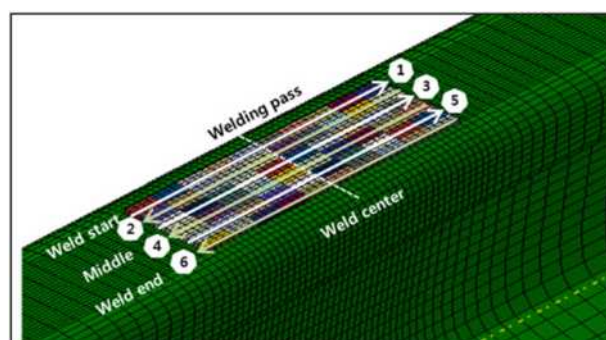


**Fig. 7.** FE welding passes by moving the point heat on the slot and cutting head weld repair [10].

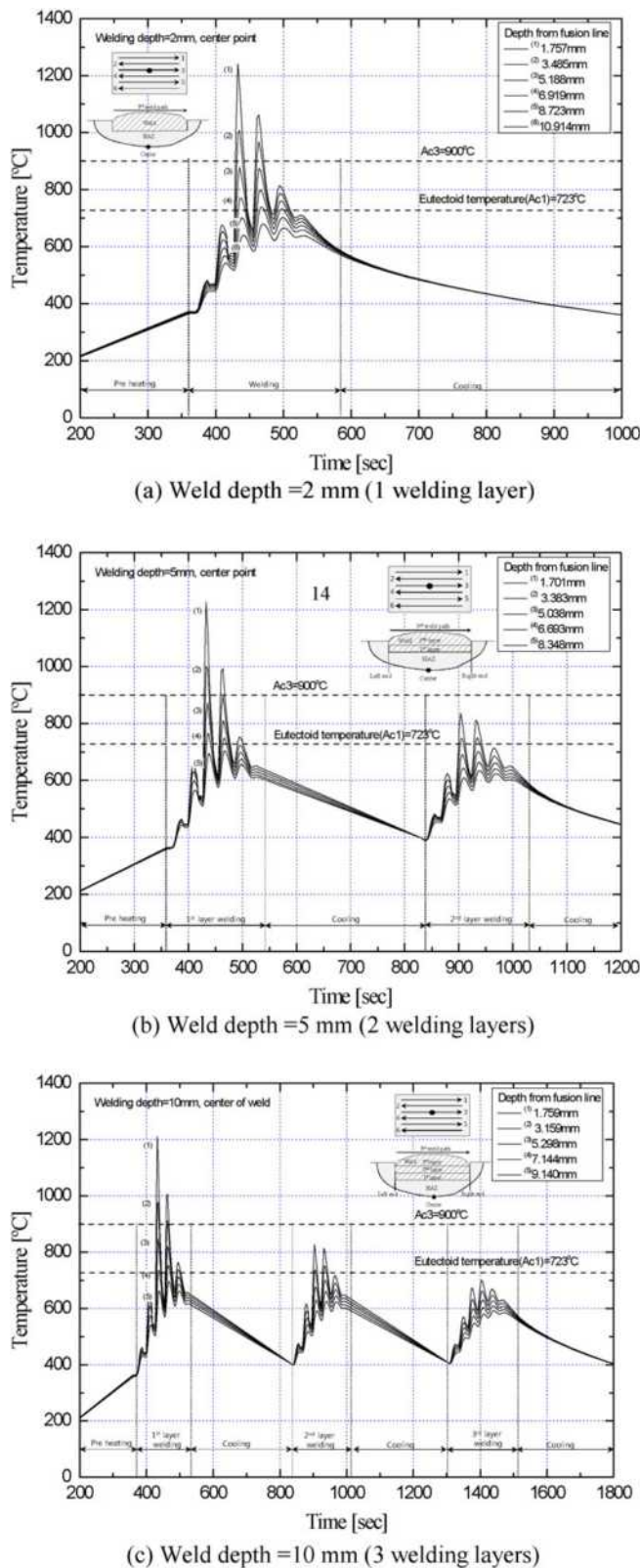


Fig. 8. Temperature distributions during the weld repair along the depth of the rail.

temperature is lower than the eutectoid temperature. Therefore, we can deduce that the weld-repair process for building up the 1st layer determines the depth of the heat-affected zone where the phase transformation occurs.

Fig. 9 presents the residual stress distributions obtained from FE analyses. In the case of the longitudinal stress distribution of the weld-repaired rail, in which high tensile stresses are observed at the surface of the rail head, they gradually become compressive stresses in the web and are finally neutralized at the bottom of the rail. The magnitude of the residual stress is much higher than that of the measured stress, as shown in Fig. 6(c). In the case of the vertical stress distribution along the depth of the rail, compressive stresses are observed at the rail head, and the magnitude increases with depth and is fully neutralized at the bottom of the rail. In the case of the shear stress distribution along the depth of the rail, the magnitudes are very low compared with those of the longitudinal and vertical stresses.

### 3.3. Discussion

The magnitude and distribution of the residual stress in a rail were obtained by both measuring the physical rail and performing an FE analysis on a computer model of the rail. The tensile residual stress was obtained by measuring the head of a new rail. In contrast, the compressive residual stress was obtained from a used rail that was cut from the servicing railway line. The transition from tensile to compressive stress is thought to be due to the high compressive contact stress between the wheel and rail when a railway service changes the residual stress in the rail head, as shown in Fig. 10. Meanwhile, a very high tensile residual stress was obtained from the simulation of the weld repair process by FE analysis. With this method, the local shrinkage of the weld pool at the rail head brings a very high tensile stress in the rail head compared with the other section rail welding methods such as the flash-butt weld, gas pressure weld, and thermite weld methods. Fig. 11 shows a comparison of the residual stress distributions of the weld-repaired rail and the flash-butt welded rail [15]. In the flash-butt welding method, the entire section of the rail is melted, and subsequently, shrinkage occurs across the entire section in different amounts; a high compressive residual stress is thus induced at the rail head. Generally, the compressive stress at the rail head prevents a crack growth by closing the crack face; the flash-butt weld method is thus thought to be better for preventing crack growth. Therefore, it is necessary to relieve the high tensile stress at the head of the weld-repaired rail for practical use in the rail industry.

## 4. Fatigue crack growth in the weld-repaired rail

### 4.1. Analysis model

In this section, a crack growth in a weld-repaired rail under fatigue loading is predicted. Semi-elliptical shaped cracks of three different depths (2, 5 and 10 mm) were modeled to be initiated at the boundary between the weld pool and the HAZ. Repeated fatigue loading was applied to the crack while a series of trains passed over the crack. The total stress was then determined based

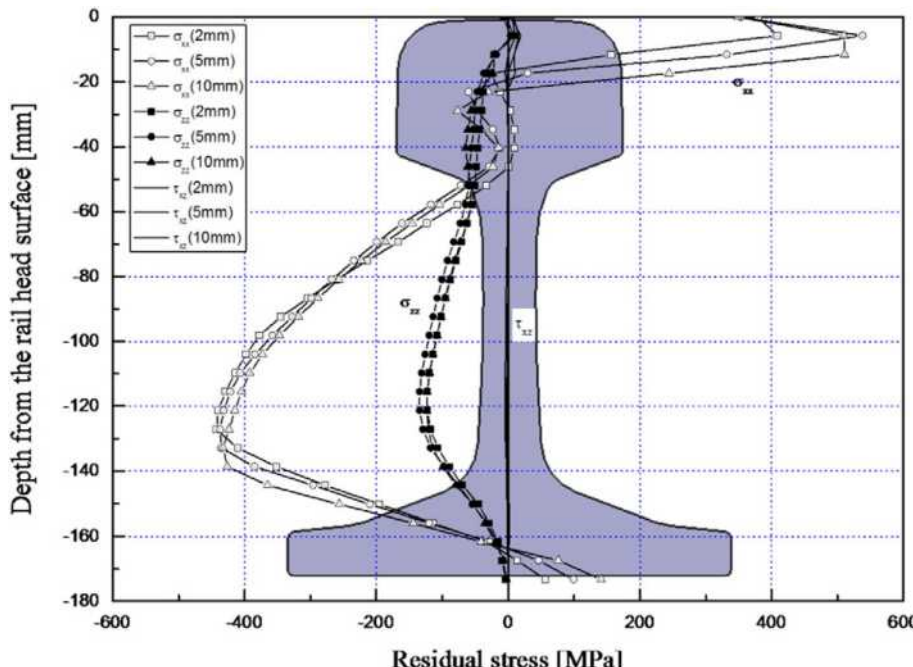
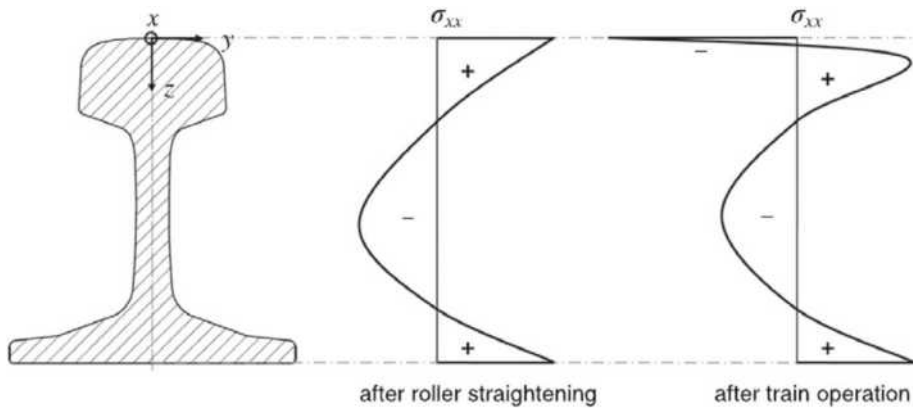


Fig. 9. Residual stress profiles along the depth of the rail.



**Fig. 10.** Residual stress profiles of the rail in the center-line after roller straightening and after train operation [22,23].

on the global bending ( $\sigma_B$ ), contact ( $\sigma_c$ ), thermal ( $\sigma_T$ ), and residual ( $\sigma_r$ ) stresses as shown in Fig. 12. The contact and bending stresses varied with the distance between the wheel position and the crack location, while the thermal and residual stresses were sustained regardless of the distance. Particularly, the contact stress along the rail was calculated from the Hertz contact theory [24], and the bending stress was calculated by the application of the elastic beam theory by Zimmermann [25]. The thermal stress was calculated from the temperature difference between the stress-free neutral temperature  $T_n$  and the railway operating temperature  $T_o$  as  $\sigma_T = 1.14 \times 10^{-5} E (T_n - T_o)$ , and the weld residual stress was used as the aforementioned analyzed and measured data. Each stress component at the crack tip was superposed as below.

$$\sigma_{\text{total}} = \sigma_B + \sigma_c + \sigma_T + \sigma_r. \quad (1)$$

Fig. 13 depicts the schematics of the weld-repaired crack, modeled as an embedded semi-elliptical shape, which was assumed to be initiated at the boundary between the weld pool and the HAZ. The crack was modeled with an inclined angle  $\theta$  to the vertical axis of the rail and having a crack mouth length  $2b$  and a crack depth  $a$ . The depth from the rail surface to the crack mouth is denoted by  $d$ . The crack is assumed to have grown along the crack plane, and the crack aspect ratio  $a/b$  is assumed to be

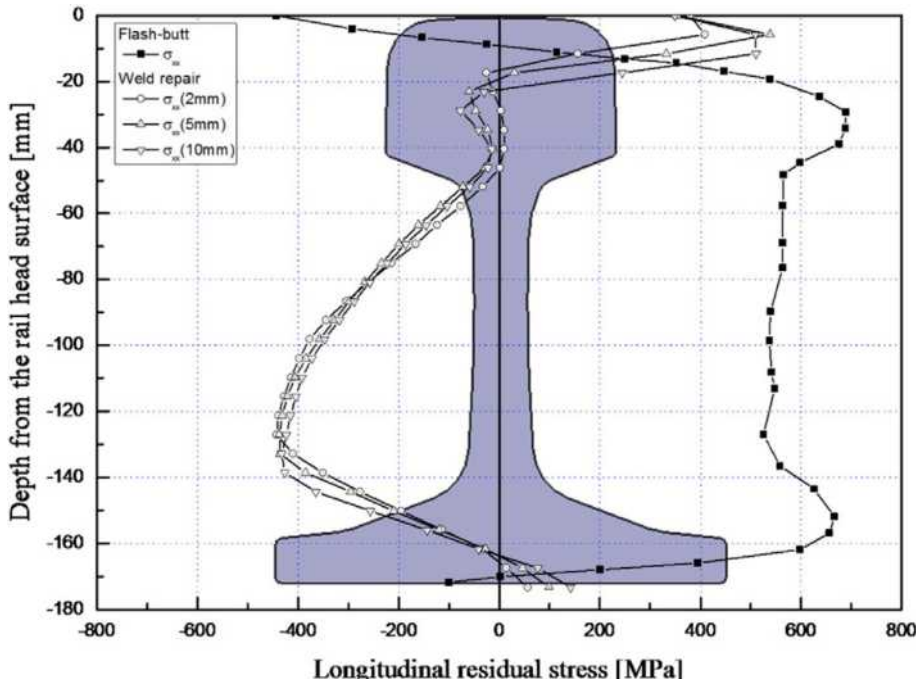


**Fig. 11.** Comparison of longitudinal residual stress distributions between the weld-repaired rail and the flash-butt welded rail [15] along the depth of the rail.

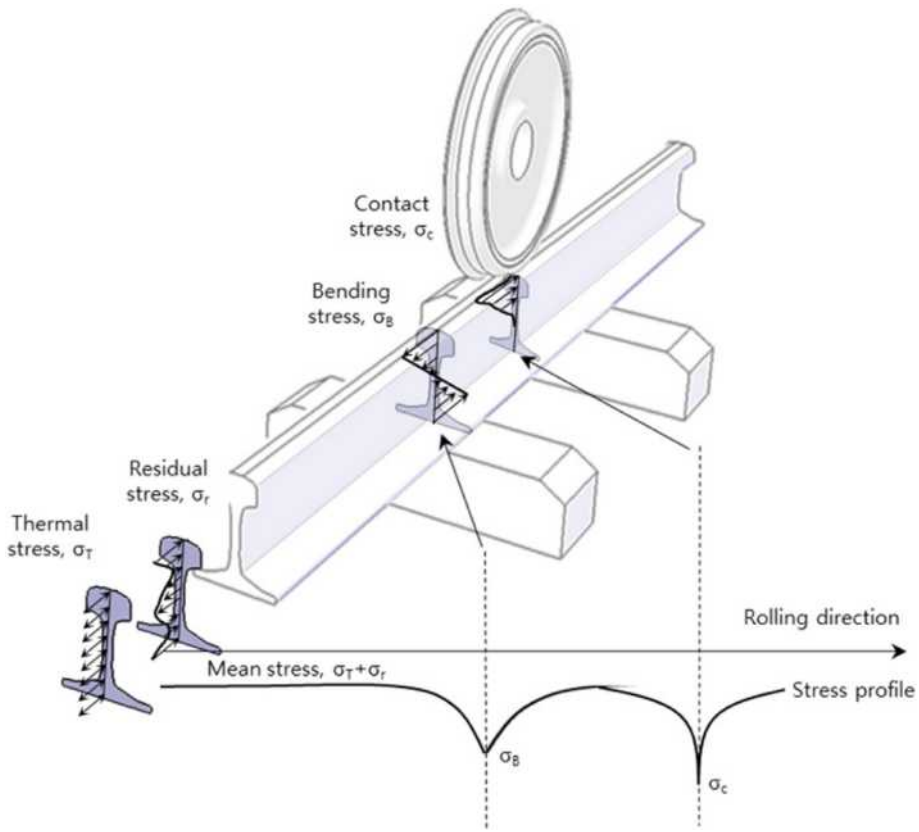


**Fig. 12.** Schematics of loading in a rail during a wheel rolling over a crack [3].

maintained during growth. The contact-induced loading and the thermal and residual stresses were applied to the crack face. The resulting stress intensity factor (SIF) for a semi-elliptical crack, as suggested by Jeong [26], was implemented as follows:

$$K = 1.12 M \sigma \frac{\sqrt{\pi a}}{E(k)} \quad (2)$$

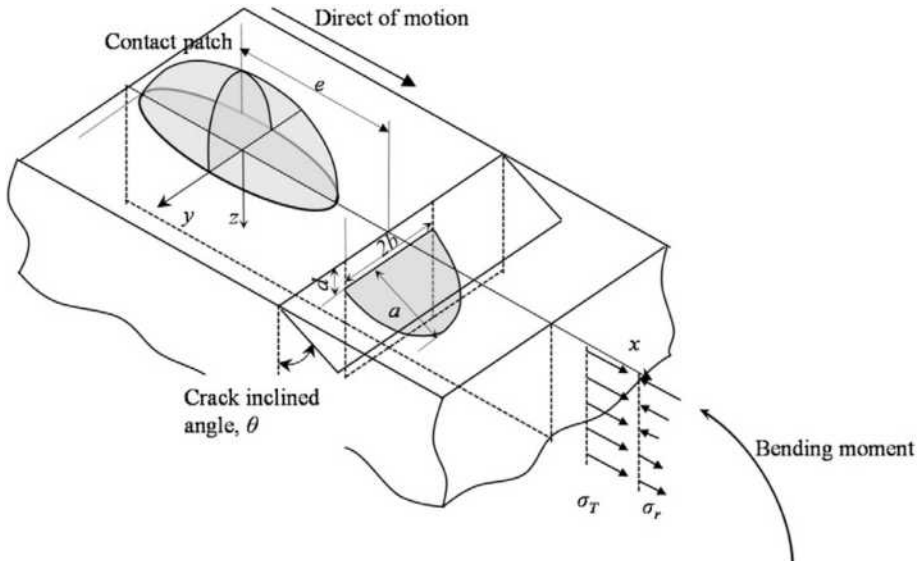


**Fig. 13.** Schematic of the weld-repaired crack model.

where  $M$  is an empirical factor to account for the finite cross-section of the rail head and  $E(k)$  is the elliptic integral of the second kind:

$$E(k) = \int_0^{\frac{\pi}{2}} \sqrt{1-k^2 \sin^2 \theta} d\theta$$

$$k = \sqrt{1-(a/b)^2}.$$

The stress intensity factors were converted into crack growth rates using the following crack growth curve [26] for rail-wheel contact on a pearlite rail.

$$\frac{da}{dN} = 1.74 \times 10^{-13} \frac{\Delta K^4}{(1-R)^{1.63}} [m/cycle] \quad (3)$$

where  $da/dN$  is the crack growth per cycle,  $\Delta K$  is the stress intensity factor range, and  $R$  is the superposed stress ratio.

#### 4.2. Parametric study

Crack growth analyses were conducted under complex loading in which a series of trains passed over a cracked rail several thousand times. Particularly, a high-speed railway operating condition was incorporated, and two types of simulation were performed. The first simulation is for a crack located in the head of the non-repaired rail, in which the used and weld-repaired statuses of the residual conditions are applied, as shown in Fig. 6(c). The other simulation is for the crack located in the head of the weld-repaired rail, in which the residual stress obtained by FE analysis is applied, as shown in Fig. 9. While the crack growth rate curves of the base and weld materials might differ, in this study, we ignored the difference because the identification itself is another considerable issue. The same crack growth rate curve was used for both simulations so that further investigation is necessary for a more accurate prediction of crack growth.

Table 3 shows a list of input variables for the simulation. A train set with a 920-mm diameter railway wheel, which is the conventional high-speed railway wheel size, was used for the simulation, and a UIC60 rail with a 300-mm crown radius was used. The axle load was 17 tons; the initial crack size was assumed to be the crack depth,  $a = 0.5$  mm; and the crack length was  $2b = 2.0$  mm. Therefore, the crack aspect ratio  $a/b$  was set as 0.5 and was maintained during the entire simulation process. As described previously, the depth from the rail surface to the crack was assumed to be constant at 5 mm in the first parametric study and to vary between 2, 5 and 10 mm in the second study.

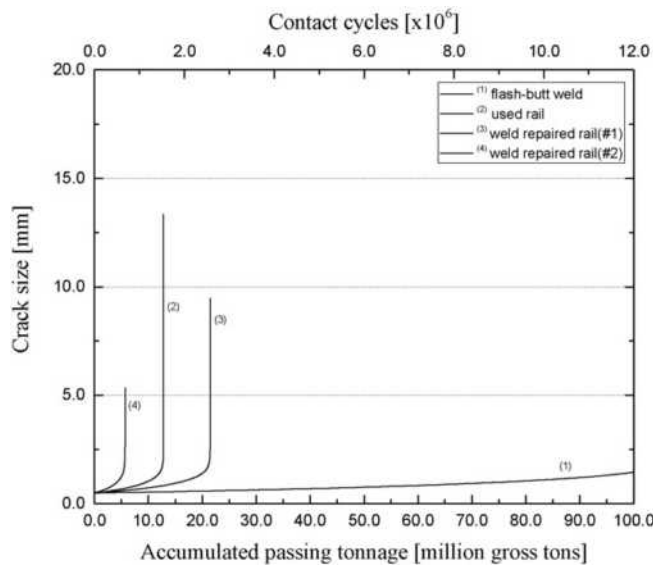
To study the effect of the residual stress on the crack growth rate, parametric crack growth studies with the four different residual stress profiles shown in Figs. 6(c) and 11 were performed. The crack location of 5 mm was used in all cases to ensure the same contact stress conditions. Fig. 14 shows the calculated crack growth curves of the four different states of residual stress. The differences in the crack growth rate are significant. The high compressive residual stress in the rail head of the flash-butt weld denoted as (1) shows the longest crack growth life, and the low compressive residual stress of the weld-repaired rail (4) shows a comparatively short crack growth life. In contrast, the weld-repaired rail with a higher compressive stress at the rail surface (3) shows a longer crack growth life than that of case (4), so it is found that the compressive stress at the rail head is beneficial to delay the crack growth in the rail.

Fig. 15 shows the predicted crack growth curve on a weld-repaired rail with different repair depths of 2, 5 and 10 mm using the residual stresses obtained by the FE analysis shown in Fig. 9. The differences in the crack growth speed among the repair depths are large. The 2-mm deep crack denoted as (1) has the longest life until the crack reaches unstable crack growth, and this is thought to be because the tensile residual stress of the 2-mm deep weld-repair case is the smallest. The 10-mm deep crack has the second longest life, and this is thought to be because although the magnitude of the tensile stresses of the 5-mm and 10-mm deep weld-repair cases are almost the same; the contact stress of the 10-mm depth is low, so the crack growth of the 10-mm deep crack of the rail is slower than that of the 5-mm deep crack.

**Table 3**

List of the input values for the simulation.

Wheel radius, $R_w$ [mm]	Rail radius, $R_R$ [mm]	Wheel load, $P$ [ton]	Elastic modulus, $E$ [MPa]	Poisson ratio, $\nu$	Peak contact pressure, $p_0$ [MPa]	Contact patch radius
460	300	8.5	207,000	0.3	1174	7.21      5.68
Crack shape	Initial crack depth, $a$ [mm]	Initial crack length, $2b$ [mm]	Crack aspect ratio $a/b$	Crack location, $d$ [mm]	Surface friction coef., $u_{cf}$	
Semi-elliptical	0.5	2.0	3.0	2, 5, 10	0.45	



**Fig. 14.** Fatigue crack growth with the residual stress of a used rail.

#### 4.3. Discussion

The longitudinal residual stress in a rail head plays an important role in the growth of cracks because the direction of the crack growth is perpendicular to the direction of the force applied. Tensile residual stress opens the crack when a train set passes over the crack and accelerates the crack growth. In contrast, compressive residual stress closes the crack and decelerates the crack growth. Therefore, it is very important to change the tensile stress to compressive stress at the rail head to reduce the unanticipated initiation and propagation of the crack. The transition from tensile to compressive stress due to contact stress is beneficial to prevent the crack from growing, especially on the rail surface. Although the 2-mm deep weld repair shows the longest life due to the comparatively low tensile stress magnitude, the 10-mm deep weld repair is recommended, considering the good quality of welding.

#### 5. Conclusions

In this study, failure analyses on a fractured weld-repaired rail were performed, and the residual stresses at various stages of the rail were obtained. The fatigue crack growth in the weld-repaired railway rail was also simulated by assuming a semi-elliptical

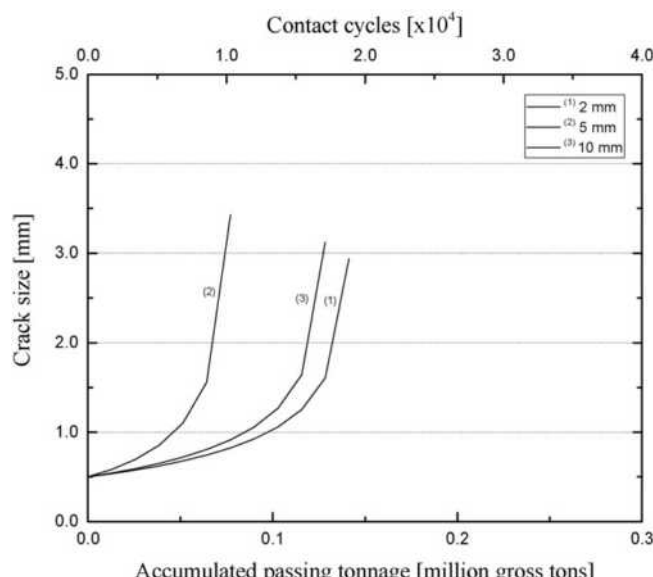


**Fig. 15.** Fatigue crack growth with the residual stress of the weld-repaired rail.

crack to be initiated at the boundary between the weld and heat-affected zones. Based on these successive analyses, the following key findings were observed.

1. Many pores, and lamella cracks, a rapid drop of material hardness, a transition in the chemical composition and microstructure of the material, and a high longitudinal tensile residual stress were found in the fractured rail. This observation is consistent with that of crack growth in other weld-repaired rails, and these are the causes of weld-repaired rail failure.
2. The longitudinal residual stresses in the heads of the new and weld-repaired rail were highly tensile, but changed into compressive stress with a magnitude of approximately 150 MPa soon after train operation because of the high compressive contact stress.
3. The residual stress distribution generated in the head of the rail greatly influenced the crack growth speed. Moreover, among the three weld-repair conditions, the crack growth at the deepest depth of 10 mm from the surface led to a longer life of the crack until unstable crack growth occurred. These trends are consistent with previous observations relating to the crack initiation life of weld-repaired rails.

## Acknowledgments

This study was supported by a grant from the R&D Program of the Korea Railroad Research Institute, Republic of Korea (PK1502d-2).

## References

- [1] S.L. Grassie, Traction, curving and surface damage of rails, part 2: rail damage, *Proc. Inst. Mech. Eng. F Rail Rapid Transit* 229 (3) (2015) 330–339.
- [2] S. Pal, W.J.T. Daniel, C.H.G. Valente, A. Wilson, A. Atrens, Surface damage on new AS60 rail caused by wheel slip, *Eng. Fail. Anal.* 22 (2012) 152–165.
- [3] E. Magel, M. Roney, J. Kalousek, P. Sroba, The blending of theory and practice in modern rail grinding, *Fatigue Fract. Eng. Mater. Struct.* 26 (2003) 921–929.
- [4] BS EN 15594, Railway applications—track—restoration of rails by electric arc welding, British Standard, 2009.
- [5] A. Allie, H. Aglan, M. Fateh, Microstructure-fracture behavior relationships of slot-welded rail steel, *Miner. Met. Mater. Soc. ASM Int.* 42A (2011) 2706–2715.
- [6] D. Workman, R. Kral, Flash butt wedge repair of weld head defects, *Proceedings of the ASME/ASCE/IEEE 2011 Joint Rail Conference* 2011, pp. 1–7.
- [7] Z. Zheng, H. Qi, H. Zhang, D. Ren, Laser repairing of damaged steel rail with filler wire, *Proceedings of Measuring Technology and Mechatronics Automation* 2014, pp. 383–386.
- [8] H.A. Aglan, S. Ahmed, K.R. Prayakarao, M. Fatch, Effect of preheating temperature on the mechanical and fracture properties of welded pearlitic rail steels, *J. Eng.* 5 (2013) 837–843.
- [9] D. Bajic, G.V. Kuzmenko, I. Samardzic, Welding of rails with new technology of arc welding, *Metalurgija* 52 (2013) 399–402.
- [10] S.H. Lee, S.H. Kim, Y.S. Chang, H.K. Jun, Fatigue life assessment of railway subjected to welding residual and contact stresses, *J. Mech. Sci. Technol.* 28 (2014) 4483–4491.
- [11] AWS D15.2/D15.2 M, Recommended practices for the welding of rails and related rail components for use by rail vehicles, American Welding Society, 2013.
- [12] Y. Chen, F.V. Lawrence, C.P.L. Barkan, J.A. Dantzig, Heat transfer modelling of rail thermite welding, *Proc. Inst. Mech. Eng. F Rail Rapid Transit* 220 (2006) 207–217.
- [13] Y. Chen, F.V. Lawrence, C.P.L. Barkan, J.A. Dantzig, Weld defect formation in rail thermite welds, *Proc. Inst. Mech. Eng. F Rail Rapid Transit* 220 (2006) 373–384.
- [14] Z. Cai, M. Nawafune, N. Ma, Y. Qu, B. Cao, H. Murakawa, Residual stresses in flash butt welded rail, *Trans. JWRI* 40 (1) (2011) 79–87.
- [15] B.L. Josefson, J.W. Ringsberg, Assessment of uncertainties in life prediction of fatigue crack initiation and propagation in welded rails, *Int. J. Fatigue* 31 (2009) 1413–1421.
- [16] H. Desimone, S. Beretta, Mechanisms of mixed-mode fatigue crack propagation at rail butt-welds, *Int. J. Fatigue* 28 (2006) 635–642.
- [17] A. Allie, H.A. Aglan, M. Fateh, Mechanical and fracture analysis of welded pearlitic rail steels, *J. Mech. Mater. Struct.* 5 (2) (2010) 263–276.
- [18] Y. Terashita, M. Tatsumi, Analysis of damaged rail weld, *Q. Rep. RTRI* 44 (2) (2003) 59–64.
- [19] A. Skyttebol, A. Josefson, J.W. Ringsberg, Fatigue crack growth in a welded rail under the influence of residual stresses, *Eng. Fract. Mech.* 72 (2005) 271–285.
- [20] V.A. Profillidis, *Railway engineering*, Ashgate Publishing Company, 2000 89–104.
- [21] P.J. Webster, X. Wang, G. Mills, G.A. Webster, Residual stress changes in railway rails, *Physica B* 180&181 (1992) 1029–1031.
- [22] M. Steenbergen, R. Dollevoet, On the mechanism of squat formation on train rails – part II: growth, *Int. J. Fatigue* 47 (2013) 373–381.
- [23] S.L. Srimani, J. Basu, An investigation for control of residual stress in roller-straightened rails, *J. Strain Anal.* 38 (3) (2003) 261–268.
- [24] Engineering Science Data Unit, *Contact phenomenon III: calculation of individual stress components in concentrated elastic contacts under combined normal and tangential loading*, HIS 85007 (1994).
- [25] V.A. Profillidis, *Railway engineering*, Ashgate Publishing, 2000 68–74.
- [26] D.Y. Jeong, Correlations between rail defect growth data and engineering analyses, part 1: laboratory tests. UIC/WEC Joint Research Project on Rail Defect Management, 2003 12–15.



## Use of adhesives in repair of cracks in ship structures

R. C. Allan, J. Bird & J. D. Clarke

**To cite this article:** R. C. Allan, J. Bird & J. D. Clarke (1988) Use of adhesives in repair of cracks in ship structures, Materials Science and Technology, 4:10, 853-859, DOI: [10.1179/mst.1988.4.10.853](https://doi.org/10.1179/mst.1988.4.10.853)

**To link to this article:** <http://dx.doi.org/10.1179/mst.1988.4.10.853>



Published online: 18 Jul 2013.



Submit your article to this journal 



Article views: 28



View related articles 



Citing articles: 9 View citing articles 

## Overview

# Use of adhesives in repair of cracks in ship structures

The structures of modern warships frequently contain significant quantities of aluminium alloy: a material especially prone to fatigue induced cracking. The satisfactory repair of such cracks is often vital if the fighting efficiency of a warship is to be maintained properly and would usually be carried out by welding. The welding of aluminium and its alloys is often difficult and onboard is further complicated by the necessity to remove inflammable linings, cables, and items of equipment to reduce the fire risk and provide access for the repair. Consequently, repair welds are often carried out from the most accessible side and are seldom full penetration. The finished weld is invariably little more than a sealant with a fatigue life inferior to that of the original plate. Initiation of further cracking in the repair weld can be prevented by adhesively bonding a reinforcement across the weld to provide a strength at least as good as that of the original plate and a stiffness sufficient to prevent the onset of further cracking. The use of adhesively bonded steel and carbon fibre patches in typical ship applications are described and the factors governing patch design, methods of surface preparation to ensure good bond durability in a marine environment, and choice of adhesives are discussed.

MST/834

R. C. Allan  
J. Bird  
J. D. Clarke

© 1988 The Institute of Metals. Manuscript received 24 December 1987; in final form 5 February 1988. The authors are with the Admiralty Research Establishment, Dunfermline, Fife, Scotland. An earlier version of this paper was presented at the conference 'Structural adhesives in engineering' held at the University of Bristol on 2-4 July 1986 and organised by The Institution of Mechanical Engineers.

## Introduction

Aluminium has been used in the shipbuilding industry for many years: from special applications such as liquid methane tanks for the Methane Pioneer and others to the deck and superstructure construction in merchant ships such as Oriana,<sup>1</sup> Canberra,<sup>2</sup> and Queen Elizabeth II. The superstructures and deckhouses in those vessels were made entirely of aluminium, whereas other vessels, such as the United States, had composite superstructures with aluminium attached to steel beams and stiffeners.

Aluminium has also been used in the decks and superstructures of warships: the Iranian destroyers built by Vickers in the 1960s, the Van Trompe Class destroyers of The Netherlands Navy, the FFG1, FFG7, and others of the US Navy, and recently the Type 21 frigates of the Royal Navy. There have also been proposals for all aluminium warships, but no such ship has yet been built.<sup>3</sup>

Aluminium is attractive to a designer in that it has a density and a modulus which are both one-third that of steel and a specific strength greater than that of steel. Thus, in addition to weight saving, it has the advantage that for a given strain the applied stress will be one-third that of steel, enabling long continuous superstructures to be designed without the need for expansion joints.

When designing a ship, the superstructure can be regarded as contributing to the strength of the hull girder or otherwise. However, even if the superstructure is not designed to contribute to the longitudinal strength of the ship, it will develop significant stress during hull bending. In addition, design features and stress concentrations can significantly increase the local stress level. Thus, special care must be taken in design to limit the stress in the aluminium superstructure, subject to the full hull bending moment.

The combination of induced stress and stress concentrations often results in fatigue damage in long aluminium superstructures attached to conventional steel hulls (Fig. 1). Although this can be alleviated by use of an expansion joint, this is not a complete solution as this only tends to concentrate the stresses elsewhere, often with more serious consequences, such as the fatigue failure of longitudinal stiffeners in deckheads (Fig. 2).

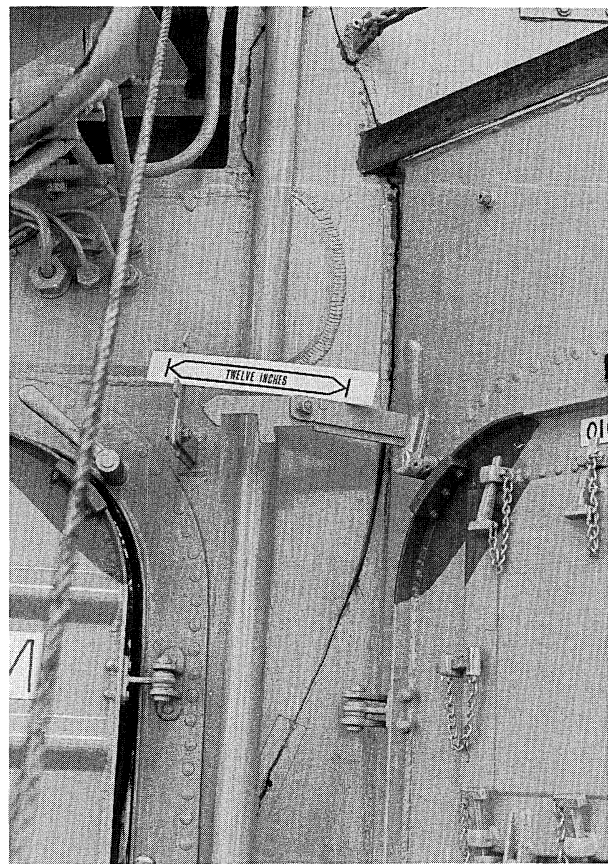
It is obvious that large cracks must be repaired to maintain the structural strength and prevent ingress of sea water to sensitive areas. However, if welding is used, the fatigue performance will be inferior to that of the original aluminium plate (Fig. 3).<sup>4</sup> For weld repair, services may have to be stripped out below decks to prevent damage, particularly to electrical cables. Also, because of the difficulties of aluminium weld repair in a shipyard, the quality of the repair is likely to be poor. Thus, however the weld repair is carried out future performance will be inferior to that of the original structure.

Where fatigue cracking occurs, the problem results from insufficient material being available to maintain the strain induced stress at an acceptable level. This could be solved by either replacing the original plating with thicker plate, which would increase the superstructural weight, or by locally strengthening the structure with a material of higher modulus.<sup>5,6</sup> This action would locally reduce the applied strain and thus the imposed stress in the aluminium, thereby reducing the likelihood of fatigue damage.

High modulus materials such as steel or carbon fibre would suffice depending on application and environment, although boron fibres might also be considered. These materials could be bonded to the aluminium plate in sufficient thickness to achieve the required reduction in stress level, the patch being tapered to avoid imposing a local stress concentration at the patch boundary.

The use of adhesively bonded patches to repair structures has been examined by many investigators and their use has increased dramatically over recent years. Adhesively bonded repairs of ship structures are invariably extremely cost effective because they can be carried out from the most accessible side and require no stripping out of equipment etc. from compartments in the immediate vicinity of the area to receive the patch. Where it is possible to repair cracks without the necessity to remove equipment this is done; the reinforcement is added for cosmetic purposes, but the weld will have little or no penetration and virtually no strength.

Unfortunately, the analytical techniques that have been devised for the design of patches are more applicable to the thinner structures used in aircraft. However, there are sufficient similarities with the repair of aircraft and reinforcement of other structures such as bridges<sup>7-9</sup> to



1 Typical crack in aluminium alloy superstructure

encourage the use of adhesively bonded patches in ship repair, although there are particular restraints which must be observed.

In the present paper, the work carried out at ARE (Dunfermline) to determine the strength of steel and carbon patches applied to aluminium plate material and the application of the technique to the repair of aluminium decks in Type 21 frigates of the Royal Navy are described and the performance of these patches in service is discussed.

## Design considerations

The most serious cracking experienced in warships has usually been caused by the stress arising from vertical bending of the hull girder resulting from wave action. This produces alternating compressive and tensile stresses in the deck and bottom structure in the longitudinal direction. Since the bottom structure is relatively free of stress concentrations, most of the cracking occurs in the decks: at openings, at ends of superstructure sections, or at changes in deck plating thickness, and nearly always initiates in a welded joint.

During its life a warship will experience about  $3 \times 10^7$  wave encounters. Most of these will be of small wave height and the resultant stresses will be correspondingly small, but there will be a reducing number of higher stresses. Measurements on warships at sea by ARE (Dunfermline) have shown that the probability distribution of the maximum stress in each wave encounter over a long period is approximately exponential. Analytical methods are available for calculating the fatigue damage for a particular welded joint configuration and probability



2 Example of deckhead cracking

distribution of stress range.<sup>10</sup> It is usually assumed that the fatigue curve can be represented by

$$N_f = A(\Delta\sigma)^{-b} \quad \dots \dots \dots \quad (1)$$

where  $N_f$  is the number of cycles to failure,  $\Delta\sigma$  is the stress range, and  $A$  and  $b$  are empirical constants. For most joints in steel and aluminium  $b \approx 3$ .

If the cumulative probability distribution of stress range is given by

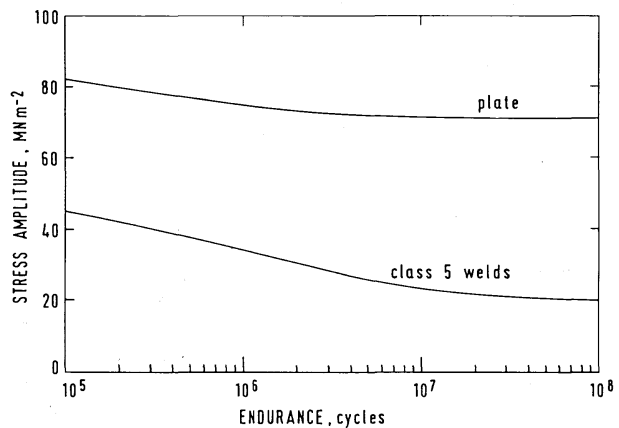
$$P(\Delta\sigma) = \exp(-\alpha\Delta\sigma/\Delta\sigma_0) \quad \dots \dots \dots \quad (2)$$

where  $\Delta\sigma_0$  is the maximum stress range expected in a ship life corresponding to a probability of exceedance per wave encounter of  $1/\alpha$ , then the Palmgren-Miner damage accumulation law gives the following expression for the fatigue usage  $D$  in a ship life

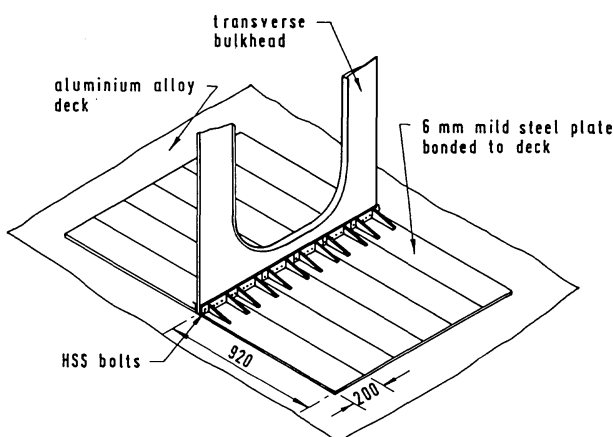
$$D = \sum \frac{N_i}{N_{f(i)}} = \frac{\alpha N_L b!}{A} (\Delta\sigma_0)^b \quad \dots \dots \dots \quad (3)$$

where  $N_L$  is the number of cycles in a ship life. There are a number of additional stress cycles resulting from hull vibrations following impacts between the hull and the sea surface, but the correction required for these is generally fairly small. Crack initiation is assumed to occur when the value of  $D$  is of the order of 1.0.

If the contributions to  $D$  from different parts of the fatigue curve are examined for typical welded joints and loading configurations, it is found that most damage



3 Fatigue design curve for N8 aluminium alloy



4 Repair of internal deck of frigate using bonded steel patches joined by bolting through bulkhead

results from the midrange (i.e.  $10^4$ – $10^5$  cycles) of the fatigue curve.

It can be seen from equation (3) that the fatigue life of a joint is proportional to  $(\Delta\sigma)^b$ , so that for  $b = 3$  the life can be doubled for a stress reduction of only about 20%. If a patch is bonded over a repaired weld and the patch is long enough and the adhesive thin enough for there to be insignificant shear in the region of the weld, then transverse sections can be assumed to remain plane under load. The longitudinal stress in the plate next to the weld  $\sigma_1$  is then given by

$$\sigma_1 = \frac{\sigma_0}{1 + (E_2 t_2 / E_1 t_1)} \quad \dots \dots \dots \quad (4)$$

where  $\sigma_0$  is the stress in the plate in the absence of the patch reinforcement,  $E_1$  and  $E_2$  are the elastic moduli of the plate and patch respectively, and  $t_1$  and  $t_2$  are the thicknesses of the plate and patch respectively.

In this relationship, it is assumed that the adhesive carries an insignificant longitudinal load and that the supporting structure (stiffeners and bulkheads) effectively eliminates bending effects.

For internal applications, where sea water corrosion and differential expansion effects resulting from temperature fluctuations are not a problem, steel patches have been used successfully on aluminium decks. For such patches,  $E_2/E_1 = 3.0$ . If the patch thickness were, say, half the original plate thickness, the plate stress would be reduced to a factor 0.4 times the original value giving a factor of 15.6 increase in fatigue life. In practice, such large increases in fatigue strength are not possible for a number of reasons. The fatigue strength of the repaired weld is never as good as the original and very often has a large area of lack of fusion internally. Therefore, it is not possible to grind down the weld bead without losing a large fraction of the weld metal and the patch has had to be recessed to accommodate the weld bead. The adhesive does reduce the load carried by the patch to some extent, and the fatigue strength of the adhesive is a governing factor. If the deck is not flat, e.g. at a transition in plate thickness where both stepped steel patches and laminated carbon fibre patches have been used, the step increases the flexibility of the patch and reduces its effectiveness. Nevertheless, despite these factors, a substantial improvement in fatigue life can still be obtained.

An alternative approach is to use patches without a repair weld, then, provided the patch is strong enough, the governing factor is the fatigue strength of the adhesive joint. This can be improved by the choice of adhesive and the reduction of stress concentration at the end of the patch as discussed below.

In some instances, cracking has occurred close to, and on both sides of, a transverse bulkhead. Then, to avoid cracking at the bulkhead, the patches on either side have had to be joined by bolting through the bulkhead, thus obtaining a continuous load path (Fig. 4). The steel patches were applied as longitudinal strips 200 mm wide for ease of handling.

## Surface preparation

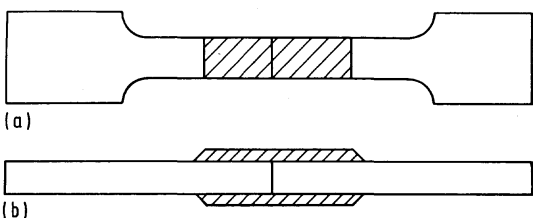
The method chosen for preparing aluminium alloy surfaces for bonding must achieve strong durable bonds. The use of flammable or corrosive liquids is not generally acceptable onboard ship. The use of organic degreasing agents entails considerable fire risk, since their vapours can be drawn into ventilation systems and spread throughout the ship. Also to be avoided are aggressive chemicals which can penetrate cracks and other openings to attack and damage wiring and equipment contained within the ship structure. Chemical paint strippers have also been known to degrade adhesive bonds, even though every effort has been made to remove all traces of the stripper from surfaces to be bonded.

Therefore, the preparation of adherend surfaces onboard ship is limited to simple degreasing using a commercial low toxicity solvent such as Genklene (1:1:1 trichlorethane) applied by wiping with lint free cloths, followed by grit blasting with 60/80 size alumina grit to produce a clean, bare metal surface.

A freshly grit blasted surface of aluminium and its alloys is very active and extremely susceptible to contamination from atmospheric moisture, dust, and grease which can adversely affect the performance of the bonded joint. To reduce the possibility of contamination to a minimum as short a time as possible should elapse between grit blasting and adhesive application. Large areas are more conveniently prepared in stages to minimise the time taken between surface preparation and application of adhesive. This is especially so where large carbon fibre patches are involved, although, as a consequence, the first ply of the laminate to be laid will contain several butt joints. Provided generous overlaps are used at the joints, no significant loss of strength and stiffness of the finished patch should occur, because all subsequent plies can usually be laid in continuous lengths. Both steel and carbon fibre patches are finished with a 10:1 taper at the ends to reduce stress concentration.

Bond durability greater than that offered by simple degreasing and grit blasting is especially desirable for marine bonded joints and might be achieved using alternative methods of surface preparation. Phosphoric acid anodising, for example, is well established in the aircraft industry as a proven method of surface preparation leading to the formation of strong durable adhesive joints in aluminium alloys. Combining the phosphoric acid with colloidal silica to form a gel is one method of making the process more manageable, but after anodising there remains a considerable quantity of aggressive chemical to be completely and safely removed – a not inconsiderable task if the restraints imposed onboard ship are to be observed.

Previous work<sup>11</sup> has demonstrated that  $\gamma$ -glycidoxypropyltrimethoxysilane (Union Carbide A187 silane) can be used as a coupling agent on grit blasted aluminium alloy surfaces with the effect of increasing the durability of structural adhesive joints. Application of a 1 or 5 vol.-% aqueous solution of A187 silane results in a slight improvement in initial joint strength and considerably increased durability of joints immersed in water when compared with untreated joints.

*a* central weldment; *b* outer weldment

## 5 Specimen used in bond strength test

Silane priming of grit blasted surfaces is very convenient to use onboard ship and, although without the same reputation as phosphoric acid anodising, is still capable of producing more than adequate joint durability to meet the surface requirement.

Some adhesives incorporate silane in their formulation, but for ship application experience has shown that it is better to apply the silane in a separate process. This has the advantage of direct control and when applied very quickly after grit blasting helps to seal a highly active aluminium alloy surface.

## Patch material and adhesives

For ship repairs, two patch materials of modulus higher than that of the usual marine aluminium alloy have been found to work well. The choice of patch material has been largely governed by situation, patch area, and the relative flatness of the area to be patched.

Mild steel patches are cheap, readily fashioned, and well suited for patching interior surfaces well away from weatherdecks. The plating used for steel patches is typically 6 mm thick and can usually be persuaded by the strategic application of pressure from weights and shoring to accommodate slight undulations in, say, a deck surface, to achieve thin bondlines. Where variations in a surface are of a very minor nature, the use of a gap filling adhesive will suffice. All the repairs involving steel patches carried out so far on HM ships have been with Permabond E04 or E32, which are both cold setting, gap filling, epoxy adhesives.

Less flat areas, especially those containing changes in plate thickness and curved surfaces, are more conveniently reinforced with patches of carbon fibre composite laminated directly onto a ship structure using cold setting epoxy resin. A typical carbon fibre patch consists of eight plies of unidirectional woven roving of  $340 \text{ g m}^{-2}$  nominal mass laminated with Ciba-Geigy 1927 epoxy resin and

hardener. The resin has a low initial viscosity enabling easy penetration of the carbon fibre and bonds well to the aluminium alloy plating of a ship superstructure.

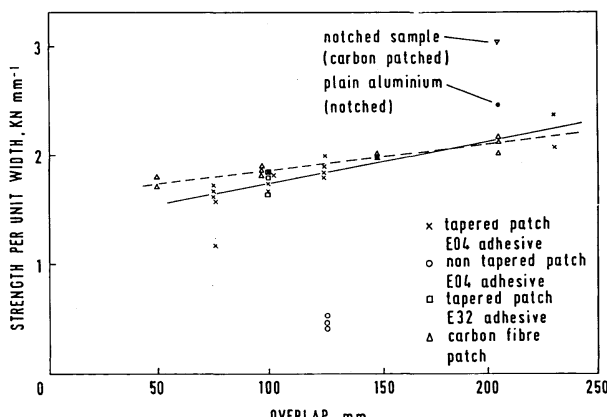
There is a particular problem in that if, in the presence of water, the aluminium alloy is in electrical contact with the carbon fibre of the patch, severe stress corrosion of the metal may occur leading to serious loss of bond strength. Although the carbon fibre in a laminated patch is effectively sealed and electrically isolated from the metal structure by the resin matrix, a moisture barrier of 0.15 mm thick aluminium foil is bonded over the patch to overlap it by about 100 mm all round. The aluminium foil is in turn protected by two plies of  $300 \text{ g m}^{-2}$  chopped strand glass laminate finished with a heavy epoxy resin flow coat.

## Bond strength

Estimates of bond strength were made using aluminium alloy samples of the type shown in Fig. 5. Steel patches were bonded with either Permabond E04 or E32 epoxy adhesives. Fully cured, preformed carbon fibre patches laminated with Ciba-Geigy 1927 epoxy resin were bonded to the aluminium using Permabond F241 acrylic adhesive. In all cases, the patch material was attached to both sides of the sample to ensure axiality of stressing when the samples were tested to failure in tension.

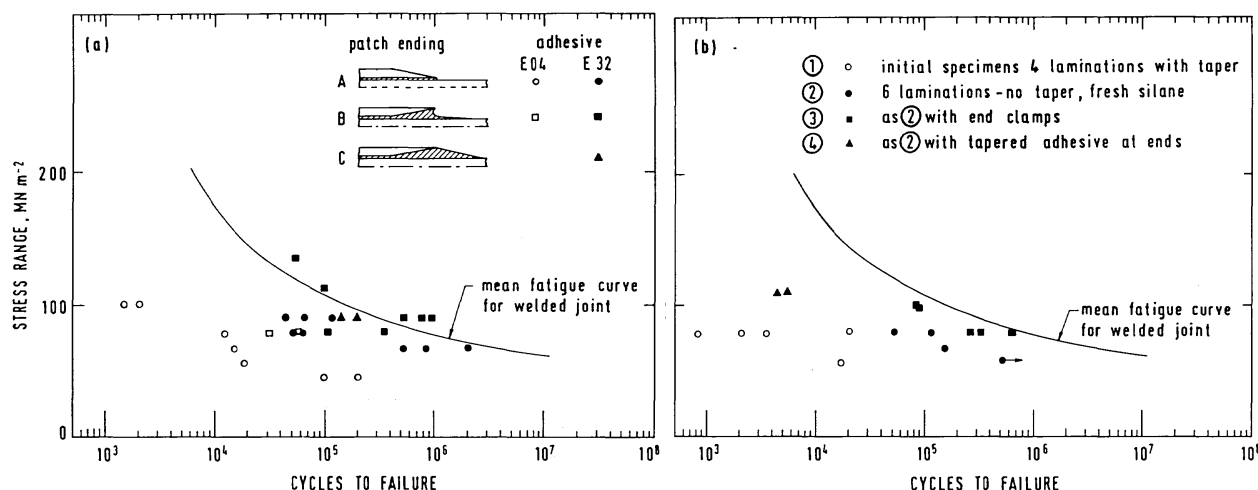
Using E04 adhesive and steel patches, the bond strength can be shown to vary in relation to the overlap (Fig. 6). The samples were all made by patching across abutting aluminium ends. To have some uniformity in expressing the failure load, the failure load per unit width is reported rather than the failure load per overlap area. The former method will give a better indication of any increase in strength. A number of the samples were tested without tapering the ends of the patches and the effective decrease of the failure stress due to the stress concentration at the patch ends can be judged (Fig. 6). Similar results are reported for the E32 adhesive in comparison with the strength of E04 provided the base material is correctly prepared.

The carbon fibre patches used in the tests were either laminated directly onto the suitably prepared aluminium test coupons using 1927 resin or laid-up previously as a separate patch, fully cured, and finally bonded to the testpiece using F241 adhesive. In all cases, patches with tapered ends were used. It can be seen that the strength of the carbon fibre patch is similar to that of the steel patch for the range of overlap tested. Also, in a number of cases, as an alternative to patching abutting aluminium ends, notched aluminium samples were used. The average failure stress for these samples (Fig. 6) is less than for the additive failure stress of carbon patched abutting aluminium and plain aluminium samples alone.



## 6 Effect of overlap on bond strength

To compare adhesives and joint designs, fatigue tests have been carried out on welded joints reinforced with patches and patched unwelded joints. The plate material in each case was 8 mm N8 aluminium alloy and the patches were either 5 mm steel or unidirectional carbon fibre with 4 or 6 laminations. The completed specimens (similar to those used for static strength, Fig. 5) were 700 mm long, 75 mm wide at the grips, with a radius transition to a uniform 50 mm over the central 300 mm. The patch width was also



a effect of patch geometry and adhesive type; b effect of taper, number of laminations, and clamping

### 7 Fatigue strength of a bonded steel-aluminium joints and b CFRP patched specimens

50 mm and the patch overlap was 100 mm each side in all cases (i.e. 200 mm patch length).

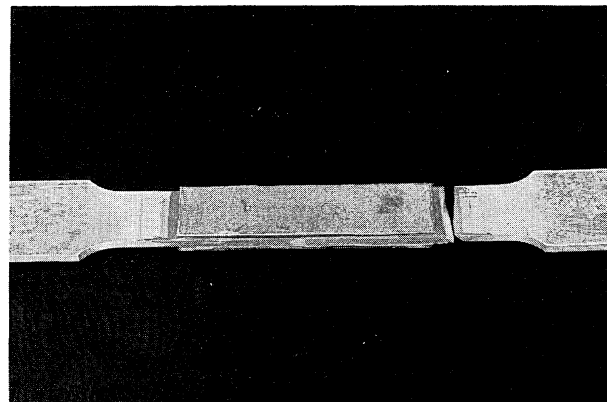
Although in practice patches applied to ships have been on one side only, the test specimens were patched on both sides to avoid bending effects. They were also tested in cyclic tension to avoid bending by buckling under compression. This is considered to be a more severe test (in terms of fatigue life for a given stress range) than the actual situation of compression-tension cycling. A minimum stress/maximum stress ratio  $R$  of 0.1 was used throughout and the test frequency was limited to 1 Hz to avoid heating effects. The steel patches had a 10:1 taper over the first 50 mm of each end to reduce the stress concentration at the ends. These were originally bonded with the longer flat surface in contact with the plate. Then, following the results reported by Adams and Wake,<sup>12</sup> it was decided to invert the patches, since the increased adhesive at the ends would be more effective in reducing the stress concentration. In each case the bond thickness over the central region was  $0.08 \pm 0.03$  mm. Also, Lees<sup>13</sup> has suggested that Permabond E32 should have a better fatigue life than E04 which had been used in the early tests and in ship repairs. Both these improvements were effective as can be seen in Fig. 7a, in which results for unwelded butt jointed specimens can be compared with the mean curve obtained for welded butt joints. The results are plotted in terms of tensile stress in the aluminium to enable direct comparison to be made with the weld for a typical plate thickness, but it must be borne in mind that the fatigue strength of the adhesive joint will be a function of the shear loading on the bond and so will vary with plate thickness.

The change from E04 to E32 adhesive increases the fatigue life by about an order of magnitude and the use of inverted patches gives a further increase of about a factor 4. Standard bonding procedure with inverted patches produces a profile approximating to that shown for type B in Fig. 7a. An attempt was made to improve this by adding further adhesive after the original bond had set and profiling to give a smooth taper (type C). This did not have the desired effect, since the adhesive cracked at the point of maximum thickness and the life was less than that of the specimens without this additional taper. Static testing gave a similar difference. A type C specimen failed at 83 kN compared with 90 and 91 kN for two type B specimens. Admittedly only three type C specimens were tested, but the results do suggest that the strength of type C joints is significantly lower than that of type B. Stress analyses are being carried out to investigate this difference and it is hoped to define the optimum taper configuration.

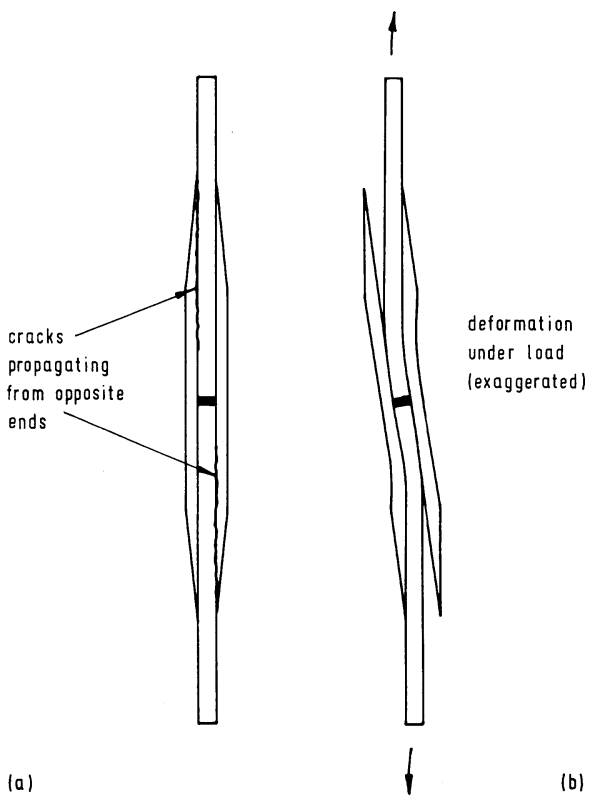
However, the type B patches with E32 adhesive appear adequate for double sided repairs to 8 mm plate, since most of the results lie above the weld fatigue curve and one specimen failed in the aluminium alloy at the end of the adhesive taper (Fig. 8).

The steel patched weld reinforcement specimens gave similar results, with inverted patches and E32 adhesive being the most successful. Most of the specimens failed in the aluminium at the start of the 37 mm radius of the width transition at an endurance of 3–4 times the mean value for a weld. However, it was possible for the patch reinforcement to have a detrimental effect on the fatigue life of the weld if the fatigue strength of the bond was inadequate. This occurred in some cases using E04 adhesive without an adhesive taper to reduce the stress concentration. The bond failure tended to initiate at opposite ends of the two patches, as illustrated in Fig. 9. This form of failure, once initiated, was maintained by the bending of the specimen which increased the peel stresses at the cracked ends. Fatigue failure ultimately occurred in the heat affected zone of the weld under the increasing direct stress as the reinforcement was reduced, plus the additional bending introduced by the asymmetry of the remaining reinforcement. This form of failure is less likely to occur in a ship because of the supporting structure, but the possibility must be borne in mind.

The CFRP specimens were produced by laminating directly onto the aluminium following the same procedure used for ship repairs. For some specimens a taper was



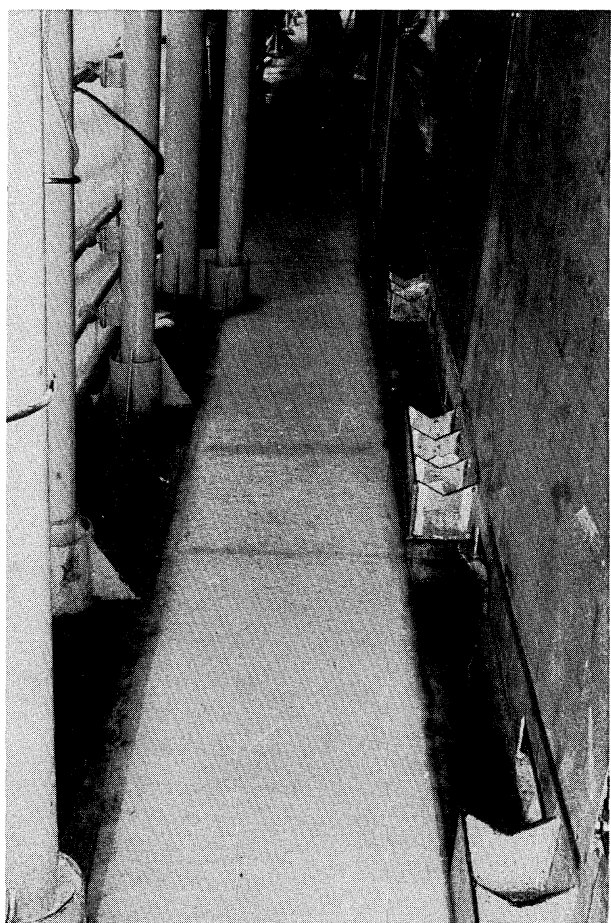
8 Steel patch specimen which failed by fatigue of aluminium



### 9 Typical mode of failure by fatigue

introduced by making successive laminations approximately 10 mm shorter. Again, both butt joints and welded specimens were tested. Initial results were disappointing. Butt joints failed at lifetimes two orders of magnitude lower than that of the weld. It was later found that improved results could be obtained for both welded and unwelded specimens if fresh silane were used for each batch. A further improvement was obtained with end clamps to produce compressive stresses in the adhesive at the ends of the patch. The clamps were bolted to the aluminium outside the patch area. The bolts had to be highly torqued so that the compressive stress generated in the aluminium prevented crack initiation from the bolt hole. An attempt was also made to improve the fatigue strength by building up an epoxy layer over the region of the ends of the patch before laminating so that the stress was relieved at the end in a manner similar to the type C steel patch specimens. These did not give a significant improvement since a crack initiated fairly rapidly normal to the plate surface at the position of maximum adhesive thickness. This then turned and propagated along the bondline to the aluminium plate. Again it is probable that finite element analysis could be used to derive an improved geometry. Results are shown in Fig. 7b in terms of the nominal stress range in the aluminium.

It can be seen that the clamped specimens are only just below the weld curve. For the CFRP reinforced weld specimens, clamped patches and unclamped patches bonded with fresh silane gave lifetimes 3–10 times that of a butt weld. Therefore, the endurance of these specimens was similar to the E32 bonded steel patches, although none of the CFRP specimens failed in the aluminium. Failure was by propagation of cracks along the bondline in a manner similar to that illustrated for steel specimens in Fig. 9. CFRP patches have proved satisfactory in ship repairs where the overlap was large, but when space is limited and the patches have to be small it appears that inverted taper steel patches bonded with E32 adhesive would be the best choice.



10 Example of deck repair using large CFRP (carbon fibre reinforced plastic) patch

### Conclusions

The use of adhesives for attaching high modulus patch materials to aluminium structures has been shown to be a useful technique where the correct surface preparation has enabled the development of adequate adhesive strength.

It has been possible successfully to use large carbon fibre patches on deck structures (Fig. 10) to accommodate both an undulating surface and changes in deck height. Where samples have been tested with short overlaps the steel patches have been shown to have a superior fatigue strength to carbon fibre patches. This could be related to the properties of the adhesive. For bonded steel patches Permabond E32 adhesive has been shown to give a better fatigue life than E04 adhesive.

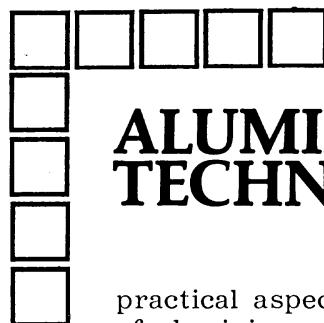
In some instances, it may be possible to use aluminium patches in place of steel, where thermal effects are a problem, provided the aluminium is thick enough to take the load.

Tapered patches have been found to be superior both for static strength and fatigue behaviour. Tapering the adhesive is more effective than tapering the patch. It would be possible to reinforce areas within an as-built structure to reduce their sensitivity to crack initiation.

The fatigue strength of patched simple butt joints has been shown to be as good as that of patched welded joints. Therefore, it may be possible to use patching without first carrying out a weld repair.

## References

1. L. REDSHAW: in Proc. Symp. on 'Welding in shipbuilding', 1962, Abington, Cambridge, The Welding Institute.
2. F. St. M. BRIERLY: *Light Met.*, April 1960.
3. C. H. POHLER, A. B. STAVOURY, J. E. BEACH, and F. F. BORRIELLO: *Nav. Eng. J.*, Oct. 1979, **91**, (5), 33.
4. 'The structural use of aluminium', British Standard Code of Practice CP 118.
5. A. A. BAKER: *Composites*, 1978, **9**, (1), 11.
6. B. DAVIS: 'Strengthening of Brinsworth Road Bridge' (Design and assembly with engineering adhesives), Cranfield Institute of Technology, 1983.
7. K. B. ARMSTRONG: in Proc. SAMPE Conf. on 'Engineering with composites', London, Mar. 1983.
8. K. W. ALLAN, S. Y. T. CHAN, and K. B. ARMSTRONG: *Int. J. Adhes. Adhes.*, 1982, **2**, (4), 239.
9. A. A. BAKER: *Compos. Struct.*, 1984, **2**, 153-181.
10. W. H. MUNSE, T. W. WILBUR, M. L. TELLALIAN, K. NICOLL, and K. WILSON: 'Fatigue characterisation of fabricated ship details for design', US Ship Structure Committee Report SSC 318, 1983.
11. W. A. DUKES, R. A. GLEDHILL, and A. J. KINLOCK: Preprints of 'Organic coatings and plastics', (ACS Philadelphia Meeting), Vol. 35, (1), p. 546.
12. R. D. ADAMS and W. C. WAKE: 'Structural adhesive joints in engineering'; 1984, London, Elsevier Applied Science Publishers.
13. W. A. LEES: personal communication, Permabond Adhesives Ltd, Eastleigh, Hants., 1984.



# ALUMINIUM TECHNOLOGY '86

Proceedings of an international conference held to mark the centenary of the Hall-Heroult molten salt electrolysis method of producing aluminium.

Papers cover the current fundamental metallurgical science of alloy production and properties, together with the more practical aspects and the principles involved for the diverse applications aerospace, architecture, electronic discs, packaging and transport.

## SUBJECT AREAS

- the aluminium industry: Overview delivered at the Plenary Session
- primary technology
- treatment of the melt
- casting technology
- deformation processing
- texture analysis
- recrystallisation
- corrosion and quench sensitivity
- aluminium-lithium alloys
- properties of aluminium alloys
- welding and brazing technology
- alloys for specific applications
- formability
- process modelling
- rapid solidification technology
- composites
- advances in equipment and control: melting and casting
- advances in equipment and control: deformation and processing

BOOK 391 280x210mm 850pp ISBN 0 904357 85 6 Casebound Published 1986

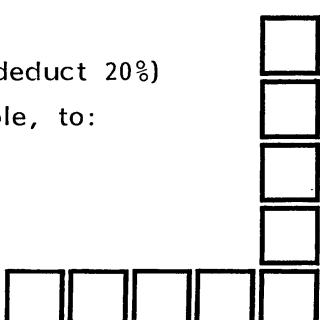
## PRICE:

UK: £59.50 Overseas: US\$125.00 (Institute of Metals members deduct 20%)

Orders with remittance, quoting membership no. where applicable, to:

**THE INSTITUTE OF METALS**  
Subscriber Services Department  
1 Carlton House Terrace  
London SW1Y 5DB

Tel. 01-839 4071 Telex 8814813



# FATIGUE IMPROVEMENT OF WELD REPAIRED CRANE RUNWAY GIRDER BY ULTRASONIC IMPACT TREATMENT

T. Tominaga<sup>a</sup>K. Matsuoka<sup>a</sup>Y. Sato<sup>b</sup>T. Suzuki<sup>c</sup>

<sup>a</sup> Steel Structure Development Center, Nippon Steel Corporation

<sup>b</sup> Kimitsu works, Nippon Steel Corporation

<sup>c</sup> Material Characterization Research Laboratory, Nippon Steel Corporation  
(Japan)

## ABSTRACT

The fatigue improvement method using ultrasonic impact treatment was examined. This method was applied to in-plane-gusset detail and out-of-plane gusset detail of existing crane runway girders. Comparison with other fatigue improvement methods was based on fatigue tests performed on small-scale welded specimens, and UIT gave the best result. Also, applicability to mild steel and the influence of repair welds was examined through girder fatigue tests. Fatigue improvement was obtained for 400 MPa class mild steel, even after repair welding.

**IIW-Thesaurus keywords:** Combined processes; Fatigue improvement; Low carbon steels; Maintenance; Post weld operations; Repair; Steels; Ultrasonic processing; Unalloyed steels.

## 1 INTRODUCTION

Crane runway girders (hereafter CRG) are the structures that support rails for cranes. They resemble bridge structures and, as with bridges, fatigue is a design criterion. Moreover, in the absence of a deck structure, working stresses in CRGs are usually larger than in bridges. Actually many fatigue cracks have been found in these structures [1]. Also the CRG structures built before the early 1970s have flange gusset details which though not used now, give poor fatigue performance. The same detail has been the source of fatigue problems in Shinkansen railway bridge structures [2].

Weld toe grinding treatment has already been applied to many of these structures, but they are now approaching

the end of the estimated fatigue life of these. To extend the fatigue life further, some kind of additional treatment was needed. Therefore, various fatigue improvement methods were compared and their effects were evaluated. As a result ultrasonic impact treatment (UIT) was selected.

With regard to the application of UIT to flange gussets, out-of-plane gussets and vertical stiffeners, the following issues are examined.

- (a) Comparison with other fatigue improvement methods on performance or ease of operation.
  - (b) Applicability of UIT to mild steels.
  - (c) Possible influence of repair welds.
  - (d) Quality control of UIT.
- (b) was considered because, for fatigue improvement methods based on the introduction of compression residual stress are known to be more effective when applied to high strength materials. Low Temperature

Doc. IIW-1860-07 (ex-doc. XIII-2170r1-07) recommended for publication by Commission XIII "Fatigue behaviour of welded components and structures".

Transformation welding material (hereafter LTT) is also more effective for high strength steels [3]. Also, many of Fisher's investigations of UIT were conducted using specimens made from HPS70 (ASTM 709), which are 600 MPa class steels [4]. However, existing old CRG structures are mostly built from 400 MPa class mild steels.

It is also known that the toughness of ferrite-pearlite steels can be reduced as a result of large compressive strain [5]. Only 1-2 mm in depth is affected by UIT, and so no such decrease of toughness is expected. Even so, this effect was also examined.

For subject (c), the problem envisaged was the large residual stress induced from repair welds. Many existing CRGs are already repaired by welding. Repair welds are conducted under conditions of high restraint, so high residual stresses are usually induced in a large area of the structure. The concern was that large tensile residual stress would reduce the beneficial effect of the compressive stress induced by UIT.

With regard to (d), a standard quality control method for UIT is already provided by Applied Ultrasonics, the company providing the UIT equipment. However, this does not include any means of controlling the residual stress level. So, from that point of view, additional quality control parameters were examined.

The resulting study included fatigue tests on welded joint specimens and large-scale components, Charpy impact tests, residual stress measurements and treatment tests to develop the application of UIT to CRGs.

## 2 EVALUATION OF FATIGUE PERFORMANCE BY SMALL SCALE WELDED JOINT SPECIMENS

### 2.1 Test parameters

Specimens consisting of plates with in-plane attachments welded to their edges (Figure 1) were used to

represent flange gusset type joints in CRGs. The weld toe condition (as-welded, toe ground or UIT) and the presence or not of a repair weld were the parameters investigated, as summarized in Table 1. The specimen geometry and details of the repair welds are shown in Figure 1. The flange gusset fillet weld size was 6 mm. Flange gussets are usually attached with full-penetration welds. However, to examine the effect of weld defects, no special care was taken to achieve these in the present specimens with the result that slight lack of penetration defects remained at the weld roots. The specimens were made from SS400 steel with L-55 weld filler material with the properties shown in Table 2.

Details of the repair welds are also shown in Figure 1. These simulated the repair of fatigue cracking from the toe of the weld around the end of the gusset, as indicated in Figure 2 a). In practice, the end of the gusset is cut away before repair, Figure 2 b), to allow sufficient access for the welding. As a result, the gusset length is reduced by around 50 mm and the repair weld does not coincide with the gusset fillet weld, Figure 2 c) and d). To simulate this, the repair welds in the present specimens were located 30 mm from the gusset ends, as indicated in Figure 1. The repair welds were made into 45 degree grooves ground into the plate to leave a 6 mm root gap. A backing plate was used and the weld was made with an interpass temperature of 50-200 °C. After the repair welding, the backing plate was gas-

**Table 1 – Specimen details**

No	Toe condition	Repair weld	Test stress (MPa)
1	as-welded	No	100
2			150
3		Yes	100
4			150
5	ground	No	100
6			150
7		No	100
8			150
9	UIT	Yes	100
10			150

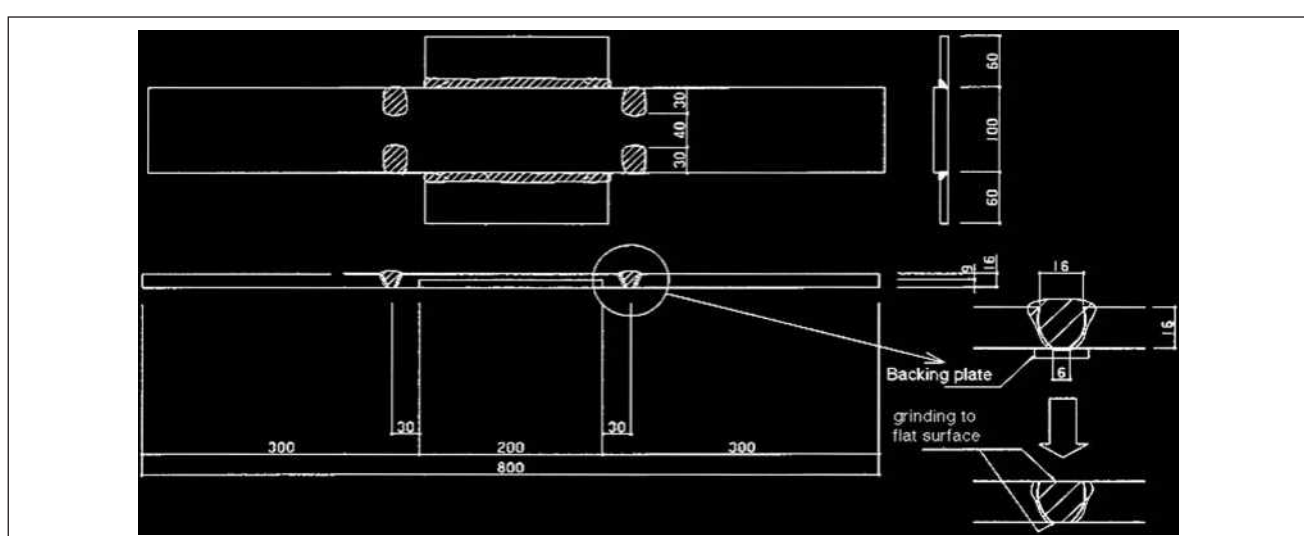


**Figure 1 – Geometry of joint specimen**

**Table 2 – Mechanical properties of materials**

Spec.	Thickness (mm)	YS (MPa)	UTS (MPa)	Elongation (%)	Note
SS400	16	286	433	34	main plate
SS400	9	311	449	31	gusset
L-55	φ 4	486	567	30	weld material

cut and the weld cap and root were ground flush with the adjacent plate surfaces.

With regard to the two weld toe improvement techniques used, both of which were applied to as-welded toes, grinding was performed with a 5 mm diameter burr grinder while UIT was carried out using a 27 kHz Esonix tool with 3 mm pins. The treatments were applied to the weld toes at the ends of the gusset and for 30 mm along the fillet weld length; the gusset side of the weld toe was not treated.

## 2.2 Fatigue test results

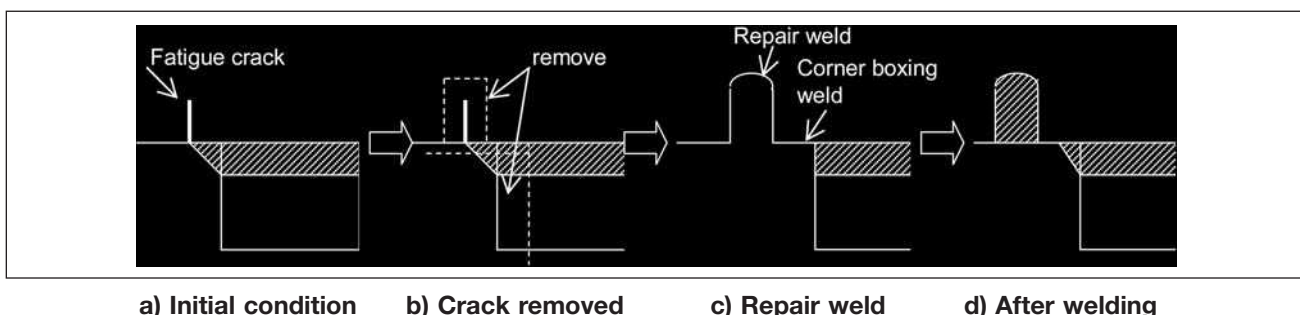
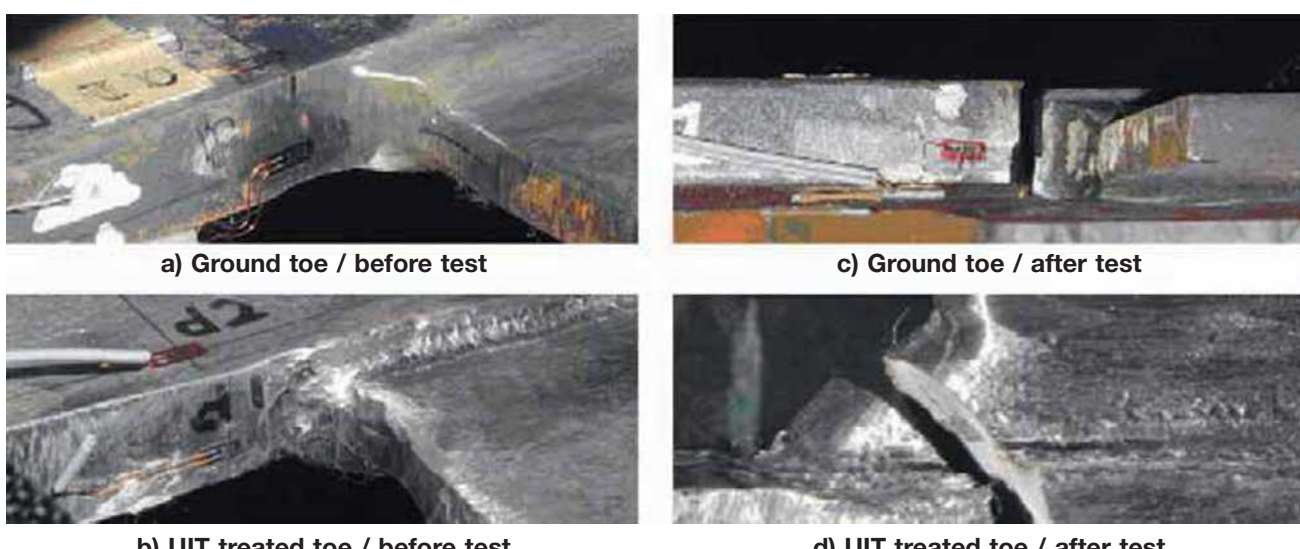
Fatigue tests were conducted at stress ranges of 100 MPa and 150 MPa, both at  $R = 0.1$ . These stresses were based on field measurements made on Nippon Steel CRGs, from which the maximum stress ever measured in a girder flange was 108 MPa.

Examples of weld toes before and after testing are shown in Figure 3. Both the ground and UIT treated surfaces were very smooth.

The fatigue test results are shown in Figure 4. Compared with grinding, UIT produced the best improvement in fatigue life. Furthermore, the benefit of UIT was not reduced as a result of the presence of repair welds. However, their presence has reduced the fatigue lives of the as-welded specimens. Examples of fatigue cracks produced in the ground and UIT treated types of specimen are shown in Figure 3. The UIT specimens failed from the weld root while the others failed from the weld toe. Thus, UIT provided effective improvement in the fatigue performance of the weld toe.

## 2.3 Residual stress and toe profiles

The effect of UIT was investigated further on the basis of examination of the weld toe profile and the residual

**Figure 2 – Weld repair procedure****Figure 3 – Welded details**

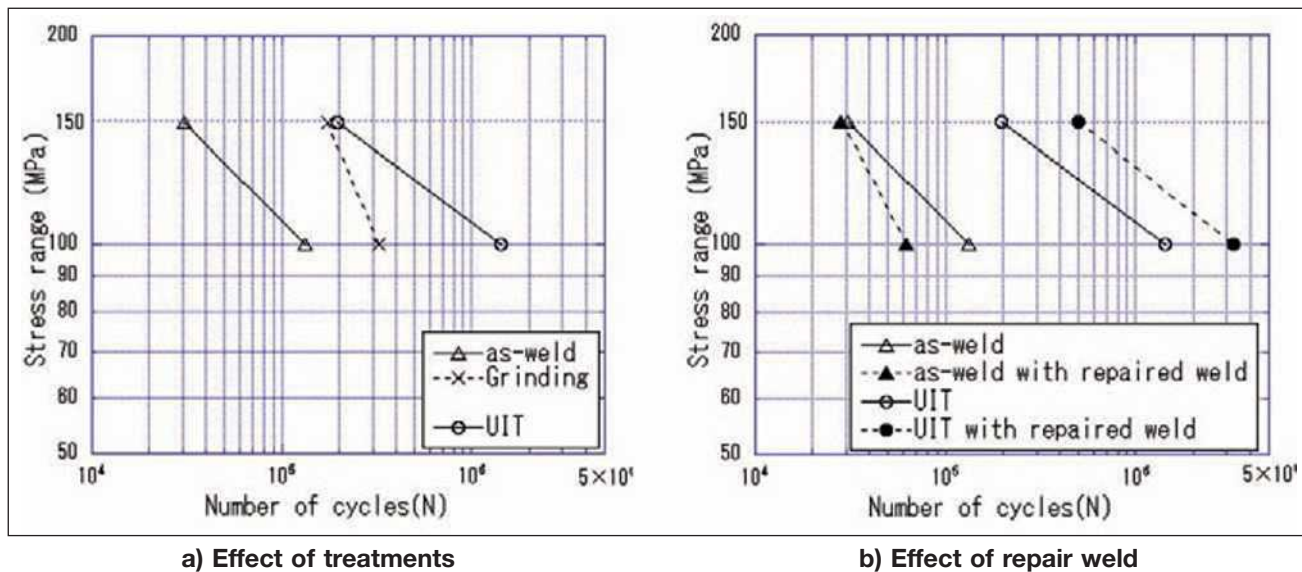


Figure 4 – Fatigue test results

stress in the specimen. The weld profiles were replicated using silicon rubber and used to measure the weld toe radius and flank angle along both sides of the weld bead. Corresponding stress concentration factors were calculated by Atokawa's method for considering a cruciform joint [6]. This was multiplied by 1.5 to allow for the additional stress concentrating effect of the flange gusset to give the final estimate of  $K_t$ . After the fatigue testing, residual stresses were measured in the tested specimens near weld toes that did not experience any fatigue cracking. Strain gauges were attached 5 mm from the weld toe. The cutting method was used to measure residual stress, the cutting position being as shown in Figure 5, and residual stresses deduced from the strain changes when the material containing the gauge was cut out (see Figure 5). The gauge position 5 mm from weld toe is too far to measure the resi-

dual stress at the toe, but it is considered suitable for measuring the residual stress from the repair weld.

Details of the toe profiles and average value of  $K_t$  are shown in Figure 6.  $K_t$  for UIT treated toes is about 75 % of that for the as-welded.

The results of the residual stress measurements are shown in Table 3. These show that the repair weld has introduced tensile residual stress in the as-welded specimens. However, the fact that the residual stress was compressive after UIT in specimens with

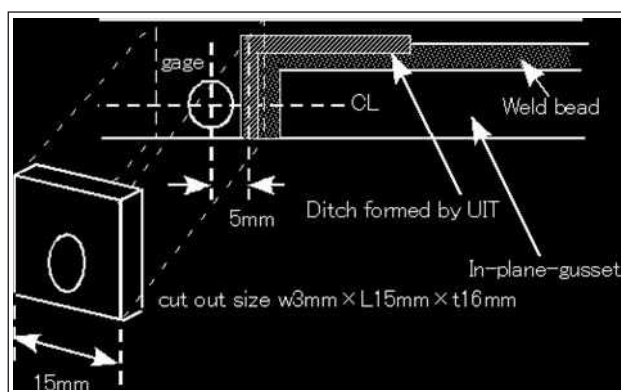


Figure 5 – Geometry of cutting method

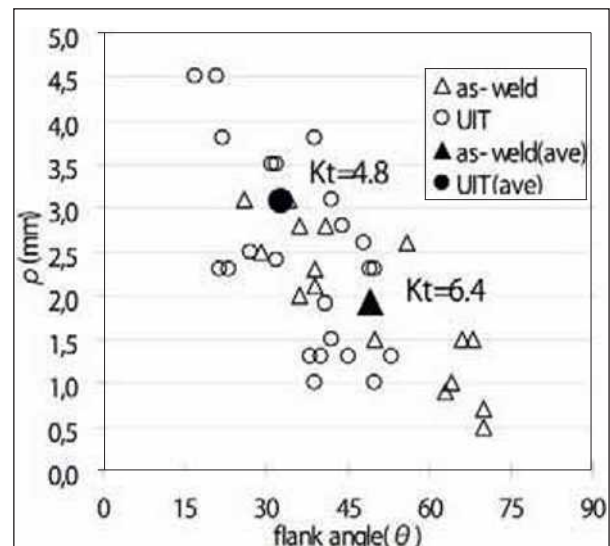


Figure 6 – Toe profiles and stress concentration factor

Table 3 – Results of residual stress measurements

No	Toe condition	Repair weld	Test stress (MPa)	Residual stress (MPa)
1	as-welded	No	100	-21
3		Yes	100	121
9	UIT	No	100	-65
11		Yes	100	-63

or without repairs indicates that this tensile stress was then changed to a compressive residual stress by UIT. Compressive residual stress was measured in the as-welded specimen without UIT. This might be due to stress re-distribution from fatigue test loading.

Thus, these results confirm that UIT is beneficial in terms of reduced stress concentration and the introduction of compressive residual stress. They also verify that residual stress improvement by UIT is not affected by the presence of a repair weld.

### 3 LARGE SCALE FATIGUE TESTS

### 3.1 Test parameters

Large scale fatigue tests were conducted on two specimens with the geometry shown in Figure 7. This was a welded plate girder structure with in-plane gussets, out-of-plane gussets and vertical stiffeners. To examine the effect of steel strength [subject (b)], it was fabricated from 400 MPa class mild steel. To examine the effects of UIT [subject (a)] and repair welds [(subject (c)], tests were conducted according to the procedure shown in Table 4.

Specimen No. 1 was the case of UIT without a repair weld, so the UIT treatment was conducted before the initial loading started. (Toes were not ground, before UIT.) Specimen No. 2 was the case of a toe ground beam in which, after initiating a fatigue crack, the crack

was repaired by welding. Then, UIT treatment was conducted after weld repair, giving a UIT with repair weld case. (Repair welded toes were not ground, before UIT.) In this way, for each specimen, both the effect of UIT (N1 and N2) and the effect of repair welding on the benefit of UIT (N1 and N = Ne2 - N2) could be examined.

The toe grinding and UIT conditions were the same as those used to treat the small-scale welded joint specimens. For the UIT treatment time, 32 weld toes in out-of-plane gussets on one side of a web could be treated in about 26 minutes, including the time taken for the operator to change position. Therefore about 50 seconds of treatment time was needed for each weld detail including the position changing. The treatment was done in the flat position. Examples of weld toes at the end of gussets after UIT are shown in Figure 8.

### **3.2 Test procedure**

The applied fatigue test load was 50-460 kN, which produced a stress of 15-154 MPa in the flange at the centre of the bending section. The highest stress for in-plane flange gussets detail was 15-154 MPa, with 12-125 MPa for out-of-plane gussets. These stresses are very high compared with the allowable stress for 400 MPa class steel.

Small, 1 mm gauge length, strain gauges were attached near each weld detail, 5 mm from the weld toe. By

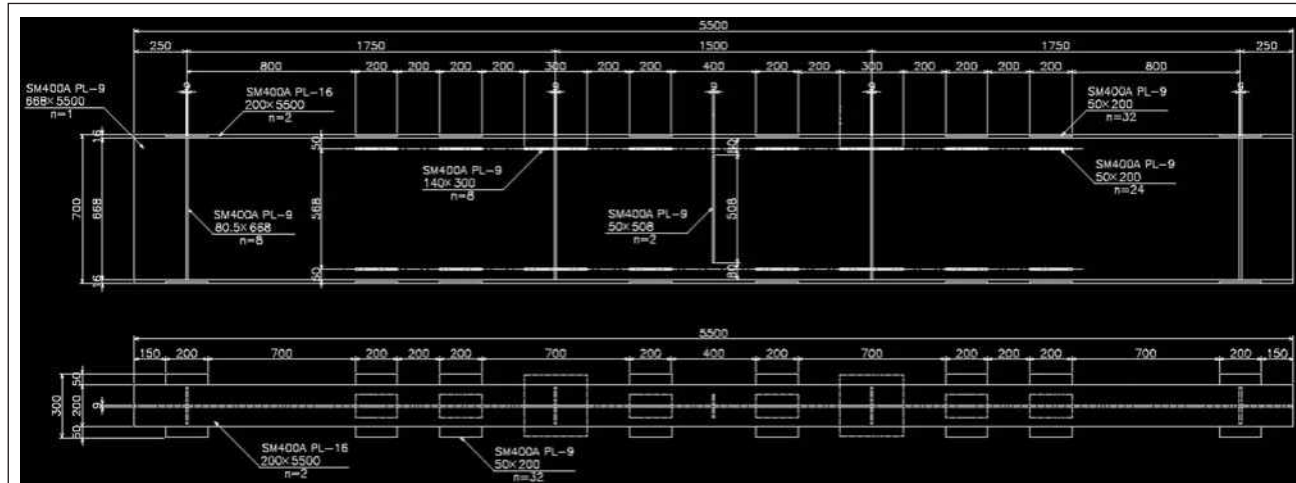


**Figure 7 – Geometry of large scale specimen**

**Table 4 – Test procedure for each specimen**

Condition	No. 1	No. 2	Loading cycles
Initial	UIT	grinder	0
Repairing method	crack removal and bolted splice	repair weld and UIT	N1, N2
Finished condition			
N1	: Number of cycles, when crack initiated in No. 1 specimen (for each crack).		
Ne1	: Total loading cycles of No-1 specimen.		
N2	: Number of cycles, when crack initiated in No. 2 specimen (for each crack).		
Ne2	: Total loading cycles of No-2 specimen.		



a) Weld toe at end of in-plane gusset

b) Weld toe at end of out-of-plane gusset  
(boxing weld)

Figure 8 – UIT treated details on flanges

placing them very close to the toe, the local stress change due to applied load was measured. Among the attached strain gauges, 24 highly stressed details were monitored continuously during the fatigue testing. If a local stress change was observed, the loading was stopped immediately and the weld toe checked by magnetic particle testing (MT) for evidence of fatigue cracking. At the same time, a static loading test was conducted.

When the crack length reached 10 mm, the fatigue endurance was recorded as  $N_f$  cycles. When the length of cracks at flange gusset details exceeded 10 mm, they were removed by grinding, or gas cutting. The cracks at out-of-plane gussets were stopped by drilling holes at their tips (stop-hole). In the case of specimen No.1, when many cracks had initiated and the remaining cross-section became too small, the parts where cracks had been removed were stiffened by bolting additional plates over them. For specimen No. 2, after removing cracks by grinding or gas cutting, repair welding was conducted. The repair welds were made using 4 mm S-16 electrodes (YP: 460 MPa, UTS: 540 MPa), and ceramic soft backing. To improve the root fatigue performance, the weld size at the end of the flange gusset was increased by making the repair weld in two passes (see section 3.4). The resulting repair welds around the ends of the gussets were not

ground but simply treated with UIT to prevent fatigue cracking from weld toe.

The aim of this procedure was to achieve as many fatigue loading cycles as possible, so that many fatigue cracks could be observed.

### 3.3 Strain changes due to the first applied loading

Longitudinal gusset details in the as-welded condition usually contain very high tensile residual stress, sometimes greater than yield, due to welding. However, re-distribution of such stresses can take place during the first applied loading. If a fatigue improvement method that controls the residual stress is applied, this re-distribution at the first cycle should be affected by the improvement method. So, useful information is often obtained from the stress measurement data obtained during the first loading cycle.

Typical stress-strain curves at the first cycle for both details are shown in Figure 9. UIT treated and untreated cases are shown for both flange gusset (hereafter FG) and out-of-plane gusset (hereafter WG). The comparison is also done for both the tension and compression sides of the beam. For the normal weld on the tension side, large plastic strains were induced and

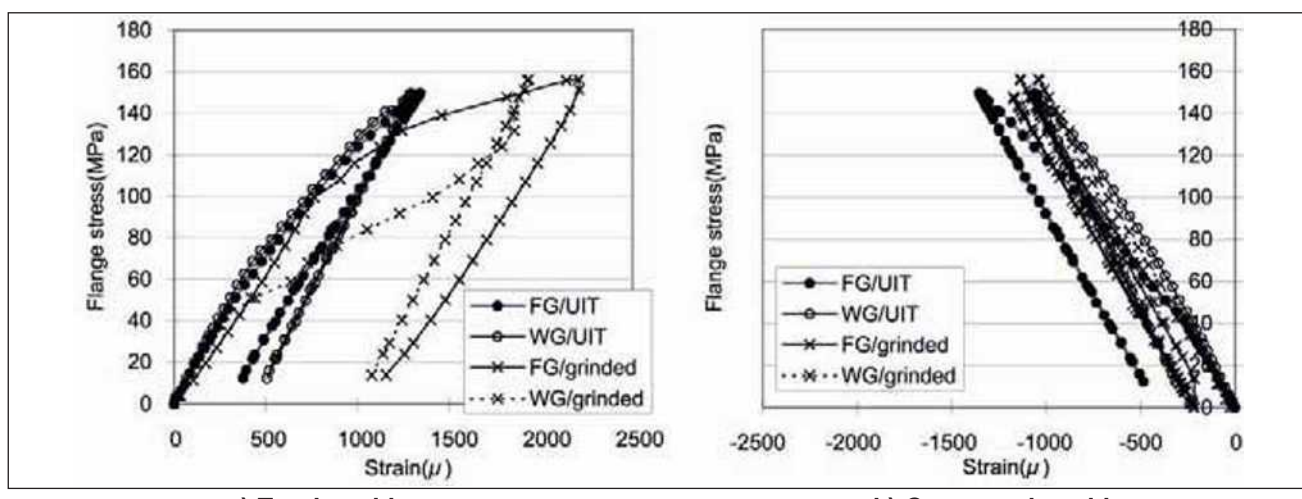


Figure 9 – Stress-strain relation during first loading cycle

tensile residual strains were left. This is consistent with the presence of high tensile residual stress, such that the subsequent application of additional tensile stress from loading produces extensive plasticity. In contrast, large plasticity did not take place in the UIT treated details and the residual strains were smaller. This is because before applying the loading the material was in compression, from the compressive residual stress induced by applying UIT. Also, for the compression side, the residual strains are slightly larger for the UIT treated details, due to the residual stress induced by UIT. In this way, tensile residual stresses provide residual strain for the tension side and compressive residual stresses provide residual strain for the compression side. Thus, from the first time loading residual strain, the stress condition at welded toes can be estimated roughly. Relations of residual strain and applied nominal stress for all the welded toes in the specimens are shown in Figure 10. One graph is for the flange gussets and other is for the out-of-plane gussets. UIT treated cases have smaller residual strain on the tension side, but larger in the compression side. Residual strains for untreated cases are larger for out-of-plane gussets than flange gussets. A possible explanation for this is that the stress concentration factor for the out-

of-plane gusset is higher than that of flange gussets. But the slopes of the stress-load curves in Figure 9 are almost the same for out-of-plane gussets and flange gussets.

Residual strains obtained from first loading of details containing repair welds are also shown in Figure 10. All these cases refer to UIT treated welds. However, comparing the data for normal UIT and repair weld UIT, no significant difference can be found. Tensile residual stress might be induced by the repair weld in a comparatively large area, but the stress condition formed by UIT at each detail is not affected by the original residual stress condition, before UIT treatment.

### 3.4 Repair welds

Repaired welded details are shown in Figure 11. For the flange gussets, Figure 11 b), it proved to be very difficult to produce good welds due to welding position limitations. As noted previously, to increase the root fatigue resistance, the weld size at the end of the gusset was made larger than that of the original welds (6 mm).

Repair welding changes the residual stress in a relatively large area surrounding the repair. This is evi-

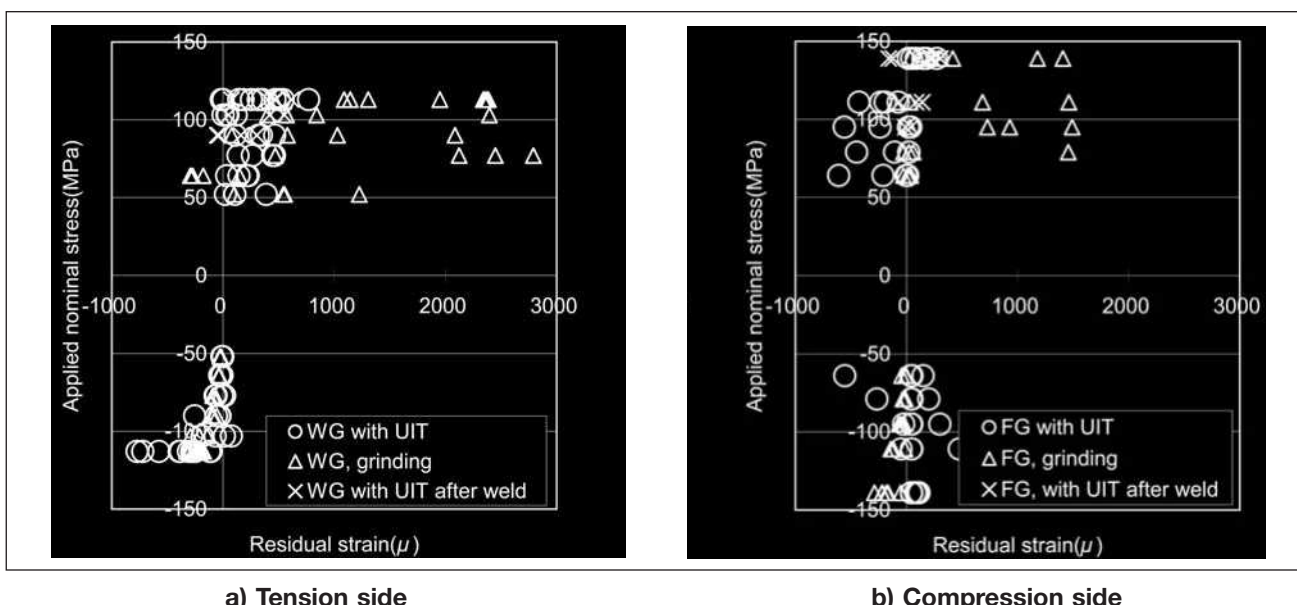


Figure 10 – Residual strain-applied stress relation



Figure 11 – Repaired welded details

dent from Figure 12 which shows the change of strain following repair welding close to location B3. It will be seen that the strain change was over 600 micro strain at the flange edge on the opposite side to the repaired flange. This is an increase in tensile residual stress of about 120 MPa, assuming all the strain is elastic. The strain change has dropped to 200 micro strain at B2, 200 mm from the repair weld, but is still 100 micro strain (20 MPa) 400 mm away. Also, for the upper flange, the compressive stress increased.

A total of nine repairs were carried out but re-application of UIT for relevant adjacent details that had been

UIT treated previously was not carried out. But from the obtained data, if the repaired welding is conducted and there is UIT treated (treated before the repair welding) detail within 300-400 mm, re-treatment is favourable to recover residual stress condition.

### 3.5 Fatigue performance

Typical fatigue cracks are shown in Figure 13 and the fatigue test results are plotted in Figure 14, together with relevant design S-N curves from the Japanese

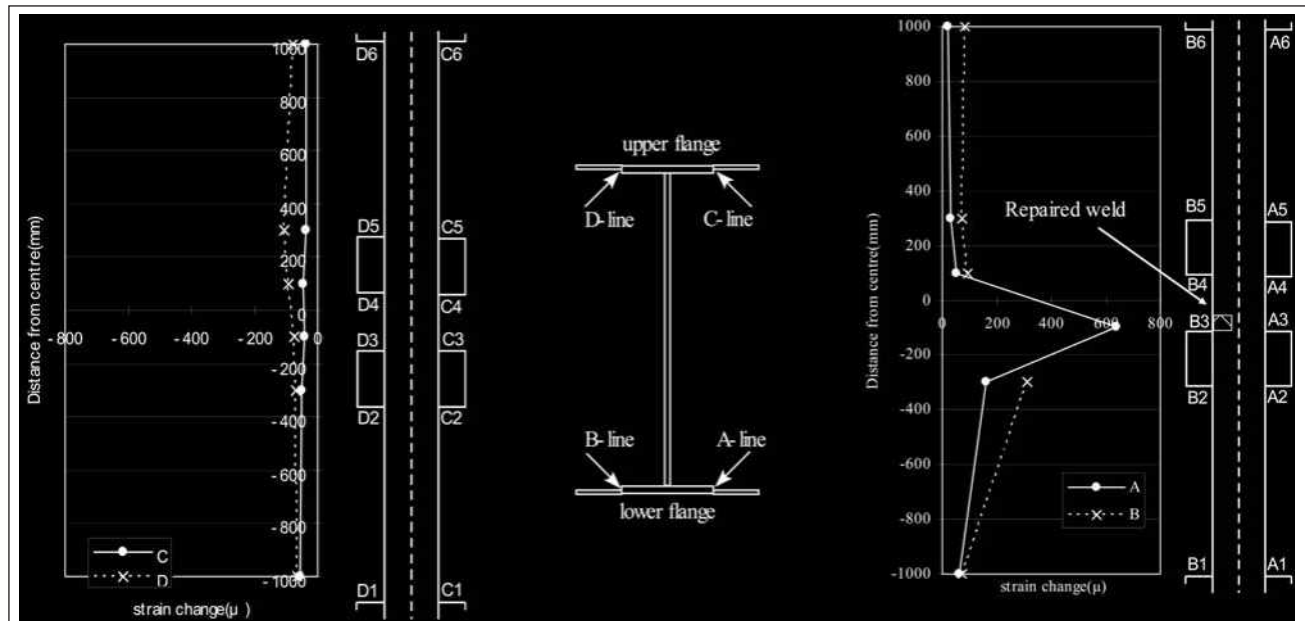


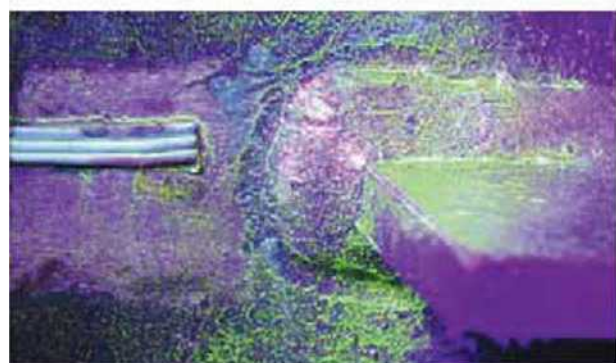
Figure 12 – Strain distribution change due to repaired weld



a) Flange gusset / ground



c) Flange gusset / UIT



b) Out-of-plane gusset / ground



d) Out-of-plane gusset/ UIT

Figure 13 – Typical fatigue cracks

JSSC fatigue design code. Specimen No. 1, which started with weld toes treated by UIT, was tested for 2.01 million cycles. Specimen No. 2, which started with ground weld toes, continued for 1.36 million cycles, at which time a fatigue crack initiated at the fillet weld between the flange and web end, the test had to be terminated. (This detail was UIT treated in specimen No. 1 and there was no evidence of fatigue cracking). In Figure 14, "No crack" means there was no evidence of cracking from the detail at the end of the fatigue test. Symbols with the arrow are results without fatigue cracks. Fatigue classes are classified by JSSC (Japan Society of Steel Construction) standards.

For the ground welds, toe cracks initiated at a very early stage of loading. However, all the fatigue cracks in UIT treated details initiated at the weld root. In the case of the flange gussets, for a stress range of 139 MPa the first crack initiated at about 110 000 cycles for the ground toe compared with about 390 000 cycles, 3.5 times longer, in the UIT treated detail. In fact, there was a significant decrease of strain in the toe ground

case after about 70 000 cycles. This may have been due to crack initiation, in which case the margin between crack initiation in toe ground and UIT details increases to more than 5. At lower applied stress ranges the difference is larger, corresponding to a factor of about 8.8 at a stress of 111 MPa. Similar effects were observed in the out-of-plane gussets. At a stress range of 113 MPa, the first crack in a toe ground detail was observed at 260 000 cycles, compared with 1.36 million cycles for the UIT case, about 5.2 times higher. The flange gusset detail is classified as JSSC Class H. Referring to Figure 14, toe grinding increased the performance by one class to G. However, UIT improved it by three classes, to E. For the out-of-plane gusset, only G-E class performance was obtained by grinding, whereas again UIT improved the performance by three classes, to D. For some details treated by grinding, there was no improvement. Many of the grooves formed by grinding were more than 1 mm depth. Thus, these comparatively short lives were attributed to over-grinding.

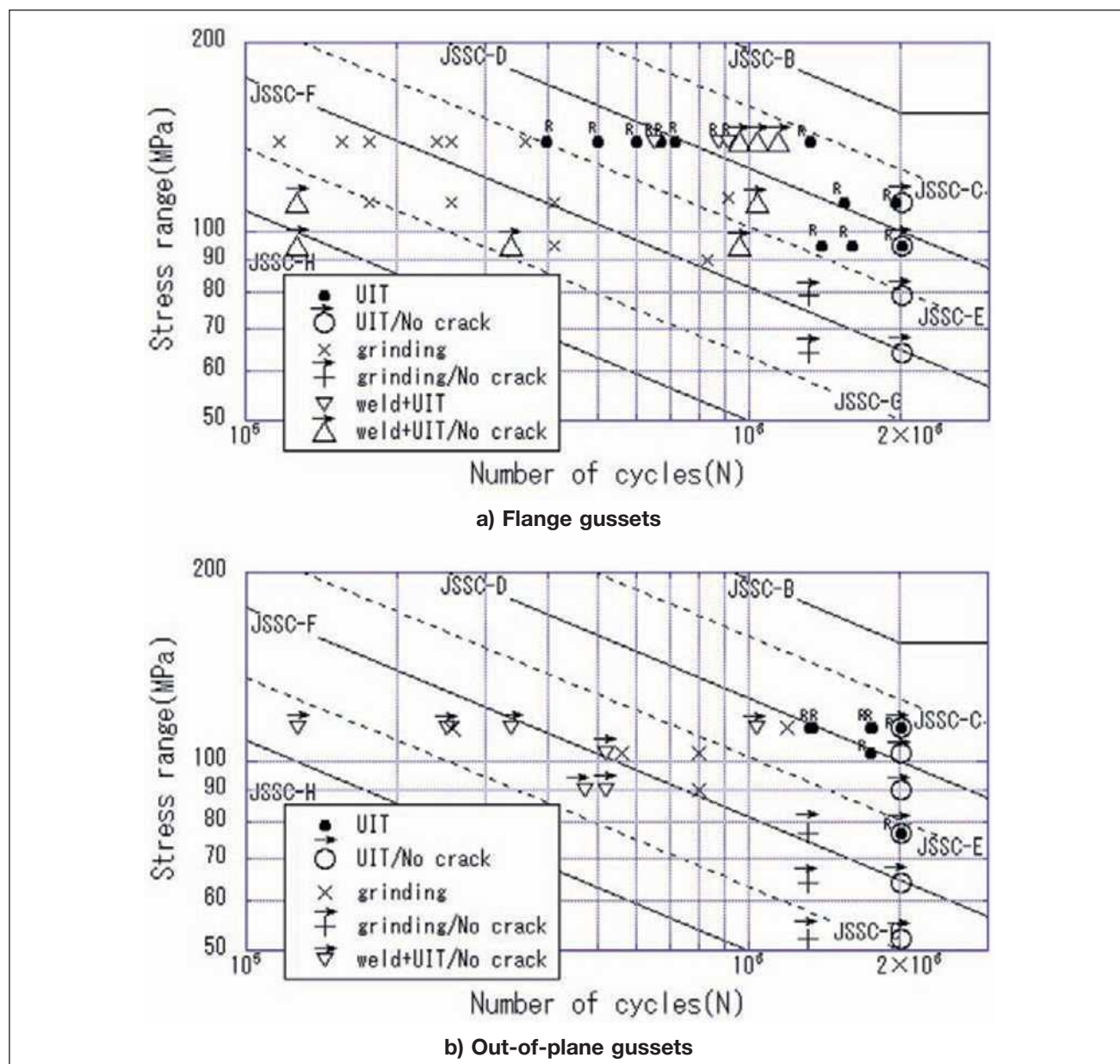


Figure 14 – S-N relations

No fatigue cracks initiated from the edges of UIT treated weld repaired gussets. However, some cracks initiated from the repair weld. As the repair welding conditions were very poor, cracks initiated from weld defects within the weld metal. However, even in that case, about 650 000 cycles were achieved. This is longer than the lowest life of 390 000 cycles achieved by UIT treatment of normal welds, a result that is believed to reflect the extra benefit obtained by increasing the weld size when making the repair welds.

Similarly no fatigue cracks initiated from UIT treated repaired out-of-plane gusset details. The maximum fatigue life obtained from these details was 1.03 million cycles, which is very close to the life of 1.32 million cycles obtained from the UIT treated normal weld, without a repair. If it had not been necessary to terminate the test due to fatigue cracking from the flange to web fillet, clearly a greater improvement may have been obtained.

## 4 TREATMENT TESTS

### 4.1 Ease of operation

To compare the 'ease of operation' of UIT to other improvement methods [subject (a)], basic treatment tests were conducted. Acceleration of the tool and noise were measured. Figure 15 shows the configurations of the basic treatment test and the measuring equipment. The UIT tool was set on the support frame and the treatment was applied onto steel plates under constant load. An acceleration meter was set on the tool and a microphone was located 2 m from the tool.

Measurements were also made during hammer peening (HP) and the results compared. For the hammer peening, a compressed air powered ACJ-16 (product of NITTO KOHKI Co.) gun was used. The tip of the tool was modified to a shape suitable for peening. The force needed to keep the tool in contact with the plate during treatment was 3.5 kgf for UIT, and 20 kgf for HP.

The measured acceleration and noise are given in Table 5. Both the noise and acceleration were smaller in the case of UIT, especially the latter.

As UIT is powered by an ultrasonic generator, the density of impulses is very large. Consequently, uniform

**Table 5 – Acceleration and noise**

Tool	Acceleration rms ( $\text{m/s}^2$ )	Max acceleration ( $\text{m/s}^2$ )	Noise (dB)
UIT	16 ~ 18	90	69 ~ 74
HP	562 ~ 631	1 200	83 ~ 87

deformation of the steel surface can be produced. An example of a uniform and smooth treated surface is shown in Figure 16.

### 4.2 Residual stress

To find the parameter for controlling residual stress [subject (d)], a further basic treatment test was conducted, again using the configuration shown in Figure 15. The test plate was placed on slider, and moved back and forth manually. Both operating parameters and the plate treated were varied and measurements made on surface geometry and residual stress produced.

The parameters varied were pin type, power, treatment speed, number of treatment passes, treatment time, applied force, welding, and steel strength. The test plate size was 300 mm length and 100 mm width. Both 9 mm and 28 mm thickness plates were used. Geometry measurements were made using a contact roughness meter having 1 micron accuracy. Residual stresses were measured by X-ray diffraction (RIKEN 20 kV/10 mA). A 2 mm collimator was used because no significant difference was found between the results for 1 mm and 2 mm collimators.

One of the sets of results is shown in Figure 17. A close relation is found between the width of the groove

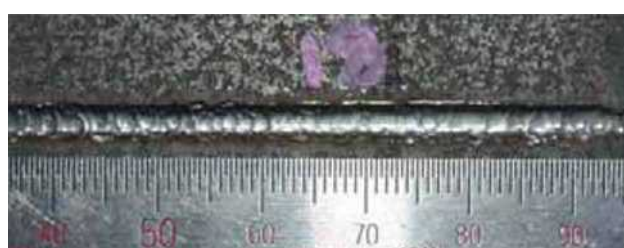


**Figure 16 – Surface deformation produced by UIT**

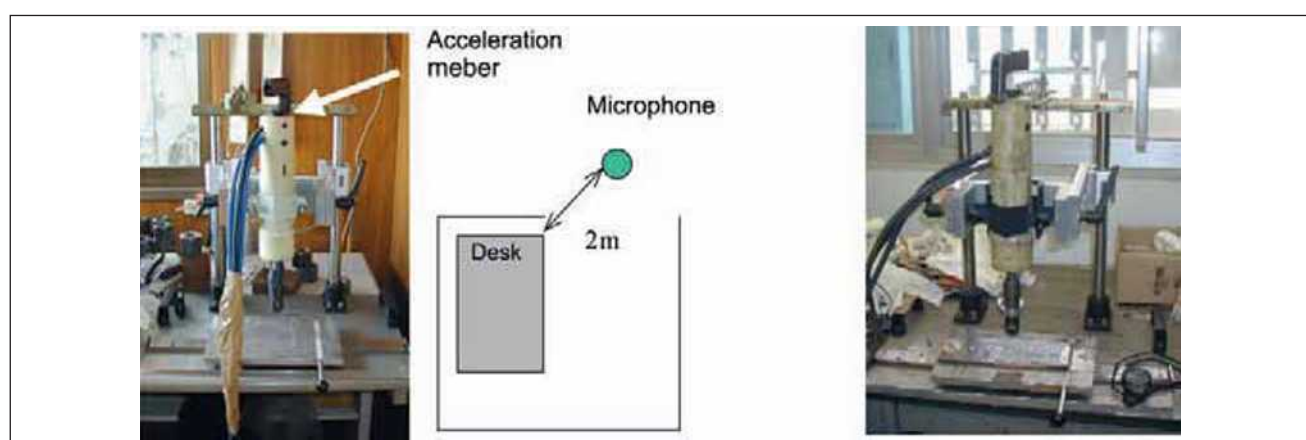


**Figure 15 – Configuration of treatment and measurements**

produced by deformation of the surface metal and the magnitude of the induced compressive residual stress acting transverse to the groove direction. So the size of the groove formed is selected as an important quality control parameter, leading to the requirement of a groove width of 4 mm.

#### 4.3 Field efficiency test

Test treatment was conducted on existing structures to examine the practicability of applying UIT in the field as compared with grinding. Using the full scale girder model shown in Figure 18, test treatment was conducted by UIT and grinding in the flat, horizontal, and overhead positions. After using in one position, the equipment set was dismantled, carried to a new location, and then set up again. The treatment length for each operating position was 2 m. Scaffolding was required in order to apply treatment in the horizontal and overhead positions. The grinder was air driven

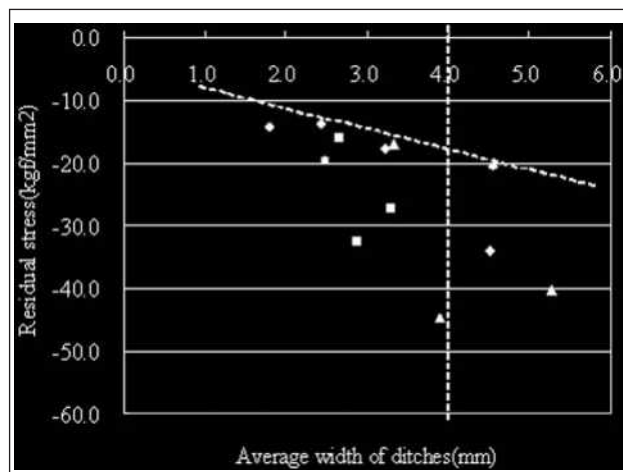


Figure 17 – Relation between residual stress and UIT groove width



and was applied using a high strength tool with a cone shaped tip. The time consumed carrying out each treatment was measured to examine the relative efficiency in field conditions of the two treatment methods.

The test results are shown in Table 6. The average treatment speed of UIT was about 4 times faster than that of grinding. The physical burden from UIT treatment is much smaller than that from a grinder with the result that the treatment time rate can be higher. The estimated treatment length in one day, calculated from the treatment time rate, is shown in Table 7. This shows that the treatment efficiency of UIT can be 4.4 to 6.6 times greater than that of grinding.

Table 6 – Measured treatment time

	UIT 27 kHz	Grinder
Average treatment speed [cm/min]	43.0	11.0
Equipment transfer time [min]	10.0-10.8	0.5-0.9
Break time/ treatment time [min]	0/10	8.0/45.2

Table 7 – Treatment efficiency

UIT		Grinder	
Treatment time rate	Treatment length of toes of welds	Treatment time rate	Treatment length of toes of welds
35 %	6 540 cm/day	30 %	1 410 cm/day
50 %	9 340 cm/day	-	-

#### 5 TOUGHNESS OF WELDED JOINTS

UIT causes plastic deformation of the metal surface and hence the introduction of compressive residual stress. It has been suggested that the depth of plastic deformation up to 1.5-2.5 mm, and the depth of the residual compressive stress field extend up to 15 mm



Figure 18 – Condition of field treatment test

[7]. This residual stress decreasing effect has not yet been verified. However, if such a large-scale effect really exists, it should be confirmed that there is no degradation in the fracture toughness of the material as a result of UIT treatment, especially for ferrite-pearlite steel [subject (b)]. Therefore, a simple examination was conducted involving the use of Charpy impact tests to detect evidence of possible reduced toughness following the application of UIT.

In particular, the influence on toughness of the following parameters was investigated.

- a) With or without UIT.
- b) With or without welding.
- c) Direction C and L; (L is rolling direction of the plate, C is the transverse).

Three tests were performed for each parameter leading to 24 Charpy tests, all conducted at 0 degrees C.

The geometries of the specimens are shown in Figure 19. They were made from 16 mm thick SN490

steel plate with the chemical composition and mechanical properties, from the mill sheet data, shown in Table 8. For the welded sample, in order to produce a re-heated zone (heat-affected zone of both beads) with poor toughness, 2 weld beads are laid side by side. The weld material was YM-26 and the heat input was 2.5 kJ/mm. UIT was applied along the centre of the plate in the L-direction using 27 kHz tool with 3 mm diameter pins at a treatment density of 3 sec/cm. For the welded specimen, the treatment was applied between the two weld beads. The Charpy specimen notches were placed just under the groove produced by UIT. The Charpy specimens were standard 10 mm size, with a 2 mm deep notch.

The Charpy test results obtained are presented in Table 9. It will be seen that the UIT has not influenced the toughness of the steel in either the L or C direction. The toughness of the welded specimens was lower but again not influenced by the application of UIT.

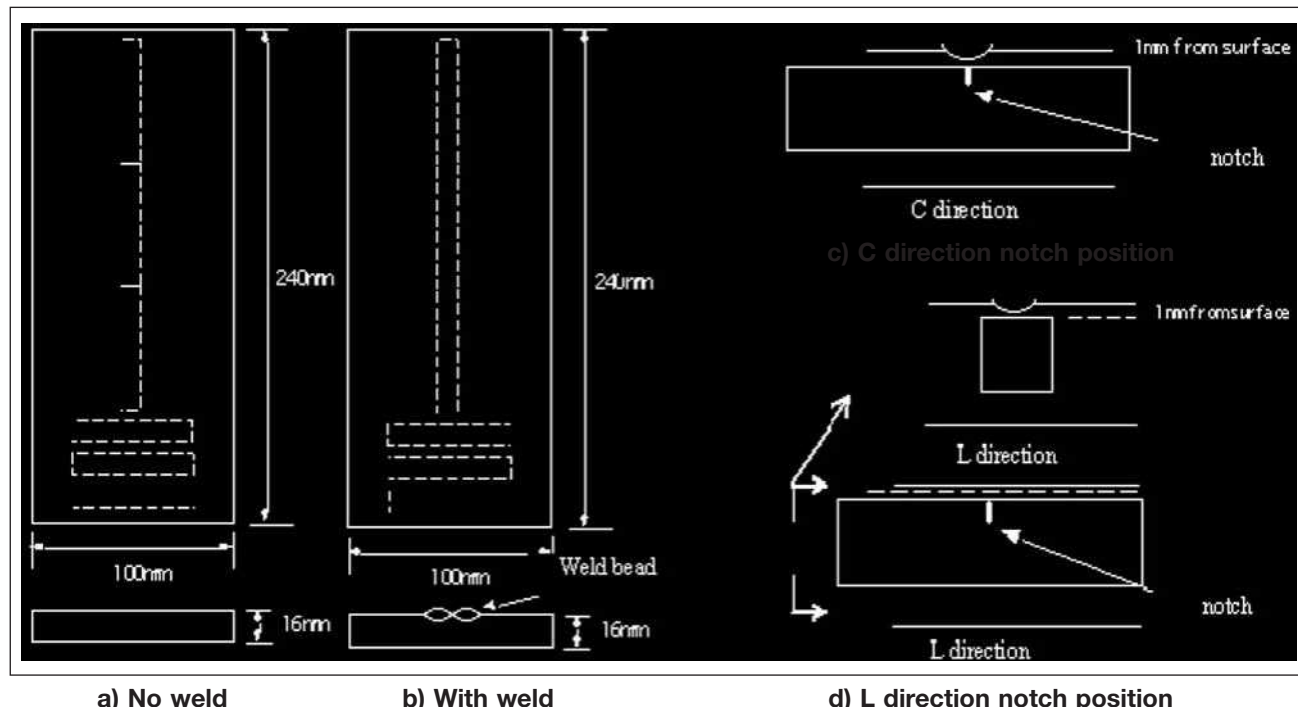


Figure 19 – Geometry of specimens

Table 8 – Chemical compositions

C	Si	Mn	P	S	Ni	Mo	Cr	CEQ	YS (MPa)	TS (MPa)	EL (%)
0.16	0.35	1.44	0.025	0.005	0.02	0.01	0.03	0.42	352	543	25

(※ unit: weight%)

Table 9 – Charpy results

Condition		C-direction		L-direction	
		Charpy (J)	Ave.	Charpy (J)	Ave.
No welding	UIT	209.1, 224.7, 231.3	221.7	213.6, 189.9, 223.2	208.9
	no UIT	216.2, 227.2, 222.8	222.1	175.3, 214.6, 217.2	202.4
Welding	UIT	109.2, 104.4, 108.7	107.4	111.6, 108.2, 104.4	108.1
	no UIT	108.7, 116.4, 116.9	114.0	97.3, 113.5, 109.2	106.7

## 6 CONCLUSIONS

In this study, the conditions needed for the application of UIT to existing welded 400 MPa class mild steel structures and its effect in terms of improved fatigue resistance were examined on the basis of fatigue tests on small-scale welded joints and large scale welded structures, together with Charpy impact tests. The following conclusions may be drawn.

- a) UIT improved the fatigue performance of flange gusset details, both original welds and repair welds, by an amount equivalent to a 3-class increase in the JSSC fatigue design rules (life increase of approximately 8). Toe grinding was less effective, around one-class increase.
- b) The benefit of UIT was not reduced in the presence of an adjacent weld repair.
- c) UIT was also more efficient than grinding in the treatment of weld toes at the ends of both in-plane and out-of-plane gussets. UIT was also more favourable than hammer peening with regard to ease of operation, including noise level.
- d) There was no evidence that the plastic deformation due to UIT reduced the fracture toughness of the steel.
- e) The most effective measure of quality control for weld toe UIT treatment was the size of the groove produced.



**Figure 20 – UIT treatment work**

As a result of the study described in this paper, Nippon Steel started to apply UIT to CRGs. Figure 20 shows the treatment being carried out on one CRG. The result of such treatment of existing steel structures will be more healthy, safe and economical operation of facilities.

## ACKNOWLEDGEMENTS

We appreciate the support and good advice from Dr. Statnikov of Applied Ultrasonics on UIT treatment.

We also appreciate the kind and practical advice from Prof. Wohlfahrt of T.U. Braunschweig and his colleagues on the X-ray residual stress measurement technique.

## REFERENCES

- [1] Tenjousoukoubari Konnwakai: Report of crane girders fatigue damages, JSSC, 1976, Vol. 12, No. 128, pp. 9-22.
- [2] Miki C., Sugimoto I., Kaji H., Megishi H., Ito Y.: A Study on fatigue strength improvement of flange gusset in existing steel railway bridges, Journal of structural mechanics and earthquake engineering, 1998.1, No. 584/I-42, pp. 67-77.
- [3] Tominaga T., Miki C., Takahashi K., Kasuya T., Morikage Y.: Fatigue improvement method for existing bridge by low temperature transformation welding materials, Journal of structural mechanics and earthquake engineering, 2004.4, No. 759/I-67, pp. 355-367.
- [4] Takamori H, Fisher J.W.: Tests of large girders treated to enhance fatigue strength, Transportation research record 1696, paper no. 5B0093, 1999.
- [5] Sasaki E., Arakawa T., Miki C., Ichikaw A.: Required fracture toughness of steel to prevent brittle fracture during earthquakes in steel bridge piers, Journal of structural mechanics and earthquake engineering, 2003.4, No. 731/I-63, pp. 93-102.
- [6] Ushirokawa O., Nakayama E.: Stress concentration factor at welded joints, Ishikawajimaharima Gihou, 1983, Vol. 23, No. 4.
- [7] Statnikov E.Sh.: Application of operational ultrasonic impact treatment (UIT) technology in production of welded joints, IIW Doc. XIII-1667-97, 1997.

# WELD REPAIR FOR FATIGUE-CRACKED JOINTS IN STEEL BRIDGES BY APPLYING LOW TEMPERATURE TRANSFORMATION WELDING WIRE

C. Miki, T. Hanji and K. Tokunaga

## ABSTRACT

When repairing fatigue damage by welding, the fatigue strength of cracked joints needs to be restored and also improved to prevent the reoccurrence of cracks. In this study, a new welding wire called low temperature transformation (LTT) welding wire, which enables the introduction of compressive residual stresses around a weld bead and the reduction of weld deformation, was applied to the weld repair. Its applicability was investigated by fatigue tests with compact tension specimens and a plate girder specimen. The compact tension specimens revealed that compressive residual stresses introduced by LTT welding wire have positive effects on crack initiation and propagation behaviour. The plate girder specimen indicated that the fatigue lives of cracked joints are restored and also improved by weld repair with LTT welding wire. Therefore, weld repair with LTT welding wire makes it possible to improve the fatigue strength of cracked joints.

*IIW-Thesaurus keywords:* Fatigue cracks; Low temperature; Transformation; Consumables; Repair; Residual stresses; Welded joints.

## 1 Introduction

Bolted splices are widely used in steel structures as repair and retrofitting methods for fatigue damage [1], in which additional steel plates are attached to cracked parts with bolts to reduce acting stress. The bolted splice can be a powerful retrofitting method. However, when considering its working speed, it is not always efficient for relatively minor fatigue damage. Besides, the bolted splice cannot be applied to some fatigue cracks because of limited workspace around them.

One of the proper repair methods for minor fatigue damage can include gouging and re-welding. Weld repair will be the more cost-efficient solution and will shorten the work period, compared with the conventional bolted splice method, because no additional members such as splice plates are required. However, with weld repair, there is the possibility of inducing weld defects or residual deformation which may reduce the fatigue strength of repaired joints. In previous research on weld repair [2, 3], it has been presented that the fatigue strength of repaired joints, which depends on weld quality, can recover to the same level as the initial conditions, if cracks are completely removed. That means, even though cracked joints are restored to the initial condition with sound weld repairs, cracks will reoccur in repaired parts because the fatigue strength

of cracked joints is originally low in most of the cases. Therefore, after conventional weld repair, the fatigue strength of repaired joints must be improved by post-weld treatments [4], or stresses acting on repaired joints must be reduced by bolted splices in order to prevent the reoccurrence of cracks.

Recently, there have been studies on the improvement of fatigue strength by the use of a newly-developed welding wire, known as low transformation temperature (LTT) welding wire [5-9]. LTT welding wire enables the introduction of compressive residual stress in the vicinity of the weld bead and the reduction of weld residual deformation, which leads to the increase of fatigue strength without any post-weld treatment. Considering these advantages, previous research has attempted to use LTT welding wire in the repair of fatigue cracks initiated from welded joints, and demonstrated the possibility that weld repair through the use of LTT welding wire can restore and also increase the fatigue strength of repaired joints [10].

In this study, the efficiency of weld repair via the use of LTT welding wire was investigated in detail. Crack propagation behaviour and redistribution of residual stress in a compressive residual stress field introduced by LTT welding wire were examined, then a plate girder specimen repaired by LTT welding wire was tested to reveal the fatigue strength of the repaired girder.

## 2 Fatigue crack behaviour

### in a compressive residual stress field introduced by weld repair

#### 2.1 Test specimens and loading methods

The configurations and dimensions of a specimen are shown in Figure 1. Compact tension (CT) specimens were made of steel plates with 9.0 mm thickness. The mechanical properties and chemical compositions of the material are given in Table 1. A 3.0 mm-long and 0.15 mm-wide notch was machined from the specimen as a trigger of crack initiation. After fatigue cracks originated from the notch and propagated to about 20 mm in length, they were gouged as illustrated in Figure 2 and repaired by welding. This type of crack and groove shape were adopted, on the assumption that weld repair was to be applied to stop holes drilled at the crack tip in actual steel structures.

The mechanical properties and chemical compositions of the welding wire are given in Table 2. The welding condition is given in Table 3. In this study, TIG welding was employed because it is more suited to weld repair than other welding methods. Three specimens were tested

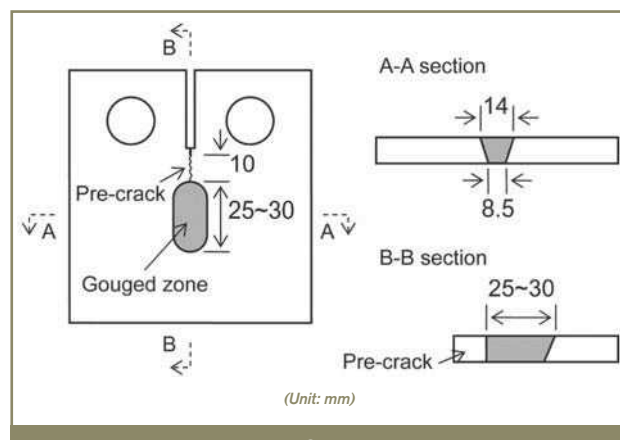


Figure 2 – Groove shape

Table 3 – Weld repair condition for CT specimen

Current [A]	Voltage [V]	Speed [cm/min]	Heat input [J/cm]
130	10~11	20.5	4 185

overall. Two were repaired using LTT welding wire and one with conventional welding wire. The specimens were clamped and welded as shown in Figures 3 and 4. Welding sequences were almost the same, but the resulting weld layers were slightly different among the specimens, as illustrated in Figure 5.

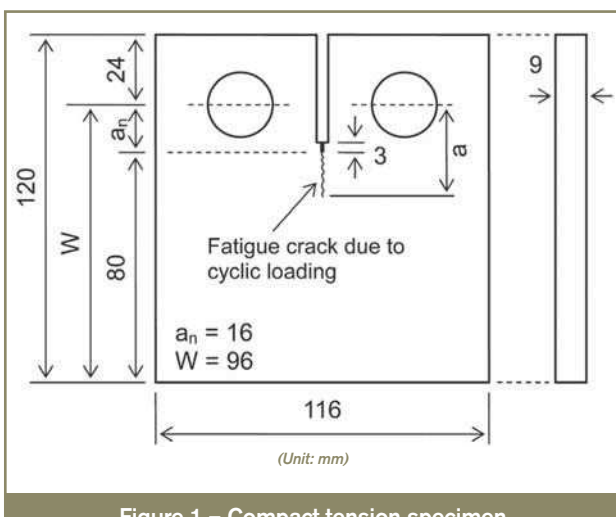


Figure 1 – Compact tension specimen

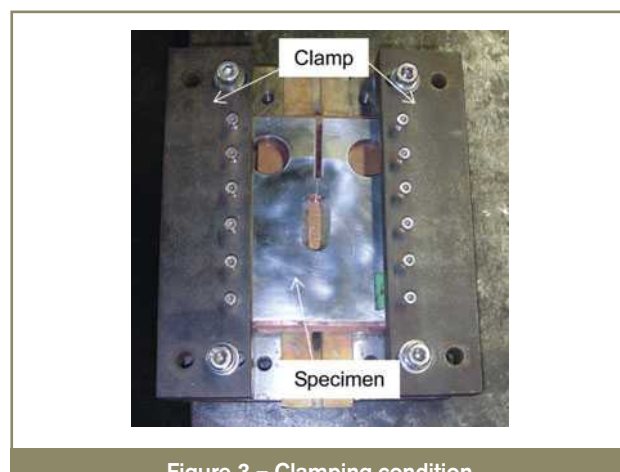


Figure 3 – Clamping condition

Table 1 – Mechanical properties and chemical compositions of material for CT specimen

Yield strength [MPa]	Tensile strength [MPa]	Elongation [%]	Chemical composition [%]								
			C	Si	Mn	P	S	Cu	Ni	Cr	Mo
439	556	25	0.15	0.38	1.53	0.01	0.002	0.03	0.03	0.01	0.001

Table 2 – Mechanical properties and chemical compositions of welding wire for CT specimen

Welding wire	Yield strength [MPa]	Tensile strength [MPa]	Ms [°C]	Chemical composition [%]							
				C	Si	Mn	P	S	Cu	Cr	Ni
LTT	808	852	350	0.055	0.17	0.25	0.007	0.004	—	—	10
Conventional	470	570	600	0.09	0.25	0.65	0.006	0.002	0.31	0.61	0.6

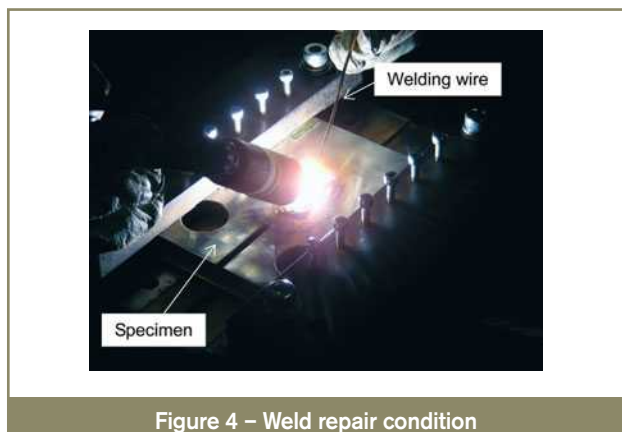


Figure 4 – Weld repair condition

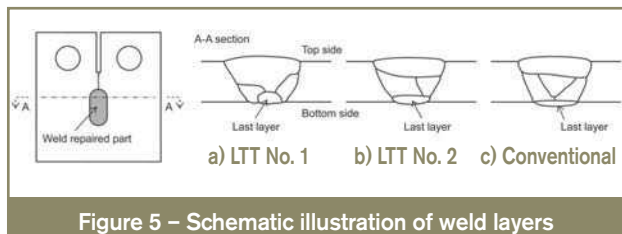


Figure 5 – Schematic illustration of weld layers

Sinusoidal wave with the frequency of 15 Hz to 20 Hz was used in the test. The details of testing procedures are described in 2.3.

42

## 2.2 Initial distribution of residual stress and its redistribution due to crack growth

### 2.2.1 Residual stress measurement methods

Residual stress, introduced by weld repair, and its redistribution due to crack propagation, were measured by strain gauges attached to the specimen surface, based on previous experiments [11]. The location of the gauges is shown in Figure 6. Initial residual stress distributions can be obtained from released strains by sectioning after specimen rupture. And, by subtracting the strain released due to crack propagation, measured periodically during the test, from the initial distribution, redistributed residual

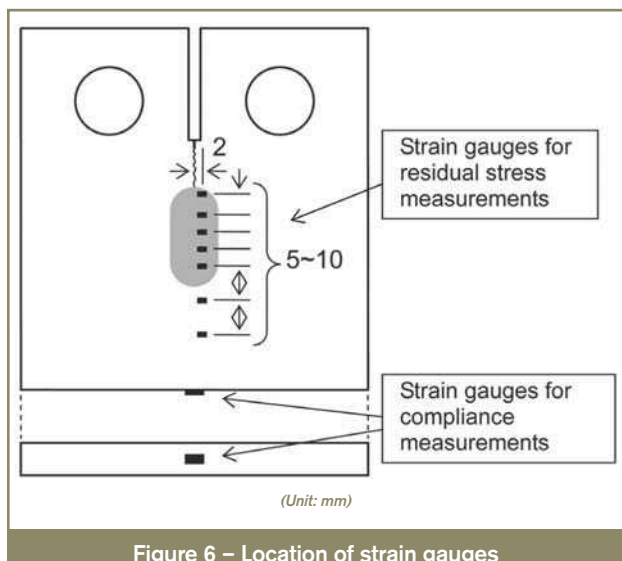


Figure 6 – Location of strain gauges

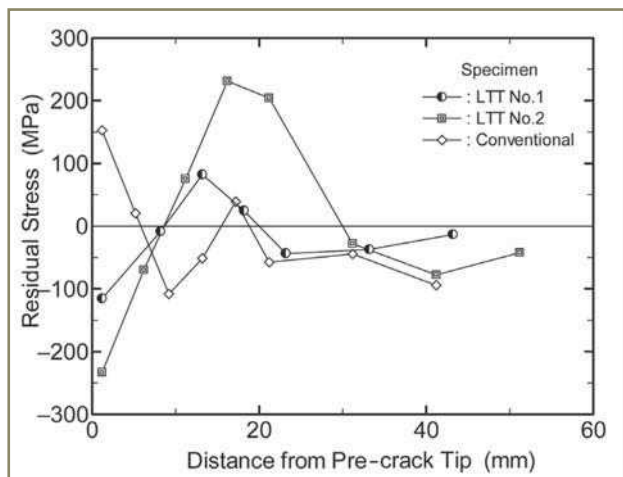


Figure 7 – Initial residual stress distribution

stress can be calculated. At the same time that strain measurements were taken during the test, fatigue crack growth was also observed on both specimen surfaces, using a digital camera with 10-power magnifying lens.

In the specimen repaired by using conventional welding wire, the experiment could not be continued due to an unexpected crack, initiated from a corner of a rectangular slit. While the cause of this phenomenon is unexplained, it might be a case specific to CT-type specimens which have a single-edge crack and low constraint around the slit. This issue will need to be investigated in detail in the future. Therefore, this specimen was artificially cut along the expected crack path, and only initial residual stress distribution was measured by using the same sectioning method.

### 2.2.2 Measurement results

Figure 7 shows the initial residual stress distribution measured on the top side of each specimen. Abscissa means the distance from the tip of the pre-crack in the crack propagation direction. It can be found that compressive residual stress is introduced around the tip of the specimen repaired with LTT welding wire, while tensile residual stress occurs in the specimen repaired with conventional welding wire. Furthermore, the magnitude of the compressive residual stress varies between the LTT specimens, which may be affected by differences in the weld layers.

Figure 8 indicates the redistribution behaviour of residual stress in the LTT specimen. The coordinate system is the same as in Figure 7. A solid line represents the initial distribution, and broken lines represent the distributions in some crack lengths. The residual stress distributions are different between the top and bottom sides because of multi-layer welding. According to previous research [11], in the case of a crack originating in a tensile residual stress field, residual stress near the crack tip remains tense after crack propagation, due to its redistribution. Similar redistribution behaviour has been reported when a crack occurs in a compressive residual stress field, that is,

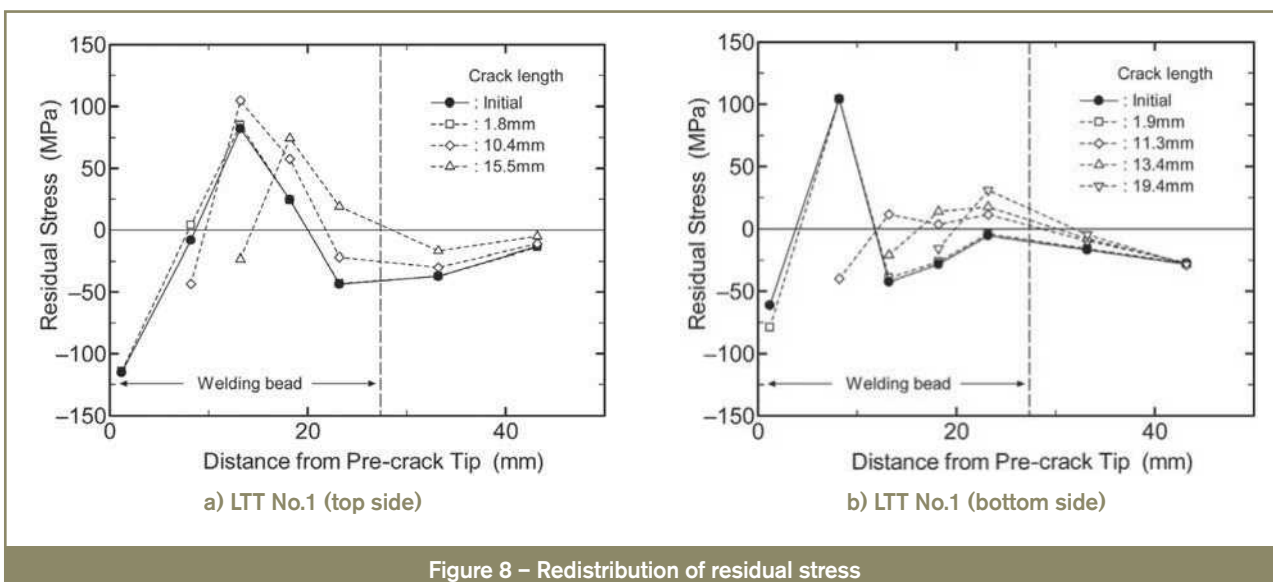


Figure 8 – Redistribution of residual stress

residual stress around the crack tip is redistributed to be compressed by crack growth [12]. In the graph, the same tendency as in the previous study [12] can be observed. The compressive residual stresses act at the crack tip in every crack length, due to the redistribution of the residual stress.

### 2.3 Fatigue crack initiation and propagation behaviour

Fatigue crack initiation and propagation were observed during the tests, and the effect of compressive residual stresses introduced by weld repair on the cracking behaviour was investigated.

#### 2.3.1 Experimental procedures

In order to detect crack occurrence in the specimen before and after repair, a tip of the notch or the pre-crack was photographed by a digital camera at certain cycles on both surfaces. If the crack could not be observed in images before several millions of loading cycles, the test was suspended and re-started after increasing the load range. Similar procedures were repeated until the crack could be detected at the tip. In this study, crack initiation life was defined as the number of cycles when the crack of 1.0 mm length was found. The loading conditions when the crack was first detected were 1.4~14.0 kN, 1.2~14.0 kN and 1.5~15.0 kN in the specimens before repair, 1.95~19.5 kN in LTT No. 1 specimen, 1.96~19.6 kN in LTT No. 2 specimen.

In the specimens before repair, crack propagation tests were conducted with a limiting reduction rate in stress intensity factor to a value proposed in ASTM E647-08 [13]. The test was launched after growing the crack to at least 2 mm, and crack size measurements were made at intervals recommended by ASTM, that is, a minimum crack extension size was 0.25 mm [13]. The crack growth was measured on both sides from images taken by the digital camera. In the repaired specimen, the crack propagation

tests were performed under the same loading conditions as the crack initiation tests. Crack size measurements followed ASTM recommendations [13].

At the same time as the crack measurement, crack closure loads were also measured by the unloading elastic compliance method [14]. A strain gauge for the compliance method was attached as shown in Figure 6.

#### 2.3.2 Crack initiation life

Generally, in notched specimens, the maximum stress range at the notch tip  $\Delta\sigma_{\max}$  can be expressed in the following equation, supposing that the notch-tip radius is extremely small in comparison with the notch length [15].

$$\Delta\sigma_{\max} = \frac{2}{\sqrt{\pi}} \frac{\Delta K}{\sqrt{\rho}} \quad (1)$$

where

$\rho$  is the radius of the notch tip and

$\Delta K$  is the stress intensity factor range calculated by assuming a notch as a fatigue crack.

The stress intensity factor range for a CT specimen can be calculated with the following equations,

$$\Delta K = \frac{\Delta P}{t\sqrt{W}} f(\alpha) \quad (2a)$$

$$f(\alpha) = \frac{(2+\alpha)}{(1-\alpha)^{3/2}} (0.886 + 4.64\alpha - 13.32\alpha^2 + 14.72\alpha^3 - 5.6\alpha^4) \quad (2b)$$

where

$\Delta P$  is the applied load range,

$t$  is the plate thickness of the specimen and

$\alpha = a/W$ ,  $a$  and  $W$  are given in Figure 1.

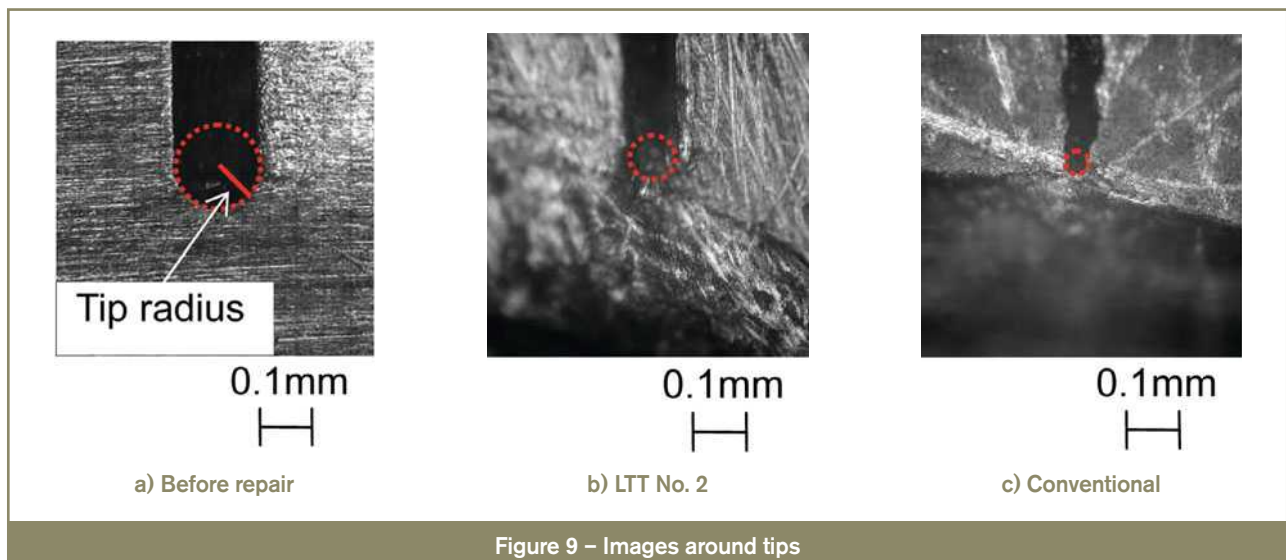


Figure 9 – Images around tips

According to Equation (1), a parameter of the stress intensity factor range, divided by the square root of the notch-tip radius, may be one of the predominant factors in fatigue crack initiation of notched specimens. This has been verified in previous experiments [16, 17]. Therefore, this study tried to correlate the crack initiation life of the specimen to the maximum stress range calculated from the stress intensity factor range and the notch tip radius.

44

The tip radius was measured with an optical microscope in advance of the experiment. Example images around the tip are indicated in Figure 9, and the measurements are summarized in Table 4. The tip radii of the specimens repaired with LTT welding wire are larger than that repaired with conventional welding wire. The reason for such may be as follows: repaired portions with LTT welding wire expand near room temperature during the cooling process, encouraging the opening of the crack. On the other hand, portions repaired using conventional welding wire cool down, with shrinkage occurring around room temperature, causing the crack to close. The measured tip radii can support the expansion and shrinkage at repaired portions. As a result of the expansion during the cooling process of the LTT-repaired portions, compressive residual stress could be introduced in the vicinity of the pre-crack tip, as shown in Figure 7.

The test results are presented in Figure 10 in terms of the maximum stress range calculated by Equation (1) versus the crack initiation life. As mentioned above, the crack initiation life is the number of cycles to the crack length of 1.0 mm. In the graph, a curve proposed by Barsom [16] is also shown in reference to the relationship. It was obtained from experiments where a notch-tip radius was 0.2 mm and the crack initiation life was defined as the

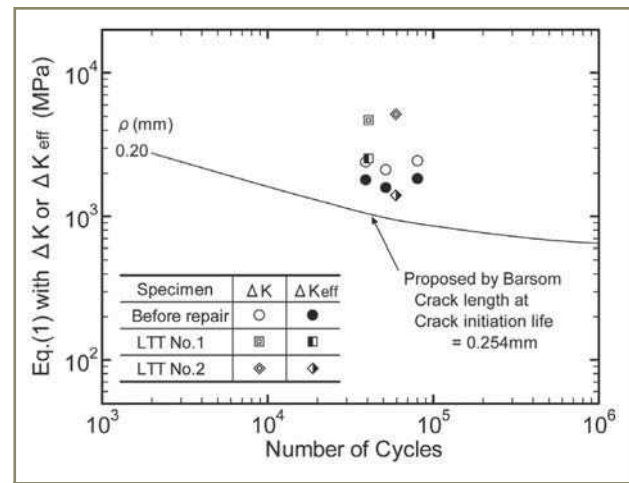


Figure 10 – Crack initiation life

number of cycles to 0.254 mm crack length. The results after repair are located higher than before repair. It means that a higher intensity of stress was required to generate cracks in the repaired specimen than in the specimen before repair. These differences in the maximum stress range for crack initiation may be caused by compressive residual stress due to the weld repair and the differences in yield strength of materials. In this study, further discussion was carried out from the viewpoint of crack closure by compressive residual stresses as described below.

### 2.3.3 Crack propagation behaviour

The relationships between the crack growth rate and the stress intensity factor range are indicated in Figure 11. The mean design curve proposed by the Japanese Society of Steel Construction [18] is also shown. The crack propagation behaviour differs in every specimen. The results of

Table 4 – Measurements of tip radius

Specimen	Before repair (machined notch)	LTT welding wire		Conventional welding wire
		No. 1	No. 2	
Tip radius [mm]	0.079	0.051	0.040	0.027

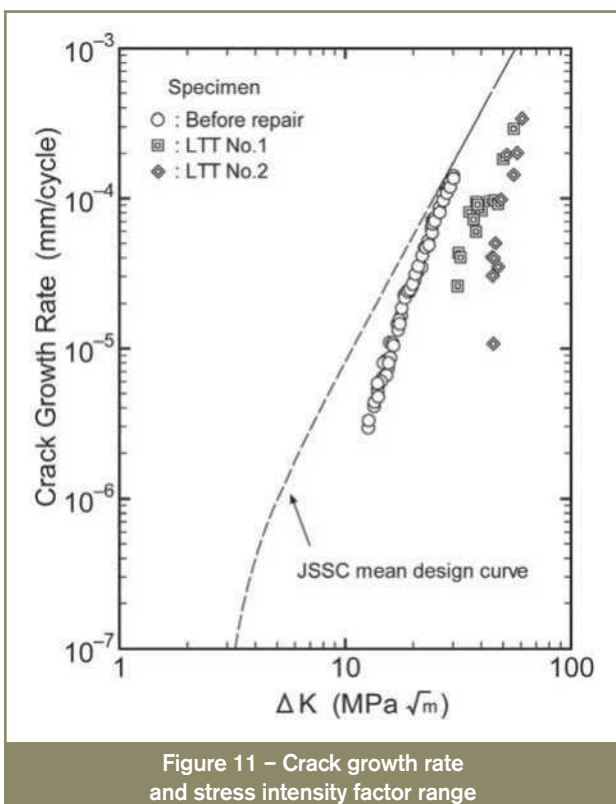


Figure 11 – Crack growth rate and stress intensity factor range

the repaired specimen lie on the right side of the results before repair, which indicates that the crack growth rate was declined by the weld repair. Also, there are slight differences between the repaired specimens due to the magnitude of the initial compressive residual stress at pre-crack tips shown in Figure 7.

### 2.3.4 Crack closure

Previous research has indicated that residual stress can affect crack closure behaviour and, consequently, change crack propagation characteristics when a crack runs in residual stress fields [19, 20]. In this study, the test results were discussed further in view of the crack closure behaviour.

Crack opening ratio  $U$ , which is a ratio between the load range while the crack opens and the entire load range, is calculated with the following equation,

$$U = \frac{P_{\max} - P_{cl}}{\Delta P} = \frac{\Delta K_{eff}}{\Delta K} \quad (3)$$

where

$P_{\max}$  is the maximum value of the applied load,

$P_{cl}$  is the load at which the crack opens under cyclic loading and

$\Delta K_{eff}$  is the effective stress intensity factor range defined by Elber [21].

Here, it is assumed that the portion of the cycle that is below the crack opening point does not contribute to fatigue crack growth because there is no change in crack-tip strain during the cyclic loading of a closed crack.

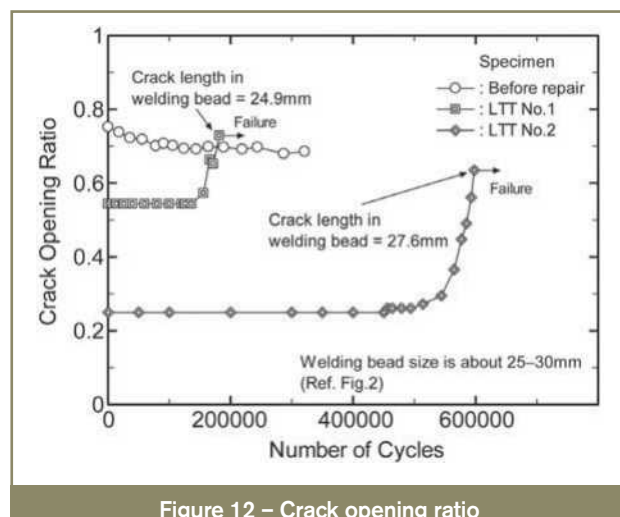


Figure 12 – Crack opening ratio

The crack opening ratio is correlated with the number of cycles in Figure 12. Abscissa is the number of cycles after the crack was detected, which means the cycles for crack propagation. The results demonstrate that the crack tip before repair is almost open over the entire load range, while less than half of the entire load range contributes to crack growth in the LTT-repaired portions. It can be assumed that these differences in the crack opening ratio lead to the differences in the crack initiation and propagation behaviour before and after repair, as shown in Figures 10 and 11. Therefore, the test results were rearranged by using the effective stress intensity factor range calculated with Equation (3).

Rearranged results are shown in Figures 10 and 13, respectively. In aspects of crack initiation and propagation, the test results before and after repair have good

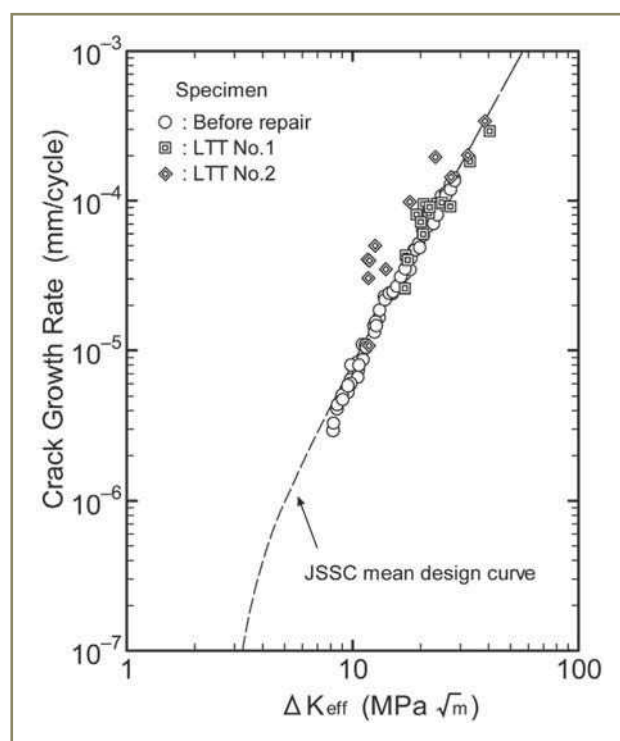


Figure 13 – Crack growth rate and effective stress intensity factor range

agreement with each other. Consequently, it can be confirmed that compressive residual stress introduced by weld repair with LTT welding wire has an influence on crack initiation and propagation behaviour. That means, even in actual structures, if cracks could be repaired by any welding with the introduction of compressive residual stresses, the fatigue life of repaired joints could be improved, as compared to that before repair.

In the next section, the effectiveness of the weld repair by applying LTT welding wire was verified by a fatigue test of a large-scale plate girder specimen.

## 3 Fatigue test of a plate girder specimen

A fatigue test on a large-scale plate girder specimen was carried out in order to induce fatigue cracks and to reveal the fatigue strength of the specimen before repair.

### 3.1 Specimen

The configuration and dimensions of the specimen are shown in Figure 14. The mechanical properties of the material are given in Table 5. A plate girder specimen has two types of welded joints on its web plate, which are out-of-plane gusset joints and cross-beam connections with coped end holes. The length and thickness of all attachments are 200 mm and 12 mm, respectively. The welded joints were placed in such a way that they would be subjected to approximately the same nominal stress range. This study focused only on the out-of-plane gusset joints represented in the left side of Figure 14.

Table 5 – Mechanical properties of the material for the girder specimen

Yield strength [MPa]	Tensile strength [MPa]	Elongation [%]
583	614	35

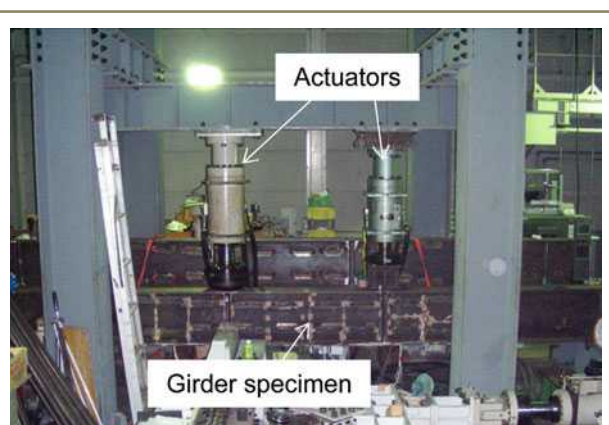


Figure 15 – Appearance of loading

### 3.2 Experimental procedures

Figure 15 provides a view of the experiment. The load was applied to the specimen by 4-points bending. A sinusoidal wave with the frequency of 1.0 Hz to 1.3 Hz was used in the test. Nominal stress range at the joints was about 70 MPa. Fatigue cracks were observed by Magnetic Particle testing at intervals. The loading was stopped to repair cracks after 4 million cycles.

### 3.3 Fatigue life before weld repair

Fatigue test results of the specimen before repair are shown in Figure 16. The fatigue life was defined as the number of cycles when the crack propagated to 10 mm in length on the web (total crack length was about 48 mm). In the graph, fatigue strength curves proposed by JSSC are also presented. The fatigue strength of this out-of-plane gusset detail scatters from JSSC-G to E class, and the lowest is located slightly below JSSC-F class.

## 4 Application of weld repair to the plate girder specimen

The plate girder specimen was repaired by LTT welding wire and re-tested to investigate its fatigue strength.

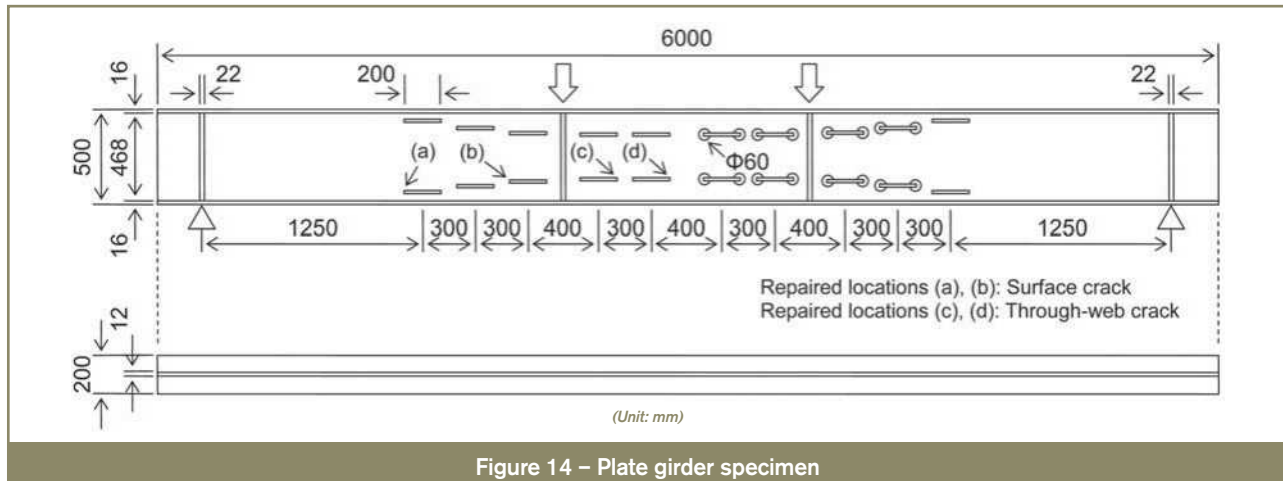
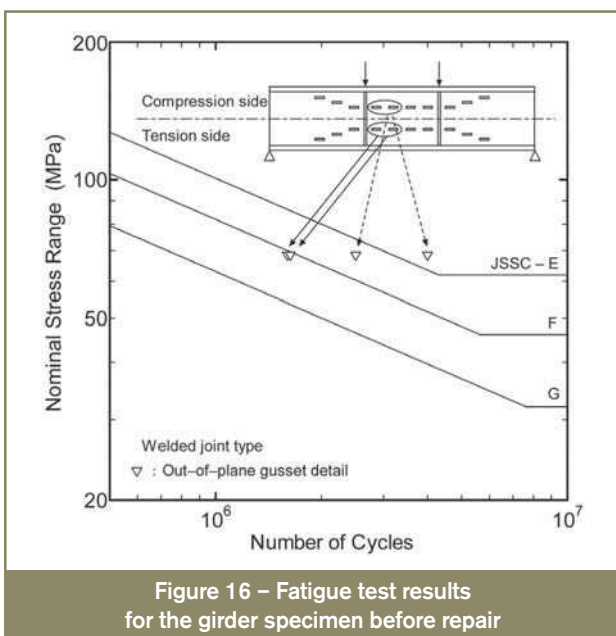


Figure 14 – Plate girder specimen



**Figure 16 – Fatigue test results for the girder specimen before repair**

The test was performed using the same procedures as before repair. Due to crack growth from longitudinal welds between the lower flange and the web, the test had to be ended after about 3.5 million cycles.

#### 4.1 Weld repair procedures

As concluded in Section 2, compressive residual stresses introduced by weld repair have retardation effects on

crack initiation and propagation, leading to improvement in the fatigue strength of cracked joints. In this study, the cracks were repaired by using both LTT and conventional welding wires, based on the preliminary examination results. The preliminary test revealed that, due to welding heat cycles, multi-pass welding with LTT welding wire sometimes makes it difficult to introduce compressive residual stress around the toe of an attachment weld, and causes weld defects in its deposit. In order to overcome this difficulty, conventional welding wire was used for filling the gouged zone after the removal of cracks, and then additional welds using LTT wire were added to the welds made with conventional wire. The mechanical properties and chemical compositions of the welding material are given in Table 6.

Four locations (a) ~ (d) in Figure 14 were selected from the attachments in the tension side to clearly indicate the effect of compressive residual stresses by weld repair. Surface cracks and through-web cracks existed in (a), (b) and (c), (d), respectively. Figure 17 illustrates the schematic procedure of the weld repair. In repair types B and C, cracks are removed completely before repair, while cracks are consciously left in the web in repair types A and D. The remaining crack depth for the through-web crack was determined from the gouging depth, and for the surface crack, it was estimated from the surface length of the crack [22, 23]. Table 7 summarizes the weld repair cases. A view of the area around the weld toe before and

**Table 6 – Mechanical properties and chemical compositions of the welding wire for the plate girder specimen**

Welding wire	Yield strength [MPa]	Tensile strength [MPa]	Ms [°C]	Chemical composition [%]							
				C	Si	Mn	P	S	Ni	Cr	Mo
LTT	614	1 117	250	0.029	0.15	0.19	0.022	0.007	7.07	15.66	–
Conventional	540	640	–	0.07	0.42	1.12	–	–	0.73	–	0.22

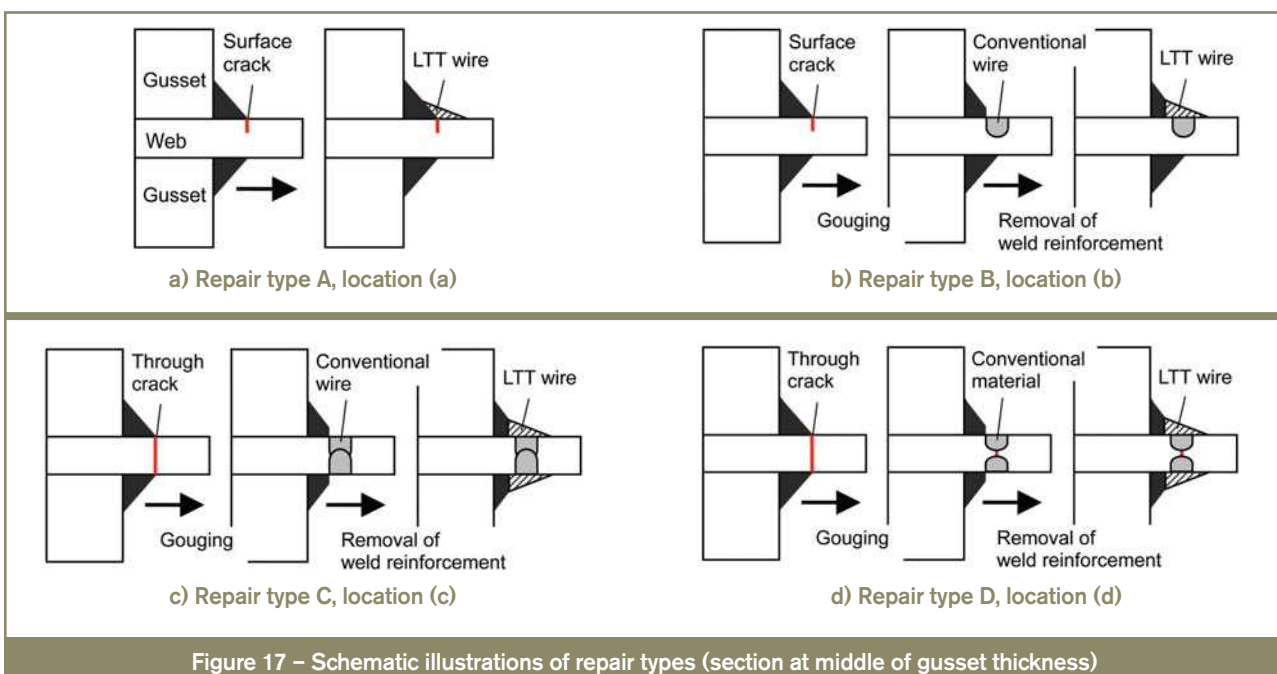


**Figure 17 – Schematic illustrations of repair types (section at middle of gusset thickness)**

**Table 7 – Summary of weld repair cases**

Repair location	a	b	c	d
Crack shape	Surface	Surface	Through	Through
Repair type	A	B	C	D
Remaining crack depth [mm]	3~5 <sup>a)</sup>	0	0	2

<sup>a)</sup> Depth for surface crack was estimated from crack length on a surface.

after repair is shown in Figure 18. Table 8 provides the weld repair condition as determined according to the preliminary examination results.

## 4.2 Crack initiation and propagation

### 4.2.1 Visual observation

Figure 19 shows fatigue cracks observed during the test. The cracks were detected at two out of four repaired locations. At location (d), where the crack remained inside the web, a crack occurred from the boundary between the repaired portion and the original weld. At location (b), where the crack was completely removed, a crack originated at a weld on the opposite of the gusset plate from the repaired one, and it penetrated through the web. Another minor crack was also observed at the weld toe of the repaired portion in location (b). However, no crack was detected at locations (a) and (c).

### 4.2.2 Microscope observation

After the test, the repaired portions were cored and examined by optical microscopy. Images taken during the microscopy are shown in Figures 20 and 21. In location (d), crack re-initiation and a little propagation can be observed at the tip of the remaining crack, aside from the crack at the boundary between the repaired portion and the original weld. However, both cracks did not penetrate the web. At location (a), although a crack re-initiated from

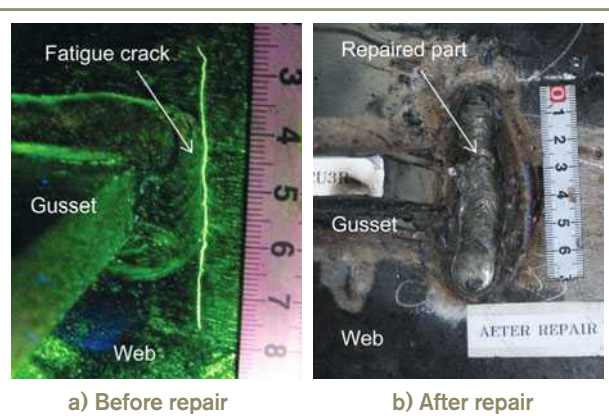


**Figure 18 – Appearance of the gusset area before and after repair**

**Table 8 – Weld repair condition for the plate girder specimen**

Current [A]	Voltage [V]	Speed [cm/min]	Heat input [J/cm]
165	36	18	19 800

the remaining crack tip, it hardly grew into the deposit of LTT welding wire. This might be because weld repair with LTT welding wire resulted in retardation or arrest of crack growth.

## 4.3 Fatigue life after weld repair

Figure 22 indicates the fatigue test results after repair, together with those before repair. In the graph, the results of the repaired location which did not fail during the test are represented with arrows. The fatigue strength of location (c), where no crack was re-initiated, is higher than JSSC-E class. And, at locations (a) and (d), where remaining cracks existed in the web, the fatigue strength is also satisfied with E class, although some cracks were re-initiated from the remaining crack. Therefore, it can be concluded that weld repair with LTT welding wire provides the possibility of restoring and also improving the fatigue strength of a cracked joint.

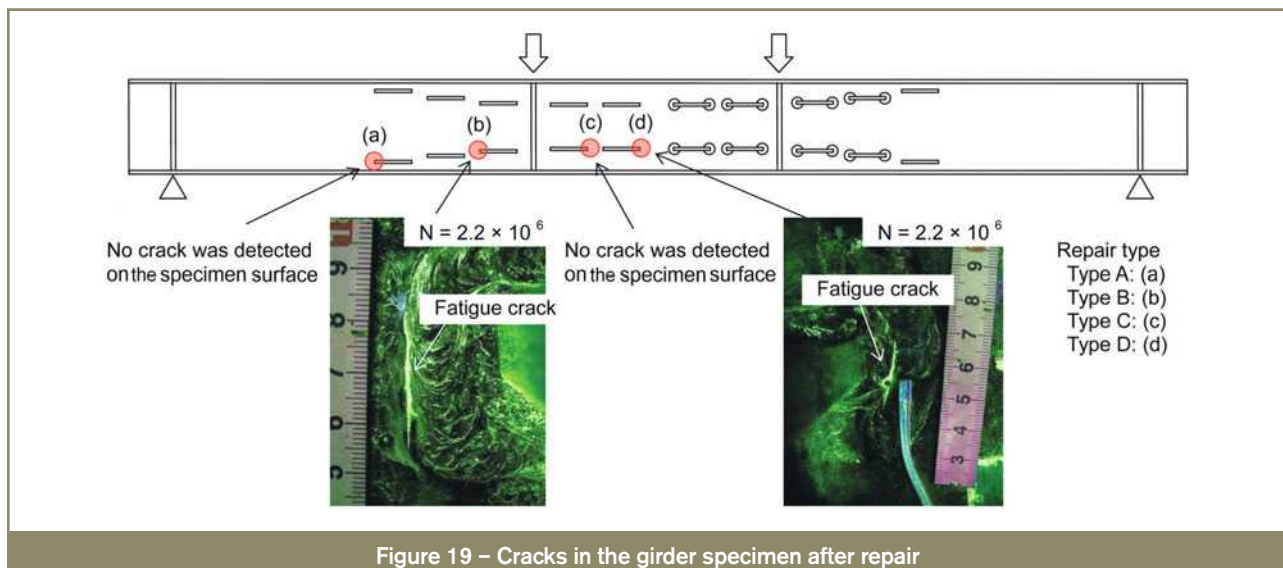


**Figure 19 – Cracks in the girder specimen after repair**

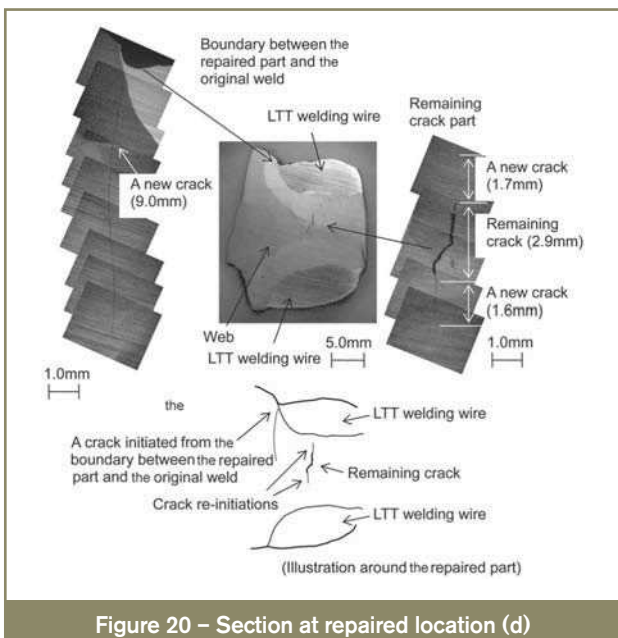


Figure 20 – Section at repaired location (d)

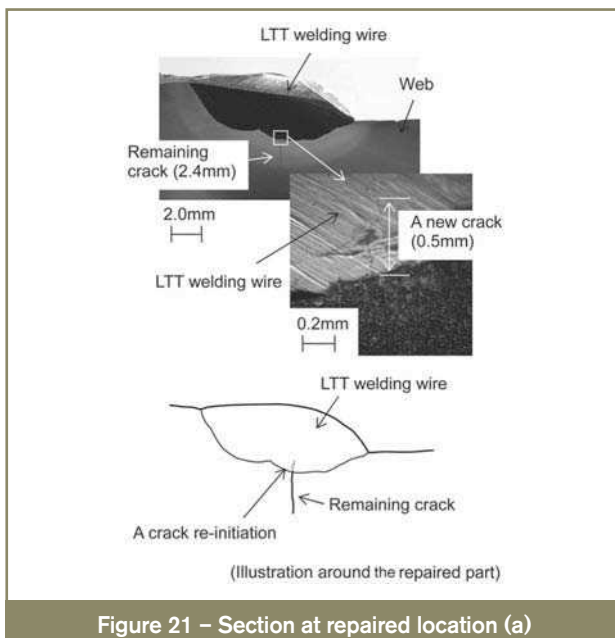


Figure 21 – Section at repaired location (a)

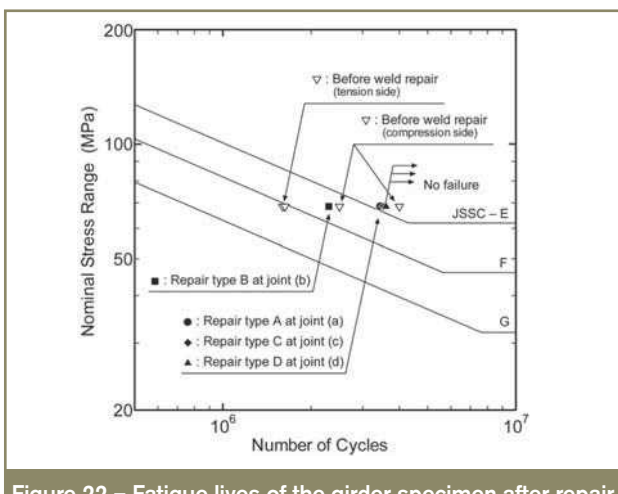


Figure 22 – Fatigue lives of the girder specimen after repair

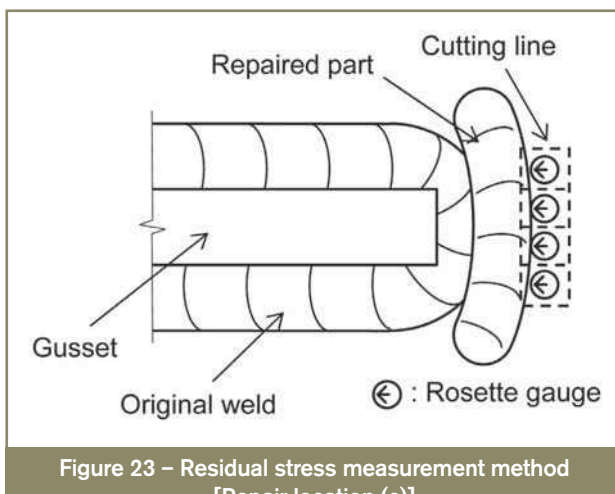


Figure 23 – Residual stress measurement method [Repair location (c)]

#### 4.4 Residual stress measurements

Residual stress around the repaired part was measured at location (c) using the sectioning method. Figure 23 shows the locations of rosette gauges and cutting lines. Measurement results are represented in Figure 24. It is demonstrated that high compressive residual stresses are introduced around the repaired part, which can lead to the improvement of the fatigue strength of the repaired joint.

## 5 Summary

- In the case of a crack occurring in a compressive residual stress field, residual stress around the crack tip is re-distributed to become compression by crack propagation.
- It can be revealed that compressive residual stress introduced by weld repair with LTT welding wire has a positive effect on crack initiation and propagation behaviour.
- In a plate girder specimen, the fatigue lives of cracked joints were restored and also improved by repair with LTT welding wire.

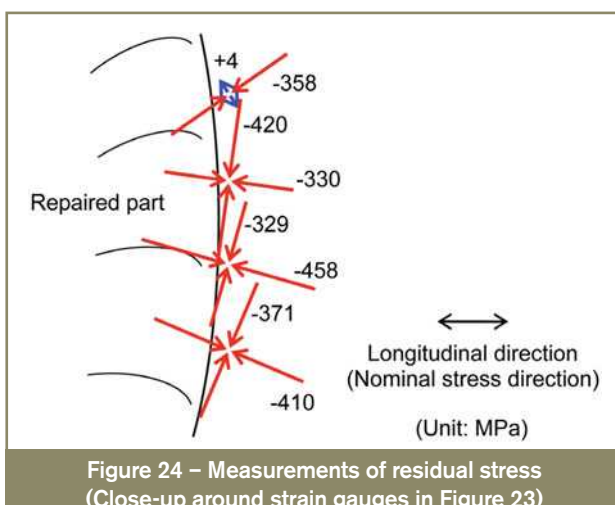


Figure 24 – Measurements of residual stress (Close-up around strain gauges in Figure 23)

- Residual stress measurements reveal that high compressive residual stresses were introduced around a repaired portion.
- It can be concluded that weld repair with LTT welding wire provides the possibility of improving the fatigue strength of a cracked joint.

## Acknowledgements

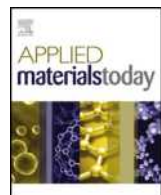
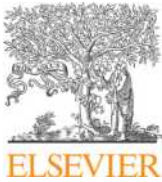
The authors gratefully acknowledge the support of the Grant-in-Aid for Scientific Research (S) (18106010) in Japan.

## References

- [1] Miki C.: Retrofitting engineering for fatigue damaged steel structures, IIW Doc. XIII-2284-09, 2009.
- [2] Wylde J.G.: The fatigue performance of repaired fillet welds, The Welding Institute Research Report, 1983, no. 215.
- [3] Yamada K., Sakai Y., Kondo A. and Kikuchi Y.: Weld repair of cracked beams and residual fatigue life, Proceedings of JSCE, 1986, no. 374/I-6, pp. 373s-382s.
- [4] Miki C., Takenouchi H., Mori T. and Ohkawa S.: Repair of fatigue damage in cross bracing connections in steel girder bridges, Proceedings of JSCE, 1989, no. 404/I-11, pp. 31s-39s.
- [5] Ohta A., Watanabe O., Matsuoka K., Siga C., Nishijima S., Maeda Y., Suzuki N. and Kubo T.: Fatigue strength improvement by using newly developed low transformation temperature welding material, Doc. IIW-1439, Welding in the World, 1999, vol. 43, no. 6, pp. 38-42.
- [6] Ohta A., Maeda Y., Nguyen N.T. and Suzuki N.: Fatigue strength improvement of box section beam by low transformation temperature welding wire, Doc. IIW-1481, Welding in the World, 2000, vol. 44, no. 5, pp. 26-30.
- [7] Miki C. and Anami K.: Fatigue strength improvement of welded joint by addition welding with low temperature metallurgical transformation electrode, IIW Doc. XIII-1827-00, 2000.
- [8] Ohta A., Suzuki N., Maeda Y. and Maddox S.J.: Fatigue strength improvement of lap welded joints by low transformation temperature welding wire – Superior improvement with strength of steel, Doc. IIW-1583, Welding in the World, 2003, vol. 47, no. 3/4, pp. 38-43.
- [9] Tominaga T., Ishikawa T. and Miki C.: Fatigue life improvement of existing bridge girders by low temperature transformation electrode, IIW Doc. XIII-1999-03, 2003.
- [10] Ohta A., Maeda Y. and Suzuki N.: Fatigue life extension by repairing fatigue cracks initiated around box welds with low transformation temperature welding wire, Doc. IIW-1507, Welding in the World, 2001, vol. 45, no. 5/6, pp. 3-8.
- [11] Miki C., Nishino F., Hirabayashi Y. and Takena K.: Influence of residual welding stress on fatigue crack growth rate, Proceedings of JSCE, 1983, no. 330, pp. 161-168.
- [12] Kitsunai Y., Kobayashi H., Narumoto A., Ishizuka T., Iida K. and Yoshihisa E.: Effect of residual stress on fatigue crack growth behavior of STS 42 steel weldments, Journal of JSMS, 1987, vol. 36, no. 409, pp. 1077-1083 (in Japanese).
- [13] ASTM E647-08: Standard test method for measurement of fatigue crack growth rates, 2008.
- [14] Kikukawa M., Jono M., Tanaka K. and Takatani M.: Measurement of fatigue crack propagation and crack closure at low stress intensity level by unloading elastic compliance method, Journal of JSMS, 1976, vol. 25, no. 276, pp. 899-903 (in Japanese).
- [15] Barsom J.M. and Rolfe S.T.: Fracture and fatigue control in structures, 3rd edition, ASTM International, 1999.
- [16] Barsom J.M. and McNicol R.C.: Effect of stress concentration on fatigue-crack initiation in HY-130 steel, ASTM STP 559, 1974, pp. 183-204.
- [17] Clark W.G. Jr.: Evaluation of the fatigue crack initiation properties of type 403 stainless steel in air and steam environments, ASTM STP 559, 1974, pp. 205-224.
- [18] Japanese Society of Steel Construction, Fatigue design recommendations for steel structures, 1993.
- [19] Kitsunai Y.: Effect of specimen size and configuration on fatigue crack growth behavior of mild steel butt welded joints, Journal of JSMS, 1983, vol. 32, no. 354, pp. 304-309 (in Japanese).
- [20] Murakami R. and Akizono K.: On the estimation of fatigue crack growth rate at welding residual stresses fields, Quarterly Journal of JWS, 1984, vol. 2, no. 4, pp. 144-150 (in Japanese).
- [21] Elber W.: Fatigue crack closure under cyclic tension, Engineering Fracture Mechanics, 1970, vol. 2, no. 1, pp. 37-45.
- [22] Yamada K., Makino T., Baba C. and Kikuchi Y.: Fatigue analysis based on crack growth from toe of gusset end weld, Proceedings of JSCE, 1980, no. 303, pp. 31-41 (in Japanese).
- [23] Mori T. and Miki C.: Aspect ratios of surface fatigue cracks originated in fillet welded joints, Journal of Structural Engineering, JSCE, 1995, vol. 41A, pp. 829-838 (in Japanese).

## About the authors

Prof. Chitoshi MIKI ([miki@cv.titech.ac.jp](mailto:miki@cv.titech.ac.jp)) and Mr Kohei TOKUNAGA ([tokunaga.kab@m.titech.ac.jp](mailto:tokunaga.kab@m.titech.ac.jp)), Master Course Student are both with the Department of Civil Engineering, Tokyo Institute of Technology, Tokyo, (Japan). Mr Takeshi HANJU ([hanji@civil.nagoya-u.ac.jp](mailto:hanji@civil.nagoya-u.ac.jp)), formerly Postdoctoral Research Assistant with the Department of Civil Engineering, Tokyo Institute of Technology is now Associate Professor with the Department of Civil Engineering, Nagoya University, Aichi (Japan).



## Short communication

## Repairing large cracks and reversing fatigue damage in structural metals

Charles R. Fisher<sup>a</sup>, Hunter B. Henderson<sup>b</sup>, Michael S. Kesler<sup>b</sup>, Pingping Zhu<sup>c</sup>, Glenn E. Bean<sup>d</sup>, M. Clara Wright<sup>e</sup>, John A. Newman<sup>f</sup>, L. Catherine Brinson<sup>g</sup>, Oscar Figueroa III<sup>h</sup>, Michele V. Manuel<sup>i,\*</sup>

<sup>a</sup> Naval Surface Warfare Center – Carderock Division, 9500 MacArthur Blvd, West Bethesda, MD 20817, USA

<sup>b</sup> Oak Ridge National Laboratory, 1 Bethel Valley Rd, Oak Ridge, TN 37830, USA

<sup>c</sup> Fiat-Chrysler Automobiles, 800 Chrysler Dr, Auburn Hills, MI 48326, USA

<sup>d</sup> The Aerospace Corporation, 2310 E. El Segundo Blvd, El Segundo, CA 90245, USA

<sup>e</sup> NASA – John F. Kennedy Space Center, Kennedy Space Center, FL 32899, USA

<sup>f</sup> NASA – Langley Research Center, 1 NASA Dr, Hampton, VA 23666, USA

<sup>g</sup> Northwestern University, 2145 Sheridan Road, Tech A214, Evanston, IL 60208, USA

<sup>h</sup> University of Florida, 100 Rhines Hall, PO Box 116400, Gainesville, FL 32611, USA

<sup>i</sup> University of Florida, 100 Rhines Hall, PO Box 116400, Gainesville, FL 32611, USA

## ARTICLE INFO

## Article history:

Received 16 November 2017

Received in revised form 29 June 2018

Accepted 8 July 2018

## Keywords:

Self-healing

Thermodynamics

Design

Metal-matrix composite

Shape-memory alloy

## ABSTRACT

**Self-healing materials** represent a paradigm shift from traditional materials development, enabling intrinsic repair of functionality (such as strength) after a catastrophic failure as opposed to part replacement. Several healing mechanisms have been demonstrated in polymeric and ceramic materials, but few in metallic systems. This study demonstrates a **novel liquid-assisted self-healing metal-matrix composite (MMC)** designed to be capable of over 90% strength recovery after a healing cycle. The aluminum (Al)-based matrix is reinforced with continuous nickel-titanium (NiTi) shape-memory alloy (SMA) reinforcements. Using a tailored heat treatment for healing, a paired effect of crack closure from the SMA reinforcement and partial liquefaction of the matrix occurs. These effects result in a compressive force across the crack surface, and, coupled with increased diffusion rates from the liquefied matrix, produces consolidation and healing in the composite structure. This work provides experimental and computational evidence for the healing mechanism under both tensile and fatigue conditions.

© 2018 The Authors. Published by Elsevier Ltd. This is an open access article under the CC BY license (<http://creativecommons.org/licenses/by/4.0/>).

## 1. Introduction

Self-healing materials can be considered biomimetic, replicating the way biological systems are able to restore functionality after a catastrophic failure. While self-healing polymers and ceramics have been described extensively in the literature, the development of self-healing metallic systems has been inhibited by several factors: increased healing activation energy, small atomic volume for crack filling, and slow diffusion rates when healing using solid-state mechanisms [1]. Despite these difficulties, there is a need for materials that have self-healing capability with higher strength and toughness in structural applications where metals are traditionally used. A structural self-healing metal would be particularly advantageous in applications where part replacement is difficult or impossible. Other applications include components that are challenged by infrequent service, require high reliability, or operate in

remote conditions. Self-healing MMCs with the ability to repeatedly heal could also benefit traditional applications where the higher initial cost of a material would be offset by decreased repair costs over time.

Only a few mechanisms of self-healing in metals have been proposed, with liquid-assisted healing considered a prime candidate for recovery from large-scale material failure. This mechanism is based on a thermodynamics-driven design methodology first described by Olson [2–4], and consists of a metallic matrix reinforced by longitudinal shape memory alloy (SMA) wires to form a composite. This matrix is designed to possess semi-solid character at elevated temperatures, allowing the material to form a liquid phase that facilitates healing.

The damage and healing cycle of the self-healing composite involves careful interaction between the metallic matrix and SMA reinforcement with temperature, as illustrated in Fig. 1. After damage occurs and a crack propagates through the MMC, load is transferred from the matrix alloy to the crack-bridging SMA reinforcement. These reinforcements remain intact while accommodating strain due to their shape memory effect [5]. To recover

\* Corresponding author.

E-mail address: [mmanuel@mse.ufl.edu](mailto:mmanuel@mse.ufl.edu) (M.V. Manuel).

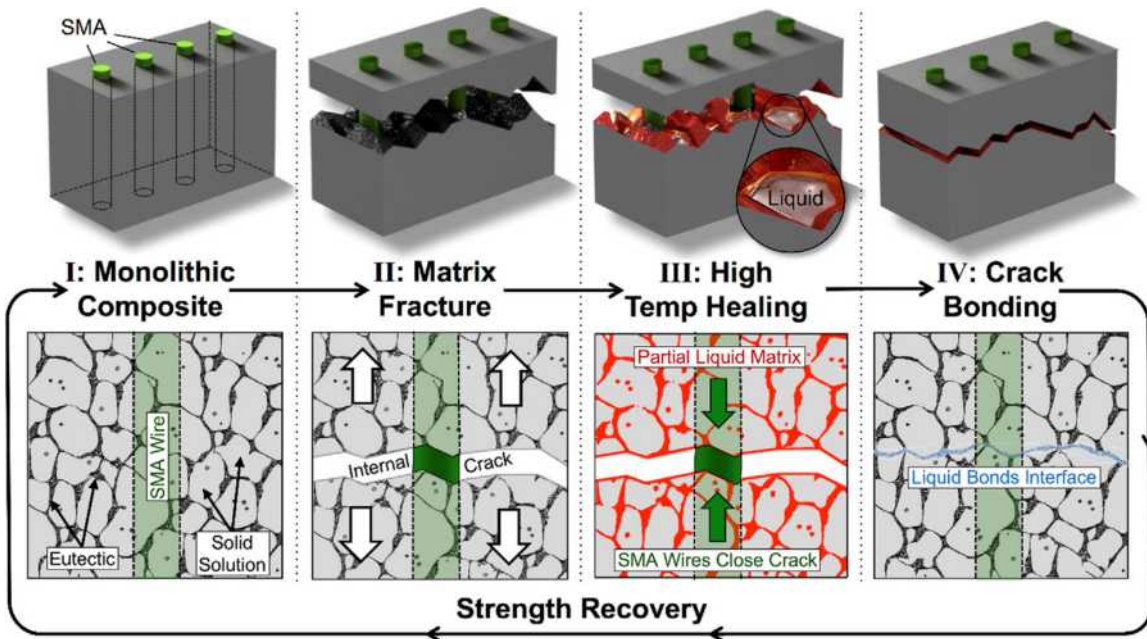


**Fig. 1.** The healing cycle for liquid-assisted self-healing metal-matrix composites. The system consists of a metallic matrix with a eutectic micro-constituent shown in black and reinforcing SMA wires shown in green (I). After catastrophic failure, the SMA wires deform to bridge the crack (II). To heal the sample, a high temperature healing treatment is initiated, during which the eutectic component melts and SMA wires close the crack (III). During cooling, the eutectic component freezes, welding the crack surfaces and eliminating the crack (IV). (For interpretation of the references to color in this figure legend, the reader is referred to the web version of the article.)

the damage, the MMC is heated above the SMA's austenite start ( $A_s$ ) temperature. This initiates shape recovery of the SMA, pulling the crack together as the SMA reinforcements return to their initial length. Concurrently, the increased temperature causes softening and liquefaction of the eutectic micro-constituent in the matrix, which enables the recovery of plastic strain in the matrix as well as crack filling. Combined with the crack closure force provided by the SMA reinforcement completely reverting to their original length, the MMC welds itself together and, upon cooling, results in a solidified composite able to realize its pre-cracked, original strength.

## 2. Self-healing MMC design

To demonstrate the self-healing effect in a structural alloy, the aluminum–silicon (Al–Si) system was used as the matrix. Si additions to Al decrease eutectic temperature and provide increased castability [6], while the eutectic microstructure of the Al–Si enables reliable equilibrium partial-liquid heat treatment. Alloys with a Si content below 3 wt% Si additions are prone to hot-shortness during casting [7], so an Al–3 at.% Si (3.1 wt% Si) was selected. Using the PANDAT thermodynamic software system [8], a temperature of 592 °C for Al–3Si was calculated to yield 20% liquid and 80% solid, a combination which has been found to maintain structural stability throughout an elevated temperature healing cycle while possessing enough liquid phase to enable healing [9,10].

## 3. Tensile strength recovery

To fabricate the composite for tension experiments, liquid Al–3Si was cast over continuous NiTi SMA wire reinforcements into a dog bone shaped graphite mold. Each composite had three parallel SMA wires along the tensile axis, resulting in 2 vol% SMA reinforcement. Subsequently, each specimen was heat treated at the healing temperature (592 °C) for 24 h to stabilize the microstructure, then mechanically tested in tension. Tensile tests of three individual composite specimens resulted in average values of 39.4 MPa

for 0.2% offset yield strength ( $\sigma_y$ ), 93.6 MPa for ultimate tensile strength (UTS), and 3.9% for strain to failure. After inducing matrix failure, each specimen was put through the 592 °C, 24 h healing cycle and tested again in tension. Post-healing, the composites possessed an average strength recovery of 91.6% compared to the initial test (see Healing efficiency model in Section 7). Fig. 2A shows before and after healing mechanical testing data, with corresponding optical images of the fractured area within each tensile specimen. It should be noted that all cracks extended through the entire cross-section of each composite specimen. A representative video of the healing heat-treatment for an Al–3Si matrix reinforced with 2 vol% NiTi SMA wires, showing both shape recovery and partial matrix liquefaction to enable healing, is presented as Movie S1.

Fig. 2B is a schematic of how each composite constituent component behaves prior to failure. Since the reinforcement is in the form of longitudinal fibers, strain is assumed to be equivalent between the Al–3Si matrix and SMA reinforcement before cracks form in the matrix. Since the SMA deforms by detwinning to the same strain as when the matrix fails and cracks, these quantities are nearly equivalent. Thus, in the absence of wire prestrain, a certain amount of matrix plasticity is required for the crack to be clamped by the SMA wires. Conversely, the matrix should not be more ductile than the recoverable strain of the SMA. A highly plastic matrix would strain the SMA reinforcement beyond its recoverable strain, reducing shape recovery capability. These results show that extensive damage can be reversed in a structural materials system given a compatible mechanical response between the matrix and reinforcement.

## 4. Computational simulation of crack closure

To gain more insight into the mechanics of crack closure and healing, a finite element (FE) approach [11] was used with the post-crack condition as a starting point. The initial conditions of the model are as follows. First, the SMA reinforcements are given a 6% pre-strain, which is elongation of the SMA prior to matrix cracking (due to matrix plasticity). The reinforcements were fixed to the

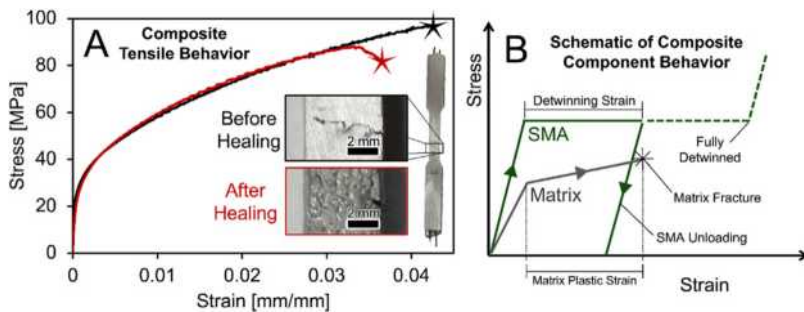


**Fig. 2.** (A) Mechanical test information for an Al-3Si/SMA longitudinally-reinforced composite. Note the inset macro-images correspond to the before and after healing heat treatment of a crack along the dog bone-shaped specimen. (B) Schematic of constituent component (SMA reinforcement and matrix) mechanical behavior internal stress as a function of applied strain. Note that plastic strain in the matrix and detwinning strain in the SMA reinforcement before failure are roughly equivalent.

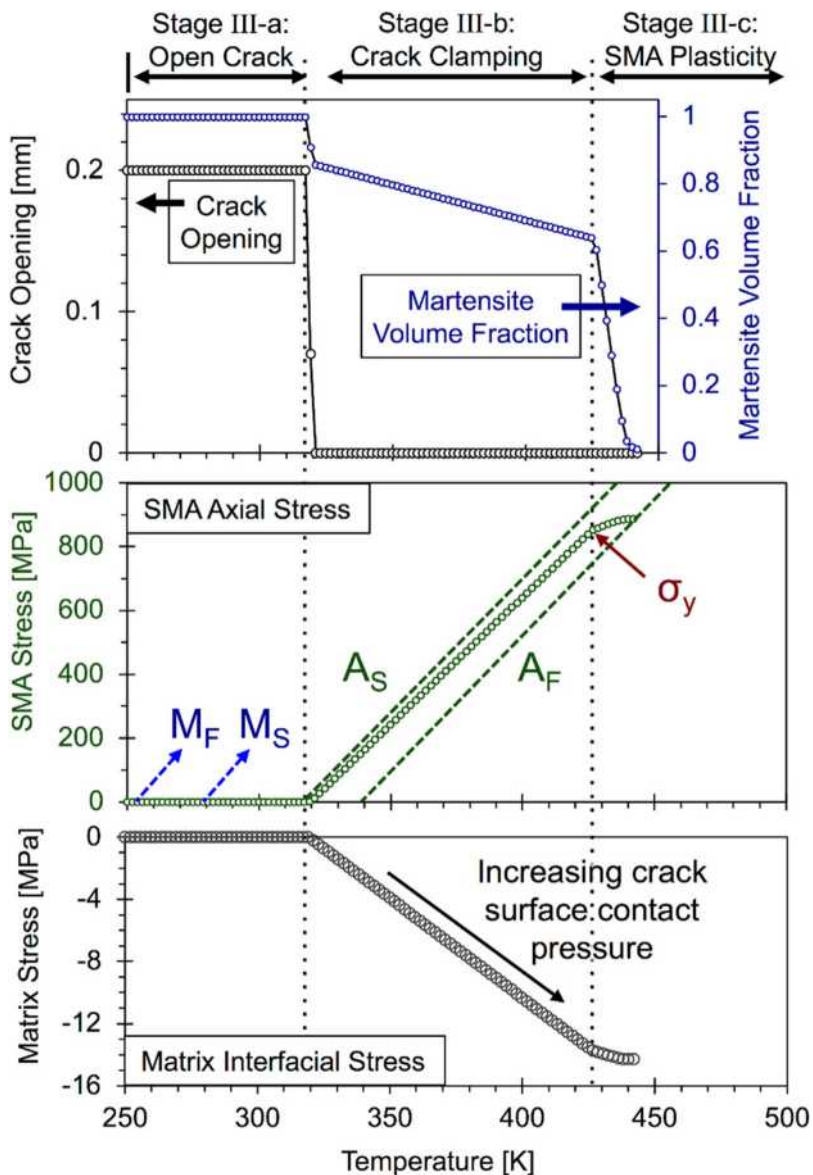


**Fig. 3.** Finite element simulation of the crack closure process (Stage III from Fig. 1) as a function of temperature, with crack opening, martensite volume fraction, and SMA and Al-3Si matrix stress displayed. As the sample is heated, an austenitic phase transformation in the wires closes the crack and initiates crack surface contact pressure that increases with temperature. Note that the stress in the SMA is tensile (positive) and the stress on the matrix interface is compressive (negative).

Al-3Si matrix at both ends (i.e., axial displacement at each composite end is uniform), while otherwise fully debonded along the length of the reinforcement. Lastly, the initial gap is set at 0.2 mm in the center of the 30 mm long matrix, equivalent to the cracks

exhibited by the experimental tension specimens. The composite responded to heating in three stages of behavior, as shown in Fig. 3. In the figure,  $M_S$ ,  $M_F$ ,  $A_S$ ,  $A_F$ , and  $\sigma_y$  represent the SMA martensite and austenite start and finish temperatures and yield stress,

respectively. In Stage III-a, from 250 K to 318 K ( $-23^{\circ}\text{C}$  to  $45^{\circ}\text{C}$ ), no movement occurs. In Stage III-b, the SMA begins to transform from martensite to austenite and quickly closes the gap in the matrix. As temperature is further increased, more martensite transforms and the stress in the SMA reinforcement increases, illustrating the crack clamping mechanism. Note that the transformation temperatures are a function of stress. In Stage III-c, the SMA reaches the temperature dependent yield stress and begins to accommodate strain by slip, and the transformation to austenite completes. The transformation of the matrix to partial liquid above the eutectic temperature of 850 K ( $577^{\circ}\text{C}$ ) is not included in the model, but the remaining clamping force ensures that the interface would remain in contact to bond effectively.

This modeling effort illustrates the need for pre-strained SMA reinforcements to enable crack closure and healing in the MMC through a crack clamping mechanism. Without the pre-strain in the SMA reinforcements, the sample would experience crack closure but no crack clamping force (as illustrated by the increase in the crack surface contact pressure in Fig. 3). The compressive force helps to ensure adequate contact between the crack faces and facilitates healing efficacy. Overall, investigations found the elevated temperature compressive strength of the matrix, the bond strength between the matrix and SMA reinforcements, and the ductility of the composite material play a major role in determining self-healing capabilities as these factors affect the amount of strain imparted on the SMA reinforcements and directly relates to the recovery force during healing.

## 5. Fatigue life recovery

In Al alloys, especially for aerospace and space applications, material failure is most likely to occur from fatigue [12]. Therefore, to investigate the healing mechanism in a more representative

failure condition, fatigue testing was conducted on Al-3Si reinforced with NiTi SMA reinforcements using middle tension [M(T)] fatigue crack growth rate tests. The results from M(T) fatigue testing can be seen in Fig. 4. On the scale in Fig. 4B and C, 0 mm represents the center of the sample and 12 mm represents the outer edge. In all four tests, the crack length decreased as a result of the healing cycle, as the matrix bonded to itself, and the crack growth rate decreased after healing. The micrographs in Fig. 4D–G show that upon initial testing, cracking propagates mostly intergranular, following the eutectic regions (matching the failure path seen in tensile testing), while after healing the crack path becomes more tortuous. Since the preferential crack propagation path in Al-3Si is along the brittle eutectic, microstructural modification, such as morphology changes and growth, during the healing treatment redirects the crack path and thus the sample exhibits a toughening behavior. These early tests indicate that, in addition to the strength recovery after catastrophic failure previously discussed, the healing cycle is also effective at repairing fatigue damage and thus may be beneficial in extending fatigue life.

## 6. Conclusion and future work

These initial investigations into an Al-3Si matrix reinforced with 2 vol% NiTi SMA wires resulted in 91.6% healing efficiency on average under tensile conditions, and showed promise for healing fatigue cracks. While the overall strength of the tested MMCs is below industry standards for cast aluminum alloys, the methodology of liquid-assisted self-healing MMC design is applicable to other metallic systems outside of Al-Si. Any system exhibiting a solid + liquid region at a temperature which will not adversely affect the thermal properties of SMA wires has self-healing potential. Future designs will seek to improve strength to that of

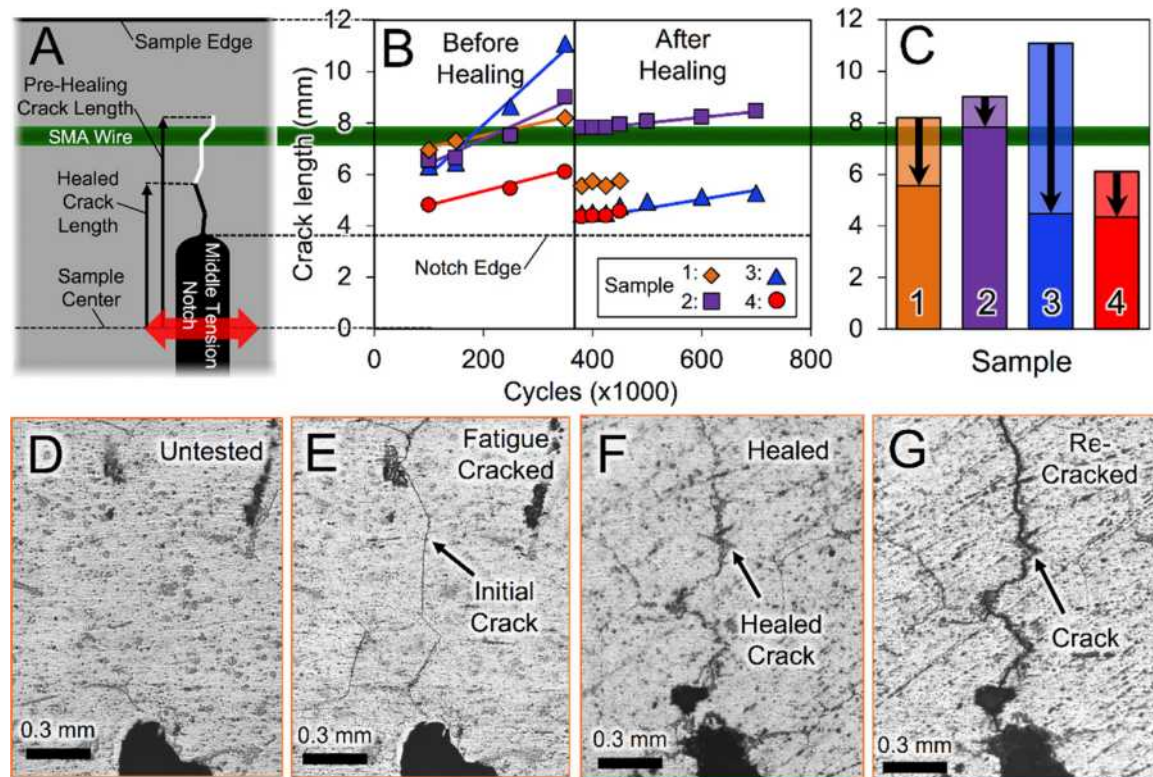


**Fig. 4.** (A) Schematic of area of interest in the M(T) notch specimens, (B) fatigue data showing decreased crack growth rate relative the location of the embedded SMA reinforcement, (C) crack length before and after healing. Micrographs of a (D) untested specimen, (E) post-fatigue cracking, (F) post-healing, and (G) after a second M(T) fatigue test.

commercial Al alloys while maintaining the high healing efficiency found in the Al–Si composite system. These structural materials could be incorporated into a number of technologies in the future, where functionality can be restored after a loss of mechanical integrity.

## 7. Experimental

### 7.1. Preparation of composite

A master alloy was prepared by melting Al (shot, 99.99%, Alfa Aesar) and Si (lump, 99.9999%, Alfa Aesar) at 850 °C until a liquid solution and casting into a graphite mold. Appropriate amounts of this master alloy and Al to obtain an Al-3 at.% Si alloy were melted at 750 °C until a liquid solution. A graphite mold coated with boron-nitride with custom designed ends to hold wires was heated to 350 °C with the NiTi wires (Ni-49.3 at.% Ti, Ø = 0.87 mm, Memry Corporation) already aligned. The Al–Si melt was poured over the NiTi wires and allowed to cool. The composite was heat-treated at 592 °C for 24 h to set the post-heal microstructure. The matrix composition was confirmed via inductively coupled plasma atomic emission spectroscopy (ICP-AES). Each healing cycle was performed by vacuum encapsulating the composite in a Pyrex tube and heat-treating at 592 °C for 24 h.

### 7.2. Tensile testing

Specimens were fabricated according to the sub-size tensile specimen dimensions in ASTM E8M: Standard Test Methods for Tension Testing of Metallic Materials [13]. Tensile testing was completed on an Instron 5582 mechanical testing machine at a strain rate of 1.0%/min. Strain was measured with an extensometer (Model 3542, Epsilon Technology Corporation) attached to the gauge area.

### 7.3. Fatigue testing

Four middle tension [M(T)] fatigue crack growth rate specimens were fabricated with geometry based on ASTM E647: Standard Test Method for Measurement of Fatigue Crack Growth Rates [14]. Fatigue testing was completed on an MTS 321.12 hydraulic load frame in strain control, with maximum stress of 80% yield strength (32 MPa), stress ratio  $R=0.1$ , and frequency of 80 Hz. Pre-cracks were initiated at a central machined notch and all tests were halted at 350,000 cycles. Subsequently, each M(T) specimens underwent a healing cycle of 24 h at 592 °C before being re-tested. Crack size was measured optically from the center of each M(T) specimen.

### 7.4. Healing efficiency model

The healing efficiency of a composite was determined by comparing the ultimate tensile strength (UTS) of the virgin composite against the post-heal UTS of the same specimen via the following Eq. (1):

$$\frac{\text{UTS}_{\text{virgin}}}{\text{UTS}_{\text{healed}}} \times 100\% = \% \text{Healed} \quad (1)$$

## Supporting information

Supplementary Movie S1 of the healing during heat-treatment is available.

## Acknowledgements

The authors would like to thank our funding partners at the Florida Space Grant Research program (NNX10AM01H), National Science Foundation (CMMI-0824352) and the National Aeronautics and Space Administration (NNX12AQ42G, NNX13AR53A, and NNX12AP71A).

## Appendix A. Supplementary data

Supplementary data associated with this article can be found, in the online version, at [doi:10.1016/j.apmt.2018.07.003](https://doi.org/10.1016/j.apmt.2018.07.003).

## References

- [1] S. Van der Zwaag, N.H. van Dijk, H.M. Jonkers, S.D. Mookhoek, W.G. Sloof, Self-healing behaviour in man-made engineering materials: bioinspired but taking into account their intrinsic character, *Philos. Trans. R. Soc. A* 367 (2009) 1689–1704.
- [2] G.B. Olson, Computational design of hierarchically structured materials, *Science* 277 (1997) 1237–1242.
- [3] G.B. Olson, Designing a new material world, *Science* 288 (2000) 993–998.
- [4] G.B. Olson, Beyond discovery: design for a new material world, *CALPHAD* 25 (2001) 175–190.
- [5] C.M. Wayman, T.W. Duerig, An introduction to martensite and shape memory, in: T.W. Duerig, K.N. Melton, D. Stockel, C.M. Wayman (Eds.), *Engineering Aspects of Shape Memory Alloys*, Butterworth-Heinemann, United Kingdom, 1990, pp. 3–20.
- [6] A.M. Russell, K.L. Lee, *Structure–Property Relations in Nonferrous Metals*, John Wiley and Sons, Inc., New Jersey, 2005.
- [7] P.H. Jennings, A.R.E. Singer, W.I. Pumphrey, Hot-shortness of some high-purity alloys in the systems Al–Cu–Si and Al–Mg–Si, *J. Am. Inst. Met.* 74 (1948) 227–248.
- [8] S.L. Chen, F. Zhang, S. Daniel, F.Y. Xie, X.Y. Yan, Y.A. Chang, R. Schmid-Fetzer, W.A. Oates, Calculating phase diagrams using Pandat and PanEngine, *J. Mater.* 53 (2003) 48–51.
- [9] M.V. Manuel, Principles of self-healing in metals and alloys: an introduction, in: S.K. Ghosh (Ed.), *Self-Healing Materials: Fundamentals, Design Strategies, and Applications*, Wiley-VCH, Weinheim, Germany, 2009.
- [10] M.V. Manuel, G.B. Olson, Biologically inspired self-healing metals, in: N. aan Zee (Ed.), *Proc. 2nd Int. Conf. on Self-Healing Mater.*, Springer, New York, 2009.
- [11] P. Zhu, Z. Cui, M.S. Kesler, J.A. Newman, M.V. Manuel, M.C. Wright, L.C. Brinson, Characterization and modeling of three-dimensional self-healing shape memory alloy-reinforced metal-matrix composites, *Mech. Mater.* 103 (2016).
- [12] R.J. Wanhill, Fatigue crack initiation in aerospace aluminum alloys, components, and structures, in: N. aan Zee (Ed.), *Proc. 1st Int. Conf. on Self-Healing Mater.*, Springer, New York, 2007.
- [13] ASTM E8M-04, 2004, Standard Test Methods for Tension Testing of Metallic Materials [Metric], ASTM International, West Conshohocken, PA, 2004 [www.astm.org](http://www.astm.org).
- [14] ASTM E647-15e1, Standard Test Method for Measurement of Fatigue Crack Growth Rates, ASTM International, West Conshohocken, PA, 2015 [www.astm.org](http://www.astm.org).

# Fatigue behaviour of welded joints with cracks, repaired by hammer peening

C. M. BRANCO<sup>1</sup>, V. INFANTE<sup>1</sup> and R. BAPTISTA<sup>2</sup>

<sup>1</sup>ICEMS/IST, Lisbon University of Technology, Lisbon, Portugal, <sup>2</sup>ESTG/IPT, Polytechnical Institute of Setúbal, Setúbal, Portugal

Received in final form 18 February 2004

**ABSTRACT** Rehabilitation of a welded structure, which involves repair of cracked joints, is achieved when the local treatment for repair gives a fatigue strength in the joint equal or above the fatigue strength of the uncracked original detail. If the treatment is properly applied the rehabilitation of the detail is assured, and the nature of the weld toe improvement methods can produce a joint, after repair, with a fatigue strength and residual life greater than the initial detail. The paper presents the results obtained on a fatigue study on the rehabilitation of non-load carrying fillet welded joints loaded in bending at the main plate and with fatigue cracking at the weld toes of the attachment in the main plate and through the plate thickness. Residual stresses were measured at the surface, with X-ray diffraction. The residual stresses induced by hammer peening at the weld toe were found to be greater along the longitudinal direction of the plate than in the transverse direction. The peak residual stresses near the weld toe were found to be close to yield in compression, justifying the great benefit of hammer peening. Results of a derived gain factor,  $g$ , in fatigue life were obtained as a function of the crack depth repaired by hammer peening.

**Keywords** fatigue, hammer peened; improvement techniques; life prediction; weld specimens.

## INTRODUCTION

The present trend is to use welded structures to the maximum of their life potential. To achieve this aim, considerable effort should be made to inspection, monitoring and repair of the damaged zones. Life extension of ageing structures is possible to achieve without putting in danger the integrity of the structures, if repair methods are introduced. Current research deals with the fatigue behaviour of welded joints in a structural steel subjected to the so-called 'local post-welding improvement techniques', and is a follow-up of research work carried out by the authors in this field.<sup>1,2</sup>

The local treatment for repair should give a fatigue strength not below the fatigue strength of the original detail before it was damaged. If the treatment is properly applied, the nature of the weld toe improvement methods can produce a joint, after repair, with a fatigue strength and residual life higher than the initial detail, if this was

not subjected to an improvement treatment. The repair treatment may arrest the original fatigue cracks.

Most of the life improvement techniques, as applied to original or new welds, were established in the 1960s and early 1970s.<sup>3–5</sup> A number of investigations have confirmed the benefit to be gained from improvement techniques, and large increases in the fatigue strength are usually obtained. In spite of this, some reluctance has been observed towards the introduction of improvement techniques into design recommendations, and only recently one method, toe grinding, has been allowed for in the design of offshore structures<sup>6</sup> and pressure vessels.<sup>7</sup>

An analysis of an extensive amount of data available in the literature was made by Lieurade and co-workers.<sup>8</sup> Four improvement techniques (*grinding, TIG dressing, hammer peening and shot peening*) for four types of joints (*butt, T-joints, cruciform and longitudinal joints*) were taken into account in this study.<sup>8</sup> All the S-N curves were above those of as-welded assemblies. The best results were obtained with hammer peening.

The rather large increase in the fatigue strength, due to the use of improvement techniques, can be explained by

Correspondence: C. M. Branco. E-mail: cmbranco@dem.ist.utl.pt

the significant increase of a so-called initiation phase. During the initiation phase, the extension of existing 'crack-like' defects is slowed down or even stopped. The duration of this phase increases with the local fatigue life (or the decrease in the stress range).

In a review recently presented by Maddox,<sup>9</sup> conclusions and recommendations were defined for hammer peening which is now part of an official IIW document of the Commission XIII.<sup>10</sup>

Damaged weld toes can be treated locally, and most frequently while the structure is in service. If the repair is successfully applied, after the treatment, a significant life extension period can be obtained. This will avoid the need for repair welding that would be the case if the detail had to be rewelded and set back into service again.

A report of significant fatigue life extensions in repaired welds by air-hammer peening is presented in Ref. [11]. In another work by the same authors<sup>12</sup> it is shown that air-hammer peening of the local weld toe region is a reliable technique for repairing welds with shallow surface cracks up to 3 mm long.

The more traditional fusion rewelding repair procedures are susceptible to induced metallurgical problems associated with the formation of brittle phases or another embrittling phenomenon.

There is evidence, from tests on welded steel beams, that improvement techniques, notably those relying on the introduction of compressive residual stresses, are less effective in large welded structures containing high tensile residual stresses, due to welding, than when they are used to treat small-scale specimens. That is undoubtedly

linked to the fact that the increase in fatigue life, resulting for an improvement technique—particularly one relying on compressive residual stresses—tends to decrease with increase in applied tensile mean stresses.

However, recent results obtained on real structures were very good as far as the benefit of hammer peening is concerned.<sup>13</sup>

Recently the authors have published data in this area, both for as-welded and defective welds.<sup>14–16</sup>

The results presented in this paper cover the effect of hammer peening, mainly as a repair technique for fatigue cracks at the weld toe. Results are presented also on the impact forces, distribution of residual stresses induced by the process and S-N data for the repaired cracks.

## EXPERIMENTAL DETAILS

### Material, specimens and improvements processes

Table 1 gives the composition and the nominal mechanical properties of the base and weld metal used in this study—a medium strength structural steel of the 400 MPa yield class (St 52-3, DIN 17100 specification) with a weld metal in a overmatching condition. The welds were made by the covered electrode process more details of which can be found in Ref. [13]. The mechanical properties were also obtained at room temperature in tensile, compressive and LCF tests carried out in cylindrical specimens of 8–9 mm diameter and 25 mm gauge length machined from 12.5 mm thick steel plates. The results are presented in Table 2.

**Table 1** Chemical compositions of base metal and weld metal

C	Si	Mn	Cr	Mo	Ni	Ti	Al	V	Cu	Co	Nb	P	S
<b>Base metal (St 52-3 steel)</b>													
0.131	0.413	1.44	0.063	0.024	0.034	0.009	0.029	0.043	0.018	0.013	0.005	0.011	0.005
<b>Weld metal (E 11018-G; over matched)</b>													
0.08	0.45	1.28	0.50	0.37	1.87							0.017	0.01

**Table 2** Parameters of the monotonic and cyclic stress-strain curves [13]. St 52-3 steel

	$\sigma_{0.2}$ (MPa)	$\varepsilon_{0.2}$ (%)	E (MPa)	$\sigma_R$ (MPa)	$\sigma_f$ (MPa)	$\varepsilon_R$ (%)	$K'$	$n'$	$r^2$
(A) Tension (monotonic) and reversed cycling ( $R = -1$ )									
Average	415.3	0.56	200302	571.2	356.5	14.27	—	—	—
	406.9	0.50	218254	569.4	358.3	15.04	—	—	—
Average	411.1	0.53	214273	567.3	357.4	14.65	1015.31	0.1535	0.966
(B) Compression (monotonic) and reversed cycling ( $R = -1$ )									
Average	0.27	205949	696.5	696.5	12.77	—	—	—	—
	0.31	203625	638.0	638.0	7.92	—	—	—	—
Average	0.29	204787	667.3	667.3	10.35	1015.31	0.1535	0.966	

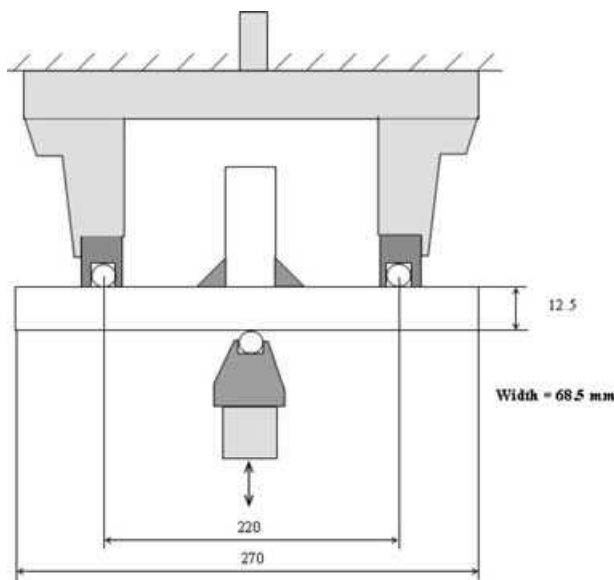


Fig. 1 Geometry of the specimens and loading arrangement. 3PB.  $R = 0.1$ . T-joint. St 52-3 steel.

The cyclic stress-strain curve of the material was obtained with one step level tests in cylindrical specimens and under reversed cycling ( $R = -1$  and, also,  $R = 0$  in tension and compression). The material exhibited mainly cyclic strain hardening behaviour. Values of the strain hardening coefficient and exponent were obtained in tension and compression.<sup>13</sup> In Table 2:  $\sigma_{0.2}$  and  $\varepsilon_{0.2}$  are the yield stress and strain, respectively, for 0.2% offset parallel line to the elastic line, with Young's modulus,  $E$ ,  $\sigma_R$  is  $\sigma_{UTS}$ ,  $\sigma_f$  is the failure stress ( $\sigma_f > \sigma_R$ )  $\varepsilon_f$  is the rupture strain for  $\sigma_f$ .  $K'$  and  $n'$  are the cyclic strain hardening coefficient and exponent, respectively, of the Ramberg-Osgood-type curve. This was obtained with a correlation coefficient of  $r^2$  (Table 2).

Macros of the cruciform joints of the fatigue specimens are shown in Fig. 2 as indicated. The specimen is a non-load carrying T-joint failing from the weld toe in the thickness direction. The dimensions of the specimens and details of the loading arrangement are given in Fig. 1. In the macros of Fig. 2 the boundaries of the base metal, weld metal and HAZ are clearly visible. The material has a pearlitic-ferritic-type microstructure with an average grain size of 20  $\mu\text{m}$ . In the macros of Fig. 2 it is possible to detect the differences in geometry of the local geometric parameters at the weld toe, the radii,  $\rho$  and the tangent angle,  $\theta$ . The toe grinding technique changes the values of  $\rho$  and  $\theta$  at the weld toe as can be seen in Fig. 2.

Toe grinding was carried out with a small portable grinding fitted with a rotary barrel type tool rotating at high speed along the width of the specimen. The operation procedures were those recommended in Ref. [10].

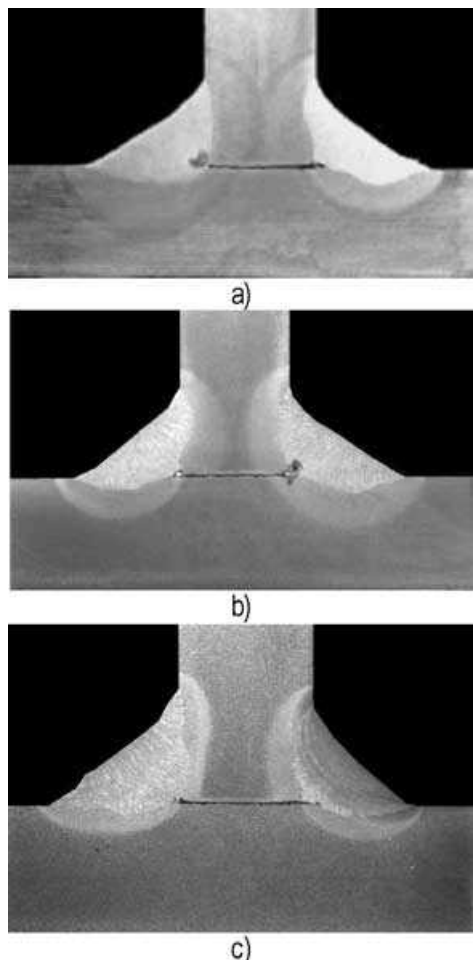


Fig. 2 Macros of the welded joints. T-joint. St 52-3 steel (a) as-welded; (b) toe ground; (c) hammer peening at weld toe.

For hammer peening, a small portable pneumatic hammer was used (Fig. 3), fitted with a special hard metal tool, instrumented with four strain gauges bonded in full bridge (Fig. 3) to measure the impact forces and stresses during the hammer peening working cycles. The tool diameter was approximately 8.5 mm, the air pressure was 3.5 bar and four passes, along the transverse direction of the specimen, were applied.<sup>10</sup> The frequency was 3000 blows/min.

#### Local geometry at weld toe

Values of  $\rho$  and  $\theta$  at the weld toe were obtained by optical measurement using an  $x$ - $y$  co-ordinate table with an accuracy of 0.01 mm and 0.1 degrees, respectively. More than 100 measurements were obtained and the statistical data is given in Table 3 for the as-welded and hammer-peened specimens. A Gaussian-type correlation was obtained and the main parameters are given in Table 3 and Fig. 4a the



**Fig. 3** Hammer-peening tool (high strength steel) to measure the impact forces. T-joint (Fig. 1).

**Table 3** Statistical data of the measurements of radius and tangent angle at weld toe. T-joint (Fig. 1)

	Mean value	Standard deviation	Quadratic error
<b>As-welded</b>			
Radius	3.56 mm	2.1 mm	4.38 mm
Angle	27.33°	10.6°	112.64°
<b>Hammer-peened</b>			
Radius	3.05 mm	1.2 mm	1.44 mm

latter being the probability density function. The empirical fit of the probability of occurrence of the value above, is shown in Fig. 4b for the radius and for the as-welded specimens only. Analysis of the results indicates that there is a very small difference in the values of  $\rho$  between the as-welded and hammer-peened specimens. However for toe grinding  $\rho$  is greater than for as-welded and hammer peening (Fig. 2b & c). Hence the benefit of hammer peening for an increased fatigue life is due mainly to the introduction of compressive residual stresses.

Due to the morphology of the surface, in the weld toe region, after hammer peening, it was not possible to measure accurately the angle at the weld toe in the hammer-peened specimens.

### Fatigue and hardness tests

The fatigue tests were carried out under constant amplitude loading in a  $\pm 250$  kN capacity servo-hydraulic fatigue test machine. The frequency was 10–15 Hz, and the stress ratio,  $R = 0.1$ . The bulk of the tests was carried out until complete failure of the specimen or up to a number of cycles close to  $6.0 \times 10^6$ , time when the fatigue test was stopped.

In the majority of the specimens, including all the cracked ones subjected to repair, six strain gauges were bonded very close to the weld toes of the attachment. These strain gauges measured the variation of the local strain at the weld toe and along the width of the specimen, caused by the initiation and propagation of the fatigue cracks at the weld toe through the thickness direction of the longitudinal plate. The strain data were used to establish the onset of fatigue crack tip marking and to define the crack geometry to be repaired, afterwards, by

hammer peening. The strain gauge data are presented in Ref. [13].

Misalignment was checked in some specimens, using strain gauges, and it was found to be negligible.

Vickers data with 1 kg was obtained along the longitudinal directions of the plate, close to the upper and lower surfaces. The variation of hardness along the thickness of the specimen at the weld toe and in the crack propagation direction was also obtained. The main objective of these tests was to compare the hardness distributions for the as-welded and hammer-peened specimens.

## RESULTS AND DISCUSSION

### Analysis of the hammer-peening process

The variation of the hammer peening impact forces and stresses in the tool, as measured by the strain gauges, is depicted in Fig. 5. The duration of the treatment (working cycles) is indicated in Fig. 5. The mean values quoted in Fig. 5 are the static values that produce the same area under the dynamic stress or load cycle imposed by the tool in the material.

In the fast cycle (approximately 3 s duration) the mean force is significantly larger than in the slow cycle (approximately 35 s duration). The latter cycle follows the procedures recommended in Ref. [10] giving an impact speed between 50 and 100 mm/min in the direction of the length of the weldment (width of the specimen). With these results (Fig. 5) it is expected that the residual stresses in fast cycles will be higher than in the recommended slower impact cycles. Work is in progress to assess this behaviour.

The fatigue tests were only carried out with specimens treated with 'fast' cycle (Fig. 5a).

### Hardness data

In the hammer-peened joints, an increase in hardness was obtained, and the hardness profile, through the plate thickness, shows peak values close to 260 HV near the surface at the weld toe zone (Fig. 6). Figure 6 also shows that the depth of the zone affected by the hammer peening is about 2.5 mm, i.e. the material has hardened up to this depth, and this could be the limit of the residual stress field created by hammer peening. This result also indicates that the treatment could be effective if the crack is inside this hardened zone, where the hardness increases

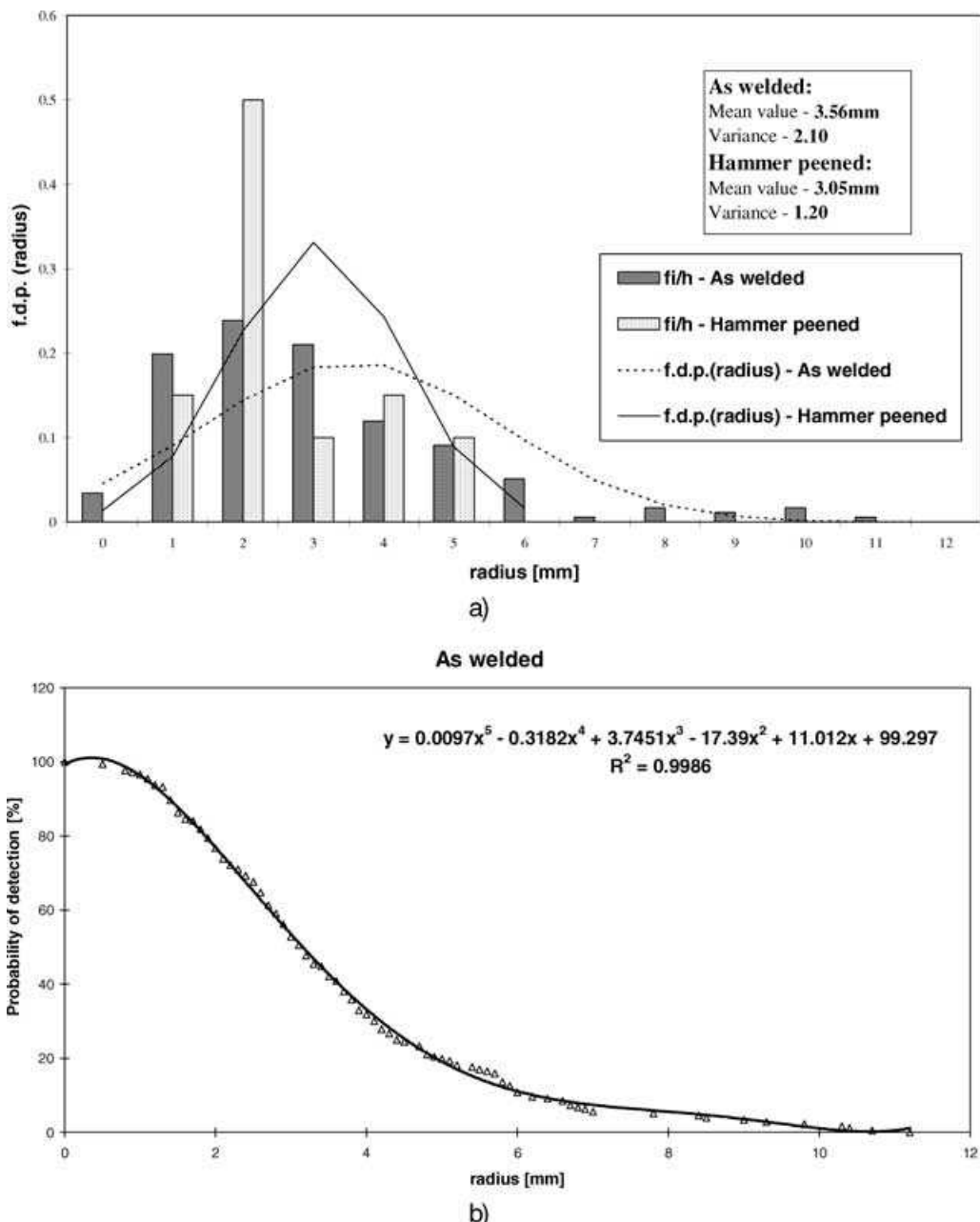


Fig. 4 Statistical data of the local geometry at the weld toe. T-joint (Fig. 1). St 52-3 steel (a) P.D.F. for the radius  $\rho$  (as-welded and hammer-peened joints); (b) probability of occurrence of the value above for the radius  $\rho$ . As-welded joints.

from near the value 190 HV of the base metal up to near 260 HV at the surface at the weld toe in the WM/HAZ hammer-peened zone.

#### Fatigue data in the welded joints

Two typical plots of the variation of strain in the weld toe region are shown in Figs 7a and b. These can be used to detect crack initiation life,  $N_i$ , and also to define a crack marking death, at the associated number of cycles,  $N_{bm}$ ,

or the number of cycles of crack propagation,  $N_{bh}$ , before hammer peening was carried out  $N_{bh}$ .

The crack initiation life,  $N_i$  was defined for the first variation in strain in the strain gauge(s) due to the nucleation of the crack near the strain gauge closest to the crack. (strain gauge 5 in Fig. 7a and strain gauge 2 in Fig. 7b). The depth of the repaired cracks was defined as indicated in Fig. 7.

Specimens failed by crack propagation from the weld toe and through the plate thickness.

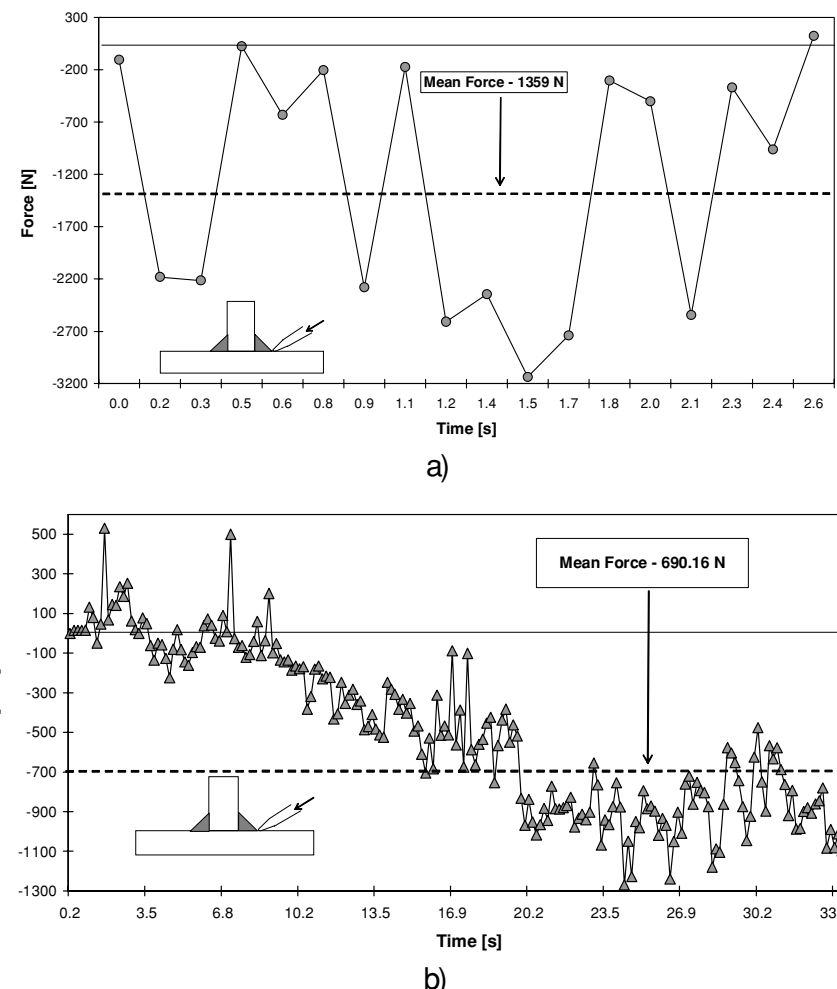


**Fig. 5** Variation of impact forces and stresses measured in the hammer-peening tool (Fig. 3) during the treatment at weld toe (one pass). (a) Fast hammer-peening cycle; (b) slow hammer-peening cycles (recommended in Ref. [10]).

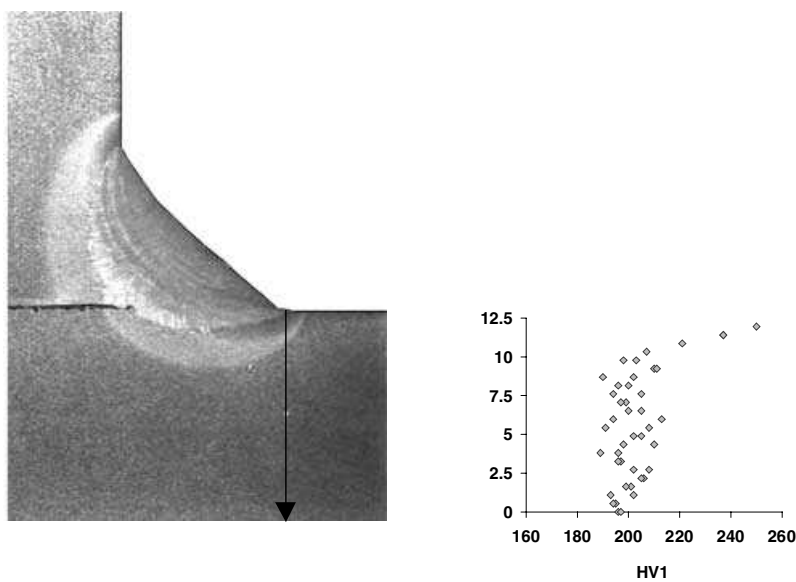


**Fig. 6** Hardness plot along the plate thickness  $y_i$  in the weld toe line for the hammer-peened joints. HV1. T-joints. St 52-3 steel.

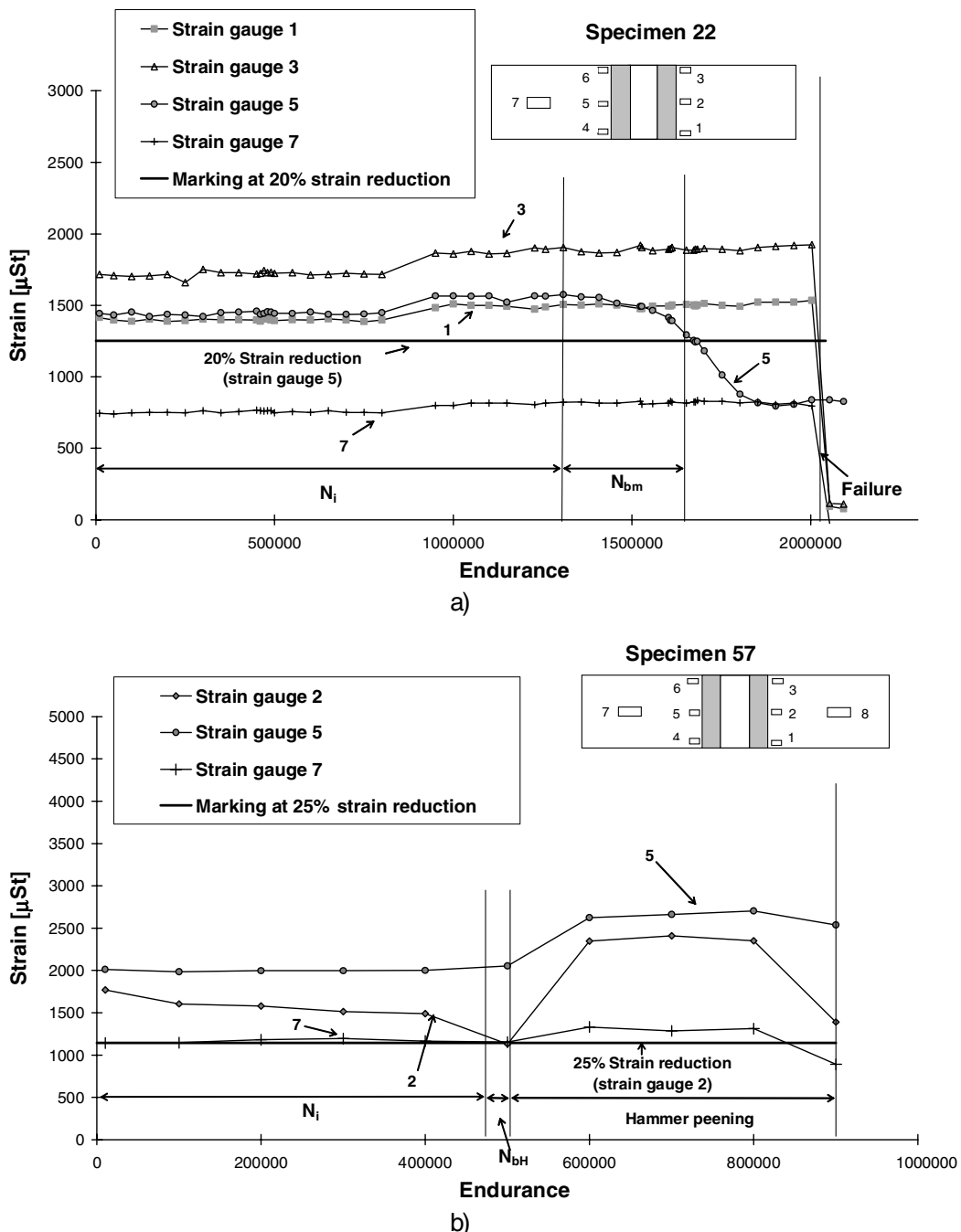


**Fig. 7** Variation of strain, at weld toe region, with the number of cycles to detect crack initiation and define number of cycles to detect crack initiation and define number of cycles of marking.  $N_{bm}$ . T-joints (Fig. 1).  $R = 0.1$ . St 52-3 steel (a) as-welded with marking of a crack depth  $a_H = 1.67$  mm.  $\Delta\sigma = 325$  MPa (20% of strain reduction); (b) specimen repaired by hammer peening of a crack of  $a_H = 1.27$  mm (25% reduction of strain)  $\Delta\sigma = 325$  MPa.

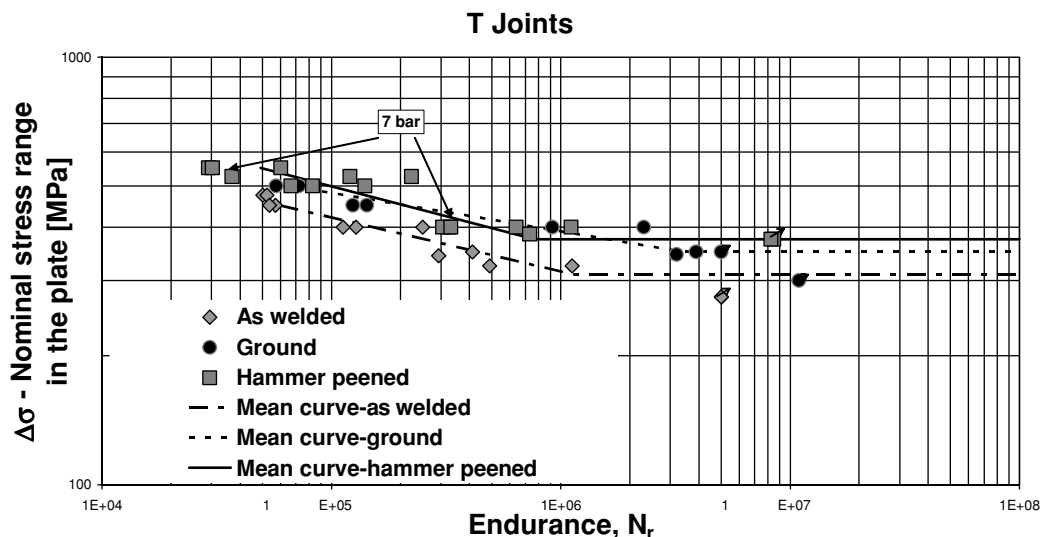
An improvement in fatigue behaviour was obtained in the treated joints. Thus, for fatigue lives above  $10^6$  cycles, hammer peening provides higher fatigue strength since higher fatigue limit stresses were obtained ( $\approx 350$  MPa). Progressively higher fatigue crack initiation periods were obtained in the toe ground and

hammer-peened joints, as reflected by the higher values of  $m$  in the equation of the S-N curve (Table 4 and Fig. 8).

The results (Fig. 8) show that the fatigue strength of this detail is very high. Comparisons can be made with available fatigue design S-N codes.<sup>17,18</sup>

**Table 4** Values of  $K_o$  and  $m$  for the non-repaired specimens. S-N curves.  $N_r = \frac{K_0}{(\Delta\sigma)^m}$  T-joint. 3 PB.  $R = 0.1$  (Fig. 1)

Ref. ( $R = 0.1$ )	$M$	$K_o$	$r^2$	Gain in fatigue strength ( $2 \times 10^6$ cycles)	Gain in fatigue strength ( $3 \times 10^6$ cycles)	Gain in fatigue life ( $\Delta\sigma = 350$ MPa)
As-welded	8.263	$4.99 \times 10^{26}$	0.9469	1	1	1
Toe grinding	11.068	$4.93 \times 10^{34}$	0.9380	$(367.4/294.0) = 1.25$	$(350.0/294.0) = 1.19$	$(3.4 \times 10^6/4.7 \times 10^5) = 7.22$
Hammer peening	6.751	$1.85 \times 10^{23}$	0.7866	$(325.6/294.0) = 1.11$	$(375.0/294.0) = 1.27$	$(1.2 \times 10^6/4.7 \times 10^5) = 2.60$

**Fig. 8** S-N data and best fit of data for the as-welded, toe ground and hammer-peening joints. T-joint (Fig. 1). Unrepaired specimens.  $R = 0.1$ . 3PB. St 52-3 steel.**Table 5** S-N data for the repaired joints by hammer-peening T-joint (Fig. 1)

Ref.	$\Delta\sigma$ (MPa)	$N_i$ (cycles)	$N_r$ (cycles)	Condition
22	325	1 357 537	2 024 529	As-welded only with fatigue marking
23	325	260 000	489 201	As-welded only with fatigue marking
24	325	65 100	1 398 259	As-welded initially and repaired by hammer peening
26	400	75 000	156 255	As-welded initially and repaired by hammer peening
27	400	10 000	230 613	As-welded initially and repaired by hammer peening
28	400	100 000	379 581	As-welded initially and repaired by hammer peening
29	300	2 080 000	3 401 893	As-welded initially and repaired by hammer peening
53	400	100 000	543 810	As-welded initially and repaired by hammer peening
		261254*	—	As-welded initially and repaired by hammer peening
54	325	360 000	514 619	As-welded initially and repaired by hammer peening
57	325	470 000	3 506 191	As-welded initially and repaired by hammer peening
		263809*	—	As-welded initially and repaired by hammer peening
57	400	—	900 266	As-welded initially and repaired by hammer peening
38	500	10 000	111 939	Hammer-peened initially and repaired by hammer peening
46	500	85 000	144 252	Hammer-peened initially and repaired by hammer peening
47	500	30 000	93 809	Hammer-peened initially and repaired by hammer peening

Note:  $\Delta\sigma$  is the nominal stress range in bending in the weld toe area. It was only possible to obtain  $N_{iaH}$  values after hammer peening in a few specimens (Table 5).

\* $N_{iaH}$ —Number of cycles of crack initiation after hammer peening.

Fatigue endurance was defined as the number of cycles,  $N_r$ , to initiate and propagate fatigue cracks up to final failure.

### Results of fatigue life in the repaired joints

The S-N data is given in Table 5 and these results are plotted in Figs 9 and 10 for comparison with the appropriate S-N curves for the unrepaired joints shown in Fig. 8. It is seen that, for the initial untreated welded joints (Fig. 8), an increase in fatigue life was obtained after repair by hammer peening (Fig. 9) because all the data points (Table 5) of the

repaired joints are above the S-N curve of the unrepaired as-welded joints. Also, the results of the repaired joints are very close to the S-N curve of the specimens which were subjected initially to the hammer-peening treatment (Fig. 10). Therefore repair of fatigue cracks by hammer peening gives an improved life in comparison with the unrepaired joints and only a negligible variation of fatigue life was obtained as against the fatigue life results obtained in the joints subjected to hammer peening initially (with no fatigue cracks). Then repair by hammer peening of existing fatigue cracks gives a very similar improvement in fatigue life as if the treatment was applied initially.

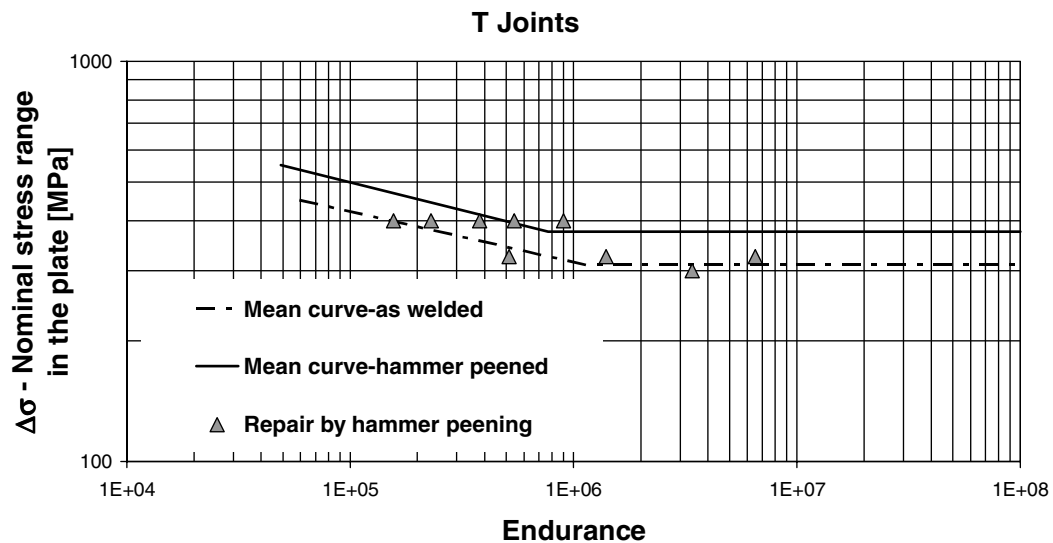


Fig. 9 S-N results for the as-welded specimens with fatigue cracks repaired with hammer peening. T-joints (Fig. 1).  $R = 0.1$ . 3PB. St. 52-3 steel.

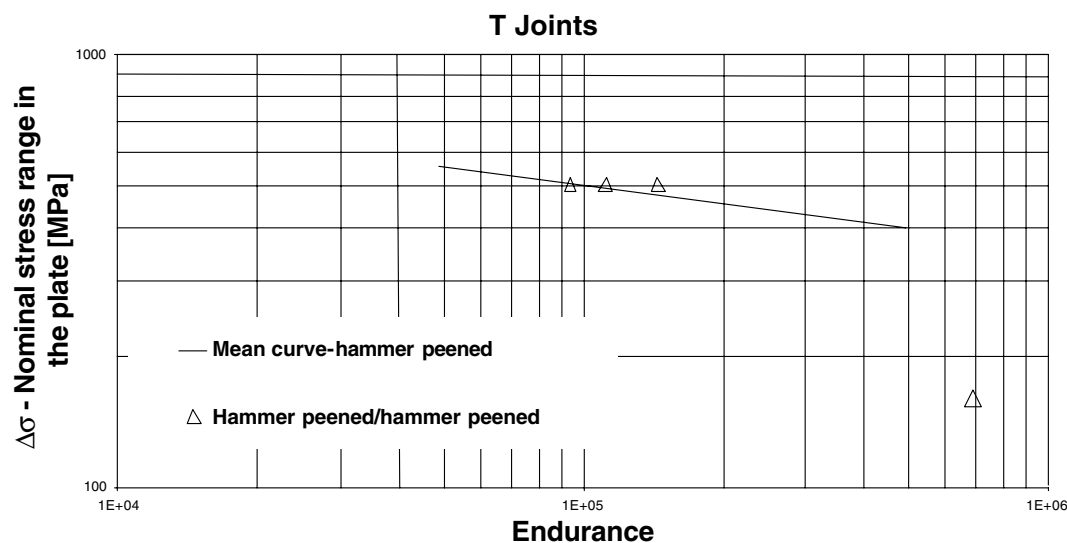


Fig. 10 S-N results for hammer-peened specimens with fatigue cracks repaired by hammer peening. T-joints (Fig. 1).  $R = 0.1$ . 3PB. St 52-3 steel.

**Table 6** Fatigue life data for as-welded specimens with cracks treated (repaired) by hammer peening.  $R = 0.1$ . T-joint (Fig. 1)

Specimen	$\Delta\sigma$ (MPa)	$\Delta\sigma$ (as-welded) (MPa)	$a_H$ (mm)	$c_H$ (mm)	$N_{bH}$ (cycles)	$N_i$ (cycles)	$N_{paH}^{**}, N_{aH}^*$
24	325	307	2.41	5.36	202306	65100	1130853*
26	400	400	3.18	18.29	42321	75000	38934**
27	400	382	2.50	7.72	88458	10000	132155*
28	400	360	4.0	9.21	109237	100000	170344**
29	300	276	3.3	5.81	427107	2080000	1194786**
53	400	344	1.44	11.96	38746	100000	405064*
54	325	347	6.1	26.84	132775	360000	21914**
57	325	275	1.27	3.69	—	470000	—
57	400	324	1.27	3.69	—	—	394075*

$N_{paH}^{**}$ , Calculated values of  $N_{paH}$ ;  $N_{iaH} = 261254$  cycles.

For the repaired joints (Fig. 9) a correlation was not fitted to the results since crack depth is another variable, but comparisons can be made on a basis of constant stress or for a range of fatigue lives.

From data in Fig. 9 it is apparent that a crack may not change significantly the compressive residual stress field of hammer peening. For initial hammer-peened joints (Table 5) a second hammer-peening treatment applied for repair of an existing crack does not provide any significant improvement in fatigue life as shown in Fig. 10. This is due to the fact that the beneficial effect of hammer peening is mainly a consequence of the initial residual stress field left in compression, due to hammer peening, as will be analysed later.

For the conditions in Fig. 10 the material attains a shake down state in the initial treatment by hammer peening, and any additional impact stresses induced by a second set of hammer peening will not change significantly the residual stress field.

Detailed work is in progress in this area using an elastic-plastic 3D FE model to compute the residual stresses caused by hammer-peening operations.<sup>19</sup>

Gain factors  $g_N$  and  $g_s$  to quantify the beneficial effects of hammer peening in repair could be defined as:

$$g = \frac{N_r}{N_e}. \quad (1)$$

For  $g_N$ ,  $N_r$  is the fatigue life of the repaired joint and  $N_e$  is the expected fatigue life of the joint if it was not repaired. The  $g$  factor depends on the crack depth,  $a_H$  of the repaired crack and also on the applied stress range. No correlation was obtained with the stress range but a correlation was obtained with the crack depth. This is valid since for these specimens stress range variation in the fatigue specimens was small (Table 5).

In Eq. (1a)  $N_r$  and  $N_e$  are given by the equations

$$N_r = N_i + N_{bH} + N_{aH}, \quad (2)$$

where  $N_i$  is the crack initiation life before the first crack for repair starts (Figs 7a & b);  $N_{bH}$  is the fatigue life in crack propagation (Figs 7a & b) and Table 6 before repair by hammer peening was carried out in a crack with dimensions  $a_H$ ; and  $c_H$  and  $N_{aH}$  is the fatigue life after repair which will include crack initiation and crack propagation periods (Fig. 7a & b). Both  $N_{bH}$  and  $N_{aH}$  were obtained experimentally:

$$N_{aH} = N_{iaH} + N_{paH}. \quad (3)$$

$N_{iaH}$  was obtained experimentally and  $N_{paH}$  can also be calculated.<sup>13</sup>

Finally,  $N_e$  will be given by the equation:

$$N_e = N_i + N_{bH} + N'_{aH}, \quad (4)$$

where  $N'_{aH}$  is the fatigue life (in crack propagation) that would be obtained in the specimen if repair by hammer peening was not introduced.

$N'_{aH}$  is therefore the number of cycles to propagate an initial crack from the size ( $a_H$ ;  $c_H$ ) to the size for the failure criterion ( $a_H = B/2$ ) where  $B$  is the specimen plate thickness. This failure criterion is acceptable as seen in the macros of fracture surfaces in Fig. 11a and b, since the applied nominal stress range has not varied very significantly in the specimens (Table 5).

Calculated values of  $N_{paH}$  were obtained from integration of the Paris law of the material with values of constant  $C$  and exponent  $m$  obtained in crack propagation tests carried out on the same material<sup>20</sup>  $C = 1.36 \times 10^{-11}$  [mm/cycle];  $m = 3.34$ . The appropriate LEFM K solution was taken from B57910.<sup>21</sup>

For the specimens in Table 5 the results obtained for the terms in Eqs (2)–(4) are presented in Tables 6 and 7 and the values of the gain factor  $g_N$  (Table 7) are plotted in Fig. 12 against crack depth of the repaired crack.

More appropriate values of  $C$  and  $m$  should have been used to predict the  $N_{paH}$  values in the hammer-peened material (Fig. 11b). However, it is known in the

literature<sup>8,9</sup> that the values of  $C$  and  $m$  do not vary significantly with the hardness and strength in carbon steels. Therefore crack propagation behaviour in the hammer-peened zone is expected to have values very similar to the metal leading also to similar values of  $N_{paH}$  for both regions. Thus, the increase in fatigue life in hammer-peened joints is due to increased crack initiation life induced by the compressive residual stresses in the critical areas. A discussion on residual stress values is presented in the section 'Residual stress management'.

For the initial as-welded joints the gain factor  $g_N$  increases for small repaired crack depths and one order of

magnitude in fatigue life  $g \approx 10$  could be obtained for crack depths in the region 1–1.5 mm. For crack depths above 3 mm, the increase in fatigue life is very small (Fig. 12) ( $g_N$  between 1 and 2.5) and for crack depths above 5 mm, the value of  $g_N$  is very close to 1 (no benefit). Therefore, repair by hammer peening is effective if the crack tip region is still within the depth of the region where hardness has increased due to the hammer-peening treatment (Fig. 6). The scatter obtained in the results of Fig. 12 should be mainly attributed to the values of stress range,  $\Delta\sigma$ , in the specimens which were not constant (Tables 6 & 7) although with a small variation.

For the initial hammer-peened specimens, and as expected from above and from the S-N curves in Fig. 10, the gain factor is very small (Fig. 12 & Table 7). In the majority of specimens the number of cycles after repair by hammer peening,  $N_{aH}$ , was greater than  $N_{bH}$ . This is due to the greater crack initiation phase after hammer peening ( $N_{iaH} > N_{paH}$  in Eq. (3)). Work is in progress to predict the crack initiation phases using LCF data obtained in the base metal (Table 2) applied to local stress-strain models.<sup>22</sup> Also for the specimens subjected to the second hammer peening for repair (Fig. 10) prediction of  $N_{aH}'$  should be made taking into account the strain hardening and increase in hardness induced by the initial hammer peening applied after welding.

The gain factor for strength,  $g_S$  was calculated for the fatigue endurance,  $N_r$  of the repaired specimens. The values of  $g_S$  are in Table 7 and the plot  $g_S$  against crack depth  $a_H$ , as in Fig. 12, is in Fig. 13. In Eq. (1b) for  $g_S$ ,  $\Delta\sigma$  is the applied stress range in the fatigue tests of the repaired specimens and  $\Delta\sigma_{aw}$  is the fatigue strength for the as-welded specimen and for the same value of  $N_r$ , whose values are in Table 7. The results for  $g_S$  show some scatter due to the difference in  $N_r$  values from specimen to specimen. However  $g_S$  is always greater than 1, and increases

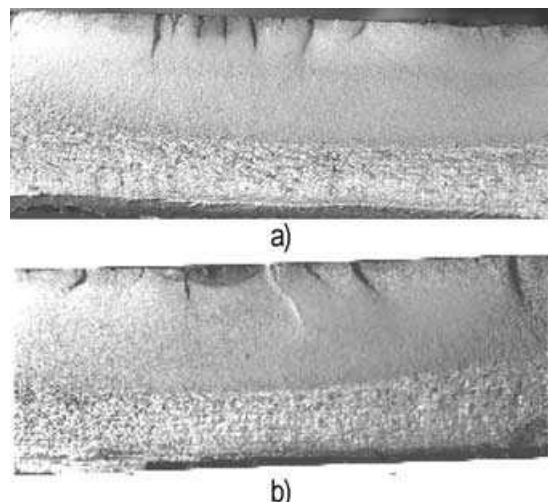


**Fig. 11** Macros of fracture surfaces of fatigue specimens. T-joints (Fig. 1). 3PB.  $R = 0.1$  St 52-3 steel. (a) As-welded only with fatigue marking at 40% strain reduction.  $a_H = 3.86$  mm.  $\Delta\sigma = 325$  MPa.  $N_T = 489201$  cycles. (b) Repaired by hammer peening of a crack depth of 1.27 mm. Fatigue marking of 25% strain reduction.  $\Delta\sigma = 325$  MPa.  $N_T = 900266$  cycles.

**Table 7** Continuation of Table 6 and also Hammer-peening specimens repaired by hammer peening.  $R = 0.1$ . T-joint (Fig. 1)

Specimen	$\Delta\sigma$ (as-welded) [Mpa]	$a_H$ (mm)	$N_{paH}^{**}, N_{aH}^*$	$N_e$	$N_r$	$g_N$	$g_S$
24	307	—	344398**	344399	1398259	4.06	1.06
26	400	—	124523*	125004	156255	1.25	1.00
27	382	—	126741**	126710	230613	1.82	1.05
28	360	—	230795*	208561	379581	1.82	1.11
29	276	—	2603875*	2074325	3401893	1.64	1.09
53	344	—	147153**	415122	543810	1.31	1.16
54	347	—	493360*	139086	514619	3.70	0.94
57	275	—	594434**	6255953	3506181	1.04	1.18
57	324	—	—	82211	900206	10.95	1.23
38	417	2.37	36107	86107	111939	1.30	1.20
46	404	3.98	19330	137383	144252	1.05	1.24
47	426	2.87	33507	80870	93809	1.16	1.17

$N_{iaH} = 263809$  cycles.

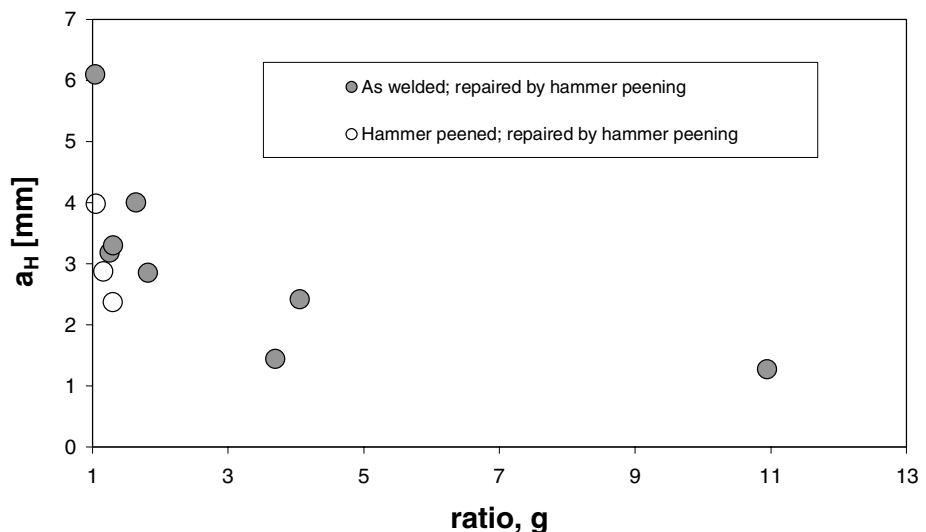


Fig. 12 Gain factor,  $g_N$ , in fatigue life, against depth of fatigue crack repaired by hammer peening. T-joints (Fig. 1).  $R = 0.1$ . 3PB. St 52-3 steel.

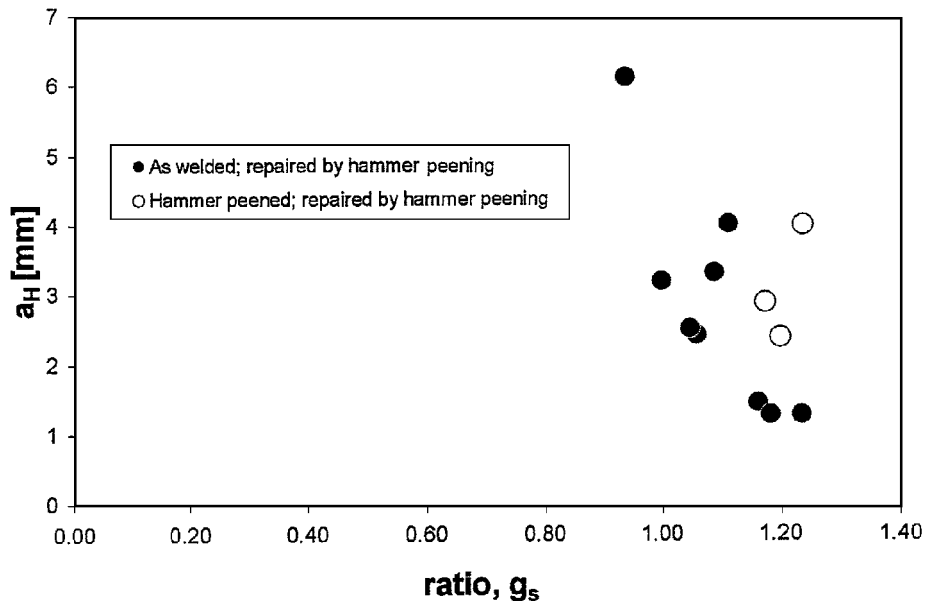


Fig. 13 Gain factor,  $g_s$  is strength against depth of fatigue crack repaired by hammer peening and for the  $N_r$  values. T-joints (Fig. 1).  $R = 0.1$ . 3PB. St 52-3 steel.

when the depth of the repaired crack decreases (Fig. 13). This result indicates that the fatigue strength of the repaired joints is above the as-welded joint (Figs 13 & 9). Hence, with repair by hammer peening there is gain in fatigue life and fatigue strength from very tiny cracks up to cracks with a depth close to half of the thickness of the specimens.

Scatter in the results of gain factors can be reduced by testing treated specimens with variable crack depths, and fixed (few) stress ranges, to obtain  $g_N$ , or with fixed (few) crack depths and variable stress ranges, to obtain  $g_s$  data.

#### Residual stress measurements

Values of the residual stresses were obtained in some selected specimens by X-ray diffraction at the weld toe and at 1–3 and 5 mm from the weld toe in the longitudinal  $x$ -direction. The residual stresses were obtained for different types of specimens, as-welded and hammer-peened after a fatigue test. The objectives of these tests were to quantify the residual stresses introduced by the hammer-peening process. The residual stresses decrease as the  $x$ -distance increases (Table 8(a) & 8(b)).

**Table 8a** Values of the longitudinal residual stress,  $\sigma_x$  (MPa) at the surface along the longitudinal direction,  $x$  from the weld toe. X-ray diffraction (for orientation see axes in Fig. 1)

	Weld toe $x = 0$	$x = 1$ mm	$x = 2$ mm	$x = 3$ mm	$x = 5$ mm
As-welded not tested	–	–	–18	–	14
Hammer-peened	–334	–298	–258	–185	–7

**Table 8b** Values of the transverse residual stress,  $\sigma_z$  (MPa) at the surface along the longitudinal direction,  $x$  from the weld toe. X-ray diffraction. (for orientation see axes in Fig. 1)

	Weld toe $x = 0$	$x = 1$ mm	$x = 2$ mm	$x = 3$ mm	$x = 5$ mm
As-welded before fatigue testing	22	–	–	–	11
Hammer-peened	–439	–288	–213	–172	–22

The results (Table 8(a) & 8(b)) have shown that the residual stresses in the  $x$ -direction are usually significantly higher than in the transverse  $z$ -direction. This effect is predicted in the theory of welding. Both in the  $x$ - and  $z$ -directions, the residual stresses in the hammer-peening condition are above those of the as-welded condition. The maximum value of residual stresses is compressive, and occurs in the location at the weld toe and in the transverse  $z$ -direction.

Because the residual stress is of yield magnitude in compression its effect is beneficial for the fatigue behaviour of the joint, thus explaining the large increase in fatigue strength obtained for the hammer-peened joints. The results also show that the effect of hammer peening, in terms of residual stresses, is localized near the weld toe where the treatment is applied since, at the zone 5 mm away from the weld toe  $x = 5$  mm, the residual stresses are negligible (Table 8(a)). The residual stresses decrease as the longitudinal distance from the weld toe increases (Table 8(a) & 8(b)).

The residual stresses in the as-welded tested specimens are low, at least 5 mm away from the weld toe. Some relaxation effect of stresses may occur after the fatigue tests.

## CONCLUSIONS

For non-load carrying T-joints loaded in 3PB in the main plate, gain factors,  $g$ , were obtained to assess the fatigue lives of repaired fatigue cracks at the weld toe, using the hammer-peening process. A correlation was found between  $g$  and the crack depth,  $a_H$ , of the repaired crack.

The results of hardness distributions at the weld toe have shown that the depth in the thickness direction of the zone affected by hammer peening is about 2.5 mm, the limit of the compressive residual stress fields induced by hammer peening.

For the as-welded joints with fatigue cracks of known size obtained by marking, and repaired by hammer peening, the fatigue lives were found to be significantly above the fatigue lives of the initial as-welded specimens only.

Beneficial effects of repair were found to be greater (high values of gain factors,  $g$ ) in small repaired fatigue cracks with depths below 2.5 mm.

For specimens initially subjected to hammer peening, treatment repair of the fatigue cracks by hammer peening did not produce any significant increase in fatigue life. However the fatigue data obtained in the repaired specimens fitted rather well with the S-N curve for the as-welded hammer-peened specimens without fatigue cracks. Hence the benefits of hammer peening, in terms of increase in fatigue life, are identical whether there is or is not a fatigue crack at the weld toe.

In the hammer-peened specimens, values close to the yield stress in compression were obtained at the weld toe region using the X-ray diffraction technique, which is the main reason for the great increase in fatigue life when hammer peening is applied.

## Acknowledgements

This project was financed by FCT, in Portugal, under the PRAXIS XXI program (Contract 3.1/CEG, 2705/95). The specimens were kindly supplied by The Welding Institute (TWI), Cambridge, U.K. The authors express their gratitude for the support and useful discussions with Dr S.J. Maddox, of TWI.

## REFERENCES

- 1 Branco, C. M. and Dickerson, T. Final Report of ECSC/EEC project Weld Improvement Methods for Low Cycle Fatigue Applications, Contract Nr. 7210 – MC/931, CEMUL/IST, July 94 (in cooperation with TWI, UK, under contract ECSC 7210 – MC/801).

- 2 Branco, C. M. and Gomes, E. C. (1995) Development of fatigue design curves for weld improved joints. In: *Proceedings of the International Conference on Fatigue Design 95, FD95, Helsinki, Finland*, Vol. III, pp. 9–21.
- 3 Maddox, S. J. (1991) *Fatigue Strength of Welded Structures*, Abington Publishing, Cambridge, UK.
- 4 Branco, C. M., Fernandes, A. A. and Castro, P. T. (1999) *Fatigue of Welded Structures (in Portuguese)*, Cap. 11, Ed. Calouste Gulbenkian Foundation, Lisbon.
- 5 Booth, G. S. (1999) (8 edn) *Improving the Fatigue Performance of Welded Joints*, The Welding Institute, Cambridge, UK.
- 6 Offshore Installations; Guidance on Design, Construction and Certification, UK Department of Energy, HMSO, Fourth Edition, 1990.
- 7 *British Standard Specifications for Unfired Fusion Welded Pressure Vessels*, BS5500, 1990, British Standards Institution, London, UK.
- 8 Huther, I., Lieurade, H. P., Sonissi, R., Nussbaumer, A., Chabrolin, B. and Janosh, J. J. (1996) Analysis of results on improved welded joints. *Weld. World* **37**, 242–266.
- 9 Maddox, S. J. (1998) The application of fatigue life improvement techniques to steel welds. In: *IIW Commission XIII Workshop on Improvement Methods, International Institute of Welding, Proceedings of the 51st Annual Assembly, Hamburg, Germany*.
- 10 Haagensen, P. J. and Maddox, S. J. (2001) Specifications for Weld Toe Improvement by Burr Grinding, TIG Dressing and Hammer Peening for Transverse Welds. IIW Document, Commission XIII, Working Group 2, WG2, International Institute of Welding.
- 11 Fisher, J. W. and Dexter, R. J. (1994) Weld improvement for fatigue life extension. In: *Proceedings of the International Conference on Fatigue*, Toronto, Canada, 9–10 May 1994, AWS, pp. 82–87.
- 12 Fisher, J. W. and Dexter, R. J. (1994) Field experience with repair of fatigue cracks. In: *Proceedings of International Conference on Fatigue*, Toronto, Canada, 9–10 May 1994, AWS, pp. 82–87.
- 13 Infante, V. (2002) An Analysis of the Improvement of the Fatigue Behaviour of Welded Joints (in Portuguese), *PbD Thesis*, IST, Lisbon University of Technology, Portugal.
- 14 Infante, V. and Branco, C. M. (2000) A comparative study on the fatigue behaviour of repaired joints by hammer peening. Doc. XIII 1836-2000, 53rd IIW Meeting, Florence, Italy, International Institute of Welding, Commission XIII.
- 15 Infante, V. and Branco, C. M. (2000) A study on the fatigue behaviour of damaged welded joints repaired by hammer peening. In: *Proceedings of ECF13, 13th European Conference on Fracture*, (Edited by San Sebastian). ESIS.
- 16 Infante, V., Branco, C. M. and Baptista, R. An analysis of the effect of hammer peening on the repair of fatigue cracked welded joints. In: *Proceedings of ECF14, 14th European Conference on Fracture, Cracow, Poland, September 2002*, ESIS, Vol. II, pp. 13–21.
- 17 Eurocode 3: Design of Steel Structures, Part 1, General Rules for Buildings, Commission of the European Communities, 1990.
- 18 Fatigue design of welded joints and components. International Institute of Welding, IIW (Edited by A. Hobbacher). Abington Publishing, Cambridge, UK, 1996.
- 19 Baptista, R. (2002) A Study of the Hammer Peening Parameters on the Fatigue Behaviour of Welded Joints, *MSc Thesis*, IST, Technical University of Lisbon.
- 20 Infante, V. and Gomes, E. C. (1999) Fatigue performance of TIG and plasma welds in thin sections. *Int. J. Fatigue* **22**, 589–602.
- 21 British Standards Institution. (2000) Guidance on methods for the acceptance of flaws in structures. Annex J, PD6493, BS7910, UK.
- 22 Glinka, G. (1988) Relations between the strain energy density distribution and elastic-plastic stress-strain fields near cracks and notches and fatigue life calculations. ASTM, STP 942, pp. 1022–1047.

# REHABILITATION AND REPAIR OF WELDED ELEMENTS AND STRUCTURES BY ULTRASONIC PEENING



Y.  
Kudryavtsev<sup>1a</sup>



J.  
Kleiman<sup>1</sup>



A.  
Lugovskoy<sup>2</sup>



L.  
Lobanov<sup>3</sup>



V.  
Knysh<sup>3</sup>



O.  
Voitenko<sup>3</sup>



G.  
Prokopenko<sup>4</sup>

<sup>1</sup> Integrity Testing Laboratory Inc. (Canada)

<sup>2</sup> Atoll (Ukraine)

<sup>3</sup> Paton Welding Institute (Ukraine)

<sup>4</sup> Institute of Metal Physics (Ukraine)

E-mail: <sup>a</sup> ykudryavtsev@itlinc.com

## ABSTRACT

The Ultrasonic Peening (UP) is the most efficient technique for increasing the fatigue life of welded elements as compared to such existing improvement treatments as grinding, TIG-dressing, shot peening, hammer peening, etc. The results of experimental investigation of the efficiency of UP for rehabilitation and repair of welded elements and structures with the goal of preventing the origination and propagation of fatigue cracks are considered in this document. UP treatment was applied to large-scale welded specimens in as-welded condition, after 50 % of expected fatigue life and after repair of fatigue cracks. Also, different techniques for restraining and repair of fatigue cracks were analyzed and compared: overloading; drilling of the crack tips; drilling of the crack tips with installation of high strength bolts; local explosive treatment; local heat treatment; welding with and without UP of weld toe zones. As an example, the practical application of UP for rehabilitation and repair of welded elements of highway and railway bridges are also discussed.

**IIW-Thesaurus keywords:** Bridges; Combined processes; Fatigue life; Fatigue tests; Peening; Reference lists; Repair; Railways; Roads; Structures; Ultrasonic processing; Welded joints; Work hardening.

## 1 INTRODUCTION

Ultrasonic Peening (UP) is a leading technology in the application of High Power Ultrasound (HPU) for fatigue life improvement of welded components and structures [1-4]. The UP technology is based on more than 30 years of extensive research and development by an international group of experts in the use of HPU for industrial applications. One of the first publications on this topic can be attributed to Prof. G. Prokopenko and his colleagues as early as 1974 [5]. During the different stages of its development, the UP process was also known as ultrasonic treatment (UT) [5-7], ultrasonic impact technique/technology/treatment (UIT) [8-10] or ultrasonic impact peening (UIP) [11-12]. A brief histori-

cal review of UP development is provided in IIW Document XIII-2010-04 [1].

The most recent design of the UP equipment is based on "Power on Demand" concept. Using this concept, the power and other operating parameters of the UP equipment are adjusted to produce the necessary changes in residual stresses, stress concentration and mechanical properties of the surface layers of materials to attain the maximum possible increase in fatigue life of welded structures. The basic UP system is suitable for most fatigue improvement applications with the power consumption of 300-500 watts. More powerful UP systems can be designed and produced for special applications. Basic UP systems for manual and robotic applications are shown on Figure 1.

The degree of fatigue strength improvement due to post-weld treatment depends on the mechanical properties of the base material, the geometry of the welded joint, the parameters of cyclic loading and other factors. This is

Doc. IIW-1806-07 (ex-doc. XIII-2076-05) recommended for publication by Commission XIII "Fatigue of welded components and structures".



**Figure 1 – Basic UP systems for manual (left) and robotic (right) applications**

particularly the case when UP treatment is applied. In order to improve the effectiveness of the UP treatment with respect to minimum time-, labour- and power-consumption a software package for "Optimum Application of Ultrasonic Peening" has been developed. This software tool is based on an original predictive model that considers the above mentioned variables [1].

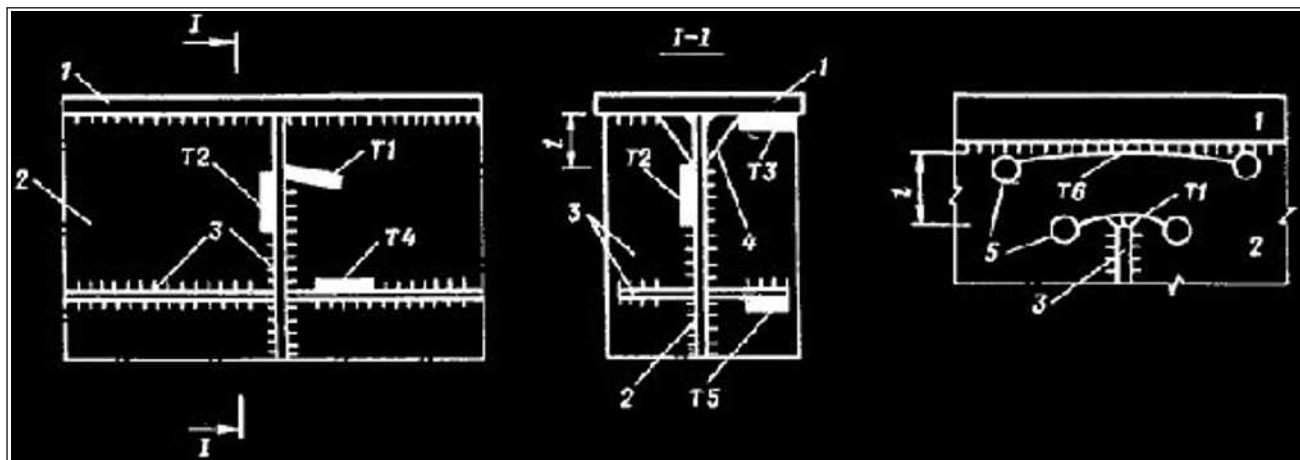
The UP technology has been applied successfully for the fatigue life improvement of different machine parts and welded structures in a number of different industries including: Railway and Highway Bridges, Shipbuilding, Construction Equipment, Mining, Automotive and Aerospace.

The current paper reports the results of an experimental investigation of the efficiency of UP for the rehabilitation and repair of welded elements and structures with the goal of preventing the initiation and propagation of fatigue cracks. The UP treatment was applied to large-scale welded specimens in the as-welded condition, after 50 % of expected fatigue life and after the repair of

fatigue cracks. Also, the efficiency of using the UP treatment in repair of fatigue cracks was assessed in comparison with other techniques. The following techniques for retarding the growth of fatigue cracks were considered; overloading; hole drilling of the crack tips; hole drilling of the crack tips combined with the installation of high strength bolts; local explosive treatment; local heat treatment; welding without and with UP treatment of weld toe zones. As an example, the practical applications of UP for rehabilitation and repair of welded elements of highway and railway bridges are also considered in this document.

## 2 APPLICATION OF UP FOR REHABILITATION OF WELDED ELEMENTS AND STRUCTURES

One example of the effective application of UP is the fatigue life improvement of welded joints of highway and railway bridges. Published reports and direct observations of welded bridges have shown that the typical zones of fatigue crack initiation are the ends of vertical welded stiffeners [8], i.e., crack types T1 and T2 in Figure 2. The effectiveness of applying UP for the prevention of fatigue crack initiation and retarding propagation in such locations was studied experimentally using fatigue testing of large-scale welded samples, see Figure 3. Fatigue testing showed that UP could prevent the initiation of fatigue cracks for these types of welded details for the studied cyclic loading conditions. It was shown that UP treatment of the weld toe over a length of about 100 mm from the end zones of the welded stiffeners could produce a significant increase of the fatigue strength of this welded detail and could eliminate the initiation of fatigue cracks. Figure 3 shows the zone of crack initiation in un-treated test specimens and the UP treated areas for improved test specimens. The UP treatment of weld toe produced an easily visible groove [8, 9].



**a) Railway bridge**

**b) Railway bridge**

**c) Highway bridge**

T1-T6 - Zones of fatigue crack initiation

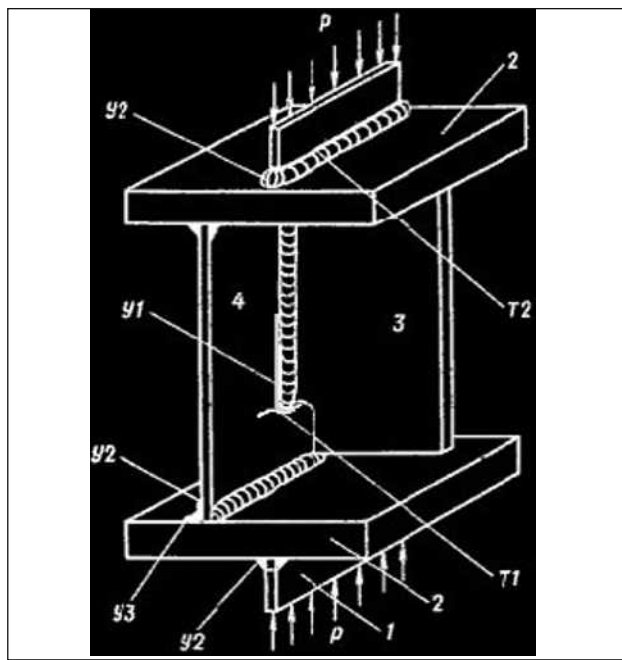
1, 2, and 3 - Upper flange, web and stiffeners of the bridge span

4 - Openings in the stiffener

5 - Holes produced to prevent the propagation of fatigue cracks

1 - Zone of local bending of the web [8]

**Figure 2 – Schematic presentation of the location of fatigue cracks in welded elements of bridges**



T1 - Zone of fatigue cracks initiation

Y1 - Zone of UP treatment

3 - Welded stiffener

4 - Web

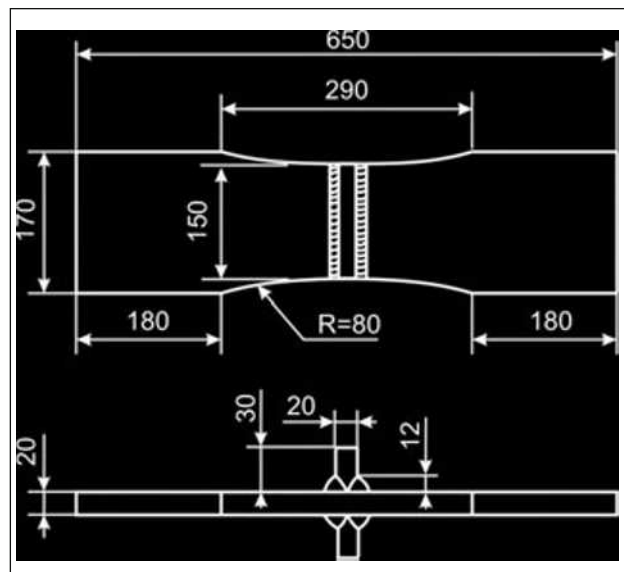
**Figure 3 – Drawing of welded sample imitating the attachment of the vertical stiffener to the web for fatigue testing in as-welded condition and after UP [8]**

### Effectiveness of UP applied after 50 % of expected fatigue life of welded elements

Virtually all previous test programs using UP were intended to demonstrate the efficiency of the technology for new welded constructions. Previous tests illustrated that UP could be effectively applied for the prevention of fatigue crack initiation in new welded bridges. However, there was also a need to investigate the effectiveness of the method for bridges already in service. The goal was to examine the effectiveness of UP when applied to bridge details already exposed to cyclic loading conditions corresponding to several years in service. This section describes fatigue testing of welded details when UP treatment was applied after 50 % of the expected fatigue life of welded elements in the as-welded condition.

Three series of large-scale welded samples were subjected to fatigue testing to evaluate the effectiveness of UP application to the existing welded structures:

1. in as welded condition,
2. UP was applied before fatigue testing,
3. UP was applied after fatigue loading with the number of cycles corresponding to 50 % of the expected fatigue life of samples in as-welded condition.



(Dimensions in mm)

**Figure 4 – General view of welded sample for fatigue testing**

The general view of welded sample for fatigue testing is shown on Figure 4.

Mechanical properties and chemical composition of base material are presented in Tables 1 and 2.

All welded samples were tested at stress ratio  $R = 0$  ( $\Delta\sigma = \sigma_{max}$ ). The results of the fatigue testing are presented in Figure 5.

As can be seen from Figure 5, the UP produced a significant increase in the fatigue strength of the welded joints for both series of UP treated samples. The increase in the mean fatigue strength (at  $N = 2 \cdot 10^6$  cycles) of the welded samples was 49 % (from 119 MPa to 177 MPa) for UP treated samples before fatigue loading and was 66 % (from 119 MPa to 197 MPa) for samples treated with UP after fatigue loading corresponding to 50 % of the expected fatigue life of the samples in as-welded condition. The resulting increase in fatigue life due to UP treatment was a factor of 5-10 times depending on the level of applied loading. With reference to Figure 5, the higher increase of fatigue life of UP treated welded elements for fatigue curve #3 could be explained by a more beneficial redistribution of residual stresses and/or "healing" of fatigue damaged material by UP in comparison with the fatigue curve #2. Additional research work is now in progress to explain this and similar results.

**Table 1 – Mechanical properties of base material**

$\sigma_y$ MPa	$\sigma_u$ MPa	$\delta$ %	$\psi$ %
260	465	37.6	63

**Table 2 – Data on chemical composition of base material**

%							
C	Si	Mn	S	P	Cr	Ni	Cu
0.210	0.205	0.52	0.019	0.007	0.04	0.04	< 0.01

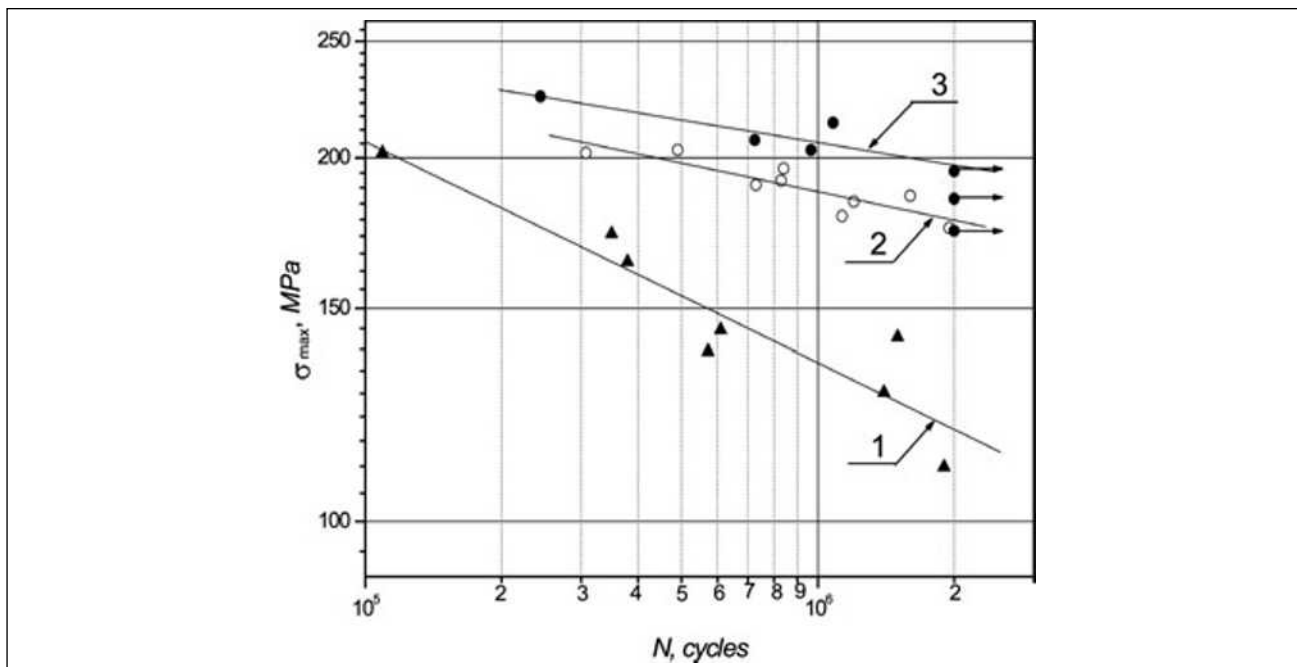


**Figure 5 – Fatigue curves of welded samples (transverse non-load-carrying attachment):**

1 – in as welded condition, 2 – UP was applied before fatigue testing,

3 – UP was applied after fatigue loading with the number of cycles corresponding to 50 % of expected fatigue life of samples in as-welded condition

In cases where experimental data is lacking for specific materials, loading conditions or joints improved by UP, the improvement factors described in IIW recommendations on fatigue life improvement of welded elements for different peening techniques [13, 14] can be applied to estimate the expected increase of fatigue strength of welded elements by UP. This benefit factor is 1.3 for steels with the yield strength less than 355 MPa, and 1.6 – for steels with the yield strength of more than 355 MPa. The benefit factor for aluminium alloys is 1.6. This factor could be applied to increase the limit stress range (at 2·10<sup>6</sup> cycles) of UP treated welded element. A benefit factor of, for instance 1.3, corresponds to a 2.2 times increase in fatigue life of the welded element [13, 14].

### 3 APPLICATION OF UP FOR REPAIR OF FATIGUE CRACKS IN WELDED ELEMENTS AND STRUCTURES

In the previous section it was shown that UP treatment is an effective way for rehabilitation of welded structures. Throughout this document, rehabilitation is defined as the prevention of possible fatigue crack initiation in existing welded structures that are in service. The UP could also be effectively used during the repair of fatigue cracks.

The results of experimental investigation of the efficiency of traditional and advanced techniques for fatigue life improvement of structural elements with fatigue cracks are considered in this chapter. Large-scale specimens containing fatigue cracks were subjected to further

fatigue testing after a number of fatigue crack restraining and repair techniques were applied. These techniques included: overloading, drilling of the crack tips, drilling of the crack tips combined with the installation of high strength bolts, local explosive treatment, local heat treatment, repair welding with and without UP of weld toe zones.

A number of large scale specimens, see Figure 6, with observable fatigue cracks were subjected to further fatigue loading both without any repair and using one of the previously mentioned repair procedures. In all cases the cyclic loading was zero-to-tension ( $R = 0$ ) with the maximum stress of 155 MPa. The fatigue testing of large scale specimens showed that the repair of fatigue crack by welding with the subsequent UP treatment provided longest fatigue life in comparison with other ways to prolong the service life of structural elements with fatigue cracks. The results of fatigue testing of specimens with cracks subjected to the above-mentioned improvement techniques are summarized in Figure 7. This figure shows the number of fatigue cycles to complete separation of the test pieces following the repair procedure.

A predictive model and software for fatigue assessment of welded elements with cracks in the as-welded condition and after the application of common improvement techniques based on the introduction of beneficial compressive residual stresses in the zone of crack tip have been developed and experimentally verified [15]. In some specimens and real welded structures the residual stresses were measured by non-destructive ultrasonic method [16, 17]. This information was further used to compute of the effect of compressive residual stresses on fatigue crack propagation.

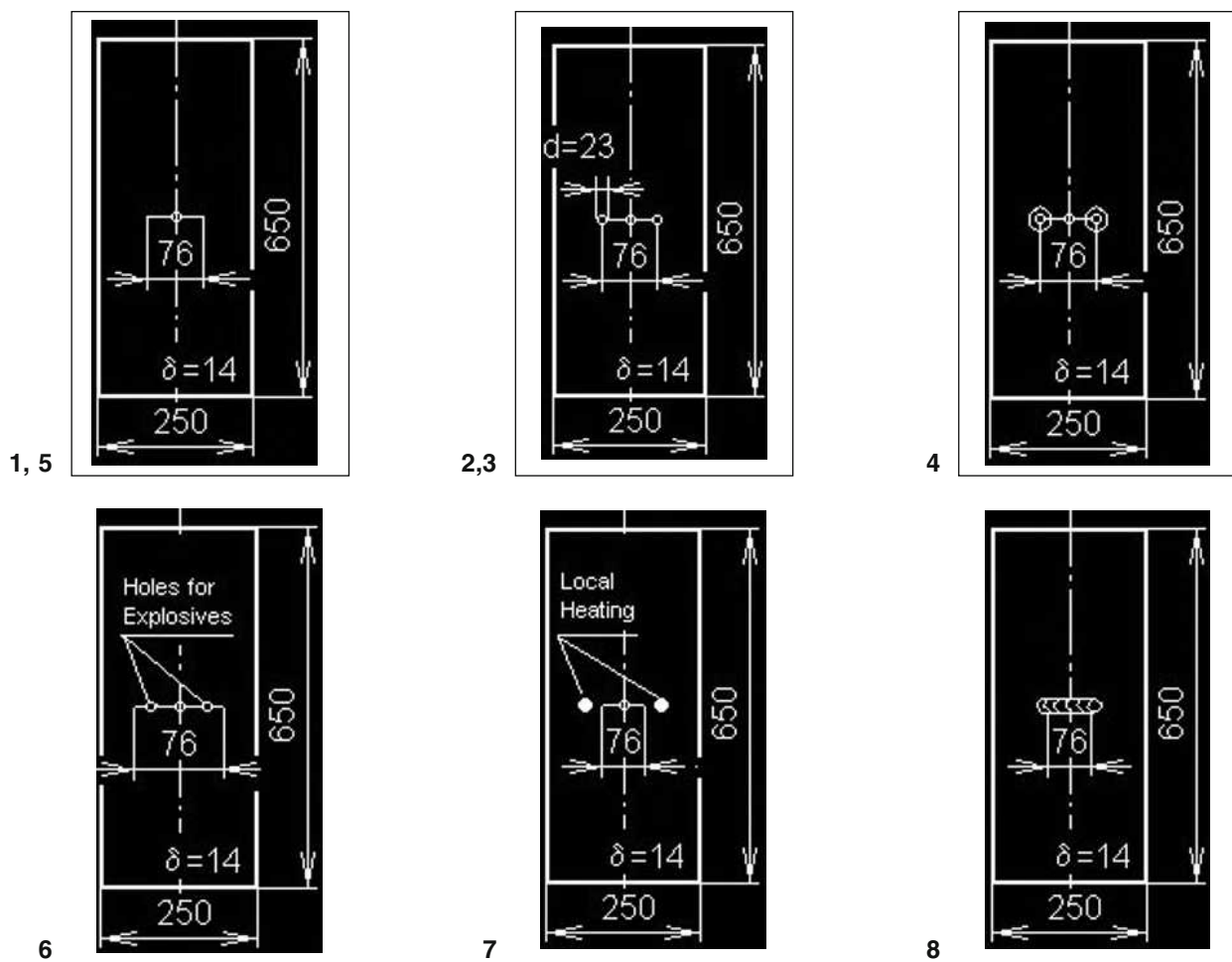
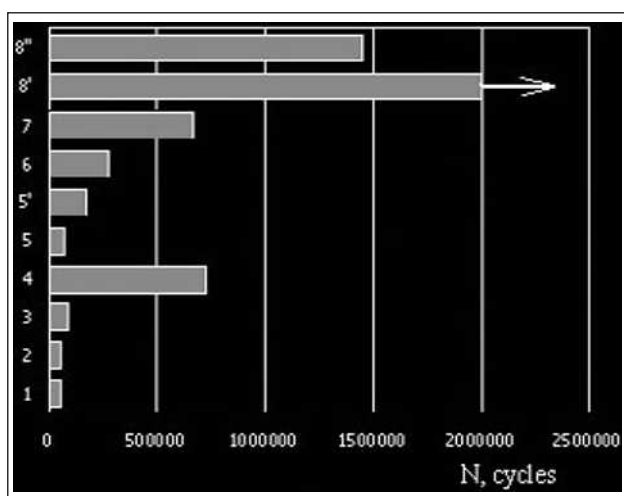


**Figure 6 – Drawings of specimens with fatigue cracks for further fatigue testing at the following conditions:** 1 - initial condition (no repair), 2, 3 - drilling of the crack tips with and without cold working, 4 - drilling of the crack tips combined with installation of high strength bolts, 5 - overloading, 6 - local explosive treatment, 7 - local heat treatment, 8 - welding with and without UP of weld toe zones



1 - Initial condition, 2 and 3 - Drilling of the crack tips with and without cold working,  
 4 - Drilling of the crack tips with installation of high strength bolts,  
 5 - Overloading (yield strength), 5' - Overloading (0.7 yield strength),  
 6 - Local explosive treatment, 7 - Local heat treatment,  
 8' - Repair by welding with UP treatment of the weld toe zones,  
 8'' - Repair by welding without UP

**Figure 7 – Comparison of the efficiency of different techniques of restraining and repair of fatigue cracks**

#### 4 EXAMPLES OF PRACTICAL APPLICATION OF UP FOR REHABILITATION AND REPAIR OF WELDED STRUCTURES

##### 4.1 Rehabilitation: prevention of fatigue crack initiation

Based on the fatigue data and the solution described in Chapter 2, UP was applied during the rehabilitation of welded elements of a highway bridge over the Ohio River in the USA, see Figures 8 and 9. The bridge was constructed about 30 years ago. The welded details of the bridge did not have macroscopic fatigue cracks. The motivation for application of the UP for fatigue life improvement of this bridge was the fatigue cracking in welded elements of another bridge of approximately the same age and design. The stages of preparation for UP treatment of the bridge and the process of UP treatment of one of the welded vertical stiffeners are shown on Figures 8 and 9. More than two thousand welded details of the bridge structure that were considered to be fatigue critical were UP treated. The total length weld toe treated using UP treated was about 500 meters.



**Figure 8 – Ultrasonic Peening of a welded bridge:  
Preparation for UP treatment  
(Two UP Systems/Lifts)**



**Figure 9 – Ultrasonic Peening of a welded bridge:  
UP of the end of one of welded vertical stiffeners**

#### 4.2 Repair of fatigue crack

During the regular inspection of the railway bridge over Dnepr River in Ukraine, a fatigue crack was found in one of the welds of the bridge span. The fatigue crack was located in the weld connecting the upper flange and the web. The length of the crack was about 1 meter. The location of fatigue crack in welded element of bridge span is shown on Figure 10.

The fatigue crack was repaired using standard welding procedures. To prevent possible recurrence of fatigue cracks at the same location, the repaired zone was UP treated. The process of UP treatment of repaired zone in welded element of bridge span is shown on Figures 10 and 11.

#### 5 CONCLUSIONS

The effectiveness of Ultrasonic Peening for repair and rehabilitation of fatigue loaded welded structures had been studied using large-scale laboratory specimens and has been applied to in-service bridge structures. The following conclusions can be made.

1. Ultrasonic Peening is a relatively new and promising technique for fatigue life improvement that could be effi-

ciently used for rehabilitation and repair of welded elements and structures.

2. The application of Ultrasonic Peening for treatment of welded elements of existing structures provides, practically, the same increase in fatigue life of welded elements that could be achieved by treatment after/during construction.
3. The results of fatigue testing of large-scale specimens showed that the welding and subsequent application of Ultrasonic Peening provides the highest endurance of specimens with fatigue cracks as compared with other considered techniques for fatigue life improvement.
4. The modern equipment for Ultrasonic Peening could be efficiently applied for rehabilitation and repair of welded elements of highway and railway bridges and other areas.

#### REFERENCES

- [1] Kudryavtsev Y., Kleiman J., Lobanov L., Knysh V., Prokopenko G.: Fatigue life improvement of welded elements by Ultrasonic Peening, International Institute of Welding, IIW Document XIII-2010-04, 2004, 20 p.



**Figure 10 – Photo showing the location of fatigue crack in welded element of bridge span and application of UP during the repair of crack**



**Figure 11 – Enlarged view of the zone of repair (welding + UP treatment) of fatigue crack in welded element of bridge span**

- [2] Kudryavtsev Y., Kleiman J., Prokopenko G., *et al.*: Effect of Ultrasonic Peening on microhardness and residual stress in materials and welded elements, X International Congress and Exposition on Experimental and Applied Mechanics, Costa Mesa, California USA, June 7-10 2004, (on CD).
- [3] Kudryavtsev Y., Kleiman J., Prokopenko G., *et al.*: Computerized complex for Ultrasonic Peening of parts and welded elements, 32<sup>nd</sup> Annual Ultrasonic Industry Association Symposium, New York, NY, USA, October 21-23 2002 (on CD).
- [4] Kudryavtsev Y., Kleiman J., Prokopenko G., *et al.*: Mechanism and efficiency of Ultrasonic Peening in fatigue improvement, SEM Annual Conference & Exposition on Experimental and Applied Mechanics, Milwaukee, Wisconsin, USA, June 10-12 2002, (on CD).
- [5] Polozky I., Nedoseka A., Prokopenko G., *et al.*: Relieving of welding residual stresses by ultrasonic treatment, Paton Welding Journal, 1974, No. 5., pp. 74-75 (in Russian).
- [6] Krivko V., Prokopenko G.: Ultrasonic treatment of welded joints, Welding Production, 1979, No. 5, pp. 32-33 (in Russian).
- [7] Mikheev P., Nedoseka A., Parkhomenko A., *et al.*: Efficiency of ultrasonic treatment application for increase of fatigue strength of welded joints, Paton Welding Journal, 1984, No. 3, pp. 4-7.
- [8] Kudryavtsev Y., Korshun V., Kuzmenko A.: Improvement of fatigue life of welded joints by the ultrasonic impact treatment, Paton Welding Journal, 1989, No. 7. pp. 24-28.
- [9] Kudryavtsev Y., Mikheev P., Korshun V.: Influence of plastic deformation and residual stresses, created by ultrasonic impact treatment, on the fatigue strength of welded joints, Paton Welding Journal, 1995, No. 12, pp. 3-7.
- [10] Trufiakov V., Mikheev P., Kudryavtsev Y., Statnikov E.: Ultrasonic impact treatment of welded joints, International Institute of Welding, IIW Document XIII-1609-95, 1995.
- [11] Trufyakov V., Mikheev P., Kudryavtsev Y., Reznik D.: Ultrasonic impact peening treatment of welds and its effect on fatigue resistance in air and seawater, Proceedings of the Offshore Technology Conference, OTC 7280, 1993, pp. 183-193.
- [12] Trufyakov V., Mikheev P., Kudryavtsev Y., Reznik D.: Fatigue endurance of welded joints, Residual stresses and fatigue improvement treatments, Ship Structure Symposium "93", Arlington, Virginia, USA, November 16-17 1993, pp. N1-N14.
- [13] Haagensen P., Maddox S.: IIW Recommendations on post weld improvement of steel and aluminium structures, International Institute of Welding, IIW Doc. XIII-1815-00, 2000.
- [14] Hobbacher A.: Recommendations for fatigue design of welded joints and components, International Institute of Welding, IIW Doc. XIII-1965-03/XV-1127-03, 2003.
- [15] Kudryavtsev Y., Kleiman J., Knysh V., Mikheev P.: Fatigue life improvement of structural elements with fatigue cracks, SEM Annual Conference & Exposition on Experimental and Applied Mechanics, Milwaukee, Wisconsin, USA, June 10-12 2002 (on CD).
- [16] Kudryavtsev Y., Kleiman J., Gushcha O.: Ultrasonic measurement of residual stresses in welded railway bridge, Structural Materials Technology: An NDT Conference, Atlantic City, NJ, February 28-March 3 2000, pp. 213-218.
- [17] Kudryavtsev Y., Kleiman J., Gushcha O., *et al.*: Ultrasonic technique and device for residual stress measurement, SEM International Congress and Exposition on Experimental and Applied Mechanics, Costa Mesa, California, USA, June 7-10 2004 (on CD).

## Offshore fatigue crack repair by grinding and wet welding

J. E. RODRÍGUEZ-SÁNCHEZ<sup>1</sup>, A. RODRÍGUEZ-CASTELLANOS<sup>2</sup>,  
F. PÉREZ-GUERRERO<sup>3</sup>, M. F. CARBAJAL-ROMERO<sup>4</sup> and S. LIU<sup>5</sup>

<sup>1</sup>Instituto Mexicano del Petróleo, Coordinación de Aguas Profundas, Eje Central Lázaro Cárdenas Norte 152, 07730 México Distrito Federal, Mexico,

<sup>2</sup>Instituto Mexicano del Petróleo, Dirección de Ingeniería, Eje Central Lázaro Cárdenas Norte 152, 07730 México Distrito Federal, Mexico, <sup>3</sup>Instituto Mexicano del Petróleo, Coordinación de Aguas Profundas, Eje Central Lázaro Cárdenas Norte 152, 07730 México Distrito Federal, Mexico, <sup>4</sup>Instituto Politécnico Nacional, Sección de Estudios de Posgrado, Avenida de las Granjas 682, 02350 México Distrito Federal, Mexico, <sup>5</sup>Colorado School of Mines, Metallurgical & Materials Engineering, Hill Hall 254 Golden, Colorado 80401, USA

Received in final form 25 Oct 2010

**ABSTRACT** A fatigue crack repair option based on crack removal by grinding and subsequent filling of the resultant groove by wet welding is presented. Author's experimental and fracture mechanics analysis experience on fatigue crack removal by grinding has demonstrated that a fatigue life extension factor of 2 to 3 is feasible for crack removal done before crack penetration has reached 30% of the plate thickness. However, it has also been demonstrated when groove is left empty, that fatigue life extension after crack removal is mainly due to the stage of fatigue initiation because crack propagation after removal has a higher rate than in as-welded condition. To overcome this situation, this work proposes for an underwater application like in the offshore industry, that filling the grinded groove by means of wet welding would produce a crack repair with a longer fatigue life than the empty groove case.

**Keywords** crack repair; fatigue life; grind; groove; notch; offshore repair; wet weld.

### NOMENCLATURE

$a$	= crack depth
$C$	= material constant
$da/dN$	= crack growth rate
$m$	= material constant
$Y$	= modification factor (Y factor)
$\Delta K$	= stress intensity range $K_{\max} - K_{\min}$
$\Delta\sigma$	= surface stress range of uncracked welded joint at the crack site

### INTRODUCTION

Fatigue cracks in offshore structures are frequently found during inspection campaigns, and their effect on the structural integrity can become quite relevant depending on the redundancy of the structure. For the case of jacket structures it is widely known that hot spot stress locations at main tubular welded joints are prone to fatigue cracking, fortunately jackets are quite redundant structures that can safely continue operating with some cracked joints considering that they are regularly inspected to monitor crack growth depth and length. This practice of en-grossing NDT inspection plans to sustain integrity when fatigue cracks are found is mainly due to the fact that

underwater fatigue crack repairs are not an easy task to perform, otherwise a repair would partially reinstate the as-welded condition and general visual inspection would be enough to sustain integrity after a fatigue crack repair is performed.

Present practice for fatigue crack repair of jackets tubular joints basically relies on mechanical clamps rather than on crack removal. However, clamping solutions require considerable economical resources for the fabrication and installation of the clamps and frequent stress monitoring of the studs during the operating life of the jacket. Therefore, the fatigue crack repair option presented in this paper is a feasible option to reduce the economical resources required for fatigue crack repair of offshore jackets.

Correspondence: José Efraín Rodríguez-Sánchez. E-mail: ersanche@imp.mx

This paper gathers author's experience obtained experimentally and in the field on fatigue crack repairs and on wet welding procedures. It has to be stated that at this stage of wet welding technology, it is only applicable up to 100 m of water depth, thus what is presented here has the same limitations. The repair procedure presented combines crack removal by grinding and subsequent filling of the groove by means of wet welding trying to reinstate the as-welded condition. The grinding experience assures that the crack is adequately removed and the wet welding experience provides a procedure that leads to maximize the weld quality of the repair. Additionally, because the grinding tool is available as it was used for the crack removal, the tool can also be used to improve the weld toe profile to reduce the stress concentrations and extend the fatigue initiation life. It is known that after crack removal by grinding when the groove is left empty, the fatigue life extension is due to the fatigue initiation stage because crack propagation stage has a higher rate than in as-welded condition.<sup>1</sup> Therefore, for a crack removal to reduce the fatigue propagation to a similar rate of the as-welded condition it has been considered the application of wet welding. Thus, the repair procedure presented has been conceived as follows:

To remove the crack and reinstate as-welded conditions

- 1 Fatigue crack removal by grinding
- 2 Groove filling with wet weld to reduce the fatigue crack propagation rate due to the stress riser effect of the groove

To extend fatigue initiation life

- 3 Wet weld toe profiling
- 4 Induce surface compressive stresses

## FATIGUE CRACK REMOVAL BY GRINDING

Grinding of fatigue cracks has been used mainly in underwater offshore applications to remove the crack tip and stop crack propagation. For the case of welded tubular joints and welded plates, the profile of the groove along the crack length produced by grinding is highly relevant on the fatigue life of the repaired component. For the case of crack re-initiation after crack removal by grinding, the profile of the groove prescribes the location of crack initiation along the groove. Analytical and experimental work on crack repair geometry has been done where the concept of short repair is introduced and its usefulness demonstrated for the case of removal of fatigue cracks by grinding in underwater conditions.<sup>2</sup> Crack initiates at the location of highest stress, which for the as grinded condition occurs at the bottom of the groove or at both ends of the groove where the groove reaches the plate surface. Occurrence of one or the other case would depend on the groove geometry; the second case is known as short repair. The main advantage of a short repair is that after a crack removal is performed and if crack re-initiation occurs, this would always be at the groove ends located at the top of the plate, reinstating the original plate thickness for crack propagation and also facilitating the inspection of the repair because plate surface inspection is easier than inspection in a narrow groove.<sup>2</sup> Crack re-initiation for repairs that do not comply with the short repair conditions will always take place on the bottom of the groove. From Fig. 1, groove ends and bottom of the groove locations for a surface crack short repair are illustrated.

It is worth pointing out that if a repair profile is left empty this is, not filling the groove with wet weld, a short repair

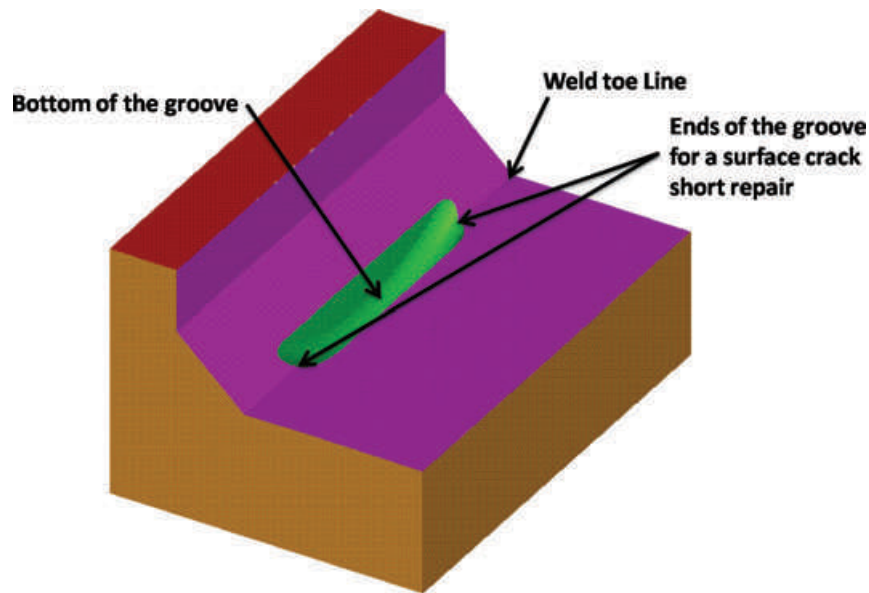


**Fig. 1** Locations of groove ends and bottom of the groove for a surface crack short repair on a *t*-butt welded connection.

profile is only effective for the removal of surface cracks. For the case of edge cracks after crack removal is performed and leaving the groove empty, crack re-initiation will always take place on the bottom of the repair.<sup>2</sup> Thus, the wet weld groove filling benefit is to erase the repair profile shape that defines if crack re-initiation starts on the surface of the plate or on the bottom of the repair making feasible to perform the repair procedure proposed in this work for surface and edge cracks.

For the case of fatigue crack repairs by grinding and subsequently filled with wet weld, it has been considered that the use of short repairs is not recommended because the profile requirement is stringent and no benefits are expected due to the profile geometry because the groove stress distribution effect is erased by the wet weld filling that tends to reinstate the as-welded condition. Additionally, it is expected that the use of longer grooves facilitates the application of wet welds.

Grooves are generally machined by divers using rotating burrs and quality control of the groove profile geometry becomes difficult due to the amount of force required to penetrate into the metal, thus burrs skip sideways before a deep groove track is obtained resulting in poor groove profile geometry. The use of wet weld to fill the groove can help to overcome the difficult task of assuring the quality of the groove profile because the groove profile effect is erased by filling the groove.

#### **GROOVE FILLING WITH WET WELD**

Wet welding has been used by offshore oil operators in the Gulf of Mexico for the repair of offshore structures damaged by hurricanes, boat impacts, dropped objects from the decks, etc. It is well known that fatigue cracks typically initiate at the weld toe and propagate though the thickness of the structural component. As mentioned earlier, crack removal is an option to extend the fatigue life for crack depths up to 30% of plate thickness. However underwater inspection of a narrow groove is difficult, thus, risk of incomplete crack removal by grinding is feasible, which would lead to increased fatigue crack propagation rate instead of extending the fatigue life. Therefore, an effective option to assure that crack propagation is halted, even if the crack is not totally removed, is by fusing the crack tip when melting the bottom of the groove during wet weld deposition. Although a total removal of the crack is intended by design, if a crack tip is left unintentionally its size is minimum due to the inspection equipment accuracy and can be fused while wet weld is deposited.

Once a fatigue crack has been detected a decision has to be made whether it is only grinded out leaving an empty groove or in addition to grinding out the crack, filling the groove with wet weld. The first case is preferably applica-

ble to surface cracks repaired with short repairs, limited to a crack depth removal up to 30% of plate thickness. The second case is preferably recommended for edge crack repairs because crack re-initiation will always take place on the bottom of the groove making underwater inspection even more complicated. However, it is worth pointing out that the uncertainty of total crack removal for both cases remains an issue due to inspection equipment accuracy. Thus, groove filling with wet weld is always recommended if resources are available to increase the reliability of the repair.

#### **POROSITY OF WET WELDS**

Porosity is one of the main disadvantages of wet welding, it was reported in 1986 that porosity in welds deposited with commercial electrodes increased from 1% at 5 m water depth to approximately 8% at 60 m water depth, see data represented by D4301, D4313 and D4327 in Fig. 2 where nomenclature refers to commercial electrodes.<sup>3</sup>

By 2002, research efforts led to reduced porosity in wet welds, from approximately 0.8% at 21 m water depth to 1.6% at 60 m water depth. These welds were produced using rutile electrodes with low titanium and low boron additions (see also Fig. 2).<sup>4</sup> From the same figure, by 2007, enhanced rutile grade electrodes with ultra low carbon in the steel rod produced wet welds with less than 1% porosity at 50 m water depth.<sup>5,6</sup> These electrodes were water proofed with varnish to protect the electrode flux coating from water absorption from the surroundings. Advances in porosity mitigation made wet welding a truly underwater structural repair option. Shielded metal arc welding (SMAW) process with direct current electrode positive (DCEP) has been the preferred process for wet welding with rutile grade electrodes. Wet welds made with direct current electrode negative (DCEN) polarity and rutile electrodes exhibit deeper penetration and more porosity than the DCEP wet welds.<sup>7</sup>

#### **POROSITY AND FATIGUE**

Matlock *et al.* reported results from fatigue tests performed on three types of welds fabricated with commercial rutile E6013 electrodes.<sup>8,9</sup> The types of multiple-pass welds in these works were: surface weld, hyperbaric or habitat weld and underwater wet weld.

Surface welds are typically considered pore-free and their data were used to define the base line for comparison. The hyperbaric dry welds contained low porosity, in the range of 3%. The wet welds contained considerably higher porosity with approximately 12% porosity. Porosity was measured on the fracture surfaces of tested specimens.

Crack growth rate ( $da/dN$ ) values of the surface weld are lower than the wrought carbon steel, but higher than the

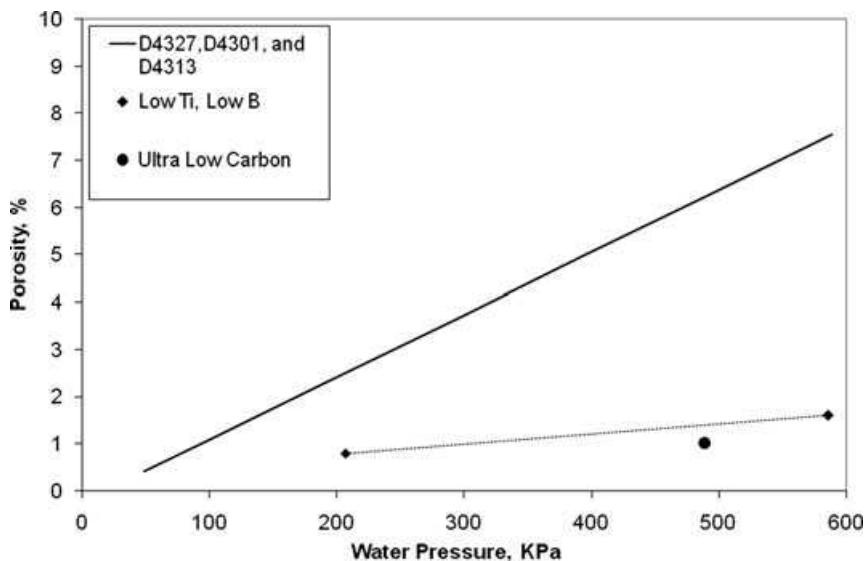


Fig. 2 Effect of pressure on weld porosity of commercial,<sup>3</sup> low Ti – low B<sup>4</sup> and ultra low carbon electrodes.<sup>5,6</sup>

habitat weld. At low stresses the wet weld reported smaller  $d\alpha/dN$  values than the surface and the habitat welds. However at high stresses the wet weld presented higher  $d\alpha/dN$  values. These results imply that at low stresses porosity was beneficial in retarding the fatigue crack propagation. Pores acted like pinning sites at the crack front, arresting the crack growth for finite number of stress cycles.<sup>8,9</sup> However, it is important to mention that the porosity values achieved in wet welds made at 50 m water depth were at the order of 1%, which is considerably less than the 12% reported in this fatigue study.<sup>5,6</sup>

## MECHANICAL PROPERTIES

Another problem that has limited the application of wet welding is related to poor mechanical properties of the weld metal. The main reason behind the reduced mechanical properties is associated with the loss of alloying elements such as carbon, manganese and silicon. On the other hand, oxygen content in the weld metal increases with water depth until a saturation value is reached. It is well known that the above mentioned alloying elements have strong affinity for oxygen at the arc fusion welding temperatures. Carbon forms carbon monoxide gas (CO) that contributes to porosity formation while silicon and manganese form non-metallic inclusions in the weld metal.<sup>5,6,10</sup> Parts of the CO bubbles and oxide inclusions escape from the weld pool and the remaining gas bubbles and second phase particles are trapped in the weld metal. Only if the alloying elements are distributed in solid solution in the steel matrix of the weld, they contribute to the mechanical properties of the weld metal. Pores and

non-metallic inclusions are detrimental to the mechanical properties.

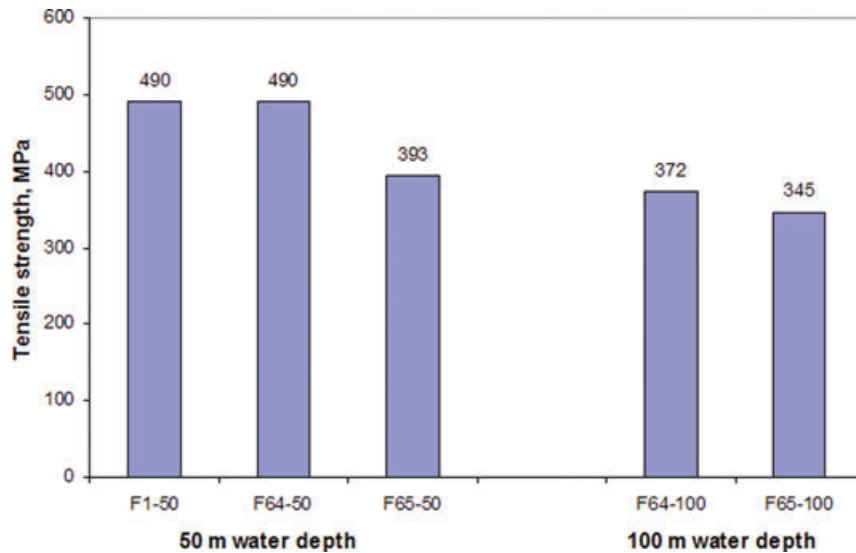
From Fig. 3 a tensile strength of 490 MPa has been reported for wet welds made with experimental E6013 rutile grade electrodes with alloying additions at 50 m water depth (see F1–50 and F64–50).<sup>5,6</sup> For wet welds made with similar electrodes, but with ultra-low carbon steel core rods, a tensile strength of 393 MPa was observed (see F65–50). As expected, the 100 m water depth welds showed lower tensile strengths, 372 and 345 MPa for the F64–100 and F65–100 electrodes, respectively. Porosity was shown to reduce in Fig. 2 with the ultra low carbon content steel rods; however, strength was also reduced for the same reason. Other cause of strength decrease is the increase of water depth and an increasing loss of alloying elements and increasing volume fractions of non-metallic inclusions. Strength reduction due to water depth can be overcome by replenishing the alloying elements in the flux coating of the electrode.

Fig. 4 shows a wet weld bead made with ultra-low carbon electrode on a plate. The weld exhibited good weld bead morphology with very well-defined ripples, which are evidence of constant feeding and good arc stability. Note also the absence of typical spatter present in wet welds.

Among commercial electrodes for dry applications, the E6013 rutile grade electrodes can be modified to produce acceptable wet welds with less than 2% porosity.

## LOCATION OF FATIGUE CRACKS

Fatigue cracks in offshore jackets are more frequently found in tubular welded joints close to the splash zone



**Fig. 3** Tensile strength of wet welds made at 50 and 100 m water depth using rutile base electrodes with alloying additions.



**Fig. 4** Weld bead of rutile grade electrode with ultra-low carbon content in the steel rod deposited at 50 m water depth.<sup>5,6</sup>

of the jacket. Other locations of high incidence of fatigue cracks are the welds that join top submerged horizontal framings that provide lateral support to well conductor pipes to the jacket in drilling platforms. In offshore floating structures, fatigue cracks can develop in the welded joints of the plate framing that provide stiffness to the caissons or hulls. A beneficial factor in both cases is the relative low water depth where these fatigue cracked joints are located which favour high quality wet welding applications.

#### WET WELD STRESS-STRAIN PROPERTIES

Wet weld stress-strain properties were obtained experimentally from ASTM tensile tests performed in a research project to produce wet weld electrodes<sup>5,6</sup>; this study demonstrated that porosity is randomly distributed in the weld, thus a mean value of the stress-strain properties of the wet welds made with F1 rutile electrodes previously presented was used. Fig. 5 shows the mean wet weld stress-strain curve and a stress curve of ASTM A-36 structural steel; it can be observed that wet weld ultimate resistance is close to the experimentally obtained from an A-36 structural steel. A-36 steel is mainly used for tubular members of offshore jacket structures in the Gulf of Mexico, for the case of tubular joints they are usually fabricated with high strength steel; in this paper A-36

was considered because steel for tubular joints can vary depending on stress level and location of the fabrication yard; it has to be noted that location of crack initiation is not dependent on steel type or yield strength.

Young's modulus ( $E$ ) is determined from the linear range of the stress-strain curves in Fig. 5. In Fig. 6, linear equations were fitted and  $E$  is obtained from the first derivative of these equations. Thus,  $E_{\text{wetweld}} = 199 \text{ GPa}$  and  $E_{\text{A-36}} = 228 \text{ GPa}$ .

#### ESTIMATED FATIGUE LIFE EXTENSION BY CRACK REMOVAL AND GROOVE FILLING WITH WET WELD

Extensive analysis and experimental tests have been performed on fatigue life extension for the case of crack removal by grinding.<sup>1,2,11</sup> Thus, a similar process based on fracture mechanics was proposed to analyze the effects of groove filling by means of wet weld deposition after fatigue crack removal. Fatigue life extension is estimated by comparison of the number of cycles needed to initiate and propagate a crack from as grinded condition as compared with groove wet weld filled condition. It is worth mentioning that crack initiation cannot be determined from fracture mechanics calculations, thus only crack propagation can be analyzed using fracture mechanics.

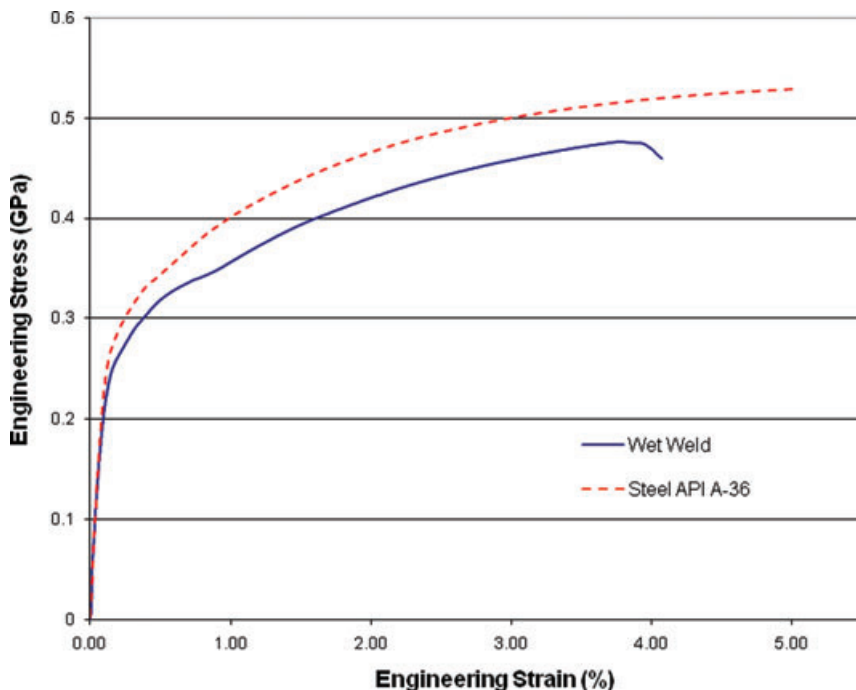


Fig. 5 Engineering stress–strain curves from tensile tests of ASTM-A36 and a wet welded specimen.

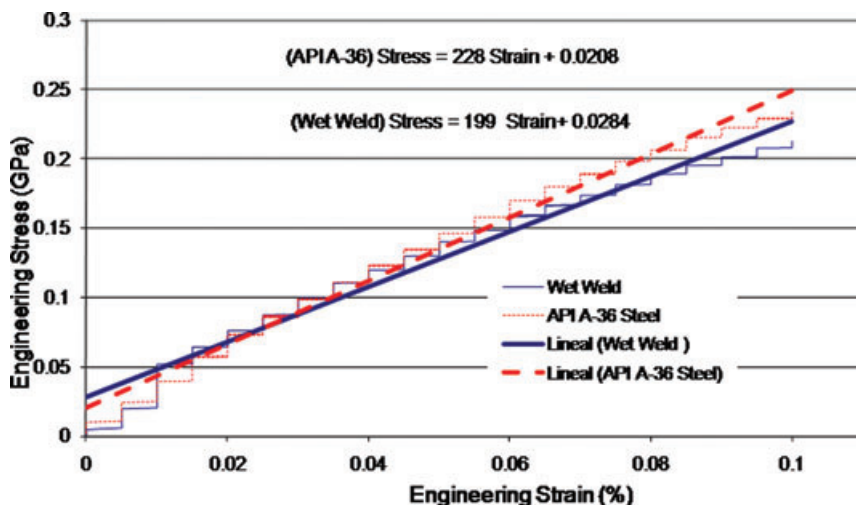


Fig. 6 Linear range of stress–strain curves.

Crack initiates at the location of highest stress, which for the as grinded condition occurs at the bottom of the groove or at both ends of the groove where the groove reaches the plate surface. Occurrence of one or the other case would depend on the groove geometry; the second case is known as short repair.<sup>2</sup> Wet weld stress–strain properties were considered for the fracture mechanics analysis where the stress distribution through the thickness is used to estimate the fatigue life.

Stress distribution was obtained from a T-butt finite element analysis where a fatigue crack was removed by

grinding and the groove was filled with wet weld. A finite element analysis of a fatigue crack repaired T-butt was produced; the model represents the case where a fatigue crack was removed by grinding a groove of radius  $R$  and the groove was filled with wet weld (see Fig. 7).

Experimentation on T-butts welded plate specimens has been used extensively to explain fatigue behaviour of more complex welded structures. Testing T-butt specimens was considered convenient because it is more economical than on full scale tubular connections. Although particular stress distributions found in tubular connections are

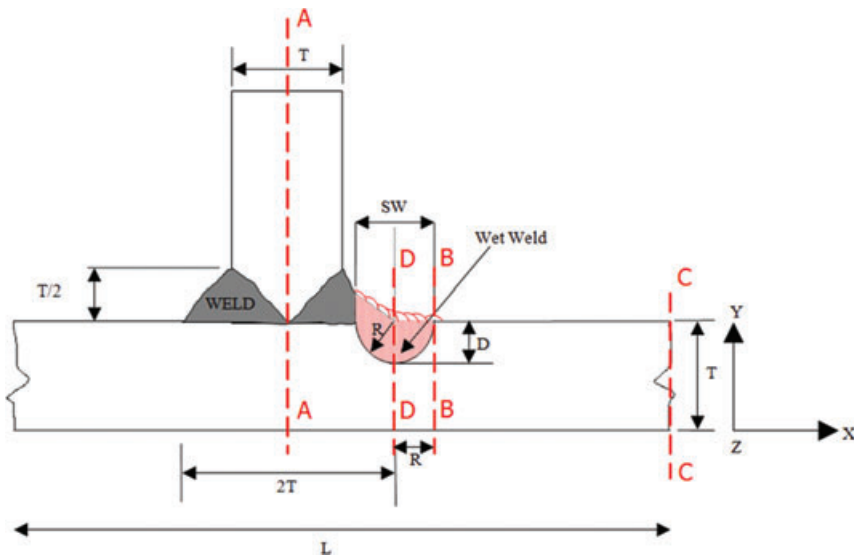


Fig. 7 T-butt model and crack repair geometry for stress analysis.

not reproduced when testing on T-butt specimens, extrapolation of the results to tubular welded connections is possible and is based on extrapolation of the Y factor determined for fatigue cracked repaired T-butt plates to tubular joints to estimate fatigue lives by fracture mechanics procedures. The extrapolation of Y from plates is a normal procedure for the determination of Y for tubular joints. In fact, the majority of the theoretical Y equations for tubular joints were developed from plates and then affected by a moment release procedure.<sup>12</sup> The moment release procedure is used to consider the so-called load shedding effect present during crack growth in tubular joints; this effect is not present in crack growth of plates. The load shedding effect is based on the observation that in circular sections as the crack grows through the thickness, the bending moment decreases while the membrane force remains constant. Therefore, the bending stress has to be corrected by a reduction function known as moment release, as proposed by Aaghakouchak *et al.*<sup>12</sup>

In Fig. 7, the shaded area at the weld toe is the groove filled with wet weld where the crack was removed. The wet weld stress properties used in the finite element model are those obtained from Figs 5 and 6. The base metal is ASTM A-36 steel. To optimize the time of analysis, model symmetry was taken into account and it was only modelled from section A-A to the right hand side; boundary conditions were implemented along section A-A where x, y and z displacements were constrained and rotations freed. Bending stress along sections B-B and D-D by application of stress along section C-C was computed using the ANSYS software package for finite element analysis. Section B-B is located at the intersection of the groove with the plate surface, and this is at a distance R from the weld toe as indicated in Fig. 7. According to Fig. 7, T-butt and

Table 1 T-butt and repair dimensions used for FEA models

Model	T (mm)	SW (mm)	L (mm)	R (mm)	D (mm)
1	20	8	400	4	4
2	20	8	400	4	8

repair dimensions considered for the finite element analysis (FEA) are given in Table 1. Repair geometry shown in Fig. 7 corresponds to model 1 dimensions according to Table 1; repair dimensions for model 2 produce a 'U' shaped groove repair with vertical walls, because D is deeper than R having its centre located below the weld toe along section D-D.

Stress concentration factors (SCF) computed from FEA of model 1 according to Table 1 are shown in Fig. 8. In this figure, SCF distributions through the thickness are calculated for the following conditions: as welded (unrepaired), grinded up to depth  $D = 4$  and groove filled with wet weld (repaired) at sections D-D and B-B. The flat plate condition is included only for comparison purposes. SCF in Fig. 8 for sections D-D or B-B is the ratio of top surface stress/nominal stress, where the nominal stress considered for this study is the plate bottom surface stress at section D-D or B-B, because weld toe effect is negligible at the bottom surface of the plate; computed stresses were produced by bending loading in all cases. SCF is defined as the ratio of FEA calculated stress/FEA nominal calculated stress, where the nominal stress is a stress unaffected by any stress concentration.

It can be seen from Fig. 8 that at the weld toe, section D-D, for the depth range  $0.1 < x/T < 1.0$ , the as welded and grinded  $D = 4$  + wet weld filled groove SCF distributions

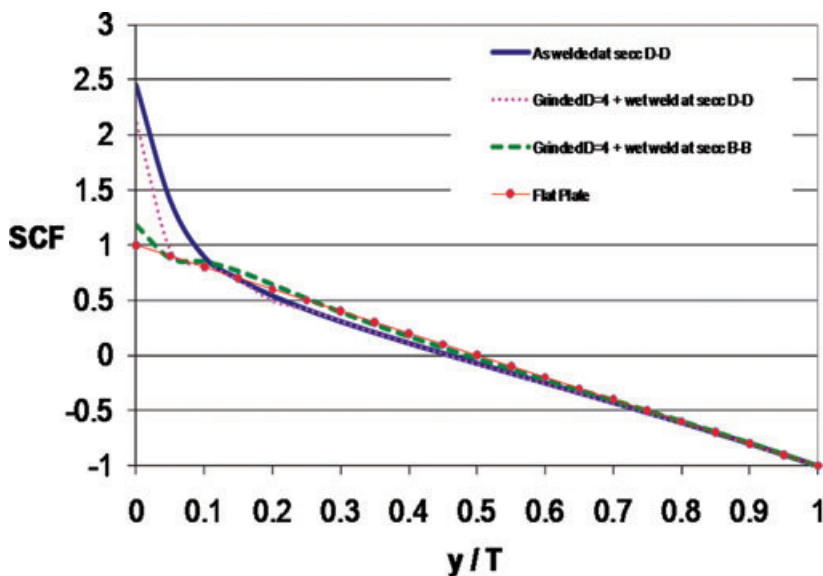


**Fig. 8** SCF through the thickness for various conditions.

are the same. For depth range  $0 < x/T < 0.1$  the deviation is due to the elasticity modulus difference, because weld shape and its dimensions remained identical in the FEA model for the as-welded and grinded models. This effect would increase if wet weld quality was lower than the experimentally tested. It is worth highlighting that the only difference between the as welded and the grinded  $D = 4+$  wet weld groove filled models is the elasticity modulus value;  $E_{\text{wet weld}} = 199 \text{ GPa}$  is 13% less than  $E_{\Delta-36} = 228 \text{ GPa}$ . Fig. 8 also shows that at section B-B for depth range  $0.1 < x/T < 1.0$ , the flat plate condition and the grinded  $D = 4+$  wet weld filled groove SCF distributions are the same because weld toe effect is negligible at section B-B,  $\text{SCF} = 1.2$ .

It is widely known that the fatigue process has three stages: initiation, propagation and failure and fracture mechanics is only applicable for fatigue life estimation in the propagation stage. Thus, performing the fracture mechanics procedure described in Rodríguez-Sánchez *et al.* (2005)<sup>11</sup> for fatigue life estimation of the as-welded and grinded  $D = 4+$  wet weld filled leads to similar results because stress distribution through the thickness for both cases is similar. Additionally, fatigue initiation which is highly dependent on surface conditions and which could make a difference between the as-welded and grinded  $D = 4+$  wet weld filled cannot be estimated by fracture mechanics, thus it is worth considering experimental fatigue testing for its assessment.

The analysis of model 2 according to Table 1, T-butt as-welded and grinded  $D = 8+$  wet weld showed a similar trend of SCF stress distributions through the thickness as described previously for model 1, thus SCF stress distributions for model 2 do not provide additional in-

formation for the study and are not presented in this work.

As has been mentioned previously, the repair method by filling the groove with wet weld and the as-welded condition would have a similar fatigue life during crack propagation as they have similar through-thickness stress distribution. Thus, it has been considered that to make a difference in the fatigue initiation stage, weld toe profiling can be implemented to reduce the weld toe SCF after wet welding and in addition if equipment is available, inducing compressive residual stresses to inhibit fatigue crack initiation is also an option; following sections explain these procedures.

#### WELD TOE PROFILING TO EXTEND THE FATIGUE INITIATION STAGE

Once wet welding has been used to fill the groove produced during crack removal, weld toe profiling has been considered in this study because the grinding tool is available as it could be also used to remove the crack (see Fig. 9).<sup>13</sup> Weld toe profiling can improve fatigue life by a factor of 2 approximately by extending the crack initiation stage. Weld profiling has the purpose to produce a smooth transition between the weld and the plate or pipe repaired. This practice has demonstrated fatigue life extension of welded components, as such the American Bureau of Shipping S-N curves allow a credit of 2.2 on fatigue life when suitable toe grinding and NDE are provided. A robust review of the weld toe grinding effects on fatigue life extension is given in Rodríguez-Sánchez *et al.* (2008).<sup>1</sup>

## INDUCING RESIDUAL STRESSES BY PEENING FOR FATIGUE LIFE EXTENSION

Peening is the process of impacting a metal surface with hard objects causing plastic deformation on the surface. The impact objects can be hard small particles, a bunch of needles or even a simple hammer and the process would be known as shot peening, needle peening or hammer peening, respectively.

The mechanisms of fatigue improvement using peening are:

- Cold work
- Residual compressive stress.

The cold work process is used in the industry to improve the strength of metals by changing the metallurgical conditions of the surface resulting in an increased surface hardness and refined grain structure. With the increased hardness, the brittleness is also expected to increase; consequently there is a limit to which cold working may be applied without danger of fracture.

The residual compressive stress is probably the most important benefit of peening in terms of fatigue improvement. Residual stress is produced because the surface layer of material is deformed beyond its yield point by peening; however, it cannot deform freely as the material underneath is not affected by the peening and therefore has not been plastically deformed. So, a compressive residual stress is developed in the surface material due to the constraint imposed by the deeper layers.<sup>14</sup>

It has been found by researchers that the fatigue improvement by peening is mainly due to the residual compressive stress rather than due to the cold work hardening process. Occasional high tensile loads, such as many components experience in service, reduce the beneficial effects

of peening because plastic deformation resulted at points of high stress concentration when the loading is applied.

A residual compressive stress reduces the effective range of fatigue stress, reduces crack growth and can even stop cracks from growing completely. However, there are still difficulties in making quantitative predictions of the effect on fatigue life as a result of a particular peening process. Fracture Mechanics procedures have not been easily applied for peened components; moreover, peening has a greater effect on the crack initiation phase where fracture mechanics cannot be applied. Peening leaves a surface far from being smooth which may cause crack starting points.

The following rules of thumb are recommended for the application of shot peening but the concept can be extended for other methods of peening. If the component under consideration is achieving a reversed bending endurance limit close to 0.5 of the tensile strength in steels or 0.25 in other alloys, further improvement by peening is unlikely. The maximum residual compressive stress induced by shot peening is approximately 60% of the ultimate tensile strength in compression; this ratio is common to all metallic materials.<sup>14</sup>

The general conclusion on the behaviour of cracks growing from a peened surface in fatigue is that surface effects, which may be regarded as minute cracks, already exist in the surface but that their initial growth rate is considerably slower than that of cracks which are eventually initiated in an as-welded (unpeened) surface.

## EXPERIMENTAL FINDINGS ON THE INDUCTION OF RESIDUAL STRESSES

Although, underwater shot peening for the improvement of fatigue crack resistance has not been used in practice, it was considered convenient to include it in this study because other applications of shot blasting such as marine growth removal are currently in use in underwater

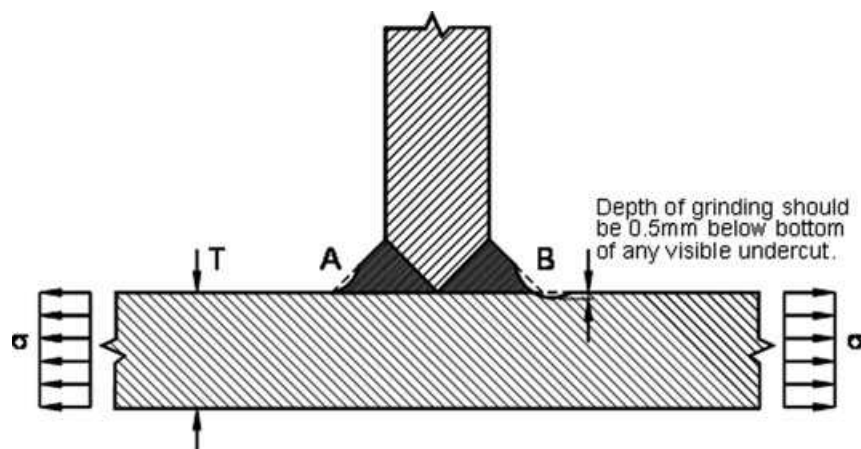


Fig. 9 Weld toe profiling to improve fatigue life.<sup>13</sup>

conditions. Hence, adjustments to currently used techniques based on shot blasting suggest that shot peening in underwater conditions might be possible. Hammer and needle peening have been used in underwater conditions proving its effectiveness inducing residual stresses; however its application into narrow grooves as in geometries presented in Table 1 appear complicated. It was decided to test shot peening in this work because it is a technique widely used in air conditions for residual stress induction and has the feasibility that the shots can reach the bottom of the groove for the geometries presented in this work.

Two T-butt welded specimens as in Fig. 7 having both an edge repair D4R2 (repair of constant section all across the specimen width) machined in as-welded condition were fatigue tested. Specimen UPD4R2 was tested after machining the edge repair and no subsequent treatment was applied. Specimen LPD4R2 was shot peened after the edge repair was machined. The purpose for testing these two identical shaped specimens was to determine the benefit of compressive residual stresses induced by shot peening on the fatigue life of repaired specimens. Both specimens were tested until failure and multiple cracking and coalescence was observed in the bottom of the edge repair.

With the application of equipment such as the Alternate Current Potential Drop (ACPD) which is able to provide crack growth measurements, the crack growth rate per cycle ( $da/dN$ ) can be determined experimentally and knowing the fatigue constants of the material ( $C$  and  $m$ ), it is possible to determine the stress intensity factor from Paris law expressed in Eq. (1).<sup>15</sup>

$$\Delta K = \left( \frac{1}{C} \frac{da}{dN} \right)^{\frac{1}{m}}. \quad (1)$$

On the other hand, the stress intensity factor range  $\Delta K$  in repaired welded joints can be described by Eq. (2).

$$\Delta K = Y \Delta \sigma \sqrt{\pi a}. \quad (2)$$

Equation (2) is a general expression that can be applied to any crack geometry and loading mode by considering the corresponding Y factor. From observation of Eqs (1) and (2), the Y factor value has a direct effect in the stress intensity factor and this one in the crack growth rate. Y factor for the case of the crack geometries present in welded joints varies as a function of parameters such as plate width, crack geometry, stress field, geometrical discontinuities and structural restraints.

For the calculation of the fatigue life of an offshore crack repaired welded joint by crack removal, the Y factor should include the particular characteristics of the crack growing in the repaired notch and propagating through the thickness of the welded member under the membrane

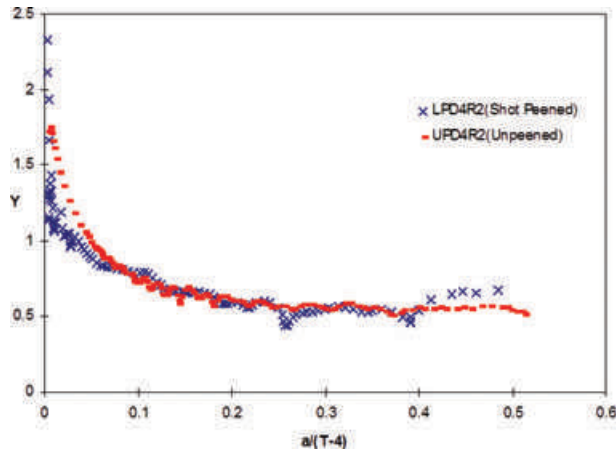


**Fig. 10** Experimental Y factors for edge crack repaired specimens in unpeened and peened conditions.

and bending stresses produced by the wave loading on the structure.

Fig. 10 shows experimental Y factors for the edge repaired specimens UPD4R2 and LPD4R2 in unpeened and peened conditions, respectively; it can be observed that the unpeened curve is smoother than that for the peened specimen in the range  $0 < a/(T-4) < 0.08$ ; this may be explained by a multiple crack initiation effect, possibly caused by the mildly rough surface left by the shot particles. Another observation from the same figure is obtained considering the point where the two curves intersect which is at  $a/(T-4) = 0.08$  being  $T = 30$  mm for these specimens; at this point the crack is 2 mm deep; this coincides with the approximate thickness of the residual stress compressive layer. This could be indicating the sensitivity of ACPD to residual stress.

Fig. 10 compares the experimentally determined Y factors for an unpeened and lightly peened specimens and shows in general a lower value of Y for the peened specimen in the range  $0 < a/(T-4) < 0.08$ . This finding could mean that peening reduced the crack growth rate in this region. However, because the Y values are only slightly lower for the peened specimen, it has to be considered that other factors such as the crack aspect ratio or the accuracy of the measurement technique may have been involved that affected the Y values. It is, for example, possible that the presence of residual stress and its relaxation as the crack grows could have had an influence on the ACPD readings. Therefore, it is not possible to draw a firm conclusion from the experimental data obtained from only two specimens.

#### GENERAL GUIDELINES TO IMPLEMENT THE REPAIR PROCEDURE

The proposed fatigue crack repair procedure initiates removing the crack by grinding it out. To decrease the

contribution of crack propagation, this work also proposed filling the grinded groove with wet weld.

Grinding can be performed either by burr grinding or by disc cutting. The use of disc grinding is discouraged because grinding marks could become crack initiators. However, fatigue initiation for the proposed procedure does not rely on the surface finish left after grinding out the crack, because wet welding erases the grinding marks.

Wet welding can be performed by using E6013 rutile grade electrodes with alloying additions. These electrodes can produce acceptable wet welds for the conditions where cracks typically occur in fixed and floating offshore structures for the oil industry. These locations are in shallow waters or nearby the splash zone, respectively.

To delay fatigue initiation, it has been proposed in this work to perform weld toe profiling to produce a smooth transition from the wet weld to the plate. This practice does not increase the repair complexity because the same grinding tool used for crack removal can be used for weld toe profiling after wet welding. Attention should be paid to the force control on the grinding tool to avoid burr or disc skipping on the plate surface.

Finally, as it was experimentally tested and results presented in this work, induction of compressive residual stresses on the repaired surface can improve the resistance against fatigue initiation; this practice should be recommended as optional because its benefits could be erased by an overloading which for the case of offshore structures is highly possible under storm conditions.

## CONCLUSIONS

A crack repair procedure based on crack removal by grinding, subsequent filling of the produced groove with wet welding and weld toe profiling with an optional induction of compressive residual stresses on the surface has been proposed to reinstate as-welded fatigue life.

Wet welding technology has improved considerably in recent years. Techniques required for performing the proposed crack repair procedure are of common use in the offshore oil industry, thus the proposed procedure which combines grinding, wet welding and shot peening is feasible for industrial application.

The proposed procedure can reinstate the original fatigue life of a crack repaired joint regardless of crack depth before repair. Fatigue initiation for the proposed procedure does not rely on the surface finish left after grinding out the crack, because wet welding erases the grinding marks. Use of weld toe profiling after wet welding is recommended. An extensive testing program should be performed before the proposed procedure is industrially used, the collected data would support its effectiveness.

It is a common practice to determine Y factor data from T-butt specimens and extrapolate it to tubular joints by

incorporating the load shedding effect. Thus, conclusions presented in this work can be applicable to offshore platforms.

Effectiveness of the proposed procedure does not rely on a complete removal of the crack as in the case of crack repair by grinding removal leaving an empty groove. An effective option to assure that crack propagation is halted, even if the crack is not totally removed due to crack detection capabilities of the inspection equipment, is by fusing the crack tip when melting the bottom of the groove during wet weld deposition.

## REFERENCES

- 1 Rodríguez-Sánchez, J. E., Rodríguez-Castellanos, A., Carabajal-Romero, M. and Ayala-Uraga, E. (2009). Controlled weld toe profiles for fatigue life extension of T-Butt joints: an application to FSOs & FPSOs. *Int. J. Offshore Mech. Arctic Eng.* **131**, 1–8.
- 2 Rodriguez-Sánchez, J. E., Dover, W. D. and Brennan F. P. (2004). Application of short repairs for fatigue life extension. *Int. J. Fatigue* **26**, 413–420.
- 3 Suga, Y. and Hasui, A. (1986). On formation of porosity in underwater weld metal. *Int. Inst. Weld.* **IX**, 1388–1386.
- 4 Liu S. and Rowe M (2002). Progress in underwater wet welding, The Quintessential SMA Consumables. *ASM International Conference on Trends on Welding Research, Pine Mountain, Georgia*.
- 5 Perez Guerrero, F (2007). The mechanism of porosity formation in underwater steel welds using SMAW process. Ph.D. Thesis, Colorado School of Mines.
- 6 Liu, S. and Perez, F (2007). *Phase III Joint Research Program between MMS and IMP Underwater Wet Welding for Offshore Structures and Pipelines in the Gulf of Mexico: Enhanced Reliability and Integrity of Underwater Wet Welds*. Final report.
- 7 Liu, S. and Perez, F. (2004). *Joint Research Program between MMS and IMP Underwater Wet Welding for Offshore Structures and Pipelines in the Gulf of Mexico: Process Maturation and Technology Transfer*. Final report.
- 8 Matlock, D. K., Edwards, G. R., Olson, D. L. and Ibarra, J (1983). An evaluation of the fatigue behavior in surface, habitat, and underwater wet welds. *International Institute of Welding Conference, Trondheim, Norway*. 303–310.
- 9 Ibarra, S., Liu S. and Olson, D. L (1995). Underwater wet welding of steel. *Weld. Res. Coun. Bull.* **401**, 1–39.
- 10 Perez-Guerrero, F. and Liu, S (2007). Explaining porosity formation in underwater wet welds. *26th International Conference on Offshore Mechanics and Arctic Engineering, American Society of Mechanical Engineers*.
- 11 Rodríguez-Sánchez, J. E., Dover, W. D., Brennan, F. P. and Rodríguez-Castellanos, A. (2005). Fracture mechanics analysis of fatigue crack repaired joints. *Int. J. Offshore Mech. Arctic Eng.* **127**, 182–189.
- 12 Aaghakouchack, A.A., Glinka, G. and Dharmavasan, S. (1989). A load shedding model for fracture mechanics analysis of fatigue cracks in tubular joints. *OMAE 89 Conference*.
- 13 NORSO standard N-004 Rev. 2, October 2004.
- 14 Marsh, K. J. (1993). *Shot Peening: Techniques and Applications*. Engineering Materials Advisory Services Ltd.
- 15 Paris, P. C. and Erdogan, F. (1963). A critical analysis of crack propagation laws. *Trans. ASME, J. Basic Eng.* **85**, 528.

## **FATIGUE IMPROVEMENT OF WELDED ELEMENTS AND STRUCTURES BY ULTRASONIC PEENING**

**Yuri Kudryavtsev**

Structural Integrity Technologies Inc.  
Markham, Ontario, Canada

**Jacob Kleiman**

Structural Integrity Technologies Inc.  
Markham, Ontario, Canada

### **ABSTRACT**

The ultrasonic impact treatment (UIT) is relatively new and promising process for fatigue life improvement of welded elements and structures. In most industrial applications this process is known as ultrasonic peening (UP). The beneficial effect of UP is achieved mainly by relieving of tensile residual stresses and introducing of compressive residual stresses into surface layers of a material. The secondary factors in fatigue improvement by UP are decreasing of stress concentration in weld toe zones and enhancement of mechanical properties of the surface layers of the material. Fatigue testing of welded specimens showed that UP is the most efficient improvement treatment as compared with traditional techniques such as grinding, TIG-dressing, heat treatment, hammer peening and application of LTT electrodes. The developed computerized complex for UP was successfully applied for increasing the fatigue life and corrosion resistance of welded elements, elimination of distortions caused by welding and other technological processes, residual stress relieving, increasing of the hardness of the surface of materials. The UP could be effectively applied for fatigue life improvement during manufacturing, rehabilitation and repair of welded elements and structures. The areas/industries where the UP process was applied successfully include: Shipbuilding, Railway and Highway Bridges, Construction Equipment, Mining, Automotive, Aerospace. The results of fatigue testing of welded elements in as-welded condition and after application of UP are considered in this paper. It is shown that UP is the most effective and economic technique for increasing of fatigue strength of welded elements in materials of different strength. These results also show a strong tendency of increasing of fatigue strength of welded elements after application of UP with the increase in mechanical properties of the material used.

### **INTRODUCTION**

The ultrasonic impact treatment (UIT) is one of the most efficient techniques for fatigue life improvement of welded elements and structures [1-7]. In most industrial applications this process is also known as ultrasonic peening (UP) [8-12]. The beneficial effect of UIT/UP is achieved mainly by relieving of harmful tensile residual stresses and introducing of compressive residual stresses into surface layers of materials, decreasing of stress concentration in weld toe zones and enhancement of mechanical properties of surface layers of the material. The fatigue testing of welded specimens showed that the UP is the most efficient improvement treatment when compared with such traditional techniques as grinding, TIG-dressing, heat treatment, hammer peening, shot peening and application of LTT electrodes [1, 13, 14].



Fig.1a. Basic ultrasonic peening system for fatigue life improvement of welded elements and structures [6]

The developed system for UP treatment (total weight - 11 kg) includes an ultrasonic transducer, a generator and a laptop (optional item) with software for optimum application of UP - maximum possible increase in fatigue life of parts and welded elements with minimum cost, labor and power consumption. In general, the basic UP system shown in Figure 1a could be used for treatment of weld toe or welds and larger surface areas if necessary.

Also the special ultrasonic system was designed to perform underwater UP at the depth of up to 30 meters [26]. Figure 1b shows the process of underwater UP of welded samples in preparation for their subsequent fatigue testing.



Fig.1b. The process of underwater ultrasonic peening by using of the specially designed tool

The most recent design of the UP equipment is based on "Power on Demand" concept. Using this concept, the power and other operating parameters of the UP equipment are adjusted to produce the necessary changes in residual stresses, stress concentration and mechanical properties of the surface layers of materials to attain the maximum possible increase in fatigue life of welded elements and structures. From other side, this approach prevent the possibility to overwork the treated surface and decrease the efficiency op UP.

The effects of different improvement treatments, including the UP treatment, on the fatigue life of welded elements depend on the mechanical properties of used material, the type of welded

joints, the parameters of cyclic loading and other factors. For effective application of UP, depending on the above-mentioned factors, a software package for Optimum Application of UP was developed that is based on original predictive model. In the optimum application, a maximum possible increase in fatigue life of welded elements with minimum time/labor/cost is thought [15].

The developed technology and computerized complex for UP were successfully applied for increasing of the fatigue life of welded elements, elimination of distortions caused by welding and other technological processes, relieving of residual stress, increasing of the hardness of the surface of materials and surface nanocrystallization. The areas/industries where the UP was applied successfully include: Railway and Highway Bridges, Construction equipment, Shipbuilding, Mining, Automotive and Aerospace to name a few.

### **PRINCIPLES, TECHNOLOGY, EQUIPMENT FOR UP *Freely Movable Strikers***

The UIT/UP equipment is based on known technical solutions from the 40's of last century of using working heads with freely movable strikers for hammer peening. At that time and later on, a number of different tools based on using freely movable strikers were developed for impact treatment of materials and welded elements by using pneumatic [16, 17] and ultrasonic [18-24] equipment. A more effective impact treatment is provided when the strikers are not connected to the tip of the actuator but could move freely between the actuator and the treated material. Figure 2 shows a standard set of easy replaceable working heads with freely movable strikers for different applications of UP.



Fig.2. A set of interchangeable working heads for UIT/UP [7]

### ***Ultrasonic Impact and Effects of Ultrasound***

The UP technique is based on the combined effect of high frequency impacts of the special strikers and ultrasonic oscillations in treated material. Some specific features of the ultrasonic impact treatment of metals are described in [16]

where it is shown that the operational frequency of the transducer and the frequency of the intermediate element-striker are not the same.

During the ultrasonic treatment, the striker oscillates in the small gap between the end of the ultrasonic transducer and the treated specimen, impacting the treated area [18-21]. This kind of high frequency movements/impacts in combination with high frequency oscillations induced in the treated material is typically called the ultrasonic impact.

There are a number of effects of ultrasound on metals that are typically considered: acoustic softening, acoustic hardening, acoustic heating, etc. In the first of these (acoustic softening that is also known as acoustic-plasticity effect), the acoustic irradiation reduces the stress necessary for plastic deformation. In general, the effect of ultrasound on the mechanical behavior could be compared with the effect of heating on a material. The difference is that acoustic softening takes place immediately when a metal is subjected to ultrasonic irradiation. Also, relatively low-amplitude ultrasonic waves leave no residual effects on the physical properties of metals after acoustic irradiation is stopped [25].

#### **Technology and Equipment for Ultrasonic Peening**

The ultrasonic transducer oscillates at a high frequency, with 20-30 kHz being typical. The ultrasonic transducer may be based on either piezoelectric or magnetostrictive technology. Whichever technology is used, the output end of the transducer will oscillate, typically with amplitude of 20 – 40  $\mu\text{m}$ . During the oscillations, the transducer tip will impact the striker(s) at different stages in the oscillation cycle. The striker(s) will, in turn, impact the treated surface. The impact results in plastic deformation of the surface layers of the material. These impacts, repeated hundreds to thousands of times per second, in combination with high frequency oscillations induced in the treated material result in a number of beneficial effects of UP.

The UP is an effective way for relieving of harmful tensile residual stresses and introducing of beneficial compressive residual stresses in surface layers of parts and welded elements. The mechanism of residual stress redistribution is connected mainly with two factors. At a high-frequency impact loading, oscillations with a complex frequency mode spectrum propagate in a treated element. The nature of this spectrum depends on the frequency of ultrasonic transducer, mass, quantity and form of strikers and also on the geometry of the treated element. These oscillations lead to lowering of residual welding stresses. The second and the more important factor, at least for fatigue improvement, is surface plastic deformation that leads to introduction of the beneficial compressive residual stresses.

In the fatigue improvement, the beneficial effect is achieved mainly by introducing of the compressive residual stresses into

surface layers of metals and alloys, decrease in stress concentration in weld toe zones and the enhancement of the mechanical properties of the surface layer of the material. The schematic view of the cross section of material/part improved by UP is shown in Figure 3 with the attained distribution of the stresses after the UP. The description of the UP benefits is presented in Table 1.

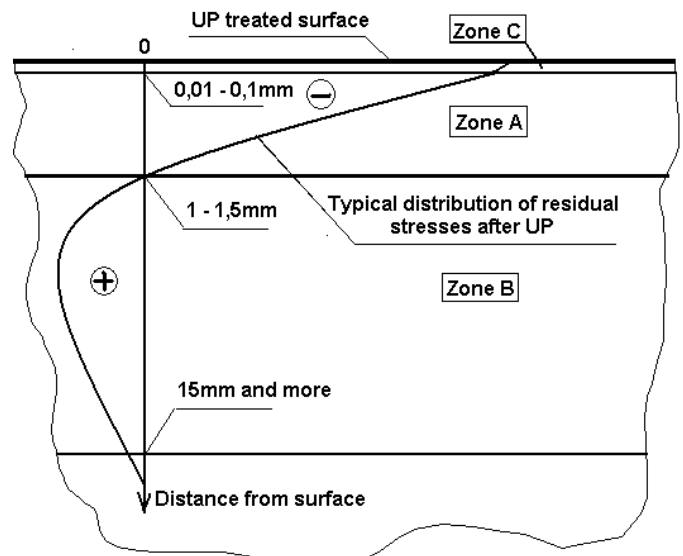


Fig.3. Schematic view of the cross section of material/part improved by Ultrasonic Peening [9]

Table 1. Zones of Material/Part Improved by Ultrasonic Peening [9] (see Figure 3 for illustration of the zones)

Zone	Description of zone	Distance from surface,	Improved characteristics
A	Zone of plastic deformation and compressive residual stresses	1 – 1.5 mm	Fatigue, corrosion, wear, distortion
B	Zone of relaxation of welding residual stresses	15 mm and more	Distortion, crack propagation
C	Zone of nanocrystallization (produced at certain conditions)	0.01 – 0.1 mm	Corrosion, wear, fatigue at elevated temperature

The most important, from the fatigue improvement point of view, is the zone A where the beneficial compressive residual stresses are induced by UP due to the plastic deformation of the surface layers of material [4]. The zone of nanocrystallization C could be produced by UP at certain conditions [27]. This

zone is characterized by a small depth of only 10-100 micrometers and does not contribute significantly to the fatigue increase of welded elements by UP. In case of surface nanocrystallization the fatigue cracks initiate under this thin layer.

Figure 4 illustrates the concept of the fatigue life improvement of welded elements by UP. In case of welded elements, it is enough to treat only the weld toe zone – the zone of transition from base metal to the weld, for a significant increase of fatigue life. The width of the zone of UP treatment is typically 2-5 mm.

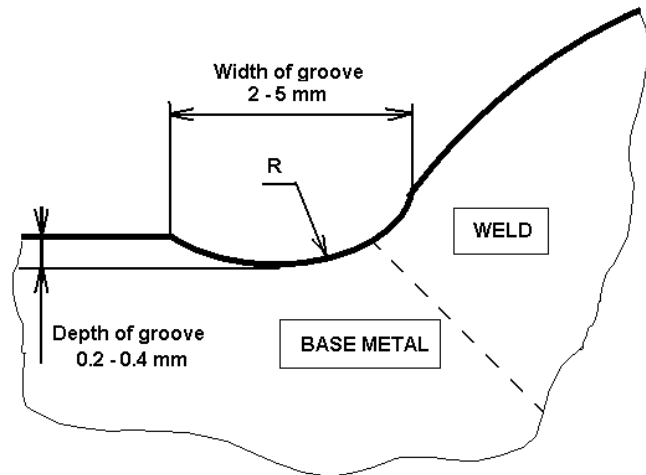


Fig.4. Profile of weld toe improved by Ultrasonic Peening [9]

A so-called groove, shown in Figures 4 and 5, characterized by certain geometrical parameters is produced by UP. This groove is a result of a surface plastic deformation of material during UP [2, 4].



Fig.5. The view of the butt welds in as-welded condition (left side sample) and after application of UP (right side sample) [7]

## APPLICATION OF UP FOR FATIGUE IMPROVEMENT

The UP could be effectively applied for fatigue life improvement during manufacturing, rehabilitation and repair of welded elements and structures. Examples of all three applications will be described below.

### *Manufacturing and Rehabilitation*

Three series of large-scale welded samples, designed as shown in Figure 6, were subjected to fatigue testing to evaluate the effectiveness of UP application to the existing welded structures: 1 – in as welded condition, 2 – UP was applied before fatigue testing, 3 – UP was applied after fatigue loading with the number of cycles corresponding to 50% of the expected fatigue life of samples in as-welded condition [9]. Material properties: yield strength – 360 MPa, ultimate strength – 420 MPa. The samples were tested at stress ratio R=0. Test frequency – 5 Hz.

All considered in this paper welded specimens were UP treated with the following standard parameters: speed of treatment – 0.4 meter/minute, level of amplitude of oscillation - 4, working head – one row, four pins, diameter of pin - 3mm.

The results of fatigue testing of the large-scale welded samples imitating the transverse non-load-carrying attachments (Fig. 6) with UP applied to specimens in as-welded condition and also after 50% of expected fatigue life are presented in Figure 7.

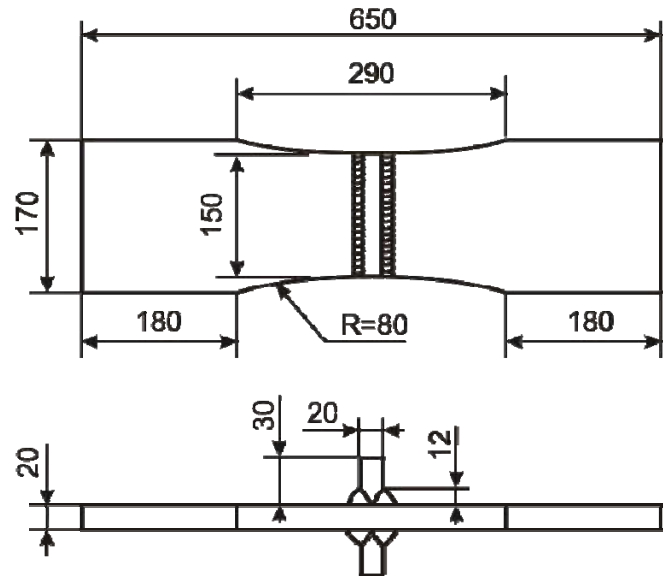


Fig.6. The general view of welded sample for fatigue testing

The UP caused a significant increase in fatigue strength of the considered welded element for both series of UP treated samples. The increase in limit stress range at  $N=2 \cdot 10^6$  cycles of welded samples is 49% (from 119 MPa to 177 MPa) for UP treated samples before fatigue loading and is 66% (from 119 MPa to 197 MPa) for UP treated samples after fatigue loading,

with the number of cycles corresponding to 50% of the expected fatigue life of the samples in as-welded condition. A slightly higher increase of fatigue life of UP treated welded elements for fatigue curve #3 could be explained by a more beneficial redistribution of residual stresses by UP after cyclic loading than in as-welded condition and/or by "healing" of fatigue damaged material by recrystallization [27] during UP in comparison with the fatigue curve #2.

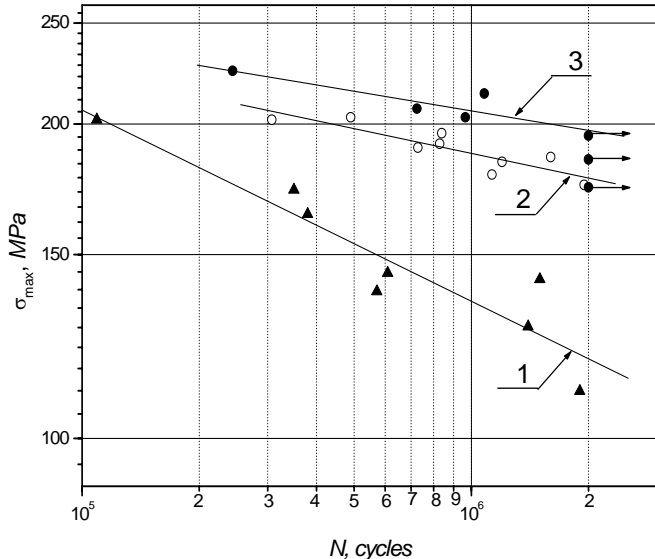


Fig.7. Fatigue curves of welded elements (transverse non-load-carrying attachment): 1 – in as welded condition, 2 – UP was applied before fatigue testing, 3 – UP was applied after fatigue loading with the number of cycles corresponding to 50% of expected fatigue life of samples in as-welded condition

### Weld Repair

In this paper the rehabilitation is considered as a prevention of possible initiation of fatigue cracks in existing welded elements and structures that are in service. The UP could also be effectively used during the weld repair of fatigue cracks [7, 10].

Figure 8 shows the drawing of a large-scale welded specimen containing non-load carrying longitudinal attachments designed for fatigue testing [7]. Material properties: yield strength – 360 MPa, ultimate strength – 420 MPa. Such specimens were tested in as-welded condition and after weld repair with and without application of UP.

The testing conditions were zero-to-tension stress cycles ( $R=0$ ) with different level of maximum stresses. Test frequency - 5 Hz.

The fatigue testing was stopped and the number of cycles was recorded when the length of fatigue crack on surface reached 20 mm. Then, the fatigue crack was repaired by gouging and welding and the fatigue test was continued. After repair, a

number of samples were subjected to UP. The weld toe of the "new" weld was UP treated. The results of fatigue testing of welded specimens in as-welded condition and after weld repair of fatigue cracks are presented in Figure 9.

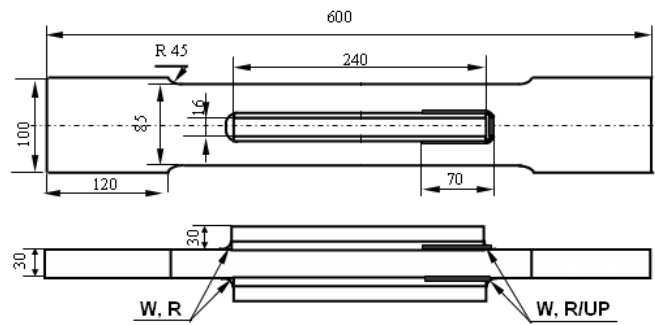


Fig.8. Drawings of welded specimens for fatigue testing at different conditions: W – as-welded condition; R - repair by gouging and welding; R/UP – repair by gouging, welding and UP

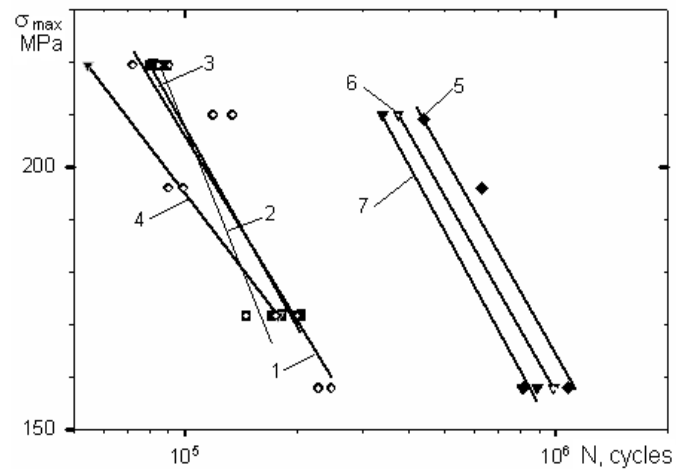


Fig.9. Results of fatigue testing of welded elements:  
1 - as-welded condition, 2, 3 and 4 – after first, second and third weld repair, 5, 6 and 7 - after first, second and third weld repair with application of UP

The fatigue testing of large scale specimens showed that the repair of fatigue cracks by welding is restoring the fatigue strength of welded elements to the initial as-welded condition. Second and third repair of fatigue cracks also practically restored the fatigue life of repaired welded elements to initial as-welded condition.

The application of UP after weld repair increased the fatigue life of welded elements by 3-4 times. Practically the same significant fatigue improvement of repaired welded elements by UP is observed also after second and third repair of fatigue cracks in welded elements.

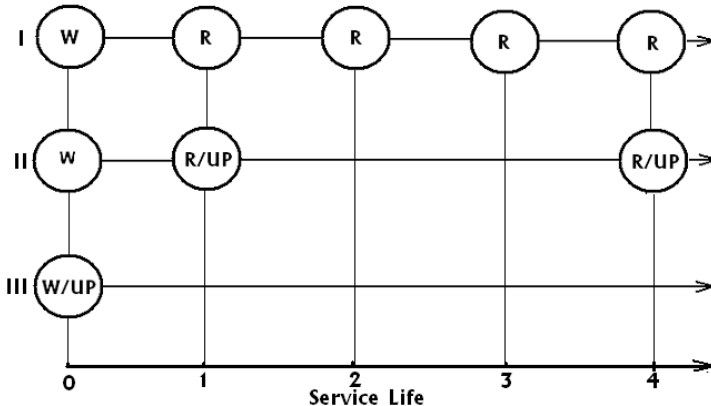


Fig.10. Diagram showing the endurance of welded elements:  
 Line I - fatigue crack is repaired by gouging and welding,  
 Line II - fatigue crack is repaired by gouging, welding and UP,  
 Line III – UP is applied before/during the first phase of service  
 life, W – as-welded condition, R - repair by gouging and  
 welding, R/UP – repair by gouging, welding and UP,  
 W/UP- welding and UP

A comparison of the efficiency of weld repair of fatigue cracks with and without application of UP is presented in Figure 10. This diagram illustrates the fatigue behavior of the same welded elements in cases when UP is not applied (I), when UP is applied after weld repair (II) and UP is applied before/during the first phase of service life (III). Here, 1 unit of service life corresponds to ~ 240,000 cycles of loading at the stress range 158 MPa and to ~ 75,000 at the stress range 220 MPa. Every circle, marked R or R/UP, in Fig.10 starting from the number 1 on service life axis indicates a fatigue fracture and a repair of the welded element. As can be seen from Fig.10, the benefit from application of UP for weld repair and rehabilitation of welded elements is obvious.

## ULTRASONIC PEENING OF HSS WELDED ELEMENTS

### 700 MPa yield strength steel

Four series of large-scale welded samples were subjected to fatigue testing to evaluate the effectiveness of UIT/UP application for fatigue life improvement of welded elements made from 350 MPa and 700 MPa yield strength steels [13]. The fatigue specimens were designed as 80 mm wide by 8 mm thick steel plates with longitudinal non-load carrying fillet welded attachments, as shown in Figure 11.

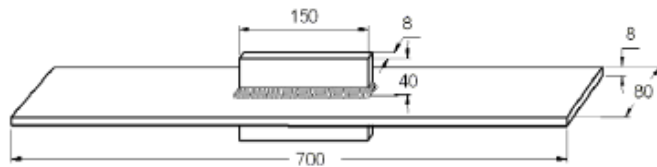


Fig.11. Welded specimen for fatigue testing of 350 and 700 MPa yield strength steel welded elements [13]

All testing has been conducted under constant amplitude axial tension in servo-hydraulic fatigue testing machines. The applied stress ratio has been  $R=0.1$ , with test frequencies varying from 2 to 6 Hz depending on load levels. Failure is defined to have taken place upon complete separation of the specimen. The results of fatigue testing are presented in Figure 12.

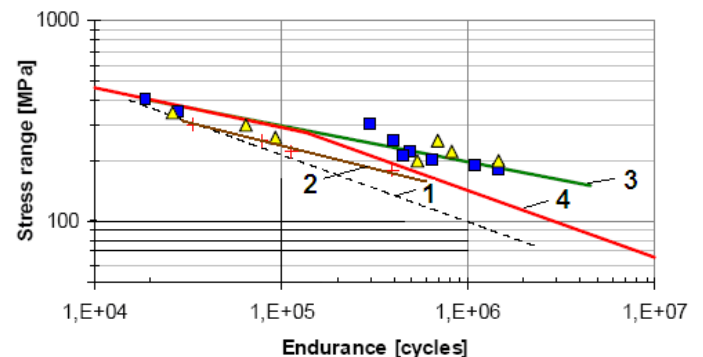


Fig.12. Fatigue test results for 350 and 700 MPa yield strength steel welded specimens [13]: 1- in as-welded condition, 350 MPa and 700 MPa yield strength steels, 2 - after UIT, 350 MPa yield strength steel, 3- after UIT/UP, 700 MPa yield strength steel, 4- FAT 112 design curve

As can be seen from Figure 12, the UIT/UP provided significant increase in fatigue performance of considered welded element for 700 MPa yield strength steel. The increase in limit stress range at 2 millions cycles of loading was 81% for welded samples treated by UIT/UP in comparison with as-welded condition, while TIG-dressing provided a 36% increase in limit stress range of welded element (see Table 2).

TABLE 2. INCREASE IN LIMIT STRESS RANGE OF WELDED ELEMENT AT 2 MILLIONS CYCLES OF LOADING [13]

S-N curve	Slope m	FAT value [MPa]	Improvement at FAT value [%]
As-welded S355 and S700	-3 (fixed)	71.3	-
UIT/UP S700	-5 (fixed)	129.4	81
Robotized TIG-dressing S700	-3 (fixed)	97.0	36.0

### 960 MPa yield strength steel

Four series of large-scale welded samples were subjected also to fatigue testing to evaluate the effectiveness of UIT/UP application for fatigue life improvement of welded elements made from 960 MPa yield strength steel [14]. The fatigue specimens were designed as 50 mm wide by 6 mm thick steel

plates with longitudinal non-load carrying fillet welded attachments, as shown in Figure 13.

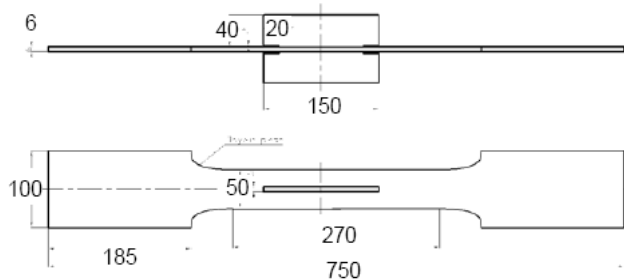


Fig.13. Specimen geometry for fatigue testing of 960 MPa yield strength steel welded elements [14]

The testing has been conducted under constant amplitude using  $R = -1$ . All of the as-welded specimens failed at the weld toe at the end of the longitudinal stiffeners. For the improved by UIT/UP welds, tested using constant amplitude loading, a variety of other failure modes were observed. The results of fatigue testing are presented in Figure 14.

As can be seen from Figure 14, the UIT/UP treatment with an instrument based on piezoelectric transducer provided the highest increase in fatigue performance of considered welded element for 960 MPa yield strength steel in comparison with the efficiency of application of magnetostrictive transducer and LTT electrodes.

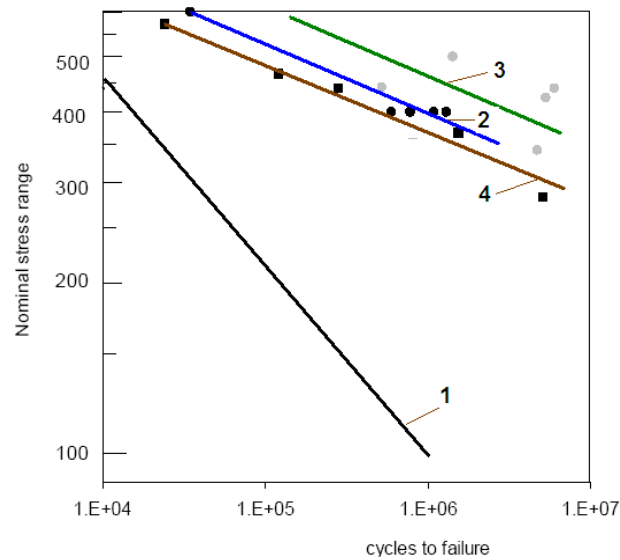


Fig.14. Fatigue test results for 960 MPa yield strength steel welded specimens [14]: 1- in as-welded condition (results of approximation of fatigue data received earlier), 2 and 3 - after UIT/UP based on using magnetostrictive and piezoelectric transducers respectively, 4- after application of LTT electrodes

## INDUSTRIAL APPLICATIONS OF UP

As was demonstrated, the UP could be effectively applied for fatigue life improvement during manufacturing, rehabilitation and repair of welded elements and structures. The UP technology and equipment were successfully applied in different industrial projects for rehabilitation and weld repair of parts and welded elements. The areas/industries where the UP was applied successfully include: Railway and Highway Bridges, Construction Equipment, Shipbuilding, Mining, Automotive and Aerospace.

An example of application of UP for repair and rehabilitation of welded elements subjected to fatigue loading in mining industry is shown in Figure 15. Around 300 meters of welds, critical from fatigue point of view, were UP treated to provide improved fatigue performance of two large grinding mills located near Labrador City, NL, Canada..



Fig.15. Application of UP for rehabilitation of welded elements of a large grinding mill

The second example is based on the fatigue data and the solution described in [10]. The UP was also applied during the rehabilitation of welded elements of a highway bridge over the Ohio River in the USA. The bridge was constructed about 30 years ago. The welded details of the bridge did not have macroscopic fatigue cracks. The motivation for application of the UP for fatigue life improvement of this bridge was the fatigue cracking in welded elements and failure of one of the spans of another bridge of approximately the same age and design. More than two thousand and five hundred welded details of the bridge structure that were considered to be fatigue critical were UP treated.

## CONCLUSIONS

1. Ultrasonic Impact Treatment (UIT/UP) is a relative new and promising technique for fatigue life improvement of welded elements and structures in materials of different strength including HSS with the yield strength of 700-1000 MPa. The results of fatigue testing show a strong tendency of increasing of fatigue strength of welded elements after application of UP with the increase in mechanical properties of the material used. It allows using to a greater degree the advantages of the HSS in welded elements, subjected to fatigue loading.
2. The fatigue testing of welded specimens also showed that the UP is the most efficient improvement treatment as compared with post weld techniques such as TIG-dressing and application of LTT electrodes.
3. The developed computerized complex for UP was successfully used in different applications for increasing of the fatigue life of welded elements, elimination of distortions caused by welding and other technological processes, relieving of residual stress, increasing of the hardness of material surfaces and surface nanocrystallization. The areas/industries where the UP was applied successfully include: Railway and Highway Bridges, Mining, Construction Equipment, Shipbuilding, Automotive and Aerospace.

## REFERENCES

1. V. Trufyakov, P. Mikheev and Y. Kudryavtsev. Fatigue Strength of Welded Structures. Residual Stresses and Improvement Treatments. *Harwood Academic Publishers GmbH, London. 1995. 100 p.*
2. Y. Kudryavtsev, V. Korshun and A. Kuzmenko. Improvement of Fatigue Life of Welded Joints by Ultrasonic Impact Treatment. *Paton Welding Journal. 1989. No. 7. p. 24-28.*
3. V. Trufyakov, P. Mikheev, Y. Kudryavtsev and D. Reznik. Ultrasonic Impact Peening Treatment of Welds and Its Effect on Fatigue Resistance in Air and Seawater. *Proceedings of the Offshore Technology Conference. OTC 7280. 1993. p. 183-193.*
4. Y. Kudryavtsev, P. Mikheev and V. Korshun. Influence of Plastic Deformation and Residual Stresses Created by Ultrasonic Impact Treatment on Fatigue Strength of Welded Joints. *Paton Welding Journal. 1995. No. 12. p. 3-7*
5. V. Trufiakov, P. Mikheev, Y. Kudryavtsev and E. Statnikov. Ultrasonic Impact Treatment of Welded Joints. *International Institute of Welding. IIW Document XIII-1609-95. 1995.*
6. Y. Kudryavtsev and J. Kleiman. Fatigue Improvement of Welded Elements and Structures by Ultrasonic Impact Treatment (UIT/UP). *International Institute of Welding. IIW Document XIII-2276-09. 2009.*
7. Y. Kudryavtsev and J. Kleiman. Increasing Fatigue Strength of Welded Elements and Structures by Ultrasonic Impact Treatment. *International Institute of Welding. IIW Document XIII-2318-10. 2010.*
8. Patent of USA # 6467321. 2002. Device for Ultrasonic Peening of Metals.
9. Y. Kudryavtsev, J. Kleiman, L. Lobanov et al. Fatigue Life Improvement of Welded Elements by Ultrasonic Peening. *International Institute of Welding. IIW Document XIII-2010-04. 2004. 20 p.*
10. Y. Kudryavtsev, J. Kleiman, A. Lugovskoy et al. Rehabilitation and Repair of Welded Elements and Structures by Ultrasonic Peening. *International Institute of Welding. IIW Document XIII-2076-05. 2005. 13 p*
11. Y. Kudryavtsev, J. Kleiman, A. Lugovskoy et al. Fatigue Life Improvement of Tubular Welded Joints by Ultrasonic Peening. *International Institute of Welding. IIW Document XIII-2117-06. 2006. 24 p.*
12. Y. Kudryavtsev, J. Kleiman and Y. Iwamura. Fatigue Improvement of HSS Welded Elements by Ultrasonic Peening. *Proceedings of the International Conference on High Strength Steels for Hydropower Plants, July 20-22, 2009. Takasaki, Japan.*
13. P. Haagensen. Progress Report on IIW WG2 Round Robin Fatigue Testing Program on 700 MPa and 350 MPa YS Steels. *International Institute of Welding. IIW Document XIII-2081-05. 2005.*
14. G. Marquis and T. Björk. Variable Amplitude Fatigue Strength of Improved HSS Welds. *International Institute of Welding. IIW Document XIII-2224-08. 2008.*
15. Y. Kudryavtsev. Residual Stress. *Springer Handbook on Experimental Solid Mechanics. Springer – SEM. 2008. P. 371-387.*
16. Patent of USA No. 2,356,314. 1944. Scaling Tool. Reo D. Grey and James R. Denison.
17. Patent of USA No. 3,349,461. 1967. Descaling Tool. Joseph F. Niedzwiecki.
18. Krilov N. A., Polishchuk A. M. Using of ultrasonic apparatus for metal structure stabilization. *Physical background of industrial using of ultrasound. Part 1. LDNTP. Leningrad.-P. 70-79. 1970.* (in Russian)
19. Patent of USA No. 3,609,851. 1971. Metal Working Apparatus and Process. Robert C. McMaster and Charles C. Libby.
20. Patent of USA No. 3,595,325. 1971. Intermediary Impact Device. Charles C. Libby and William J. White.
21. C. Feng and K. Graff. Impact of a Spherical Tool against a Sonic Transmission Line. *The Journal of the Acoustical Society of America. Volume 52, Number 1 (Part 2), 1972. pp. 254-259.*
22. I. Polozky, A. Nedoseka, G. Prokopenko et al. Relieving of welding residual stresses by ultrasonic treatment. *The Paton Welding Journal. 1974. № 5.- p. 74-75. (in Russian)*
23. Author's Certificate (USSR) # 472782. 1975. Ultrasonic head for strain hardening and relaxation treatment. E.

Statnikov, L. Zhuravlev, A. Alexeyev, Yu. Bobylev, E. Shevtsov, V. Sokolenko and V. Kulikov. (in Russian)

24. Author's Certificate (USSR) # 601143. 1978. Ultrasonic multiple-strikers device. G. Prokopenko and V. Krivko. (in Russian)

25. B. Langenecker. Effects of Ultrasound on Deformation Characteristics of Metals. *IEEE Transactions on Sonics and Ultrasonics*. Vol. SU-13, No. 1, March 1966, pp. 1-8.

26. Yuri Kudryavtsev, Jacob Kleiman and Alexander Lugovskoy. Underwater Ultrasonic Peening of Welede Elements and Structures. Proceedings of the 4th International Conference on INTEGRITY, RELIABILITY & FAILURE (IRF2013), Funchal, Portugal, 23-27 June, 2013.

27. N.R. Tao, Z.B. Wang, W.P. Tong et al. An investigation of surface nanocrystallization mechanism in Fe induced by surface mechanical attrition treatment. *Acta Materialia*, 50, 2002, 4603-4616.

PII: 0102-1123(96)00029-1

## Fatigue damage repair: a comparison of some possible methods

C.S. Shin, C.M. Wang and P.S. Song<sup>t</sup>

Department of Mechanical Engineering, National Taiwan University, No. 1, Sec. 4,  
Roosevelt Road, Taipei, 10617 Taiwan, ROC

<sup>t</sup>Department of General Courses, Chung Cheng Institute of Technology, Twhsi,  
Taoyuan, Taiwan, ROC

(Received for publication 15 March 1996)

When a fatigue crack is discovered in an engineering component, some expeditious temporary repair may be needed before more thorough treatment is available. Conventional repair methods, such as grinding removal of the crack and stop drilling, are often employed. In this work, the method of drilling crack-flank holes near to but not at the crack tip has been studied. It was found that retardation still occurred. Moreover, if the holes were drilled a small distance ahead of the tip, the crack was likely to grow into the hole, achieving a considerable amount of life extension. The effects of inducing artificial crack closure by infiltrating epoxy resin, alumina powder and a mixture of both have also been investigated. These were compared with the effect of overload-induced retardation. In all the methods studied, different degrees of crack growth retardation have been achieved, and they have the potential to be developed into practical fatigue crack repair methods. Copyright © 1996 Elsevier Science Limited

(Keywords: fatigue repair; hole drilling; artificial infiltration; crack closure)

It is well known that fatigue fracture accounts for a great number of mechanical failures. When a fatigue crack is discovered in a critical component during routine maintenance, replacement of the component may not be feasible, as there may not be stocks, or the available down-time is too limited. Some expeditious temporary fixing may then be needed to allow the component to operate safely until more elaborate repair or replacement can be arranged.

Different methods for repairing fatigue damage have been studied, and some of these are being employed in practical application. Early work found that by removing the surface layer of a smooth specimen repeatedly from time to time, the specimen fatigue life can be extended indefinitely<sup>1-4</sup>. Intermittent heat treatment had been employed in the hope of reversing early cyclic damages<sup>5-9</sup>. Despite the varying degrees of success reported in some of these works, the difficulty of treating full-scale components and the lack of consistent performance rendered these early attempts futile for practical engineering applications. Above all, these attempts were based on the infinite life design concept, which will invariably break down when pre-existing flaws occur.

A number of more practical methods have been employed for cracked components. One simple repair technique is to grind away the fatigue crack altogether if it is shallow<sup>10</sup>. If this will significantly weaken the structure, a weld overlay or welding of replacement

parts may be required after grinding. When welding is involved, one has to take precautions to avoid the problems commonly associated with the welding process, such as residual stresses, stress corrosion cracking, and hydrogen embrittlement<sup>11</sup>.

One may also drill a stop hole to remove the crack tip singularity<sup>12-14</sup>. In this case, the crack has to be re-initiated before growth can continue. The stop hole may further be cold expanded to introduce favourable residual stress to delay crack re-initiation and subsequent growth<sup>13,14</sup>. Residual stresses that reduce fatigue crack growth rates may also be introduced by pressing steel balls or rollers to plastically deform the material in the vicinity of the crack tip region<sup>14-17</sup>. In grinding or stop drilling, one must take care to remove the crack tip completely. *In-situ* drilling is difficult to control precisely, and often the fatigue crack tip is not easily located. If the hole is drilled a little bit behind, thereby missing the crack tip, the crack may behave as if it is a short crack growing out of a notch. Such notch cracks can have anomalously high growth rates<sup>18</sup>, making the outcome of the repair unpredictable. An alternative method is to drill a pair of holes on the crack flank. The stress intensity factor for the resulting configuration is lower than before, and crack retardation has been observed<sup>19</sup>.

In the case when a crack is too long for grinding and the crack tip is not easily accessible for drilling, other crack repair methods must be sought. Stop drill-

ing is also impracticable for surface cracks or corner cracks emanating from holes because these crack fronts are non-uniform through the thickness. Adhesive patching with composite materials across a crack has been used in the aircraft industry to retard the growth of a fatigue crack. However, patching has been applied mainly to thin-walled components, and its effect on thick components under large applied loading may be limited.

## FATIGUE CRACK REPAIR BY INFILTRATION

It is well known that a tensile overload can cause fatigue crack growth retardation (e.g. ref. 20). This beneficial effect has been made use of as a by-product in the proof testing of pressure vessels to increase their fatigue life<sup>21</sup>. The deliberate use of tensile overload to prolong fatigue life may risk causing a momentary stretch growth or even catastrophic fracture. It would be very useful if we could induce the mechanisms that cause overload retardation by some means other than applying a tensile overload directly. The mechanisms underlying overload retardation may be varied<sup>22-28</sup>, yet premature crack closure stands out to be one of the most significant mechanisms<sup>29-31</sup>. In a recent study of the overload effect in AISI 304 stainless steel, plasticity-induced crack closure has been identified to be the major mechanism for crack growth retardation<sup>31</sup>. Residual plastic deformation leaves extra material behind on the crack flanks, causing premature crack closure and reduction in the effective crack-driving force.

It seems that foreign materials may be introduced into the crack flanks to achieve a similar purpose. Vecchio *et al.*<sup>32</sup> had tried to introduce a spurious asperity such as needle tip into the wake of the crack tip. They found that by so doing the crack closure load increased from an original 5–10% to ~50% and even ~70% of the loading range. According to Elber's modified Paris law<sup>28</sup>, such a great reduction in crack opening duration predicts a large reduction in crack growth rate. In reality, it was observed that growth rates had reduced only slightly, to ~75–88% of the original rate<sup>32</sup>. This discrepancy probably occurred because the asperity behind the crack tip triggered the closure instrumentation but did not really cause much closure at the crack tip, where fatigue damage occurred. In a preliminary attempt the present author has shown that careful infiltration of epoxy resin into a fatigue crack can bring the growth rate down to ~4–10% of the original value in some compact tension specimens<sup>33</sup>. This order of reduction is similar to that caused by a 100% overload<sup>33</sup>. In the current work, the infiltration and hole-drilling crack repair methods have been applied to 3 m long 165 mm diameter seamless piping. Their effects on the fatigue crack growth behaviour were studied. The same repair techniques have also been applied to small three-point bending specimens machined from the pipe. This is to check how well small specimens reflect the effect of crack repair on full-scale components. It is hoped that the results may provide some guidelines on the development of practical *in-situ* repair methods for fatigue-cracked mechanical components.

## EXPERIMENTAL PROCEDURES

### Pipe experiments

A four-point bending fixture that can accommodate up to 170 mm diameter piping was constructed<sup>34</sup>. The inner and outer spans of the bending fixture are 1 m and 2.52 m respectively. At each of the four gripping points, free longitudinal motion and rotation of the pipe were allowed through appropriate roller and bearing arrangements. Three metre long seamless AISI 304 stainless steel pipes, with outer diameter 165 mm and thickness 11 mm, were tested. A Shimadzu 500 t servo-hydraulic machine was used for the pipe experiments. Fatigue testing was carried out under a constant stress intensity range ( $\Delta K$ ) of 45 MPa m<sup>0.5</sup> using a sinusoidal waveform. The load ratio (minimum load/maximum load) was fixed at 0.1. Owing to the large load-line displacements involved, the testing frequency achieved by the machine was only about 0.5 Hz. A through-thickness starter notch subtending a half-crack angle of 40° was saw-cut in the mid-section of the pipe. Details of the experimental set-up and stress intensity calibration have been documented in ref. 34.

Owing to a limited budget and the high equipment rental and specimen costs, a series of different repair methods had to be performed on the same pipe. To avoid complication in data interpretation, a minimum of 3 mm of stable growth (constant growth rate) was allowed before a new repair was carried out. The following sequence of repairs had been performed:

1. A first set of holes was drilled on both sides of the crack, as shown in *Figure 1*. The hole diameter  $d$  was 4.5 mm, and the distance  $L$  of the hole centres from the crack tip was 5 mm.
2. A second set of holes was then drilled. This time  $d = 2.7$  mm and  $L = 2$  mm.

During the drilling operations, the average strains near the crack tip were closely monitored by strain gauges stuck just clear of the crack tip. This was to make sure that, in the entire drilling process, no unwanted plastic deformation had been introduced that

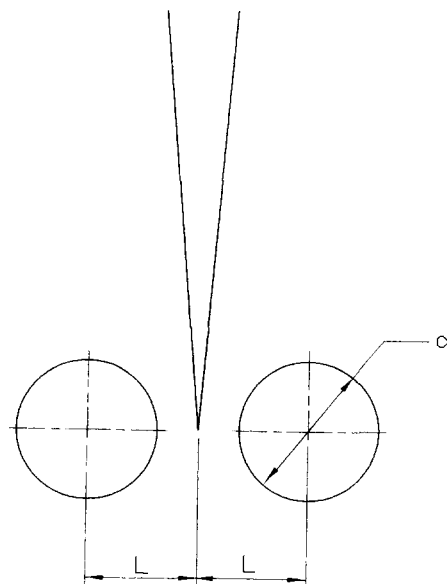


**Figure 1** Relative positions between the drilled holes and the crack

might complicate the results. *Table 1* shows the maximum strains measured, which are small and well within the elastic limit. It is therefore reasoned that the effect of the associated residual stress on the growing crack is probably insignificant.

3. Infiltrations of epoxy resin. A partial vacuum was created in the interior of the pipe by a vacuum cleaner with sealing plastic tape at suitable places. The crack was held open by applying 90% of the maximum loading to facilitate infiltration.
4. Infiltration of alumina powder in the form of an aqueous suspension. Four infiltrations were attempted. The average diameters of the powder were 380 nm, 585 nm, 690 nm and 1100 nm respectively.

To serve as a control, a single tensile overload ( $K_{\text{overload}} = 88.7 \text{ MPa m}^{\frac{1}{2}}$ ) was applied in a second pipe specimen cycled under the same constant baseline  $\Delta K$  of  $45 \text{ MPa m}^{\frac{1}{2}}$ . This corresponded to an overload ratio  $[(K_{\text{overload}} - K_{\min})/\Delta K]$  of 1.86.

Throughout the tests, data on the crack length  $a$  and the number of cycles  $N$  were recorded automatically by a reversing d.c. potential drop system hooked up to an IBM PC. This method has been shown to have sufficient accuracy in a previous work<sup>34</sup>. Periodic manual measurement of the crack length confirmed the accuracy of the acquired data.

#### Three-point bending specimen tests

Three-point bending (3P) specimens of length 145 mm and width 30 mm were machined from the same pipe after the crack repair experiment. The longitudinal axes of the 3P specimens run parallel to the long axis of the original pipe so that fatigue crack growth in the pipe and the 3P specimens occurred in parallel planes. In order to obtain flat specimens from the curved pipe section, the specimen thickness had to be reduced from 11 mm to 9 mm. Fatigue tests were carried out by an MTS 810 closed-loop servohydraulic machine. A constant baseline  $\Delta K$  of  $25 \text{ MPa m}^{\frac{1}{2}}$  was employed in all tests to give a similar value of growth rate as in the pipe specimen. The stress intensity calibration given in ASTM E399<sup>35</sup> was employed to compute the crack driving force. The applied stress intensity range was smaller, as the remaining ligament of the 3P specimen was much smaller than that of the pipe specimen, giving rise to considerable differences in crack closure response and growth rate under the same  $\Delta K$ .

A sinusoidal waveform with a frequency of 10 Hz was used. Crack length was monitored using the reversing d.c. potential drop method mentioned in the last section. As in the pipe experiment, the above series of hole drilling, infiltration as well as the overload tests were carried out on 3P specimens. In this case,

**Table 1** Crack tip strain recorded during hole drilling on pipe specimen

Hole diameter	After drilling the first hole	After drilling the second hole
4.5 mm	-32 $\mu\epsilon$	-47 $\mu\epsilon$
2.7 mm	-66 $\mu\epsilon$	-84 $\mu\epsilon$

each repair was performed on a different specimen. The hole-drilling experiment was repeated five times. Hole diameters were all 2.7 mm, and the distance between the hole centre and the crack plane was 2 mm. As in the pipe specimen, the average crack tip strains were monitored during each drilling operation. The maximum crack tip strain recorded among the five specimens was  $-293 \mu\epsilon$ . This is larger than those from the pipe specimen, but is still well within the elastic limit of the material.

Infiltration of the 3P specimens was first carried out in vacuum, making use of capillary action. Details of the process have been reported in a previous paper<sup>34</sup>. During infiltration, the crack was pulled open using 90% of the maximum cyclic load, as in the case of the pipe specimen. After encountering failure in infiltrating alumina powder, a number of other methods were tried<sup>36</sup>. It was found that using pressurized nitrogen as propellant to drive the infiltrant into a crack gave a higher and more consistent success rate. As a result, a later series of tests employed the new method to infiltrate alumina-reinforced epoxy resin into the 3P specimen cracks.

#### Crack closure measurement

In each of the above tests, crack opening load was measured by the compliance method aided by an offset procedure similar to that proposed by Kikukawa *et al.*<sup>37</sup>. The relevant displacement for compliance information was measured with a strain gauge straddling the crack just behind the crack tip. Crack tip strain gauges were normally fixed with the specimen removed from the testing machine. A low-pass filter with a cut-off frequency of 1 Hz was used to reduce electrical noise. As a result, the testing frequency was reduced to 0.05 Hz during closure measurement to avoid distortion of the signals. The degree of crack closure,  $U$ , was defined as the fraction of the load range for which the crack is open:

$$U = \frac{K_{\max} - K_{\text{op}}}{K_{\max} - K_{\min}} = \frac{\Delta K_{\text{eff}}}{\Delta K} \quad (1)$$

where  $K_{\text{op}}$  is the stress intensity at which the crack started to become fully open and  $\Delta K_{\text{eff}}$  is the effective range of stress intensity available for growing a crack.

## RESULTS AND DISCUSSION

#### Baseline fatigue crack propagation data

In general, fatigue crack growth rate and  $\Delta K$  may be related through Paris' law:

$$\frac{da}{dN} = C(\Delta K)^m \quad (2)$$

Elber<sup>28</sup> suggested taking premature crack closure into account. In this case, the crack growth rate may be correlated through  $\Delta K_{\text{eff}}$ :

$$\frac{da}{dN} = C_c(\Delta K_{\text{eff}})^{m_c} \quad (3)$$

where  $\Delta K_{\text{eff}}$  is as defined in Equation (1).

In the current work, constant-loading-amplitude crack growth tests were carried out at a load ratio of 0.1 in 3P specimens, with crack closure closely monitored. It was found that in the small 3P specimens,

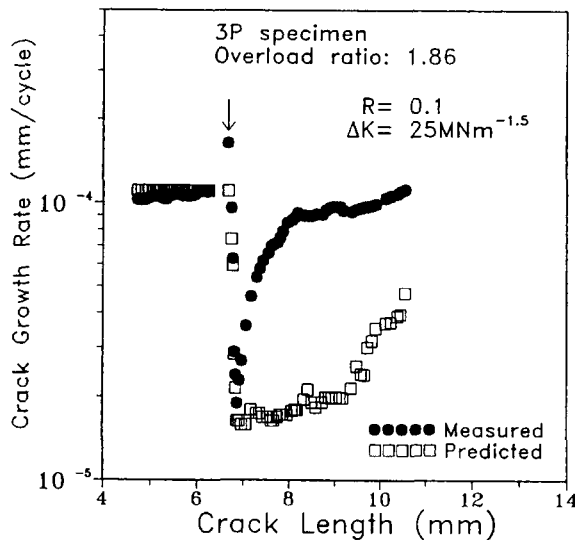


**Figure 2** Crack growth rate versus crack length behaviour of the 3P specimen suffering a tensile overload. Arrow shows the crack tip position during overload

fatigue cracks stayed open throughout the whole loading cycle, and so the coefficients and exponents in Equations (2) and (3) are virtually the same. Thus  $C = C_c = 5.39 \times 10^{-10}$  and  $m = m_c = 3.8$ ;  $da/dN$  is in  $\text{mm cycle}^{-1}$  and  $\Delta K_{\text{eff}}$  is in  $\text{MPa m}^{\frac{3}{2}}$ . Available growth rate data span a  $\Delta K_{\text{eff}}$  range from 20 to 60  $\text{MPa m}^{\frac{3}{2}}$ . It is reasoned that in larger specimens where sufficient elastic enclave exists to bring about premature crack closure,  $C$  and  $m$  will be different from that reported above. On the other hand, as Equation (3) has taken closure into account,  $C_c$  and  $m_c$  should still remain the same. Hence in later crack growth rate prediction only Equation (3) will be used.

#### Retardation caused by single overload

The black circles in Figures 2 and 3 show the effect of a single tensile overload on the crack growth rate in the 3P and pipe specimens respectively. The general

trends of behaviour are similar in the two specimens. The overload ratio as defined above was 1.86 in both cases. On applying the overload, the pipe crack growth rate increased immediately from  $2 \times 10^{-4} \text{ mm cycle}^{-1}$  to  $4.74 \times 10^{-4} \text{ mm cycle}^{-1}$ , while that in the 3P specimen increased from  $1.05 \times 10^{-4} \text{ mm cycle}^{-1}$  to  $1.64 \times 10^{-4} \text{ mm cycle}^{-1}$ . The application of the overload stretched open the crack, giving rise to the observed instantaneous acceleration. Since the pre-overload crack in the 3P specimen was already nearly fully open, the effect of further stretching by the overload was limited, and so the instantaneous acceleration in the 3P specimen was not as pronounced as that in the pipe specimen. In both cases, deceleration to the minimum growth rates occurred relatively more steeply than the subsequent acceleration back to normal conditions. The minimum growth rate reached in the pipe specimen was  $9.28 \times 10^{-5} \text{ mm cycle}^{-1}$ , occurring at 12.9 mm from the point of overload. In the 3P specimen, the minimum growth rate was  $1.9 \times 10^{-5} \text{ mm cycle}^{-1}$ , occurring at 0.6 mm from the point of overload.

The overall crack lengths affected by the overload transient were  $\sim 4$  mm in the 3P specimen and  $\sim 27$  mm in the pipe specimen. Life extensions in terms of number of cycles were 17 000 and 95 000 for the 3P and pipe specimens respectively.

Figures 4 and 5 show the development of crack closure in the 3P and pipe specimens respectively. The crack in the 3P specimen was nearly fully open before the overload. Following the overload, crack closure decreased abruptly to 0.6. It then increased gradually. In the pipe specimen, the crack closure value  $U$  stayed more or less constant around 0.76 before the overload. On applying the overload, the crack became fully open ( $U = 1$ ) immediately. Thereafter,  $U$  decreased abruptly at first and then more gradually until a minimum of 0.46 was reached. Afterward it rose gradually. In both the 3P and pipe specimens, the positions of minimum crack growth rate corresponded well to those of the minimum  $U$  value. Over the crack length under test, crack closure did not regain the pre-overload  $U$  values.

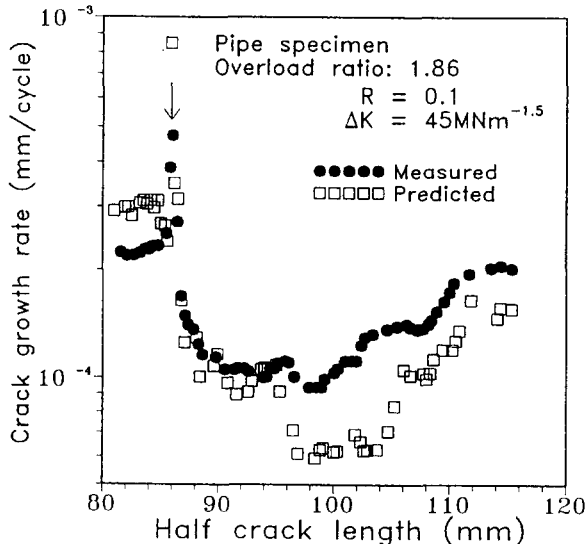


**Figure 3** Crack growth rate versus crack length behaviour of the pipe specimen suffering a tensile overload. Arrow shows the crack tip position during overload

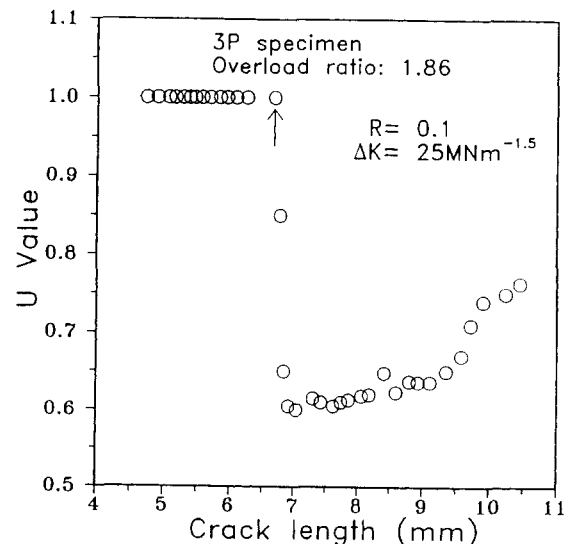


**Figure 4** Crack closure versus crack length behaviour of the 3P specimen suffering a tensile overload. Arrow shows the crack tip position during overload

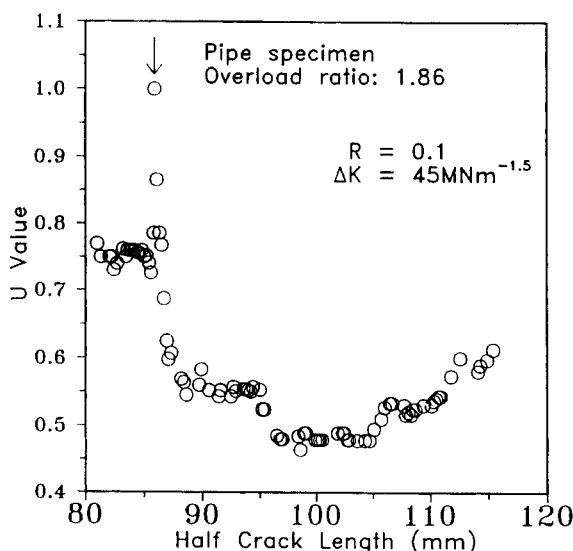


**Figure 5** Crack closure versus crack length behaviour of the pipe specimen suffering a tensile overload. Arrow shows the crack tip position during overload

The quantitative differences in the amount of retardation achieved and the overload-affected zone sizes are presumably due to the difference in size between the two kinds of specimen. This size effect will give considerable difference in the overall elastic-plastic response, which affects the crack opening displacement, the crack closure development, and hence the crack growth rate. In the pipe specimen, which has a large remaining ligament, the ligament was nominally elastic with a localized overload plastic zone. This favoured the development of a greater amount of crack closure, and resulted in more growth retardation. In the 3P specimen, the remaining ligament was small. The crack opening displacement under the same  $\Delta K$  was therefore larger. This gave rise to a higher growth rate as well as a less pronounced overload retardation effect. The occurrence of this *size effect* suggests that using small specimens to evaluate the overload retardation effect on full-scale components is likely to seriously underestimate the beneficial effect.

The open squares in Figures 2 and 3 are predictions based on the measured crack closure values and Elber's correction of Paris law (Equation (3)). The predicted crack growth rates agree well with observed rates from the beginning up to the point of minimum growth rates. Thereafter, Equation (3) tends to underestimate moderately in the pipe specimen and heavily in the 3P specimen. The cause of these underestimations is due to the phenomenon of 'discontinuous closure' identified in a previous paper<sup>31</sup>. Discontinuous closure arose when the exceptionally large humps of residual plastic wake some distance behind the crack tip, created by the overload, came into contact and triggered the closure instrumentation while the crack tip region still stayed open. Thus closure instrumentation will record an  $U$  value smaller than what is actually seen by the crack tip. As a result, the effective crack driving force,  $\Delta K_{\text{eff}}$ , as well as the crack propagation rate, are underestimated. The difference in the degrees of underestimation is probably due to the difference in elastic constraints in the two specimens, as discussed before.

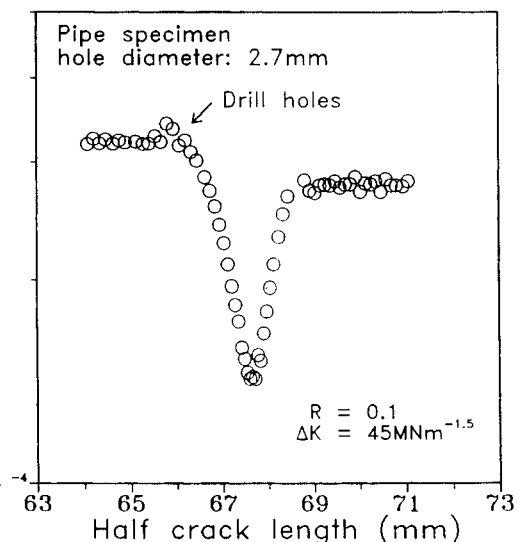


**Figure 6** Effect of drilling holes near the crack tip on the crack growth behaviour in pipe specimen. Arrow shows the crack tip position during hole drilling

#### Retardation caused by crack-flank holes

Drilling the first set of 4.5 mm diameter crack-flank holes did not cause any observable change in crack growth rate in the pipe specimen. It was reasoned that the holes, being 5 mm from the crack plane, were too far away to exert enough influence on the crack. As a result, a second set of holes was drilled only 2 mm from the crack plane. The diameter must necessarily be reduced in order not to drill away part of the crack. Figure 6 shows the development in growth rate for this case. The hole centres were in line with the instantaneous crack tip on drilling. The crack growth rate gradually decreased from  $3.2 \times 10^{-4}$  mm cycle<sup>-1</sup> to  $1.41 \times 10^{-4}$  mm cycle<sup>-1</sup> after a crack growth increment of 1.2 mm. Thereafter, growth rate increased gradually back to normal. The overall affected crack length was 2.5 mm.

The corresponding effect on the 3P specimen (3PH1) is shown in Figure 7. Before drilling holes, the crack

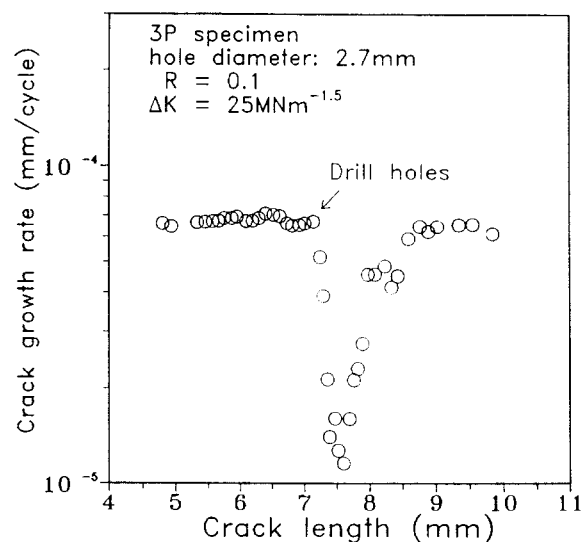


**Figure 7** Effect of drilling holes near the crack tip on the crack growth behaviour in 3P specimen. Arrow shows the crack tip position during hole drilling

growth rate was  $6.5 \times 10^{-5}$  mm cycle $^{-1}$ . This gradually decreased to a minimum rate of  $1.16 \times 10^{-5}$  mm cycle $^{-1}$  after a crack growth increment of 0.5 mm. The total crack length affected was 1.5 mm. Qualitatively, the same behaviour was observed in both pipe and 3P specimens. The amount of life extension was  $\sim 5000$  cycles in the pipe specimen and  $\sim 40\,000$  cycles in the 3P specimen. This difference may be attributable to the difference in the changes in stress intensity factor, as the same hole size was used in the large pipe and small 3P specimens. However, as the stress intensity for the current configuration of a crack approaching two holes is available only for an infinite plate, further numerical analysis is needed to clarify the above postulation. In contrast to the overload experiments, although the amounts of life extension were again different, the affected crack length increments were similar and of the same order of magnitude as the hole diameter in both the pipe and 3P specimens. This suggests that extents of the effect of a pair of holes are similar in large and small specimens. The current result indicates that if we use standard laboratory specimens to evaluate the beneficial effect of hole drilling on full-scale components, care should be taken against possible overestimation of the amount of life extension.

To study the sensitivity of this repair method to the accuracy of hole alignment and location, some further experiments with hole drilling have been carried out in 3P specimens. In a second and third specimen (3PH2 and 3PH3), *in-situ* drilling under unfavourable conditions was simulated. The hole centres were located by a centre punch, and a hand drill was used. The resulting hole locations were not precise, but were as close to the desired position as the hand tool allowed. It was later revealed that the centre axes of the holes were not perfectly perpendicular to the surface of the specimens. On testing, the crack on the front surface of 3PH2 grew into one of the holes, and stopped growing. However, it was later discovered that the crack on the back surface had not grown into a hole. Growth of this crack probably continued on the back surface and through the thickness, leading to a sudden re-emergence of the crack on the front surface 2.9 mm ahead of the hole position. As load shedding to maintain a constant  $\Delta K$  was based on the front surface crack length, the crack might have seen a driving force larger than intended ( $25 \text{ MPa m}^{1/2}$ ) for some length of time. As it re-emerged on the front face, the calculated  $\Delta K$  was  $32 \text{ MPa m}^{1/2}$ . Despite the occurrence of a larger  $\Delta K$ , a life extension of 25 000 cycles was obtained.

In 3PH3, crack branching was observed on the front surface, and one minor branch grew into a hole. No branching or growing into hole occurred on the back (Figure 8). A life extension of 11 000 cycles over an affected crack length of 1.4 mm was obtained.

From the above three tests, it seems that the amount of life extension generated is sensitive to the correct positioning and accurate alignment of the holes. Moreover, as the hole centres were in line with the crack tip, it was not easy for a crack to grow into a hole. Even if that happened, it might probably have occurred over a small part of the thickness, and could not lead to long life extension.

Instead of keeping in line with the instantaneous crack tip, holes were drilled 1 mm (3PH4) and 4 mm

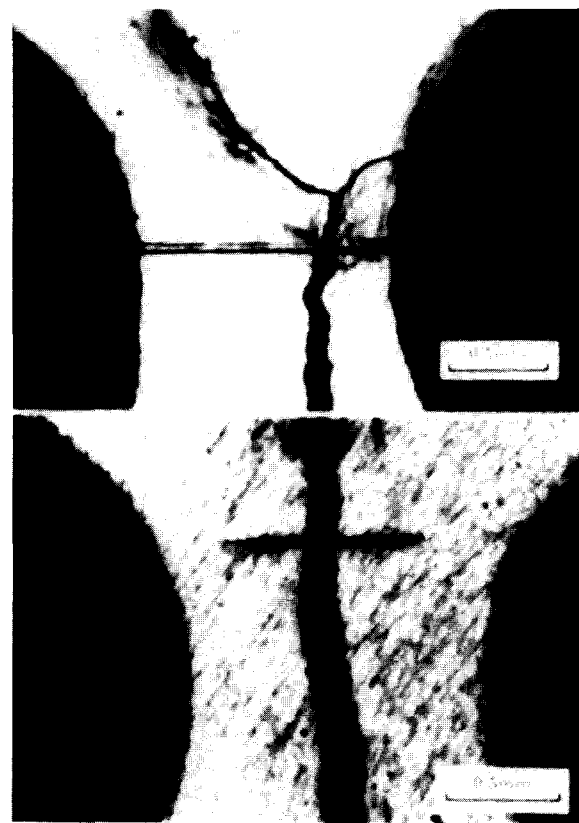


**Figure 8** Crack branching on the front surface of 3PH3, with one branch growing into a hole. No branching occurred on the back surface

(3PH5) ahead of the crack tip in the 3P specimens. Three phenomena are worth noting in these cases. First, the crack started to decelerate once the holes were drilled. As a result, a longer retardation-affected crack length could be achieved. Second, on growing near the hole, crack branching sometimes occurred, with each hole attracting one branch of the crack. A larger amount of retardation in growth rate than for the unbranched crack was then obtained. Third, the attraction of the crack might sometimes be great enough to deflect it and make it grow into the holes. Crack branching and deflection by itself can reduce the crack tip stress intensity by a considerable amount<sup>26</sup>. If the crack grows into a hole, the crack tip singularity is removed altogether (Figure 9). The third effect is

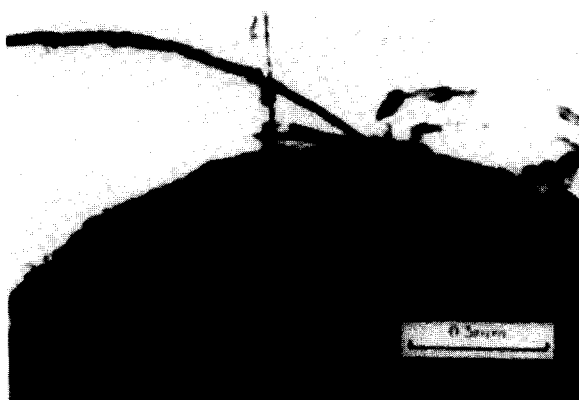


**Figure 9** Crack deflection and growth into a hole on the front surface of 3PH4

the most beneficial, as it caused a very favourable extension of the total fatigue life. In 3PH4, although a crack on only one surface was observed to grow into a hole, such behaviour might have occurred over a considerable portion through the thickness, resulting in a life extension of 126 000 cycles. In 3PH5, cracks on both the front and back surfaces grew into the same hole. The resulting life extension was 112 000 cycles. Thus the life extension in terms of the number of cycles in 3PH4 and 3PH5 amounted to seven to eight times that achieved by the above-mentioned 1.86 times overload.

Good precision is difficult to procure in *in-situ* drilling. Simulated drilling showed that the hole centres might not be well aligned, and that the holes might not be perpendicular to the specimen plane. As a result, the hole on one surface may be slightly ahead of the crack tip, although it was intended to be in line with the tip. If this happened, a crack on that surface might grow into the hole while one on the other surface did not. The life extension achieved would then be less than achieved by those growing into the hole completely but still comparable with or larger than those that grew clear of the holes. In all cases, the 3P specimens repaired by the hole-drilling method derived much better extension in fatigue life than from the corresponding 1.86 times overload.

From this series of crack-flank hole experiments, it may be concluded that the best technique to employ is to drill holes close enough to the crack plane while slightly ahead of the current crack tip. A favourable amount of life extension can be obtained, as the crack tends to be attracted and grows into one of the holes. In this way, stringent requirements on drilling precision to remove the crack tip completely are not required, yet the same effect can be attained. Even if the crack misses the holes, a considerable amount of retardation will still be generated due to a reduction of crack driving force. The drawback of this type of method is that it cannot be conveniently applied to surface cracks or to fluid-tight vessels.

#### *Retardation caused by infiltration of epoxy resin*

The black circles in Figures 10 and 11 show the effect of epoxy resin infiltration on fatigue crack growth rate in the pipe and 3P specimens respectively. Immediate retardation was attained, and the crack growth rate gradually returned to normal.

The pre-infiltration crack growth rate was  $2.8 \times 10^{-4} \text{ mm cycle}^{-1}$  in the pipe specimen. This dropped immediately to  $5 \times 10^{-5} \text{ mm cycle}^{-1}$ , and then gradually increased back to the normal rate. The affected crack length was 3.6 mm, and the resulting life extension was 12 600 cycles. In the 3P specimen, the growth rate dropped from  $1.05 \times 10^{-4} \text{ mm cycle}^{-1}$  to  $3.69 \times 10^{-5} \text{ mm cycle}^{-1}$  immediately on infiltration. It took a crack growth increment of 3.2 mm to regain the original growth rate. The resulting life extension obtained was 15 400 cycles.

The development of crack closure behaviour (Figures 12 and 13) closely matched the development of growth rate transients. A large decrease in  $U$  value was recorded. In the pipe specimen,  $U$  dropped from 0.7 to 0.21. In the 3P specimen,  $U$  dropped from 1 to 0.36. These amounts of decrease were larger than that caused by the 1.86 times overload. The minimum

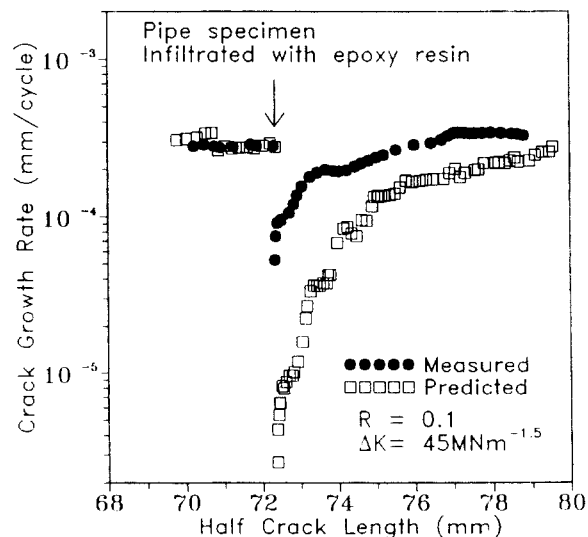


**Figure 10** Effect of suction infiltration with epoxy resin on crack growth behaviour in the pipe specimen. Arrow shows the crack tip position during infiltration

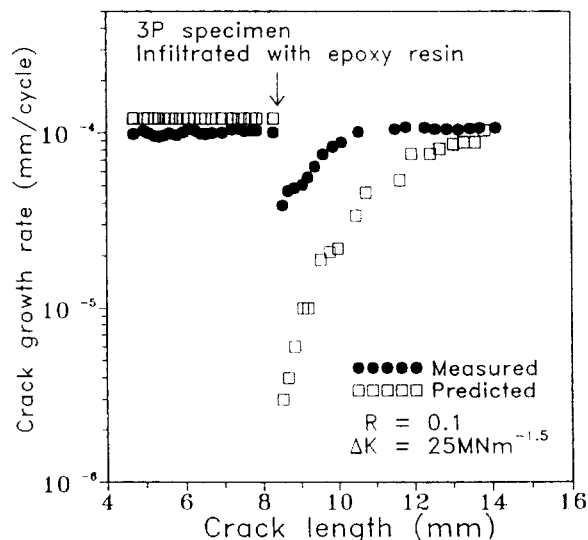


**Figure 11** Effect of vacuum infiltration with epoxy resin on crack growth behaviour in the 3P specimen. Arrow shows the crack tip position during infiltration

growth rates resulting from infiltration were also lower than that due to the overload. These phenomena may be understood in the following terms. Large decreases in  $U$  value and growth rate occurred because the cracks were pulled open at 90% of maximum load so that the crack flanks were fully filled with epoxy resin. The thickness and extent of resin filled were much larger than that in the overload case. However, as the overloaded crack grew, continual release of residual plastic wake material occurred. This helped to maintain a low level of crack opening for a considerable crack growth increment. In the infiltrated cases, no such continual supply of extra wedging material took place. Thus retardation could not be sustained for as large a crack growth increment as that in the overload case for the infiltrated pipe specimen. As a result the overall life extension achieved was much less. In the 3P specimen, continual release of extra plastic wake was offset by the increasing crack opening due to the small

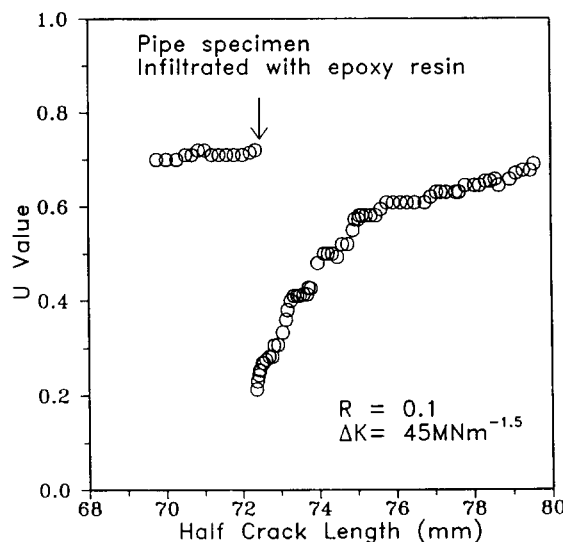


**Figure 12** Effect of suction infiltration with epoxy resin on crack closure behaviour in the pipe specimen. Arrow shows the crack tip position during infiltration

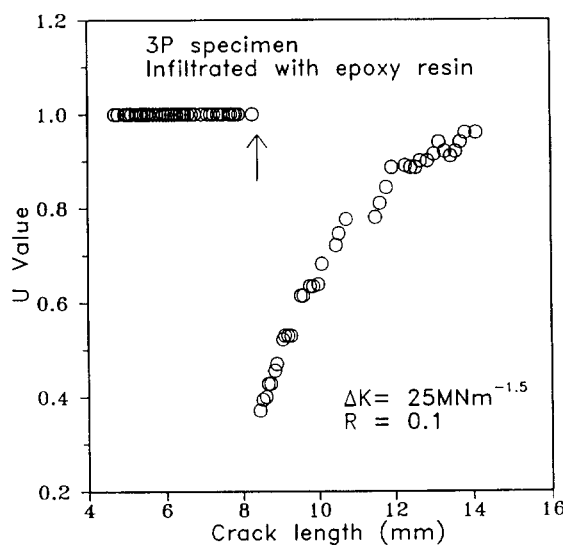


**Figure 13** Effect of vacuum infiltration with epoxy resin on crack closure behaviour in the 3P specimen. Arrow shows the crack tip position during infiltration

remaining ligament size. The overload retardation effect was therefore not extensive, and the amount of life extension was comparable to the infiltrated case.

The open squares in Figures 10 and 11 represent the prediction based on measured crack closure and Equation (3). Serious underestimation occurs throughout the whole crack growth transient. On fracturing the 3P specimen after test, a trace of the infiltrated epoxy resin could be found on the fracture surface. However, judging from the position of the epoxy resin, it was evident that the resin had probably not gone all the way into the instantaneous crack tip region. We have therefore had a similar situation as that of Vecchio *et al.*'s needle tip<sup>32</sup>, as mentioned above, and Equation (3) will obviously give serious underestimation of growth rate. It is reasoned that a much more favourable life extension should be obtained if we have more efficient methods to ensure that the resin reaches the crack tip region.

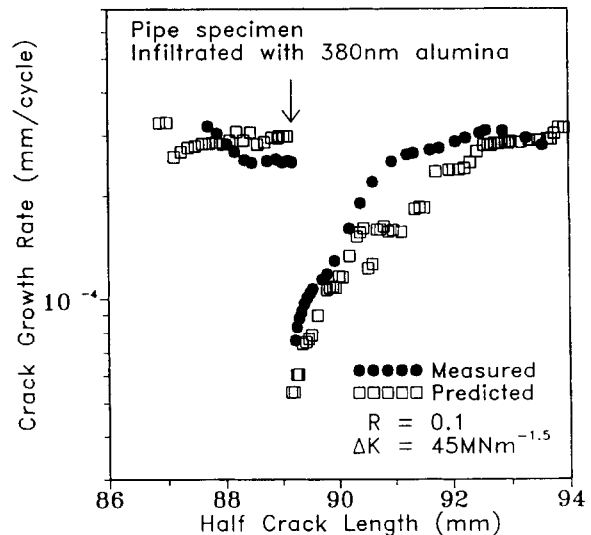


**Figure 14** Effect of suction infiltration with 380 nm alumina powder on crack growth behaviour in the pipe specimen. Arrow shows the crack tip position during infiltration

#### Retardation caused by infiltration of alumina powder

Infiltration of aqueous alumina suspension into the 3P specimen was carried out using the same technique as that for epoxy resin. No observable change in crack growth rate was noted. Some success was obtained with the pipe specimen. The black circles in Figures 14–17 show respectively the effect of infiltration of 380 nm, 585 nm, 690 nm and 1100 nm diameter alumina powder on crack growth rate in the pipe specimen. No retardation is observed in Figures 15 and 17, while immediate retardation occurred in Figures 14 and 16. The best retardation effect was achieved with the 380 nm diameter powder. The growth rate immediately dropped from  $2.6 \times 10^{-4} \text{ mm cycle}^{-1}$  to  $7.6 \times 10^{-5} \text{ mm cycle}^{-1}$ . The affected crack length was 2.5 mm and the extension in life was 7000 cycles. The next best retardation was achieved with the 690 nm diameter powder. In this case, the growth rate immediately dropped from  $2.9 \times 10^{-4} \text{ mm cycle}^{-1}$  to

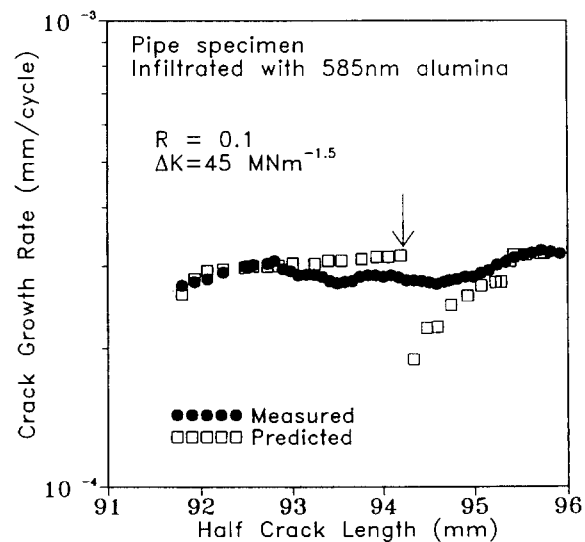


**Figure 15** Effect of suction infiltration with 585 nm alumina powder on crack growth behaviour in the pipe specimen. Arrow shows the crack tip position during infiltration

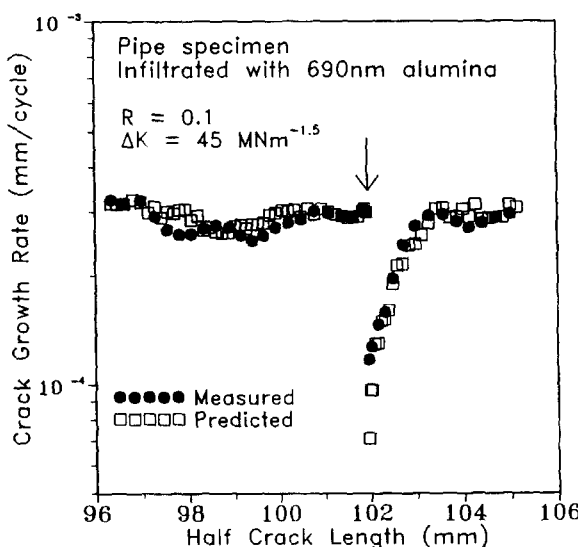


**Figure 16** Effect of suction infiltration with 690 nm alumina powder on crack growth behaviour in the pipe specimen. Arrow shows the crack tip position during infiltration

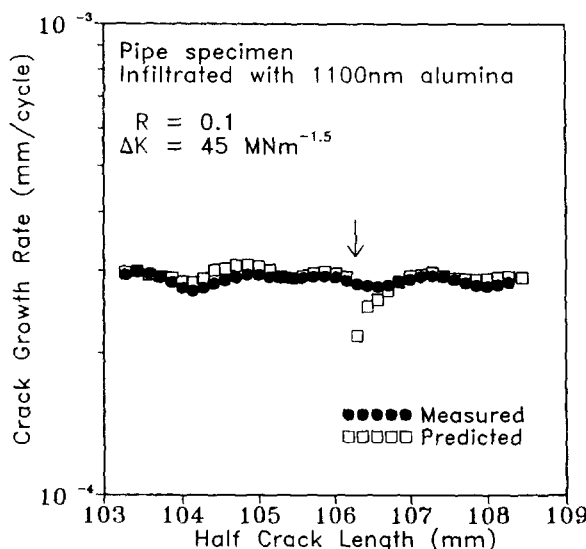


**Figure 17** Effect of suction infiltration with 1100 nm alumina powder on crack growth behaviour in the pipe specimen. Arrow shows the crack tip position during infiltration

$1.16 \times 10^{-4}$  mm cycle $^{-1}$ . The affected crack length was 1.4 mm and the extension in life was 2900 cycles. The development in crack closure matched that of the growth rate (*Figures 18 and 20*). In the remaining two cases (*Figures 19 and 21*), although no retardation was observed, there was a marked drop in *U* value for the 585 nm diameter powder. A slight but distinct drop in *U* value also occurred for the 1100 nm powder. The open squares in *Figures 14–17* show the crack growth rate calculated using Equation (3) and the recorded *U* values. Unlike the overload and epoxy resin infiltrated cases, the predicted growth rate agrees very well with the measured. No serious underestimation exists, implying that the phenomenon of discontinuous closure has probably not occurred.

The absence of retardation in some of the cases was probably caused by the failure of alumina powder to get into the crack. The crack tip opening displacement in the pipe specimen was estimated to be at least

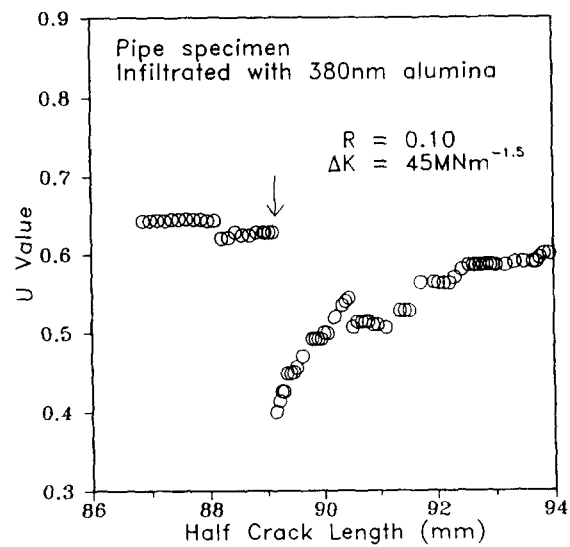


**Figure 18** Effect of suction infiltration with 380 nm alumina powder on crack closure behaviour in the pipe specimen. Arrow shows the crack tip position during infiltration

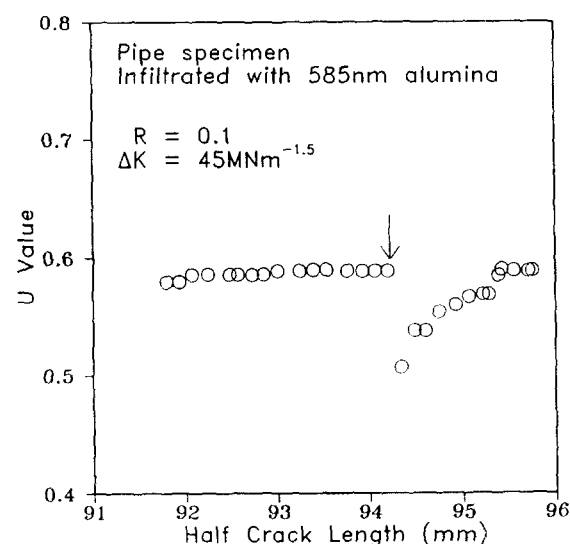


**Figure 19** Effect of suction infiltration with 585 nm alumina powder on crack closure behaviour in the pipe specimen. Arrow shows the crack tip position during infiltration

7400 nm. Hence failure of infiltration was not caused by large particle size. It is probably due to the inefficiency of the aqueous carrier and the infiltration method. In the pipe specimen, infiltrant was to some extent drawn into the crack by a partial vacuum. In the 3P specimens, although infiltration was done in a better vacuum, capillary action alone operated. This explains why a limited success was obtained in the pipe specimen but a total failure occurred in the 3P specimens. A more efficient carrier and infiltration method are needed.

Previous work using epoxy resins of different hardness<sup>33</sup> suggested that a harder infiltrant might be more effective in bringing about retardation. In the current case, the harder alumina is apparently less effective than the softer epoxy resin. Besides the possible difference in the infiltration efficiency of these two materials, the small particle size of alumina powder may also be responsible. Assuming a successful infiltration, epoxy

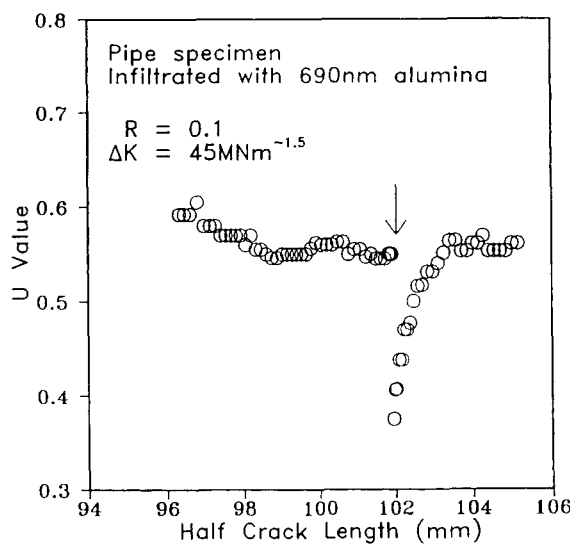


**Figure 20** Effect of suction infiltration with 690 nm alumina powder on crack closure behaviour in the pipe specimen. Arrow shows the crack tip position during infiltration

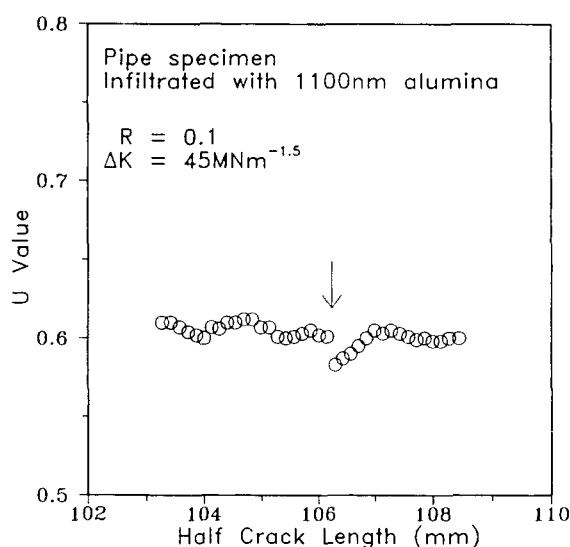


**Figure 21** Effect of suction infiltration with 1100 nm alumina powder on crack closure behaviour in the pipe specimen. Arrow shows the crack tip position during infiltration

resin can take up fully the space between the crack flanks, while only a single or a few layers of alumina powder can probably be built up on the fracture surface. The additional amount of crack closure brought about by alumina will be much less than that caused by epoxy resin, noting that the crack tip opening displacement is much larger than the alumina particle size. This is also the likely reason for no serious underestimation in the predicted growth rates in Figures 14–17. One improvement may be to employ powder with a wide range of sizes so that the largest allowable particles can get into the crack and induce the maximum amount of closure. The other possible way is to mix alumina powder with epoxy resin so that an alumina-reinforced epoxy resin composite is infiltrated. Preliminary results of the latter options are reported next.

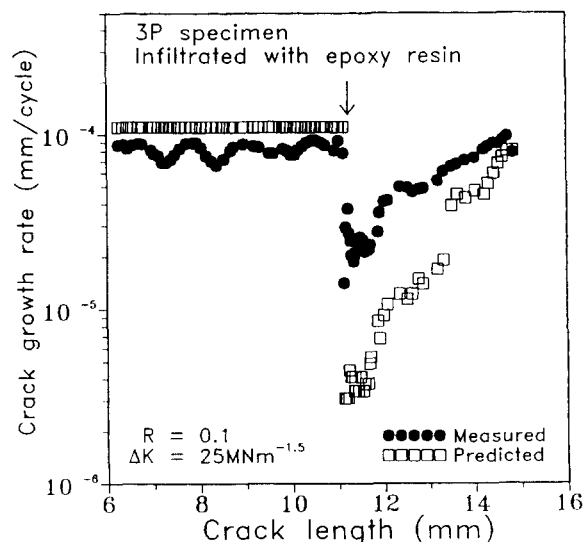


**Figure 22** Effect of pressure infiltration with epoxy resin on crack growth behaviour in the 3P specimen. Arrow shows the crack tip position during infiltration

#### Retardation caused by infiltration of epoxy resin reinforced by alumina powder

Following the failure in infiltrating aqueous alumina suspension, a new technique using pressurized nitrogen to force infiltrant into a crack was developed<sup>36</sup>. Epoxy resin was infiltrated into a 3P specimen again using this new technique. For comparison purposes, epoxy resin mixed with 0.2 µm and 0.5 µm mean diameter alumina powder (weight ratio = 1 : 1) was also used. The black circles and open squares in Figures 22–24 show respectively the measured and predicted growth rates for these three cases. The growth transients and the deviation between the measured and predicted responses exhibit qualitatively the same trends as that discussed above for the 3P specimen infiltrated with epoxy resin (i.e. Figure 11). The affected crack lengths in the four cases were similar. Being more efficient in transporting material into a crack, the pressure infil-

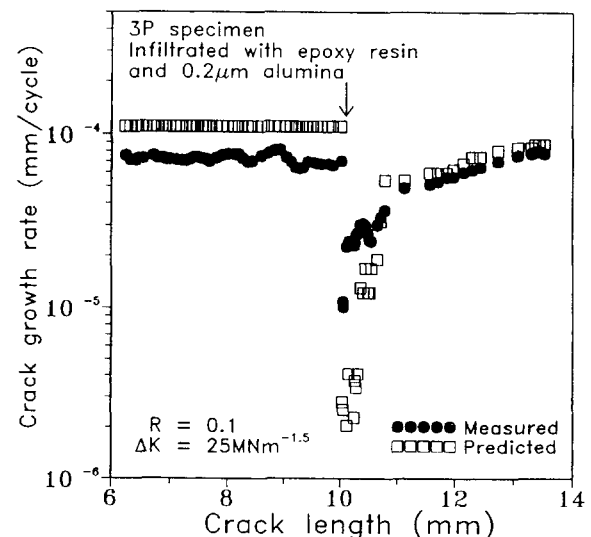


**Figure 23** Effect of pressure infiltration with epoxy resin plus 0.2 µm alumina on crack growth behaviour in the 3P specimen. Arrow shows the crack tip position during infiltration

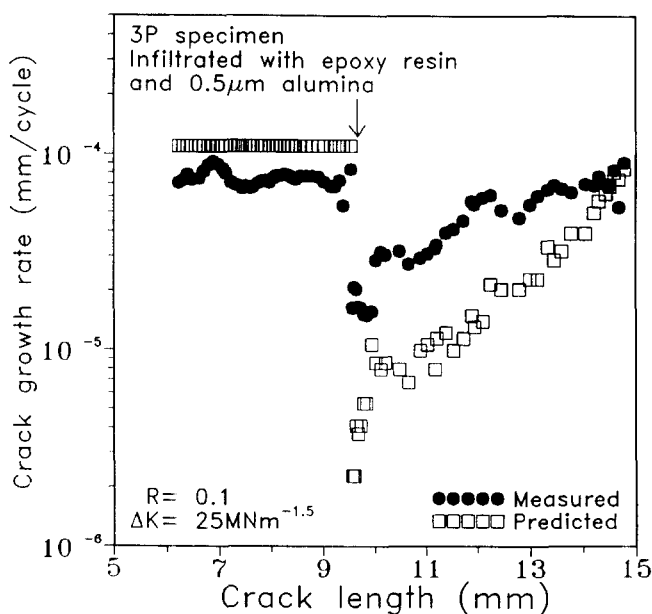


**Figure 24** Effect of pressure infiltration with epoxy resin plus  $0.5 \mu\text{m}$  alumina on crack growth behaviour in the 3P specimen. Arrow shows the crack tip position during infiltration

tration method brought about lower minimum growth rates and longer life extensions (see Table 2).

Comparison between the current three cases showed that reinforcing epoxy resin with different-sized alumina powder did not cause significant differences in retardation and life extension. Subsequent examination of the fracture surfaces suggested that the differences in growth response and life extension were probably associated with how well the resin filled up the crack to the crack tip. Reinforcement with a wider range of particle size and particle mechanical properties is needed to clarify whether a harder infiltrant will give a better repair.

The five methods employed above all induced retardation in growth rate and hence extension in fatigue life to different amounts. The most straightforward parameter to quantify the beneficial effect of a repair method is the amount of life extension, expressed in number of cycles. The severity of retardation (minimum growth rate/baseline growth rate) and the

overall affected crack growth increment also reflect the effectiveness of a repair method. Though not as direct as life extension, the latter two parameters tend to shed some light on the direction towards which a particular method should be improved. Tables 2 and 3 document these three parameters for each of the tests in the 3P and pipe specimens respectively. Overload retardation is the most convenient method to apply in general. It may be applied to most configurations. Its retardation effect is fairly certain, and repeated applications can easily be achieved. However, the major drawback that probably precludes its use on practical components is that it carries the risk of causing stretch-tearing growth or even catastrophic fracture. This risk is difficult to avoid, as in most engineering applications the exact fracture toughness of the material concerned is often not known. On the other hand, hole drilling and infiltration do not carry the above risk.

Of the five methods investigated, hole drilling gave the longest life extension, and by drilling ahead of a crack the requirement of strictly removing the crack tip is not necessary, yet a very favourable effect can still be obtained. In the case where hole drilling is not appropriate, infiltration is a potential candidate. Currently the infiltration technique needs to be improved before it can have practical value. It is reasoned that, to be successful, we must be able to infiltrate foreign materials well into the crack tip region in a reproducible manner. Moreover, the thickness of the infiltrated materials should be large enough to cause a sufficient amount of crack closure so that the crack growth rate can be decreased to a very low level. If this cannot be achieved, repeated applications should be attempted.

The above comparison between pipe and 3P specimens showed that the beneficial effect of overload on pipe specimen cannot be accurately predicted from small 3P specimens. Further numerical analysis on stress intensity factor will clarify whether we can predict from small specimens the effect of hole drilling on full-scale components. Although the effect of infiltration repair depends very much on whether infiltration has taken place, current results show that the responses of the pipe and 3P specimens are similar. This suggests that the more economical tests on standard specimens

**Table 2** Summary of the effectiveness of various repair methods on 3P specimens

Method	Severity of retardation <sup>a</sup>	Affected crack growth increment (mm)	Life extension (no. of cycles)
1.86 times overload	0.18	3.9	17 000
Crack-flank holes (3PH1)	0.18	1.5	40 000
Hand tool (3PH2)	Stopped <sup>b</sup>	—	25 000
Hand tool (3PH3)	0.17	1.4	11 000
1 mm ahead of tip (3PH4)	Stopped	—	126 000
4 mm ahead of tip (3PH5)	Stopped	—	112 000
Aqueous alumina infiltrant	1	—	—
Vacuum-infiltrated epoxy resin	0.35	3.2	15 400
Pressure-infiltrated epoxy resin	0.17	3.1	36 000
Epoxy resin + 0.2 $\mu\text{m}$ alumina	0.27	3.2	31 000
Epoxy resin + 0.5 $\mu\text{m}$ alumina	0.16	4.2	60 000

<sup>a</sup>Severity of retardation = Minimum growth rate/baseline growth rate.

<sup>b</sup>Crack grew into a hole and stopped on the front surface only.

**Table 3** Summary of the effectiveness of various repair methods on pipe specimen

Method	Severity of retardation <sup>a</sup>	Affected crack growth increment (mm)	Life extension (no. of cycles)
1.86 times overload	0.46	27	95 000
4.5 mm crack-flank holes	—	—	—
2.7 mm crack-flank holes	0.44	2.5	5 000
Epoxy resin infiltrant	0.18	3.6	12 600
380 nm alumina infiltrant	0.29	2.5	7 000
585 nm alumina infiltrant	—	—	—
690 nm alumina infiltrant	0.4	1.4	2 900
1100 nm alumina infiltrant	—	—	—

<sup>a</sup>Severity of retardation = Minimum growth rate/baseline growth rate.

may be used to investigate the possible extension in life under infiltration repairs.

## CONCLUSIONS

The effects on crack growth caused by hole drilling near the crack tip and artificial induction of crack closure by tensile overload, infiltration with epoxy resin, alumina powder and a mixture of both have been studied in 165 mm diameter pipe and three-point bending specimens. Except for a poor infiltration technique to transport aqueous alumina suspension into 3P specimens, all five methods achieved crack growth retardation and successfully extended the fatigue life, to different extents. The introduction of an overload may risk fracturing the cracked structure, and so is not a good candidate for fatigue crack repair technique. Crack-flank hole drilling and infiltration are relatively safe. In this preliminary work, hole drilling was more effective than infiltration in extending the fatigue life. The best retardation effect was obtained by drilling very near to the crack plane while slightly ahead of the crack tip. More efficient infiltration techniques are needed for this method to be of practical value.

## ACKNOWLEDGEMENTS

The authors gratefully acknowledge the financial support provided by the National Science Council under the projects NSC-83-0401-E-002-087 and NSC-84-2212-E-002-024.

## REFERENCES

- Thompson, N., Wadsworth, N.J. and Louat, N. *Phil. Mag.* 1956, **1**, 113
- Christensen, R.H. In 'Metal Fatigue' (Eds. G. Sines and J.L. Waisman) McGraw-Hill, New York, 1959, pp. 376-412
- Bentele, M. and Lowthian, C.S. *Aircraft Eng.* 1952, **24** (276), 32
- Raymond, M.H. and Coffin, L.F. *J. Basic Eng.* 1963, **85** (4), 548
- Sinclair, G.M. and Dolan, T.J. In 'Proc. First US National Congress of Applied Mechanics', ASME, New York, 1952, p. 647
- Sandor, B.I. In 'Achievement of High Fatigue Resistance in Metals and Alloys', ASTM STP 467, American Society for Testing and Materials, Philadelphia, 1970, pp. 254-275
- Wright, M.A. and Greenough, A.P. *J. Inst. Met.* 1964-65, **93**, 309
- Ivanova, V.S., Antikain, P.A. and Sabitova, N.S. *Metallovedenie i Termicheskaya Obrabotka Metallov* 1965, No. 1, Jan., 7
- Cousland, S.McK. and Sargent, K.R. *J. Inst. Met.* 1963-1964, **92**, cited in ref. 10
- Popp, H.G., Wilber, L.G. and Erdeman, V.J. In 'Metal Fatigue Damage—Mechanism, Detection, Avoidance and Repair' (Ed. S. Manson), ASTM STP 495, American Society for Testing and Materials, Philadelphia, 1971, p. 228
- Linnert, G.E. 'Welding Metallurgy', Vol. 2, American Welding Society, New York, 1967
- Broek, D. 'Elementary Engineering Fracture Mechanics', 4th edn. 1986, Martinus Nijhoff Publishers, The Hague
- de Rijk, P. Nat. Aerospace Inst. Amsterdam Report TR 70021, 1970, cited in Ref. 12
- van Leeuwen, H.P. *et al.* Nat. Aerospace Inst. Amsterdam Report TR 70029, 1970, cited in ref. 12
- Eggwirtz, S. Swedish Aerospace Inst. FFA Report TN-HE-1270, 1969, cited in ref. 12
- Blazewicz, W. Results reported in Schijve, J. *Eng. Fract. Mech.* 1979, **11**, 182
- Landy, M.A., Armen, H. Jr. and Eindoff, H.L. In 'Fatigue in Mechanically Fastened Composite and Metallic Joints', ASTM STP 927, American Society for Testing and Materials, Philadelphia, 1986, pp. 190-220
- Shin, C.S. and Smith, R.A. *Eng. Fract. Mech.* 1988, **29** (3), 301
- Miyagawa, H. and Nisitani, H. *Bull. Jpn. Soc. Mech. Eng.* 1985, **28** (244), 2219
- von Euw, E.J.F., Hertzberg, R.W. and Roberts, R. In 'Stress Analysis and Growth of Cracks, Proc. 1971 National Symposium on Fracture Mechanics', Part I, ASTM STP 513, American Society for Testing and Materials, Philadelphia, 1972, pp. 230-259
- Novotny, I.G. *Proc. Inst. Mech. Eng.* 1986, **C268/86**, 249
- Christensen, R.H. 'Metal Fatigue', McGraw-Hill, New York, 1959
- Schijve, J. and Brock, D. *Aircraft Eng.* 1962, **34**, 314
- Jones, R.E. *Eng. Fract. Mech.* 1973, **5**, 585
- Suresh, S. *Scr. Metall.* 1982, **16**, 995
- Suresh, S. *Eng. Fract. Mech.* 1983, **18** (3), 577
- Elber, W. *Eng. Fract. Mech.* 1970, **2**, 37
- Elber, W. In 'Damage Tolerance in Aircraft Structures', ASTM STP 486, American Society for Testing and Materials, Philadelphia, 1971, pp. 230-242
- Shin, C.S. and Fleck, N.A. *Fatigue Fract. Eng. Mater. Struct.* 1987, **9** (5), 379
- Fleck, N.A. In 'Basic Questions in Fatigue', Vol. 1 (Eds. J.T. Fong and R.J. Fields) ASTM STP 924, American Society for Testing and Materials, Philadelphia, 1988, pp. 157-183
- Shin, C.S. and Hsu, S.H. *Int. J. Fatigue* 1993, **15** (3), 181
- Vecchio, R.S., Crompton, J.S. and Hertzberg, R.W. *Int. J. Fract.* 1986, **31**, R29
- Shin, C.S. and Hsu, S.H. *Eng. Fract. Mech.* 1992, **43** (4), 677
- Shin, C.S., Tseng, R.P. and Jao, W.T. *Int. J. Pressure Vessels Piping* 1994, **57**, 169
- 'Standard Test Method for Plane-Strain Fracture Toughness of Metallic Materials', ASTM E399-90, American Society for Testing and Materials, Philadelphia, 1990
- Song, P.S., Wang, C.M. and Shin, C.S. In 'Proc. 1994 Far East Conference on NDT (FENDT '94) and ROCSNT Ninth Annual Conference', Taipei, ROC, Nov. 1994, pp. 221-228
- Kikukawa, M., Jono, M. and Tanaka, K. In 'Proc. ICM2', Boston, 1976, pp. 254-277



## **Refill Friction Stir Spot Weld Repair of a Fatigue Crack**

*Prepared by:*

Sean Long Fox

Undergraduate, Metallurgical Engineering

*Faculty Advisors:*

Dr. Michael West

REU Site Director, Department of Materials and Metallurgical Engineering

Dr. Bahrat Jasthi

Research Associate, SDSMT Advanced Materials Processing Center

Dr. Alfred Boysen

Professor, Department of Humanities

*Program Information:*

National Science Foundation

Grant #: 0852057

Research Experience for Undergraduates

Summer 2010

South Dakota School of Mines and Technology

501 E Saint Joseph Street

Rapid City, SD 57701

## TABLE OF CONTENTS

<b>Abstract.....</b>	<b>3</b>
<b>Introduction.....</b>	<b>4</b>
<b>Broader Impact.....</b>	<b>5</b>
<b>Procedure.....</b>	<b>6</b>
<b>Materials Prep.....</b>	<b>6</b>
<b>Pre-cracking and Fatigue Crack Growth.....</b>	<b>7</b>
<b>Fatigue Test.....</b>	<b>8</b>
<b>Optimization of Parameters.....</b>	<b>8</b>
<b>Surfacing and Penetration.....</b>	<b>11</b>
<b>Stitch Welding.....</b>	<b>12</b>
<b>Cold Spray.....</b>	<b>12</b>
<b>Results.....</b>	<b>15</b>
<b>Discussion/Conclusion.....</b>	<b>16</b>
<b>Future Work.....</b>	<b>16</b>
<b>References.....</b>	<b>17</b>

## **ABSTRACT**

The main objective of this project is to repair a fatigue crack using Refill Friction Stir Spot Weld Technology. This involved developing a procedure to stitch, or overlap, single spot weld to repair fatigue cracks. A pre-cracking procedure was also developed to provide simulated fatigue cracks on which repairs could be made. First, the welding parameters were optimized for 2024 Al T3 with a thickness of .125 inches. 2024 powder is then deposited using Cold Spray Deposition to fill the pre-crack. The welds were then overlapped and repairs were made. The repairs were found to have defects and the defects are characterized to show how they reduced fatigue life. Good repairs are also characterized and show improvement in fatigue life over cracked samples. Improved repair methods are discussed to allow for better repairs in the future.

## INTRODUCTION

Fatigue life is a very important factor in many applications. For instance, a plane wing will undergo fatigue cycles as the wing flutters during flight. Over time this cyclic fatigue will cause fatigue cracks. With every cycle, the fatigue crack grows larger. Many times these fatigue cracks act as an indicator that the part in question must be replaced. These replacements are costly and require constant manufacturing. Recently, a new friction stir process was developed called Refill Friction Spot Welding. With this new idea, Harms and Wende of Germany has developed a small RFSW machine. The RFSW process differs from traditional friction spot welding. The friction stir refill process uses a pin and sleeve (shoulder) that move independently from each other. While both pin and sleeve are rotating, the sleeve is plunged into the material to be welded. At the same time, the pin retracts upward; drawing plasticized material up as well. Once the sleeve has reached its full depth, both sleeve and pin return to their original position. As the pin moves down, it re-introduces the plasticized material back into the weld. This method of friction stir spot welding has been shown to be superior to the fixed pin of friction spot welding. Using the RFSW process, a procedure for repairing existing fatigue cracks could be developed. Repairing a part can be much more cost effective when compared with simply replacing the part. It is with this goal in mind that a procedure for RFSW fatigue crack repair will be developed.

In order to repair a fatigue crack, it must first be created in a sample that can be analyzed. 2024 Aluminum in a T3 state will be used as the material to be tested. A thickness of 0.125 inches will be used as it is a common size for many Al skin applications. This thickness is also near the limit of the RFSW machine's welding depth. A sample configuration was selected as per ASTM E647 for a notched sample. The specimen is a dog bone configuration. The samples are then machined under high tolerances and a pre-crack is introduced into the test cross section. The pre-crack acts as a stress concentrator and helps to grow the fatigue crack. The crack will be

grown under cyclic loading condition in a MTS 810 tensile testing machine. Once a fatigue crack is present, the pre-crack volume loss must then be filled to allow for proper surfacing during RFSW repair. For this a Cold Spray Process will be used to introduce 2024 Al powder into the pre-crack. Then, stitch welds will be used to repair the fatigue crack that remains in the sample. A stitch weld is simply overlapping welds to form a continuous repair. Once repaired, the sample will then undergo addition fatigue test to show the resulting fatigue life. This is then compared to the fatigue life of parent metal samples and to that of unrepairs samples. The un-repaired samples simply have the unrepairs fatigue crack present. Ultimately this will show whether the procedure outlined in this project will give an improved fatigue life for this material.

## BROADER IMPACT

In order for a part to develop a fatigue crack the part simply must undergo cyclic stress at a level below the materials flow stress. The crack will generally form near a stress concentrator. Sharp ninety degree angles, or areas of weakness, make good stress concentrators. Once the crack is started it will spread to a point when the part may fail in a catastrophic manner. Replacement parts are costly and they rely on their supply. One good example of how fatigue cracks can be harmful would be the United States Military's aging equipment. For instance, the F-15 eagle is an aircraft that has been around since the early 1970's. As this aircraft flies through the air, the tips of the wings flutter up and down. This causes fatigue cracks to form in the wing. A replacement wing is a costly option, but what if it could be effectively repaired? Time, money, and resources could be saved with an effective repair procedure. Solution such as this are needed to caring aging equipment into the future without having to maintain the associated infrastructure. This means that a piece of machinery could still be used even without parts being actively manufactured. The military example is not where the possibilities end. The private sector could also benefit much from an effective fatigue crack repair process.

## PROCEDURE

### Materials Preparation

The materials that were used in this project were 2024 Aluminum in the T3 state. The 2024 Aluminum plate was 0.125 inches thick. Originally, this material was a single plate. This plate was then sheered to a dimension with approximated 0.125 inches excess in each dimension. It should be noted that the length (12in) of the specimen is the original direction of rolling. The raw sheered plates where then squared to within .1 inches of their final dimensions. This was done using a manual milling machine, with great care taken to achieve high tolerances. Instead of the traditional 0.02 inches tolerances, 0.01 inches was selected. Precisely machined samples are needed to ensure good results. ASTM E466 was the standard referred to while finalizing the sample configuration. The rectangular plates then needed some final milling to introduce the reduced section. This milling was performed using a CNC milling machine. The radius of the reduced section was 0.5 inches. The final pass in the CNC was a high tolerance and surfacing pass. This means that only 0.005 inches were removed on the last pass in order to maintain the high tolerance. The samples were stacked 8 high or 1 inch thick for the CNC milling process. Figure 1 illustrates the final specimen and the location of the pre-crack, while Figure 2 shows the Solidworks model used to develop the tool paths for final CNC milling.

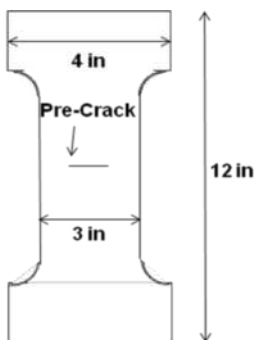


Figure1: Sample Configuration

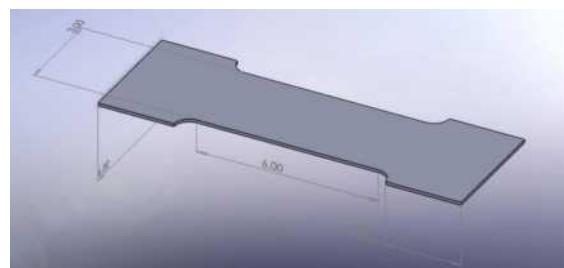


Figure 2: Solidworks Coupon Model

## Pre-Cracking and Fatigue Crack Growth

The pre-crack growth procedure was setup using a Dremel power tool. The tool had a 1/8 inch thick disk made of silicon carbide. The procedure was to cut a .80 inch deep and .75 inch long slot out of the fatigue coupon to initiate a fatigue crack growth.

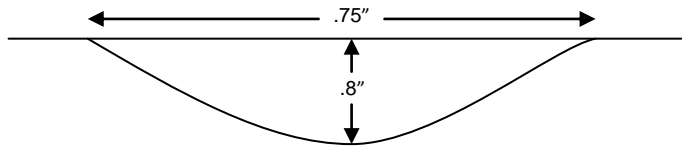


Figure 3: Pre-Crack Dimension (front)

Figure 3 shows the diagram and shows the dimensions of the pre-crack.

This was the first step in artificially creating a fatigue crack. After the pre-crack was initiated the coupon was then loaded into a tensile test machine. The coupons were run in cyclic fatigue to broaden the width and depth of the fatigue crack. The range for the load of the cyclic fatigue was from .675 kips to 6.75 kips. The 6.75 kips is thirty percent of the flow stress of the material. The range of the load needed to be low to ensure a plastic region did not form around the crack. The test were performed at 20 Hz and reached approximately 50,000 cycles. Figure 4 shows a close look on a finished fatigue crack. It can be seen that the pre-crack dominates the visual; however there are microscopic cracks on each side of the pre-crack. The total width of the crack was approximately .78 inches to .65 inches. A closer look at this macroscopically indicates that indeed a crack was propagated in the pre-crack. In Figure 5, it shows the crack at a 50x resolution.



Figure 4: Fatigue Crack Width

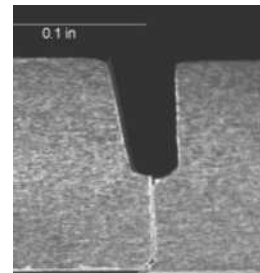


Figure 5: Fatigue Crack Macro (side)

## Fatigue Test

The cyclic fatigues of the samples are broken up into three categories. The categories consist of parent, un-repaired and repaired samples. Each category will have 4 load levels applied to them. These are expressed as percentage of flow stress. The load levels include 20% at .45 kips to 4.5 kips, 30% at .675 to 6.75 kips, 40% at .9 kips to 9.0 kips and 50% at 1.125 kips to 11.25 kips. Making the total flow stress for the coupon to be 22.5 kips. These are the cyclic fatigues lower and upper limits and will proceed until failure of the material is reached. In Figure 6, an unrepaired sample that was run until failure is shown.

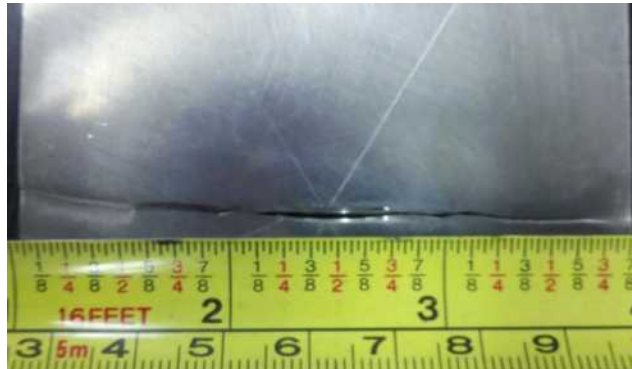


Figure 6: Failure of an Un-Repaired Sample

## Optimization of Parameters

For the welding part of the project, optimized parameters are needed. Previous work was done using this exact procedure of optimization, however, the state of RFSW machine was unsteady at that time. A parameter matrix was developed and can be seen below in Figure 7. In order to show the best combination of weld time and rotational speed, each must be varied to show the overall affect on weld defects. By increasing these variables an increase in the mixing and heat input may be seen. In order to see the best combination, 1400 to 1600 rpm was tested, with the total weld time varying from 6 to 10 seconds. It should be noted that the total weld time includes

the plunge time and the retraction time. In this experiment the plunge time is equal to the retraction time. The clamping pressure is constant at 3.5 bar. Clamping pressure is applied through a standard pneumatic c-gun which forms the frame of the RFSW. The clamp, or gun, is actuated at the beginning of the welding cycle and lifts the material up to the clamping ring, which contains the sleeve and pin. Additional clamping is applied to the front and the back of the plate in the form of secured blocks. This prevents the coupon from rotating during the welding process. After the welds were made for the parameter matrix, the samples were polished down to a one micron diamond polish and then etched with Kellar's.

The parameter matrix in Figure 7 shows the results of the parameter development process. The sections marked no weld are the result of the machine retaining most of the material that was plasticized. This resulted in a large hole in the aluminum plate. This most certainly indicates unacceptable parameters. Early in the parameter investigation, parameters were explored below the range shown in the chart with a particularly bad result, current limits were triggered. This means that the force required to rotate the tools required an amount of current outside the operational range of the RFSW machine. The parameters expressed on the chart are the lowest within the operation range of the machine. This tells us that with bad welds at higher variable levels and force limits on the low end of the matrix, an optimized parameter should be within the matrix. Another consideration in the welding procedure is the surfacing. An addition welding step was added at the end of the welding process in order to give the best surfacing possible. This was kept constant as a 1 mm plunge, 1 sec total weld time, and 1400 rpm plunge. As a result, the material along the surface is returned to the 2024 aluminum plate and a nearly flush surface is achieved. This surfacing step will be discussed in further detail.

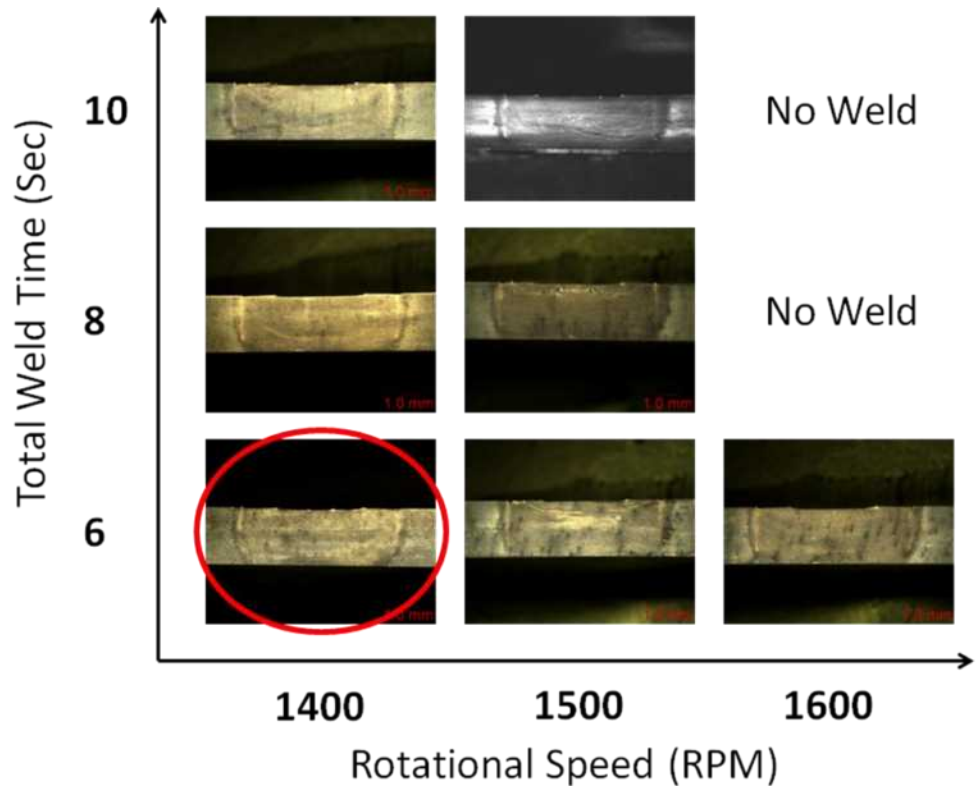


Figure 7: Developmental Matrix

Within the matrix, observations were made to show the best set of parameters. The criterion of a good weld involves observation of the formation of defects. In the 1500 rpm set of samples, a lack of mixing near the surface can be seen. In 1500 rpm sample, the six and eight second welds show voiding near the surface as a result of the lack of mixing. These features can very easily initiate fatigue cracks and thus are seen as un-acceptable welds. Another consideration is the mixing along the walls of the weld. A thin light colored line can be seen in all welds along the left and right sides of each weld. This feature is caused by the sleeve plunging into the plate. The 1400 rpm, 6 second sample shows the best mixing in the walls of the weld. Using these observations, it was decided that the 1400 rpm, 6 second weld, is the most optimized

parameter. Once again it is important to keep in mind that at variable levels below this yield no welds due to machine limits.

## **Surfacing and Penetration**

Beyond the variation of RPM and Time, there are two other major factors in showing a good weld from a fatigue standpoint: penetration and surfacing. When it comes to penetration, this machine is at its limit with 3.175 mm (0.125 inch) thick material. Luckily the area under the pin is stirred and a full depth plunge is not necessary. As a result, the plunge depth for all welds is 2.8 mm. As seen in the parameter matrix, all welds were stirred all the way to the bottom surface. This is important because the fatigue crack to be repaired extends through entire thickness of the plate. The other major factor left to discuss is surfacing. Right angles and indentations along the surface may be initiation sites for fatigue cracks, so the surface must be as flush as possible. This is accomplished by ensuring that there has been no volume loss from the fatigue cracking process, and by having a proper home position for the pin and sleeve. The volume loss is addressed by filling the pre-crack using a cold spray process. This process will be discussed in greater detail later. The home position is set by having the proper pin, sleeve, and clamping ring alignment. When the part is clamped, it is pressed upwards against the downward facing clamping ring. Within the clamping ring is the sleeve and pin. The bottom surface of these three components must be aligned when the tool is first installed into the machine. Further adjustments can be made after twenty conditioning welds using identical material. These conditioning welds fill the tool with aluminum, and prevent additional volume loss. Once the surface is as flush as possible the tool is ready to make repairs.

## **Stitch Welding**

A single weld will not repair the entire fatigue crack. In order to stir the entire length of the crack, single spot welds must be overlapped into what is referred to as a stitch weld. In the previous year's study it was found that tensile strength varies with varying overlaps. Using digital image correlation to illustrate stress distribution around each configuration of stitch weld and the hardness across each configuration, an optimized stitch weld was found. It was shown that overlapping 4 welds by 0.216 inches, centered about the center of the fatigue crack, would give the best properties. This study was a comparison of configurations with identical weld conditions so this study is used for this project as well.

## **Cold Spray**

Cold spray deposition will be used to fill the pre-crack that was created to grow the fatigue cracks. It is critical to make up for the volume loss, or else risk creating a fatigue initiation point along the surface. The cold spray process involves injecting a particle into a stream of gas and impacting the particle onto a substrate. The idea is that the particle needs enough energy to plasticize and bond with the surfacing. Energy is transferred from the gas to the particle as it accelerates within a nozzle. Generally the nozzle will involve converging and diverging chambers. The gas is also heated to allow for higher velocities. A cold spray deposition trial can be seen in Figure 8.



Figure 8: Cold Spray Deposition Trial with 2024 Al Powder (400 mesh)

Abdulaziz Alhulaifi is currently preparing a dissertation on the subject. With Abdulaziz's work we have a better understanding of the process. The critical velocity can be calculated using Equation 1. This equation is the result of the energy balance. Note that the melting point for the material, 2024 Al in this case, is reduced by 30%. This is because only 70% of the melting temperature is needed for plasticization. The  $C_p$  and  $T_m$  come from Al 2024 known properties. The  $T_i$  is the temperature of the gas. The gas is generally heat between 250°C and 450°C. The gas can be varied, but compressed air between 80psi and 140psi has been the gas of choice up to this point. Using this equation the critical velocity for the 2024 Al powder was found to be 590 m/s. Additionally, the size of the sprayed particle is crucial for achieving a deposit. The 2024 Al powder begins as 140 mesh, which means 105 microns is the largest size particle.

$$V_{critical} = \sqrt{C_p (0.7T_m - T_i)}$$

Equation 1: Critical Velocity

After attempting to spray the 105 micron size material, it was found that no particles were sticking to the substrate. The variables were explored in depth with no positive result. In order to overcome this, the powder was sieved to reduce the size of particle sprayed. 44 micron and 37 micron particles were sieved. The pressure of the compressed air was varied from 80 psi to 140 psi and the temperature of the gas from 250°C to 450°C with only minimal deposition. The pressure is limited by the range that the lab air compressor can operate in. The deposition occurred with the 37 micron particle at max pressure and temperature. Loss was very large as few particles actually deposited. The possibility of strain hardened particles was explored. First, a polished sample was examined for geometry. This can be seen in Figure 9 below. Clearly the Al powder particles are small spheres, most likely from being atomized. Meaning it is less likely that they are strain hardened. Second, a micro hardness test was needed. A sample was prepared in an epoxy mount. This sample was then tested for Vicker's hardness. After 20 points were tested it was found that the average hardness was about 125 on the Vicker's scale. This is within 10 of the known 2024 Al hardness value, thus it was confirmed that no strain hardening occurred. After consulting Abdulaziz, he calculated that the system was not reaching the critical velocity and adjustments would be needed.

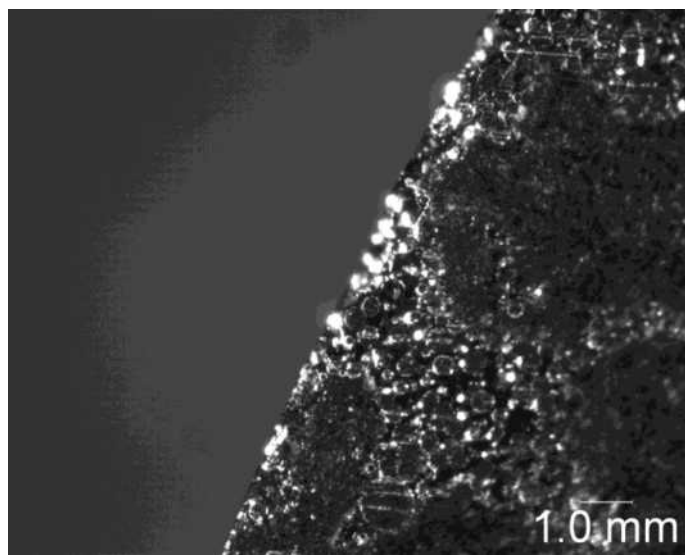


Figure 9: 2024 Al Powder in Bakelite at 2.5x

## RESULTS

The cold spray process has not yet yielded a deposition. As a result, the final repairs have not yet been made. The fatigue testing of the parent material has been complete and can be seen in Figure 10. These values form the basis of a comparison with repaired and unrepaired samples.

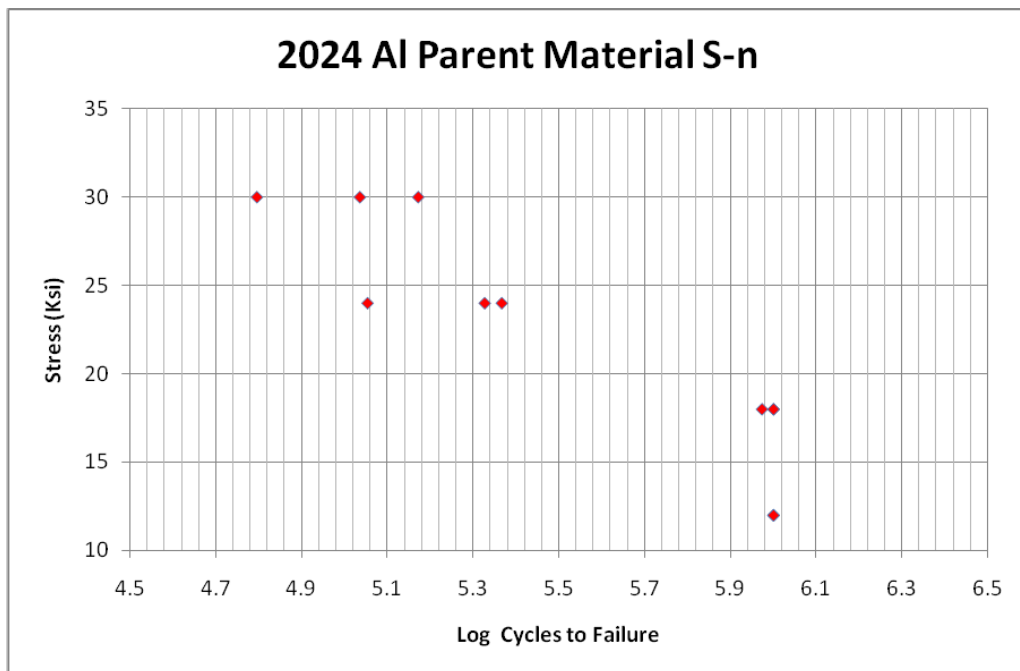


Figure 10: 2024 Al Parent Metal Fatigue Results

## CONCLUSION/DISCUSSION

### Future Work

Cold spray deposition and final repairs have yet to be completed. The cold spray deposition will require further investigation. In order to achieve this deposition, one of two methods will be used. One method involves depositing pure aluminum into the pre-crack. This method would involve a tertiary study on the effect of the pure aluminum addition on the properties of the resulting RFSW. If found the improve properties (tensile and fatigue), or if the properties remain unchanged, the method will be used for final repair. The second method for 2024 Al cold spray deposition involves further investigation into depositing the 2024 Al powder. Using the data from the previous attempts to deposit this material, we know that we must achieve a higher velocity. This may be achieved by one of several ways. First, the cold spray nozzle could be extended. This will give the particles more time to accelerate to the critical velocity. Another way this may be accomplished is simply by changing the distance from the end of the nozzle to the substrate from 13mm to 20mm. This may have a similar effect to the longer nozzle solution. Lastly, the gas used in the cold spray deposition process could be changed. Regardless of the gas chosen, the high pressure tanks that are delivered can provide much higher pressure than 140 psi. This may allow us to achieve double the pressure previously used. The gas may also be varied. Helium, and possibly nitrogen, may be used to propel the aluminum particles as well. The density of the helium gas may allow for higher impact velocities. The nitrogen gas will behave in a similar manner to the compressed air, but serve as a higher pressure source. Once the cold spray deposition process is finalized, final repair and testing can begin.

## **REFERENCES**

Russel, SG. 2001. Static, Fatigue and Crack Growth Behavior of FSW 7075 T-6 and 2024 T-3 Aluminum Alloys. TMS Friction Stir Welding and Processing, Vol. 1, Pg 93

Oberembt, Clark. 2008 Effects of Process and Parameters on Joint Properties of Refill Friction Stir Spot Welded Magnesium-Aluminum Alloy. SDSMT Thesis.

Alhulaifi, Abdulaziz. 2009. Cold Spray Modeling for Spraying Nano Particle Powders. SDSMT Research Proposal.

Uematsu and Tokaji. 2008. Effect of Re-filling Probe Hole on Tensile Failure and Fatigue Behaviour of Friction stir Spot Welded Joints in Al–Mg–Si Alloy. International Journal of Fatigue, Vol. 10-11, Pg 1956-1966.

Uemetsu, 2009. Comparison of Fatigue and Tensile Behaviour Between Resistance Spot Welds and Friction Spot Welds. Science and Technology of Welding and Joining. Vol 14, Pg 62.

Referenced ASTM Standards:

ASTM E647- Measuring Fatigue Cracks

ASTM E466- Fatigue Test Practices

ASTM E468- Reporting Fatigue Test Results



## Fatigue Life Prediction of Repaired Welded Structures

J. T. P. Castro, J. L. F. Freire

Mechanical Engineering Department, Catholic University of Rio de Janeiro, Rio de Janeiro 22453-900, Brazil

&

R. D. Vieira

Mechanical Engineering Department, CEFET-RJ and StrainLab Stress Analysis, Rio de Janeiro 22461-900, Brazil

### *ABSTRACT*

*This paper discusses the fatigue life prediction of welded structures which had cracked in service and were repaired by welding reinforcing plates over the cracked sections. The maximum working stress histories under actual loading conditions were measured and the fatigue lives of the welded repairs were predicted using international design codes. These damage evaluations were compared with the actual numbers of cycles to failure obtained in industrial operation.*

### 1 INTRODUCTION

This paper discusses the fatigue life prediction of three repaired welded steel traveling cranes which are used for ingot manipulation in a steel slab rolling mill. Each crane is composed of two parallel all-welded bridges which have box girder shapes and support a traveling trolley. The two bridges have 30 m spans and are connected at their end sides by head girders which are supported on wheels and rails. All 12 end sides of the three traveling cranes developed fatigue cracks in the transition regions which connect the bridges to the head girders, after six years of normal operation, and were repaired by welding reinforcing plates directly over the cracked regions (Fig. 1).

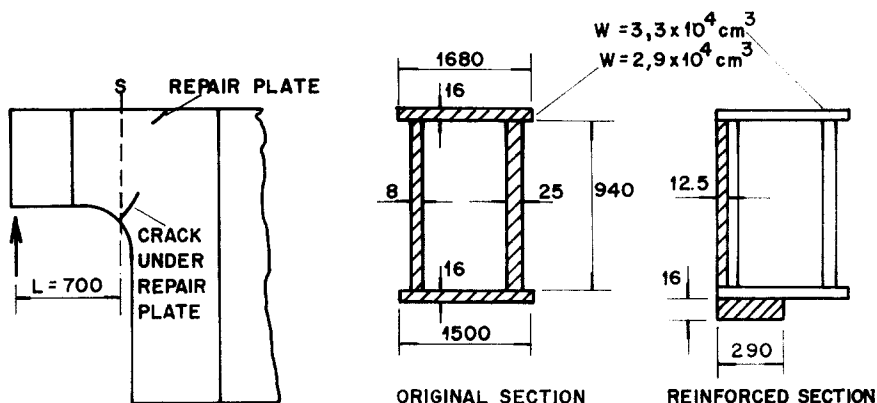


**Fig. 1.** The reinforcing plates and the cross-sections before and after repairing.

To predict the fatigue life of these welded repairs, working stresses were measured under normal operation and fatigue damage was calculated using several welded structures design codes (IIW,<sup>1</sup> ECCS,<sup>2</sup> AWS,<sup>3</sup> BSI,<sup>4</sup> AISC,<sup>5</sup> NBR<sup>6</sup>). The following sections report the stress measurement results, the fatigue damage calculations, and the evaluation of the reliability of these calculations using data from failures which occurred under normal operation.

## 2 STRESS ANALYSIS

Two elementary models were used to estimate the nominal stress in the structure critical sections. The first model considered the structure as a simple supported beam. The second model used a finite element commercial package. The transition region connecting the bridge to the head girder was modeled by 2D six-node elements. This simple model showed that the stress concentration at the critical sites was larger than 2·0.

The two models were used to indicate the levels of stresses which should be measured in a static experimental stress analysis. Combined with the cracks which appeared in the original cranes, these two models have also shown the best locations for the strain gages in the critical region of the repaired structure.

One of the repaired cranes was instrumented using welded uniaxial (U) strain gages, bonded triaxial rosettes (R) and also reflective photoelastic coatings, as shown in Fig. 2.

The experimental stress measurements were made in two steps. In the first, a quasi-static incremental loading was applied to the crane by lifting ingots of known weights and slowly moving the traveling trolley from one

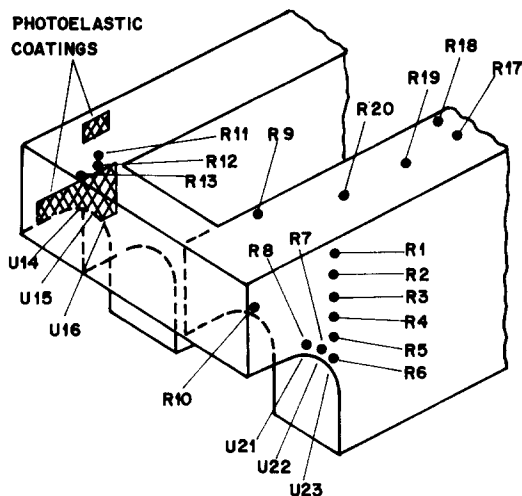


Fig. 2. Location of the uniaxial strain gages (U), rosettes (R) and photoelastic coatings.

bridge end to the other. It was concluded that the maximum static stress was 3.7 times the nominal stress calculated using the simple-supported beam theory and it occurred in the reinforcing repair plate at the same location where cracks have initiated in the non-reinforced structure. This position coincides with the location of the strain gage U23 shown in Fig. 2.

The second experimental step involved the dynamic strain measurements of the most loaded strain gages while the traveling crane was operated in its actual production service. The measured dynamic signals were recorded in a FM tape recorder and correlated with each kind of service executed by the traveling crane. A typical loading history is presented in Fig. 3. This strain history represents the actual variations of the stress ranges ( $\Delta\sigma$ ) which occur in the most loaded point of the structure. It already includes the stress concentration due to the structure geometry (transition region), but does not take into account the geometric imperfections due to the welding details. These imperfections, together with other strength reduction factors, are conveniently considered by the design codes.

### 3 THE FATIGUE DAMAGE EVALUATION

Fatigue damage was evaluated using five design codes,<sup>1-5</sup> a S-N Wohler Gerber procedure<sup>7</sup> and the Brazilian NBR 8400<sup>6</sup> standard for hoisting structures. The principal difference among these damage evaluation procedures is that the first five consider that fatigue damage is only dependent

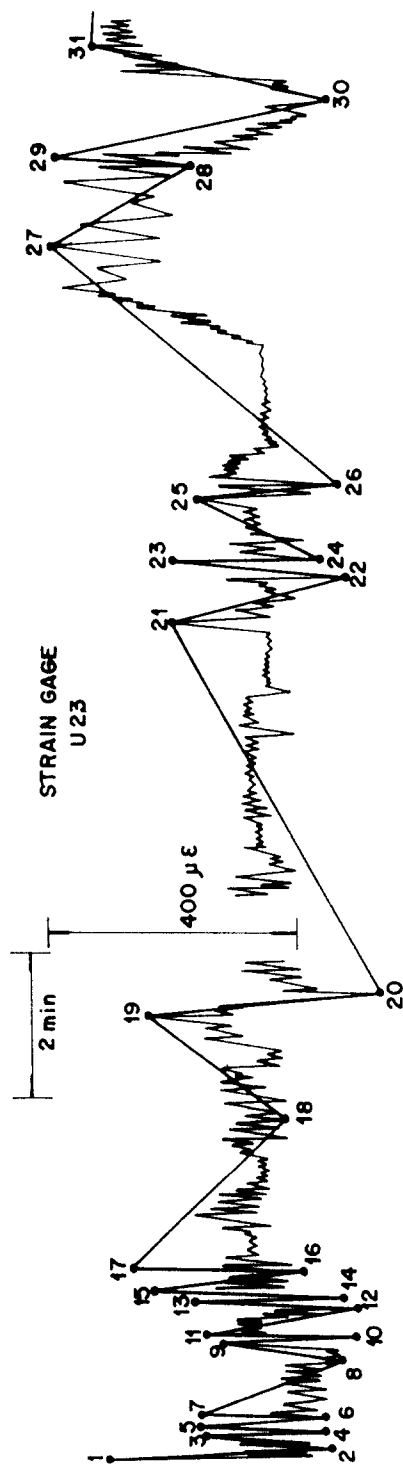


Fig. 3. Typical strain-loading history.

on the stress range. The last two procedures also include the mean stresses as variables which influence the fatigue damage.

For complex loading histories such as the one presented in Fig. 3, all design codes and methods are unanimous in proposing the use of the Palmgren-Miner linear cumulative damage rule.<sup>7</sup>

Cycle counting was carried out by applying the rain-flow<sup>8,9</sup> counting procedure to the typical loading history presented in Fig. 3. To avoid the inclusion of small load excursions that do not cause fatigue damage, the load history was filtered by using the race-track<sup>8</sup> method with an amplitude high-pass filter fixed in  $\Delta\sigma = 38 \text{ MPa}$ .

This value is the fatigue limit of the IIW class 50 welding detail. This means that any value of  $\Delta\sigma$  smaller than 38 MPa will not cause any fatigue damage on welded joints of this class (or higher class). Use of this limit assumes that no crack has already been developed. In Fig. 3, the filtered history is presented by a gross continuous trace with numbers identifying each peak that was considered for the rain-flow counting procedure.

Table 1 resumes the fatigue damage evaluation which was determined using the IIW design methodology. The procedures carried out for the

**TABLE 1**  
Lives  $N_i$  Corresponding to Each Measured Stress Range (in  $10^4$  Cycles) for the IIW Welding Detail Classes 50 to 100

$\Delta\sigma_i$ (MPa)	No. $n_i/2$ of half-cycles	Life $N_i$ for the welding classes:						
		50	56	63	71	80	90	100
38	6	523						
39	2	478						
41	2	401						
43	6	339	504					
45	2	290	430					
48	2	321	343	518				
50	2	200	298	449				
53	2	163	243	366				
68	2	68	101	153	233	353		
69	1	65	96	145	221	336	506	
84	1	33	48	73	111	169	254	368
88	1	28	41	62	94	143	216	313
103	1	16	24	36	54	83	124	180
Damage caused by the event ( $\times 10^{-6}$ )		12.5	7.69	4.53	2.56	1.68	0.93	0.57
No. of similar events allowed ( $\times 10^5$ )		0.80	1.30	2.18	3.90	5.96	10.7	17.4

other methodology<sup>2-7</sup> are quite similar and only their final results will be reported in Table 2.

Table 1 presents the lives  $N_i$  corresponding to each measured stress range  $\Delta\sigma_i$  and to each welding class detail strength of the IIW design methodology. Its first column lists the measured stress ranges and the second lists the number of half-cycles each stress range acted in the piece, as counted by the rain-flow method in the filtered history of Fig. 3.

Columns 3-9 list the fatigue lives (considering a 97.3% reliability) the structure would have if it was loaded only by the corresponding  $\Delta\sigma_i$ , for each class of welding detail proposed by the IIW. The blank spaces mean that the stress range does not cause any damage to the structure, because it is below the fatigue limit of that particular welding detail.

The penultimate line of Table 1 lists the fatigue damage that each measured event would cause in welding details from class 50 to class 100. These damage values were obtained by the application of the Miner's rule, i.e.  $\sum n_i/N_i = 1$ .

Finally, the last line presents the total lives expected for each welding detail class, in number of 'typical loading history' events.

For example, the damage that the Fig. 3 loading history would cause in a class 50 details is  $12.5 \times 10^{-6}$ . Therefore, fatigue failure of a IIW class 50 detail would be expected before 80 000 'typical load history' events in only 2.7% of the cases (the IIW fatigue strength curves are specified for a 97.3% reliability).

To close the fatigue analysis, it is necessary to classify the welded repair in one of the IIW classes. Inspection of the weld fillets in the field revealed

TABLE 2

Comparison Between the Various Prediction Methods. Predicted Fatigue Life in  $10^3$  'Typical Load Events' (about 110 000 'typical load events' per year)

Method	Original structure		Repaired structure	
	Joint class	Predicted life	Joint class	Predicted life
IIW	80 or 100	342 or 800	63 or 71	218 or 390
ECCS	80 or 90	252 or 361	64 or 72	187 or 268
AWS	B	356	D or C	60 or 227
BS5400	E or D	257 or 376	F or F	161 or 237
AISC	B-3	500 or 2000	E-3	100 or 500
Gerber				150
NBR			Group 6, K-3	200

many imperfections such as cold spots, overlaps and undercuts. Moreover, the (unremoved) original plate worked as a backing bar. Therefore, it was decided to classify the joint as belonging to a low class, the 71 or the 63. For those classes, the repairs' expected fatigue lives were, respectively, 390 000 and 218 000 'typical loading history' events. As each crane repeats this loading history 110 000 times per year, the 97·3% expected life of the welded repairs would range from two to four years.

The validity of the above predictions depends on the success achieved on the determination of the strain-loading history for the critical point as well as on the actual strength of the welding details.

A possible source of information to support the above analysis is to apply the loading history of Fig. 3 to the original structures which had all their critical points cracked after six years of operation. Figure 2 shows that the repaired critical section had its inertia increased by approximately 15%. Considering that the operational conditions of the traveling crane did not change throughout the years, the typical loading history, presented in Fig. 3, could be increased by a factor of 1·15 and be used to calculate the fatigue damage of the original structures. A new race-track-rain-flow calculation was carried out for this modified loading history and compared to the original structure weld class detail. In this case, the class detail was upgraded because all the original weldings were carried out under good fabrication and inspection conditions. Life predictions for the original structures resulted in 342 000 and 800 000 events, respectively, for the 80 and 100 weld class details, which means three to seven years of service operation. These predictions are compatible with the actual service lifes which did not exceed six years.

The fatigue lives calculated for the original and the repaired crane structures using the IIW design procedure are presented in Table 2 together with the predictions calculated using other design procedures. It can be seen that life predictions indicate fatigue failures for the repaired cranes from approximately one to three years in most cases. Care should be taken when comparing the lives predicted in Table 2, since the reliabilities embedded in the different methods are not equal.

A final verification of the fatigue damage evaluations presented in Table 2 for the repaired structures uses a recent information that one of the 12 repairs has cracked after one year in service. This first to fail welded repair specimen has a 5·61% median rank.<sup>7</sup> Considering a normal failure distribution and a standard deviation of 15%,<sup>10</sup> the mean life expected for the 12 repairs is 144 000 events. The 2·7% failure life (which considers a 97·3% reliability) is calculated to be equal to 93 000 events. It

can be seen that those numbers are compatible with the fatigue lives predicted in Table 2 for the repaired structures.

#### 4 CONCLUSIONS

The transition regions between the bridge and the head girders of three traveling cranes presented cracks after six years of normal operation. These critical sections were repaired by welding reinforcing plates over the original cracked plates. The present paper showed that it is possible to predict the expected life of the repaired structures by determining the working stresses in the critical regions using experimental methods, and by comparing the race-track filtered and rain-flow counted load history with the fatigue strengths for weld details presented by several design codes or methodologies.

It was concluded that all methodologies indicated that the expected repair lives would range from one to three years. This period of time is smaller than the lives achieved by the original structures. Although the reinforcement plates reduced the working stresses by 15%, the procedure used to weld the repairs lowered the strength of the weld details in larger proportions.

The methodologies used in the life predictions had their accuracy satisfactorily evaluated by their application to the field data generated by the previously fatigue damaged structures. The first crack which appeared in the repaired structure after one year of normal operation also confirmed the accuracy of those predictions.

#### ACKNOWLEDGMENTS

The Secretaria de Ciéncia e Tecnologia of the Brazilian Government and StrainLab Stress Analysis Ltd, of Rio de Janeiro, Brazil partially financed this work. Eng. Alvaro Pio from Cia. Siderúrgica Tubarão kindly provided the field support for the measurements.

#### REFERENCES

1. IIW 693-81: Design recommendations for cyclic loaded steel structures. *Welding in the World*, 7/8 (1982).
2. ECCS, *Fatigue Design Rules*, European Convention of Constructional Steel-work, Nov. 1983.

3. AWS D1.1, Structural welding code, 1981.
4. BS 5400, Steel concrete and composite bridges code, 1980.
5. AISC, Specification for the design, fabrication and erection of structural steel for buildings, 1978.
6. NBR 8400, Cálculo de Equipamentos para Levantamento e Movimentação de Cargas. Associação Brasileira de Normas Técnicas, Rio de Janeiro, 1984.
7. Shigley, J. E. & Mischke, C. R., *Mechanical Engineering Design* (5th edn). McGraw Hill, New York, 1989.
8. Rice, R. C., *SAE Fatigue Design Handbook*. Society of Automobilistic Engineers, Warrendale, PA, 1988.
9. Dowling, N. E., Fatigue life prediction for complex load versus time histories. *J. Eng. Mater. & Technol.*, **105** (1983) 206–14.
10. Mischke, C. R., Prediction of stochastic endurance strength. *J. Vibration, Acoustics, Stress and Reliability in Design*, **109** (1987) 113–22.



# Application of short repairs for fatigue life extension

J.E. Rodriguez-Sanchez <sup>a,\*</sup>, W.D. Dover <sup>b</sup>, F.P. Brennan <sup>b</sup>

<sup>a</sup> Instituto Mexicano del Petroleo, Eje Central Lazaro Cardenas 152, Edificio SIPE, No. 28, Piso 1, Cubiculo 105, 07730 Mexico D.F., Mexico

<sup>b</sup> University College London, Department of Mechanical Engineering, Torrington Place, London WC1 7JE, UK

Received 15 March 2002; received in revised form 22 April 2003; accepted 18 July 2003

## Abstract

The application of a new fatigue crack repair concept defined as ‘short repair’ is presented. This concept is based on crack removal by cutting. The objective of using a short repair is to extend the fatigue life of cracked welded connections. A short repair is an option to repair fatigue cracks, particularly for offshore structures where diving intervention is of high risk and the application of remote operated vehicles is an alternative.

Short repairs were machined on welded T-butt plates by disc cutting. Experimental data have been analysed to determine crack growth rates, crack initiation and fatigue life extension after crack repair. Conclusions and recommendations are given.

© 2003 Elsevier Ltd. All rights reserved.

**Keywords:** Fatigue; Repair; Crack

## 1. Introduction

Fatigue cracks in offshore structures are originated by the effect of wave forces acting on the structure. Fatigue cracks occur at the welded connections where structural members join. A structural member can disconnect from a joint as cracks propagate through the member thickness. This situation reduces the load capacity of the structure leading to a loss of safety and even a collapse.

Fatigue crack repairs are of high relevance to maintain the integrity of offshore structures. Fatigue crack repair options depend on the crack growth extension; in early stages of growth, grinding is applicable to remove cracks. For the cases when cracks have propagated through the thickness disconnecting one or more members of a joint, a mechanical or grouted clamp is applicable to reinstall the load transmission between members. Inspection of offshore structures for fatigue crack detection in early stages of growth can reduce the cost and effectiveness of a repair since a grind repair can be used instead of a clamp.

Fatigue crack grind repair has been investigated for about 20 years, demonstrating that grinding is a feasible

option for the repair of fatigue cracks. In this research, the grind repair profiles used have shown that if cracks reinitiate, this occurs in the bottom of the repair groove. Thus, fatigue life after repair relies on the remaining member thickness through which the crack propagates. On the other hand, short repairs have a depth/length ratio that if cracks reinitiate after being removed, this occurs out of the groove at the repair ends. Thus, cracks that reinitiate have the intact plate thickness for propagation. Additionally, short repairs facilitate subsequent inspection activities since inspection on a surface has a higher probability of detection compared with the inspection of a narrow groove in underwater conditions.

The short repair concept is based on two robust studies. First, the stress concentration gradient was studied using finite elements theory on three-dimensional models. It was found that for short repairs the maximum stress concentration is a function of the radius and depth of the repair, and is always located at the repair longitudinal ends, out of the repair groove. Thus, if cracks reinitiate, these always occur at these points [4], see Fig. 1. A fracture mechanics analysis of crack shape development under pure bending fatigue loading using stress intensity factors calibrations was undertaken by Scott and Thorpe [5]. Their calculated results are in accordance with the experimental crack shape development for short repairs described in this paper.

\* Corresponding author. Tel.: +52-55-3003-7266; fax: +52-55-3003-7255.

E-mail address: ersanche@imp.mx (J.E. Rodriguez-Sanchez).

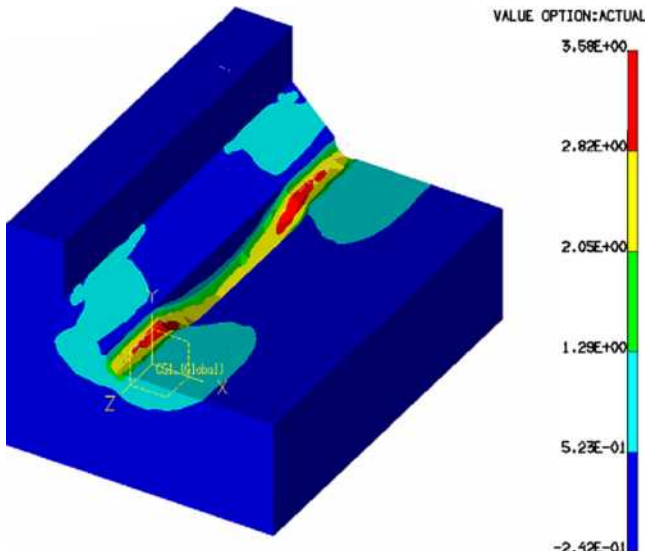


Fig. 1. Stress concentrations at the repair ends determined by 3-D finite element analysis.

Second, research on crack shape evolution was made; this work showed that crack shape ratio is definitive to determine if a crack propagates in depth or in length. This concept was taken to design a repair profile with a shape factor such that if cracks reinitiate, the repair shape first induces a repair extension in length rather than in depth. This is a different approach to explain why cracks reinitiate at the repair ends in short repairs. A comprehensive study of crack shape development under the bending loading of surface defects for the design of short crack repairs is presented in [6].

## 2. T-butt-welded specimens

Experimentation on T-butt-welded plate specimens has been used extensively to explain fatigue behaviour of more complex welded structures. The specimens used for the experimental work here are T-butt-welded plate connections in the as-welded condition and T-butts with short repairs machined. Although, particular stress distributions found in tubular connections (geometric stresses) are not reproduced when testing T-butt specimens, extrapolation of the results to tubular welded connections is possible.

### 2.1. Specimens design

T-butts under a uniform cyclic distribution of nominal stress develop edge cracks along the weld toe in most of the cases. Edge cracks are not the interest of this study since cracks on offshore tubular joints are normally surface cracks. Increasing the weld toe radius at both sides of a central as-welded weld toe region is a reliable procedure to obtain surface cracks on T-butts, whilst main-

taining a uniform distribution of nominal stress along the plate width. A uniform distribution of nominal stress along the plate width makes fracture mechanics calculations and extrapolation of the results easier. Tubular joint repair could well include crack removal and removal of adjacent weld toe regions to increase the weld toe radius. Additionally, the increase of the weld toe radius reduces the stress concentration factor at the repair ends. Thus, fatigue life is also increased where cracks reinitiate.

### 2.2. Dimensions

A 20-mm plate thickness was used for the T-butt-welded specimens, main and attachment plates were of the same thickness, specimen width was 300 mm. Fig. 2 shows the specimen dimensions.

### 2.3. Manufacture and material properties

Specimens were manufactured using steel which had to comply with the requirements defined in BS EN 10025 Grade S355J2G4 [1].

T-butt specimens were cut out in pairs from a T-butt-welded joint 400 mm wide × 700 mm long which had 50 mm from both longitudinal ends cut-off. The purpose was to eliminate the plate ends where defects accumulate due to poor fusion during welding. The attachment plate was bevelled to 45° for a full penetration weld.

## 3. Applied loading

It was considered convenient for the purposes of the research to test only under bending loading since it was identified that, for tubular joints, the stress field near the weld is predominantly bending, even under axial loading [2].

A four point bending set-up was used for testing. This set-up produces a constant moment distribution between

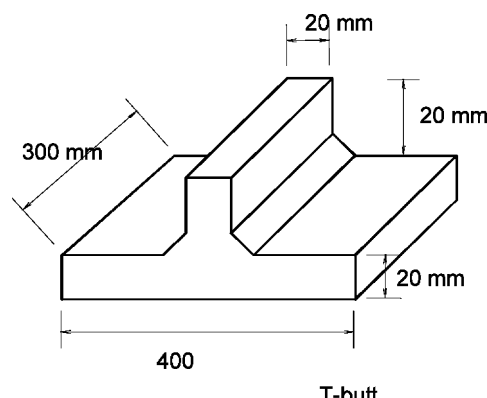


Fig. 2. T-butt specimen dimensions.

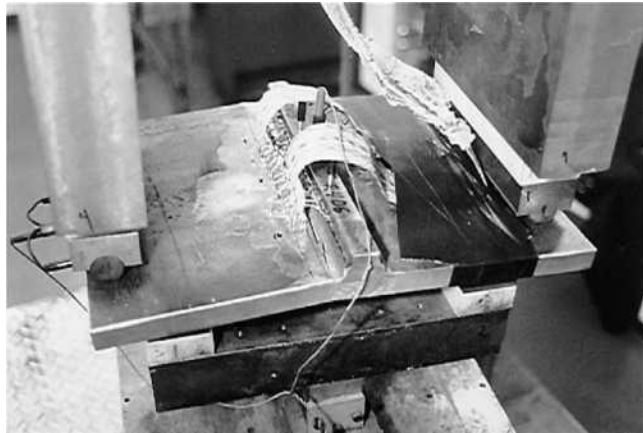


Fig. 3. Loading set-up and instrumentation of a T-butt specimen after failure.

the two internal loading points, see Fig. 3. All the tests were performed under load control, so even when the stiffness of the specimen changed the magnitude of the load cycle applied did not change.

### 3.1. Fatigue crack depth monitoring

Crack depth evolution was monitored from early stages of growth using the alternating current potential difference (ACPD) technique applied by a U-10 crack microgauge. The technique requires the injection of an alternating current on the surface of the specimen. The current follows the contour of surface-breaking defects, such as cracks, and since the potential gradient on the metal surface and on the crack faces is assumed to be linear, measurements of the potential difference across the crack and adjacent to the crack can be used for the calculation of the crack depth.

## 4. Fatigue test programme

Table 1 shows the fatigue tested specimens and relevant experimental parameters that will be introduced through the remainder of this section.

With the experience gained from previous experimentation, a comparison study was planned considering four T-butt specimens. The purpose was to quantify the fatigue life extension of repaired specimens against specimens in the as-welded condition. Thus, specimens 1 and 2 represented the case of as-welded condition. Prior to testing, these specimens had weld toes machined R4D0.5, except in a central 30 mm long region on one side of the specimen. This forced crack initiation at the centre of the specimen avoiding multiple initiation and then edge cracking. The average measured weld toe radius of the as-welded region was 0.8 mm. The repaired condition was represented by specimens 3 and 4; they had machined repairs prior to testing of dimensions R4D6L60 and R4D9L60, respectively. Repairs were made with a disc cutter. The weld toes were left in as-welded condition and the average measured weld toe radius was 0.8 mm. Dimensions and other experimental parameters are presented in Table 1. Results will be presented in Section 6.

It is clear that it would be preferable to determine the fatigue life extension on the same T-butt. In this work the as-welded and the repaired cases were represented by different T-butt specimens. Fatigue life extension was determined by addition of the number of cycles of the as-welded T-butt, when the crack reached the depth dimension of the repaired T-butt plus the fatigue life of the repaired specimen. Contribution from prior fatigue loading is not considered in the repaired specimens since repairs were carried out on as-welded condition. However, previous experimentation demonstrated that fatigue life extension determined from a single T-butt fatigue loaded in the as-welded condition and then repaired with increased weld toe radius regions adjacent to the repair reported approximately the same fatigue life extension as the approach presented here using two T-butts. Removal of weld defects at the weld toes adjacent to both sides of the repair, increasing the weld toe radius by cutting 0.5 mm deep with the same tool used for crack removal, extends the fatigue life since crack initiation is inhibited. This procedure was also used to inhibit fatigue cracking along the weld toe on the T-butt side where

Table 1  
Fatigue tested specimens and relevant experimental parameters

Specimen	Connection/Manufacture	T (mm)	W (mm)	Repair/Procedure	Nominal stress (MPa)	Life (million cycles)	Comments
1	T-butt/Automatic welding	20	300		300	0.195	AW, F, SC
2	T-butt/Automatic welding	20	300		250	0.21	AW, BF, SC
3	T-butt/Automatic welding	20	300	R4D6L60/DC	200	0.384	F, SC
4	T-butt/Automatic welding	20	300	R4D9L60/DC	200	0.2525	F, SC

R, repair radius; DC, disc cutter; AW, As-welded tested; D, repair depth; SC, surface crack; F, specimen tested until failure; L, repair length; BF, test stopped before failure.

neither as-welded nor repaired fatigue life was determined. As mentioned before, tubular joint repair could well include crack removal and removal of adjacent weld toe regions to increase the weld toe radius.

An advantage of this approach is that during experimentation the time spent on inspection after crack removal is not required. During the progress of the experimental work it was demonstrated that if a minimum length of the crack front is left after the crack removal, the effect of the repair is practically nil. This and future research will help to define an adequate depth allowance to ensure that the crack front is totally removed depending on the inspection technique used.

#### 4.1. Test stress levels

Experience obtained from previous experimentation suggested stress range levels for testing between 180 and 300 MPa, see Table 1. Since the determination of an S-N curve was not a concern, the stress levels for fatigue testing were kept as high as possible to shorten the testing time.

### 5. Fatigue crack repair

The objective pursued during the design of the ‘short repair’ profile was to ensure that the maximum stress concentration factor is located at the repair ends out of the repair groove; if cracks reinitiate after being removed, this occurs out of the groove at the repair ends thus, cracks that reinitiate again have the intact plate thickness for propagation.

During the experiments, three repair radii of 4, 8 and 12 mm were used and from the amount of weld cut when using radius 12 mm it is considered that in practice a review of the static load capacity of the member should be conducted prior to use of a cutting tool with radius equal or greater than 12 mm [3].

The longitudinal repair profile of the grooves machined on the specimens was always semicircular and the transverse repair profile varied from semicircular to U-shaped depending on the depth/radius ratio. A robust study based on finite element theory allowed determination of the optimum repair profile to be used and the stress concentration factor associated to a particular repair profile [3].

#### 5.1. Disc cutter machining

The repair profiles were cut using disc blade cutters driven by a numerically controlled machine. Fig. 4 shows disc cutters radii 4, 8 and 12 mm used during the study. It is obvious that this technique could not possibly be applied to a real underwater repair of a fatigue crack, but repair profiles obtained using this technique could



Fig. 4. Disc cutters used for machining repair profiles.

provide a good base line to evaluate novel applications of underwater machining, such as electrochemical machining technique (ECM) [4]. Dimensions of the repair profiles machined are shown in Table 1 and a disc cut repair D4R8L60 is shown in Fig. 5.

The use of disc blade cutters driven by a numerically controlled machine provided the opportunity of obtaining optimum quality repair profiles since it was possible to have: precise positioning of the repair in the specimen, good quality surface repair and total control of the longitudinal and transverse repair profile dimensions. The numerically controlled machine used is at University College London Mechanical Engineering Workshop.

### 6. Fatigue test results

#### 6.1. Crack growth curves

Crack growth curves relate the number of cycles to crack depth. For surface cracks the crack growth at the deepest section is usually presented. In some cases, for comparison purposes, the crack growth at the repair ends and in the bottom of the repair are presented together to illustrate how cracks develop in short repairs.



Fig. 5. Disc cut repair profile D4R8L60 on T-butt specimen.

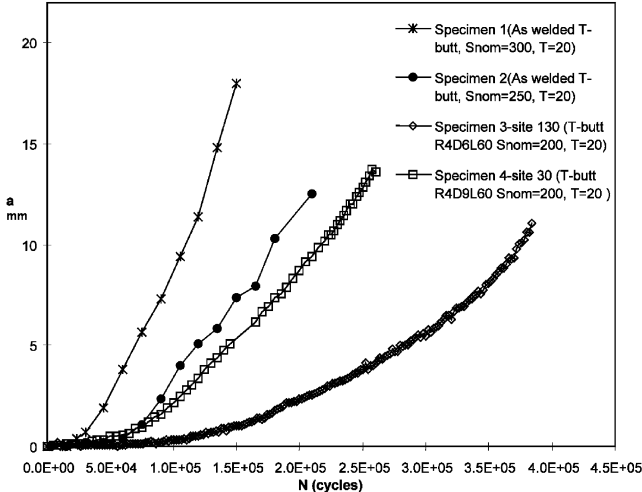


Fig. 6. Fatigue crack growth for T-butt specimens 1 to 4.

Fig. 6 shows the crack growth curves for specimens 1 to 4. The legend provides the test stress level and the specimen thickness. It can be observed that the fatigue life increases as the nominal stress level is reduced. Repaired specimens 3 and 4 were tested under the same stress level, but with different repair depths. Therefore, the stress concentration produced by the repair was reflected in the fatigue life. Results from a robust finite element study [4] showed that for repair profiles, increments of the stress concentration factor are associated to a combined effect of repair radius reduction and repair depth increment and vice versa. Specimen 3 with shallower repair R4D6L60 showed a longer fatigue life than specimen 4 with deeper repair R4D9L60. The crack growth curves presented in Fig. 6 for the repaired specimens correspond to crack initiation sites 30 for 4 and 130 for 3, which are located on the as-welded weld toes out of the repair groove, 20 mm from the repair ends, see Figs. 7 and 8.

Figs. 9 and 10 show crack growth at the repair ends outside the repair groove (sites 30, 130) and in the bottom of the groove (site 80) for specimens 3 and 4,

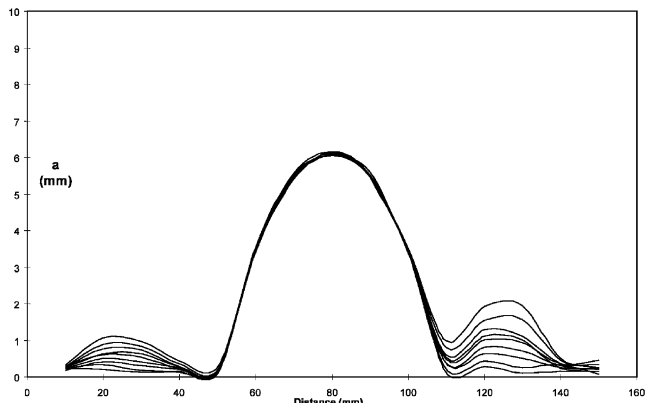
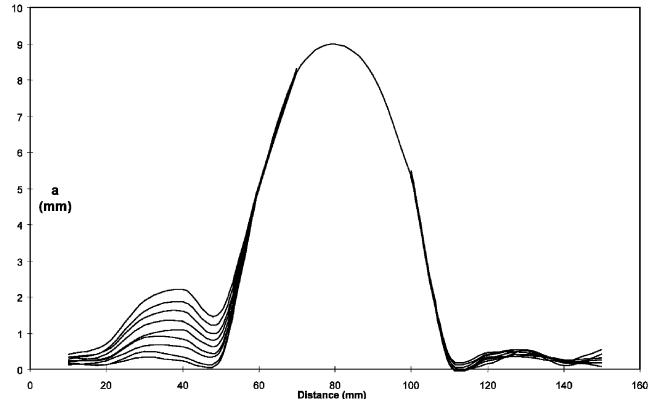
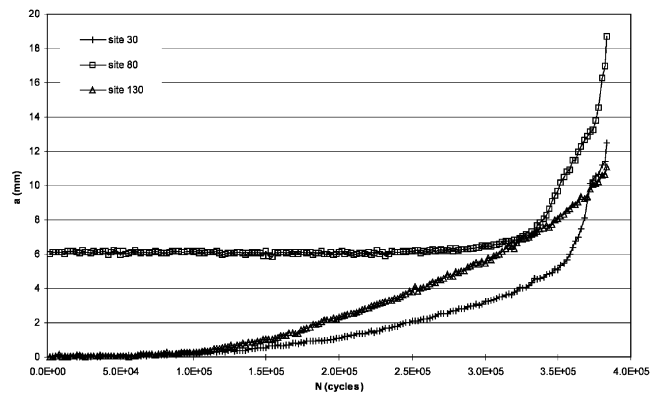
Fig. 7. Fatigue crack initiation for specimen 3 up to  $0.9 \times 10^5$  cycles.Fig. 8. Fatigue crack initiation for specimen 4 up to  $1.8 \times 10^5$  cycles.

Fig. 9. Fatigue crack growth at various sites for specimen 3.

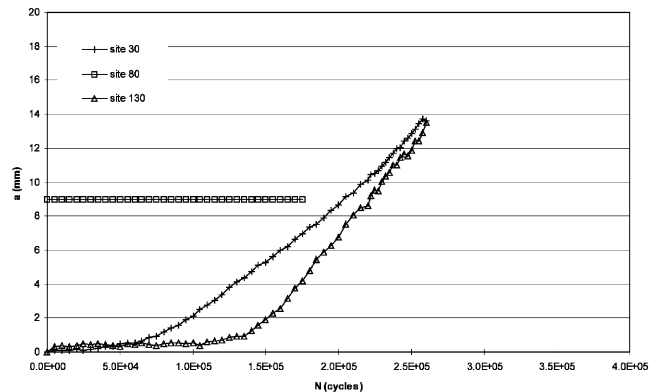


Fig. 10. Fatigue crack growth at various sites for specimen 4.

respectively. As noted here, cracks initiated at sites 30 and 130, but cracking had not initiated in the repair grooves at the number of cycles indicated. As Fig. 9 shows, cracks only initiated at site 80 after the crack at site 130 was approximately 5 mm deep, that is 1 mm before reaching the repair depth.

For specimen 3, crack initiation at site 80 started after the cracks that initiated at sites 30 and 130 had merged and continued growing as one crack; see crack growth

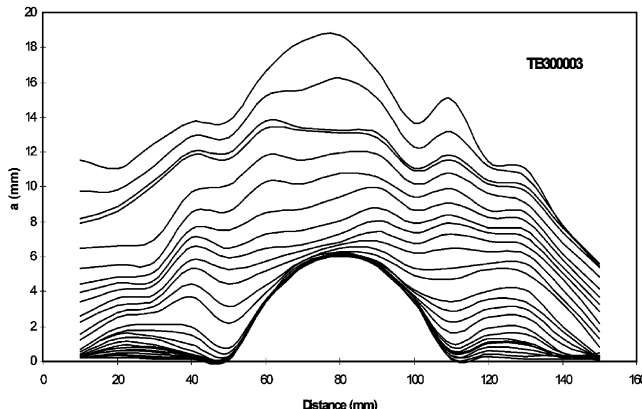


Fig. 11. Fatigue crack growth evolution for repaired specimen 3.

evolution in Fig. 11. Unfortunately, for specimen 4 it was not possible to determine crack growth in the repair groove region due to a high gain setting for the U10 crack microgauge, causing voltage overflow.

#### 6.2. Fatigue crack growth rates

Figs. 9 and 10 show that for a considerable period, crack growth rates are nil in the bottom of the repairs (sites 80) of specimens 3 and 4. This is due to the effect of short repairs that force the cracking pattern in the repaired region to grow from the repair ends on the surface, extending the repair first longitudinally and then in depth.

#### 6.3. Fatigue crack initiation

From the experimental results presented in Figs. 9 and 10 it can be observed that for the purposes of life extension it is more effective if crack initiation after repair is located outside the repair groove. This is because the new crack again has the total plate thickness for crack initiation and propagation. However, locating crack initiation outside the repair groove becomes increasingly less likely as the length of the repair increases. This is addressed when explaining crack shape development [4].

Considering 0.4 mm as the crack depth for determining initiation life the initiation to total fatigue life ratios for the specimens are presented in Table 2. Fig. 12

Table 2  
Fatigue initiation life to total fatigue life ratios

Specimen	Nominal stress MPa	Fatigue initiation life (Ni)	Total fatigue life (Nt)	Ni/Nt
1 (As-welded)	300	22 800	150 000	0.15
2 (As-welded) <sup>a</sup>	250	60 000	300 000	0.20
3 (R4D6L60)	200	112 000	383 700	0.29
4 (R4D9L60)	200	50 000	260 000	0.19

<sup>a</sup> Extrapolated total fatigue life.

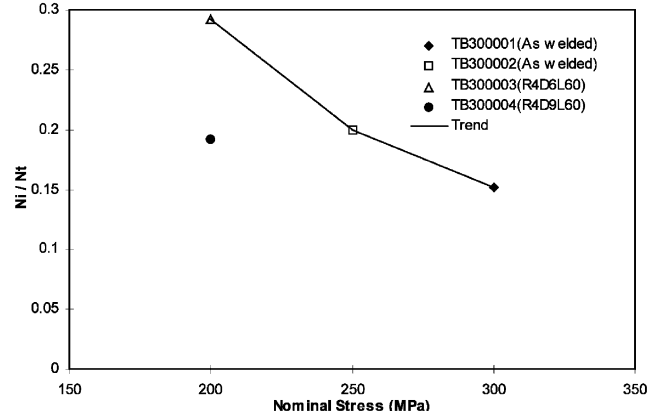


Fig. 12. Fatigue initiation to total fatigue life ratios for T-butt specimens 1 to 4.

shows the trend of initiation to total fatigue life ratio for the specimens. It can be observed that although specimens 3 and 4 were tested under the same stress level, the latter has a shorter initiation to total fatigue life ratio ( $Ni/Nt$ ) as a result of the high stress concentration produced by a deeper repair (R4D9L60) with respect to specimen 3 (R4D6L60). Therefore, specimen 4 is outside the trend defined considering as-welded specimens and it can be inferred that its initiation life is less than an as-welded specimen under the same stress. However, it is worth noting that the weld toes of specimen 4 were in as-welded condition. Thus, it is expected that  $Ni/Nt$  would increase substantially if the weld toes are machined.

#### 6.4. Fatigue life extension

Calculations of the fatigue life extension obtained after crack repairing are presented here. Calculation will be based on the approximate cubic relation between stress ranges and fatigue life, since different stress levels were used in as-welded and repaired conditions. The stress difference was due to specimens 1 and 2 which belonged to an extensive testing programme where higher stress levels were used.

To demonstrate the approximation of the cubic relation, a prediction of fatigue life for specimen 2 based on the fatigue life of specimen 1 is presented and then compared with the real data.

For  $a = 6$  mm, see Fig. 6.

Specimen	Stress range	$N \times 10^5$
1	300	0.8
2	250	1.4

From the cubic relation:  $(300/250)^3 = 1.73$ . Thus, the estimated fatigue life for specimen 2 at  $a = 6$  mm would

be:  $1.73 \times 0.8 \times 10^5 = 1.4 \times 10^5$  which is equal to the real data obtained from Fig. 6. This validation can be performed for various crack depths and close approximation to the real data would always be obtained.

Using the cubic relation verified above, prediction of fatigue life extension after repair is presented for specimens 3 and 4.

For a repair depth  $D = 6$  mm as in specimen 3, see Fig. 6.

Specimen	Stress range	$N \times 10^5$
1	300	0.8
3	200	3.1

From the cubic relation:  $(300/200)^3 = 3.38$ . Thus, the estimated fatigue life for specimen 3 at  $a = 6$  mm in as-welded condition would be:  $3.38 \times 0.8 \times 10^5 = 2.7 \times 10^5$ .

Thus, after repair the fatigue life extension obtained would be  $(2.7 + 3.1)/2.7 = 2.1$  times the as-welded fatigue life. The relation between repair depth and plate thickness is  $100 \times (6/20) = 30\%$ .

For a repair depth  $D = 9$  mm as in specimen 4, see Fig. 6.

Specimen	Stress range	$N \times 10^5$
2	250	1.7
4	200	2

From the cubic relation:  $(250/200)^3 = 1.95$ . Thus, the estimated fatigue life for specimen 4 at  $a = 9$  mm in as-welded condition would be:  $1.95 \times 1.7 \times 10^5 = 3.3 \times 10^5$ .

Thus, after repair the fatigue life extension obtained would be  $(3.3 + 2)/3.3 = 1.6$  times the as-welded fatigue life. For this case the relation between repair depth and plate thickness is  $(9/20) \times 100 = 45\%$ .

It can be deduced from the limited results presented that a 100% fatigue life extension can be obtained when repair depths are up to 30% of the plate thickness. However, results from other specimens showed that increasing the weld toe radius at the repair ends can still provide a fatigue life extension at least equal to the fatigue life in as-welded condition for repair depths up to 48% the plate thickness [4].

The results presented above are summarized in Table 3. These results are based on limited experimental data, thus an extensive validation is recommended for its application in the industry.

With regard to the effect of defect scatter associated with welding, which could lead to the assumption that

cracking can take place out of the region of the repair ends, this paper reports the findings of only two worked specimens welded automatically. However, other manually welded specimens were fatigue tested and showed crack initiation at the ends of shorts repairs. It is important to consider that the weld geometry influence on the stress distribution through the thickness under bending is up to 5% the plate thickness. Thus, after the repair is done the weld toe has been removed and the influence of the stress concentration induced by the repair geometry is much larger than the effect of the weld. This effect is increased when weld toes are machined at both sides of the repair using the same repair tool. Therefore, this practice is strongly recommended. The effect of weld defects is reduced substantially since increasing the weld toe radius by machining at both sides of the repair removes a large number of them. None of the fatigue-tested specimens (worked or not) showed crack initiation due to weld defects.

Due to the limited number of worked specimens, the fatigue testing scatter on the fatigue life extension after repair is not presented. However, for the manually welded specimens that were fatigue tested and showed crack initiation at the ends of the shorts repairs, its fatigue life extension was determined and showed that it was in the range of the worked specimens. Additionally, it can be considered that regardless of the scatter, if crack initiation after crack removal takes place on the plate surface at the repair ends as with the use of short repairs, the original plate thickness of the component is reinstalled and its fatigue life is greater than in the case when cracks initiate and are not prevented from continuing propagating through the plate thickness.

## 7. Conclusions

The application of short repairs has experimentally demonstrated that the fatigue life of cracked welded connections can be extended by a factor of two in many cases. The successfulness of fatigue life extension using short repairs depends mainly on two considerations:

- (a) The crack is totally removed before it extends further than 30% of the plate thickness;
- (b) The repair depth and length comply with a short repair profile to force crack initiation to take place at the repair ends.

The experimental results obtained also showed that the application of short repairs in some cases can provide extensions of fatigue life greater than a factor of two. This is more likely to occur when the cracks are repaired in early stages of growth and the weld toes at the repair ends are increased to remove weld defects.

Machining the repair ends can be undertaken easily

**Table 3**  
Fatigue life extension of crack repaired specimens

Specimen	Repair profile	Weld toes	Nominal stress (MPa)	Repair depth thickness ratio	Crack depth after repair (mm)	Fatigue life increment
3	R4D6L60	As-welded	200	30%	6	2.1
4	R4D9L60	As-welded	200	45%	9	1.6

by lengthening the cutting path of the same tool used to machine the short repair. For underwater conditions, this task appears especially suitable for the ECM technique.

In addition to the fatigue life extension, short repairs induce crack initiation outside the repair notch, so the total thickness for crack propagation is reinstated and easier access for inspection is provided.

## References

- [1] BS EN 10025:1993, Hot rolled products in weldable fine grain structural steels, British Standards Institution, 1993. (This specification supersedes the BS 4360:1990.)
- [2] United Kingdom Offshore Steels Research Project-Phase I, Final Report, OTH 88 282, Prepared by the Safety and Reliability Directorate for the Department of Energy, 1988.
- [3] Rodríguez JE, Brennan FP, Dover WD. Minimisation of stress concentration factors in fatigue crack repairs. *International Journal of Fatigue* 1998;20(10):719–25.
- [4] Rodríguez JE. Fatigue crack repair for offshore structures. PhD thesis, University College London, UK, 1999.
- [5] Scott PM, Thorpe TW. A critical review of crack tip stress intensity factors for semi-elliptic cracks. *Fatigue of Engineering Materials and Structures* 1981;4(4):291–309.
- [6] Rodríguez JE, Dover WD, Brennan FP. Design of crack removal profiles based on shape development of surface defects. In: Proceedings of OMAE 2003, 22nd International Conference on Offshore Mechanics and Arctic Engineering, OMAE 2003-37198. 2003.



## Considerations on corrosion and weld repair effects on the fatigue strength of a steel structure critical to the flight-safety

Marcelino P. Nascimento\*, Herman J.C. Voorwald

Department of Materials and Technology – State University of São Paulo, UNESP/FEG/DMT 333, Ariberto Pereira da Cunha Ave., 12516-410, Guaratinguetá City, São Paulo State, Brazil

### ARTICLE INFO

#### Article history:

Received 30 July 2009

Received in revised form 24 December 2009

Accepted 31 December 2009

Available online 7 January 2010

#### Keywords:

AISI 4130 steel

Fatigue behavior

Corrosion

Weld repairs

Flight-safety

### ABSTRACT

The aim of this study is to analyze the effects of corrosion and successive tungsten inert gas (TIG) welding repairs on the reverse bending fatigue strength of AISI 4130 steel used in components critical to the flight-safety. The tests were performed on hot-rolled steel plate specimens, 1.10 mm and 1.60 mm thick, by means of a SCHENK PWS equipment, with load ratio  $R = -1$ , constant amplitude, 30 Hz frequency and room temperature. It was observed that the reverse bending fatigue strength of AISI 4130 steel decreases due to the corrosion and the TIG welding and re-welding processes.

© 2010 Elsevier Ltd. All rights reserved.

### 1. Introduction

According to flight-safety foundation [1], “Aircraft accidents means an occurrence associated with the operation of an aircraft, which takes place between the time any person boards the aircraft with the intention of flight until such time as all such persons have disembarked, and in which any person suffers death or serious injury as a result of being in or upon the aircraft or by direct contact with the aircraft or anything attached thereto, or in which the aircraft received substantial damage (damage or structural failure that adversely affects the structural strength, performance, or flight characteristics of the aircraft, and which would normally require major repair or replacement of the affected component)”. Based in such definition, the accident rates (i.e., accidents per million departures) have been at 1.2, or 12,000 accidents, in the occidental world [2]. In the search for a zero accident rates, the flight-safety has been the main concern of the aeronautical authorities all over the world.

Basically, the aeronautical projects should take into account the difficulties of transporting a load against the gravity force during take-off and flight, and discharge it in an efficient way, with minimum cost and maximum safety, because failures in any of these stages will implicate catastrophic accidents, involving human lives [3]. In general, structural failures during flight are attributed to

aerodynamic overloads or fatigue of materials, as a consequence of inadequate project or any notch produced during manufacturing or maintenance of aircrafts [4–7]. Since the catastrophic accidents involving the English model “Comet” in the 1950’s, the fatigue process has been the most important project and operational consideration for both civil and military aircrafts [4,5,8]. On the other hand, many fractures of materials are also caused by corrosion as a consequence of aggressive environment.

Since the aircrafts become more complex, the environmental effects assumed great importance. As a result of older aircrafts flying nowadays, problems such as stress-corrosion cracking, corrosion-fatigue (simultaneously or separately) and wear are also expected to occur [4,5,9,10]. Due to several aggressive environments in which the aircrafts are subjected, particularly marine, corrosion is the most important factor of maintenance and inspection for the aeronautic sector [4,5,9,10]. Hence, corrosion is undoubtedly a real and critic issue acting on aircrafts, flowing with the time even on those not operational. Usually, the corrosion control is accomplished by adoption of prevention methods with high-quality periodic inspections associated to damage tolerance philosophy, for taking into account its effect on the fatigue life of a structural component [4,5,10–12]. Such issues will request extensive investment, planning, researches and development on repair methods and maintenance procedures towards assure the safe and continued airworthiness.

For several aircraft models (e.g. agricultural, military training and acrobatic) the most solicited and repaired component is one that supports the motor, called “Motor-Cradle” (Fig. 1) [13]. This

\* Corresponding author. Tel.: +55 12 3123 2865; fax: +55 12 3123 2852.

E-mail addresses: [pereira@feg.unesp.br](mailto:pereira@feg.unesp.br), [marcelino.nascimento@gmail.com](mailto:marcelino.nascimento@gmail.com) (M.P. Nascimento), [voorwald@feg.unesp.br](mailto:voorwald@feg.unesp.br) (H.J.C. Voorwald).

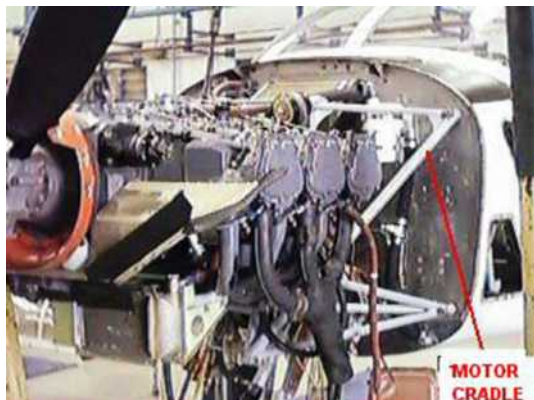


**Fig. 1.** Motor-cradle assembly in a T-25 Universal Brazilian aircraft.

component presents a geometrically complex structure made from AISI 4130 tubular steel of different dimensions and TIG welded in several angles [13,14]. For the Brazilian aircrafts T-25 Universal and T-27 Tucano, for example, besides supporting the motor in balance, the motor-cradle also maintains the nose landing gear fixed at the other extremity. Since the motor-cradle is a component critical to the flight-safety, the aeronautic standards are extremely rigorous in its manufacturing, by imposing a “zero-defect index” on the final weld seam quality (Safe-Life philosophy), which is 100% inspected by non-destructive testing/NDT [13–15]. For this reason, welded aeronautic structures are frequently subjected to successive repairs in accomplishment to current standards. As a consequence, components approved by NDT may contain a historic record of welding repairs whose effects on their structural integrity are not computed. In addition, these structures are also submitted to weld repairs along their operational life, turning this question more complex.

As a part of this research-work, an investigation on 157 motor-cradles fracture reports indicates that all of them occurred at welded joints as a result of fatigue cracks, reducing the “Time-Before-Fail” from 4.000 h to 50 h of flight [13]. Motivated by high fracture incidence of this particular component, an extensive research program to evaluate the manufacturing and maintenance weld repair effects on the structural integrity, mechanical properties and microstructural changes has been conducted [13].

Although the maintenance repairs of parts and components are a multibillion-dollar industry [16] and that, particularly for the transport sector, the welding repairs are an essential and frequently used process [17], few papers approaching this issue have been published, being all of them on either aged and degenerated materials [18,19] in petrochemical, offshore and power industries [20], by means of finite element method – FEM - [21–23].

In this paper, special emphasis was attributed to a standardized weld repair procedure, widely employed during manufacture of welded aeronautic structures and characterized by removing the previously defective weld bead and by applying a new weld seam by means of the gas tungsten arc welding/GTAW (or tungsten inert gas/TIG) process with filler metal.

The aim of this study is to analyze the effect of the corrosive process and the successive TIG welding repairs on the reverse bending fatigue strength of AISI 4130 steel specimens made from hot-rolled steel plates, 1.60 mm and 1.10 mm thick, respectively. Analyses of microstructure, microhardness and residual stresses from the base-material (BM), heat-affected zone (HAZ) and weld metal (WM), as well as the effects of the surface roughness and weld bead geometry complemented this study.

In the sequence, a brief comment on the current weld repair procedures is presented.

### 1.1. Current Welding Repair Procedure and Applications

When defects (such as porosity, impurity, undercut) are found in the welding joints, the main international standards (e.g. API, AWS, BSI and ASME) request that the defective welded joints are corrected. However, in a general form, none of the above standards make mention to number of permissible repairs.

In general, repair welding usually involves the complete shut-down of the equipment, the removal of all dead loads and the carrying out welding to original manufacturing standards [24]. Two typical procedures of weld repairs, complete repair and partial repair, include mechanics removal of the damaged material and the restoration of the geometry and integrity of the component, followed for a post-welding heat treatment (PWHT), which will depend mainly on type and thickness of material [21]. PWHT has as a function to reduce or eliminate residual stresses and to temper the metallurgical structure of heat-affected zone (HAZ). However, PWHT is very expensive, time consuming and, depending on local, difficult or impracticable.

An important application of weld repair techniques is to avoid PWHT, generating HAZ with structures of fine grains [24]. Such an objective can be reached by minimizing the size of original grain in HAZ, by minimizing the thermal contribution during the welding process or by refining the size of the initial coarse-grain region of HAZ [24]. For this purpose, two welding repair techniques are employed, viz:

- i. Half-bead welding (HBW): the beads are removed before welding the next layer.
- ii. Temper-bead welding (TBW): the subsequent weld bead partially does heat-treat the previous passes, after that the deposited weld layer is removed.

Both techniques involve removal of the upper passes and they are employed to avoid PWHT, to reduce or eliminate residual stresses, to avoid hydrogen cracking, to improve fracture toughness and to reduce welding cost and time [24].

For the aeronautic sector, in accordance with IIS/IW – 956-87 Doc [25], when repairing a weld seam in critical aeronautic components is requested that the defect is also located and removed. The removal process should be always carried out from the side that propitiates the smallest weld material loss. Soon after, to maintain the uniformity of the deposited metal along the weld seam, the repair is applied [25].

However, the weld bead removal can be uneconomical, impracticable or even impossible in certain engineering applications due to urgency or emergency, difficult access to the component or appropriate equipments. As a consequence, along the useful life of the aircraft many non-standardized weld repairs are carried out by putting upon several weld bead, without removal of the previous pass. The subject to be answered up is whether or not the weld repairs are a viable and effective procedure, capable of extending the in-service life of components and structures. At present, due to the increase of residual stresses, the distortion in the geometry and deterioration of the microstructure caused by the thermal cycles, the effectiveness of the weld repairs on cracked structures is not well understood and investigated. Differently to the considerable data volume on the effects of original weld on fatigue life for steels and aluminum from the literature, data on welds repairs are scarce. In this context, the availability of experimental data on weld repair effects on the fatigue behavior may be very useful in determining inspection intervals in high-responsibility welded structures.

## 2. Material and methods

### 2.1. Material

For the present research-work flat welded specimens from hot-rolled AISI 4130 aeronautic steel, 1.10 mm and 1.60 mm thick, were used. The chemical compositions (wt%), from the base-material and from the weld (filler) metal, are presented in Table 1 (Fe in balance). The mechanical properties obtained from smooth flat samples and original welded specimens (OR) – with central weld seam crossed to the hot-rolled plate direction –, are indicated in Table 2. The hot-rolled plates presented 65 HR<sub>A</sub> in the “as-received” condition.

The monotonic tensile tests were performed in accordance with ASTM E 8 M by means of a servo-hydraulic INSTRON test machine, applying 0.5 mm/min displacement rate and a preload equal to 0.1 kN.

### 2.2. Welding and re-welding procedures

The most commonly employed welding process for manufacturing of aeronautical structures is tungsten inert gas (TIG), or gas tungsten arc welding (GTAW), which is appropriate to weld thin thickness materials and to allow the necessary variable control, resulting in high-quality and defect-free weld beads. The TIG welding process was carried out in accordance with the Brazilian Aeronautic Industry – EMBRAER NE 40-056 TYPE 1 – Standard (for components critical to the flight-safety), with a protective 99.95% purity argon-gas and filler metal AMS 6457 B – Turballoy 4130. A Square Wave TIG 355 – Lincoln equipment was manually employed by an expert aeronautic welder. All the welding parameters were controlled, and the main ones are indicated in Table 3. Also, all the welded joints were subjected to X-ray non-destructive analysis by the Brazilian Aerospace Technical Centre (CTA/IFI), which proved the acceptable quality of the welds, according to MIL-STD-453, EMBRAER – NE-57-002 and ASTM E-390 standards.

The welding direction was always perpendicular to hot-rolling process (direction) of the plate. Before welding, samples were cleaned with chlorinated solvent to oxide removal and fixed on a backing bar, to avoid contamination and porosity in the weld root. After the welding/re-welding process neither subsequent heat treatment to residual stresses relief nor subsequent removal of the weld bead was carried out, in order to simulate the real condition of the original aeronautic structure. Due to the plate thickness,

only one weld single-pass was required. For re-welding process, a manual grinding machine capable to reach 22,000 rpm was used to remove the previous weld metal. The heat-input applied was kept constant for all the welded and re-welded specimens.

### 2.3. Corrosion process

To analyze the effects of the corrosive process on the fatigue behavior of AISI 4130 steel, specimens were submitted to atmospheric corrosion (urban environment), accelerated by means of constant wetting during thirty days. Periodically, the specimens were moved so that all the surfaces were uniformly corroded.

### 2.4. Reverse bending fatigue tests

For experimental bending fatigue tests, welded and non-welded flat specimens were manufactured according to SCHENCK model PWS requirements (Fig. 2), following the LT direction of the hot-rolled plate. The specimens were fatigue tested upon a sinusoidal load, constant amplitude, load ratio  $R = -1$ , at 30 Hz frequency and room temperature. The superficial average roughness, obtained by means of a Mitutoyo 301 equipment, with cut-off equal to 0.8 mm × 5 mm, was  $R_a = 0.24 \mu\text{m} \pm 0.16 \mu\text{m}$ .

### 2.5. Microstructural and microhardness analyses

For microstructural analysis, a Nital 2% chemical etching was applied during 5 s. Vickers microhardness measurements were obtained at 0.0254 mm intervals throughout the regions under analysis (base-material, HAZ regions and weld metal), applying a 1 N load.

**Table 3**  
TIG welding parameters.

Direct current	DCEN
Welding position	Flat
Welding voltage	12 V
Welding current	30 A
Welding average speed	19.0 cm min <sup>-1</sup>
Pre heating	NONE
Flow rate	4–12 L min <sup>-1</sup>
Theoretical heat input	1.2 kJ cm <sup>-1</sup>
Filler metal diameter	1.6 mm

**Table 1**  
Chemical compositions (wt%).

Composition (wt%)	C	Mn	P <sub>max</sub>	S <sub>max</sub>	Si	Mo	Cr	Cu
Specified BM <sup>a</sup>	0.28–0.33	0.40–0.60	0.035	0.040	0.15–0.30	0.15–0.25	0.80–1.10	0.10
Specified WMB <sup>b</sup>	0.28–0.33	0.40–0.60	0.008	0.008	0.15–0.35	0.15–0.25	0.80–1.10	0.10
Weld (filler) metal	0.30	0.50	0.004	0.003	0.25	0.18	0.91	0.042
Plate #1.10 thick	0.33	0.53	0.010	0.003	0.28	0.17	1.04	0.02
Plate #1.60 thick	0.28	0.49	0.009	0.004	0.24	0.18	0.93	0.02

<sup>a</sup> AMS 6457 B – turballoy 4130 steel.

<sup>b</sup> AMS T 6736 A (2003) – for chromium–molybdenum (4130) seamless and welded steel tubing of aircraft quality.

**Table 2**  
Mechanical properties obtained from the welded and non-welded specimens.

Specimens	Yielding (0.2% offset)	Ultimate strength	Rupture stress	Elongation (25 mm length)	Yielding/ultimate strength ratio
Base-metal	746 ± 21	843 ± 9	655 ± 26	9.80 ± 1.87	0.88 ± 0.02
Welded	671 ± 20	778 ± 17	643 ± 26	3.81 ± 0.26	0.86 ± 0.01

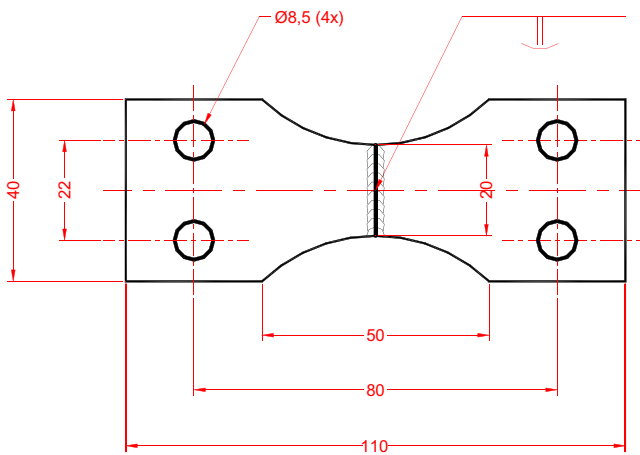


Fig. 2. Flat bending fatigue specimen (mm).

### 2.6. Residual stresses determination

The residual stresses field induced by welding and re-welding processes was determined by X-ray diffraction method, using the Raystress equipment (whose features are described in [26]) with couple exhibition,  $\varphi$  goniometer geometer, two anodes of chrome Cr- $\kappa$  radiation and registration of {2 2 1} diffraction lines, tension source of 25 kV, current of 1.5 mA, X-ray convergence angle of 50°. The accuracy of the stress measurements was  $\Delta\sigma = \pm 20$  MPa. In order to obtain the stress distribution by depth, the layers of specimens were removed by electrolytic polishing with a non-acid solution.

## 3. Results and discussion

### 3.1. Monotonic tests

First of all, it is important to pay attention to the high mechanical strength values and reasonable ductility from the hot-rolled AISI 4130 steel plate (as presented in index 2.1). It is also interesting to observe the decrease of all that mechanical properties after the first TIG welding application on AISI 4130 steel specimens, particularly the elongation (3.8% average), typical of fragile material. However, for both welded and non-welded conditions the yield tensile stress/maximum tensile stress ratio ( $\sigma_y/\sigma_m$ ) was around 0.8, which is an appropriate value for structures as the aeronautical ones [27]. Historically, values from 0.80 to 0.86 have been considered appropriate for specification, project and analysis of structural

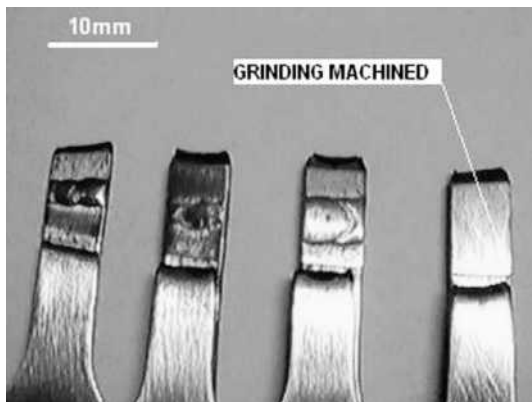


Fig. 3. Specimens fractured by monotonic tension tests.

integrity, by providing high capacity of plastic deformation and consequent margin of safety against fracture [27]. Yet, all the monotonic specimens tested, including those grinding machined, fractured at the sub-critical HAZ (SCHAZ)/base-material interface (strength-overmatch), despite any stress concentration originated at the weld toe, as illustrated in Fig. 3. This means that the influence of the microstructural variations along HAZ is more deleterious for tensile strength than the geometric features induced by the welding process. That is, for the monotonic test the material was not sensitive to stress concentration at the weld toe.

### 3.2. Reverse bending fatigue tests

#### 3.2.1. Effect of the corrosion process

Fig. 4 presents the SN (stress vs. number of cycles) curves for corroded and non-corroded AISI 4130 steel specimens. For seek of comparison with the welded specimen, it was added the fatigue curve obtained with base-material specimens (BM) 1.10 mm thick. Considering that for all the specimens just the thickness was altered (1.60–1.10 mm), it is possible to verify that the higher the thickness the lower the fatigue strength. It is in accordance with Murakami [28,29], who mentions that the larger specimens the higher amount of existent defects. Makkonen [30] also mentions that there is a great amount of microcracks previously nucleated in specimens submitted to cyclic loads, whose population increases when their dimensions increase.

From Fig. 4 it is also possible to verify that the fatigue curves diverge in the short fatigue life range/SFL ( $< 10^5$  cycles). This is due to the maximum stress at the surface, as a function of the type of fatigue test. That is, for reverse bending fatigue tests also in SFL the specimens are sensitive to fatigue-notch effect,  $K_f$ , which is defined as the ratio of the fatigue strength of a smooth specimen to the fatigue strength of a notched specimen at the same number of cycles.

It is also possible to observe in Fig. 4 the detrimental effect of the corrosive process on the reverse bending fatigue strength of the AISI 4130 steel. Thus, for 359 MPa and 303 MPa stress levels, the respective numbers of cycles were about  $1.10 \times 10^5$  and  $1.90 \times 10^5$ , corresponding to 300% and 500% reduction in comparison to those non-corroded. It is well known that the fatigue behavior of any mechanical component is sensitive to its surface finishing. Thus, since there was not simultaneity between the fatigue and corrosion processes (when the anodic condition at the

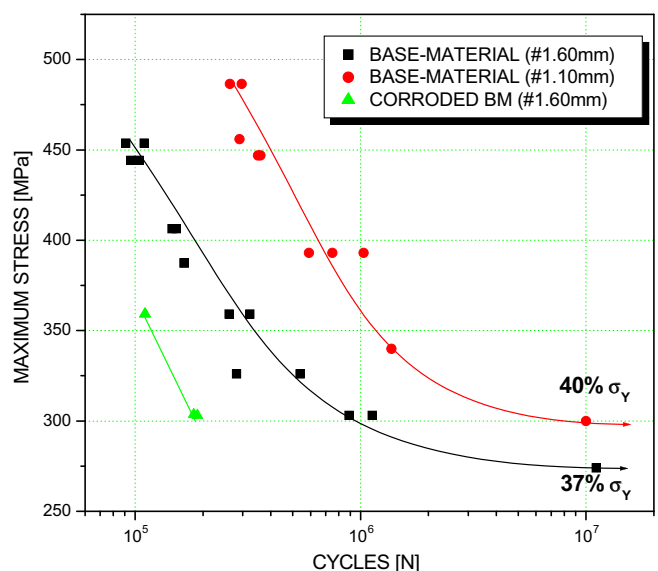


Fig. 4. SN curves for corroded and non-corroded specimens of base-material.

crack tip accelerates the corrosive process and vice versa), the main factor controlling the fatigue behavior presented is related to surface roughness of the specimens tested. In fact, the average surface roughness measured provided  $R_a = 0.24 \mu\text{m} \pm 0.16 \mu\text{m}$  for non-corroded specimens and  $R_a = 1.95 \mu\text{m} \pm 0.18 \mu\text{m}$  for those corroded. The corrosive process generated a Grant No. of pits, which gave rise to local stress concentration and reduced the number of cycles for crack nucleation. Additionally, the local stress concentration can also reduce the stress intensity factor threshold ( $\Delta K_{th}$ ) and allows that the small cracks grow [10–12]. Therefore, it is necessary to protect the surface of aeronautic structures against the aggressive environment acting on an aircraft.

### 3.2.2. Effect of the TIG welding/re-welding process

Fig. 5 presents the SN curves of welded and re-welded specimens. The horizontal line indicates the nominal stress value ( $\sigma_n \approx 247 \text{ MPa}$ ), which corresponds to yielding stress divided by the safety-factor equal to 3 (for welded components critical to the flight-safety), in accordance with the EMBRAER NE 40–056 TYPE 1 Standard.

From Fig. 5, one can observe the significant decreasing in bending fatigue strength of the AISI 4130 steel, whose endurance limit was about 37% of its yielding stress ( $\sigma_y$ ). However, the endurance limit is still above the nominal stress,  $\sigma_n$  (horizontal line). Nevertheless, a subsequent reduction in bending fatigue strength for welded specimens is observed in comparison with the base-material specimens (BM), mainly in the short fatigue life (SFL) range. In the long fatigue life (LFL) range, it is possible to verify that the endurance limit is located close to the horizontal line, corresponding to specified nominal stress ( $\sigma_n$ ). On the other hand, with the first weld repair (1R), no-subsequent reduction in bending fatigue strength is observed. For both original (OR) and first time re-welded (1R) specimens, one can observe practically the same fatigue behavior. However, the second weld repair (2R) resulted in a decreasing of the fatigue strength, with the endurance limit below the nominal stress value,  $\sigma_n$  (horizontal line). Since the aircrafts are submitted to high fatigue cycles during flight, as a result of abrupt maneuvers, wind bursts, motor vibration and helixes efforts, it is not recommended or favorable to the flight-safety the second weld repair (2R) application. This behavior is also due to the increase in volume of the weld bead with consequent increase of the stress concentration factor at the weld toe. In addition, the re-welding process can increase the HAZ dimensions and its coarse-grain re-

**Table 4**  
Vickers microhardness values (HV).

Microstructure	Original weld	one-repair	two-repairs
Base-material	$267.7 \pm 16.4$	$285.5 \pm 15.8$	$286.5 \pm 19.7$
CGHAZ	$362.9 \pm 55.7$	$373.4 \pm 22.8$	$477.80 \pm 59.15$
Weld metal	$573.2 \pm 69.8$	$507.5 \pm 47.4$	$399.9 \pm 22.8$

gion (CGHAZ), which is located exactly at the weld toe and characterized by low fracture toughness and considerable hardness (as can be verified in Table 4).

From Fig. 5, it is also possible to verify the larger scattering of the fatigue results obtained with both welded and re-welded specimens. This is due to volume variations of the deposited weld metal, the higher heating/cooling rate and the uneven stress concentration values at the weld toe notch. Fig. 5 also shows that the fatigue strength reduction due to welding process tends to be more pronounced when the number of cycles is also reduced (divergence between BM and OR fatigue curves in SFL). This observation is very important taking into account the efforts due to landing operations (typical for SFL regime) along the operational life of the aircraft. On the other hand, it is observed that the divergence between both endurance limits ( $10^7$  cycles) was low, i.e.: from 37%  $\sigma_y$  for base-material to 32%  $\sigma_y$  after welding (close to  $\sigma_n$ ). In the same way, this is a very important result, taking into account the abrupt maneuvers or wind bursts during flight (typical for LFL regime). This implicates that special cares should be adopted during design and, particularly, maintenance of welded aeronautical structures against any accidental tool marks capable to introduce local stress concentration on the structure. Since for bending loads the maximum stress occurs at the surface, the fatigue resistance is sensitive to any geometric change of material (notch-sensitivity).

From Fig. 5, comparing the first (1R) and second weld repairs (2R) fatigue curves in the SFL ( $<10^5$  cycles) regime, one can observe that the reduction was minimum, with both curves converging to a same point in high stress levels (SFL). On the other hand, one can also observe high divergence between the aforementioned curves in LFL regime, reaching a maximum at the endurance limit level ( $10^7$  cycles). Since the material is notch-sensitive in LFL, such a behavior was due to the abrupt geometric change generated by the weld bead in addition to the microstructural alterations induced by the new cooling rate. On the other hand, comparatively to the fatigue behavior of base-material (BM), as in SFL as LFL (endurance limit) regimes the tendency of the second weld repair (2R) fatigue curve shows practically the same fatigue-notch sensitivity [ $q = (K_f - 1)/(K_t - 1)$ ], or fatigue-notch factor,  $K_f$  (Eq. (1) [32]). This observation becomes evident considering the parallelism presented by both base-material (BM) and two weld repairs (2R) fatigue curves. In fact, the fatigue-notch factor values ( $K_f$ ) in  $10^7$ ,  $10^6$  and  $2.8 \times 10^5$  cycles were: 2.00, 2.15 and 2.07, respectively, which confirms the mentioned parallelism. Since the welding repair procedure applied was by removing the previous weld bead, the geometric alteration was hoped to be low (as can be seen in Table 5 ahead). Thus, the increase of the notch sensitivity (fatigue-notch factor) with the second weld repair (2R) was also due to the microstructural variations resulting of successive heating/cooling cycles imposed to the material. Therefore, based on the results obtained and considering that the welding repair is necessary, it can be admitted only one weld repair (1R) during fabrication of the critical to the flight-safety structures, without compromising their reverse bending fatigue strength. On the other hand, being necessary to make some subsequent repair along the operational life, this study indicates that cares should be adopted in the sense of avoiding abrupt maneuvers and/or overloads on the aircraft. In

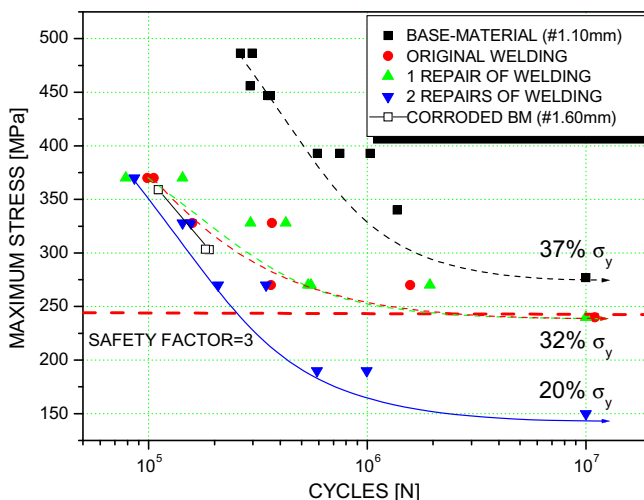


Fig. 5. Reverse bending fatigue SN curves for base-material and (re-)welded specimens (1.10 mm thick).

**Table 5**

Geometry factor values from the weld bead (in accordance with Fig. 6).

Group	W (mm)	T (mm)	Root (mm)	Angle ( $\alpha$ )	Radius (mm)	HAZ (mm)	$K_f$ (Eq. (1))
OR	$3.75 \pm 0.35$	$0.89 \pm 0.20$	$0.77 \pm 0.19$	$141.9^\circ \pm 14.4^\circ$	$1.03 \pm 0.36$	$2.89 \pm 0.25$	1.290
1R	$4.49 \pm 0.33$	$1.17 \pm 0.32$	$0.82 \pm 0.27$	$146.1^\circ \pm 8.6^\circ$	$0.75 \pm 0.21$	$3.11 \pm 0.12$	1.305
2R	$4.80 \pm 0.23$	$0.96 \pm 0.20$	$0.79 \pm 0.30$	$138.6^\circ \pm 7.5^\circ$	$0.93 \pm 0.40$	$3.22 \pm 0.23$	2.178

$$K_f = 1 + \frac{K_t - 1}{1+a/r}$$

where:  $a = 0.1659$  (Peterson's material parameter for steel);  $r$  = notch-root;  $K_f$  = fatigue-notch factor.

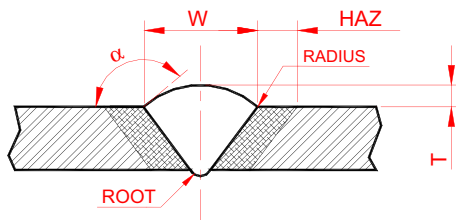


Fig. 6. Geometry factors of the welded joints (values presented in Table 5).

addition, it becomes necessary lower inspection intervals for flaws as-crack determination at the weld joints of structural components.

Finally, although it is not appropriate to directly compare both fatigue behaviors of welded specimens with those corroded due to their different thickness, it is interesting to observe the similar deleterious effect caused by the corrosive process on the fatigue strength of AISI 4130 steel.

Table 4 presents the microhardness values measured in the three interest areas. Firstly, one can observe the high microhardness values for weld metal and CGHAZ as a consequence of TIG welding and re-welding process. This is due to high cooling speed associate to the low heat-input applied, which resulted in martensitic structures. Since the heat input was kept constant for all the (re-)welding process, it is important to mention that just the weld reinforcement was removed. Consequently, the different microhardness values verified were due to remaining weld material volumes (e.g. weld root), which unevenly affected the cooling speed of the weld metal. Thus, from Table 4, one can observe that for both the original weld (OR) and the first welding repair (1R) the microhardness values were close and coherent with each other. This can explains the bending fatigue behavior presented in Fig. 5. However, it is also important to pay attention to the great dispersion of microhardness results in both CGHAZ and weld metal (standard-deviation). It is also possible to observe the highest microhardness value from the original weld metal than for all the other conditions. This implicate that probably the second welding repair promoted the tempering of the previous microstructure, but with no improvement on their bending fatigue strength, as verified in Fig. 5. After the second welding repair it is also possible to observe higher microhardness value for the CGHAZ, implicating a grain size reduction in that region, but again with no improvement on the bending fatigue strength, as illustrate in Fig. 5. It is well known that the lower the grain size the higher the material toughness. In the same way, the higher the grain size, the lower the hardness/mechanical strength.

Considering that the weld profile affects the fatigue resistance of a welded structure, Table 5 and Fig. 6 present the main geometric factors that compose a weld joint and their corresponding values, obtained by image analysis tools. Thus, from Table 5 and Fig. 6, it is possible to confirm all the results presented in Fig. 5 on the effect of welding repairs on the bending fatigue behavior of AISI 4130 steel. Therefore, it can be observed that the welding repairs reduced both angle ( $\alpha$ ) and radius at the weld toe notch that, com-

bined, are considered the main geometric factors controlling the fatigue behavior of welded components and structures [13,31]. In addition, the great scattering on the geometric factors measured is in consonance with the great scattering of the fatigue results presented by the welded specimen groups. Yet, from Table 5, we can observe: the increase of the stress concentration factor ( $K_f$ ) at the weld toe notch with the successive welding repairs; the largest extension of HAZ due to the successive heat-input applied and, consequently, the increase of the CGHAZ as well; the effect of both weld reinforcement ( $T$ ) and weld root dimensions, again, on the angle ( $\alpha$ ) and radius reduction and, consequently, on the bending fatigue strength of welded specimens. On this subject, it is important

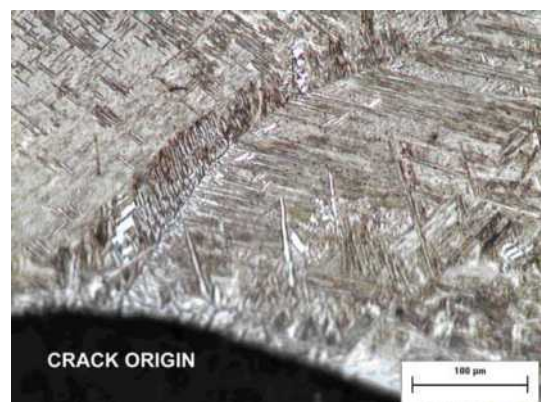


Fig. 7. Crack initiation at the weld toe of a non-fractured fatigue specimen (500×). Nital 2%.

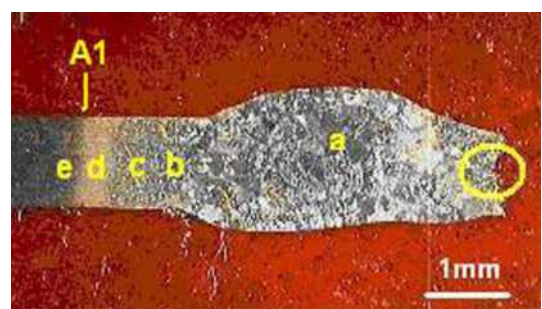
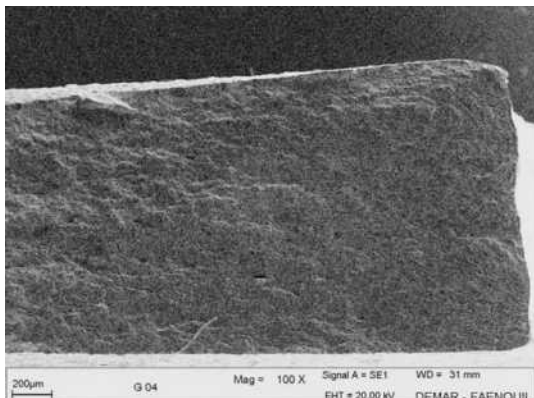


Fig. 8. Macrography of a fatigue specimen fractured by reverse bending loads. Nital 2%.



Fig. 9. Secondary crack propagation from the fracture surface of a reverse bending fatigue specimen (500×). Nital 2%.



**Fig. 10.** Edge fatigue crack origin and propagation for a fractured specimen of base-material, 1.60 mm thick.

to mention that all the welded specimens fractured at the weld toe notch, as illustrated in Figs. 7 and 8. In fact, Fig. 7 illustrates a crack in a non-fractured specimen, which initiated at the weld toe notch and propagated through grain boundary into weld metal (intergranular crack).

Fig. 8 presents the macrography of a fractured specimen that was submitted to two welding repairs (2R), in which we can observe: (a) the weld metal region with well delineated equiaxial coarse-grains; the HAZ extension with the sub-regions, (b) coarse-grain/CGHAZ, (c) fine-grain/FGHAZ, (d) inter-critical/ICHAZ and (e) sub-critical/SCHAZ near to  $A_1$  line (lower critical tempera-

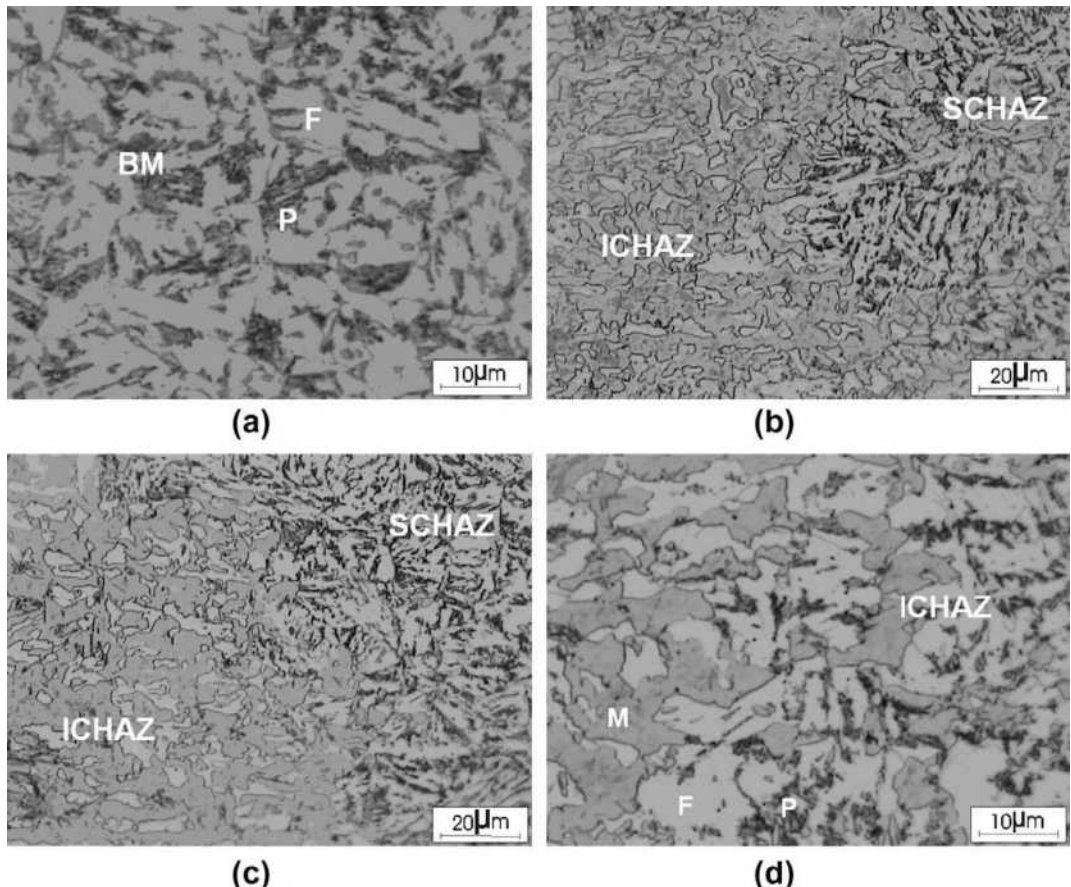
ture); as well as the welded joint irregularity as a consequence of the deformation generated by the reverse bending loads applied.

Fig. 9 presents the transgranular secondary crack, originate from the fracture surface of the specimen in Fig. 8. This secondary crack implicates that the reverse bending fatigue specimens may have been subjected to either Modes I and II or Modes I and III of loading combination (or all of them), turning the laboratorial test more severe due to friction process by both free crack surfaces, accelerating its propagation. In fact, bending loads also introduce shear stresses in the specimens (Mode II of fracture) and/or tearing stress (Mode III of fracture) whether crack initiation occurs at the edge of the specimen, as illustrated in Fig. 10. On this subject, Veidt [33] mentions that the radius in the notch root has little effect on the stress intensity factor in Mode II of fracture.

Figs. 11 and 12 present the base-material, HAZ and weld metal microstructures for all the proposed conditions. Fig. 11a shows the normal products of transformation from austenite, i.e. ferrite and perlite. From Fig. 11b-d the beginning of the transformation from perlite to austenite is observed (to martensite, upon subsequent cooling) along the SCHAZ/ICHAZ regions ( $A_1$  line).

Fig. 12 presents the microconstituent of the weld metal (original, one and two weld repairs) and respectives CGHAZ, basically constituted by martensite, which is a very hard and fragile microstructure. As aforementioned, the higher the hardness the higher the resistance to fatigue crack initiation.

Fig. 13 presents the residual stresses field in the weld metal, HAZ and base-material of all the conditions analyzed. It is well known that residual stresses are present in welded components [22,34–36] and have great effect on fatigue crack nucleation and propagation [34]. Thus, from Fig. 13, one can observe that the



**Fig. 11.** Base-material and base-material/HAZ transition microstructures: (a) Base-material (typical); (b) SCHAZ-ICHAZ of the original weld; (c) SCHAZ-ICHAZ of the first welding repair; and (d) ICHAZ of the second welding repair. Nital 2%. (F = Ferrite; P = Perlite; M = Martensite).

TIG (re-)welding process induced high compressive residual stresses for all conditions upon analysis, as weld metal as in HAZ and base-material (up to 20 mm from the fusion line). Such residual stresses were relieved internally in some point along the length of the specimens, because no deformation was verified on the samples. Yet, it is observed that all the residual stress profiles presented similar tendency, i.e., maximum values in weld metal ( $-600$  MPa for original weld;  $-450$  MPa for one weld repair and  $-330$  MPa for two weld repairs), followed by HAZ ( $-400$  MPa for original weld;  $-75$  MPa for one weld repair and  $-50$  MPa for two weld repairs) and last base-material up to 20 mm far-away from the fusion line ( $-300$  MPa for original welding;  $-160$  MPa for one weld repair and  $-100$  MPa for two weld repairs).

Many factors might have contributed to compressive residual stresses induced by the TIG (re-) welding process, viz: (i) austenite-martensite transformation (which generate up to 4% increase in volume of material) and which initiate at the surface due to higher cooling speed; (ii) the thin thickness and good mechanical properties in high temperature of the base-material, particularly low deformation in high temperature; (iii) subsequent contraction in the core of the weld metal (after the martensitic transformation at the surface) due to relatively lower cooling speed in that region; (iv) constraint to natural expansion of the weld metal and HAZ by the base-material volume around; and (v) the clamps applied at the extremities of the specimens during the (re-)welding process, etc. However, some aspects get the attention from the Fig. 13 as:

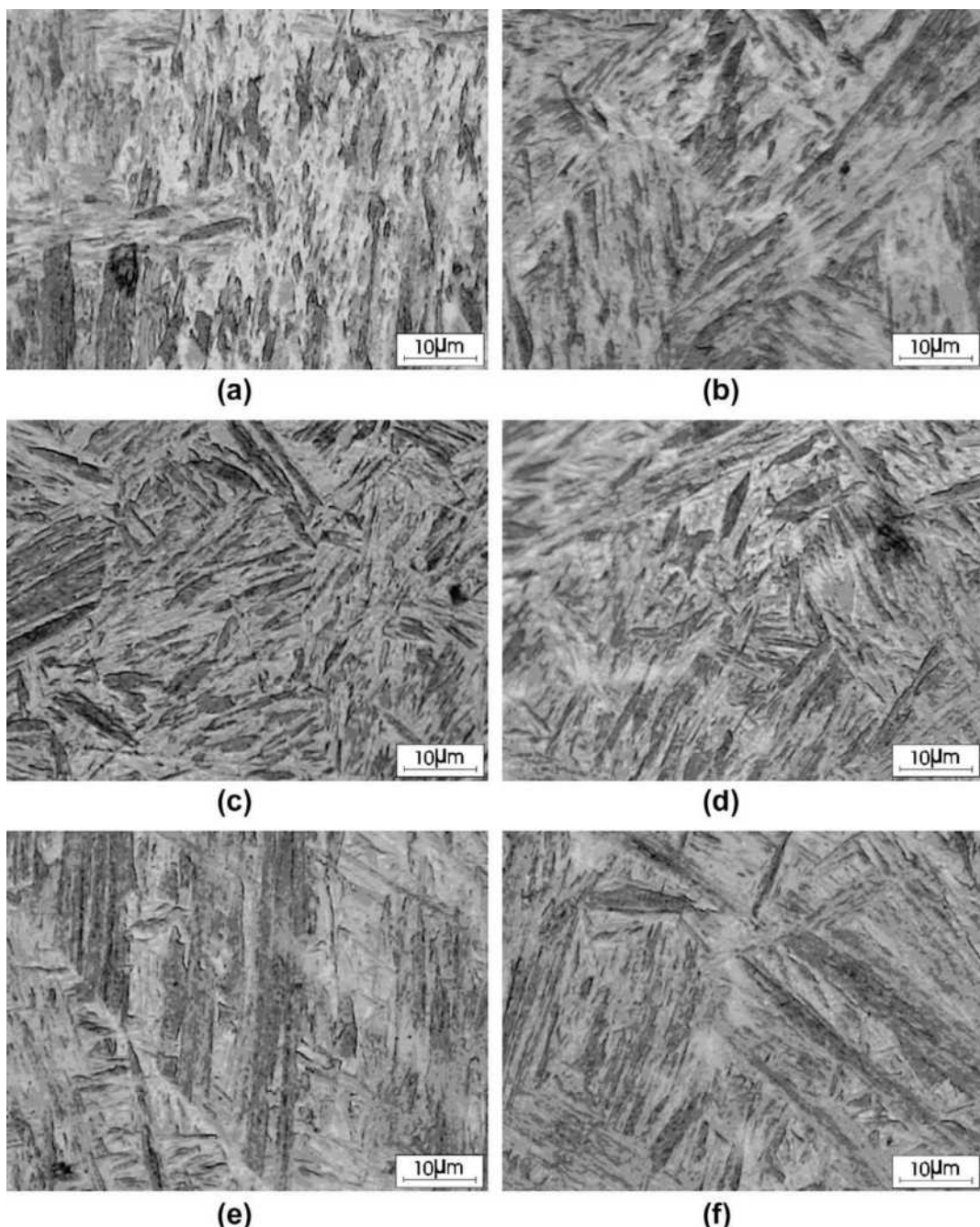


**Fig. 12.** Microscopic analysis of the weld metal and CGHAZ: (a) original CGHAZ; (b) original weld metal; (c) CGHAZ of the first welding repair; (d) weld metal of the first welding repair; (e) CGHAZ of the second welding repair; and (f) weld metal of the second welding repair. Nital 2%.

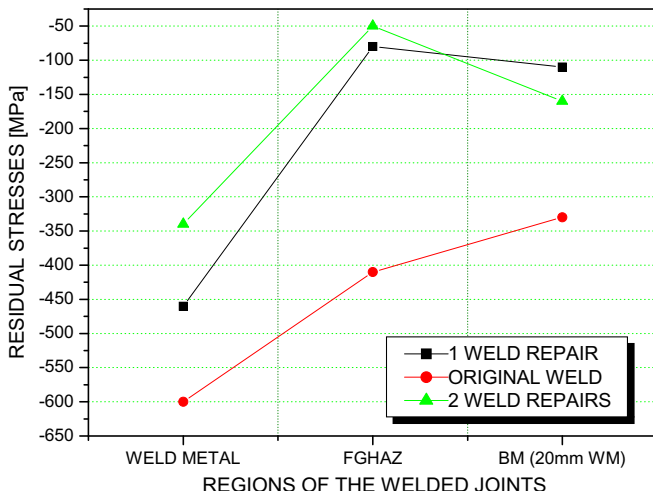


Fig. 13. Residual stress profiles of all the conditions tested.

the high values of compressive residual stresses, which were higher in the weld metal than HAZ; all the compressive stress fields were still compressive up to 20 mm distance from weld fusion line.

It is well known that the residual stresses largely affect the fatigue behavior of components, and that compressive residual stresses are benefit towards inhibit the crack nucleation. Thus, the results presented in Fig. 13 are in accordance with the fatigue behavior of specimens with original weld (OR), as well as those with one (1R) and two (2R) weld repairs presented in Fig. 5. In addition: the higher the hardness, the higher the fatigue strength as well. Consequently, from Table 4 and Fig. 5, it could be observed better fatigue behavior for the originally welded (OR) specimens in comparison with the one (1R) weld repair condition. However, considering the fatigue crack propagation stage, it is well known that the increase of the hardness increases the propagation rate ( $da/dN$ ). In this context, the existence of compressive residual stresses highlight the stress concentration effect induced by the weld geometry on the fatigue strength reduction verified. That is, although a mechanical component possess high compressive residual stresses, their effects or benefits will be minimized (or annulled in case the stress relief) when this component presents a stress concentrator (geometric factor) that reduces the number of cycles necessary to fatigue crack initiation. Thus, it is possible that the geometric stress concentration factor, which is located at the weld toe/fusion line/CGHAZ region, overcomes the compressive residual stress field induced by the (re-)welding process, relief it. Certainly, the compressive residual stresses field as far as possible delayed the fatigue crack nucleation and propagation by reducing the stress intensity factor ( $\Delta K$ ), as mentioned by Wei & Chen [34].

#### 4. Conclusions

Motivated by high fracture incidence at welded joints of a specific and critical to the flight-safety component, called "motor-craddle", experimental reverse bending fatigue tests on welded and re-welded specimens were carried out. Based on the results obtained, the following conclusions may be drawn:

1. The AISI 4130 steel possess good mechanical properties, but low elongation in the "as-received" condition (not heat-treated).
2. All the monotonic specimens tested, including those grinding machined, fractured at the sub-critical HAZ (SCHAZ)/base-material interface (strength-overmatch), despite any stress concentration originated at the weld toe.

3. The reverse bending loads significantly decrease the fatigue strength of the AISI 4130 steel, whose endurance limit were about 37% and 40% of the yielding stress ( $\sigma_y$ ) for specimens 1.60 mm and 1.10 mm thick, respectively.
4. The corrosive process strongly reduced the reverse bending fatigue strength of AISI 4130 steel.
5. In comparison with specimens from the base-material a reduction in bending fatigue strength for TIG welded specimens (OR) was observed. After the first weld repair (1R), no-subsequent reduction in bending fatigue strength was observed in comparison with the original weld. The second weld repair (2R) again resulted in decreasing of the fatigue strength in comparison with that subjected to the first weld repair. Consequently, it is not recommended or favorable to the flight-safety the second weld repair (2R) on critical to the flight-safety components.
6. The TIG (re-)welding procedure induced high compressive residual stress values in the AISI 4130 steel.
7. It was verified increase of the stress concentration factor,  $K_t$ , at the weld toe with the successive welding repairs, which overcomes the compressive residual stress field induced by the (re-)welding process. As a result, all the welded fatigue specimens fractured at that region.

#### Acknowledgement

The authors are grateful to FAPESP/Process No. 99/11948-6, CNPq and FUNDUNESP.

#### References

- [1] Flight Safety Foundation – Available from <<http://www.flightsafety.org>>; 2009 [accessed 10.2009].
- [2] National Civil Aviation Agency – Brazil. Available from <<http://www.anac.gov.br>>; 2004 [accessed 10.2003].
- [3] Godefroid LB. Fatigue crack growth under constant and variable amplitude loading in aluminium alloys of aeronautical applications. Ph.D. Thesis, COPPE/UFRJ, Brazil: Federal University of Rio de Janeiro; 1993.
- [4] Goranson UG. Fatigue issues in aircraft maintenance and repairs. Int J Fatigue 1993;19:S3–S21.
- [5] Payne AO. The fatigue of aircraft structures. Eng Fract Mech 1976;8:157–203.
- [6] Wenner CA, Drury CG. Analysing human error in aircraft ground damage incidents. Int J Ind Ergonom 2000;26:177–99.
- [7] Latorella KA, Prabhu PV. A review of human error in aviation maintenance and inspection. Int J Ind Ergonom 2000;26:133–61.
- [8] Bhaumik SK, Sujata M, Venkataswamy MA. Fatigue failure of aircraft components. Eng Fail Anal 2008;15:675–94.
- [9] Carpenter M. Managing the fleet: materials degradation and its effect on aging aircraft. Amptiac, News Lett 2001;4(5):7–19.
- [10] DOT/FAA/AR-00/22. US Department of Transportation, Federal Aviation Administration, Corrosion and Corrosion Fatigue of Airframe Materials, final report, July 2002. 2002. 79p.
- [11] Wang QY, Kawagoishi N, Chen Q. Effect of pitting corrosion on very high cycle fatigue behavior. Scripta Mater 2003;49:711–6.
- [12] Murtaza G, Akid R. Corrosion fatigue short crack growth behaviour in a high strength steel. Int J Fatigue 1996;18:557–66.
- [13] Nascimento MP. Effects of TIG welding repair on the structural integrity of AISI 4130 aeronautical steel. In: Ph.D. Thesis in mechanical engineering. State University of São Paulo/UNESP-FEG, Brazil (in Portuguese); Code CDU 620.92, 2004. 240p.
- [14] Nascimento MP, Voorwald HJC. An evaluation on the fatigue crack growth in re-welded AISI 4130 aeronautical steel. In: Eighth international fatigue congress/FATIGUE 2002, vol. 5, Stockholm-Sweden; 2002. p. 3463–72.
- [15] Nascimento MP, Ribeiro RB, Voorwald HJC. Fatigue crack growth in re-welded AISI 4130 high strength steel. In: Fourteenth European congress on fatigue/ECF 14, vol. 2, Cracow, Poland; 2002. p. 1–3116.
- [16] Vern Sutter, Robert J. Dybas, repair welding. In: ASM International, American Society for Metals, Editors, Metals Handbook, Welding, Brazing and Soldering, vol. 6, Metals Park, Ohio; 2002. p. 1103–7.
- [17] Kroes MJ, Watkins WA, Delp F. Aircraft maintenance and repair. 6th ed. New York: Glencoe – Macmillan/McGraw-Hill; 1993. 648p.
- [18] Vega EO, Hallen JM, Villagomez A, Contreras A. Effect of multiple repairs in girth welds of pipelines on the mechanical properties. Mater Charact 2008;59:1498–507.
- [19] Liming L, Xin Du, Meili Z, Guoqing C. Research on the microstructure and properties of weld repairs in TA15 titanium alloy. Mater Sci Eng A 2007;445–446:691–6.

- [20] Shankar K, Weidong Wu. Effect of welding and weld repair on crack propagation behaviour in aluminium alloy 5083 plates. Mater Des 2002;23:201–8.
- [21] Sun W, Hyde TH, Becker AA, Williams JA. Some key effects on the failure assessment of weld repairs in CrMoV pipelines using continuum damage modeling. Eng Fail Anal 2005;12:839–50.
- [22] Dong P, Hong JK, Bouchard PJ. Analysis of residual stresses at weld repairs. Int J Pres Ves Pip 2005;82:258–69.
- [23] Hyde TH, Sun W, Becker AA, Williams JA. Life prediction of repaired welds in a pressurised CrMoV pipe with incorporation of initial damage. Int J Pres Ves Pip 2004;81:1–12.
- [24] Aloraijer AS, Ibrahim RN, Ghojet J. Eliminating post-weld heat treatment in repair welding by temper bead technique: role bead sequence in metallurgical changes. J Mater Process Technol 2004;153–154:392–400.
- [25] Doc IIS/IIW-956-87. (ex. doc. XV-648-87) prepared by commission XV “fundamentals of design and fabrication for welding” of the IIW, recommendations for repairs and/or strengthening of steel structures. Welding in the world 1988; 26(11/12): 292–306.
- [26] Ivanov SA, Monim VI, Teodósio JR. New method of X-ray tensometry. In: International conference on experimental mechanics. Lisboa; 1994. p. 757–61.
- [27] Bannister AC, Ocejo JR, Gutierrez-Solana F. Implications of the yield stress/tensile stress ratio to the SINTAP failure assessment diagrams for homogeneous materials. Eng Fract Mech 2000;67:547–62.
- [28] Murakami Y. Inclusion rating by statistics of extreme values and its application to fatigue strength prediction and quality control of materials. J Res Nat Inst Stand Technol 1994;4:99–107.
- [29] Murakami Y, Usuki H. Quantitative evaluation of effects of non-metallic inclusions on fatigue strength of high strength steels. II: fatigue limit evaluation based on statistics for extreme values of inclusion size. Int J Fatigue 1989;5(11):299–307.
- [30] Makkonen M. Statistical size effect in the fatigue limit of steel. Int J Fatigue 2001;23:395–402.
- [31] Lancaster JF. Metallurgy of welding. 5th ed. London: Chapman and Hall Incorporation; 1993. 389p.
- [32] Peterson RE. Stress Concentration design factors. 5th ed. New York: John Wiley and Sons Incorporation; 1966 [155p].
- [33] Veidt M. On the Effect of notch radius and local friction on the Mode I and Mode II fracture toughness of a high-strength steel. Eng Fract Mech 1997;58:223–31.
- [34] Wei MY, Chen C. Fatigue crack growth characteristics of laser-hardened 4130 steel. Scripta Metall Mater 1994;10(31):1393–8.
- [35] Brown TB, Dauda TA, Truman CE, Smith DJ, Memhard D, Pfeiffer W. Predictions and measurements of residual stress in repair welds in plates. Int J Pres Ves Pip 2006;83:809–18.
- [36] Chiarelli M, Lanciotti A, Sacchi M. Fatigue resistance of MAG welded steel elements. Int J Fatigue 1999;1:1099–110.



## Considerations on corrosion and weld repair effects on the fatigue strength of a steel structure critical to the flight-safety

Marcelino P. Nascimento\*, Herman J.C. Voorwald

Department of Materials and Technology – State University of São Paulo, UNESP/FEG/DMT 333, Ariberto Pereira da Cunha Ave., 12516-410, Guaratinguetá City, São Paulo State, Brazil

### ARTICLE INFO

#### Article history:

Received 30 July 2009

Received in revised form 24 December 2009

Accepted 31 December 2009

Available online 7 January 2010

#### Keywords:

AISI 4130 steel

Fatigue behavior

Corrosion

Weld repairs

Flight-safety

### ABSTRACT

The aim of this study is to analyze the effects of corrosion and successive tungsten inert gas (TIG) welding repairs on the reverse bending fatigue strength of AISI 4130 steel used in components critical to the flight-safety. The tests were performed on hot-rolled steel plate specimens, 1.10 mm and 1.60 mm thick, by means of a SCHENK PWS equipment, with load ratio  $R = -1$ , constant amplitude, 30 Hz frequency and room temperature. It was observed that the reverse bending fatigue strength of AISI 4130 steel decreases due to the corrosion and the TIG welding and re-welding processes.

© 2010 Elsevier Ltd. All rights reserved.

### 1. Introduction

According to flight-safety foundation [1], “Aircraft accidents means an occurrence associated with the operation of an aircraft, which takes place between the time any person boards the aircraft with the intention of flight until such time as all such persons have disembarked, and in which any person suffers death or serious injury as a result of being in or upon the aircraft or by direct contact with the aircraft or anything attached thereto, or in which the aircraft received substantial damage (damage or structural failure that adversely affects the structural strength, performance, or flight characteristics of the aircraft, and which would normally require major repair or replacement of the affected component)”. Based in such definition, the accident rates (i.e., accidents per million departures) have been at 1.2, or 12,000 accidents, in the occidental world [2]. In the search for a zero accident rates, the flight-safety has been the main concern of the aeronautical authorities all over the world.

Basically, the aeronautical projects should take into account the difficulties of transporting a load against the gravity force during take-off and flight, and discharge it in an efficient way, with minimum cost and maximum safety, because failures in any of these stages will implicate catastrophic accidents, involving human lives [3]. In general, structural failures during flight are attributed to

aerodynamic overloads or fatigue of materials, as a consequence of inadequate project or any notch produced during manufacturing or maintenance of aircrafts [4–7]. Since the catastrophic accidents involving the English model “Comet” in the 1950’s, the fatigue process has been the most important project and operational consideration for both civil and military aircrafts [4,5,8]. On the other hand, many fractures of materials are also caused by corrosion as a consequence of aggressive environment.

Since the aircrafts become more complex, the environmental effects assumed great importance. As a result of older aircrafts flying nowadays, problems such as stress-corrosion cracking, corrosion-fatigue (simultaneously or separately) and wear are also expected to occur [4,5,9,10]. Due to several aggressive environments in which the aircrafts are subjected, particularly marine, corrosion is the most important factor of maintenance and inspection for the aeronautic sector [4,5,9,10]. Hence, corrosion is undoubtedly a real and critic issue acting on aircrafts, flowing with the time even on those not operational. Usually, the corrosion control is accomplished by adoption of prevention methods with high-quality periodic inspections associated to damage tolerance philosophy, for taking into account its effect on the fatigue life of a structural component [4,5,10–12]. Such issues will request extensive investment, planning, researches and development on repair methods and maintenance procedures towards assure the safe and continued airworthiness.

For several aircraft models (e.g. agricultural, military training and acrobatic) the most solicited and repaired component is one that supports the motor, called “Motor-Cradle” (Fig. 1) [13]. This

\* Corresponding author. Tel.: +55 12 3123 2865; fax: +55 12 3123 2852.

E-mail addresses: [pereira@feg.unesp.br](mailto:pereira@feg.unesp.br), [marcelino.nascimento@gmail.com](mailto:marcelino.nascimento@gmail.com) (M.P. Nascimento), [voorwald@feg.unesp.br](mailto:voorwald@feg.unesp.br) (H.J.C. Voorwald).

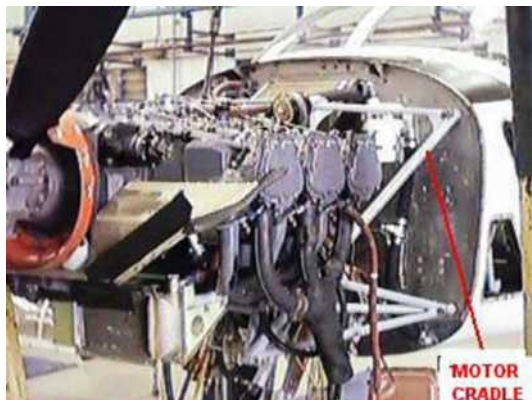


**Fig. 1.** Motor-cradle assembly in a T-25 Universal Brazilian aircraft.

component presents a geometrically complex structure made from AISI 4130 tubular steel of different dimensions and TIG welded in several angles [13,14]. For the Brazilian aircrafts T-25 Universal and T-27 Tucano, for example, besides supporting the motor in balance, the motor-cradle also maintains the nose landing gear fixed at the other extremity. Since the motor-cradle is a component critical to the flight-safety, the aeronautic standards are extremely rigorous in its manufacturing, by imposing a “zero-defect index” on the final weld seam quality (Safe-Life philosophy), which is 100% inspected by non-destructive testing/NDT [13–15]. For this reason, welded aeronautic structures are frequently subjected to successive repairs in accomplishment to current standards. As a consequence, components approved by NDT may contain a historic record of welding repairs whose effects on their structural integrity are not computed. In addition, these structures are also submitted to weld repairs along their operational life, turning this question more complex.

As a part of this research-work, an investigation on 157 motor-cradles fracture reports indicates that all of them occurred at welded joints as a result of fatigue cracks, reducing the “Time-Before-Fail” from 4.000 h to 50 h of flight [13]. Motivated by high fracture incidence of this particular component, an extensive research program to evaluate the manufacturing and maintenance weld repair effects on the structural integrity, mechanical properties and microstructural changes has been conducted [13].

Although the maintenance repairs of parts and components are a multibillion-dollar industry [16] and that, particularly for the transport sector, the welding repairs are an essential and frequently used process [17], few papers approaching this issue have been published, being all of them on either aged and degenerated materials [18,19] in petrochemical, offshore and power industries [20], by means of finite element method – FEM - [21–23].

In this paper, special emphasis was attributed to a standardized weld repair procedure, widely employed during manufacture of welded aeronautic structures and characterized by removing the previously defective weld bead and by applying a new weld seam by means of the gas tungsten arc welding/GTAW (or tungsten inert gas/TIG) process with filler metal.

The aim of this study is to analyze the effect of the corrosive process and the successive TIG welding repairs on the reverse bending fatigue strength of AISI 4130 steel specimens made from hot-rolled steel plates, 1.60 mm and 1.10 mm thick, respectively. Analyses of microstructure, microhardness and residual stresses from the base-material (BM), heat-affected zone (HAZ) and weld metal (WM), as well as the effects of the surface roughness and weld bead geometry complemented this study.

In the sequence, a brief comment on the current weld repair procedures is presented.

### 1.1. Current Welding Repair Procedure and Applications

When defects (such as porosity, impurity, undercut) are found in the welding joints, the main international standards (e.g. API, AWS, BSI and ASME) request that the defective welded joints are corrected. However, in a general form, none of the above standards make mention to number of permissible repairs.

In general, repair welding usually involves the complete shut-down of the equipment, the removal of all dead loads and the carrying out welding to original manufacturing standards [24]. Two typical procedures of weld repairs, complete repair and partial repair, include mechanics removal of the damaged material and the restoration of the geometry and integrity of the component, followed for a post-welding heat treatment (PWHT), which will depend mainly on type and thickness of material [21]. PWHT has as a function to reduce or eliminate residual stresses and to temper the metallurgical structure of heat-affected zone (HAZ). However, PWHT is very expensive, time consuming and, depending on local, difficult or impracticable.

An important application of weld repair techniques is to avoid PWHT, generating HAZ with structures of fine grains [24]. Such an objective can be reached by minimizing the size of original grain in HAZ, by minimizing the thermal contribution during the welding process or by refining the size of the initial coarse-grain region of HAZ [24]. For this purpose, two welding repair techniques are employed, viz:

- i. Half-bead welding (HBW): the beads are removed before welding the next layer.
- ii. Temper-bead welding (TBW): the subsequent weld bead partially does heat-treat the previous passes, after that the deposited weld layer is removed.

Both techniques involve removal of the upper passes and they are employed to avoid PWHT, to reduce or eliminate residual stresses, to avoid hydrogen cracking, to improve fracture toughness and to reduce welding cost and time [24].

For the aeronautic sector, in accordance with IIS/IW – 956-87 Doc [25], when repairing a weld seam in critical aeronautic components is requested that the defect is also located and removed. The removal process should be always carried out from the side that propitiates the smallest weld material loss. Soon after, to maintain the uniformity of the deposited metal along the weld seam, the repair is applied [25].

However, the weld bead removal can be uneconomical, impracticable or even impossible in certain engineering applications due to urgency or emergency, difficult access to the component or appropriate equipments. As a consequence, along the useful life of the aircraft many non-standardized weld repairs are carried out by putting upon several weld bead, without removal of the previous pass. The subject to be answered up is whether or not the weld repairs are a viable and effective procedure, capable of extending the in-service life of components and structures. At present, due to the increase of residual stresses, the distortion in the geometry and deterioration of the microstructure caused by the thermal cycles, the effectiveness of the weld repairs on cracked structures is not well understood and investigated. Differently to the considerable data volume on the effects of original weld on fatigue life for steels and aluminum from the literature, data on welds repairs are scarce. In this context, the availability of experimental data on weld repair effects on the fatigue behavior may be very useful in determining inspection intervals in high-responsibility welded structures.

## 2. Material and methods

### 2.1. Material

For the present research-work flat welded specimens from hot-rolled AISI 4130 aeronautic steel, 1.10 mm and 1.60 mm thick, were used. The chemical compositions (wt%), from the base-material and from the weld (filler) metal, are presented in Table 1 (Fe in balance). The mechanical properties obtained from smooth flat samples and original welded specimens (OR) – with central weld seam crossed to the hot-rolled plate direction –, are indicated in Table 2. The hot-rolled plates presented 65 HR<sub>A</sub> in the “as-received” condition.

The monotonic tensile tests were performed in accordance with ASTM E 8 M by means of a servo-hydraulic INSTRON test machine, applying 0.5 mm/min displacement rate and a preload equal to 0.1 kN.

### 2.2. Welding and re-welding procedures

The most commonly employed welding process for manufacturing of aeronautical structures is tungsten inert gas (TIG), or gas tungsten arc welding (GTAW), which is appropriate to weld thin thickness materials and to allow the necessary variable control, resulting in high-quality and defect-free weld beads. The TIG welding process was carried out in accordance with the Brazilian Aeronautic Industry – EMBRAER NE 40-056 TYPE 1 – Standard (for components critical to the flight-safety), with a protective 99.95% purity argon-gas and filler metal AMS 6457 B – Turballoy 4130. A Square Wave TIG 355 – Lincoln equipment was manually employed by an expert aeronautic welder. All the welding parameters were controlled, and the main ones are indicated in Table 3. Also, all the welded joints were subjected to X-ray non-destructive analysis by the Brazilian Aerospace Technical Centre (CTA/IFI), which proved the acceptable quality of the welds, according to MIL-STD-453, EMBRAER – NE-57-002 and ASTM E-390 standards.

The welding direction was always perpendicular to hot-rolling process (direction) of the plate. Before welding, samples were cleaned with chlorinated solvent to oxide removal and fixed on a backing bar, to avoid contamination and porosity in the weld root. After the welding/re-welding process neither subsequent heat treatment to residual stresses relief nor subsequent removal of the weld bead was carried out, in order to simulate the real condition of the original aeronautic structure. Due to the plate thickness,

only one weld single-pass was required. For re-welding process, a manual grinding machine capable to reach 22,000 rpm was used to remove the previous weld metal. The heat-input applied was kept constant for all the welded and re-welded specimens.

### 2.3. Corrosion process

To analyze the effects of the corrosive process on the fatigue behavior of AISI 4130 steel, specimens were submitted to atmospheric corrosion (urban environment), accelerated by means of constant wetting during thirty days. Periodically, the specimens were moved so that all the surfaces were uniformly corroded.

### 2.4. Reverse bending fatigue tests

For experimental bending fatigue tests, welded and non-welded flat specimens were manufactured according to SCHENCK model PWS requirements (Fig. 2), following the LT direction of the hot-rolled plate. The specimens were fatigue tested upon a sinusoidal load, constant amplitude, load ratio  $R = -1$ , at 30 Hz frequency and room temperature. The superficial average roughness, obtained by means of a Mitutoyo 301 equipment, with cut-off equal to 0.8 mm × 5 mm, was  $R_a = 0.24 \mu\text{m} \pm 0.16 \mu\text{m}$ .

### 2.5. Microstructural and microhardness analyses

For microstructural analysis, a Nital 2% chemical etching was applied during 5 s. Vickers microhardness measurements were obtained at 0.0254 mm intervals throughout the regions under analysis (base-material, HAZ regions and weld metal), applying a 1 N load.

**Table 3**  
TIG welding parameters.

Direct current	DCEN
Welding position	Flat
Welding voltage	12 V
Welding current	30 A
Welding average speed	19.0 cm min <sup>-1</sup>
Pre heating	NONE
Flow rate	4–12 L min <sup>-1</sup>
Theoretical heat input	1.2 kJ cm <sup>-1</sup>
Filler metal diameter	1.6 mm

**Table 1**  
Chemical compositions (wt%).

Composition (wt%)	C	Mn	P <sub>max</sub>	S <sub>max</sub>	Si	Mo	Cr	Cu
Specified BM <sup>a</sup>	0.28–0.33	0.40–0.60	0.035	0.040	0.15–0.30	0.15–0.25	0.80–1.10	0.10
Specified WMB <sup>b</sup>	0.28–0.33	0.40–0.60	0.008	0.008	0.15–0.35	0.15–0.25	0.80–1.10	0.10
Weld (filler) metal	0.30	0.50	0.004	0.003	0.25	0.18	0.91	0.042
Plate #1.10 thick	0.33	0.53	0.010	0.003	0.28	0.17	1.04	0.02
Plate #1.60 thick	0.28	0.49	0.009	0.004	0.24	0.18	0.93	0.02

<sup>a</sup> AMS 6457 B – turballoy 4130 steel.

<sup>b</sup> AMS T 6736 A (2003) – for chromium–molybdenum (4130) seamless and welded steel tubing of aircraft quality.

**Table 2**  
Mechanical properties obtained from the welded and non-welded specimens.

Specimens	Yielding (0.2% offset)	Ultimate strength	Rupture stress	Elongation (25 mm length)	Yielding/ultimate strength ratio
Base-metal	746 ± 21	843 ± 9	655 ± 26	9.80 ± 1.87	0.88 ± 0.02
Welded	671 ± 20	778 ± 17	643 ± 26	3.81 ± 0.26	0.86 ± 0.01

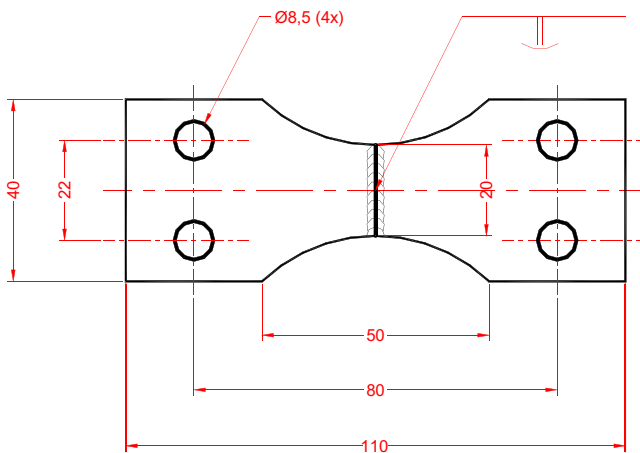


Fig. 2. Flat bending fatigue specimen (mm).

### 2.6. Residual stresses determination

The residual stresses field induced by welding and re-welding processes was determined by X-ray diffraction method, using the Raystress equipment (whose features are described in [26]) with couple exhibition,  $\varphi$  goniometer geometer, two anodes of chrome Cr- $\kappa$  radiation and registration of {2 2 1} diffraction lines, tension source of 25 kV, current of 1.5 mA, X-ray convergence angle of 50°. The accuracy of the stress measurements was  $\Delta\sigma = \pm 20$  MPa. In order to obtain the stress distribution by depth, the layers of specimens were removed by electrolytic polishing with a non-acid solution.

## 3. Results and discussion

### 3.1. Monotonic tests

First of all, it is important to pay attention to the high mechanical strength values and reasonable ductility from the hot-rolled AISI 4130 steel plate (as presented in index 2.1). It is also interesting to observe the decrease of all that mechanical properties after the first TIG welding application on AISI 4130 steel specimens, particularly the elongation (3.8% average), typical of fragile material. However, for both welded and non-welded conditions the yield tensile stress/maximum tensile stress ratio ( $\sigma_y/\sigma_m$ ) was around 0.8, which is an appropriate value for structures as the aeronautical ones [27]. Historically, values from 0.80 to 0.86 have been considered appropriate for specification, project and analysis of structural

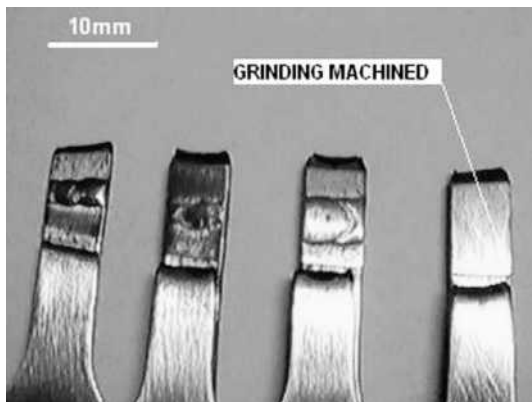


Fig. 3. Specimens fractured by monotonic tension tests.

integrity, by providing high capacity of plastic deformation and consequent margin of safety against fracture [27]. Yet, all the monotonic specimens tested, including those grinding machined, fractured at the sub-critical HAZ (SCHAZ)/base-material interface (strength-overmatch), despite any stress concentration originated at the weld toe, as illustrated in Fig. 3. This means that the influence of the microstructural variations along HAZ is more deleterious for tensile strength than the geometric features induced by the welding process. That is, for the monotonic test the material was not sensitive to stress concentration at the weld toe.

### 3.2. Reverse bending fatigue tests

#### 3.2.1. Effect of the corrosion process

Fig. 4 presents the SN (stress vs. number of cycles) curves for corroded and non-corroded AISI 4130 steel specimens. For seek of comparison with the welded specimen, it was added the fatigue curve obtained with base-material specimens (BM) 1.10 mm thick. Considering that for all the specimens just the thickness was altered (1.60–1.10 mm), it is possible to verify that the higher the thickness the lower the fatigue strength. It is in accordance with Murakami [28,29], who mentions that the larger specimens the higher amount of existent defects. Makkonen [30] also mentions that there is a great amount of microcracks previously nucleated in specimens submitted to cyclic loads, whose population increases when their dimensions increase.

From Fig. 4 it is also possible to verify that the fatigue curves diverge in the short fatigue life range/SFL ( $< 10^5$  cycles). This is due to the maximum stress at the surface, as a function of the type of fatigue test. That is, for reverse bending fatigue tests also in SFL the specimens are sensitive to fatigue-notch effect,  $K_f$ , which is defined as the ratio of the fatigue strength of a smooth specimen to the fatigue strength of a notched specimen at the same number of cycles.

It is also possible to observe in Fig. 4 the detrimental effect of the corrosive process on the reverse bending fatigue strength of the AISI 4130 steel. Thus, for 359 MPa and 303 MPa stress levels, the respective numbers of cycles were about  $1.10 \times 10^5$  and  $1.90 \times 10^5$ , corresponding to 300% and 500% reduction in comparison to those non-corroded. It is well known that the fatigue behavior of any mechanical component is sensitive to its surface finishing. Thus, since there was not simultaneity between the fatigue and corrosion processes (when the anodic condition at the

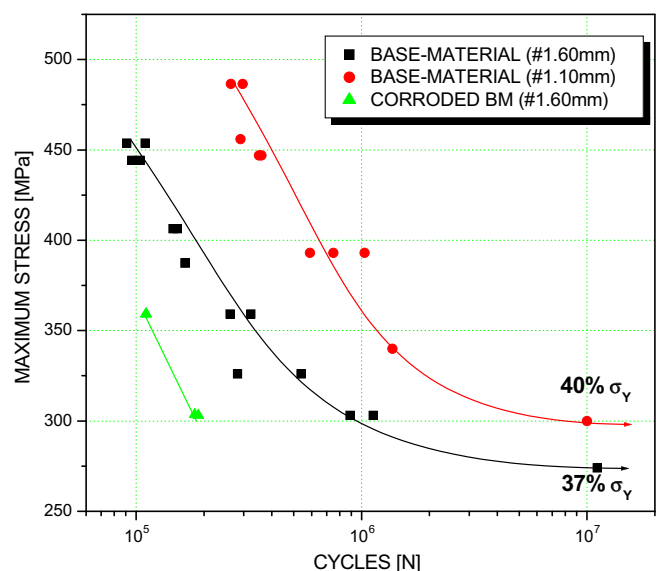


Fig. 4. SN curves for corroded and non-corroded specimens of base-material.

crack tip accelerates the corrosive process and vice versa), the main factor controlling the fatigue behavior presented is related to surface roughness of the specimens tested. In fact, the average surface roughness measured provided  $R_a = 0.24 \mu\text{m} \pm 0.16 \mu\text{m}$  for non-corroded specimens and  $R_a = 1.95 \mu\text{m} \pm 0.18 \mu\text{m}$  for those corroded. The corrosive process generated a Grant No. of pits, which gave rise to local stress concentration and reduced the number of cycles for crack nucleation. Additionally, the local stress concentration can also reduce the stress intensity factor threshold ( $\Delta K_{th}$ ) and allows that the small cracks grow [10–12]. Therefore, it is necessary to protect the surface of aeronautic structures against the aggressive environment acting on an aircraft.

### 3.2.2. Effect of the TIG welding/re-welding process

Fig. 5 presents the SN curves of welded and re-welded specimens. The horizontal line indicates the nominal stress value ( $\sigma_n \approx 247 \text{ MPa}$ ), which corresponds to yielding stress divided by the safety-factor equal to 3 (for welded components critical to the flight-safety), in accordance with the EMBRAER NE 40–056 TYPE 1 Standard.

From Fig. 5, one can observe the significant decreasing in bending fatigue strength of the AISI 4130 steel, whose endurance limit was about 37% of its yielding stress ( $\sigma_y$ ). However, the endurance limit is still above the nominal stress,  $\sigma_n$  (horizontal line). Nevertheless, a subsequent reduction in bending fatigue strength for welded specimens is observed in comparison with the base-material specimens (BM), mainly in the short fatigue life (SFL) range. In the long fatigue life (LFL) range, it is possible to verify that the endurance limit is located close to the horizontal line, corresponding to specified nominal stress ( $\sigma_n$ ). On the other hand, with the first weld repair (1R), no-subsequent reduction in bending fatigue strength is observed. For both original (OR) and first time re-welded (1R) specimens, one can observe practically the same fatigue behavior. However, the second weld repair (2R) resulted in a decreasing of the fatigue strength, with the endurance limit below the nominal stress value,  $\sigma_n$  (horizontal line). Since the aircrafts are submitted to high fatigue cycles during flight, as a result of abrupt maneuvers, wind bursts, motor vibration and helixes efforts, it is not recommended or favorable to the flight-safety the second weld repair (2R) application. This behavior is also due to the increase in volume of the weld bead with consequent increase of the stress concentration factor at the weld toe. In addition, the re-welding process can increase the HAZ dimensions and its coarse-grain re-

**Table 4**  
Vickers microhardness values (HV).

Microstructure	Original weld	one-repair	two-repairs
Base-material	$267.7 \pm 16.4$	$285.5 \pm 15.8$	$286.5 \pm 19.7$
CGHAZ	$362.9 \pm 55.7$	$373.4 \pm 22.8$	$477.80 \pm 59.15$
Weld metal	$573.2 \pm 69.8$	$507.5 \pm 47.4$	$399.9 \pm 22.8$

gion (CGHAZ), which is located exactly at the weld toe and characterized by low fracture toughness and considerable hardness (as can be verified in Table 4).

From Fig. 5, it is also possible to verify the larger scattering of the fatigue results obtained with both welded and re-welded specimens. This is due to volume variations of the deposited weld metal, the higher heating/cooling rate and the uneven stress concentration values at the weld toe notch. Fig. 5 also shows that the fatigue strength reduction due to welding process tends to be more pronounced when the number of cycles is also reduced (divergence between BM and OR fatigue curves in SFL). This observation is very important taking into account the efforts due to landing operations (typical for SFL regime) along the operational life of the aircraft. On the other hand, it is observed that the divergence between both endurance limits ( $10^7$  cycles) was low, i.e.: from 37%  $\sigma_y$  for base-material to 32%  $\sigma_y$  after welding (close to  $\sigma_n$ ). In the same way, this is a very important result, taking into account the abrupt maneuvers or wind bursts during flight (typical for LFL regime). This implicates that special cares should be adopted during design and, particularly, maintenance of welded aeronautical structures against any accidental tool marks capable to introduce local stress concentration on the structure. Since for bending loads the maximum stress occurs at the surface, the fatigue resistance is sensitive to any geometric change of material (notch-sensitivity).

From Fig. 5, comparing the first (1R) and second weld repairs (2R) fatigue curves in the SFL ( $<10^5$  cycles) regime, one can observe that the reduction was minimum, with both curves converging to a same point in high stress levels (SFL). On the other hand, one can also observe high divergence between the aforementioned curves in LFL regime, reaching a maximum at the endurance limit level ( $10^7$  cycles). Since the material is notch-sensitive in LFL, such a behavior was due to the abrupt geometric change generated by the weld bead in addition to the microstructural alterations induced by the new cooling rate. On the other hand, comparatively to the fatigue behavior of base-material (BM), as in SFL as LFL (endurance limit) regimes the tendency of the second weld repair (2R) fatigue curve shows practically the same fatigue-notch sensitivity [ $q = (K_f - 1)/(K_t - 1)$ ], or fatigue-notch factor,  $K_f$  (Eq. (1) [32]). This observation becomes evident considering the parallelism presented by both base-material (BM) and two weld repairs (2R) fatigue curves. In fact, the fatigue-notch factor values ( $K_f$ ) in  $10^7$ ,  $10^6$  and  $2.8 \times 10^5$  cycles were: 2.00, 2.15 and 2.07, respectively, which confirms the mentioned parallelism. Since the welding repair procedure applied was by removing the previous weld bead, the geometric alteration was hoped to be low (as can be seen in Table 5 ahead). Thus, the increase of the notch sensitivity (fatigue-notch factor) with the second weld repair (2R) was also due to the microstructural variations resulting of successive heating/cooling cycles imposed to the material. Therefore, based on the results obtained and considering that the welding repair is necessary, it can be admitted only one weld repair (1R) during fabrication of the critical to the flight-safety structures, without compromising their reverse bending fatigue strength. On the other hand, being necessary to make some subsequent repair along the operational life, this study indicates that cares should be adopted in the sense of avoiding abrupt maneuvers and/or overloads on the aircraft. In

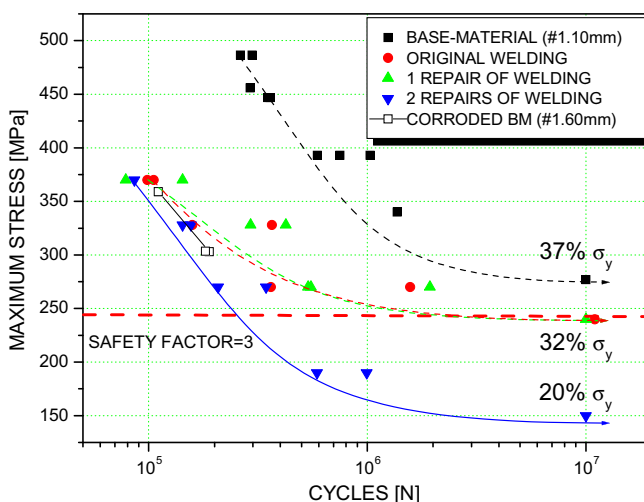


Fig. 5. Reverse bending fatigue SN curves for base-material and (re-)welded specimens (1.10 mm thick).

**Table 5**

Geometry factor values from the weld bead (in accordance with Fig. 6).

Group	W (mm)	T (mm)	Root (mm)	Angle ( $\alpha$ )	Radius (mm)	HAZ (mm)	$K_f$ (Eq. (1))
OR	$3.75 \pm 0.35$	$0.89 \pm 0.20$	$0.77 \pm 0.19$	$141.9^\circ \pm 14.4^\circ$	$1.03 \pm 0.36$	$2.89 \pm 0.25$	1.290
1R	$4.49 \pm 0.33$	$1.17 \pm 0.32$	$0.82 \pm 0.27$	$146.1^\circ \pm 8.6^\circ$	$0.75 \pm 0.21$	$3.11 \pm 0.12$	1.305
2R	$4.80 \pm 0.23$	$0.96 \pm 0.20$	$0.79 \pm 0.30$	$138.6^\circ \pm 7.5^\circ$	$0.93 \pm 0.40$	$3.22 \pm 0.23$	2.178

$$K_f = 1 + \frac{K_t - 1}{1+a/r}$$

where:  $a = 0.1659$  (Peterson's material parameter for steel);  $r$  = notch-root;  $K_f$  = fatigue-notch factor.

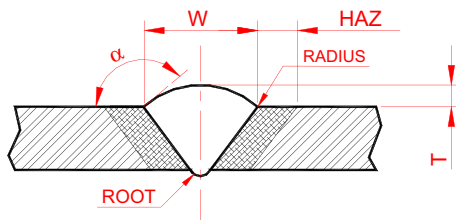


Fig. 6. Geometry factors of the welded joints (values presented in Table 5).

addition, it becomes necessary lower inspection intervals for flaws as-crack determination at the weld joints of structural components.

Finally, although it is not appropriate to directly compare both fatigue behaviors of welded specimens with those corroded due to their different thickness, it is interesting to observe the similar deleterious effect caused by the corrosive process on the fatigue strength of AISI 4130 steel.

Table 4 presents the microhardness values measured in the three interest areas. Firstly, one can observe the high microhardness values for weld metal and CGHAZ as a consequence of TIG welding and re-welding process. This is due to high cooling speed associate to the low heat-input applied, which resulted in martensitic structures. Since the heat input was kept constant for all the (re-)welding process, it is important to mention that just the weld reinforcement was removed. Consequently, the different microhardness values verified were due to remaining weld material volumes (e.g. weld root), which unevenly affected the cooling speed of the weld metal. Thus, from Table 4, one can observe that for both the original weld (OR) and the first welding repair (1R) the microhardness values were close and coherent with each other. This can explains the bending fatigue behavior presented in Fig. 5. However, it is also important to pay attention to the great dispersion of microhardness results in both CGHAZ and weld metal (standard-deviation). It is also possible to observe the highest microhardness value from the original weld metal than for all the other conditions. This implicate that probably the second welding repair promoted the tempering of the previous microstructure, but with no improvement on their bending fatigue strength, as verified in Fig. 5. After the second welding repair it is also possible to observe higher microhardness value for the CGHAZ, implicating a grain size reduction in that region, but again with no improvement on the bending fatigue strength, as illustrate in Fig. 5. It is well known that the lower the grain size the higher the material toughness. In the same way, the higher the grain size, the lower the hardness/mechanical strength.

Considering that the weld profile affects the fatigue resistance of a welded structure, Table 5 and Fig. 6 present the main geometric factors that compose a weld joint and their corresponding values, obtained by image analysis tools. Thus, from Table 5 and Fig. 6, it is possible to confirm all the results presented in Fig. 5 on the effect of welding repairs on the bending fatigue behavior of AISI 4130 steel. Therefore, it can be observed that the welding repairs reduced both angle ( $\alpha$ ) and radius at the weld toe notch that, com-

bined, are considered the main geometric factors controlling the fatigue behavior of welded components and structures [13,31]. In addition, the great scattering on the geometric factors measured is in consonance with the great scattering of the fatigue results presented by the welded specimen groups. Yet, from Table 5, we can observe: the increase of the stress concentration factor ( $K_f$ ) at the weld toe notch with the successive welding repairs; the largest extension of HAZ due to the successive heat-input applied and, consequently, the increase of the CGHAZ as well; the effect of both weld reinforcement ( $T$ ) and weld root dimensions, again, on the angle ( $\alpha$ ) and radius reduction and, consequently, on the bending fatigue strength of welded specimens. On this subject, it is important

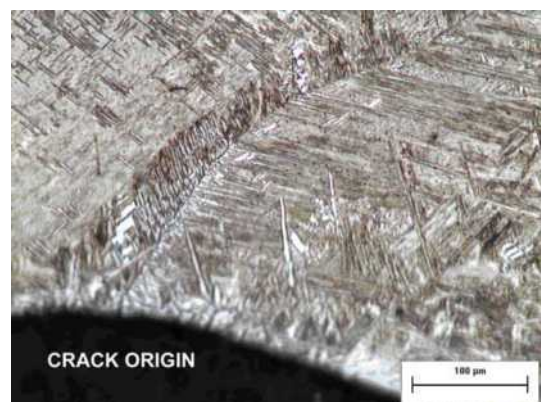


Fig. 7. Crack initiation at the weld toe of a non-fractured fatigue specimen (500×). Nital 2%.

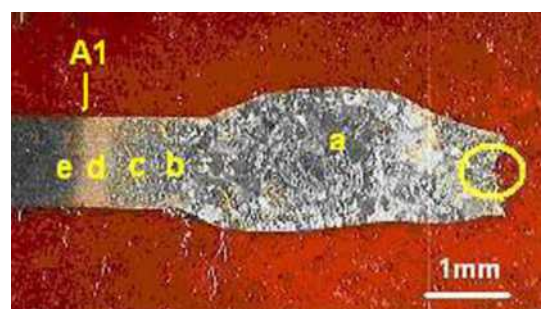
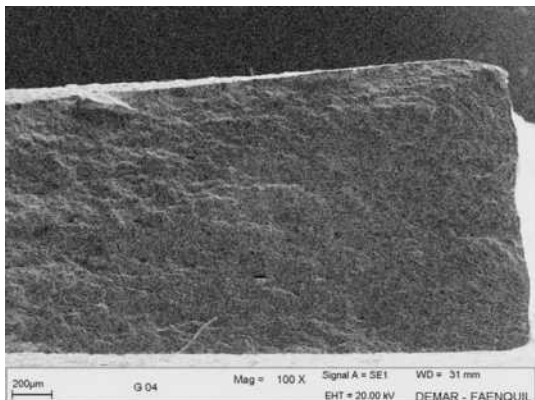


Fig. 8. Macrography of a fatigue specimen fractured by reverse bending loads. Nital 2%.



Fig. 9. Secondary crack propagation from the fracture surface of a reverse bending fatigue specimen (500×). Nital 2%.



**Fig. 10.** Edge fatigue crack origin and propagation for a fractured specimen of base-material, 1.60 mm thick.

to mention that all the welded specimens fractured at the weld toe notch, as illustrated in Figs. 7 and 8. In fact, Fig. 7 illustrates a crack in a non-fractured specimen, which initiated at the weld toe notch and propagated through grain boundary into weld metal (intergranular crack).

Fig. 8 presents the macrography of a fractured specimen that was submitted to two welding repairs (2R), in which we can observe: (a) the weld metal region with well delineated equiaxial coarse-grains; the HAZ extension with the sub-regions, (b) coarse-grain/CGHAZ, (c) fine-grain/FGHAZ, (d) inter-critical/ICHAZ and (e) sub-critical/SCHAZ near to  $A_1$  line (lower critical tempera-

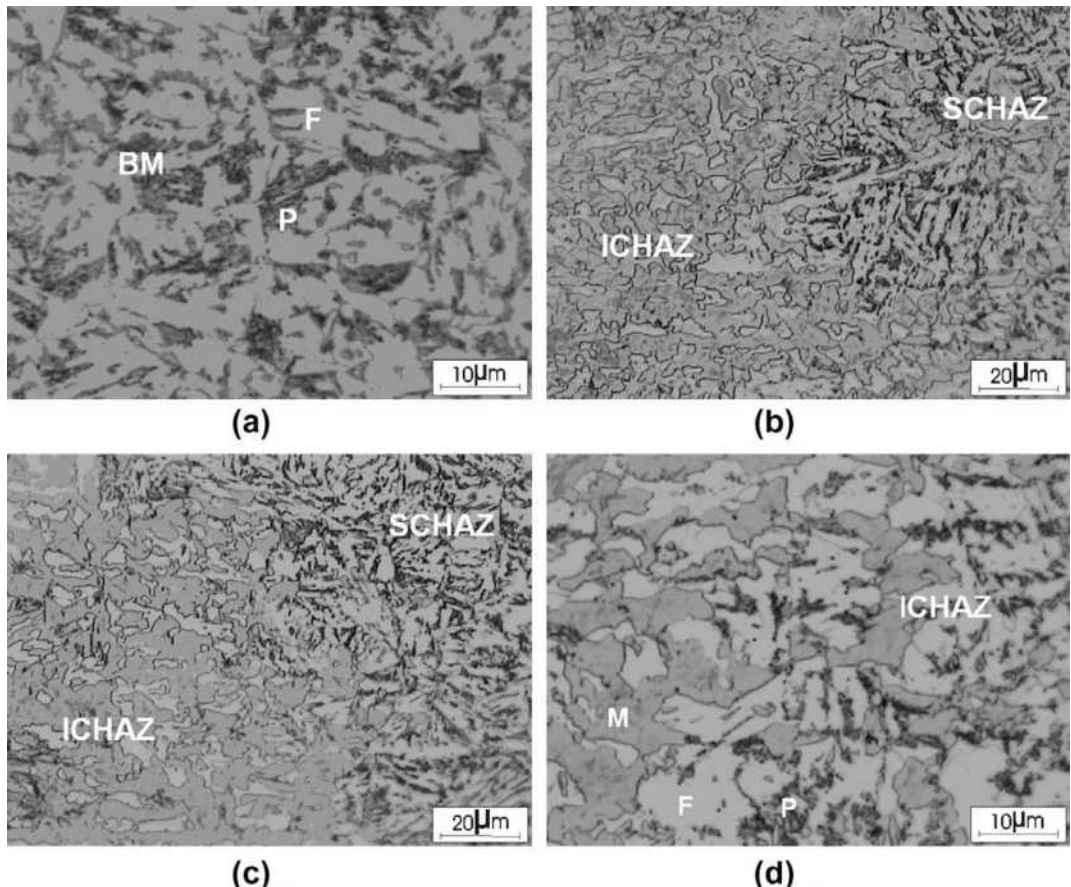
ture); as well as the welded joint irregularity as a consequence of the deformation generated by the reverse bending loads applied.

Fig. 9 presents the transgranular secondary crack, originate from the fracture surface of the specimen in Fig. 8. This secondary crack implicates that the reverse bending fatigue specimens may have been subjected to either Modes I and II or Modes I and III of loading combination (or all of them), turning the laboratorial test more severe due to friction process by both free crack surfaces, accelerating its propagation. In fact, bending loads also introduce shear stresses in the specimens (Mode II of fracture) and/or tearing stress (Mode III of fracture) whether crack initiation occurs at the edge of the specimen, as illustrated in Fig. 10. On this subject, Veidt [33] mentions that the radius in the notch root has little effect on the stress intensity factor in Mode II of fracture.

Figs. 11 and 12 present the base-material, HAZ and weld metal microstructures for all the proposed conditions. Fig. 11a shows the normal products of transformation from austenite, i.e. ferrite and perlite. From Fig. 11b-d the beginning of the transformation from perlite to austenite is observed (to martensite, upon subsequent cooling) along the SCHAZ/ICHAZ regions ( $A_1$  line).

Fig. 12 presents the microconstituent of the weld metal (original, one and two weld repairs) and respectives CGHAZ, basically constituted by martensite, which is a very hard and fragile microstructure. As aforementioned, the higher the hardness the higher the resistance to fatigue crack initiation.

Fig. 13 presents the residual stresses field in the weld metal, HAZ and base-material of all the conditions analyzed. It is well known that residual stresses are present in welded components [22,34–36] and have great effect on fatigue crack nucleation and propagation [34]. Thus, from Fig. 13, one can observe that the



**Fig. 11.** Base-material and base-material/HAZ transition microstructures: (a) Base-material (typical); (b) SCHAZ-ICHAZ of the original weld; (c) SCHAZ-ICHAZ of the first welding repair; and (d) ICHAZ of the second welding repair. Nital 2%. (F = Ferrite; P = Perlite; M = Martensite).

TIG (re-)welding process induced high compressive residual stresses for all conditions upon analysis, as weld metal as in HAZ and base-material (up to 20 mm from the fusion line). Such residual stresses were relieved internally in some point along the length of the specimens, because no deformation was verified on the samples. Yet, it is observed that all the residual stress profiles presented similar tendency, i.e., maximum values in weld metal ( $-600$  MPa for original weld;  $-450$  MPa for one weld repair and  $-330$  MPa for two weld repairs), followed by HAZ ( $-400$  MPa for original weld;  $-75$  MPa for one weld repair and  $-50$  MPa for two weld repairs) and last base-material up to 20 mm far-away from the fusion line ( $-300$  MPa for original welding;  $-160$  MPa for one weld repair and  $-100$  MPa for two weld repairs).

Many factors might have contributed to compressive residual stresses induced by the TIG (re-) welding process, viz: (i) austenite-martensite transformation (which generate up to 4% increase in volume of material) and which initiate at the surface due to higher cooling speed; (ii) the thin thickness and good mechanical properties in high temperature of the base-material, particularly low deformation in high temperature; (iii) subsequent contraction in the core of the weld metal (after the martensitic transformation at the surface) due to relatively lower cooling speed in that region; (iv) constraint to natural expansion of the weld metal and HAZ by the base-material volume around; and (v) the clamps applied at the extremities of the specimens during the (re-)welding process, etc. However, some aspects get the attention from the Fig. 13 as:

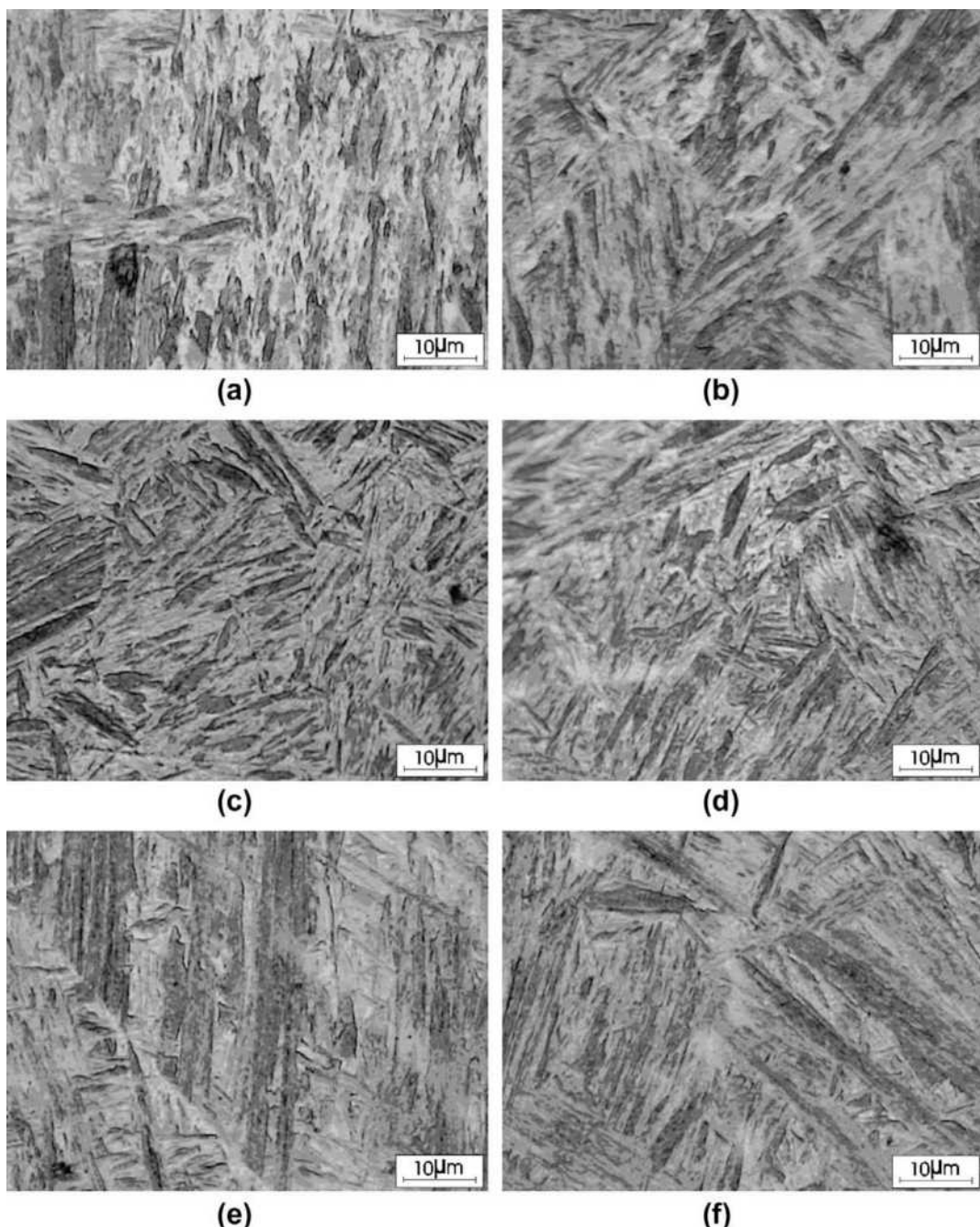


**Fig. 12.** Microscopic analysis of the weld metal and CGHAZ: (a) original CGHAZ; (b) original weld metal; (c) CGHAZ of the first welding repair; (d) weld metal of the first welding repair; (e) CGHAZ of the second welding repair; and (f) weld metal of the second welding repair. Nital 2%.

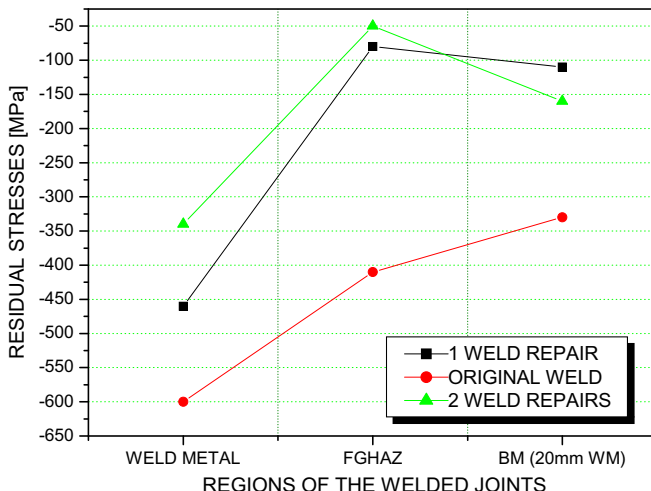


Fig. 13. Residual stress profiles of all the conditions tested.

the high values of compressive residual stresses, which were higher in the weld metal than HAZ; all the compressive stress fields were still compressive up to 20 mm distance from weld fusion line.

It is well known that the residual stresses largely affect the fatigue behavior of components, and that compressive residual stresses are benefit towards inhibit the crack nucleation. Thus, the results presented in Fig. 13 are in accordance with the fatigue behavior of specimens with original weld (OR), as well as those with one (1R) and two (2R) weld repairs presented in Fig. 5. In addition: the higher the hardness, the higher the fatigue strength as well. Consequently, from Table 4 and Fig. 5, it could be observed better fatigue behavior for the originally welded (OR) specimens in comparison with the one (1R) weld repair condition. However, considering the fatigue crack propagation stage, it is well known that the increase of the hardness increases the propagation rate ( $da/dN$ ). In this context, the existence of compressive residual stresses highlight the stress concentration effect induced by the weld geometry on the fatigue strength reduction verified. That is, although a mechanical component possess high compressive residual stresses, their effects or benefits will be minimized (or annulled in case the stress relief) when this component presents a stress concentrator (geometric factor) that reduces the number of cycles necessary to fatigue crack initiation. Thus, it is possible that the geometric stress concentration factor, which is located at the weld toe/fusion line/CGHAZ region, overcomes the compressive residual stress field induced by the (re-)welding process, relief it. Certainly, the compressive residual stresses field as far as possible delayed the fatigue crack nucleation and propagation by reducing the stress intensity factor ( $\Delta K$ ), as mentioned by Wei & Chen [34].

#### 4. Conclusions

Motivated by high fracture incidence at welded joints of a specific and critical to the flight-safety component, called “motor-craddle”, experimental reverse bending fatigue tests on welded and re-welded specimens were carried out. Based on the results obtained, the following conclusions may be drawn:

1. The AISI 4130 steel possess good mechanical properties, but low elongation in the “as-received” condition (not heat-treated).
2. All the monotonic specimens tested, including those grinding machined, fractured at the sub-critical HAZ (SCHAZ)/base-material interface (strength-overmatch), despite any stress concentration originated at the weld toe.

3. The reverse bending loads significantly decrease the fatigue strength of the AISI 4130 steel, whose endurance limit were about 37% and 40% of the yielding stress ( $\sigma_y$ ) for specimens 1.60 mm and 1.10 mm thick, respectively.
4. The corrosive process strongly reduced the reverse bending fatigue strength of AISI 4130 steel.
5. In comparison with specimens from the base-material a reduction in bending fatigue strength for TIG welded specimens (OR) was observed. After the first weld repair (1R), no-subsequent reduction in bending fatigue strength was observed in comparison with the original weld. The second weld repair (2R) again resulted in decreasing of the fatigue strength in comparison with that subjected to the first weld repair. Consequently, it is not recommended or favorable to the flight-safety the second weld repair (2R) on critical to the flight-safety components.
6. The TIG (re-)welding procedure induced high compressive residual stress values in the AISI 4130 steel.
7. It was verified increase of the stress concentration factor,  $K_t$ , at the weld toe with the successive welding repairs, which overcomes the compressive residual stress field induced by the (re-)welding process. As a result, all the welded fatigue specimens fractured at that region.

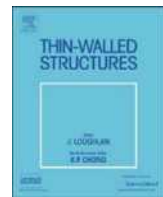
#### Acknowledgement

The authors are grateful to FAPESP/Process No. 99/11948-6, CNPq and FUNDUNESP.

#### References

- [1] Flight Safety Foundation – Available from <<http://www.flightsafety.org>>; 2009 [accessed 10.2009].
- [2] National Civil Aviation Agency – Brazil. Available from <<http://www.anac.gov.br>>; 2004 [accessed 10.2003].
- [3] Godefroid LB. Fatigue crack growth under constant and variable amplitude loading in aluminium alloys of aeronautical applications. Ph.D. Thesis, COPPE/UFRJ, Brazil: Federal University of Rio de Janeiro; 1993.
- [4] Goranson UG. Fatigue issues in aircraft maintenance and repairs. Int J Fatigue 1993;19:S3–S21.
- [5] Payne AO. The fatigue of aircraft structures. Eng Fract Mech 1976;8:157–203.
- [6] Wenner CA, Drury CG. Analysing human error in aircraft ground damage incidents. Int J Ind Ergonom 2000;26:177–99.
- [7] Latorella KA, Prabhu PV. A review of human error in aviation maintenance and inspection. Int J Ind Ergonom 2000;26:133–61.
- [8] Bhaumik SK, Sujata M, Venkataswamy MA. Fatigue failure of aircraft components. Eng Fail Anal 2008;15:675–94.
- [9] Carpenter M. Managing the fleet: materials degradation and its effect on aging aircraft. Amptiac, News Lett 2001;4(5):7–19.
- [10] DOT/FAA/AR-00/22. US Department of Transportation, Federal Aviation Administration, Corrosion and Corrosion Fatigue of Airframe Materials, final report, July 2002. 2002. 79p.
- [11] Wang QY, Kawagoishi N, Chen Q. Effect of pitting corrosion on very high cycle fatigue behavior. Scripta Mater 2003;49:711–6.
- [12] Murtaza G, Akid R. Corrosion fatigue short crack growth behaviour in a high strength steel. Int J Fatigue 1996;18:557–66.
- [13] Nascimento MP. Effects of TIG welding repair on the structural integrity of AISI 4130 aeronautical steel. In: Ph.D. Thesis in mechanical engineering. State University of São Paulo/UNESP-FEG, Brazil (in Portuguese); Code CDU 620.92, 2004. 240p.
- [14] Nascimento MP, Voorwald HJC. An evaluation on the fatigue crack growth in re-welded AISI 4130 aeronautical steel. In: Eighth international fatigue congress/FATIGUE 2002, vol. 5, Stockholm-Sweden; 2002. p. 3463–72.
- [15] Nascimento MP, Ribeiro RB, Voorwald HJC. Fatigue crack growth in re-welded AISI 4130 high strength steel. In: Fourteenth European congress on fatigue/ECF 14, vol. 2, Cracow, Poland; 2002. p. 1–3116.
- [16] Vern Sutter, Robert J. Dybas, repair welding. In: ASM International, American Society for Metals, Editors, Metals Handbook, Welding, Brazing and Soldering, vol. 6, Metals Park, Ohio; 2002. p. 1103–7.
- [17] Kroes MJ, Watkins WA, Delp F. Aircraft maintenance and repair. 6th ed. New York: Glencoe – Macmillan/McGraw-Hill; 1993. 648p.
- [18] Vega EO, Hallen JM, Villagomez A, Contreras A. Effect of multiple repairs in girth welds of pipelines on the mechanical properties. Mater Charact 2008;59:1498–507.
- [19] Liming L, Xin Du, Meili Z, Guoqing C. Research on the microstructure and properties of weld repairs in TA15 titanium alloy. Mater Sci Eng A 2007;445–446:691–6.

- [20] Shankar K, Weidong Wu. Effect of welding and weld repair on crack propagation behaviour in aluminium alloy 5083 plates. Mater Des 2002;23:201–8.
- [21] Sun W, Hyde TH, Becker AA, Williams JA. Some key effects on the failure assessment of weld repairs in CrMoV pipelines using continuum damage modeling. Eng Fail Anal 2005;12:839–50.
- [22] Dong P, Hong JK, Bouchard PJ. Analysis of residual stresses at weld repairs. Int J Pres Ves Pip 2005;82:258–69.
- [23] Hyde TH, Sun W, Becker AA, Williams JA. Life prediction of repaired welds in a pressurised CrMoV pipe with incorporation of initial damage. Int J Pres Ves Pip 2004;81:1–12.
- [24] Aloraijer AS, Ibrahim RN, Ghojet J. Eliminating post-weld heat treatment in repair welding by temper bead technique: role bead sequence in metallurgical changes. J Mater Process Technol 2004;153–154:392–400.
- [25] Doc IIS/IIW-956-87. (ex. doc. XV-648-87) prepared by commission XV “fundamentals of design and fabrication for welding” of the IIW, recommendations for repairs and/or strengthening of steel structures. Welding in the world 1988; 26(11/12): 292–306.
- [26] Ivanov SA, Monim VI, Teodósio JR. New method of X-ray tensometry. In: International conference on experimental mechanics. Lisboa; 1994. p. 757–61.
- [27] Bannister AC, Ocejo JR, Gutierrez-Solana F. Implications of the yield stress/tensile stress ratio to the SINTAP failure assessment diagrams for homogeneous materials. Eng Fract Mech 2000;67:547–62.
- [28] Murakami Y. Inclusion rating by statistics of extreme values and its application to fatigue strength prediction and quality control of materials. J Res Nat Inst Stand Technol 1994;4:99–107.
- [29] Murakami Y, Usuki H. Quantitative evaluation of effects of non-metallic inclusions on fatigue strength of high strength steels. II: fatigue limit evaluation based on statistics for extreme values of inclusion size. Int J Fatigue 1989;5(11):299–307.
- [30] Makkonen M. Statistical size effect in the fatigue limit of steel. Int J Fatigue 2001;23:395–402.
- [31] Lancaster JF. Metallurgy of welding. 5th ed. London: Chapman and Hall Incorporation; 1993. 389p.
- [32] Peterson RE. Stress Concentration design factors. 5th ed. New York: John Wiley and Sons Incorporation; 1966 [155p].
- [33] Veidt M. On the Effect of notch radius and local friction on the Mode I and Mode II fracture toughness of a high-strength steel. Eng Fract Mech 1997;58:223–31.
- [34] Wei MY, Chen C. Fatigue crack growth characteristics of laser-hardened 4130 steel. Scripta Metall Mater 1994;10(31):1393–8.
- [35] Brown TB, Dauda TA, Truman CE, Smith DJ, Memhard D, Pfeiffer W. Predictions and measurements of residual stress in repair welds in plates. Int J Pres Ves Pip 2006;83:809–18.
- [36] Chiarelli M, Lanciotti A, Sacchi M. Fatigue resistance of MAG welded steel elements. Int J Fatigue 1999;1:1099–110.



## Experimental study on repair of fatigue cracks at welded web gusset joint using CFRP strips

Hitoshi Nakamura<sup>a,\*</sup>, Wei Jiang<sup>a</sup>, Hiroyuki Suzuki<sup>b</sup>, Ken-ichi Maeda<sup>a</sup>, Takao Irube<sup>c</sup>

<sup>a</sup> Department of Civil and Environmental Engineering, Tokyo Metropolitan University, Japan

<sup>b</sup> Department of Architecture, Meisei University, Japan

<sup>c</sup> TTK Corporation, Japan

### ARTICLE INFO

Available online 9 January 2009

#### Keywords:

Carbon fiber reinforced polymer strip  
Lamination  
Repair  
Fatigue crack  
Welded joint  
Drill-hole

### ABSTRACT

This paper presents repair methods of fatigue cracks using CFRP strips. In particular, the subject of repair is fatigue cracks initiated at **welded web gusset joints**, which are the typical details in steel bridges. Several repair methods were investigated experimentally focusing on weld details. In addition, more effective repair methods were also investigated using combination of CFRP strips and drill-holes. As a result, it was found that **fatigue life after repair was significantly improved**. Therefore, the authors confirmed the feasibility of the proposed technique as a useful repair method to improve fatigue life of steel structures.

© 2008 Elsevier Ltd. All rights reserved.

## 1. Introduction

In recent years, reports of fatigue damage to steel bridges have increased in Japan with the increase of vehicle load and volume of traffic [1]. Since fatigue cracks are often initiating in narrow locations, where some members are crossing each other and have complicated details peculiar to welded joints, it is difficult to repair and reinforce them. CFRP is expected to be a useful material for repairing and reinforcement of existing steel structures [2–4], because of its lightweight, high strength and excellent corrosion resistance. In addition, the joint method for CFRP strips is very simple and is also easy to apply on site. Recently, in order to utilize CFRP effectively, many researches have been done on welded connections and fatigue strengthening [5–9].

The fundamental studies have been performed experimentally and analytically using steel flat plates [10,11], and the validity of crack repair has been verified. Aiming at application to real structures, the examination was started in consideration of the welded detail [12,13]. The subject of repair is fatigue cracks initiated at welded web gusset joints, which are the typical details in steel bridges. Therefore, the authors have proposed the practical construction method using CFRP strips to repair fatigue cracks at welded web gusset joints.

This study examined a more suitable repair method, using specimens with out-of-plane welded gusset joints, and fatigue

tests were carried out with various bonding methods of CFRP strips and varying the number of laminations. The effects of repair and the progress of fatigue cracks after repair were also considered. Moreover, in order to increase the effectiveness of the repair, CFRP strips were used in combination with drill-holes. A drill-hole is a construction method, also called a stop-hole and is generally applied as a temporary repair method on site. Drill-holes are applied to reduce the stress concentration at the tips of cracks. Several combinations of CFRP strips and drill-holes were investigated by static loading tests and fatigue tests.

## 2. Experimental procedure

### 2.1. Specimens and material properties

The specimen is shown in Fig. 1. It was fabricated with gusset plates ( $W100 \times T9 \times L140 \text{ mm}^3$ ) welded to both sides at the center of the steel plate ( $W250 \times T9 \times L1040 \text{ mm}$ ). The mechanical properties of steel, the CFRP strip, and epoxy resin adhesive are shown in Table 1. The CFRP strip is 1.2 mm in thickness. The carbon fiber is arranged unidirectionally.

In addition, in order to investigate the effects of the bonding methods and the laminations on the bond strength, the tensile shear tests were conducted using double-lap adhesive joints. The specimen is shown in Fig. 2. Its width and thickness are 100 and 9 mm, respectively. It was cut off at the dashed line as shown in Fig. 1(a). The fatigue crack was initiated at the weld toe of the web gusset plate.

\* Corresponding author.

E-mail address: [hnaka@tmu.ac.jp](mailto:hnaka@tmu.ac.jp) (H. Nakamura).

## Nomenclature

$K$	initial rigidity in linear relation of load–displacement curve
$\Delta P$	incremental applied load
$\Delta D$	incremental displacement
$\Delta\sigma_n$	nominal stress range of steel plate

$\sigma$	longitudinal stress
$a$	crack length
$D$	crack opening displacement
$N_f$	number of cycles from start of fatigue test to failure
$N_i$	number of cycles from start of fatigue test until the crack length reached 15 or 50 mm
$N_p$	number of cycles from restart after repair to failure

## 2.2. Repair method

Two series of repair methods using CFRP strips are shown in Fig. 3. The cracked specimens were repaired when the crack progressed to a length of approximately 15 mm (it is equivalent to 12% of the overall width) from the center of the specimen to both side edges by cyclic loading test. The repair methods are described as follows.

### 2.2.1. Series S

In series S as shown in Fig. 3(a), four single-layered CFRP strips ( $W25 \times T1.2 \times L100$  mm) were simply bonded to both sides of the weld bead in order to reduce the stress concentration at crack tips.

### 2.2.2. Series M

First of all, in order to improve the bonding surface, the weld bead was finished using a pencil grinder. The multi-layered CFRP strips ( $W50 \times T1.2 \times L200$  mm) with a rectangular slit in the center were bonded close to the weld bead. The single-layered CFRP strip ( $W25 \times T1.2 \times L100$  mm) was bonded on both sides. In series M as shown in Fig. 3(b), the number of laminations was considered. The effective repair is expected by the reduction in the crack opening displacement, since the crack opening is perfectly covered with multi-layered CFRP strips. Fig. 4 shows an example of repair method in series M5 with five layers.

The used adhesive hardens at ordinary temperature, and reaches the required bond strength in a day. The specimens were cured at 40 °C for a week after repair, because of elimination of dispersion caused by the curing condition of the adhesive.

## 3. Adhesion performance of double-lap joints considering gusset details

### 3.1. Experimental series and testing procedure

The experimental series is shown in Table 2. As mentioned above, the repair was performed by the two repair methods as

shown in Fig. 5. In series DL-M, the number of laminations was 1, 3, 5 or 7 layers. In series DL-S, the CFRP strip was single-layered, and its length was changed as 100 and 200 mm. The bonding surface was sandblasted. The shear tensile tests were conducted using the universal testing machine with a capacity of 1000 kN. The loading speed is 5 mm/min by displacement control. As shown in Fig. 5 and Photograph 1, strains on CFRP strips and opening displacements at joints were measured using strain gages and crip-type displacement transducers.

### 3.2. Static loading test results

The relationships between the tensile load  $P$  and the opening displacement  $D$  at the joint is shown in Fig. 6. All the series show nonlinear behavior from the low level of tensile load. In DL-M5 and DL-M7, the tensile load decreased locally at approximately 200 kN because of the yielding in the narrow section of the grip.

In order to compare the rigidity of the adhesion joint, the initial rigidity  $K$  is calculated in the linear relation of the  $P$ - $D$  curve shown in Fig. 6. The initial rigidity  $K$  is defined by the following equation:

$$K = \frac{\Delta P}{\Delta D} \quad (1)$$

where  $\Delta P$  and  $\Delta D$  are the incremental tensile load and the incremental displacement in the range from 20 to 40 kN. Fig. 7 shows the maximum tensile load  $P_{max}$  and the initial rigidity  $K$  of all the series. In series DL-S, maximum tensile load increases a little, so that the length of CFRP strips is long. In series DL-M, the

**Table 1**  
Mechanical properties of steel, CFRP strip and epoxy resin adhesive.

	Steel plate (JIS SM400A)	CFRP strip	Epoxy resin adhesive
Yield point (MPa)	293	–	–
Tensile strength (MPa)	453	2664	30
Elongation (%)	23	1.9	–
Elastic modulus (GPa)	204.5	188	1.5

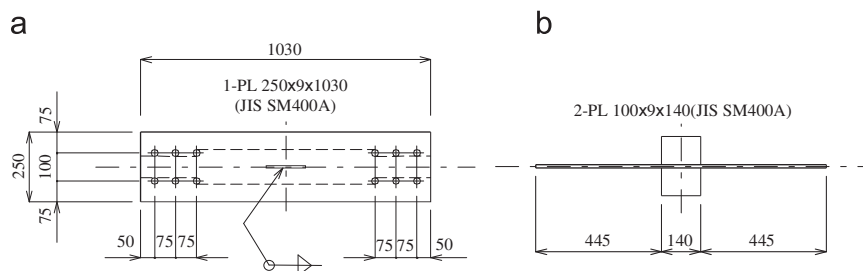


**Fig. 1.** Specimen configuration for fatigue test: (a) plan and (b) elevation.

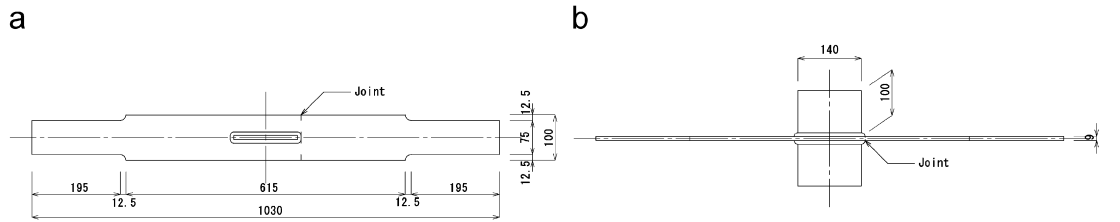


**Fig. 2.** Specimen configuration for double-lap adhesive joints: (a) plan and (b) elevation.

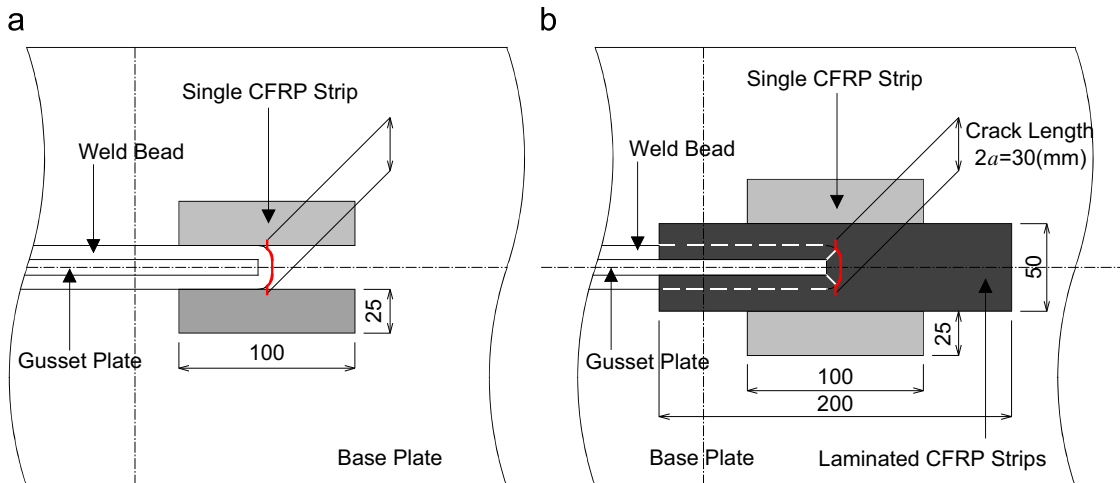


**Fig. 3.** Repair method: (a) series S and (b) series M.

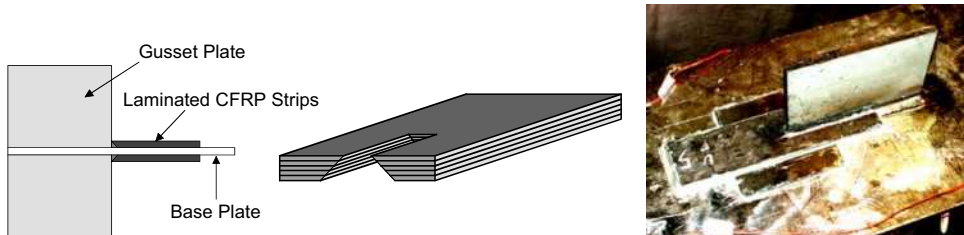
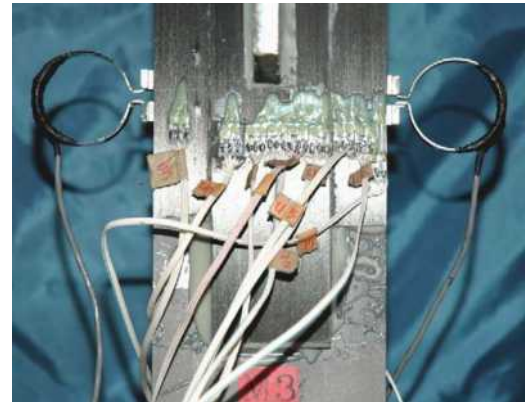


**Fig. 4.** Example of repair method in series M5.

**Table 2**  
Experimental series of double-lap adhesive joints.

Series	Repair method	CFRP strip	
		Single-layered part (mm)	Multi-layered part
DL-S1	Fig. 5(a)	100	–
DL-S2	Fig. 5(a)	200	–
DL-M1	Fig. 5(b)	100	1-layer at 200 mm
DL-M3	Fig. 5(b)	100	3-layer at 200 mm
DL-M5	Fig. 5(b)	100	5-layer at 200 mm
DL-M7	Fig. 5(b)	100	7-layer at 200 mm

maximum tensile load is higher compared with series DL-S, and increasing the number of laminations. Although the initial rigidity  $K$  is equivalent in spite of the length of CFRP strips in series DL-S, it



**Photograph 1.** Test setup of series DL-M3.

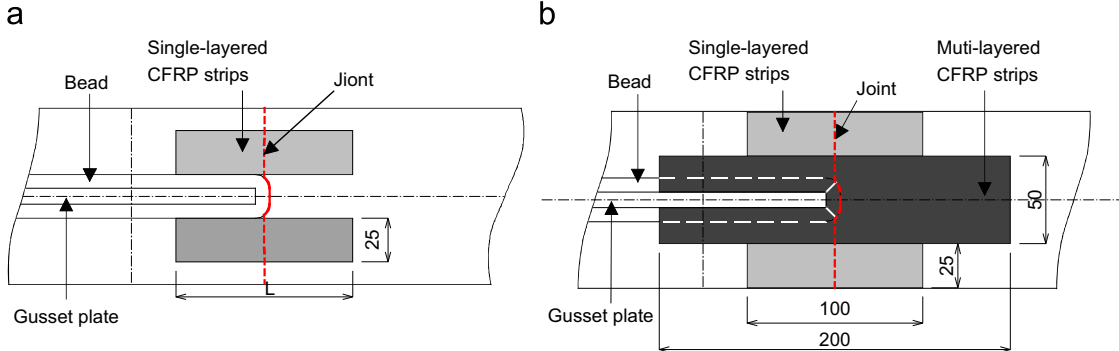


**Fig. 5.** Repair method for double-lap adhesive joints: (a) series DL-S and (b) series DL-M.

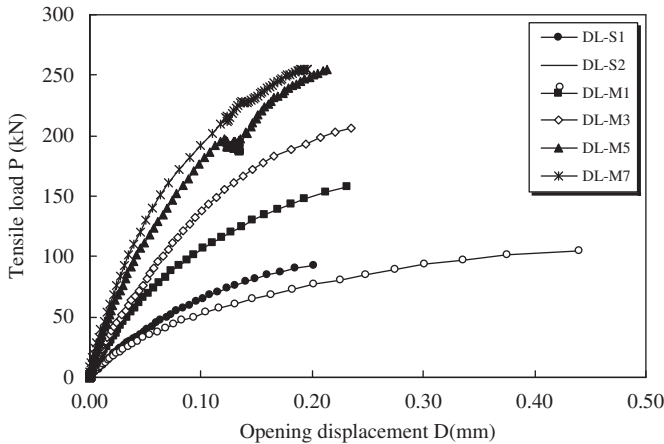


**Fig. 6.** Relationships between tensile load and opening displacements at joint.

is increased with increasing the number of laminations in series DL-M. Since the opening displacement becomes small increasing the initial rigidity, the effective repair can be expected in the case like a crack repair. Consequently, it can be considered that the required number of laminations is five layers regarding upper limits for the maximum tensile load and the initial rigidity.

Fig. 8 shows the relationships between the nominal stress  $\sigma_n$  and the tensile stresses on CFRP strips for multi-layered and single-layered parts, respectively. The nominal stress  $\sigma_n$  is the value of  $P/A$ , where  $P$  and  $A$  are the tensile load and the sectional area of the specimen, respectively. Tensile stresses were averaged for each of the multi-layered and single-layered parts using strain gages on CFRP strips. At the single-layered part of all the series, CFRP strips are subjected to the high tensile stresses of 750–1100 MPa in the ultimate. The stress of the single-layered part becomes small on increasing the number of laminations. It means that CFRP strips of multi-layered part are subjected to large tensile forces. On the other hand, the stress of the multi-layered part becomes lower as the number of laminations increases. From a viewpoint of the sharing force per layer, lamination of CFRP strips is not necessarily rational. However, as mentioned previously, since the lamination gives high rigidity, the effective reinforcement can also be expected in the case aiming at a crack repair.

Finally, an example of the fracture in DL-M7 is shown in Photograph 2. The brittle fracture including the delamination between CFRP strips was observed.

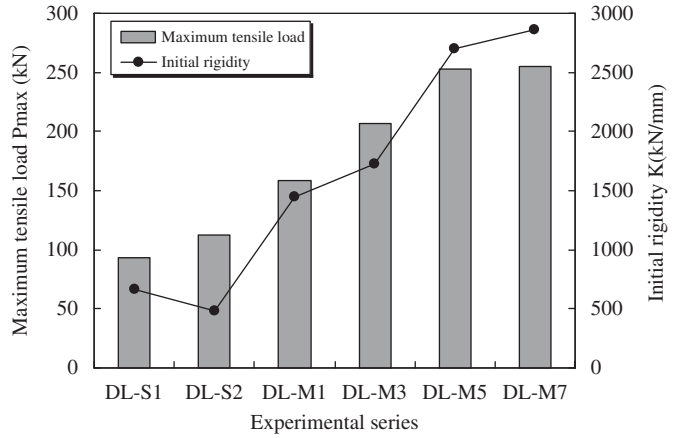


**Fig. 7.** Maximum tensile load and initial rigidity.



**Photograph 2.** An example of the fracture in series DL-M7.

#### 4. Repair effects and fatigue durability

##### 4.1. Testing procedure

The loading tests were conducted in order to verify repair effects. Fig. 9 and Photograph 3 show the loading system of the

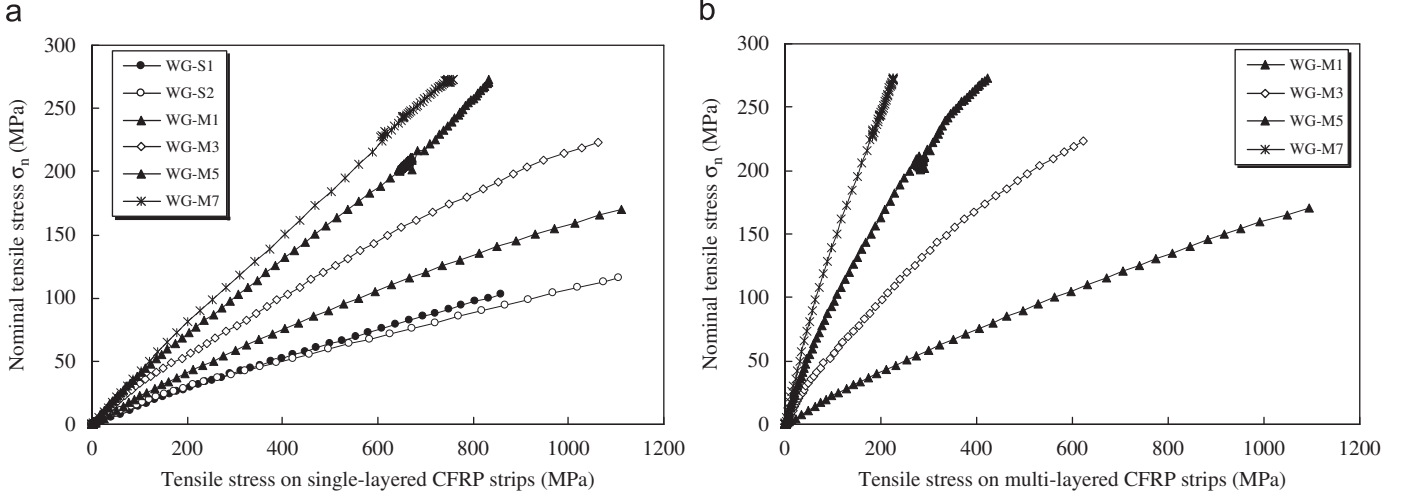


**Fig. 8.** Relationships between nominal stress and tensile stresses on CFRP strips: (a) on single-layered CFRP strips and (b) on multi-layered CFRP strips.



**Photograph 3.** Test setup of loading system.

I-shaped girder and test setup, respectively. The specimen was connected to the loading system with high-strength bolts. The load was applied by four-point bending. The uniform tensile stress was introduced into the specimen according to the uniform bending moment of the bottom flange. An electro-hydraulic servo actuator with a capacity 750 kN was used. In fatigue test, the waveform of the cyclic load was a sine wave with a frequency of 2 Hz. The minimum stress was approximately 20 MPa, and the maximum stress varied according to the nominal stress range  $\Delta\sigma_n$  from 64 to 114 MPa. The experimental series is shown in Table 3. In series M, the number of laminations was 1, 3 or 5 layers.

#### 4.2. Static loading test results

To begin with, the repair effects under the static loading are described. The cracks were initiated by fatigue test ( $\Delta\sigma_n = 100$  MPa), and the simplest repair of series S was performed, when the crack length  $a$  reached 55.7 mm (it is equivalent to approximately 45% of the overall). The static loading test was carried out before and after repair. The distribution of longitudinal stress and crack opening displacement in the steel plate were investigated. They

were measured using strain gages and clip-type displacement transducers.

In addition, in order to evaluate the validity of experimental results, elasto-plastic finite displacement analysis was carried out with 3D FEA code, Msc. Marc. Fig. 10 shows the analytical model attached to the single-layered CFRP strip. Regarding symmetric boundary condition, only  $\frac{1}{4}$  of the specimen was modeled. Same as in the experiment, the tensile stress of 120 MPa was uniformly applied.

As a result of experiment and analysis, the distribution of longitudinal stress and crack opening displacement are shown in Figs. 11 and 12. There is plastic zone by high stress concentration around the crack tip after repair. The longitudinal stresses reduced. The plastic zone decreased after repairing as shown in the analytical model. The crack opening displacements also reduced in general. For example, the crack opening displacement is lowered by about 40% in the center of the specimen. It can be seen that good agreement was achieved between the experimental and analytical results.

#### 4.3. Fatigue test results

In order to evaluate fatigue life after repair, the S-N diagram was described using the number of cycles from the restart after repair to failure,  $N_p$ . In addition,  $N_f$  and  $N_i$  were defined as follows:  $N_f$  is the number of cycles from the start of fatigue test to failure, whereas  $N_i$  is the number of cycles from the start of fatigue test until the crack length reached 15 mm. The relationship between  $N_f$ ,  $N_i$  and  $N_p$  can be shown as

$$N_f = N_i + N_p \quad (2)$$

$N_i$  is considered to be significantly depending on the dispersion of initial conditions such as residual stress and weld bead shape. In this study,  $N_i$  was equivalent to 0.4–4.2 million cycles. Consequently, the difference in  $N_p$  can be purely evaluated as the effect of repair.

Fig. 13 shows the fatigue test results arranged by the fatigue life  $N_p$  after repair to failure. In all the series, the fatigue life  $N_p$  was remarkably improved compared with the non-repaired series  $N$ . In series M, the fatigue life increased as the number of laminations increased. In particular, in series M5, the fatigue life

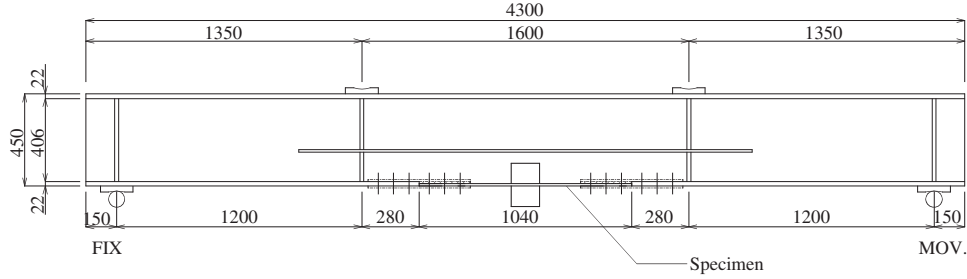


Fig. 9. Loading system.

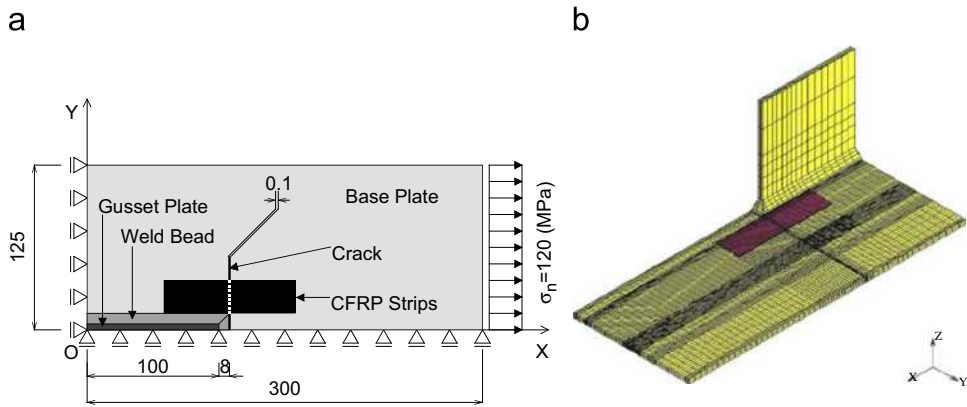


Fig. 10. Analytical model attached single-layered CFRP strip: (a) boundary conditions and (b) element division.

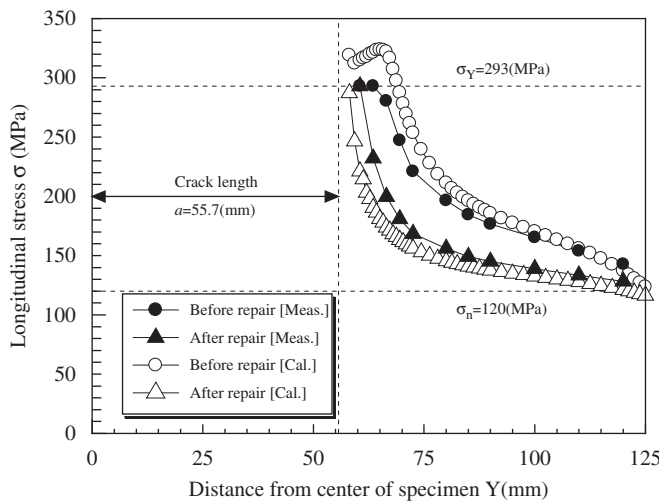


Fig. 11. Distribution of longitudinal stress.

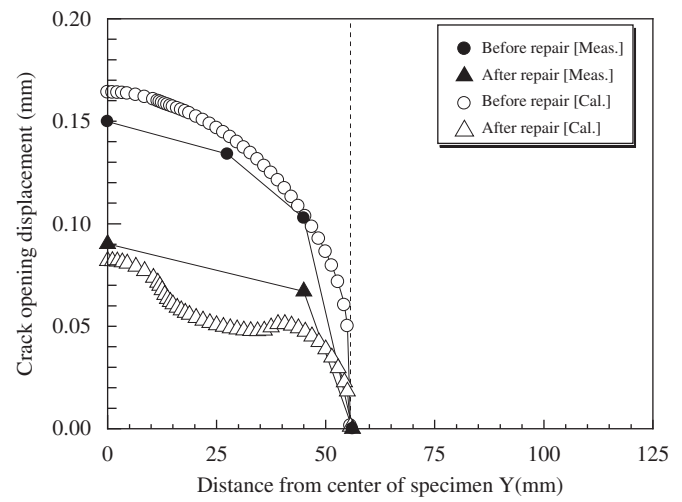


Fig. 12. Distribution of crack opening displacement.

improved remarkably in comparison with series N, indicating that a significant effect of repair was obtained. This is attributed to the fact that the crack opening was repaired by the high rigidity of multi-layered CFRP strips, and the opening displacement was sufficiently reduced. However, in this study, the fatigue limit was not obtained by series M5 within the stress range (64–114 MPa), although the fatigue life greatly exceeds 10 million cycles in the lowest stress range of 64 MPa.

Fig. 14 shows the relationship between the crack length and the number of cycles after repair in  $\Delta\sigma_n = 64$  MPa. The crack lengths were measured within about 50–70 mm, using crack gages installed at the side of CFRP strips. Since crack lengths could not be measured in the bonding area of the CFRP strips, the dotted straight lines are shown in the figure. In series S and M, the fatigue life after repair is improved. The cracks progressed slowly in the bonding area of CFRP strips as shown by the dotted line in

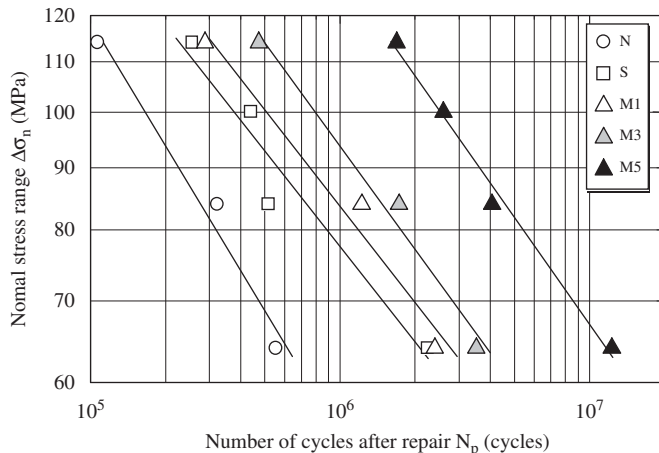
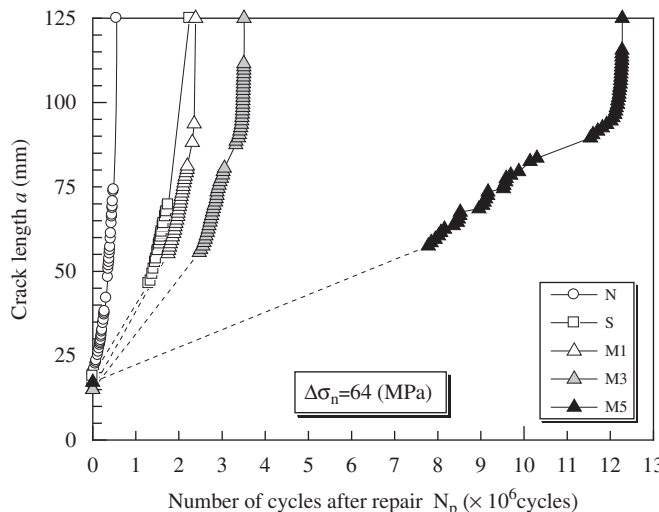
Fig. 13. S-N<sub>p</sub> diagram.

Fig. 14. Relationship between number of cycles after repair and crack length.

comparison with series N. In particular, in series M5, it was found that the crack progress was controlled effectively even after cracks crossed the bonding area. The crack propagated rapidly when crack length reached more than 95 mm (equivalent to about 75% of the overall width).

In series S, M1 and M3, CFRP strips did not debond within the bonding area. However, the cracks progressed gradually, and CFRP strips debonded when the crack length reached from 75 to 80 mm (a crack length ranging from 60% to 65% of the overall width). On the other hand, in series M5, CFRP strips debonded immediately before the specimen collapsed. In all specimens, debonding occurred in the interface of adhesive and steel plate.

In order to observe the bonding condition of CFRP strips, the fatigue test was stopped when the crack length reached approximately 100 mm (a crack length of about 80% of the overall width) in  $\Delta\sigma_n = 100$  MPa. The specimen was removed from the loading system, and then cut off. Fig. 15 shows two macrosections in series M5. The multi-layered CFRP strips were very close and bonded well to the weld bead, though some partial defects remained.

**Table 3**  
Experimental series of fatigue test.

Series	Repair method	CFRP strip	
		Single-layered part (mm)	Multi-layered part
N	Not repaired	–	–
S	Fig. 3(a)	100	–
M1	Fig. 3(b)	100	1-layer at 200 mm
M3	Fig. 3(b)	100	3-layer at 200 mm
M5	Fig. 3(b)	100	5-layer at 200 mm

## 5. Combination of CFRP strips and drill-holes

### 5.1. Variation of repair methods and testing procedure

More effective repair methods were also investigated using combination of CFRP strips and drill-holes. A drill-hole is also called a stop-hole, and is often applied as a temporary repair method on site. Drill-holes are applied to reduce the stress concentration at the tips of cracks. Several combinations of CFRP strips and drill-holes were investigated by static loading tests and fatigue tests. The basic experimental procedure is the same as that mentioned above. In the specimen configuration, the width of the specimen was 300 mm in order to install two drill-holes of 25 mm diameter. Table 4 shows the material properties of steel, CFRP strips and epoxy resin adhesive.

Regarding variation in repair methods, four series of repair methods were examined as shown in Fig. 16 and Table 5. The cracked specimens were repaired when the crack progressed to 33 mm in length from the center towards the edge. The repair methods are described as follows:

- (a) Series DH: repaired only by drill-holes.
- (b) Series DHM: repaired with multi-layered CFRP strips (5 layers) and two drill-holes.
- (c) Series DHS: repaired with single-layered CFRP strips bonded above two drill-holes.
- (d) Series DHMS: repaired combining series DHM and DHS.

The diameter of drill-holes was 25 mm, which was similar to the diameter of a high-strength bolt. By installing drill-holes, the crack length was equivalent to 50 mm per side. The repair procedures and curing conditions are as mentioned above. In addition to these repair methods, the non-repaired series N was examined to give reference value.

Procedures of static and fatigue tests are the same as mentioned above. The nominal stress range  $\Delta\sigma_n$  was 100 MPa in the fatigue test. Photograph 4 shows series DHMS as an example of repair methods. In addition, strain gages were installed on the surface of steel plate and CFRP strips, where the cracks would progress. The clip-type displacement transducers were installed in drill-holes and crack opening.

### 5.2. Static loading test results

Fig. 17 shows the longitudinal stress distribution of the steel plate in  $\Delta\sigma_n = 100$  MPa (applied load:  $\Delta P = 250$  kN) immediately after repair. The maximum stress was about five times the nominal tensile stress range  $\Delta\sigma_n$  in series DH repaired only by drill-holes. In series DHS, DMS and DHMS, it was found that the maximum stress could be reduced by the combination of drill-holes and CFRP strips. In series DHMS, which was the most

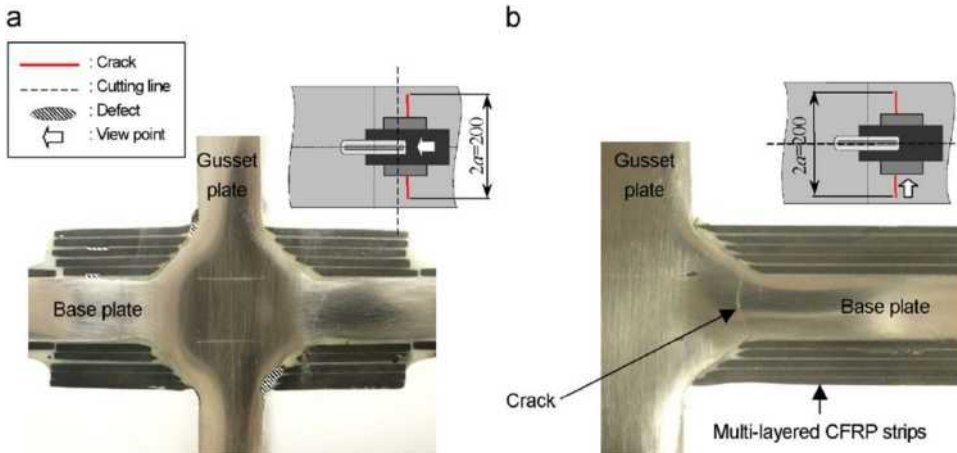


Fig. 15. Macrosections in series M5: (a) cross-sectional direction and (b) longitudinal direction.

**Table 4**

Mechanical properties of steel, CFRP strip and epoxy resin adhesive.

	Steel plate (JIS SM400A)	CFRP strip	Epoxy resin adhesive
Yield point (MPa)	285	—	—
Tensile strength (MPa)	443	2990	30
Elongation (%)	29	1.9	—
Elastic modulus (GPa)	206	172	1.5

effective repair, the maximum stress was reduced by about 50% compared with series DH.

Fig. 18 shows the longitudinal stress distribution on the CFRP strips. It can be said that the stress distribution in the multi-layered part of series DHMS was similar to that of series DHM. In the single-layered part of series DHMS, the stress distribution was lower than that of series DHS, it also showed that the stress on the steel plate was reduced as indicated above. Therefore, fatigue strength is expected to be the highest for series DHMS.

Fig. 19 shows the crack opening displacement (hereafter called the COD) in all series. In series DH, the COD after installing drill-holes (considered as 50 mm of the opening) obviously became larger compared with that before installing drill-holes (considered as 33 mm of the crack length). In series DHM, the COD could be remarkably reduced. On the other hand, in series DHS, the reduction of the COD at the center was small. In addition, the relationship between the applied load and the COD was almost linear.

### 5.3. Fatigue test results

Fig. 20 shows the  $S-N_p$  diagram.  $N_p$  was the fatigue life after repair (considered as 50 mm of the crack length) to failure, as defined by Eq. (2). The fatigue life  $N_p$  of series DH and DHM were 1.6 and 5.0 times of the non-repaired series N, respectively. In series DHMS, where the fatigue test was continuing,  $N_p$  was prolonged for 80 or more times compared to series N, and for 50 or more times compared to series DH. The sufficient effects of repair were confirmed. In addition, in series M5 with 250 mm wide specimen, the equivalent  $N_p$  from 50 mm to failure was 1.15 million cycles. The fatigue life of series DHMS was greatly improved compared with that of series M5 without drill-holes.

More detail on fatigue tests is as follows. In series DHM, the multi-layered CFRP strips debonded on one side when  $N_p$  was about 0.20 million cycles. The fatigue test was stopped because the crack generated again at the edge of drill-holes at about 0.33 million cycles. On the other hand, in series DHMS, the multi-layered CFRP strips debonded, when  $N_p$  was about 0.47 million cycles on one side and about 4.30 million cycles on the other side, respectively. However, the debonding of single-layered CFRP strips and the recurrence of the crack at the edge of drill-holes were not observed even when  $N_p$  reached to about 5.65 million cycles.

Although the stress concentration was reduced by installing drill-holes, the COD became larger. Consequently, the increase of the COD associated with installing drill-holes may have the influence on the debonding of CFRP strips.

## 6. Conclusion

For fatigue cracks initiated at the weld toe of web gusset joints, the repairs were performed using CFRP strips and epoxy resin adhesive, and the effects of repair on the bond strength and the fatigue durability were examined experimentally and analytically. The following conclusions were obtained:

- (1) It was found that the proposed repair method greatly contributed to the increase of bond strength and the reduction of the opening displacement at the joint.
- (2) The sufficient performance of adhesion joints was confirmed when the number of laminations of CFRP strips increased to five layers.
- (3) The laminating of CFRP strips was found to be effective in preventing debonding and sharing axial force.
- (4) It was confirmed that as the number of laminations of CFRP strips increases, the post-repair fatigue life improved considerably and that a sufficient effect of repair was acquired in the case of five layers.
- (5) No fatigue limit was obtained from the discussed stress range. The proposed method was positioned as a first-aid repair to prolong the fatigue life, since no crack recurrence was prevented.

Moreover, regarding the more effective repair, some repair methods combining CFRP strips and drill-holes were also investigated experimentally. The repair method by combining

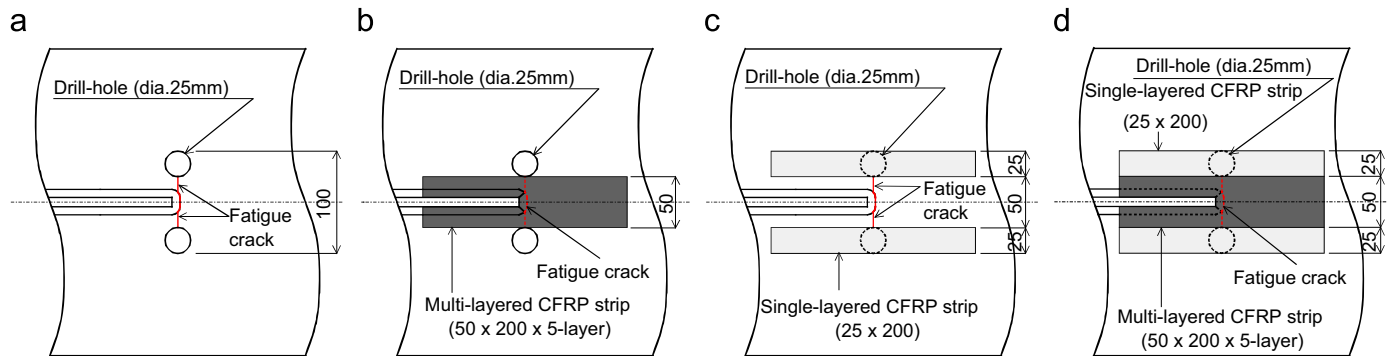


**Fig. 16.** Variation of repair methods: (a) series DH, (b) series DHM, (c) series DHS and (d) series DHMS.

**Table 5**  
Experimental series in combination of CFRP strips and drill-holes.

Series	Repair method	Drill-holes	CFRP strip	
			Single-layered part (mm)	Multi-layered part
N	Not repaired	Without	-	-
DH	Fig. 16(a)	2-Dia.25 mm	-	-
DHS	Fig. 16(b)	2-Dia.25 mm	200	-
DHM	Fig. 16(c)	2-Dia.25 mm	-	5-layer at 200 mm
DHMS	Fig. 16(d)	2-Dia.25 mm	200	5-layer at 200 mm



**Photograph 4.** Repair method in series DHMS.

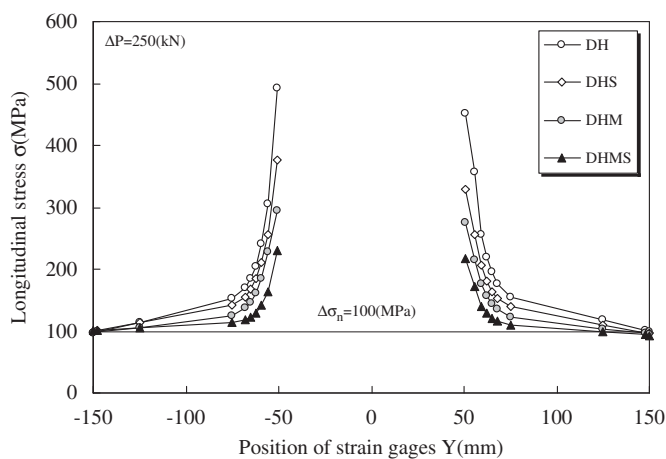


**Fig. 17.** Stress distribution of steel plate.

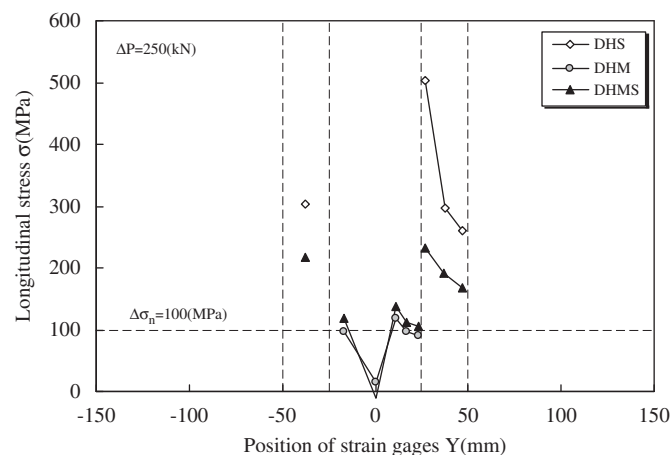


**Fig. 18.** Stress distribution of CFRP strips.

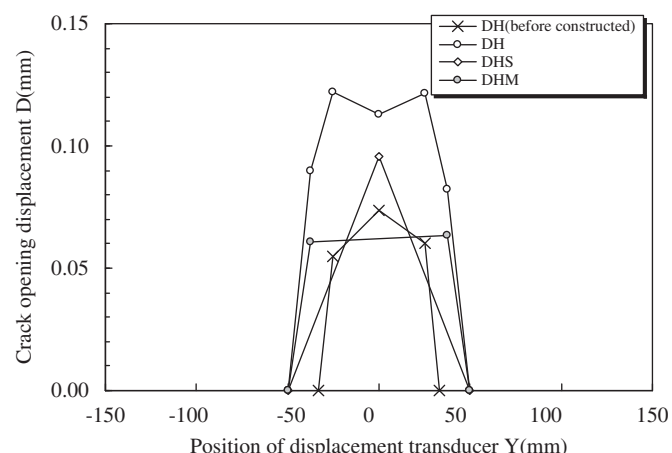


**Fig. 19.** Distribution of crack opening displacements.

CFRP strips and drill-holes was more effective compared with that without drill-holes.

It should be pointed out that the above conclusions were derived from the limited test data presented in this paper.

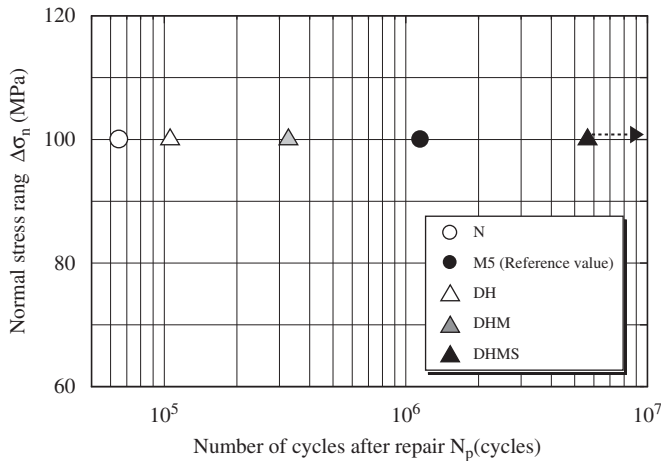


**Fig. 20.** S- $N_p$  diagram.

## References

- [1] Japan Road Association. Guidelines for fatigue design of steel highway bridges. Tokyo: Maruzen Co., Ltd.; 2002 [in Japanese].
- [2] Zhao X-L, Zhang L. State-of-the-art review on FRP strengthened steel structures. *Engineering Structures* 2007;29(8):1808–23.
- [3] Hollaway LC, Cadei J. Progress in the technique of upgrading metallic structures with advanced polymer composites. *Progress in Structural Engineering and Materials* 2002;4(2):131–48.
- [4] Smith ST. In: Proceedings of the first Asia-Pacific conference on FRP in structures—APFIS 2007, Hong Kong, 2007.
- [5] Jiao H, Zhao XL. CFRP strengthened butt-welded very high strength (VHS) circular steel tubes. *Thin-Walled Structures* 2004;42(7):963–78.
- [6] Miller TC, Chajes MJ, Mertz DR, Hastings JN. Strengthening of a steel bridge girder using CFRP plates. *Journal of Bridge Engineering, ASCE* 2001;6(6):514–22.
- [7] Bassetti A, Liechti P, Nussbaumer A. Fatigue resistance and repairs of riveted bridge members, fatigue design. Finland: Espoo; 1998. p. 535–46.
- [8] Jones SC, Civjan SA. Application of fiber reinforced polymer overlays to extend steel fatigue life. *Journal of Composites for Construction, ASCE* 2003;7(4):331–8.
- [9] Tavakkolizadeh M, Saadatmanesh H. Fatigue strength of steel girders strengthened with carbon fiber reinforced polymer patch. *Journal of Structural Engineering, ASCE* 2003;129(2):186–96.
- [10] Nakamura H, Yamasawa T, Maeda K, Doi T, Irube T, Takagi H, Suzuki H. Study on repair of steel members using CFRP strips. In: Proceedings of the 56th annual conference of JSCE, CD-ROM, 2001, 2 pages [in Japanese].
- [11] Yamauchi T, Nakamura H, Maeda K, Suzuki H. Fatigue test on repair of steel members using CFRP strips. In: Proceedings of the 57th annual conference of JSCE. 2002. p. 1339–40 [in Japanese].
- [12] Nakamura H, Moroi T, Suzuki H, Maeda K, Irube T. Repair of out-of-plane welded gusset joint using CFRP strips. *Journal of Construction Steel, JSSC* 2004;12:425–30 [in Japanese].
- [13] Jiang W, Nakamura H, Suzuki H, Maeda K, Irube T. Experimental study on adhesion characteristics of steel plate and CFRP strips. *Journal of Construction Steel, JSSC* 2006;14:595–602 [in Japanese].



## Full length article

## Fatigue behavior and remaining life evaluation of rib-to-deck joints using interior repair welds



Ming-zhe Li, Chuang Cui\*, Hao Wang, Qing-hua Zhang, Le-tian Da, Yi-zhi Bu

Department of Bridge Engineering, Southwest Jiaotong University, Chengdu, Sichuan 610031, China

MOE Key Laboratory of High-speed Railway Engineering, Southwest Jiaotong University, Chengdu, Sichuan 610031, China

## ARTICLE INFO

## Keywords:

Orthotropic steel decks  
Fatigue crack  
Reinforcement  
Interior repair welding  
Remaining life evaluation  
Fracture mechanics

## ABSTRACT

The rib-to-deck joints are one of the most critical vulnerable details of orthotropic steel deck subjected to vehicle loads. Specially, fatigue cracks initiating from the weld root and propagating along the thickness of the deck at the rib-to-deck joints is most difficult to repair. In this study, the interior repair weld is adopted to enhance the fatigue resistance of rib-to-deck joint. Three specimens of rib-to-deck joint were designed and tested to investigate the effectiveness and applicability of the interior repair weld. The fracture mechanics method associated with numerical simulation is adopted to analyze the failure mechanism and remaining life of rib-to-deck joints after reinforcement. The results indicate that the region of fatigue crack initiation will be transferred from the interior weld root before repairing to the exterior weld toe after repairing. The interior repair weld can effectively prevent fatigue crack propagation and significantly improve the remaining fatigue life of the rib-to-deck joints. The simulated fatigue life agrees well with the measurement in fatigue tests, revealing the accuracy of fracture mechanics method to estimate the remaining life.

## 1. Introduction

Orthotropic steel deck (OSD) is widely used in long-span bridge due to the benefits such as light weight, high strength and quick construction. The fatigue cracks untimely occur in OSD at the early period of service [1–3]. Specially, the rib-to-deck welded joint is one of most critical vulnerable details [4–6], and fatigue crack of rib-to-deck welded joint will accelerate the damage of pavement and compromise the durability of steel bridge, as shown in Fig. 1. Although a lot of efforts have been done to enhance the performance of cracked OSD, it is still a challenge to repair those fatigue crack in OSD [7].

The reinforcements for cracked OSD mainly include welding repair reinforcement [8,9], cold reinforcement [10–13], and integral reinforcement [14,15]. Welding repair reinforcement is the use of welding techniques to directly repair cracks by grinding and rewelding the region around the crack. Cold reinforcement mainly includes crack-arrest hole [10], grinding and impact treatment [12,13], and assembly bonding methods [16,17]. Crack-arrest hole is effective to the crack in plane plate, but not for the rib-to-deck welded joint. Impact treatment can effectively prolong fatigue life by forming residual compressive stress at the weld toe and improving the geometry of the weld toe. But this method is used to eliminate surface micro-cracks, and requires a certain operating space and hardly repairs hidden cracks. The assembly bonding methods [11,16,17] reduce the strain near the crack tip and enhance the local stiffness. Moreover, Shao et al. [18] investigated the

integral reinforcement effect of ultra-high strength concrete structural layer on the vulnerable details of OSD. Although the integral reinforcement can increase the overall stiffness of OSD, it increases the weight of the bridge, which limits its application, except for the thin UHPC layer.

The rib-to-deck welded joint is one of the most critical components of OSD [19–22] (see Fig. 1). The current reinforcement methods mainly focus on the repair of toe-deck and root-throat cracks by assembly bonding methods, such as gluing or bolting steel plate [17], FRP plate [16] or U-shaped plate [11], which are ineffective to the root-deck crack. However, the FRP plate applied at the rib-to-deck joint form a concave and cannot effectively anchored; In addition, due to thermal effect, the high temperature on the deck plate will significantly reduce the elastic modulus of epoxy glue, affecting the reinforcement effect. The remelting method was used to repair the root-deck crack taking a large proportion of fatigue cracking modes [23–25], but the remelted rib-to-deck welded joint will crack with a low lifetime due to the ineluctable weld defects during remelting. At the same time, the root-deck crack is so secluded in the interior of closed rib that it is difficult to detect at the early stage of fatigue crack propagation. Therefore, the root-deck crack is extremely difficult to repair, and the effective reinforcement of root-deck crack should be further investigated.

This paper aims to propose a new repair method for the cracked rib-to-deck welded joint, and estimate the remaining life. An interior repair

\* Corresponding author at: Department of Bridge Engineering, Southwest Jiaotong University, Chengdu, Sichuan 610031, China.  
E-mail address: [ccui@swjtu.edu.cn](mailto:ccui@swjtu.edu.cn) (C. Cui).

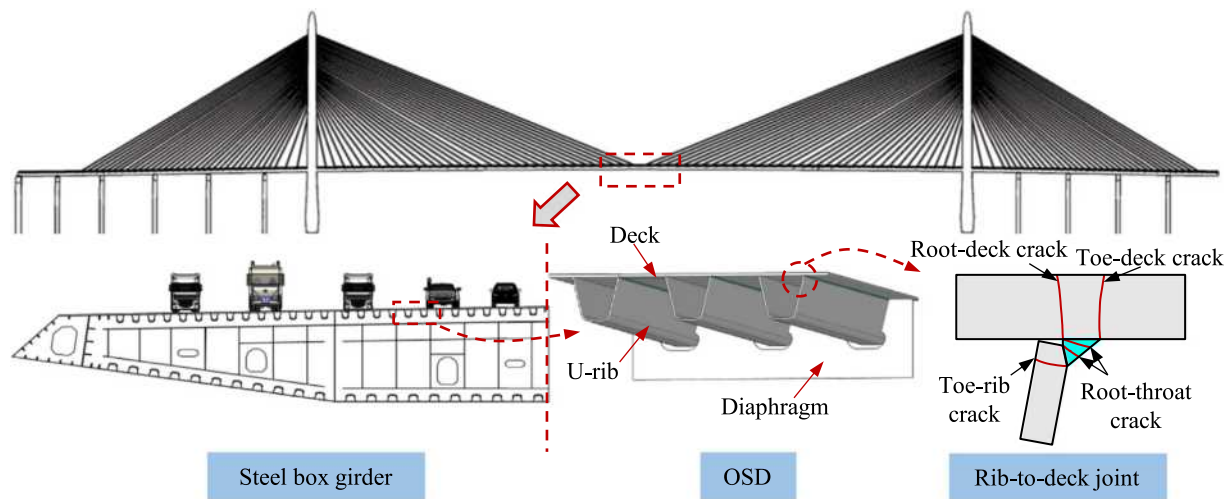


Fig. 1. The failure mode of rib-to-deck joint in OSD.

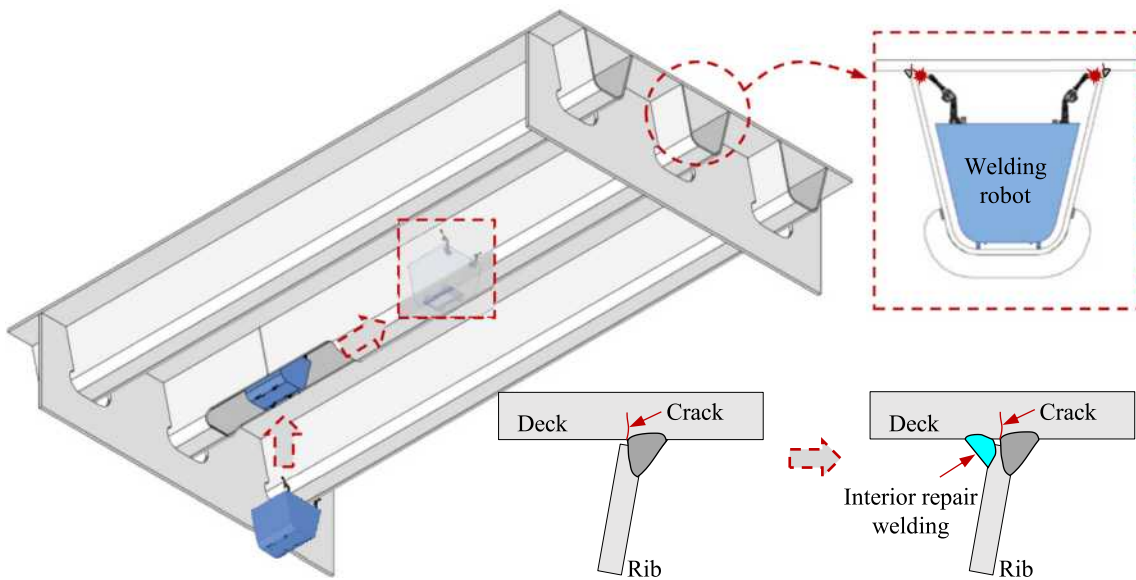


Fig. 2. The implementation process of interior repair welding.

weld was firstly proposed based on the automation welding technique. The fatigue test of rib-to-deck welded joint was conducted until the root-deck cracks appeared. Then, the reinforcement experiments of cracked rib-to-deck welded joint were carried out, and failure mechanism of enhanced rib-to-deck welded joint was analyzed. Finally, the remaining life of reinforced rib-to-deck joint was estimated by using fracture mechanics method.

## 2. Reinforcement tests of rib-to-deck joint using interior repair weld

### 2.1. Interior repair weld

The root-deck crack of rib-to-deck joint initiates from the weld root and propagates to the deck, which is located in the interior of closed U-rib. This fatigue cracking mode which is common in steel bridges is hardly reinforced by the traditional repair methods. The interior repair welding can be achieved, propelled by rapid advances in automation welding techniques which have been widely used to fabricate the double-side welded rib-to-deck joint [26–28]. Fig. 2 shows the abridged general view of interior repair welding using an automated welding

robot which can effectively close the surface of root-deck crack. To achieve interior welding repair in the real bridge, the hole at the butt weld or bolting of U-rib is cut to put the automated welding robot into the U-rib, and the welding robot passes through the hole. After interior repair welding, the hole shall be restored.

### 2.2. Specimen design

The specimens of rib-to-deck welded joint are composed of deck plate and U-rib. To investigate the enhancement effect of interior repair weld in OSDs, a special test device is designed as shown in Fig. 3(a). A specific stiffness constraint at the bottom of rib is set to adjust the stiffness of rib and ensure that fatigue crack initiates from the weld root of the joint and propagates along the thickness of deck plate. Besides, the stiffness constraint is an angle steel with a width of 300 mm, a height of 140 mm and a thickness of 8 mm. The bottom plate of longitudinal rib is connected with the angle steel by the high-strength bolts. The hinged supports are used to simulate the hinge constraint between the two sides of the deck and the pillar stiffener. The site layout of the specimen is shown in Fig. 3(b).

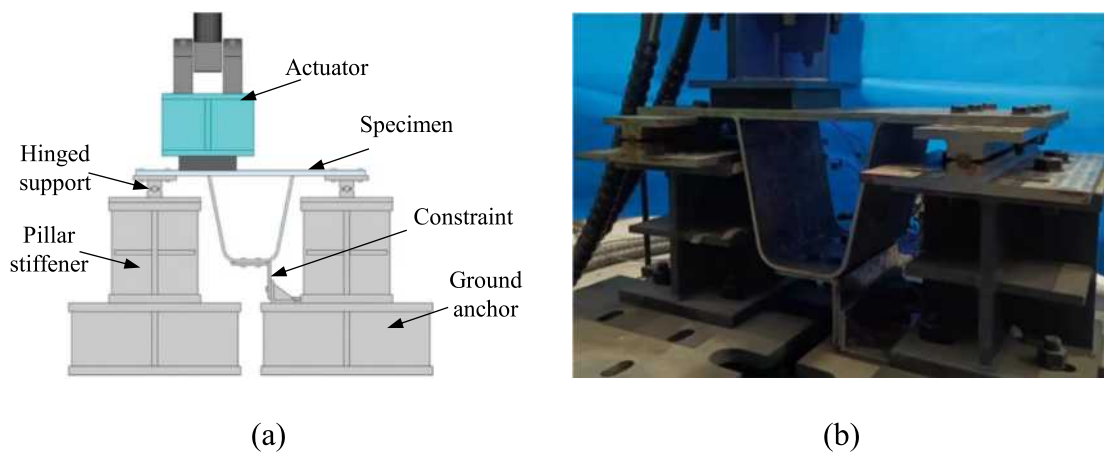


Fig. 3. Fatigue test specimen diagram: (a) fatigue test device; and (b) site layout.

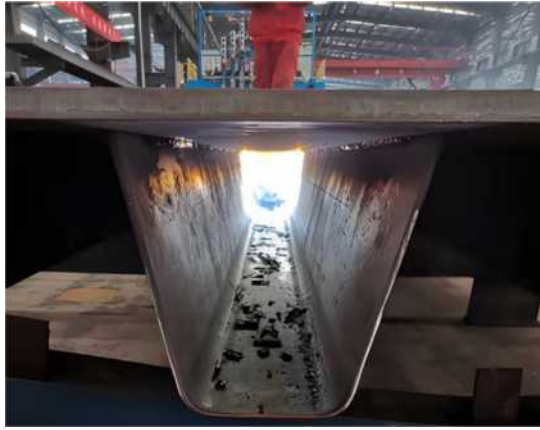


Fig. 4. Interior repair welding by the overhead fillet welds using the automated robot.

The fatigue tests were firstly conducted until the root-deck cracks appear. Then, the specimens were reinforced by the interior repair welding associated with the automation robot, as shown in Fig. 4. The specimen is not upside down and placed same as the real bridge. At last, the enhanced specimens would be reloaded using the fatigue test device in Fig. 3 until the specimens failed.

Referring to the design parameters of typical OSD, three specimens were designed, including two specimens of traditional single-side welded rib-to-deck joint and one specimen of double-side welded rib-to-deck joint as a contrast, as depicted in Fig. 5. The thicknesses of deck plate and U-rib are 18 mm and 8 mm, and the length and width of specimen are 300 mm and 800 mm, respectively. The penetration rate of both single-side weld seam and double-side weld seam of rib-to-deck joints is 75%. The size of fillet weld ( $l = h$ ) is 7 mm, the size of interior fillet weld is 6 mm, and the specimens are made of Q345qD steel with a nominal yielding strength of 345 MPa. The distance between the center line of the support and the center of the test specimen is 325 mm.

### 2.3. Test set-up and instrumentation

A rubber bearing is set between the actuator and the specimen with a length of 200 mm, a width of 200 mm, and a height of 40 mm. The transverse center of the loading position is located above the web of U-rib, and the longitudinal center of the rubber bearing overlaps with the longitudinal center of the specimen, as shown in Fig. 6. To investigate the reinforcement effort of interior repair welding and the fatigue behavior of the reinforced joints, the fatigue tests for two single-side welded rib-to-deck joints were carried out in two stages (see Fig. 6): (1)

**Table 1**  
Load Scheme of Test.

Specimens	Welding type	Loading amplitude $\Delta F$ (kN)	
		Stage I	Stage II
SRD-I	Single-side weld	45	45
SRD-II	Single-side weld	50	50
DRD-I	Double-side weld	50	-

Stage I: the specimens were loaded until the appearance of fatigue crack at the weld root of rib-to-deck joint; (2) Stage II: the cracked specimens were reinforced by the interior weld repairing method, and the enhanced specimens were reloaded until fatigue failure at the rib-to-deck welded joint. To compare fatigue behavior and failure mechanism of reinforced single-side welded rib-to-deck joint and double-sided welded rib-to-deck joint, the fatigue test of double-sided welded rib-to-deck joint was carried out as well. The loading amplitudes at each stage for different specimens are listed in Table 1.

Moreover, the strain gauges were adopted to monitor the variations of local strains at the weld root and toe under cyclic loading. Fig. 7 shows the locations of the strain gauges which are numbered in accordance with the longitudinal direction. The strain gauges with a distance of 0.4t mm from the exterior weld toe, weld root, and interior weld toe are named as ET, IR, and IT, respectively.

### 2.4. Result discussions

Firstly, the cyclic loading in Stage I was accomplished, and the monitored strains with the different number of cycles are obtained. Since the root-deck crack cannot be observed under cyclic loading due to its invisibility, it is reasonable that the macroscopic cracks occur at the weld toe or root when the strains of the critical measuring points decrease by 10% according to [2]. To monitor the fatigue crack initiation and propagation, the normalized strain by using a ratio of real-time and initial strain is adopted in this study.

The normalized strains of the measuring points at the weld toe of SRD-I and SRD-II and the weld root of DRD-I in stage I are shown in Fig. 8, where  $\epsilon_0$  is initial value of strain, and  $\epsilon$  is strain value after a certain number of cycles. It can be seen that the normalized strain at the weld root of SRD-I reduces by 10% at the location of -100mm and 50 mm from the center line of specimen after respectively 615,000 cycles and 1000,000 cycles, indicating the appearance of macroscopic cracks at the weld root. Moreover, a reduction of 10% at the weld root of SRD-II can be found at 100 mm and -75 mm away from the center line of specimen after 287,000 cycles and 447,000 cycles, respectively, revealing the potential cracks have occurred at the weld root. Correspondingly, the macroscopic crack may be obtained at the

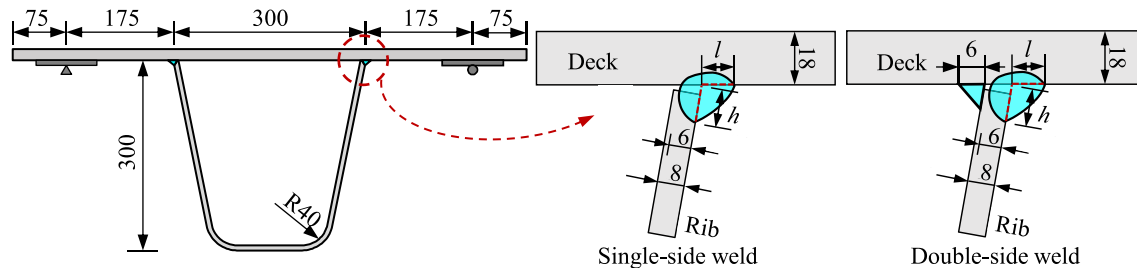


Fig. 5. Dimensions of test specimen (unit: mm).

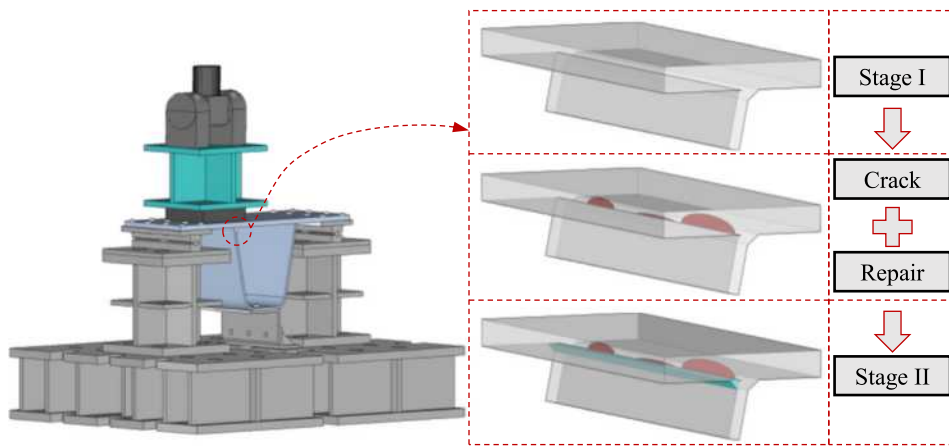


Fig. 6. The stages of test.

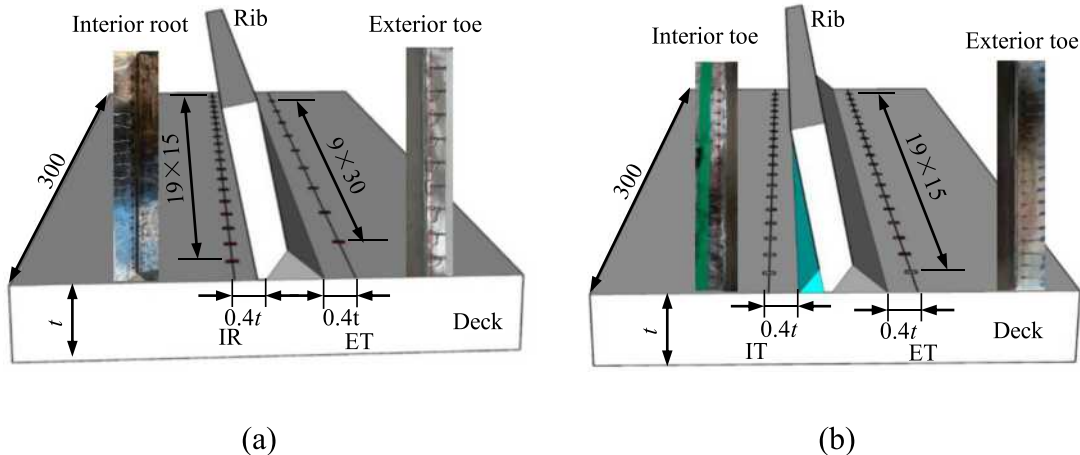


Fig. 7. Arrangement of strain measuring points on (unit: mm): (a) specimen in Stage I; (b) specimen in Stage II.

interior weld toe of DRD-I, where it is about 105 mm away from the center line of specimen after 454,000 cycles with a normalized strain decline of 10%.

Furthermore, the cracked SRD-I and SRD-II were reinforced by the interior repair welding, and the enhanced SRD-I and SRD-II were reloaded until fatigue failure. Fig. 9 shows the nominalized strains of repaired specimens under cyclic loading in Stage II. After 585,000 cycles and 830,000 cycles with a reduction of nominalized strain by 10%, it can be inferred that the macroscopic fatigue cracks may appear at the exterior weld toe of enhanced SRD-I which is respectively -75 mm, and 100 mm away from the centerline of specimen. Similarly, the cracks of reinforced SRD-II respectively propagate at 90 mm and -25 mm from the centerline of specimen after 460,000 cycles and 680,000 cycles.

At last, the cracked specimens were cut by the wire cutter to obtain the microtome sections where the cracks occurred in the different

specimens, as shown in Fig. 10. For SRD-I and SRD-II, it is clear that the cracks have firstly initiated at the interior weld root and propagated to the deck. After interior repair welding, the fatigue cracking has transferred to the exterior weld toe rather than the repaired weld root of SRD-I and SRD-II, indicating the effectivity of interior repair welding for the reinforcement of root-deck crack of the single-side welded joints. Besides, the crack of DRD-I firstly appeared at the interior weld toe, which is similar to the results in [28]. It can be seen that the dominant failure mode of DRD-I (interior toe-deck crack) differs to that of the repaired SRD-I and SRD-II (exterior toe-deck crack). The main reason is that fatigue damage has been accumulated as well at the exterior weld toes of the single-side welded joints under cyclic loading before reinforcement. According to the actual test data, the stress of weld root is greater than that of weld toe for SRD-I and SRD-II, while the stress of interior toe at DRD-I is greater than that of exterior

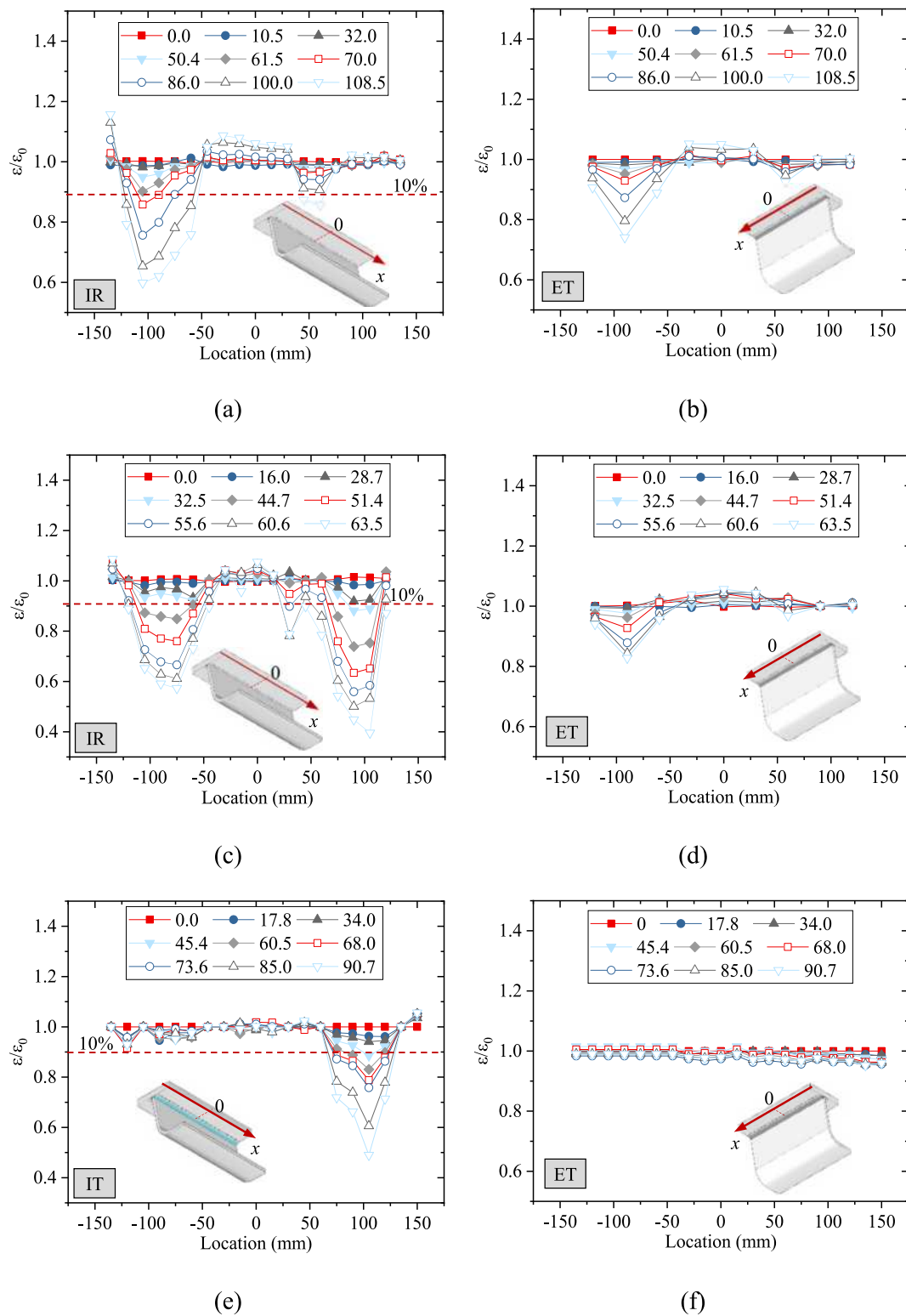


**Fig. 8.** The variation curves of nominalized strains in Stage I at: (a) interior weld root of SRD-I; (b) exterior weld toe of SRD-I; (c) interior weld root of SRD-II; (d) exterior weld toe of SRD-II; (e) interior weld toe of DRD-I; and (f) exterior weld toe of DRD-I.

weld toe. Therefore, in Stage I, cracks firstly initiate at the weld root of SRD-I and SRD-II, and at the interior weld toe of DRD-I. After the interior welding repair in Stage II, since the newly generated interior weld seams of SRD-I and SRD-II are not subjected to fatigue loading before the interior welding repair, the crack propagation rate of newly generated interior weld toe is less than the intrinsic exterior weld toe. Therefore, the fatigue crack in Stage II firstly appeared at the exterior

weld toe instead of the repaired interior weld toe where there is no fatigue damage accumulation at the beginning of Stage II.

Moreover, the stress ranges of critical measuring points where cracks initiate and grow, and the corresponding number of cycles  $N_{10}$  when the nominalized strains decrease by 10% are listed in Table 2.  $N_e$  is the corresponding number of cycles at the end of the test. It can be seen that fatigue life can be effectively improved, and the

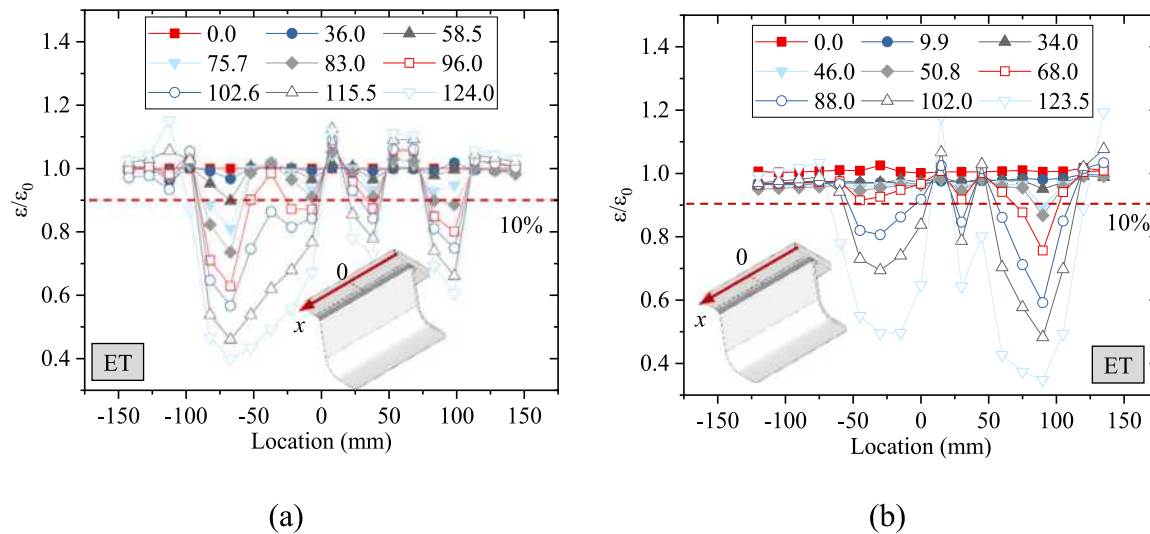


Fig. 9. The variation curves of nominalized strains at the arranged measuring points in Stage II on: (a) SRD-I; and (b) SRD-II.

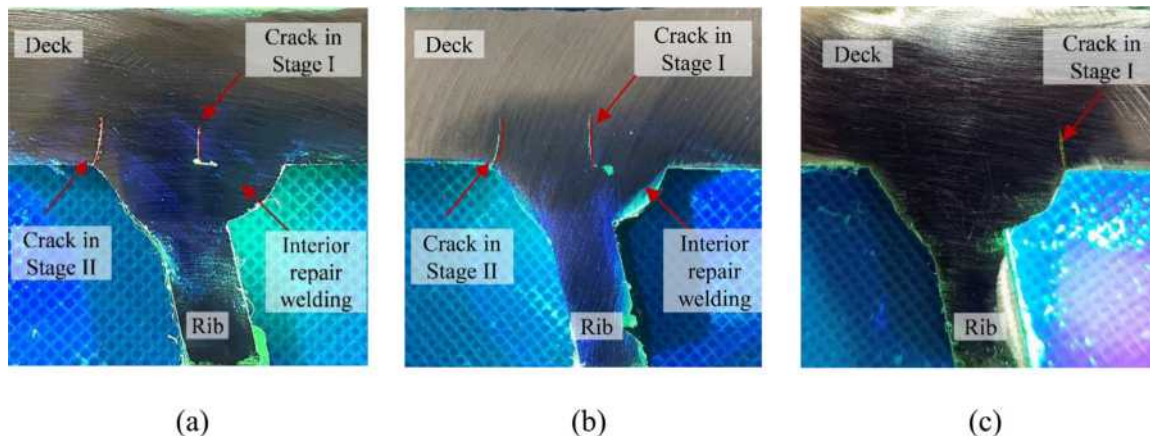


Fig. 10. The fatigue cracks of rib-to-deck after reinforcing: (a) SRD-I; (b) SRD-II; and (c) DRD-I.

**Table 2**  
Fatigue Test Results.

Stage	Specimens	Crack modes	Number of cycles ( $\times 10^4$ )	
			$N_{10}$	$N_e$
Stage I	SRD-I	Root-deck crack	61.5	108.5
	SRD-II	Root-deck crack	28.7	63.5
	DRD-I	Interior toe-deck crack	45.4	90.0
Stage II	SRD-I	Exterior toe-deck crack	58.5	124.0
	SRD-II	Exterior toe-deck crack	41.5	123.5

remaining lives of SRD-I and SRD-II have been improved by 95% and 145%. To analyze the failure mechanism and estimate the remaining life of reinforced single-side welded rib-to-deck joint, the numerical simulation should be further carried out by using fracture mechanics method.

### 3. Remaining life evaluation

#### 3.1. Linear fracture mechanics method for simulation

Although the types and number of weld defects have been sharply reduced after the application of automation welding techniques, the defect of resemble-crack extremely occurred at the unfused regions of weld root of rib-to-deck joint, as shown in Fig. 11. Similarly, the

defect of resemble-crack can be also observed at the weld toe, where the defect size is smaller than that in weld root. It has been proven in [29] that those resemble-cracks are the potential risk sources leading to cracks initiation and propagation under cyclic loading. Therefore, the fatigue performance of rib-to-deck joints including those resemble-cracks which are regarded as the initial crack can be evaluated by using the linear fracture mechanics method.

The toe-deck cracks and root-deck cracks can be found in SRD-I, SRD-II and DRD-I. Although the root-deck crack is firstly found in SRD-I and SRD-II, the fatigue damage of weld toe in SRD-I and SRD-II is simultaneously accumulated under cyclic loading in Stage I. So it can be assumed that fatigue cracks are synchronous to propagate at both weld root and weld toe with a different of initial crack size at the beginning of cyclic loading. The fatigue life can be obtained by using Paris-Erdogan formula [30,31] as below.

$$\frac{da}{dN} = C (\Delta K_{\text{eff}})^m \quad (1)$$

where  $C$  and  $m$  are the material parameters to characterize the crack propagation, with values of  $5.21 \times 10^{-13} \text{ N mm}^{-3/2}$  and 3 [32], respectively.  $a$  is the crack length, and  $N$  is the number of cycle.  $\Delta K_{\text{eff}}$  is the amplitude of equivalent stress intensity factor mixed by  $\Delta K_I$ ,  $\Delta K_{II}$  as below [32,33]. The fatigue crack growth mode of the rib-to-deck joints in OSDs is I-II mixed-mode dominated by mode I [28,34].

$$\Delta K_{\text{eff}} = \sqrt{\Delta K_I^2 + \Delta K_{II}^2} \quad (2)$$

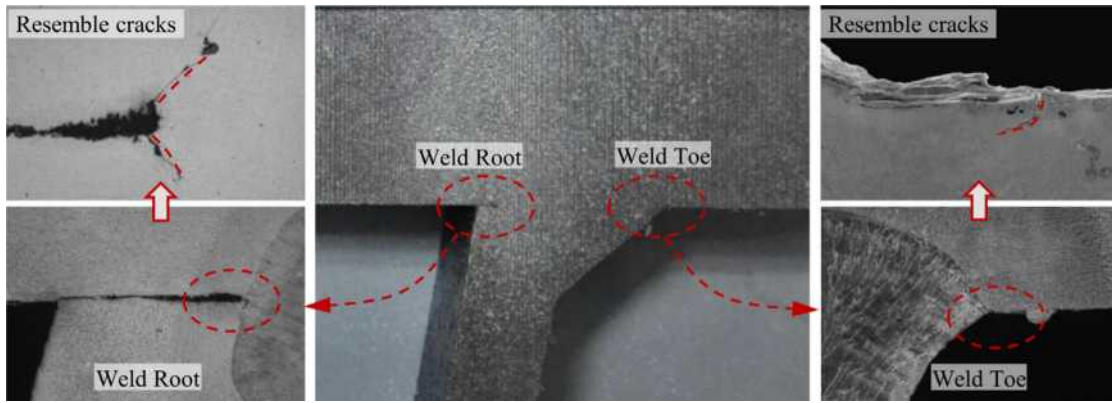


Fig. 11. Resemble-cracks of welded joints.

where  $\Delta K_I$  and  $\Delta K_{II}$  are stress intensity factor amplitudes of mode I and II crack, respectively. And the propagation angle  $\theta$  is

$$\theta = 2 \arctan \left( \frac{1 - \sqrt{1 + 8(K_{II}/K_I)^2}}{4(K_{II}/K_I)} \right) \quad (3)$$

where  $K_I$  and  $K_{II}$  are stress intensity factor of mode I and II crack, respectively.

To obtain the relationship of crack length and number of cycle, the crack propagation can be numerical simulated by using the finite element method. The resemble-cracks are considered as the initial crack. The propagation increment,  $\Delta a_{med}$ , for median node of the crack front is previously specified (see Fig. 12), and the increments,  $\Delta a_{oth}$ , for other calculation nodes of the crack front are obtained by Eq. (4).

$$\Delta a_{oth} = \Delta a_{med} \left( \frac{\Delta K_{oth}}{\Delta K_{med}} \right)^m \quad (4)$$

where  $\Delta a_{med}$  is the crack propagation increment for the median node of the crack front, and  $\Delta K_{med}$  is the corresponding stress intensity factor amplitude.  $\Delta a_{oth}$  and  $\Delta K_{oth}$  are respectively the crack propagation increments and the stress intensity factor amplitudes for other nodes of the crack front.

The crack propagation of the weld root can be directly simulated by using the above equations. Taking the propagation analysis of the root-deck and toe-deck cracks as an example,  $a_0^{Root}$  and  $a_0^{Toe}$  are the initial crack depths of the weld root and toe, respectively. Assuming that the stress intensity factor amplitude of the root-deck crack,  $\Delta K_{i,med}^{Root}$ , is greater than,  $\Delta K_{i,med}^{Toe}$ , of the toe-deck crack, for the  $i$ th propagation step, and the propagation increment,  $\Delta a_{i,med}^{Root}$ , for the median crack front of the root-deck crack is also predefined, the crack propagation increment,  $\Delta a_{i,med}^{Toe}$ , for the median crack front of the root-toe crack can be determined by Eq. (5).

$$\Delta a_{i,med}^{Toe} = \Delta a_{i,med}^{Root} \left( \frac{\Delta K_{i,med}^{Toe}}{\Delta K_{i,med}^{Root}} \right)^m \quad (5)$$

The final propagation depths of the root-deck and toe-deck cracks can be calculated by Eq. (6).

$$a_{med}^{Toe} = \sum \Delta a_{i,med}^{Toe} \cdot a_{med}^{Root} = \sum \Delta a_{i,med}^{Root} \quad (6)$$

Therefore, the crack propagation life  $N_p$  can be calculated by Eq. (7) [35]. For the same weld seam, the number of loading cycles experienced by the weld root  $N^{Root}$  and weld toe  $N^{Toe}$  should be the same.

$$N_p = N^{Toe} = N^{Root} = \sum \frac{\Delta a_{i,med}^{Root}}{C(\Delta K_{i,med}^{Root})} = \sum \frac{\Delta a_{i,med}^{Toe}}{C(\Delta K_{i,med}^{Toe})} \quad (7)$$

After the cracked joint is repaired, the determination for the initial cracks of repaired joint is of paramount importance. For the cracked

joint reinforced by the interior repair weld, the final propagation depths of the root-deck and toe-deck cracks of the cracked joint before reinforcement can be defined as the initial cracks of the repaired joint. First, the dominant crack of the repaired joint is determined according to the stress intensity factor amplitude. The crack propagation increments of the repaired joint,  $\Delta a_{i,med}^{Root}$ ,  $\Delta a_{i,med}^{Toe}$ , for the  $i$ th propagation step can be obtained by Eq. (5). Then the increments,  $\Delta a_{oth}$ , for other calculation nodes of the crack front are obtained by Eq. (4). Finally, the final propagation depths of the cracks and propagation life for the reinforced joint can be calculated by Eqs. (6) and (7). Therefore, the main framework of the evaluation process of welded joints with multiple failure modes before and after reinforcement is illustrated in Fig. 12. On the basis of the fatigue life analysis of the welded joints before repairing, the influence of multiple failure modes is considered to form a systematic analysis of the reinforced joints.

### 3.2. Numerical simulation

To simulate the crack propagation and estimate the fatigue life, the finite element models of the specimens were established. Considering the complexity of crack propagation simulation, the sub-model technique is adopted in this study, as shown in Fig. 13. The solid element SOLID45 was used to establish the global model. The solution of nodal displacements in the global model is interpolated onto the relevant parts of the boundary of the sub-model. Note that the meshes at the crack front are refined to fit the singularity of stress field at the crack tip by introducing hexahedron elements SOLID95 in the two outer layers, 15-node wedge singular element in the core layer. The part away from the crack front was transitioned by tetrahedral element SOLID92. The constraints on the both sides of deck are simply supported as same as the real condition, and the constraint on the angle steel of U-rib bottom plate is fixed support. The elastic modulus and Poisson's ratio are 206 GPa and 0.3, respectively.

Sensitivity analysis was performed to investigate the influence of mesh size on stress results. The meshing size of rib-to-deck welded joint is refined from 8 mm to 0.5 mm, and the simulated stress at the weld root under the different meshing sizes were compared in Fig. 14. Considering both the computational efficiency and meshing quality, a mesh size of 2 mm was adopted. To validate the accuracy of finite element model, taking SRD-I as an example, the calculated strains of finite element model at the arranged measuring points are compared to the measured values under a loading of 45 kN, as shown in Fig. 15. An error of less than 5% between the simulated and measured strains demonstrates the accuracy of the established finite element model, which can be further used to investigate the effect of interior repair welding on the improvement of fatigue life.

The statistical analysis of resemble-crack defect size at the single-side and double-side welded rib-to-deck welded joints in [29] were referred in this study. The size of resemble-crack at weld toe is mainly

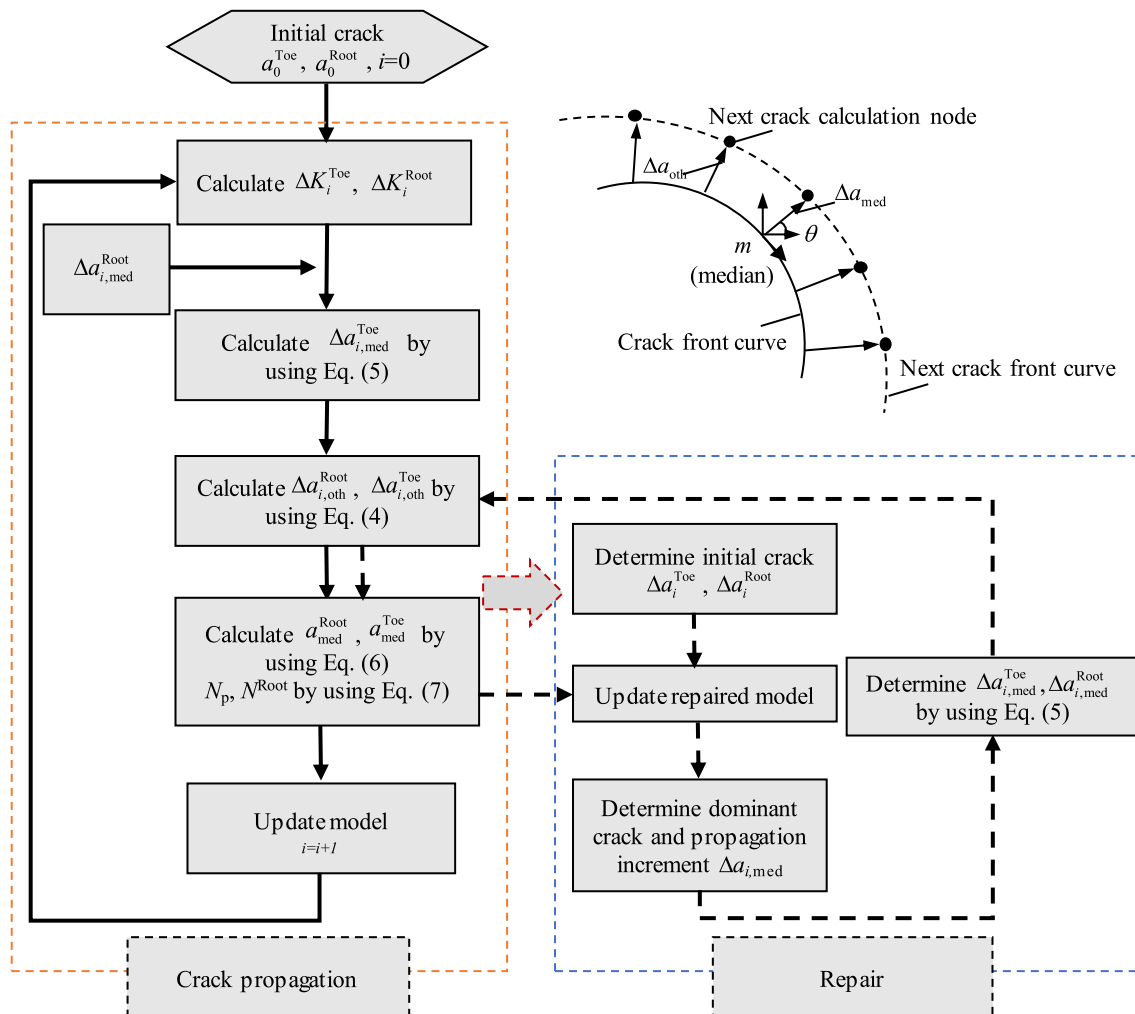


Fig. 12. The evaluation process of fatigue life of welded joints.

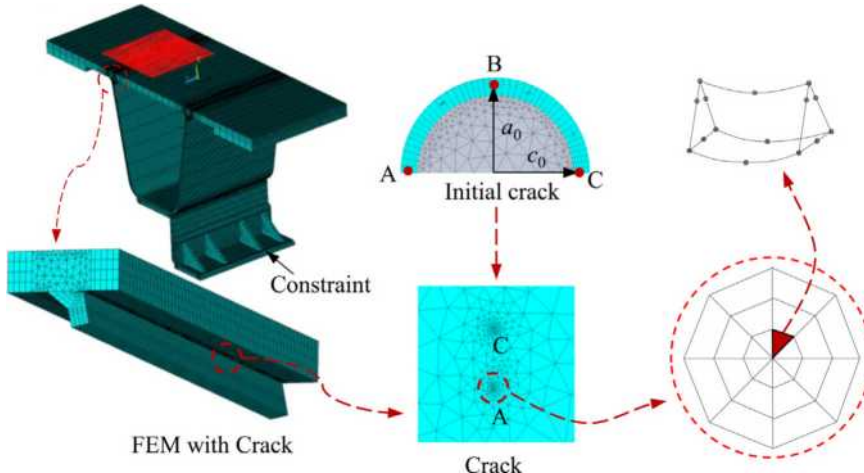
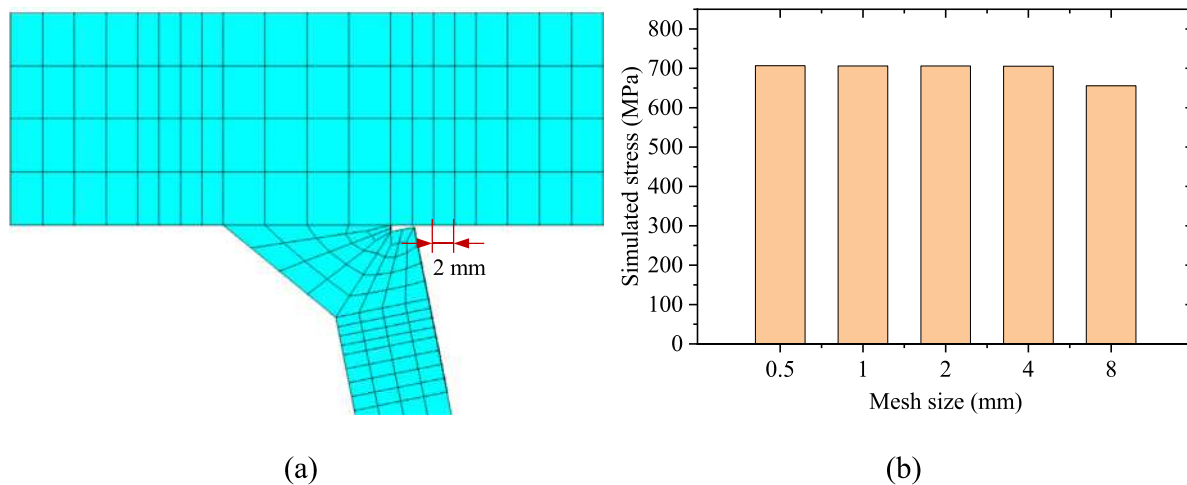


Fig. 13. Finite element model including cracks.

distributed between 20  $\mu\text{m}$  and 40  $\mu\text{m}$ , while the size of resemble-crack at weld root is mainly distributed between 100  $\mu\text{m}$  and 200  $\mu\text{m}$ . In this study, the initial size of crack depth for fracture mechanics at weld toe being determined by the fracture surface of weld toe, is approximately 40  $\mu\text{m}$ , which is in conformity with the value reported in [29]. However, the initial size of crack depth at weld root cannot be determined by

the fracture surface of weld root which has been destructed by the interior repair welding. Therefore, an average value of resemble-crack at weld root investigated in [29] is adopted in this study. Finally, the initial sizes of crack depth at weld root and toe are 40  $\mu\text{m}$  and 150  $\mu\text{m}$ , respectively. Due to the initial crack has strong association in the length direction, it is considered that the initial crack has a



**Fig. 14.** Mesh size sensitivity analysis: (a) mesh size on the finite element model; (b) simulated stress at the weld root with different mesh sizes.

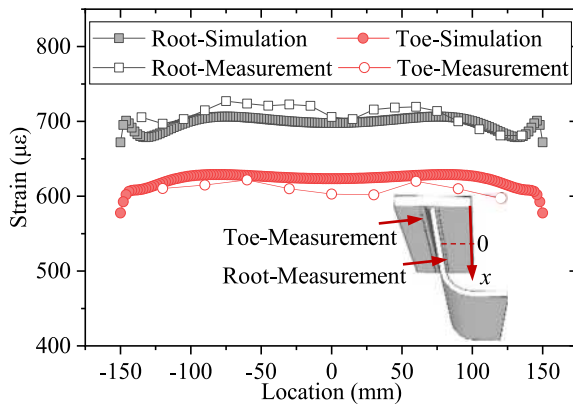


**Fig. 15.** Comparisons of testing and simulated values.

smaller depth-to-length ratio ( $a_0/2c_0$ ) [29,30,36], and the initial radius of the cracks  $a_0/2c_0$  is 0.1 in this study. Besides, the multiple crack propagations at the same seam was observed by the inspection, but they are mutually independent without coalescence. Therefore, the effect of multiple crack propagations at the same seam is ignored in the crack simulation process to facilitate the study of the mutual relationship between multiple failure modes before and after reinforcement.

The numerical simulations of fatigue crack should fully coincide with the fatigue crack initiation and propagation in the specimens (see Fig. 10) as below

(1) When the rib-to-deck joint was subjected to cyclic loading for a period of time, a visible crack was formed at the weld root, and a microcrack was formed at the weld toe as well (see Fig. 16(a)).

(2) After internal repair welding, the root-deck crack was changed into an internal defect, and the finite element model and sub-model were updated. It is assumed that the shape of the intrinsic root-deck crack remains unchanged except that the weld root is welded, as shown in Fig. 16(b).

(3) At last, the toe-deck crack at the exterior weld toe of reinforced joint still grows under cyclic loading, as shown in Fig. 16(c).

The comparison between the measured and simulated cracks of SRD-I in Stage I is shown in Fig. 17. The location and dimensions of the simulated crack are basically consistent with the maximum depth of the actual measured crack.

### 3.3. Result discussion

The stress intensity factor amplitudes at the crack tip before and after reinforcement are investigated, as shown in Fig. 18. The reduction of stress intensity factor for root-deck crack after repairing is basically 70%. Although the stress intensity factor amplitudes of the root-deck crack in SRD-I after repairing are greater than the propagation threshold  $63 \text{ MPa mm}^{1/2}$  [37], a crack propagation of 1 mm along the direction of depth needs 1,545,000 cycles with a stress intensity factor amplitude at the middle crack front (point B) of  $107.5 \text{ MPa mm}^{1/2}$ . At the same time, the crack growth per millimeter along the direction of length needs 1,217,000 cycles with a stress intensity factor amplitude at the point C of  $116.4 \text{ MPa mm}^{1/2}$ . Similarly, the stress intensity factor amplitudes of the root-deck crack in SRD-II after repairing are greater than the propagation threshold as well. A crack propagation of 1 mm along the direction of depth in SRD-II needs 1,292,000 cycles with a stress intensity factor range at the point B of  $114.1 \text{ MPa mm}^{1/2}$ . The crack growth per millimeter along the direction of length needs 1,116,000 cycles with a stress intensity factor amplitude at the point C of  $119.8 \text{ MPa mm}^{1/2}$ . However, the stress intensity factor amplitude

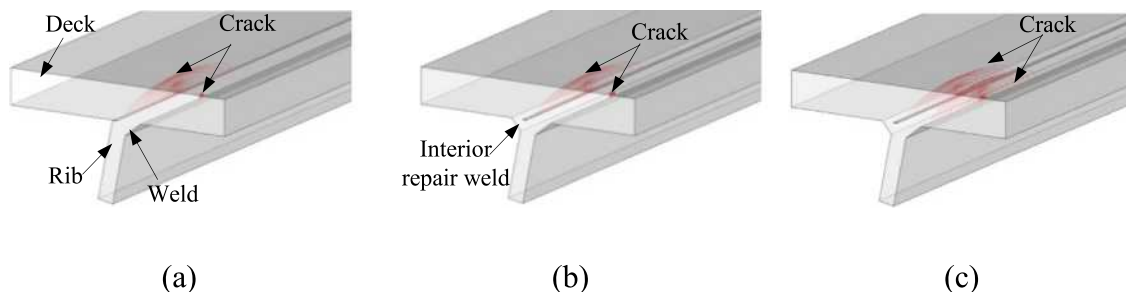


**Fig. 16.** Numerical simulation of crack propagation: (a) before interior repair welding; (b) interior repair welding; (c) after interior repair welding.

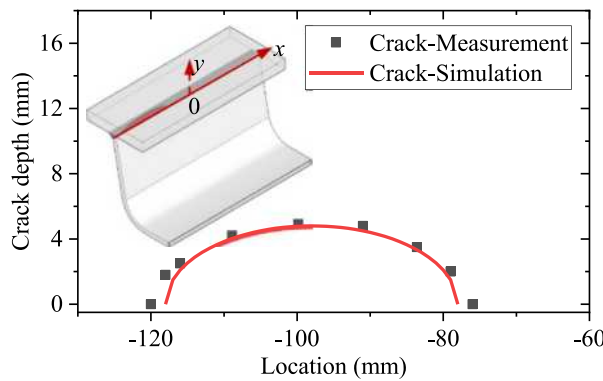


Fig. 17. Numerical simulation of crack shape of SRD-I in Stage I.

at the weld toe keeps increasing in Stage II, and the crack propagation rate continues to accelerate, gradually becoming the dominant crack.

In Stage I, for both SRD-I and SRD-II, the stress intensity factor amplitudes of toe-deck crack increases slowly at first, then increases rapidly and finally increases slowly with the rise of cycles. With the continuous propagation of the root-deck crack, the stresses at the weld toe are continuously reduced (see Figs. 8(b) and (d)), resulting in the decrease of the toe-deck crack propagation rate. Fig. 19 shows the

stress distribution of the exterior weld toe at SRD-I without the root-deck crack, with the root-deck crack, and with the interior repair welding. In Stage II, the stresses at exterior weld toe after reinforcement are redistributed, leading to a jump in the stress intensity factor range of toe-deck crack, and the crack propagation rate of toe-deck crack is faster after repair than before enhancement. Besides, the toe-deck crack propagation rate in the depth direction has a downward tendency after a certain number of cycles, while toe-deck crack propagation rate in the length direction remains an upward tendency under cyclic loading, resulting in a several times difference between depth and length of crack reported in [28,35–37]. Compared with the toe-deck crack, the root-deck crack propagation rate of rib-to-deck joint can be ignored. The interior repair weld seriously retards the propagation of the root crack.

It can be seen that the toe-deck crack propagation becomes the dominant cracking mode after interior repair welding, and considering the damage accumulation before and after reinforcement is necessary for the evaluation of welded joints with multiple failure modes.

#### 3.4. Remaining life

The crack propagations of those specimens at Stage I and II as the number of cycles increases are shown in Fig. 20. The initial crack depths at the weld toe and root in the different specimens with the different crack propagation locations are determined by the monitored strain data. Then, the remaining lives of reinforced SRD-I and SRD-II

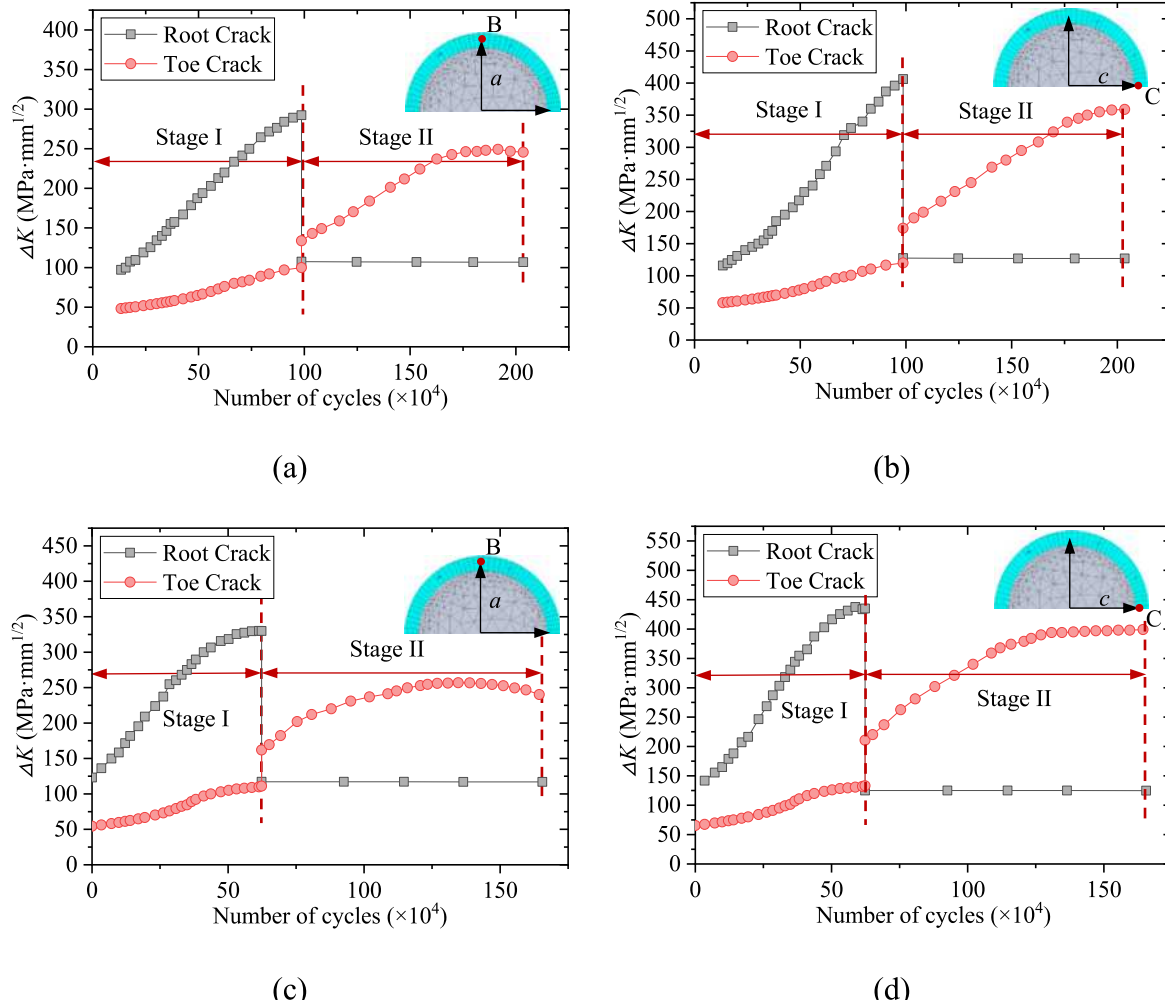


Fig. 18. The amplitude of stress intensity factor versus: (a) the cycles of SRD-I at point B; (b) the cycles of SRD-I at the point C; (c) the cycles of SRD-II at the point B; and (d) the cycles of SRD-II at the point C.

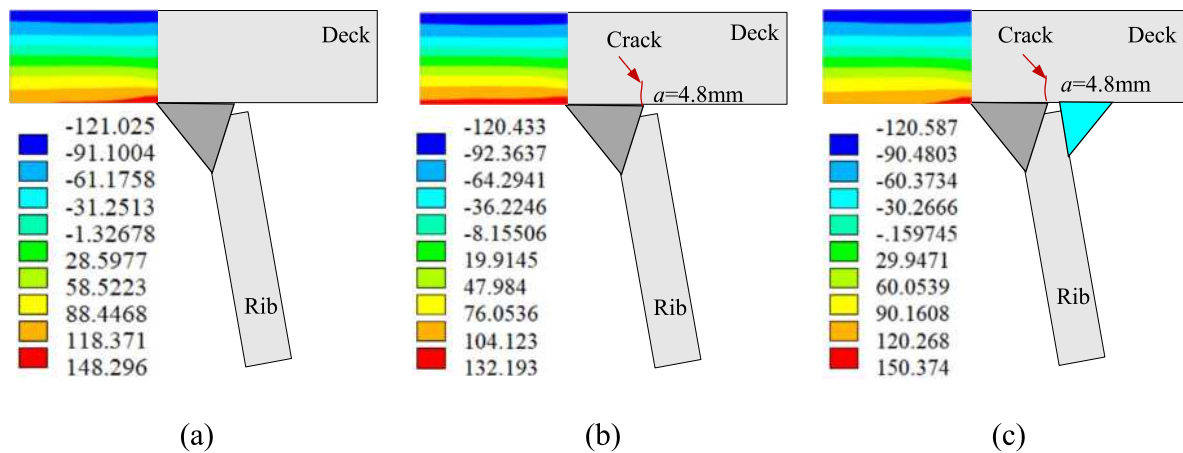


Fig. 19. The stress state of the exterior weld toe at SRD-I: (a) without root-deck crack; (b) with root-deck crack; and (c) after interior repair welding.

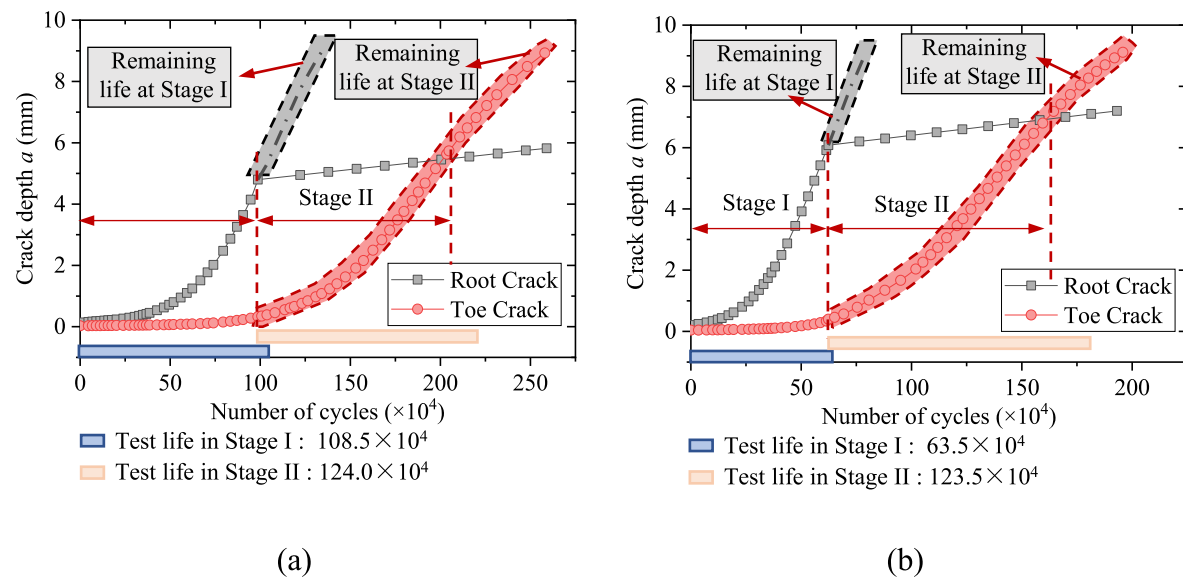


Fig. 20. The crack depth versus cycles curves for: (a) SRD-I; (b) SRD-II.

are simulated using the aforementioned method. The depth of root-deck crack in SRD-I grew to 4.8 mm at the end of Stage I, and the depth of toe-deck crack propagated to 0.32 mm. For SRD-II, the root-deck crack propagated to 6.1 mm at the end of Stage I, while the toe-deck crack extended to 0.4 mm. The depths of root-deck and toe-deck cracks at the end of Stage I are the initial cracks in Stage II. To uniformly evaluate the remaining life of welded joints, the critical crack depth in Stage II for numerical simulation is set as the half thickness of the deck plate in this study. Comparing to the experimental results of fatigue life of SRD-I and SRD-II in Table 2, the deviations of prediction results are 7.8% and 10.2%, respectively. It can be considered that the predicted results are in good agreement with the experimental values, due to the complex influencing factors of the crack propagation.

As a comparison, the crack propagation of those specimens without repairing was also simulated. It can be seen that the interior repair weld considerably prevents the propagation rate of root-deck crack and improves the fatigue life. The fatigue life is decided by the propagation of the exterior toe-deck crack after repairing. The remaining life of SRD-I is about 360,000 without repairing after cyclic loading in stage I. After interior repair welding, the remaining life increases to about 1,780,000, which is about 5 times as long as that without interior repair welding. The remaining life of SRD-II jumps from about 160,000 to more than 1,330,000 after considering the interior repair, resulting in

an increasing of more than 8 times. The fatigue lives of SRD-I and SRD-II are sharply improved by the interior repair welding. The calculated depths of root-deck and toe-deck cracks at the end of Stage I are equivalent to the existing fatigue damages at the weld toe in the calculation of remaining lives. The existing fatigue damage is the main reason for the dominant failure mode transferred from interior root-deck crack to exterior toe-deck crack after the interior repair welding. Considering crack propagation behaviors of each mode before reinforcement is the necessary condition for acceptance of the reinforced design.

#### 4. Conclusions

Based on analytical and experimental studies, the following conclusions are drawn:

- (1) The interior repair weld can effectively prevent the root-deck crack propagation, and the dominant failure mode transferred from interior root-deck crack to exterior toe-deck crack after the interior repair welding. Oppositely, failure mode at the double-sided welded rib-to-deck joint was the interior toe-deck crack.
- (2) The remaining lives of SRD-I and SRD-II with or without the interior repair welding are compared by the association of the fracture mechanics. The remaining lives of SRD-I and SRD-II after interior repair welding are respectively about 5 and 8 times that without the interior

repair welding. The interior repair weld significantly improves the fatigue life of the rib-to-deck joints.

## CRediT authorship contribution statement

**Ming-zhe Li:** Writing – review & editing, Writing – original draft, Validation, Investigation. **Chuang Cui:** Writing – review & editing, Writing – original draft, Validation, Resources, Funding acquisition. **Hao Wang:** Visualization, Validation, Investigation. **Qing-hua Zhang:** Writing – review & editing, Funding acquisition, Conceptualization. **Letian Da:** Visualization, Validation, Investigation. **Yi-zhi Bu:** Writing – review & editing, Project administration.

## Declaration of competing interest

The authors declare that they have no known competing financial interests or personal relationships that could have appeared to influence the work reported in this paper.

## Data availability

Data will be made available on request.

## Acknowledgments

This work was supported by the Research and Development Projects in Key Areas of Guangdong Province, China [grant number 2019B111106002], National Natural Science Foundation of China [grant numbers 52108176, 51978579, 51878561], Sichuan Science and Technology Program, China [grant number 2021YJ0037], the Transportation Science and Technology Project of Sichuan Province [grant number: 2020-B-02] and National Key Research and Development Program of China [2022YFB3706405].

## References

- [1] C. Wang, Y. Wang, Effectiveness and durability evaluation of cold reinforcement for Distortion-induced fatigue in steel bridges, *Eng. Fail. Anal.* 135 (2022) 106107.
- [2] M.H. Kolstein, Fatigue Classification of Welded Joints in Orthotropic Steel Bridge Decks, Delft University of Technology, Delft, 2007.
- [3] J. Fisher, J. Barsom, Evaluation of cracking in the rib-to-deck welds of the BronxWhitestone Bridge, *J. Bridge Eng.* 21 (3) (2015) 04015065.
- [4] M. Ahmadivala, J. Berthelemy, O. André, et al., A strategy for rib-to-deck crack propagation analysis and strengthening of orthotropic deck bridges, *Eng. Fail. Anal.* 134 (2022) 106057.
- [5] D.L. Wang, C. Xiang, Y.H. Ma, et al., Experimental study on the root-deck fatigue crack on orthotropic steel decks, *Mater. Des.* 203 (2021) 109601.
- [6] S. Kainuma, M.Y. Yang, Y.S. Jeong, et al., Experiment on fatigue behavior of rib-to-deck weld root in orthotropic steel decks, *J. Construct. Steel Res.* 199 (2016) 113–122.
- [7] Editorial Department of China Journal of Highway and Transport, Review on China's bridge engineering research: 2021, *China J. Highw. Transp.* 34 (02) (2021) 1–97 (in Chinese).
- [8] Z.Q. Fu, Q.D. Wang, B.H. Ji, et al., Rewelding repair effects on fatigue cracks in steel bridge deck welds, *J. Perform. Constr. Facil.* 31 (6) (2017) 04017094.
- [9] J.E. Rodriguez-Sanchez, W.D. Dover, Brennan, Application of short repairs for fatigue life extension, *Int. J. Fatigue* 26 (2004) 413–420.
- [10] Y. Lu, F. Yang, T. Chen, H. Gong, The retardation effect of combined application of stop-hole and overload on sheet steel, *Int. J. Fatigue* 132 (2020) 105414.
- [11] C. Wang, M. Zhai, L. Duan, Y. Wang, Cold reinforcement and evaluation of steel bridges with fatigue cracks, *J. Bridge Eng.* 23 (04) (2018) 04018014.
- [12] Z.Q. Fu, B.H. Ji, X.M. Kong, et al., Grinding treatment effect on rib-to-roof weld fatigue performance of steel bridge decks, *J. Perform. Constr. Facil.* 129 (2017) 163–170.
- [13] K. Yamada, T. Ishikawa, T. Kakiuchi, Rehabilitation and improvement of fatigue life of welded joints by ICR treatment, *Adv. Steel Constr.* 11 (3) (2015) 294–304.
- [14] Q.H. Zhang, Y.M. Liu, Y. Bao, et al., Fatigue performance of orthotropic steel-concrete composite deck with large-size longitudinal U-shaped ribs, *Eng. Struct.* 150 (2017) 864–874.
- [15] S.L. Wang, Z.T. Ke, Y. Gao, et al., Long-term in Situ performance investigation of orthotropic steel bridge deck strengthened by SPS and RPC solutions, *J. Bridge Eng.* 24 (6) (2019) 04019054.
- [16] J. Liu, T. Guo, D. Feng, Z. Liu, Fatigue performance of rib-to-deck joints strengthened with FRP angles, *J. Bridge Eng.* 23 (9) (2018) 04018060.
- [17] Y.Z. Wang, C.S. Wang, L. Duan, Bonding and bolting angle reinforcement for distortion-induced fatigue in steel girder bridges, *Thin-Walled Struct.* 166 (2021) 108027.
- [18] Y. Wang, X.D. Shao, J. Chen, et al., UHPC-based strengthening technique for orthotropic steel decks with significant fatigue cracking issues, *J. Construct. Steel Res.* 176 (2021) 106393.
- [19] F.B.P. DeJong, Renovation Techniques for Fatigue Cracked Orthotropic Steel Bridge Decks, Delft University of Technology, Delft, 2007.
- [20] J. Maljaars, F.V. Dooren, H. Kolstein, Fatigue assessment for deck plates in orthotropic bridge decks, *Steel Constr.* 5 (2) (2012) 93–100.
- [21] S. Teixeira, H. Kolstein, F. Bijlaard, Fatigue assessment of full-scale retrofitted orthotropic bridge decks, *J. Bridge Eng.* 22 (11) (2017) 04017092.
- [22] J.H. Choi, D.H. Kim, Stress characteristics and fatigue crack behaviour of the longitudinal rib-to-cross beam joints in an orthotropic steel deck, *Adv. Struct. Eng.* 11 (2) (2008) 189–198.
- [23] Z.G. Xiao, K. Yamada, S. Ya, et al., Stress analyses and fatigue evaluation of rib-to-deck joints in steel orthotropic decks, *Int. J. Fatigue* 30 (8) (2008) 1387–1397.
- [24] P. Wang, X. Pei, P. Dong, S. Song, Traction structural stress analysis of fatigue behaviors of rib-to-deck joints in orthotropic bridge deck, *Int. J. Fatigue* 125 (2019) 11–12.
- [25] J. Luo, X. Shao, J. Cao, M. Xiong, W. Fan, Transverse bending behavior of the steel-UHPC lightweight composite deck: Orthogonal test and analysis, *J. Construct. Steel Res.* 162 (2019) 105708.
- [26] Y. Liu, F. Chen, N. Lu, L. Wang, B. Wang, Fatigue performance of rib-to-deck double-side welded joints in orthotropic steel decks, *Eng. Fail. Anal.* 105 (2019) 127–142.
- [27] H. Yang, P. Wang, H. Qian, S. Niu, P. Dong, An experimental investigation into fatigue behaviors of single- and double-sided U rib welds in orthotropic bridge decks, *Int. J. Fatigue* 159 (2022) 106827.
- [28] C. Cui, Y. Ma, Q.H. Zhang, L.T. Da, S.H. Han, Fatigue strength and crack growth of double-side welded rib-to-deck joint in orthotropic steel decks, *J. Construct. Steel Res.* 196 (2022) 107444.
- [29] J. Li, Research on Formation Mechanism and Performance Evaluation of Dominant Fatigue Failure Modes of Orthotropic Steel Deck, Southwest Jiaotong University, Chengdu, 2021 (in Chinese).
- [30] K. Pang, H. Yuan, Assessment of three-dimensional multi-crack propagation for fatigue life prediction, *Int. J. Press. Vessels Pip.* 198 (2022) 104660.
- [31] W. Taleb, C. Gardin, C. Sarrazin, 3D predictions of the local effective stress intensity factor as the fatigue crack propagation driving force, *Int. J. Fatigue* 151 (2021) 106365.
- [32] BS 7910: Guide to Methods for Assessing the Acceptability of Flaws in Metallic Structures, BSI Standards Limited, London, 2015.
- [33] R.J. Nuismer, An energy release rate criterion for mixed mode fracture, *Int. J. Fract.* 11 (2) (1975) 245–250.
- [34] C. Cui, Y. Xu, Q. Zhang, Multiscale fatigue damage evolution in orthotropic steel deck of cable-stayed bridges, *Eng. Struct.* 237 (2021) 112144.
- [35] T. Agoda, K. Gowacka, Fatigue life prediction of welded joints from nominal system to fracture mechanics, *Int. J. Fatigue* 137 (2020) 105647.
- [36] Z. Barsoum, I. Barsoum, Residual stress effects on fatigue life of welded structures using LEFM, *Eng. Fail. Anal.* 16 (2019) 449–467.
- [37] B. Wang, W. Nagy, H. De Backer, A. Chen, Fatigue process of rib-to-deck welded joints of orthotropic steel decks, *Theor. Appl. Fract. Mech.* 101 (2019) 113–126.



## Fatigue behavior of welded coverplates treated with Ultrasonic Impact Treatment and bolting

Brian Vilhauer<sup>a</sup>, Caroline R. Bennett<sup>b,\*</sup>, Adolfo B. Matamoros<sup>b,1</sup>, Stanley T. Rolfe<sup>b</sup>

<sup>a</sup>910 Par Ln., Dell Rapids, SD 57022, United States

<sup>b</sup>University of Kansas, Civil, Environmental, and Architectural Engineering Department, 1530 W. 15th St., 2150 Learned Hall, Lawrence, KS 66045, United States

### ARTICLE INFO

#### Article history:

Received 6 April 2010

Revised 23 February 2011

Accepted 4 September 2011

Available online 4 November 2011

#### Keywords:

Fatigue

Bolts

Welds

Cracking

Rehabilitation

Retrofit

Ultrasonic Impact Treatment

Cover plate

Steel bridge

### ABSTRACT

Damage due to traffic-induced fatigue is a common problem in welded steel girder bridges. Engineers tasked with the duty of repairing fatigue-damaged bridges face difficult decisions about the choice of repair method to implement. In some instances different repair methods are used in combination, under the assumption that the combined effects of two techniques that have been shown separately to improve fatigue life will result in greater improvement. This study evaluated the interaction that may take place between different repair methods for a particular type of fatigue vulnerable detail. The detail that was chosen for the study was a welded connection between a plate and a coverplate, often used in older bridges. Specifically, this study investigated the fatigue life enhancement afforded by three retrofit methods: post-installation of tensioned bolts behind the weld, application of Ultrasonic Impact Treatment (UIT) to the weld, and a combination of the two techniques.

Results of 15 fatigue tests showed that UIT was a highly effective technique to enhance the fatigue life of coverplate end details. Weld treatment with UIT resulted in an improvement in fatigue life over control specimens by a factor of 25. This translated into an improvement in fatigue life from that of an AASTHO fatigue Category E detail to that of an AASHTO fatigue Category A detail. The bolting procedure, as implemented in this study, had a negligible effect on fatigue life. The combination of the two methods was found to be less effective than using UIT alone due to stresses induced by the bolt on the untreated portion of the weld.

© 2011 Elsevier Ltd. All rights reserved.

### 1. Introduction

Numerous aging steel highway bridges are currently developing cracks due to traffic-induced fatigue. Many of these bridges were designed at a time when little was known about the causes of fatigue crack initiation and propagation in steel structures. As a result, structural connection details having fatigue-vulnerable combinations of geometric discontinuities and large stress ranges were used in these structures. Many of these details are now recognized as undesirable and are no longer constructed. However, state Departments of Transportation (DOTs) must repair existing fatigue cracks and retrofit susceptible connection details. Due to the escalating costs of bridge replacement coupled with the large number of aging steel bridges with fatigue-susceptible details across the United States, means to efficiently extend the useable life of fatigue-prone steel bridges are critically needed.

Welded connections in steel bridge girders account for a large percentage of fatigue critical details in the national inventory. Welds are particularly susceptible to fatigue cracking because of planar or volumetric discontinuities often present in the weld or base metal, such as porosity, slag inclusions, lack of fusion, and undercut [1]. Additional factors such as geometry-induced stress concentrations, residual stresses, and distortion tend to decrease the fatigue strength of welded connections. This is particularly worthy of consideration given that many common steel bridge girder connections utilize welded connections in a wide range of applications, including cover plates, transverse and longitudinal stiffeners, connection plates, flange transitions, and web-to-flange connections.

Welded cover plates are of especial concern because this is a common detail particularly vulnerable to fatigue damage. Although welded coverplates are no longer commonly used to increase bending resistance of bridges, this was not the case 40 years ago. Many existing bridges were retrofitted with welded coverplates to increase their capacity as traffic loads intensified over time. It has since been found that welded cover plates tend to be particularly susceptible to fatigue crack initiation in the welds at cover plate terminations, and for this reason have been

\* Corresponding author. Tel.: +1 (785) 864 3235; fax: +1 (785) 864 5631.

E-mail addresses: [crb@ku.edu](mailto:crb@ku.edu) (C.R. Bennett), [abm@ku.edu](mailto:abm@ku.edu) (A.B. Matamoros), [srolfe@ku.edu](mailto:srolfe@ku.edu) (S.T. Rolfe).

<sup>1</sup> Tel.: +1 (785) 864 3235; fax: +1 (785) 864 5631.

## Nomenclature

$\Sigma_c$	stress, MPa (ksi)	$A$	constant for a particular AASHTO fatigue detail category, MPa <sup>3</sup> (ksi <sup>3</sup> )
$c$	distance from the neutral axis to an extreme fiber on the cross-section, mm (in.)	$N$	number of fatigue cycles to failure
$I$	bending moment of inertia, mm <sup>4</sup> (in. <sup>4</sup> )	$\Delta F_{TH}$	stress range corresponding to infinite life of a particular fatigue detail category, MPa (ksi)
$\delta F_n$	stress range, MPa (ksi)		

subsequently classified among the worst performing AASHTO fatigue Categories E and E' [2–4].

Improved practices have since emerged for retrofitting susceptible welded coverplates and for installing new cover plates with better performing fatigue details. One mechanism for improving performance of cover plates is to extend the coverplate into a region of compressive stress or to an inflection point, where tensile stress ranges are negligible. Another method is to remove end welds and develop the full moment capacity of the cover plate through a bolted connection. The detail resulting from the latter technique is now classified as an AASHTO fatigue Category B detail [7].

Another accepted method for improving fatigue performance of welded connections that has been successfully applied to coverplates is Ultrasonic Impact Treatment (UIT) [8–10]. Ultrasonic Impact Treatment has been shown to reduce the likelihood of fatigue cracks in weldments by relaxing tensile residual stresses introduced during welding, and by smoothing imperfections on the surface of the weld. Both effects are achieved through application of ultrasonic stress waves at the surface of the weld. The stress waves induce plastic deformations, which leave a residual compressive stresses on the order of the yield strength of the weld metal near the surface of the weld. Because fatigue cracks form primarily at imperfections in regions subjected to high tensile stress ranges, introduction of large compressive stresses and the smoothing of the surface greatly retard and may eliminate formation of fatigue cracks at the location of treatment. Since UIT is generally performed at regions having the greatest tensile stress concentrations, usually weld toes and weld discontinuities, the regions most prone to fatigue crack growth benefit the most from induced compressive stresses. When UIT treatment is performed at the toe of a fillet weld, the change in shape of the zone of plastic deformation also reduces the concentration of stress at the weld toe, as the treated surface has a larger radial shape than does an untreated weld toe.

## 2. Research significance and objective

The objective of the study was to investigate the effectiveness and interaction of various repair methods on the fatigue life of a commonly used fatigue-vulnerable connection detail. The specific repair methods evaluated were Ultrasonic Impact Treatment (UIT) of the weld, installation of tensioned bolts behind the weld, and the combination of UIT of the weld and installation of tensioned bolts. A cover plate detail was chosen for study because of the prevalence of this detail in aging steel bridges, its simplistic geometric configuration and design, and its poor fatigue performance.

Installation of bolts in an existing welded coverplate as a fatigue strengthening method requires removal of the weld at the coverplate ends so that load transfer can take place through the bolts instead of the weld. Improvements in fatigue life due to post-installation of bolts coupled with weld removal are well documented in studies by Yamada and Albrecht [3] and Simon and Albrecht [4]. In the present study, rather than expand on the fatigue related benefits of post-installing bolts in cover plates, the welds were left in place to study the interaction between post-installed tensioned bolts and welded connections treated

with UIT. For example, fatigue cracks were observed in a bridge in Kansas at connections between gusset plates from cross-bracing and girder flanges [5,6]. These connections developed a prying effect due to deformations imposed by the cross brace on the girder flange that caused fatigue cracks. Bolts were post-installed to counteract the prying effect, but questions remained about the beneficial effects of treating the welds with UIT.

## 3. Experimental program

Fifteen welded steel specimens, each representative of a girder flange with a welded cover plate, were fabricated using Grade A36 steel. Of those 15 specimens, six were control specimens receiving no treatment (designated CONTROL), three were treated with UIT along the weld toe at the cover plate ends (designated UIT), three had tensioned bolts installed near both ends of the coverplate (designated BOLT), and three had both UIT and tensioned bolts installed near both ends of the coverplate (designated UIT/BOLT). The 15 specimens were fabricated in two batches: the first batch was comprised of 12 steel specimens, after which a second batch comprised of three additional control specimens was fabricated.

### 3.1. Steel specimen design and testing program

A schematic of the steel specimens is provided in Fig. 1. A bar with dimensions PL 25.4 × 114 × 1270 mm (PL 1.00 × 4.50 × 50.0 in.) was chosen for the plate representing the girder flange, and a bar with dimensions PL 25.4 × 76.2 × 660 mm (PL 1.00 × 3.00 × 26.0 in.) was chosen for the coverplate element. The coverplate element was chosen to be as wide as possible while still allowing ample flange surface on each side to accommodate the fillet weld, while the length was chosen considering shear lag effects and St. Venant's Principle. Shielded metal arc (SMAW) 7.94-mm (0.313 in.) fillet welds were used to connect the coverplates to the flanges, with the weld applied all-around the coverplate element. This weld size and configuration are commonly used for welding bridge coverplates because it is the largest size fillet weld that can be laid in a single pass. The primary purpose of the experimental program was to compare fatigue behavior of treated and untreated specimens. Although not essential to the outcome, AASHTO detail categorization is presented here to provide a frame of reference for the results of the study. To account for the fact that the neutral axis of the cross-section was within the flange plate (rather than far above the weld toe, in the web or top flange), nominal stresses were calculated directly at the weld toe to reflect the normal bending stress at that specific location. Therefore, a stress range reported as 138 MPa (20.0 ksi) implies that this was the nominal tensile bending stress value calculated for a bare steel specimen at the toe of the weld.

After the steel substrate specimens were fabricated, tensioned bolts were post-installed at both ends of the coverplate for six of the specimens. For each coverplate retrofitted with bolts, a 25.4-mm (1.00-in.) diameter ASTM A325 carriage bolt was installed at both coverplate ends. The bolts were tightened using a calibrated pneumatic wrench to have a minimum bolt tension of 227 kN (51.0 kips), the standard minimum bolt tension specified for this

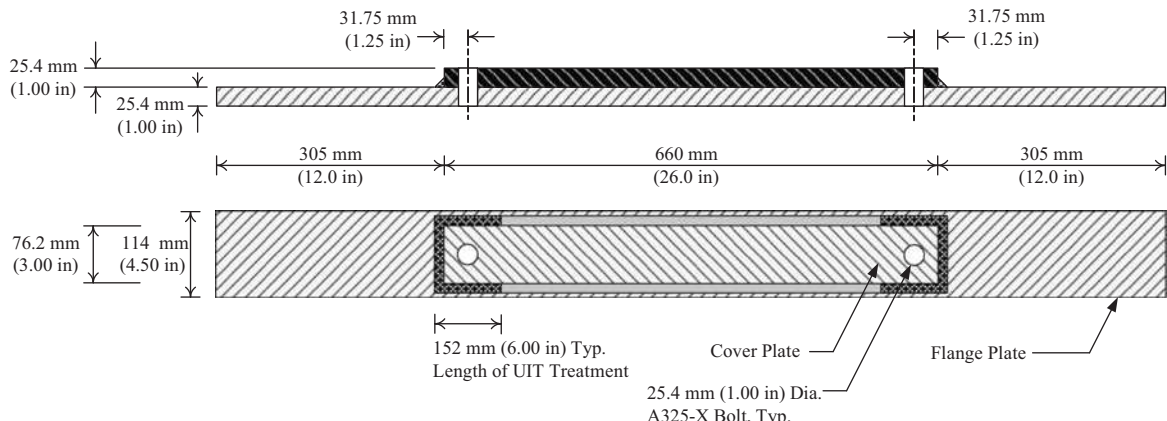


Fig. 1. Schematic of Category E' fatigue specimen.

size and grade of bolt by the American Institute of Steel Construction (AISC) [11]. The bolts were each installed with a standard flat washer on the nut-side of the connection. Because one of the reasons for installing a bolt at the end of a coverplate was to study the influence of bolt tension on the fatigue performance of the weld, the bolts were placed as close as possible to the ends of the coverplates. Therefore, the holes for the bolts were placed at the minimum edge distance of 31.8 mm (1.25 in.), measured from the edge of the coverplate to the center of the hole [11].

Each of the six specimens treated with UIT received treatment at both ends of the coverplate. Treatment was performed across the entire length of the transverse fillet weld and continued along the longitudinal fillet welds on both sides of the coverplate for a distance of 152 mm (6.00 in.), as pictured in Fig. 2. The interior portions of the longitudinal fillet welds did not receive UIT because these segments of the weld were not as prone to fatigue failure as the welds at the coverplate ends (Cat. C as opposed to Cat. E'). At the ends of each treated coverplate, additional UIT treatment was performed at points where stress concentrations were expected to exist, such as weld terminations.

### 3.2. Stress range

The procedure outlined in the AASHTO LRFD Bridge Design Specification [7] to design bridge members against fatigue failure

is a process that involves selecting a fatigue category for a member or connection detail and then determining the number of load cycles that the member or connection will be subjected to during its design life. Assigning a fatigue category is a method of quantifying the susceptibility of a member or connection to fatigue failure. AASHTO differentiates between eight fatigue categories based primarily on geometry, listed here in order of increasing severity: A, B, B', C, C', D, E, and E'.

After a member or connection has been assigned a fatigue category and the design fatigue life has been determined, a nominal design stress range for that member or connection detail can be calculated using the fatigue life equation in the 2007 AASHTO LRFD Bridge Design Specification [7]:

$$\Delta F_n = \left( \frac{A}{N} \right)^{\frac{1}{3}} \geq \frac{1}{2} (\Delta F)_{TH} \quad (1)$$

where  $\Delta F_n$  is the stress range,  $A$  is a constant for a given detail defined by AASHTO [7],  $N$  is the number of fatigue cycles to failure, and  $(\Delta F)_{TH}$  is the constant-amplitude fatigue threshold. The equation is an approximation of logarithmic behavior, with the  $^{1/3}$  factor defining the slope constant for the  $S-N$  curves. The coefficient of  $\frac{1}{2}$  on the right hand side of Eq. (1) ensures that when the design stress range is less than half of the constant-amplitude fatigue threshold, the connection detail or member will theoretically have an infinite fatigue life [12].

A literature review was conducted to estimate the increase in fatigue life associated with the retrofit methods evaluated in this study. On this basis a nominal tensile stress range at the transverse weld toe of 59 MPa (8.5 ksi) was initially chosen for the fatigue tests. For reasons discussed later, this stress range was increased gradually to 96.5 MPa (14.0 ksi), 138 MPa (20.0 ksi), and finally to 193 MPa (28.0 ksi). It should be noted that the final stress range was larger than the constant amplitude fatigue threshold for a Category A detail, which meant that the testing program had the ability to detect potential improvements in fatigue categorization up to and including Category A details.

In the course of selecting the final stress range, all three control specimens from the initial fabrication batch were tested at stress ranges lower than 193 MPa (28.0 ksi), leaving no control specimens to be tested at the final stress range. Therefore, three additional control specimens were fabricated by the same fabricator that produced the original 12 specimens. Upon visual inspection, the fillet welds on the second batch of control specimens appeared to be slightly smaller, less consistent, and of lower overall quality than the welds on the 12 original specimens. For this reason, one of the control specimens from the second fabrication batch was tested at a nominal stress range at the weld toe of 138 MPa

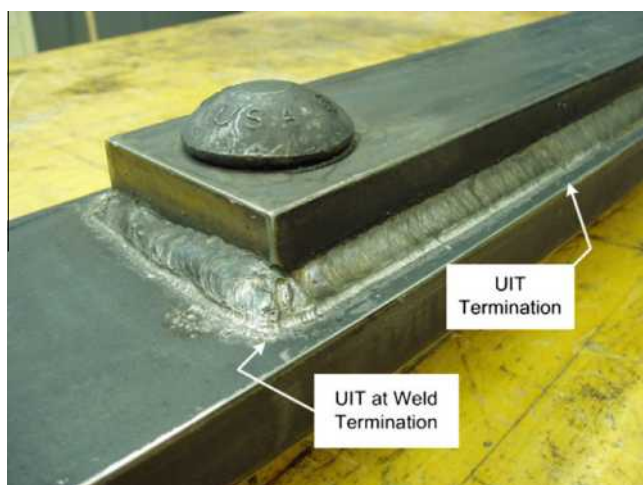
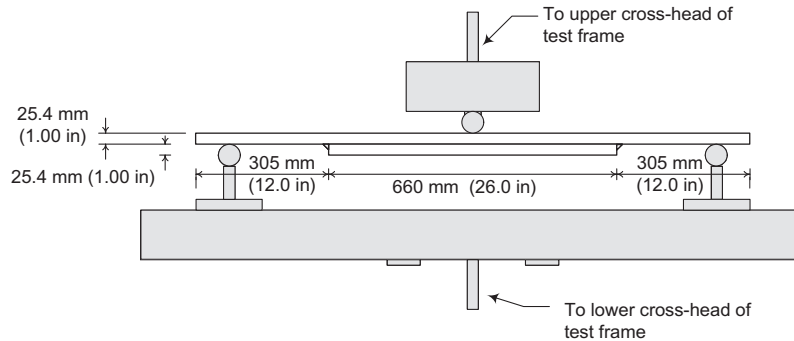
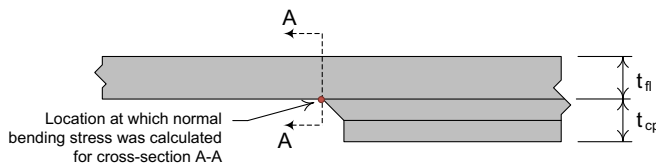


Fig. 2. Weld treated with Ultrasonic Impact Treatment; tensioned bolt installed behind an existing weld at coverplate end.



**Fig. 3.** Experimental three-point bending fatigue test set-up.



**Fig. 4.** Location of weld toe stress calculation.

(20.0 ksi), and the results were compared to the fatigue life of a control specimen from the first batch tested at a stress range of 138 MPa (20.0 ksi). This was done to ensure that the control specimens from the first and second fabrication batches had similar fatigue behavior. The other two control specimens from the second fabrication batch were tested at 193 MPa (28.0 ksi), bringing the number of specimens tested at 193 MPa (28 ksi) to 10, and total number of specimens tested to 15.

All stress ranges reported in this study are based on calculations for theoretical stress at the weld toe of the fatigue specimens. The test configuration was such that the specimens were statically determinate, with a load at the center (Fig. 3). Consequently, for an applied force,  $P$ , the moment diagram was linear with the maximum moment occurring at the center of the beam. Based on the known geometric cross-section properties of the fatigue specimens, the moment at the weld toe was computed and used to calculate the nominal stress at the weld toe using the familiar expression from beam theory:

$$\sigma = \frac{Mc}{I} \quad (2)$$

The bending moment of inertia,  $I$ , was calculated based on dimensions of the flange plate only, because the nominal bending stress being calculated was at the toe of the weld, as shown in Fig. 4. The distance from the neutral axis to the extreme fiber of interest,  $c$ , was therefore taken as 12.7 mm (0.50 in.). The bending moment,  $M$ , was taken as the moment at the location of the weld toe caused by the applied force (section A-A in Fig. 4). The loads applied to the specimens were chosen to achieve various nominal stress ranges at the location of the weld toe, as reported in Tables 1 and 2.

Differences between the configuration of a plate girder with a coverplate and the specimens evaluated in this study bring about differences in the stress demand on the weld. For example, in a welded connection between a plate girder and a coverplate, the weld is located in an area where the horizontal shear due to bending is likely to be very small. In the specimens used in this study the weld is located near the neutral axis of the specimen, in an area where the shear stresses caused by bending are close to maximum, posing a more stringent fatigue loading condition.

**Table 1**  
Fatigue testing results for ISR specimens.

Specimen ID	Stress range, MPa (ksi)	Cycles to initiation	Cycles to complete propagation failure
CONTROL 1	96.5 (14.0)	2,160,000 <sup>a</sup>	Not achieved
CONTROL 2	58.6 (8.50)	3,850,000 <sup>a</sup>	Not achieved
CONTROL 3	138 (20.0)	500,000	Not achieved
CONTROL 4	138 (20.0)	350,000	Not achieved
UIT 1	138 (20.0)	5,000,000 <sup>a</sup>	Not achieved

<sup>a</sup> Achieved run-out.

#### 4. Finite element modeling

Finite element analyses were performed using the commercial software package ABAQUS v.6.6.1 with the primary goal of examining the state of stress at the transverse welds. Two models were developed simulating the behavior of a specimen with a post-installed tensioned bolt: one model was loaded only with the bolt pressure (referred to as the “bolted” model), and the other model simulated behavior of a specimen with a load at midspan, also including the bolt load (referred to as the “bolt/bending” model).

The finite element model geometry was constructed using three-dimensional tetrahedral elements to depict half of the fatigue specimen, taking advantage of the symmetry of the specimen about the center. The mesh was comprised of approximately 50,000 nodes and 250,000 elements. The steel was modeled using an elastic-perfectly-plastic material model. The yield strength was obtained by performing 10 tension tests in accordance with ASTM E8 [13] on coupons obtained from the Gr. A36 steel bars used to fabricate the fatigue specimens.

The entire half-specimen was modeled as a single three-dimensional part instance instead of constructing the model from separate part instances and connecting them using tie constraints or other available connection techniques. Because the physical specimens had an unbonded interface between the flange and the cover plate, a slit measuring 76.2 mm (3.00 in.) wide  $\times$  0.03 mm (0.001 in.) high  $\times$  331 mm (13.0 in.) deep was placed in the center of the model to simulate an initial separation between the surfaces of the flange and coverplate. Because of the very shallow height of the slit, the two surfaces created by this slit came into contact as soon as the center load was applied to the model. Contact properties for the two surfaces of the slit were defined as true surface-to-surface hard contact in the direction normal to the surfaces. Commonly accepted static and dynamic coefficients of friction of 0.74 and 0.57, respectively, for steel-to-steel contact were used to define tangential behavior between the two surfaces.

To simulate contact between the specimen and the middle loading round in the test apparatus, the bottom edge of the flange at the specimen centerline was fixed against translation in three

**Table 2**

Fatigue testing results for HSR specimens.

Specimen ID	Stress range, MPa (ksi)	Cycles to initiation	Average cycles to initiation	Total cycles to failure
CONTROL 5	193 (28.0)	80,000 <sup>a</sup>	65,000	290,000
CONTROL 6	193 (28.0)	50,000		Not achieved
BOLT 1	193 (28.0)	80,000 <sup>a</sup>	70,000	530,000
BOLT 2	193 (28.0)	50,000		300,000
BOLT 3	193 (28.0)	70,000		400,000
UIT 2	193 (28.0)	1300,000	1700,000	Not achieved
UIT 3	193 (28.0)	2100,000		Not achieved
UIT/BOLT 1	193 (28.0)	550,000	1000,000	2400,000
UIT/BOLT 2	193 (28.0)	1070,000		Not achieved
UIT/BOLT 3	193 (28.0)	1370,000		Not achieved

<sup>a</sup> Cycle count to crack initiation determined using stiffness monitoring technique.

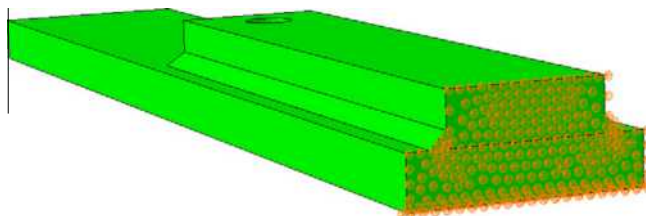


**Fig. 5.** View of finite element model, showing boundary conditions representing symmetry.

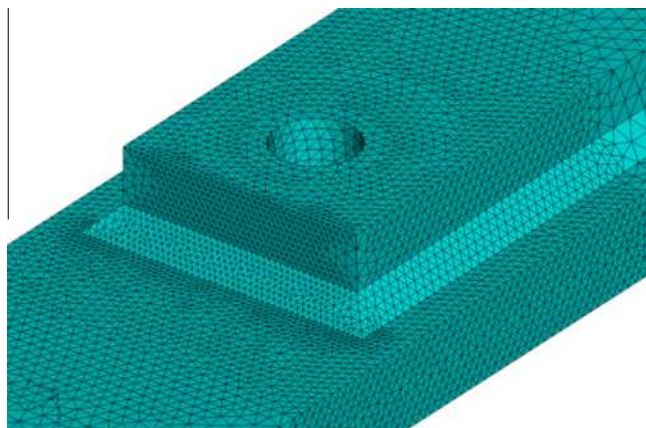


**Fig. 6.** View of finite element model containing pressures applied from a tensioned bolt.

directions. The boundary conditions at the center of the specimen (axis of symmetry) were defined so the entire cross-sectional surface at the specimen centerline was fixed against translation in the direction parallel to the longitudinal axis, and unrestrained in the other two directions, allowing displacements due to Poisson's effect in the two directions orthogonal to the longitudinal axis. A third boundary condition was applied to simulate the outside two roller supports of the three-point-bending test fixture. Fig. 5 shows the boundary conditions used to represent symmetry within the specimen.

A 25.4-mm (1.00-in.) diameter cylinder of material was removed from the flange and coverplate near the transverse weld (see Fig. 6). Circular pressure loads concentric with the cylindrical bore were applied to the top of the coverplate and the bottom of the flange, simulating forces imposed by a post installed tensioned bolt. As previously indicated, simulations were performed with and without the pressure induced by the bolt with the goal of studying the effect of the bolt tension on the state-of-stress at the weld toe.

While residual stress distributions can readily be implemented into finite element analyses using standardized distributions, the implications of doing so should be carefully weighed with modeling objectives. For this investigation, residual stresses caused by the welding process were not modeled for the following reason. Stress patterns used for modeling residual stresses must always be based off of theoretical distributions that are unlikely to represent the real variations in residual stresses that are likely to exist between specimens, and even between different segments of welds in the same specimen. Rather than compounding errors in the modeling effort, it is believed that capturing changes in load- and bolt- induced stresses presents less complicated, and potentially less erroneous, results.

## 5. Results and discussion

Five of the 15 total specimens were tested at a nominal weld toe stress ranges of 58.6, 96.5, and 138 MPa (8.50, 14.0, and 20.0 ksi) before a final stress range of 193 MPa (28.0 ksi) was chosen for the remainder of the specimens. All specimens tested at a nominal weld toe stress range less than 193 MPa (28.0 ksi) are henceforth referred to as "Intermediate Stress Range (ISR) specimens". Specimens tested at the final stress range of 193 MPa (28.0 ksi) are referred to as "High Stress Range (HSR) specimens". Experimental and analytical results are presented in the following. Results for ISR and HSR specimens are presented separately for clarity.

### 5.1. Intermediate stress range (ISR) specimens

Results for intermediate stress range specimens are summarized in Table 1, and are presented on the AASHTO S-N diagram in Fig. 7. As previously mentioned, specimen designations were assigned according to the type of treatment used. For example, the CONTROL designation corresponds to untreated specimens and the UIT designation corresponds to specimens in which the welds were treated with UIT.

The first step of the experimental program was to test several specimens at different stress ranges. This was done to determine fatigue behavior of the untreated specimens and to determine the most appropriate stress range to evaluate the strengthening methods. The first fatigue specimen tested was designated CONTROL 2, and the nominal stress range at the weld toe for this specimen was 58.6 MPa (8.50 ksi). As a reference, the fatigue life for a stress range of 58.6 MPa (8.50 ksi) estimated with Eq. (1) is approximately 635,000 cycles. Fatigue cracks were not observed during the test and the specimen achieved run-out after 3.85 million cycles. The nominal weld toe stress range for the next specimen, designated CONTROL 1, was increased to 96.5 MPa (14.0 ksi). Fatigue cracks were not observed in this specimen either, and the specimen achieved run-out after 2.16 million cycles. The next

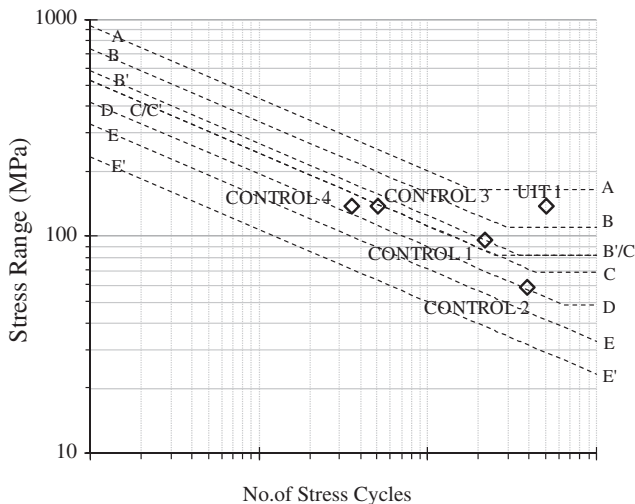


Fig. 7. S-N diagram of ISR specimen results.

specimen, designated CONTROL 3, was tested at a stress range of 138 MPa (20.0 ksi). For the first 930,000 cycles, visual inspection was performed with a dye penetrant following the standard method of inspection recommended by the manufacturer. Because load-deformation data at this point indicated that a reduction in stiffness had taken place, the method of inspection was modified to improve the ability to detect cracks. The modified inspection method differed from the manufacturer's procedure in that a developer was not utilized along with the dye penetrant. Instead, the dye penetrant was applied to the weld surface, allowed to rest briefly, then wiped off. Under the presence of a ultraviolet light, surging of the liquid dye could easily be seen, indicating opening of the crack. The presence of a 6.4 mm (0.25 in.) long crack was detected at the center of the weld toe with the modified inspection method. This rather large crack size clearly showed that crack initiation had indeed taken place prior to 930,000 cycles. In light of this, the initiation life of this specimen was estimated based on observed trends in recorded load and deflection data to be approximately 500,000 cycles. This was one of four specimens for which recorded load and deflection data were used to estimate crack initiation life. The remainder of the specimens were examined for cracks using the improved dye penetrant inspection method, and their corresponding fatigue crack initiation lives were based on the findings of those visual examinations.

The first treated specimen that was tested, UIT 1, was intended to investigate the improvement on fatigue crack initiation life associated with UIT of the welds at a nominal weld toe stress range of 138 MPa (20.0 ksi). Run-out was achieved after specimen UIT 1 reached 5 million cycles without detection of a crack. Although this run-out value was ten times greater than the crack initiation life of CONTROL 3, the goal of the project was to quantify improvement in fatigue life caused by the different treatment methods. Based on the results from these four tests, it was decided that all remaining fatigue tests would be performed at a nominal weld toe stress range of 193 MPa (28.0 ksi) so that as many specimens as possible would develop fatigue cracks instead of achieving run-out. The only exception was specimen CONTROL 4, which was tested at a nominal weld toe stress range of 138 MPa (20.0 ksi) to obtain a point of comparison for the fatigue life of the second batch of specimens.

Specimen CONTROL 4 sustained 350,000 cycles before a fatigue crack was detected. This value was 25% lower than the estimated crack initiation life of specimen CONTROL 3, which was part of the first fabrication batch of specimens and was also tested at a

nominal stress range of 138 MPa (20.0 ksi). The shorter crack initiation life of specimen CONTROL 4 is attributed to the fact that the welds on the three specimens from the second fabrication batch were of lower quality than the welds on the specimens from the first fabrication batch. Although there was a significant difference between the observed fatigue life of these two specimens from the first and second fabrication batches (CONTROL 3 and CONTROL 4), variations of this magnitude are expected in existing bridge structures due to the variability in the quality of welded connections across the national bridge inventory. For this reason, the fatigue lives of the two control specimens from the second fabrication batch tested at a nominal weld toe stress range of 193 MPa (28.0 ksi) were compared with the fatigue lives of the retrofitted specimens (which were part of the first fabrication batch) tested at a stress range of 193 MPa (28.0 ksi) without adjustment.

As evident from the S-N diagram depicted in Fig. 7, the fatigue lives of all intermediate stress range specimens exceeded the fatigue life calculated with the AASHTO fatigue design equation for a Category E' detail by a large margin, with data recorded at the level of Category D or better for each of the five specimens. Of the four ISR control specimens, the two specimens that did not achieve run-out failed after exceeding the AASHTO Category D design curve. Specimens CONTROL 2 and CONTROL 1 achieved the Category D and Category C ranges, respectively, before run-out was achieved. The ISR specimen treated with UIT achieved the AASHTO Category B range in the infinite-life region of the S-N diagram, before run-out.

To place these results into context, it is informative to examine the procedure used to develop the fatigue design equations in the AASHTO Code. Fatigue curves in the AASHTO Code were constructed based on results from numerous fatigue tests performed over a period of several decades, starting in the 1960s, on full-scale bridge girders employing various weld details. For each of the configurations tested, it was found that the presence of gouges and imperfections in a detail decreased the observed fatigue life. Consequently, there is significant variability inherent to the experimental data used to calibrate the AASTHO fatigue design equations. One of the origins of this variability is from details having identical geometric configuration but different size imperfections. For example, in one of the studies the longest fatigue life observed for a specific detail was approximately four times the shortest fatigue life observed for the same detail [1]. To ensure that an adequate margin of safety was incorporated into the design provisions, the AASHTO design equation for each detail category was calibrated so that the calculated fatigue life corresponded to the 95% confidence limit for 95% survival of all details included that category. Consequently, the AASTHO design equation for a given category represents an estimate of the fatigue life of a detail having the worst possible weld quality. The fillet welds tested in this study were determined to be of average quality or better. Given the strong correlation between weld quality and fatigue life, the fact that the specimens outperformed the AASHTO Category E' design curve by a significant margin even though their geometric configuration was similar to that of category E' details may be attributed in part to the high quality of the welds and the conservative nature of the AASHTO design curve.

In addition, different stress concentration factors exist within each fatigue design category as result of each category encompassing details with different geometric configurations. The AASTHO design curve for a given category approximately corresponds to the detail having the most vulnerable geometric configuration within the category, in addition to having the lowest weld quality. Coverplate elements on the specimens tested in the current program were only slightly thicker than the 20 mm (0.80 in.) limit that separates Category E' coverplate details from Category E coverplate details. For this reason, the geometric configuration of

the specimens tested in this study was less susceptible to fatigue damage than other Category E' details with thicker coverplates that were used in the calibration of the Category E' design curve. The combination of relatively high weld quality and less vulnerable geometric configuration accounts for the longer fatigue lives of the specimens.

The authors would like to emphasize that the main goal of this research study was to compare the performance of different strengthening techniques and the interaction between them. Reference to the AASHTO fatigue design categories is presented to provide a basis of comparison with a widely adopted classification. Although the fatigue classification of the specimen evaluated in this study may be the subject of debate, the specific fatigue design category adopted has no bearing on the relative performance of the strengthening techniques evaluated in the study.

## 5.2. High stress range (HSR) specimens

Results for HSR specimens tested at the stress range of 193 MPa (28 ksi) are provided in Table 2, and are shown superimposed on the AASHTO S-N diagram in Fig. 8.

The average fatigue life for the two control specimens tested at 193 MPa (28.0 ksi) was 65,000 cycles and the difference between their fatigue lives was 38%. It would have been ideal to select a stress range so that all specimens were loaded for at least 100,000 cycles prior to crack initiation, as suggested in the AASHTO [7] LRFD Bridge Design Specification. However, the large improvement in fatigue life displayed by the ISR UIT specimen dictated that the fatigue life of the control specimens had to be very short if the retrofitted specimens were to fail in a finite number of cycles.

The three bolted specimens were tested at a nominal weld toe stress range of 193 MPa (28.0 ksi). The average crack initiation life of the three bolted specimens was 70,000 cycles, and the difference between the least and greatest fatigue lives was 38%. The average crack initiation life for bolted specimens was nearly identical to the average initiation life of control specimens tested at the same weld toe stress range of 193 MPa (28.0 ksi). All control and bolted specimens tested at a weld toe stress range of 193 MPa (28.0 ksi) had an initiation life in the range of AASHTO [7] Category E details. Therefore, it is concluded that post-installing tensioned bolts at the ends of the coverplates without removing the welds had a negligible effect on fatigue life. The fact that fatigue life was unaffected was in part expected because without removal of the weld, load transfer was expected to take place primarily through the weld,

which was not strengthened in any fashion for these specimens. However, what these results have shown is that stresses induced by the post-installed bolts in the area surrounding the weld toe did not have a significant enough effect to improve or reduce the fatigue life of the connection.

All three of the bolted specimens were tested through crack propagation until complete failure of the specimen occurred. Specimen BOLT 1 failed completely at 530,000 cycles, BOLT 2 failed at 300,000 cycles, and BOLT 3 failed at 400,000 cycles, resulting in an average of 410,000 cycles to complete propagation failure. The length of the propagation life of each specimen appeared to be directly proportional to the length of the initiation life of that specimen. Specimens BOLT 1, BOLT 2, and BOLT 3 had propagation lives of 450,000 cycles, 250,000 cycles, and 330,000 cycles, respectively. Although the propagation lives of the three specimens were not equal, all were between 5.7 and 6.7 times longer than their respective initiation lives. These results indicated that a connection with a high-quality weld not only has a longer crack initiation life than a similar connection with a poor-quality weld, but it also has a somewhat slower rate of crack propagation rate. This phenomenon may be attributed to initiation and propagation of cracks at multiple locations in a weld of poor quality as opposed to a smaller number of locations in a weld of high quality. Because the nominal stress range would be identical for the two cases presented, the individual cracks in high-quality and poor-quality welds would be expected to propagate at equal rates after initiation. However, the presence of numerous and intersecting cracks in a weld of poor quality may have an aggregate effect and decrease the overall propagation life of the weld.

Two specimens treated with UIT were tested at a nominal weld toe stress range of 193 MPa (28.0 ksi). The first of these two specimens, designated UIT 2, underwent 1.3 million cycles before a crack was detected with dye penetrant inspection. The second specimen, designated UIT 3, underwent 2.1 million cycles before a crack was detected. The difference between the two was 38%, which coincidentally was the same difference observed between the two control specimens and also between the two bolted specimens tested at a stress range of 193 MPa (28.0 ksi). The average fatigue life of specimens treated with UIT and tested at a nominal weld toe stress range of 193 MPa (28.0 ksi) was approximately 25 times longer than the average fatigue life of untreated control specimens. The crack initiation lives of both control specimens tested at a weld toe stress range of 193 MPa (28.0 ksi) were in the range of AASHTO Category E details. Both UIT-treated specimens tested at the same stress range resulted in AASHTO Category A performance for fatigue crack initiation. Given that specimens treated with UIT in this study experienced an increase in fatigue life equivalent to that of six AASHTO fatigue categories, it was concluded that Ultrasonic Impact Treatment of the transverse weld toes was very effective in extending the fatigue life of the specimens.

Both specimens treated with UIT were tested well past the point of crack initiation to investigate crack propagation behavior. Specimen UIT 2 was loaded for 1.65 million additional cycles after crack initiation and specimen UIT 3 was loaded for 2.29 million cycles after crack initiation. The two specimens treated with UIT displayed significantly lower crack propagation rates than those of control specimens.

All three of the specimens treated with both UIT and with tensioned bolts post-installed at the end of the coverplates, referred to as combination specimens, were tested at a nominal weld toe stress range of 193 MPa (28.0 ksi). The crack initiation life of the first of these specimens, UIT/BOLT 1, was determined using recorded load and deflection data. Examining trends in data, the crack initiation life was estimated to be 550,000 cycles for UIT/BOLT 1. The fatigue lives of the other two combination specimens

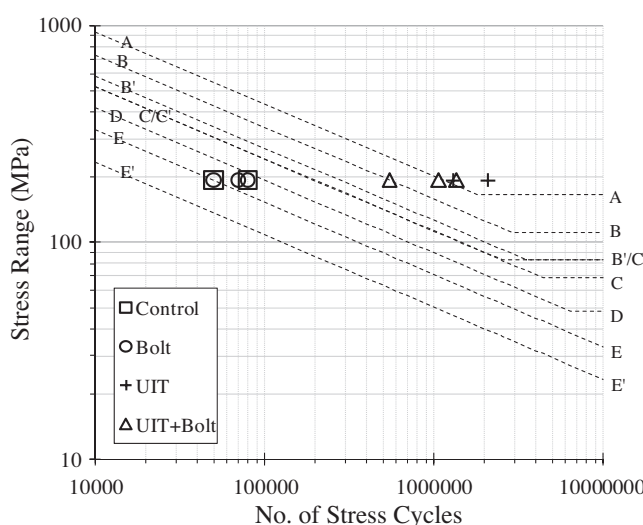


Fig. 8. S-N diagram of HSR specimen results.

were determined by visual inspection using the modified dye penetrant procedure. For specimen UIT/BOLT 2 a fatigue crack was first detected at 1.07 million cycles, while for UIT/BOLT 3 a fatigue crack was first detected at 1.37 million cycles. The average crack initiation life of these three specimens was 1 million cycles. The range of crack initiation lives was 820,000 cycles, and the difference between the specimen with the shortest life and the specimen with the longest life was 60%. Given that the fatigue lives of specimens UIT/BOLT 2 and UIT/BOLT 3 were determined with a more precise method, there was greater confidence in the results of these two specimens. When all three specimens are considered, there was more scatter in the results for the combination specimens than for any of the other three specimen types. It is reasoned that the addition of the post-installed bolt in the combination specimens added an additional state of stress subject to additional variations beyond those present in the UIT specimens, increasing the amount of scatter in the data for those specimens. Additional testing would be beneficial in determining whether this is a contributor to scatter, and would also help to show whether a similar relationship exists between bolted and control specimens.

For specimens tested at a weld toe stress range of 193 MPa (28.0 ksi), the average fatigue life for UIT/BOLT specimens was 41% lower than the average fatigue life for UIT-treated specimens. While all UIT specimens had initiation lives in the AASHTO fatigue Category A range, two of the UIT/BOLT specimens had initiation lives in the AASHTO Category B range, while the third UIT/BOLT had an initiation life in the AASHTO Category A range. Therefore, for the group of specimens tested at a weld toe stress range of 193 MPa (28.0 ksi), the majority of the combination specimens performed the equivalent of one AASHTO fatigue category worse than both UIT-treated specimens. These findings showed that Ultrasonic Impact Treatment of the welds was less effective when tensioned bolts were post-installed at the ends of the coverplates than when UIT was applied without also including post-installed tensioned bolts. Although the installation of tensioned bolts in otherwise untreated specimens was found to have a negligible effect on fatigue life, the installation of tensioned bolts in specimens treated with UIT reduced the improvement in fatigue life caused by the treatment of the welds. Even though the performance of specimens with treated welds and bolts was not as good as the performance of specimens treated only with UIT, the performance was significantly better than that observed in untreated specimens.

It was also observed that specimens treated with UIT experienced a different mode of fatigue cracking and propagation behavior than non-treated specimens. All specimens not treated with UIT (control and bolted specimens) developed fatigue cracks at the toes of the transverse welds, as shown in Figs. 9 and 10. In these specimens, cracks initiated at either the center or one of the ends of the transverse weld toe and propagated into the flange in a direction orthogonal to the longitudinal axis of the specimen. After a crack had initiated, the rate of crack growth increased exponentially until yielding of the reduced flange section caused failure. All specimens treated with UIT (UIT and combination specimens) exhibited surface cracks in the transverse weld throat near one end of the transverse weld, as illustrated in Figs. 11 and 12. On the surface, these cracks propagated along the entire length of the transverse weld throat and into the flange. These specimens displayed crack propagation plateaus, meaning that at some point during propagation the exponential rate of crack growth decreased considerably, and the fatigue crack propagated at a constant rate.

For each UIT-treated specimen, one crack propagation plateau was noted. Interestingly, in the UIT-treated specimens, not only was crack initiation life found to be greater than that for non-UIT treated specimens, but propagation life was also found to be significantly longer than that noted in non-treated specimens. The crack propagation pattern for UIT and UIT/BOLT specimens was as fol-



**Fig. 9.** Complete propagation of a crack in a non-treated (control) fatigue specimen.



**Fig. 10.** Complete propagation of a crack in a BOLT treated fatigue specimen.



**Fig. 11.** Complete propagation of a crack in a UIT-treated fatigue specimen.

lows. On the surface of a weld, a crack initiating at the weld throat near one end of a transverse weld would propagate across the entire length of the transverse weld throat. At each end of the transverse weld, the crack would then propagate around the corner of the fillet weld, moving along the longitudinal weld and toward

the flange at an angle of approximately 45°. The crack would then begin to propagate into the base metal of the flange, advancing in a direction orthogonal to the longitudinal axis of the flange.

For all specimens displaying a propagation plateau, the rate of crack propagation through the flange slowed considerably after cracking in the flange began. Based on this, the authors believe that the crack propagation plateau was reached after the crack propagated through the weld and weld-affected zone, and into good base metal of the flange. In bolted and control specimens, this would not have presented itself, as the crack did not travel through the weld, but rather through the base metal.

### 5.3. Finite element analysis results

The finite element analysis showed that the tension force in the bolt had the result of inducing tensile stresses in the transverse welds instead of compressive stresses, under no other externally-applied loads. Maximum principal stress and stress direction were used as a metric to quantify the effects of cover plate bolting on fatigue life. The surface of the transverse fillet weld had a tensile principal stress resulting from the tension force in the bolt, as shown in Fig. 13, which shows maximum principal stresses from the “bolted” model. The direction of the maximum principal stress vector from the “bolted” model was approximately parallel to the 3–3 direction (in the through-thickness direction).

According to the analysis with the bolt load, the magnitude of the principal stress at the surface of the specimen, near the middle of the transverse weld, was approximately 55 MPa (8.0 ksi). At the center of the specimen, the stress at the throat of the weld was slightly more highly stressed than the weld toe. The maximum principal tensile stress at the end of the transverse weld was higher than the stress at the middle of the transverse weld. Maximum principal tensile stresses of approximately 82.7 MPa (12.0 ksi) were induced near the ends of the transverse welds by the cover-plate bolts. These results were consistent with the fact that specimens with bolts (BOLT and UIT/BOLT specimens) developed fatigue cracks near the ends of the transverse weld instead of developing cracks near the center of the transverse weld.

The direction of maximum principal stresses under combined bending and bolt tension (“bolt/bending”) was found to be parallel to the face of the weld (at a 45 degree angle with the plane of the plates). The principal stress direction for the scenario with the combined bolt and bending agrees well with the observed crack patterns, which occurred along the length of the transverse weld, with the cracks opening in the same direction as the stress vectors are acting. This can be seen in the photographs of the cracked specimens (Figs. 9–12). The magnitude of maximum tensile principal

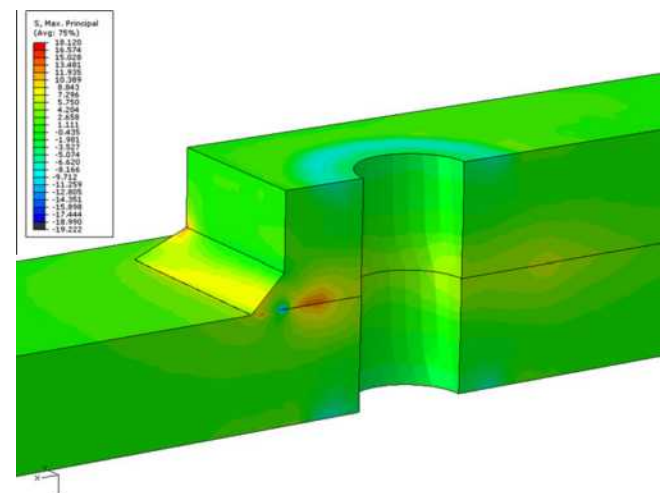


**Fig. 13.** Fringe plot of finite element modeling results showing sectioned view of maximum principal stress contours in weld region due to application of post-installed tensioned bolt in “bolted” model.

stress range experienced in the “bolt/bending” models was approximately 310 MPa (45 ksi), and occurred directly at the toe of the transverse weld.

Considering the influence of directional stresses,  $\sigma_{11}$  and  $\sigma_{33}$  should have the greatest effect on crack growth at the weld toe, as results from the finite element analyses indicate that it is a combination of these two stress components that drive this mode of crack opening. For clarity,  $\sigma_{11}$  is the directional stress acting in the longitudinal ( $x$ -) direction of the specimen,  $\sigma_{22}$  is acting in the transverse ( $y$ -) direction, and  $\sigma_{33}$  is in the though-thickness ( $z$ -) direction, as shown in Fig. 13. Considering directional stresses from the “bolt/bending” model at the toe of the transverse weld,  $\sigma_{11}$  had a tensile magnitude approximately twice that of  $\sigma_{33}$ , and three times that of  $\sigma_{22}$ . Because  $\sigma_{11}$  was the highest computed tensile stress at the weld toe, it was expected that a crack would open along this direction at the weld toe. This was consistent with the observed crack propagation pattern, in which cracks tended to initiate at the weld toe, except in specimens wherein the weld toe was treated with UIT. The relative magnitude of the computed directional stresses was also consistent with the crack propagation pattern of UI-treated specimens, in that cracking was noted at the throat of the weld, where the inclined surface made it more susceptible to cracking caused by the combined effects of  $\sigma_{11}$  and  $\sigma_{33}$ . It is hypothesized that the UI treatment induced residual stresses that counteracted  $\sigma_{11}$  and  $\sigma_{33}$  at the weld toe, making the weld throat the next most susceptible region. The low magnitude of  $\sigma_{22}$  in the weld toe region relative to  $\sigma_{11}$  and  $\sigma_{33}$  offers explanation as to why cracking along the longitudinal welds was not observed in any of the specimens.

Tests of all specimens that were treated with UIT showed that the residual compressive stresses and the smoothing of the imperfections resulting from the UIT caused a large increase in fatigue life, equivalent to an improvement of at least six AASHTO fatigue categories. The observed crack pattern for specimens treated with UIT (Figs. 11 and 12) shows that failure took place above the treated region of the weld. It was concluded that UIT effectively eliminated the vulnerability of the treated region, shifting the location of the vulnerable area to an untreated region of the weld.

In specimens with treated welds and bolts, the finite element analyses showed that there was an increase in tensile stresses in the transverse welds as a result of coverplate bolting. These specimens also developed cracks above the treated region of the weld, although at a different location along the weld. The increase in tensile stresses observed in the finite element analysis was consistent



**Fig. 12.** Complete propagation of a crack in a UIT/BOLT treated fatigue specimen.

with the fact that the combination specimens had a shorter average fatigue life than the UIT-treated specimens, and that fatigue cracks developed near the ends of the welds. In these specimens the treatment of the welds was effective in eliminating the vulnerability to fatigue failure at the weld toe, but the initiation life of the untreated region of the weld was reduced due to the increase in tensile stresses induced by the bolts.

In the case of specimens with untreated welds, the crack initiation life was dictated by the vulnerability to fatigue failure of the weld toe. This was evidenced by the fact that for specimens with untreated welds, cracks originated at the weld toe (Figs. 9 and 10). The difference in fatigue lives between specimens with and without bolts was negligible, with the bolted specimens having a slightly higher average fatigue life than the specimens without bolts. Given the range of crack initiation lives observed in the experimental study and the short fatigue lives of these specimens, this difference could not be taken as a certain indication that adding bolts tends to result in a small increase in fatigue life. In fact, the finite element analysis results suggested that a reduction in fatigue life may be expected. The difference in fatigue life between these two types of specimens was not of great significance this study, and could be investigated more precisely by testing additional specimens at a lower stress range.

## 6. Summary and conclusions

A study of the fatigue behavior of welded coverplate specimens treated with Ultrasonic Impact Treatment, post-installed tensioned bolts, and a combination of UIT and bolting has been presented. Fifteen fatigue specimens were experimentally tested at intermediate and high stress ranges so that differences in fatigue performance could be examined between the three treatment methods, and to investigate interaction effects between them. Computer simulations using a finite element model were performed to gain insight into the effects of the stress field induced by post-installed tensioned bolts behind an existing weld. Results from the study led to the following conclusions:

- UIT was found to be a very effective method of prolonging the fatigue life of the coverplate detail. When fatigue tests were performed at a nominal weld toe stress range of 193 MPa (28 ksi), the welded connection showed improved fatigue performance from that corresponding to an AASHTO fatigue Category E detail to that of a Category A detail.
- UIT-treated specimens exhibited longer crack propagation lives than non-treated specimens, in addition to longer crack-initiation lives.
- Post-installed tensioned bolts had a negligible effect on the fatigue performance of otherwise untreated specimens, indicating that the interaction between the bolt and the weld was negligible. This was not the case when the welds were treated with UIT, where the interaction was found to have a meaningful effect on fatigue life.
- Test results suggested that stresses induced by the post-installed bolt had a significant effect on the fatigue life of the portion of the transverse weld face that was not treated with UIT. This portion of the weld was closer to the point of interaction between the bolt and the coverplate. Conversely, the test results indicated that the stresses induced by the post-installed bolt had a negligible effect on the fatigue life of the treated portion of the weld (the weld toe), which was furthest from the point of interaction between the bolts and the coverplate.
- Finite element analyses showed that post-installing tensioned bolts induced tensile stresses in the untreated region of the weld. This was consistent with an experimentally observed

reduction in the fatigue life of specimens with UIT-treated welds and post installed bolts compared with the fatigue life of specimens treated only with UIT.

On the basis of the results of the fatigue testing program, application of Ultrasonic Impact Treatment to the toes of transverse fillet welds connecting coverplates to girder flanges was found to be very effective as a fatigue life enhancement technique for the fatigue-prone detail studied.

Post-installing tensioned bolts near an existing UIT treated weld was found to be a detriment to fatigue life. It is recommended that if tensioned bolts are to be used in combination with UIT, the placement of the bolts be carefully considered so that any effects of the bolts are dissipated before they reach the weld, so that no unintended interaction may reduce the fatigue life of the treated weld.

This study has illustrated that a “more is better” philosophy may not always result in a longer fatigue life, and that the interaction between retrofit measures may lead to a reduction in the effectiveness of those measures if not considered carefully.

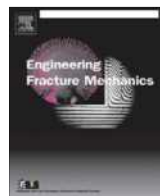
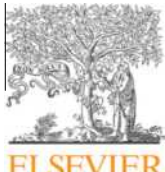
Future work on this topic is warranted. Additional tests at stress ranges utilized in this testing would lend greater statistical significance to the existing data set, while tests performed at other stress ranges would allow new distinctions to be made between the different treatment techniques. Supplementary testing of specimens at low stress ranges would allow greater differentiation to be made between the performances of bolted and control specimens, while tests performed at higher stress ranges would result in additional understanding of the performance of UIT-treated specimens.

## Acknowledgements

The authors would like to thank the Kansas Department of Transportation for funding this research and their ongoing cooperative research efforts with the University of Kansas. Additionally, the authors are grateful for donations of supplies and specimen fabrication from Builders Steel in Kansas City, MO. Finally, the authors would like express sincere thanks to Applied Ultrasonics for treating specimens with Ultrasonic Impact Treatment.

## References

- [1] Barsom JM, Rolfe ST. Fracture and fatigue control in structures. 3rd ed. West Conshohocken, PA: American Society for Testing and Materials; 1999. p. 237–280.
- [2] Fisher J, Frank K, Hirt M, McNamee B. Effect of weldments on the fatigue strength of steel beams. NCHRP Report No. 102, Washington, D.C.: Highway Research Board, National Academy of Sciences-National Research Council; 1970.
- [3] Yamada K, Albrecht P. Fatigue behavior of two flange details. *J Struct Div* 1977;103(4):781–91.
- [4] Simon S, Albrecht P. Adding fatigue life to cover plate ends. *J Struct Div* 1985;107(5):923–35.
- [5] AASHTO. LRFD bridge design specifications. 4th ed. Washington, D.C.: American Association of State Highway and Transportation Officials; 2007.
- [6] Jones J, Bennett C, Matamoros A, Rolfe S, Roddis K. Fighting fatigue in steel bridges: two case summaries, TR news. Washington D.C.: Transportation Research Board, National Research Council; 2008. p. 25–26, 259.
- [7] Anderson B, Rolfe S, Matamoros A, Bennett C, Bonnelli S. Post retrofit analysis of the tuttle creek bridge br. No. 16-81-2.24, SM Report No. 88. University of Kansas Center for Research; 2007.
- [8] Roy S, Fisher JW, Yen BT. Fatigue resistance of welded details enhanced by ultrasonic impact treatment (UIT). *Int J Fatigue* 2003;25(9–11):1239–47.
- [9] Roy S, Fisher JW. Improving fatigue strength of welded joints by ultrasonic impact treatment. Shanghai, China: IABSE Symposium: Metropolitan Habitats and Infrastructure; 2004.
- [10] Vilhauer, B. Fatigue behavior of welded connections enhanced with UIT and bolting. Thesis, presented to University of Kansas at Lawrence, KS, in partial fulfillment for the degree of Master of Science; 2007.
- [11] AISC. Steel construction manual. 13th ed. American Institute of Steel Construction (AISC); 2005.
- [12] Bennett C, Swanson J, Linzell D. Fatigue resistance of HPS-485W (70W) continuous plate with punched holes. *J Brid Eng* 2007;12(1):98–104.
- [13] ASTM E8-04. Standard test methods for tension testing of metallic materials. West Conshohocken, PA: American Society for Testing Materials; 2007.



## Fatigue crack growth behavior in weld-repaired high-strength low-alloy steel

Chunguo Zhang <sup>a,b</sup>, Stefan van der Vyver <sup>a</sup>, Xiaozhi Hu <sup>a,\*</sup>, Pengmin Lu <sup>b</sup>

<sup>a</sup> School of Mechanical and Chemical Engineering, The University of Western Australia, Perth 6009, Australia

<sup>b</sup> Construction Machinery School, Chang'an University, Xi'an 710064, PR China

### ARTICLE INFO

#### Article history:

Received 29 October 2010

Received in revised form 1 February 2011

Accepted 17 March 2011

Available online 22 March 2011

#### Keywords:

Fatigue crack growth

Weld

Buffer layer

High-strength low-alloy (HSLA)

Heat affected zone (HAZ)

### ABSTRACT

Fatigue crack growth properties and Vickers micro-hardness of a weld-repaired high-strength low-alloy steel, known for high strength, low carbon, excellent notch toughness and good weldability and formability, have been studied under the following conditions: as-received high-strength low-alloy, weld-repaired high-strength low-alloy without buffer layer, and weld-repaired high-strength low-alloy with various thickness buffer layers. Those conditions are examined to determine the respective fatigue crack growth behaviors and Vickers hardness distribution, and the effects of different weld-repaired conditions on fatigue characterizations and microscopic features of the fracture and fatigue surface. The extended-compact tension specimen geometry is adopted in this study for all tests. Paris fatigue crack growth curves and the hardness distribution across weld metal, buffer layer and parent metal has been measured together with the relevant scanning electron microscope observations along the fatigue crack growth path, with special attention at and around the interfaces between the weld metal, buffer layer and parent metal. The results show the presence of the BL of a moderate thickness has a significant influence on the fatigue crack growth behavior in the heat-affected zone and around the interface between buffer layer and parent metal. The fatigue resistance of the selected high-strength low-alloy + buffer layer + weld metal tri-metal system is higher than that of the high-strength low-alloy + weld metal bi-metal system.

Crown Copyright © 2011 Published by Elsevier Ltd. All rights reserved.

## 1. Introduction

High-strength low-alloy (HSLA) steels are known for their excellent mechanical and structural properties such as high strength, low carbon, excellent notch toughness and good weldability and formability. Because of those excellent properties, HSLA has been used in various applications including car components, transport equipments, mining equipments, lifting equipments, storage tanks, excavator buckets, high rise buildings and induced draft fans [1,2]. Utilizing the high strength property of HSLA allows reduction in section thickness, without loss of structural integrity [2]. It is noted that wear damaged sections of supporting structures manufactured from HSLA are often weld-repaired or filled by similar metals through welding [3]. The objective of the present study is to investigate an extensively weld-repaired HSLA steel of either a tri- or bi-metal system (with or without a buffer layer), which has not been systematically studied as shown in previous literatures.

Due to their high strength, HSLA steels can be difficult to repair through welding and special care is needed [4,5]. Furthermore, when these steels are welded they are often prone to softening in the weld HAZ, which exhibits low strength and

\* Corresponding author. Tel.: +61 8 6488 2812; fax: +61 8 6488 1024.

E-mail addresses: [zcguo2008@163.com](mailto:zcguo2008@163.com) (C. Zhang), [dynamic.engineering@bigpond.com](mailto:dynamic.engineering@bigpond.com) (S. van der Vyver), [xhu@mech.uwa.edu.au](mailto:xhu@mech.uwa.edu.au) (X. Hu), [lpmin@chd.edu.cn](mailto:lpmin@chd.edu.cn) (P. Lu).

## Nomenclature

HSLA	high-strength low-alloy
PM	parent metal
WM	weld metal
BL(s)	buffer layer(s)
E-CT	extended-compact tension
K	stress intensity factor (MPa $\sqrt{m}$ )
P	applied load (kN)
B	thickness of specimen (mm)
W	width of specimen (mm)
a	crack length from loading line (mm)
d	distance from specimen (mm)
SEM	scanning electron microscopy

hence is a weak link in mechanical testing indicating poor fatigue properties [6]. To avoid any detrimental effect on fatigue behavior of weld-repaired component, a number of studies have been carried out to assess the effects of the strength on fatigue properties of weld-repaired HSLA steels [7–13], the effects of welding current and speed on the fracture toughness, microstructure and hardness [14], and other relevant issues such as surface finish [15], microstructure manufacturing processes [16]. The effects of post weld heat treatments have also been discussed in [17,18]. An abnormally high fatigue crack growth rate in the WM and HAZ of a welded HSLA has been observed without any post weld heat treatment. However, with either laser multiple-temping or post weld heat treatment at 525 °C for 1 h, the fatigue performance is improved to similar to that of the base metal. It has also been shown that there is no need for post weld heat treatment if laser welding is adopted as shown in Ref. [19]. In this case, the yield strength of WM is similar to that of PM, the fatigue crack growth rates in the WM and HAZ were even lower than that in the PM for similar K range.

For thermo-mechanical control process steel weldments, the fatigue crack growth rate in the heat-affected zone is lower than that of the parent metal regardless of the post weld heat treatment [20]. A bi-metal system with strength gradient welded together [21] was also studied to investigate the fatigue crack growth characteristics through the soft parent steel and ultra strong weld of a maraging steel, which shows the high strength gradient across the weld interface has a strong influence on fatigue crack growth rate.

With different emphases to those aforementioned studies on HSLA steels, the primary objective of the present investigation is to study fatigue characteristics of an extensively weld-repaired HSLA, Bisplate, known for high strength, good toughness and weldability, and the influence of a soft buffer layer between the weld metal and parent metal on the overall fatigue crack growth behavior of the tri-metal system. This study is relevant since wear damaged sections of supporting structures manufactured from HSLA are often repaired or filled by similar metals through welding [3]. The incorporation of a soft buffer layer can assist welding of two hard metals, and can also change the characteristics of a heat-affected zone around the welded area, and thus will have a profound influence on the overall fatigue behavior of a welded structure.

## 2. Experimental procedure

### 2.1. Material and specimen

A HSLA steel widely used for earth moving and mining equipments was selected in this study. Flux cored arc welding was employed to perform the extensive welding repair, e.g. filling the section removed by erosion wear, while CO<sub>2</sub> was used as the shielding gas. The HSLA parent metal (PM), together with a weld metal (WM) and a thin buffer layer (BL) between PM and WM form a tri-metal system with different compositions and strength characteristics.

The chemical compositions and mechanical properties of PM, WM and BL are listed in Tables 1 and 2. The welding conditions and process parameters used in the welding repair including WM and BL are listed in Table 3. extended-compact

**Table 1**

Chemical compositions of tri-metal system.

Series	Element (wt.%)								
	C	Si	Mn	Cr	B	Mo	Ni	P	S
Parent metal (PM)	0.16	0.2	1.1	—	0.2	—	0.01	0.003	0.02
Weld metal (WM)	0.06	0.30	1.4	0.22	0.44	2.29	—	—	—
Buffer layer (BL)	0.03	0.59	1.66	—	—	—	—	—	—

**Table 2**

Mechanical properties of tri-metal system (typical value\*).

Series	Tensile properties			
	Tensile strength, yield (Mpa)	Tensile strength energy at break (Mpa)	Elongation at break Min (%)	Impact Min (J)
PM	690 min (750°)	790–930 (830°)	18 (26°)	40 (160°)
WM	690 min	760–840	17	30
BL	410 min	490–600	22	27

**Table 3**

Welding procedure.

Welding process	Flux cored arc welding	Flux cored arc welding
Series	Weld metal	Buffer layer
Electrode diameter (mm)	1.2	1.2
Welding consumable	100% CO <sub>2</sub>	100% CO <sub>2</sub>
Welding current (A)	230	230
Arc voltage (V)	27	27
Electrode stick-out (mm)	20	20

tension (E-CT, since CT is well-known and commonly used) specimens with machined through-the-thickness notches have been prepared following the specifications of ASTM E647 (23). The specimens were divided into four groups, i.e. as-received HSLA, weld-repaired HSLA without BL, and weld-repaired HSLA with 4 or 10 mm BLs. The soft BL is introduced to assist welding of two hard metals, and to neutralize the adverse influence of the HAZ around the extensively weld-repaired region. The metal blocks were then sliced and machined into the required dimensions (as shown in Fig. 1) to produce the extended-compact tension (E-CT) specimens for fatigue testing.

## 2.2. Vickers hardness test at 20 kilogram-force

Micro-Vickers hardness tests were carried out using a Mitutoyo AVK-C2 Hardness Tester (Akashi Corporation). Around 35 indentations near fatigue crack growth path were made across the weld metal, buffer layer and parent metal of each specimen. The distance between the centers of two adjacent indentations is about 0.9 mm. All the hardness readings were obtained using 2 kg-force load, and the full load was held for 15 s. The hardness measurements are presented in Figs. 2a–4b together with the sketches indicating their positions, and the corresponding Paris fatigue measurements.

## 2.3. Measurement of fatigue crack propagation

Four groups of E-CT specimens, (1) as-received HSLA specimens, (2) weld-repaired specimens without BL between the WM and PM, (3) weld-repaired specimens with 4 mm BL, and (4) weld-repaired specimens with 10 mm BL, were tested under the same fatigue loading condition. The Paris fatigue curves for each group were measured twice with two identical specimens, and the results are quite consistent.

The E-CT specimens were tested at the ambient condition using Instron 8501. Constant amplitude loading with haversine waveform at a frequency of 5 Hz was used, and the R ratio was set at 0 throughout the test. The fatigue pre-crack of about 1 mm was introduced with gradual increasing  $\Delta K$  in each specimen from the machined notch so that the initial crack size after fatigue pre-cracking is about 5.8 mm from the loading line. Paris fatigue curves were measured starting at around  $\Delta K_{th}$ , and a traveling optical microscope with 250 $\times$  magnification was used to monitor and measure the crack length during fatigue test. The accuracy of the measurement of crack length was close to  $\pm 0.01$  mm. Number of fatigue cycles, N, required for incremental crack growth was recorded, and the fatigue crack propagation rate,  $da/dN$ , was calculated directly by dividing the increment of crack length,  $\Delta a$ , by the elapsed number of fatigue cycles. The fatigue crack growth surface in various regions, especially around the interfaces between the PM, WM and BL was examined using SEM.

The stress intensity factor K and its variation during fatigue for E-CT specimens can be calculated following the standard equation in [22]:

$$K = (P/B\sqrt{W}) \times (2 + \alpha) / [(1 - \alpha)^{3/2} \times (1 - d/W)^{1/2}] \times (1.15 + 0.94\alpha - 2.48\alpha^2 + 2.95\alpha^3 - 1.24\alpha^4) \quad (1)$$

where P = the applied load, B = thickness, W = width of specimen,  $\alpha = a/(W - d)$ , a = crack length from load line, d = distance from specimen edge to loading line, and  $0.1 \leq (a + d)/W < 1$ .

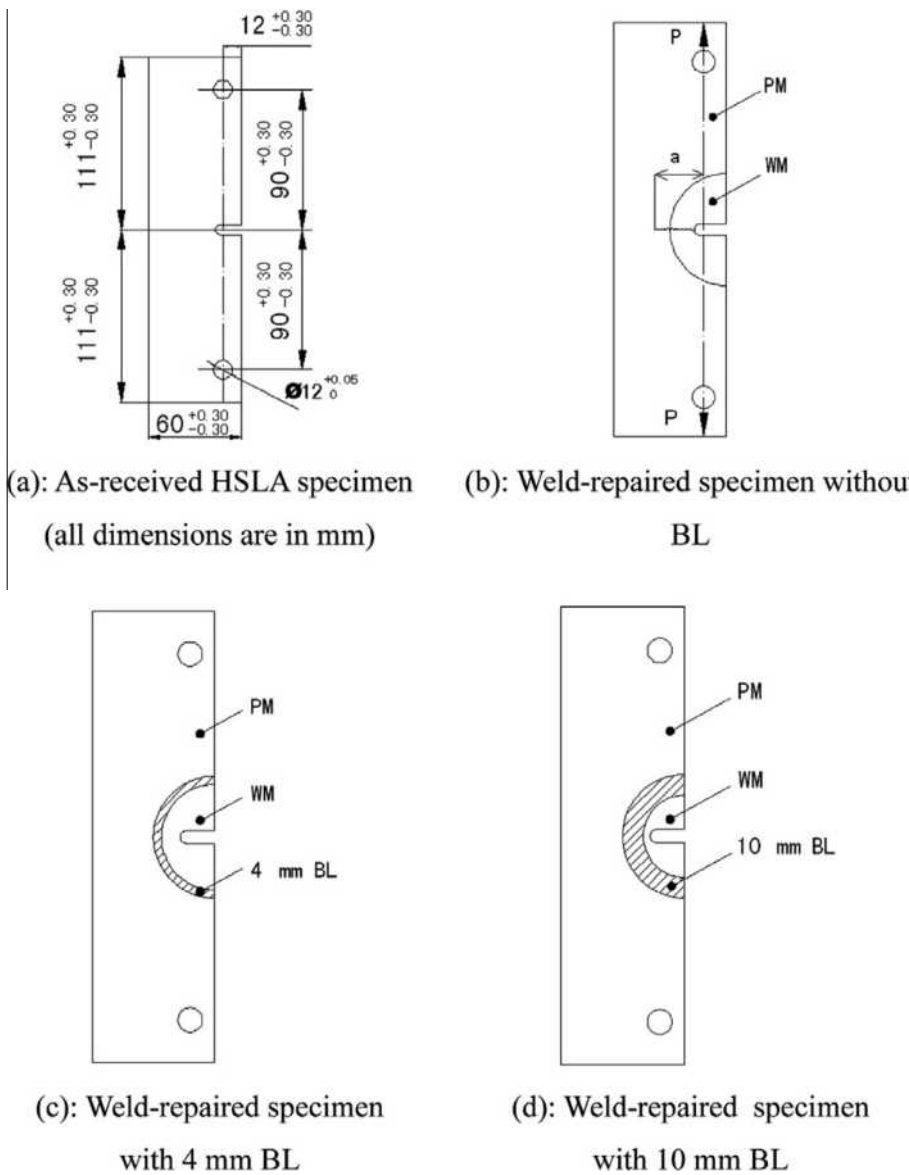


**Fig. 1.** E-CT specimens of different welding conditions, and the crack length is measured from the loading line as indicated in (b).

### 3. Results and discussion

#### 3.1. Comparison of as-received HSLA with weld-repaired bi- and tri- metals systems

Vickers hardness (VH) measurements and Paris fatigue curves from the as-received HSLA, are shown in Figs. 2a and 2b. It is clear that the results from two separate tests are very consistent, which therefore provide a good reference base so that the effects of welding, incorporating of BL and BL thickness can be studied. The comparisons with the as-received HSLA are thus shown in Figs. 3a–5b following the reference properties of as-received HSLA in Figs. 2a and 2b.

As shown in Figs. 3a and 3b, both VH and  $da/dN$  vs  $\Delta K$  from the weld-repaired HSLA without BL, fluctuate around the interface between the WM and PM, and have a larger scatter comparing with the as-received HSLA, and there is obvious reduction in VH close to the WM and PM interface and within the HAZ. The soft region around the interface and in the HAZ adjacent to the PM, and the sharp rebounding high-hardness region in the weld HAZ have also been reported in Ref. [23]. It should be mentioned that the lowest hardness at the interface shown in Figs. 3a and 3b is also corresponding to the sudden jump of  $da/dN$  at the interface shown in Fig. 3b. Furthermore, a dip of  $da/dN$  in Fig. 3b occurred at about 3 mm away from the interface, which maybe resulted from the formation of localized high-hardness weld region in the weld

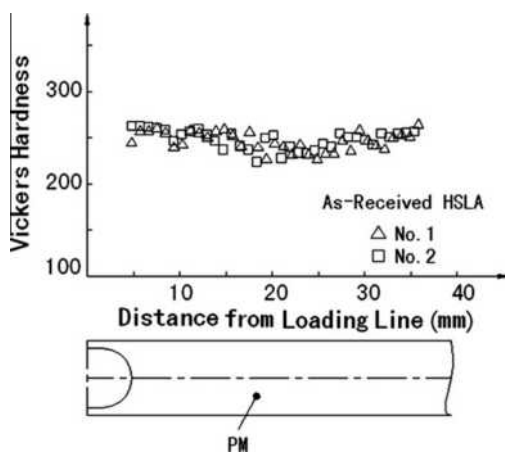


**Fig. 2a.** Vickers hardness in as-received HSLA.

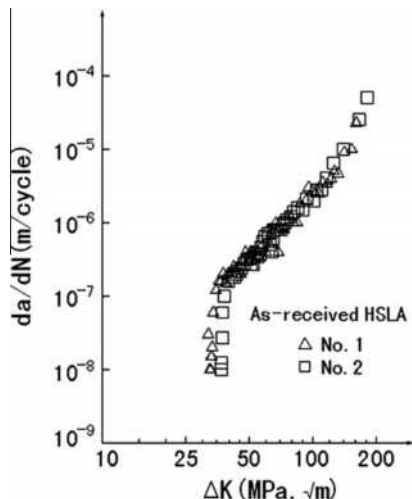


**Fig. 2b.** Fatigue behavior in as-received HSLA.

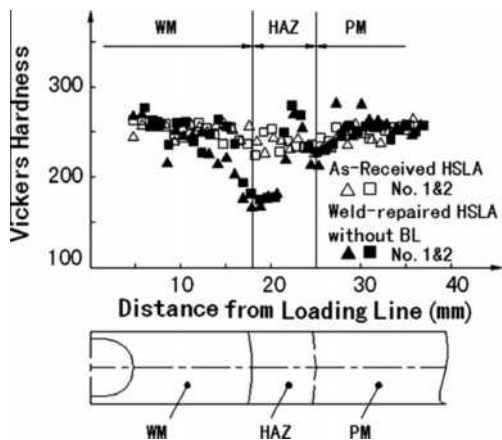


**Fig. 3a.** Vickers hardness in as-received HSLA and weld-repaired HSLA without BL.

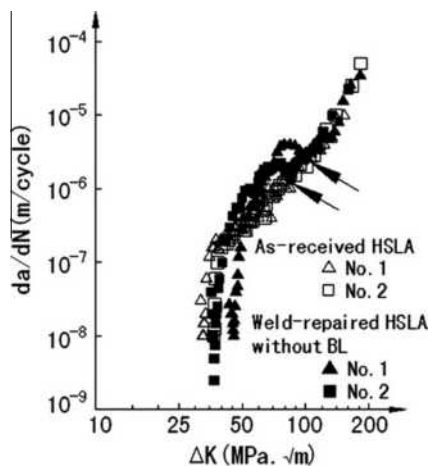


**Fig. 3b.** Fatigue behavior in as-received HSLA and weld-repaired HSLA without BL.

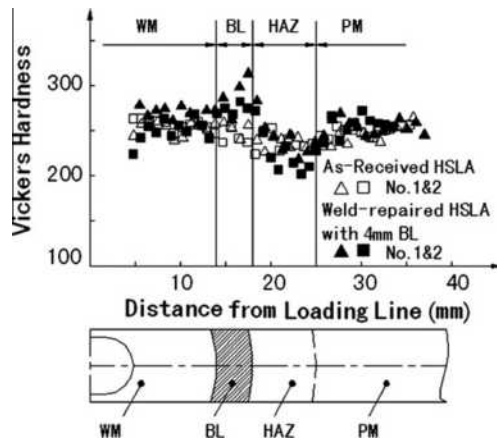


**Fig. 4a.** Vickers hardness in as-received HSLA and weld-repaired HSLA with 4 mm BL.

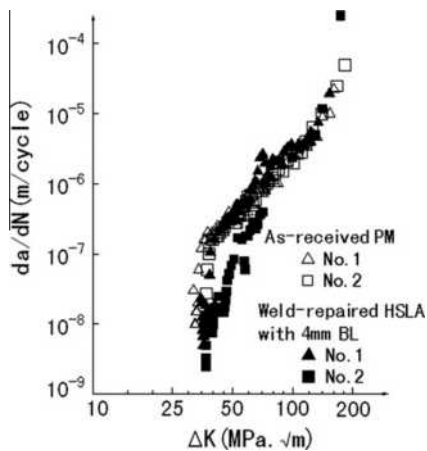


**Fig. 4b.** Fatigue behavior in as-received HSLA and weld-repaired HSLA with 4 mm BL.

HAZ shown in Fig. 3a. While the soft region exhibits poor fatigue resistance as it corresponds to higher  $da/dN$  in the 2nd stage of fatigue, it seems that the localized high-hardness region in HAZ, improves the fatigue resistance with lower  $da/dN$ .

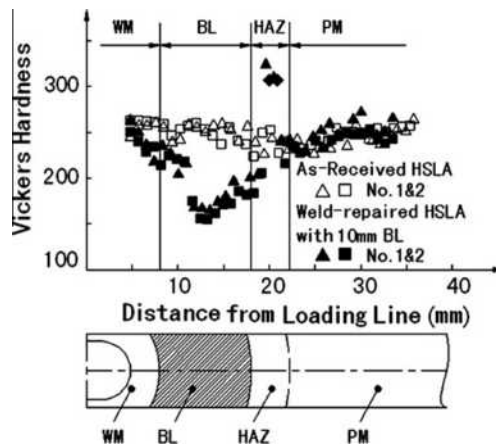


**Fig. 5a.** Vickers hardness in as-received HSLA and weld-repaired HSLA with 10 mm BL.

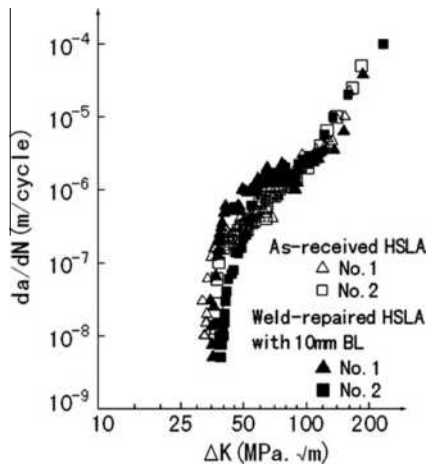


**Fig. 5b.** Fatigue behavior in as-received HSLA and weld-repaired HSLA with 10 mm BL.

As shown in Fig. 4a, the sharp reduction in VH around the WM and PM boundary and within the HAZ shown in Fig. 3a has been removed with the incorporation of a 4 mm BL. Although the BL has a lower yield strength than those of PM and WM, the micro-VH within the BL is higher than those of PM and WM. The corresponding reduction in  $da/dN$  in the 2nd stage of fatigue is also very obvious, indicating the incorporation of BL is not only beneficial to the welding process, but also improves the fatigue resistance.

In the case of 10 mm BL, VH drops substantially within the relatively thick BL as shown in Fig. 5a, but VH is increased in the HAZ. As shown in Fig. 5b,  $da/dN$  in the 2nd stage fatigue is increased within the BL, and fluctuates especially around the interface between the BL and the PM. It can be concluded from the results in Figs. 4a, 4b and 5a, 5b that the soft BL selected for this study should not be too thick as the BL by itself does not have better fatigue resistance in comparison with the PM.

Comparing the  $da/dN$  results in Figs. 3a–5b, particularly those around the interfaces between the WM and PM, WM and BL, and BL and PM, it seems that the WM and PM interface is the least fatigue resistant due to the formation of HAZ. Comparing the Figs. 3a and 4a, it can be found that the incorporation of 4 mm BL has limited the soft zone around the WM and PM interface, and the weld HAZ indicating the higher Vickers hardness as comparison with weld-repaired HSLA without BL. By incorporating a BL, the original properties at the WM and PM interface region have been positively modified in two ways. First, there is no longer a direct interface between WM and PM. Second, the HAZ properties in the PM are also modified. For the tri-metal system selected in the current study, incorporation of 4 mm BL achieves the best result. It is also noted that the interface between the WM and BL does not have much influence on  $da/dN$  and the total fatigue life. Those results indicate that the selection of WM and BL are adequate for the HSLA.

### 3.2. Influence of buffer layer and its thickness on material properties

To emphasize the influence of BL among those weld-repaired HSLA specimens, VH and Paris fatigue curves from the bi-metal system (WM and PM) are chosen as the reference properties and compared with the properties of the tri-metal system

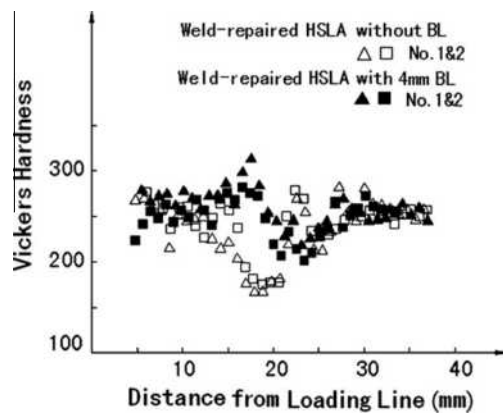


**Fig. 6a.** Vickers hardness in weld-repaired HSLA without and with 4 mm BL.

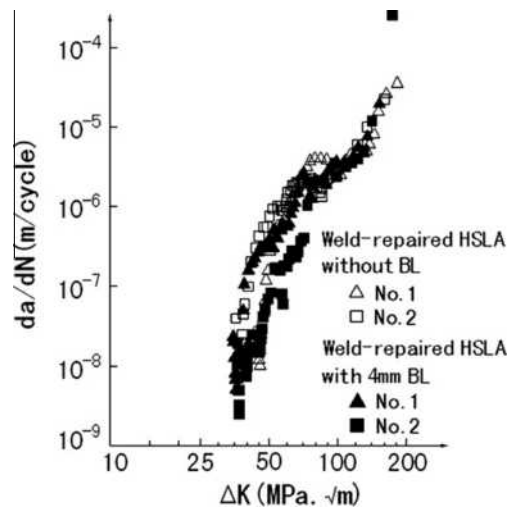


**Fig. 6b.** Fatigue behavior in weld-repaired HSLA without and with 4 mm BL.

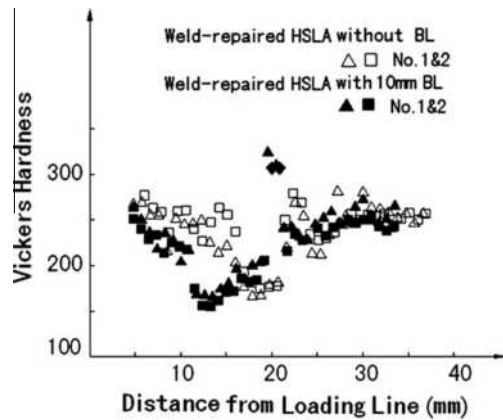


**Fig. 7a.** Vickers hardness in Weld-repaired HSLA without and with 10 mm BL.

(WM, BL and PM) as shown in Figs. 6a, 6b and 7a, 7b. To emphasize the BL thickness influence, the tri-metal systems with the 4 and 10 mm BLs are further compared in Figs. 8a and 8b.

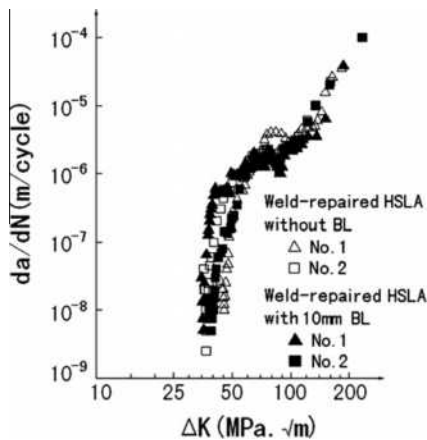


**Fig. 7b.** Fatigue behavior in weld-repaired HSLA without and with 10 mm BL.

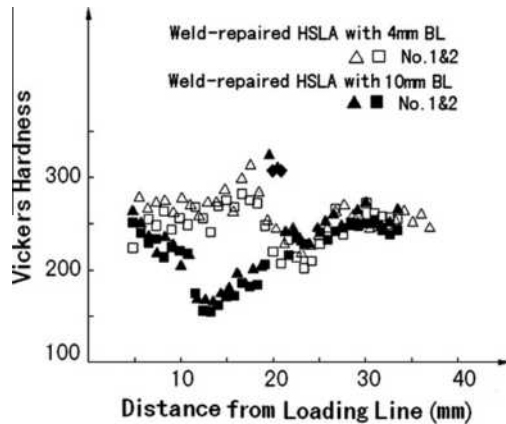


**Fig. 8a.** Vickers hardness in Weld-repaired HSLA with 4 mm and with 10 mm BL.

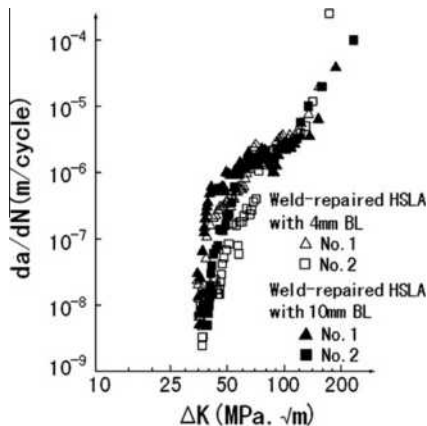


**Fig. 8b.** Fatigue behavior in weld-repaired HSLA with 4 mm and 10 mm BL.

VH of the bi-metal (WM and PM) and tri-metal (WM, 4-mm-BL, PM) systems exhibits the opposite trends within the HAZ and 4 mm BL region as shown in Fig. 6a. It is clear that the higher VH of the tri-metal in this region has resulted in slower fatigue crack growth and thus increased fatigue resistance. However, the tri-metal system (WM, 10-mm-BL, PM) with a relatively thick BL of 10 mm exhibits a substantial reduction in VH within the BL due to its low yield strength and a sudden

increase in VH within the HAZ. As a result, the overall improvement in fatigue life is not as significant as the 4-mm-BL system. The direct comparisons of two tri-metal systems (WM, 4-mm-BL or 10-mm-BL, PM) in Figs. 8a and 8b further suggest BL cannot be too thick, and incorporation of a thin BL is sufficient to alter the fatigue properties of HAZ.

### 3.3. SEM details at bi- and tri- metal interface regions

Fatigue fracture surfaces have been examined using SEM with special emphasis on the regions around the bi- and tri-metal interfaces. To correlate the microscopic observations to the relevant locations and corresponding VH and  $da/dN$  measurements, sketches for the boundary regions and  $da/dN$  curves have been numbered accordingly for the bi- and tri-metal systems.

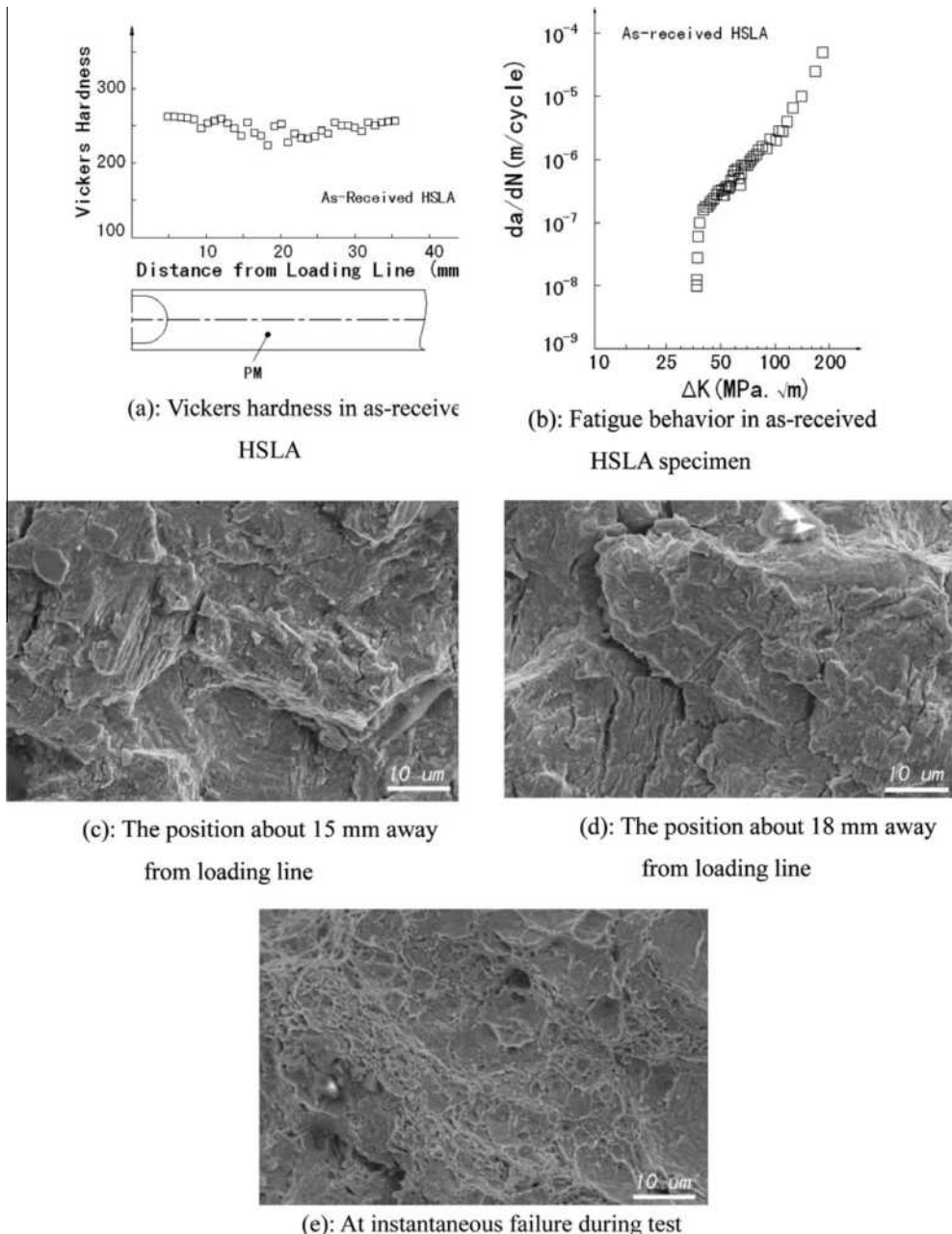


**Fig. 9.** Vickers hardness, fatigue behavior and SEM micrographs in stable and unstable crack propagation regions of as-received HSLA specimen.

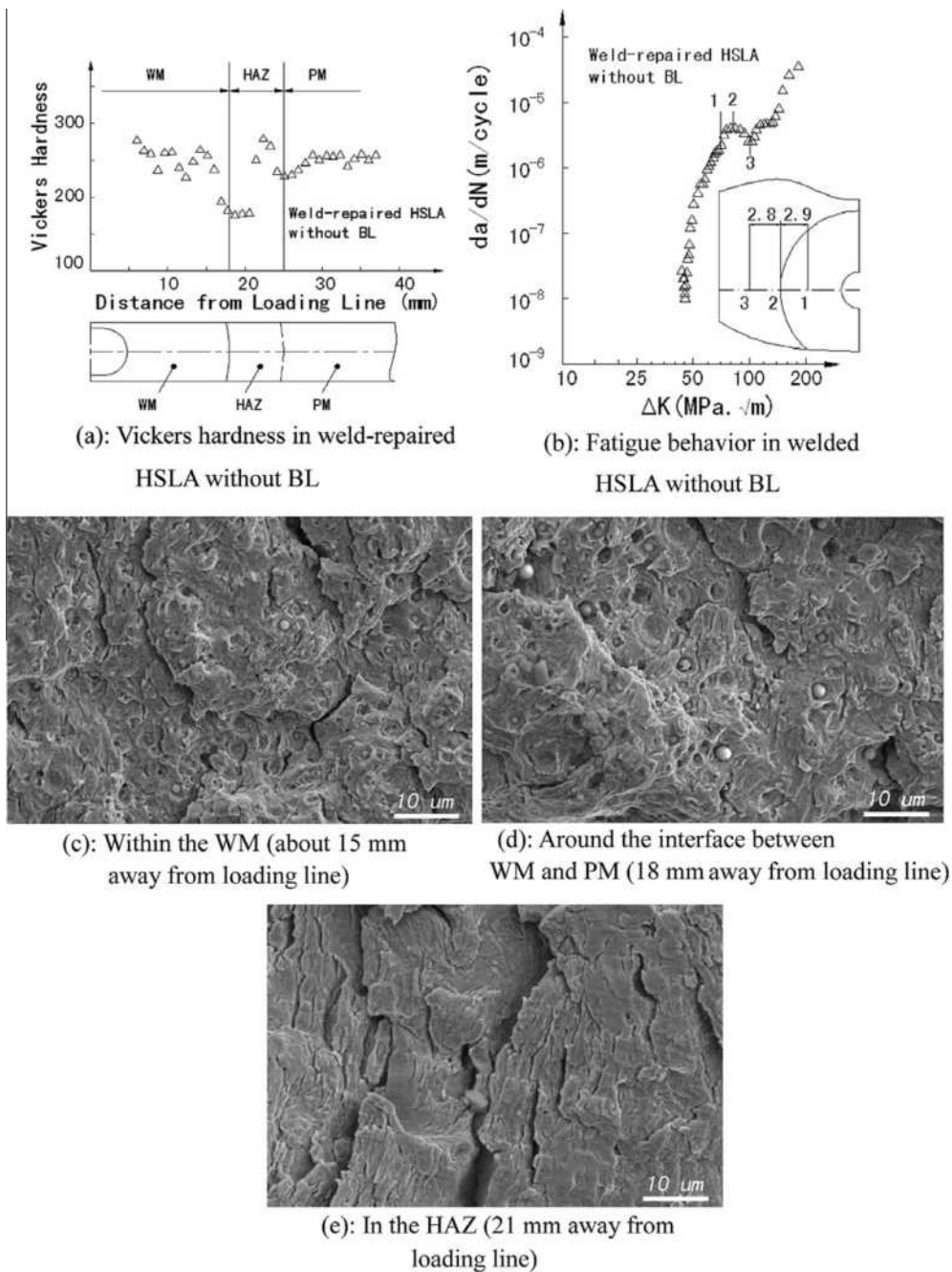


**Fig. 10.** Vickers hardness, fatigue behavior and SEM micrographs in stable crack propagation region of weld-repaired HSLA specimen without BL.

Following the above descriptions, Fig. 9 displays the details for PM, Fig. 10 displays the property, position and SEM details for the bi-metal system (WM and PM), Fig. 11 displays the details for the tri-metal system (WM, 4-mm-BL, PM), and Fig. 12 displays the details for the tri-metal system (WM, 10-mm-BL, PM).

The SEM micrographs in Fig. 9c–e for PM and Fig. 10c–e for the bi-metal system (WM and PM) show that multiple micro-cracking occurred in both systems, and it became more severe in the HAZ indicating the change in material properties. Fig. 10c and d display some spherical shaped non metallic particles from the welding process. Micro-plastic failure through micro void coalescence is evident in Fig. 9e for the PM at the final stage of unstable fracture.

The SEM micrographs, VH and fatigue crack growth measurements at comparable locations for the two tri-metal systems are shown and compared in Fig. 11 (WM, 4-mm-BL, PM), and Fig. 12 (WM, 10-mm-BL, PM). As can be seen, both VH and  $da/dN$  fluctuate within the BL and HAZ, especially around the interface between the BL and PM. Interestingly, VH within the thin

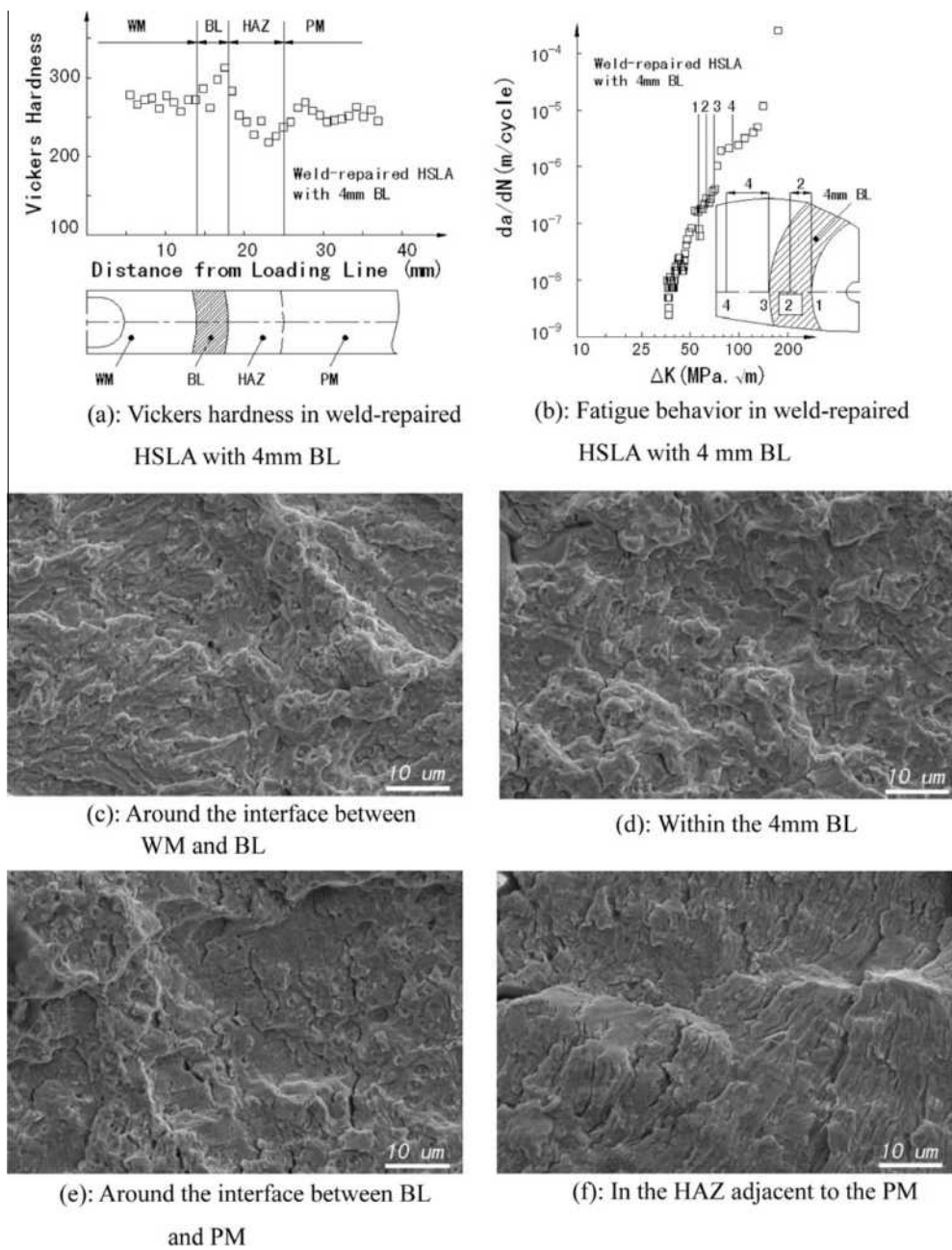


**Fig. 11.** Vickers hardness, fatigue behavior and SEM micrographs in stable crack propagation region of welded HSLA specimen with 4 mm BL.

4-mm-BL is the highest although BL has lower yield strength in comparison with WM and PM, indicating both BL and HAZ have been altered by the welding process, which has resulted in better fatigue performance for the tri-metal system (WM, 4-mm-BL, PM). While the thick 10-mm-BL displays the lowest VH, the highest VH is within the HAZ.

The SEM micrographs in Fig. 11c–f and in Fig. 12c–f provide direct comparisons for the two tri-metal systems at the WM and BL interface (c), within the BL (d), at the BL and PM interface (e), and in HAZ (f). In all those locations, the fatigue/fracture surfaces of the tri-metal system with the 10-mm-BL appear to be rougher than their counterparts of the tri-metal systems with the 4-mm-BL. This finding appears to be consistent with the relatively rough fatigue surfaces within the HAZ of the bi-metal system as both the relatively rough fatigue surfaces are corresponding to lower fatigue resistance as shown by the Paris fatigue measurements.

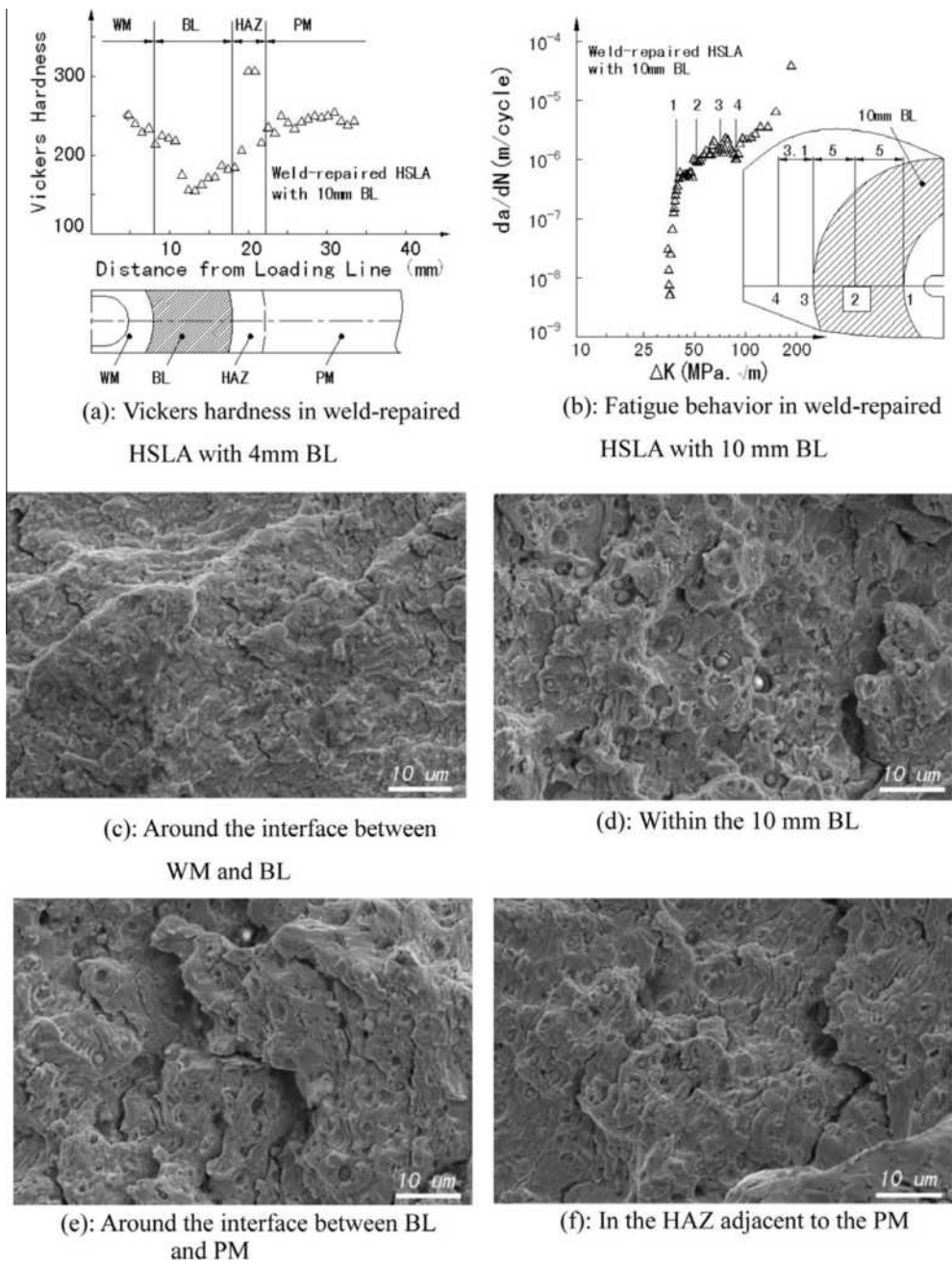


**Fig. 12.** Vickers hardness, fatigue behavior and SEM micrographs of stable crack propagation region of welded HSLA specimen with 10 mm BL.

#### 4. Conclusions

An extensively weld-repaired HSLA steel has been studied using bi- and tri- metal systems with a BL (buffer layer) as the third phase between the PM (parent metal) and WM (weld metal). For the selected tri-metal (PM, WM and BL) with the specified material compositions and properties, the thin 4-mm-BL works well by virtually removing the adverse influence of HAZ present in the bi-metal system (WM and PM) although BL has the lowest yielding strength among the three materials. The micro-VH within the BL and HAZ has been increased and the variation in VH has also been reduced leading to a substantial improvement in the fatigue resistance. However, the improvement in fatigue resistance is less significant for the tri-metal system with the thick 10-mm-BL as micro-VH drops within the thick BL and so does the overall fatigue resistance.

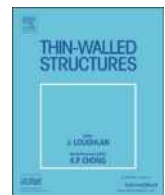
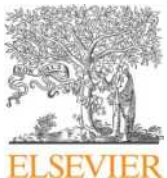
The comparable SEM micrographs of the tri-metal systems with 4-mm and 10-mm BLs at similar locations show increasing micro-fracture activities on the fatigue/fracture surface of the tri-metal system (WM, 10-mm-BL, PM), which should be related to the reduction in the fatigue resistance. The resultant “rougher” fatigue also corresponds to the lower VH region.

In summary, a soft buffer layer of a moderate thickness is beneficial as far as the fatigue life of HSLA is concerned according to the test results of the current study. This is because a thin soft buffer layer with a low carbon wt.% can effectively reduce the influence of the HAZ around the weld-repaired region. However, excessive usage of a soft buffer layer can weaken a welded structure because of its low strength. For the selected tri-metal system in this investigation, it seems the 4 mm thick buffer layer offers a promising compromising solution.

It should also be mentioned that the influence of residual stresses due to welding has not been considered in the current study. Although the micro-hardness measurements emphasized in this paper are not influenced by the residual stresses, the fatigue crack growth will be influenced. As residual stresses are structure/specimen geometry dependent, this complicated issue is beyond scope of the current paper, and can only be dealt with in the future in a separate paper.

## References

- [1] Mohan S, Prakash V, Pathak JP. Wear characteristics of HSLA steel. *Wear* 2002;252:16–25.
- [2] [http://www.bisalloy.com.au/files/Bisplate\\_Pdfs/Bisplate\\_80.pdf](http://www.bisalloy.com.au/files/Bisplate_Pdfs/Bisplate_80.pdf).
- [3] Scholl M, Devanathan R, Clayton P. Abrasive and dry sliding wear resistance of Fe–Mo–Ni–Si and Fe–Mo–Ni–S–C weld hardfacing alloys. *Wear* 1990;135:355–68.
- [4] Bisalloy steels. Bisplate technical manual. P48, <[www.bisalloy.com.au](http://www.bisalloy.com.au)>.
- [5] A.V. Borozdin, A.A. Pavlov, V.A. Kroskin. Experience with the use of high strength low alloy steels. Translated from Khimicheskoe i Neftyanoe Mashinostroenie; 1991. p. 31–2.
- [6] Mohandas T, Reddy GM, Kumar BS. Heat-affected zone softening in high-strength low alloy steels. *J Mater Process Technol* 1999;88:284–94.
- [7] Yamasaki T, Kawai Y, Maeda Y. Fatigue life of welded and bolted repair parts. *J Struct Eng* 1984;10:2499–512.
- [8] Mutoh Y, Sakamoto I. Fatigue crack propagation in the weld bond region of a type 304 stainless steel weldment. *Advances in fracture research*. Oxford: Pergamon Press; 1984. p. 1695–702.
- [9] Ravi S, Balasubramanian V, Nasser SN. Fatigue life prediction of strength mis-matched high strength low alloy steel welds. *Mater Des* 2006;27:278–86.
- [10] Ravi S, Balasubramanian V, Nasser SN. Assessment of some factors influencing the fatigue life of strength mis-matched HSLA steel weldments. *Mater Des* 2004;25:125–35.
- [11] Smith C, Pistorius PG, Wannenburg J. The effect of a long post weld heat treatment on the integrity of a welded joint in a pressure vessel steel. *Int J Press Vess Pip* 1997;70:183–95.
- [12] Ravi S, Balasubramanian V, Nasser SN. Effect of mis-matched ratio (MMR) on fatigue crack growth behavior of HSLA steel welds. *Eng Fail Anal* 2004;11:413–28.
- [13] Singh V, Raju PVSS, Namboodhiri TKG, Rao PR. Low-cycle fatigue behavior of a low-alloy high-strength steel. *Int J Fatigue* 1990;12:289–92.
- [14] Prasad K, Dwivedi DK. Some investigations on microstructure and mechanical properties of submerged arc welded HSLA steel joints. *Int J Adv Manuf Technol* 2008;36:475–83.
- [15] Liu J, Yue ZF, Liu YS. Surface finish of open holes on fatigue life. *Theor Appl Fract Mech* 2007;47:35–45.
- [16] Yu MT, Topper TH, Wang L. The effect of microstructure on the mechanical behavior of a low carbon. *Int J Fatigue* 1988;10:249–55.
- [17] Tsay LW, Li YM, Chen C, Cheng SW. Mechanical properties and fatigue crack growth rate of laser-welded 4130 steel. *Int J Fatigue* 1992;14:239–47.
- [18] Ohta A, Sasaki E, Niher M, Kosuge M, Kanao M, Inagaki M. Fatigue crack propagation rates and threshold stress intensity factors for welded joints of HT80 steel at several stress ratios. *Int J Fatigue* 1982;233–7.
- [19] Tsay LW, Chung CS, Chent C. Fatigue crack propagation of D6AC laser welds. *Int J Fatigue* 1997;19:25–31.
- [20] Tsay LW, Chern TS, Gau CY, Yang JR. Microstructure and fatigue crack growth of EH36 TMCP steel weldments. *Int J Fatigue* 1999;21:857–64.
- [21] Ukadgaonker VG, Bhat S, Jha M, Desai PB. Fatigue crack growth towards the weld interface of alloy and maraging steels. *Int J Fatigue* 2008;30:689–705.
- [22] Piascik RS, Newman Jr JC. An extended compact tension specimen for fatigue crack growth and fracture testing. *Int J Fracture* 1995;76:43–8.
- [23] Omweg GM, Frankel GS, Bruce WA, Ramirez JE, Koch G. Performance of welded high-strength low-alloy steels in sour environments. *Corrosion* 2003;59:640–53.



## Full length article

# Fatigue improvements of cracked rectangular hollow section steel beams strengthened with CFRP plates



Tao Chen\*, Xian Wang, Ming Qi

Department of Structural Engineering, Tongji University, Shanghai 200092, China

## ARTICLE INFO

**Keywords:**

Rectangular hollow section steel beam  
Fatigue crack propagation life  
Prestressed carbon fiber reinforced polymers plate  
Finite element modeling  
Parametric study

## ABSTRACT

Concerns over means to improve fatigue behavior of cracked rectangular hollow section (RHS) steel beams exist. This paper presents the details of strengthening schemes that was carried out using prestressed or high modulus carbon fiber reinforced polymer (CFRP) plates. A set of fatigue tests were conducted and results indicated that prestressed CFRP technique could increase fatigue crack propagation life 35.57 times longer than that of un-repaired one. The results also indicated that high modulus CFRP is effective at increasing fatigue life. Following crack propagation lives were calculated based on finite element models and close agreement with test results were observed. Thereafter, a parametric study was conducted considering the influence of various parameters such as the CFRP prestressing level, plate width and modulus on the fatigue life of the strengthened specimens. The findings of this paper can be employed to formulate design guidance for RHS beams under fatigue loading.

## 1. Introduction

Hollow section steel members have been adopted as structural members in bridges, civil buildings, offshore structures and even cranes. These members are often subjected to bending under external actions during service, and they may have structural deficiencies due to fabrication or harsh environments [1–4]. Fatigue cracking is a predominant problem for structures subject to repeated loading [3,5]. Thus, a critical need exists for repair techniques that allow convenient rehabilitation. However, traditional welding or bolting methods involve additional heavy plates and other applications that lead to fatigue sensitive defects [6,7]. In recent decades, carbon fiber reinforced polymer (CFRP) materials have been adopted as a popular repairing material for steel members [8–11]. Previous investigations showed the fatigue lives of repaired specimens can be greatly extended by non-prestressed CFRP repair methods [1,12–16] and even increased 21.5 times over that of control specimens using prestressed CFRP repair method [12]. Extensive research has focused on prestressed CFRP patched elements subjected to uniaxial loading [13,15,17,18].

A great deal of attention has also been paid to structural elements subjected to bending moments. Most of them have been conducted on the "I" section steel beams [16,19–21] and circular hollow section (CHS) beams [4,8,22] strengthened with CFRP materials. Linghoff et al. [23,24] conducted four-point bending tests on steel beams with I cross-sections strengthened with various configurations of CFRP laminates. Increased moment capacity was found. Finite element analyses of steel

beams were also performed as a parametric study to capture the behavior of the strengthened specimens. Experimental research has also shown the effectiveness of CFRP rehabilitation on damaged CHS members under three-point bending [22]. Fatigue performance of the CFRP strengthening system has been reported. Colombi and Fava [25] carried out fatigue tests on nine cracked steel beams, each with an I cross section strengthened with a CFRP plate. Fatigue crack growth was retarded and fatigue life was prolonged. Jiao et al. [26] investigated eight notched steel beams strengthened with strand CFRP sheets. The specimens were subjected to fatigue loadings and fatigue life enhancement was achieved. CFRP strengthening was confirmed as an ideal way to rehabilitate cracked steel beams after comparing fatigue performance with traditional strengthening methods [27]. In the aforementioned studies, artificial slot was employed to simulate the initial damage degree instead of welded details. The purpose is to eliminate scatter of fatigue results due to welding that can introduce residual stress, kinds of imperfections such as pores, blowholes, under cuts and heat affected zone.

The prestressing technique is often used to strengthen steel beams by CFRP plates to exploit its high strength. Walbridge et al. [28] carried out fatigue tests on strengthened I-beams with welded cover plates. The results indicated that a significant fatigue life enhancement can be achieved by applying prestressed CFRP strips to the cover plates. Numerical analysis with a fracture mechanics model were performed to predict fatigue life with reasonable results. Due to the complexity of weld details, artificial notched steel elements were introduced.

\* Corresponding author.

E-mail address: [t.chen@tongji.edu.cn](mailto:t.chen@tongji.edu.cn) (T. Chen).

Ghafoori et al. [16] investigated notched steel I-beams strengthened with prestressed CFRP and developed a theoretical method to calculate the prestressing levels in CFRP by controlling the stress intensity factor at the crack tip. The prestressed CFRPs were further employed to increase the buckling strength of steel I-beams with experimental and numerical approaches [29]. In regards to the strengthening of a rectangular hollow section (RHS) structural members, research focused on monotonic loadings [30,31], but limited research dealt with fatigue problems [32,33]. Field application with prestressed CFRP laminates were reported by Koller et al. [33]. A cracked steel pendulum was monitored and fatigue cracks ceased to propagate for nine years. In summary, the prestressed CFRP strengthening method is effective for steel members with open and closed sections.

Previous research indicates the fatigue performance improvement with hollow section steel members. However, to further explore the application of prestressed CFRP in this area, systematic experimental and numerical efforts are required. The aim of this paper is to examine and compare the fatigue life improvements of CFRP-strengthened RHS steel beams with different CFRP moduli and prestressing levels with un-strengthened ones. Firstly, six strengthened specimens were tested under four-point fatigue bending. The results were compared to that of the un-strengthened control specimens. Subsequently, a numerical simulation technique for studying the cracking behavior of RHS steel beams subjected to fatigue loading was developed and validated against experimental testing data. A study was then carried out on the effects of several strengthening related parameters as they relate to the response of the cracked beams using validated numerical models.

## 2. Experimental investigation of fatigue crack propagation life

### 2.1. Experimental program

The specimens were fabricated by patching CFRP plates to the bottom notched steel beams. Fig. 1 shows the basic geometry of the strengthened cracked RHS steel beams considered in this study. They were 700 mm long with an RHS cross section, which measured 100 mm × 50 mm × 6 mm. Initial damage was simulated by a notch on the bottom of the steel beam. It was cut by wire electrical discharge machining. The width of the notch was 0.18 mm and the crack depths were 10 mm or 30 mm. The lower surface was sandblasted and cleaned with acetone before applying adhesive and patching with a CFRP plate. Two types of CFRP plates with normal or high modulus were used and they had dimensions of 500 mm long and 20 mm wide. As for the prestressed CFRP plate, they were tensioned with a hydraulic jack.

Four series of tests, with a total of eight specimens, involving different combinations of CFRP types, prestressing levels and initial damage levels were considered. The test matrix are presented in Table 1. Series A consists of two un-retrofitted beams with a 10 mm or 30 mm initial crack as the control ones. Series B and C includes specimens repaired with normal modulus CFRP plates that are designated by NC followed by either N or P, indicating non-prestressed or prestressed CFRP plates, respectively. Series D is two specimens repaired with non-prestressed CFRP plates of high modulus. HC refers to the used type of

**Table 1**  
Test matrix.

Series	No.	Initial crack depth (mm)	CFRP prestressing level (%)	CFRP modulus ( $\times 10^5$ MPa)	Loading ranges 2 P (kN)	Fatigue life (Cycles)
A	RHS-1	10	/	/	8–80	31,168
	RHS-2	30	/	/	5.5–55	13,803
B	NC-N-1	10	0	1.91	8–80	104,362
	NC-N-2	30	0	1.91	5.5–55	64,599
C	NC-P-1	10	22	1.91	8–80	232,055
	NC-P-2	30	22	1.91	5.5–55	491,014
D	HC-N-1	10	0	4.60	8–80	112,173
	HC-N-2	30	0	4.60	5.5–55	194,579

**Table 2**  
Material properties of steel, CFRP and adhesive.

Property	Steel	CFRP-1	CFRP-2	Adhesive
$f_y$ (MPa)	298	–	–	–
$f_u$ (MPa)	368	3089	1500	28.6
$E_1$ (GPa)	190	191	460	1.9
$E_2$ (GPa)	–	10.8	18.4	–
$\nu_{12}$	0.30	0.27	0.30	0.36
$G_{12}$ (GPa)	–	6.0	7.7	–
$t$ (mm)	6.00	1.40	1.55	0.40

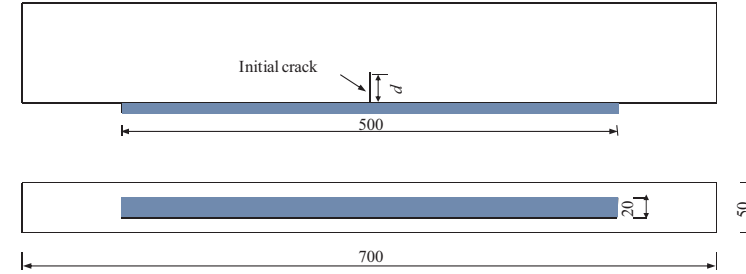
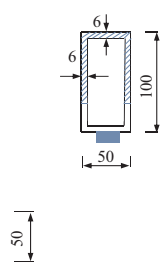
CFRP plate with high Young's modulus.

Tensile coupon tests were performed for steel tubes and results showed in Table 2. All the steel tubes were fabricated from one batch of material. The material properties of the steel, CFRP plates and adhesive are given in Table 2.

### 2.2. Specimen preparation

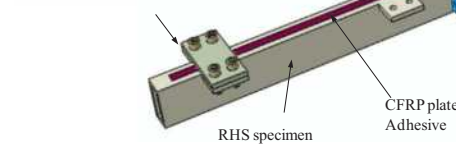
The specimen preparation consists of surface grinding, applying adhesives and patching CFRP plates. A major challenge of exploiting the high tensile strength of CFRP is prestressing the CFRP plate during specimen preparation. In this research, an instrumentation was employed to fulfill the prestressing process (Fig. 2). A bare specimen was positioned with the prestressing instrumentation. Thereafter, a CFRP plate was bolted at one end with the specimen using mechanical anchorage systems. The other end was clamped by steel plates that lined to the far end steel plate trough steel bars. Subsequently, a hydraulic jack was used to pull the steel bars. Strain gauges were mounted on CFRP plate surface to monitor the prestressing level until designed values. The anchorage systems was also used to fix both CFRP plate ends to delay or prevent debonding between CFRP plate and steel beam for non-prestressed CFRP repaired specimens. Thereafter, specimens were subjected to fatigue loading, and propagation phenomena were recorded.

**Fig. 1.** Geometry configurations (unit: mm).





Anchorage system

CFRP plate  
Adhesive

RHS specimen

Clamping plates

Steel bar

Hydraulic jack

Fig. 2. Prestressing instrumentation.

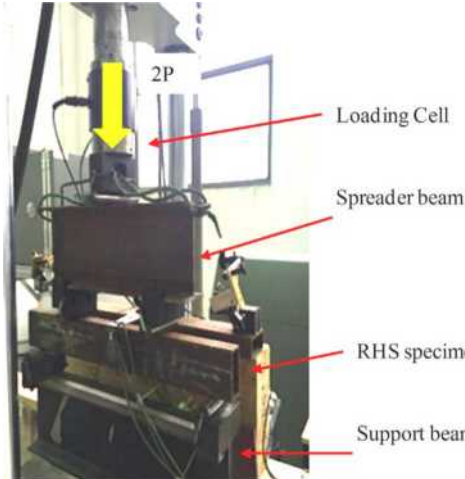


Fig. 3. Test setup.

### 2.3. Test setup

The fatigue tests were conducted on a MTS servo hydraulic testing machine with a capacity of 250 kN as shown in Fig. 3. Simply supported boundary conditions were applied at the ends of the specimens. A vertical load was applied to the center of spreader beam. All specimens were tested under an 8 Hz constant amplitude sinusoidal tension-tension fatigue loading with a loading ratio of 0.1. Different load ranges were applied to specimens with various initial crack depths (Table 1). The objective was to limit the fatigue crack propagation life less than one million cycles for all specimens.

### 2.4. Experimental results

The last column of Table 1 also summarizes the fatigue crack propagation life of all specimens. It can be observed that CFRP strengthened specimens can considerably increase fatigue life of cracked specimens. With regard to non-prestressed CFRP strengthened specimens, the fatigue lives were 3.35–14.10 times longer than that of controlled specimens. It was also found that high modulus CFRP achieved better fatigue performance. Meanwhile, the prestressed technique improved the fatigue life up to 7.45–35.57 times that of unrepairs steel beams. It also enhanced the utilization efficiency of CFRP material. Regardless of the initial crack depth, all repaired specimens had enhanced fatigue crack propagation lives.

The specimens that failed by fracture of the RHS steel beams were accompanied by rupture or pulling out of the CFRP patch from the steel beams. Fig. 4 shows typical failure patterns of strengthened specimens after the failure. Fig. 4(a) shows specimens failed with end slippage at

the anchorage region. Fig. 4(b) displays typical CFRP failure at anchorage region, while Fig. 4(c) illustrates representative CFRP breakage for specimens repaired by high modulus CFRP plates.

### 3. Fatigue crack growth prediction

In the context of linear elastic fracture mechanics (LEFM), the modeling of the fatigue crack propagation can be performed with stress intensity factors ranges from the crack front. Stress intensity factors can be obtained with numerical models specified with various crack depths. With integration of a propagation law, the number of cycles to propagated can be determined.

Several models have been developed to account for other factors based on the empirical form proposed by Paris and Erdogan [34]. In this study, the NASGRO Eq. (1) [35] was employed to estimate the crack propagation life. The equation is expressed as,

$$\frac{da}{dN} = \frac{C \cdot (1-f)^m \cdot \Delta K^m \cdot \left(1 - \frac{\Delta K_{th}}{\Delta K}\right)^p}{(1-R)^m \cdot \left(1 - \frac{\Delta K}{(1-R)K_c}\right)^q} \quad (1)$$

$$\Delta K = K_{\max} - K_{\min} = K_{\max}(1-R); R = (K_{\min}/K_{\max}) \quad (2)$$

where  $a$  = crack length;  $N$  = number of fatigue cycles;  $da/dN$  = instantaneous crack growth rate;  $\Delta K$  = stress intensity factor range;  $R$  = stress ratio;  $C$  and  $m$  = material parameters;  $p$  and  $q$  = the exponents,  $\Delta K_{th}$  = the threshold stress intensity factor range;  $f$  = the crack opening function;  $K_c$  = the critical stress intensity factor;  $K_{\max}$  = the maximum stress intensity factor and  $K_{\min}$  = the minimum stress intensity factor.

Fatigue crack closure effect is considered by introducing crack opening function,  $f$ , which is defined as [36]:

$$f = \frac{K_{op}}{K_{\max}} = \max\{R; A_0 + A_1 \cdot R + A_2 \cdot R^2 + A_3 \cdot R^3\} \quad 0 \leq R \leq 1 \quad (3)$$

where,

$$A_0 = (0.825 - 0.34\alpha + 0.05\alpha^2) \left[ \cos\left(\frac{\pi}{2}\right) SR \right]^{1/\alpha} \quad (4)$$

$$A_1 = (0.415 - 0.017\alpha) SR \quad (5)$$

$$A_2 = 1 - A_0 - A_1 - A_3 \quad (6)$$

$$A_3 = 2A_0 + A_1 - 1 \quad (7)$$

$$SR = \frac{S_{\max}}{\sigma_0} \quad (8)$$

where  $\alpha$  = the plain stress/strain constraint factor with a value of 2.5 for current steel as recommended by BEASY [37];  $S_{\max}$  = the maximum applied stress;  $\sigma_0$  = the flow stress, taken to be the average of the uniaxial yield stress and uniaxial ultimate tensile strength of the

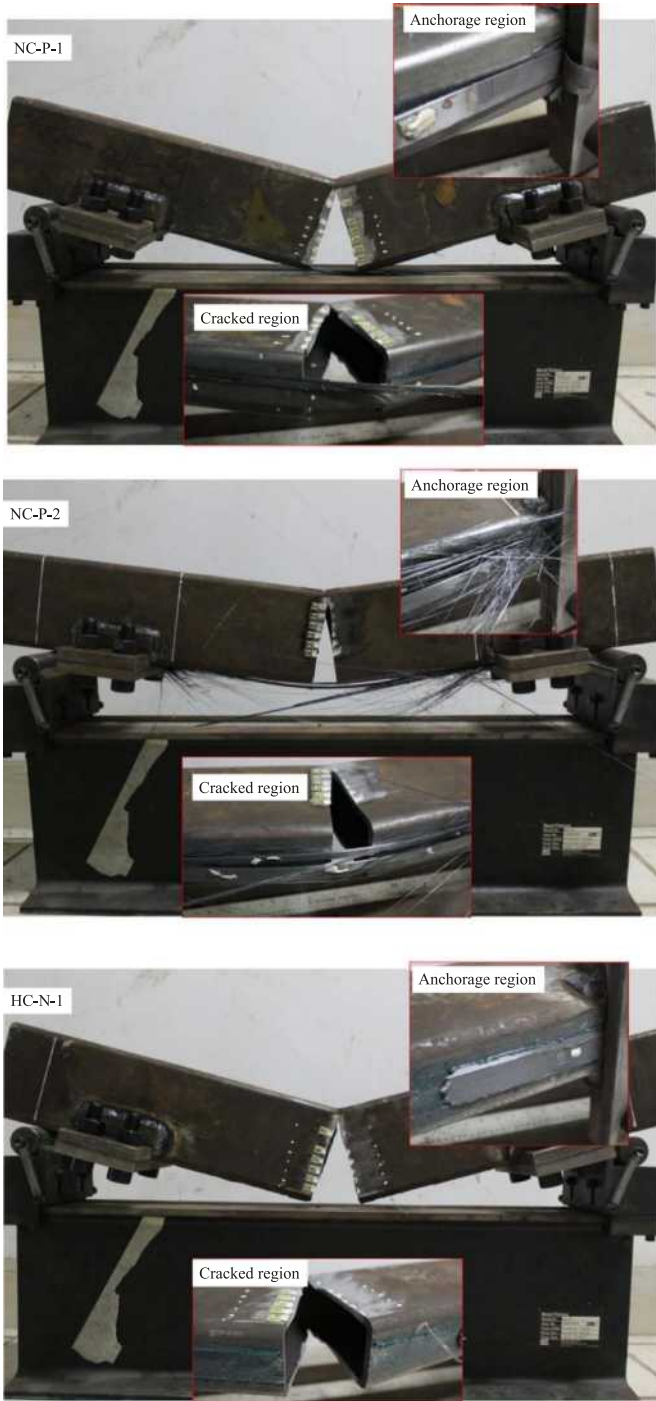


Fig. 4. Final failure of strengthened specimens.

material and  $K_{op}$  = the opening stress intensity factor below which the crack is closed.

### 3.1. Numerical model description

Finite element models were developed based on tested specimens by using the commercial finite element software package ABAQUS to predict the stress intensity factors. To reduce computational time consumption, a half finite element (FE) model was developed due to symmetry. The numerical model is mainly comprised of steel beam, CFRP plate and adhesive layer. A general view of the three-dimensional model is presented in Fig. 5. The supports were also modeled and specified with constraints as test settings. Two concentrated loads were

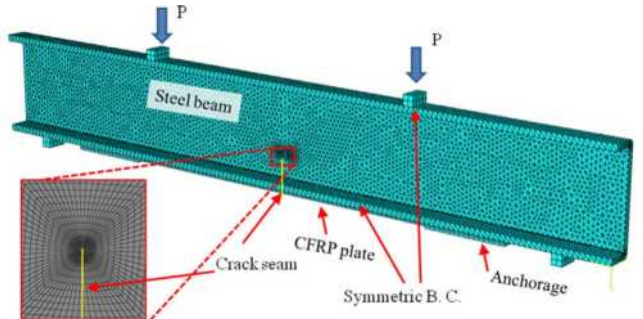


Fig. 5. Half FE model details.

applied to the top of the specimens. The prestressing stress of the CFRP plate can be simulated by applying an initial stress or by decreasing the temperature of CFRP plates [38]. The later approach was adopted in this study. We defined a decreasing temperature field to the CFRP plates before loading step. This can introduce prestress to the prescribed prestressing level after several iterations.

The adopted geometries and material properties were the same as those used for the tested specimens. The steel and CFRP materials were modeled as a linear, elastic material with Poisson's ratios of 0.3 and 0.2, respectively. The adhesive layer was modeled with cohesive elements (COH3D8) of mesh size 0.4 mm × 5 mm. The triangular cohesive zone model (CZM) formulation was chosen for its simplicity. And the traction separation law assumes an initial linear elastic behavior followed by a linear damage evolution. Damage initiation was specified by the maximum nominal stress criterion. The initial stiffness were determined from the adhesive material properties. The normal modulus ( $E$ ) is 1900 MPa and shear modulus ( $G_1, G_2$ ) are both 699 MPa. Debonding was not modeled considering the fatigue loading levels are not high during the test [39].

The steel was modeled using 3D, 10-node quadratic tetrahedron elements while the CFRP was modeled using 3D, 8-node elements with reduced integration. A mesh convergence study was conducted to achieve reliable results and guarantee simulation efficiency. Two concentrated loads were applied to the two rigid blocks. Supports were also defined as experimental settings. Crack tip singularity was modeled using classical wedge-shaped crack tip elements able to capture the crack tip feature. The SIFs at the crack front of cracked RHS steel beams were determined by the J-integral approach. Fig. 6 illustrates SIF values with crack lengths of specimens with a 30 mm initial crack depth. It can be observed that CFRP plate repairing brought down the SIFs compared to bare specimens.

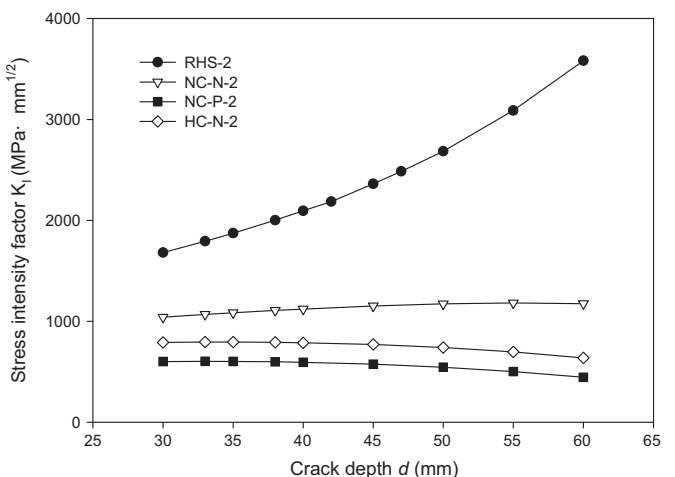


Fig. 6. Stress intensity factor values.

### 3.2. Validation using experimental results

To validate the numerical simulation technique of the cracked beams under fatigue loading, the results from the numerical simulations were compared with those from the experimental testing data. The fatigue life calculation method is well established in LEFM for cracked members. It includes following procedures: (i) SIF values extracted from numerical simulation with various crack depths; (ii) fitting equations for dotted numerical results; (iii) crack propagation life by integrating Eq. (1) as

$$N = \int_{a_i}^{a_f} \frac{(1-R)^m \cdot \left(1 - \frac{\Delta K}{(1-R)K_c}\right)^q}{C \cdot (1-f)^m \cdot \Delta K^m \cdot \left(1 - \frac{\Delta K_{th}}{\Delta K}\right)^p} \quad (9)$$

The initial crack depth,  $a_i$ , was defined for a tested beam. The final crack depth,  $a_f$ , was determined as 60% of beam height. With the employment of the NASGRO crack growth equation, the effects of stress ratio, which is 0.1 as used in the fatigue test, is considered. Material constants  $C$  and  $m$ , which are  $3.98 \times 10^{-13}$  (da/dN in mm/cycle and  $\Delta K$  in MPa mm $^{1/2}$ ) and 2.88, were adopted as recommended by the British Standards Institution (BSI) for steel in air [40]. Constants  $p$  and  $q$  are both assumed as 0.5 by referring to the NASGRO database in Beasy [37]. The values of  $\Delta K_{th}$  and  $K_c$  are recommended by BSI as 148.6 MPa mm $^{1/2}$  and 6950 MPa mm $^{1/2}$ , respectively.

Experimental data and numerical predictions are presented in Fig. 7 for comparison. Moreover, Fig. 7 shows a reasonably good agreement between the simulated and experimental results in terms of fatigue life.

### 4. Parametric study

The fracture mechanics method with finite element model was then used to perform several parametric studies on RHS steel beams. Several RHS steel beams with a 10 mm initial crack were selected as specimens to be repaired with various parameters. The considered parameters are CFRP width  $W_c$ , Young's modulus of CFRP  $E_c$  and a prestressing stress level of CFRP plate. The width ranges from 10 mm to 30 mm. Young's modulus of CFRP plates were specified as  $1.00 \times 10^5$  MPa,  $1.91 \times 10^5$  MPa and  $3.00 \times 10^5$  MPa. With prestressed CFRP, two levels were chosen at 12% and 22%, which correspond to 384 MPa and 680 MPa in CFRP plates as summarized in Table 3. Their effects on crack propagation life were discussed under the same fatigue loadings of the specimen RHS-1 that range from 8 kN to 80 kN.

#### 4.1. Influence of CFRP plate width

To investigate the influence of the amount of the repairing CFRP on

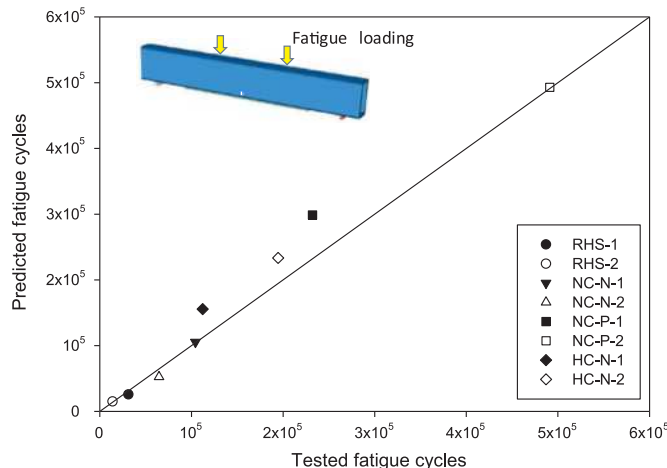


Fig. 7. Comparison of experimental fatigue life and numerical results.

**Table 3**  
Parametric study matrix.

Group	CFRP width $W_c$ (mm)	CFRP modulus $E_c$ ( $\times 10^5$ MPa)	CFRP prestressing level (%)
E	10	1.91	0, 12, 22
F	30	1.91	0, 12, 22
G	10	1.00	0, 12, 22
H	10	3.00	0, 12, 22
I	30	1.00	0, 12, 22
J	30	3.00	0, 12, 22
K	20	1.00	0
L	20	3.00	0

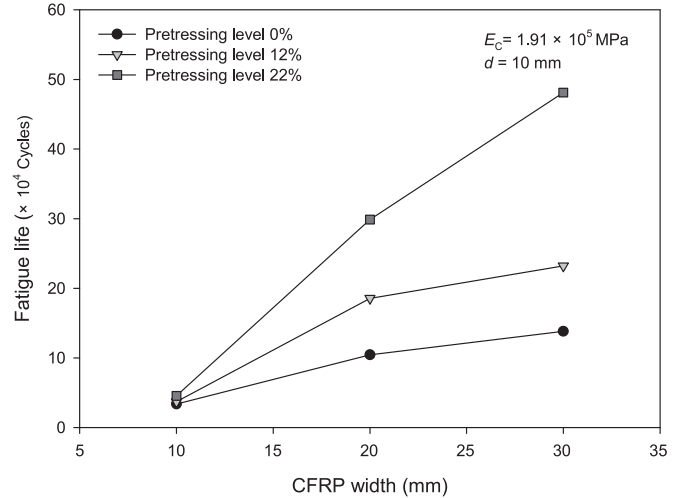


Fig. 8. Influence of CFRP plate widths on fatigue life.

fatigue life of the cracked RHS beams, three different widths of 10 mm, 20 mm and 30 mm were considered with other identical geometric parameters. Meanwhile, the prestressing levels in CFRP plates were also considered. Their fatigue crack propagation lives are plotted in Fig. 8. It is clear that by increasing CFRP widths, the fatigue propagation life increases. When the cracked specimens were patched with non-prestressed CFRP plates with various widths, the fatigue life was increased from  $3.39 \times 10^4$  cycles to  $13.81 \times 10^4$  cycles. With prestressing level of 22% CFRP repaired specimens, the fatigue life was increased from  $4.54 \times 10^4$  cycles to  $48.12 \times 10^4$  cycles when plate widths increased from 10 mm to 30 mm.

Fig. 9 illustrates the fatigue life ( $N$ ) ratio,  $R_N$ , between repaired and

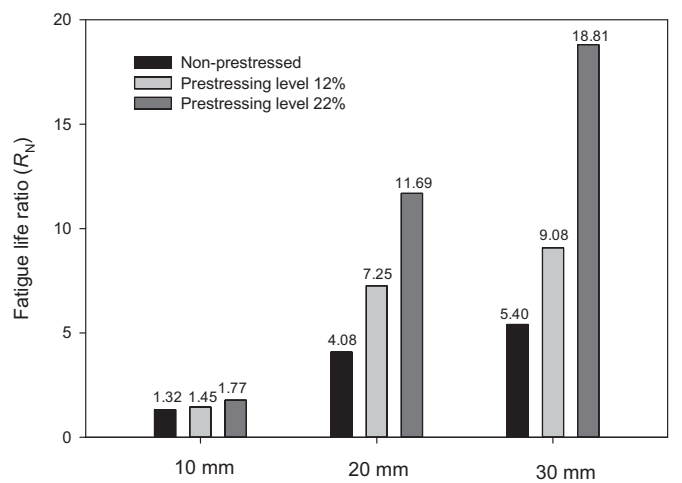


Fig. 9. Increment of crack propagation life with respect to the CFRP plate widths.

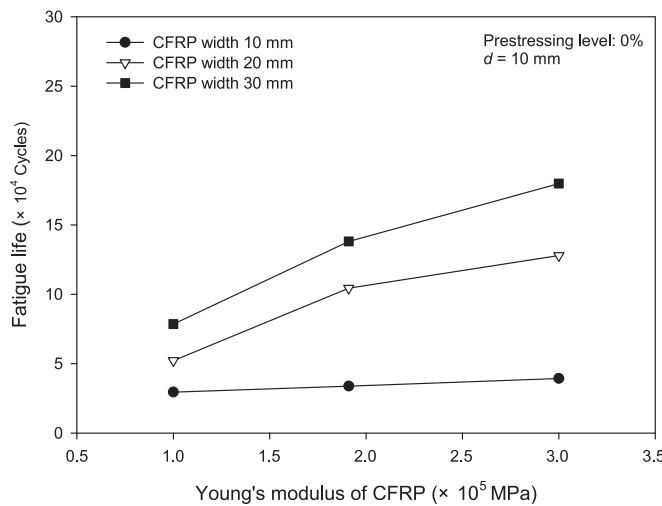


Fig. 10. Influence of CFRP moduli on fatigue life.

un-repaired specimens predicted by a numerical approach. When specimens were repaired with non-prestressed CFRP plates,  $R_N$  increased from about 1.32–5.40 (an increment of about 308%) when the CFRP widths increased from 10 mm to 30 mm. When the prestressing level in CFRP plates were 22% of the ultimate strength,  $R_N$  increased from about 1.77–18.81 (an increment of about 960%) with the augment of CFRP width. The increment effect was significant for higher prestressing levels.

#### 4.2. Influence of CFRP plate modulus

In this section, cases using non-prestressed CFRP plates with various Young's moduli were analyzed on the fatigue crack propagation life. All parameters were same except for the CFRP modulus, which was taken as  $1.00 \times 10^5$  MPa,  $1.91 \times 10^5$  MPa and  $3.00 \times 10^5$  MPa, respectively. A general trend in Fig. 10 is that a higher value of the CFRP modulus resulted in a longer fatigue crack propagation life.

The results were discussed with modulus and plate width. It can be observed from Fig. 11 that the fatigue life ratios,  $R_N$ , were about 1.15, 1.32 and 1.54 when CFRP width was 10 mm. The  $R_N$  were about 3.07, 5.40 and 7.03 when the CFRP width was 30 mm. It can be concluded that the CFRP modulus had a moderate effect on fatigue life increment compared to CFRP width.

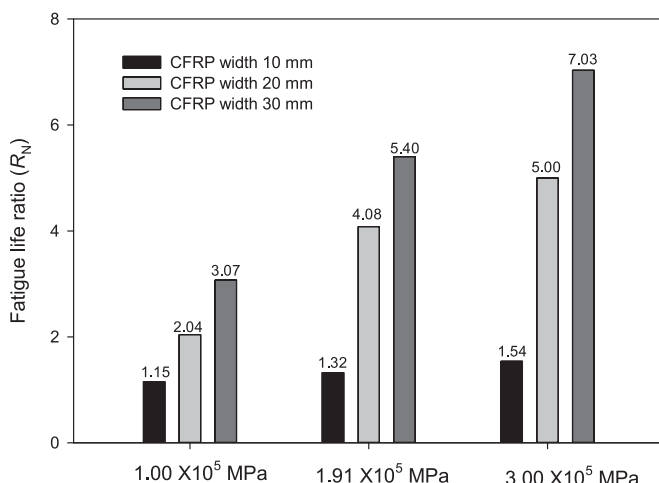


Fig. 11. Increment of crack propagation life with respect to the CFRP moduli.

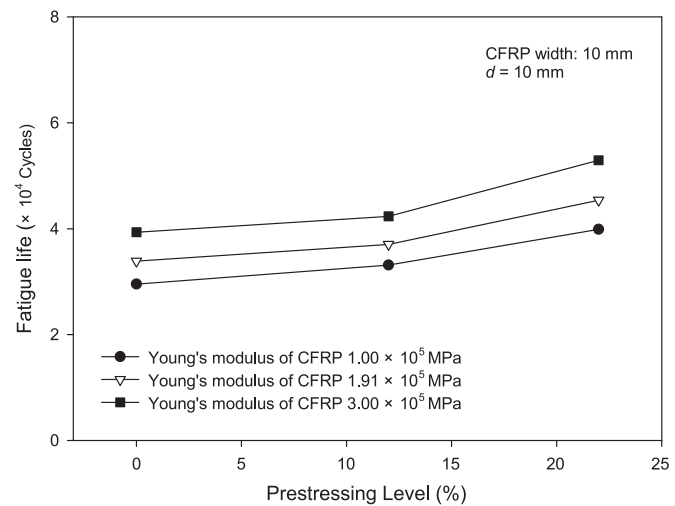


Fig. 12. Influence of CFRP prestressing levels on fatigue life.

#### 4.3. Influence of CFRP plate prestressing level

To study the effect of CFRP plate prestressing levels on fatigue lives, specimens were patched with CFRP plates of certain widths. The prestressing levels were 12% and 22% considering the test scheme. They were compared with non-prestressed CFRP repaired specimens. Fig. 12 illustrates fatigue lives with prestressing levels when the CFRP width was 10 mm. It is evident that higher prestressing levels result in longer lives. The fatigue lives increased to about 1.32, 1.45 and 1.77 times that of the unrepairs specimens when the CFRP modulus was  $1.91 \times 10^5$  MPa (Fig. 13). When the CFRP width increased to 30 mm, the fatigue life ratios,  $R_N$ , were significantly enhanced to 5.40, 9.08 and 18.81 (Fig. 9). It can be concluded that higher prestressing levels yield better fatigue life enhancement with wider CFRP plates.

#### 5. Conclusions

This paper presents the effects of the CFRP strengthening method on the fatigue crack propagation life of RHS steel beams through application of a validated numerical approach. Fatigue tests were carried out to cracked RHS steel beams with various initial crack depths, material moduli and prestressing levels in CFRP. Thereafter, three-dimensional finite element models were developed based on the configurations of the test specimens. Fatigue life prediction with numerical approach was validated with experimental data with reasonable accuracy. A

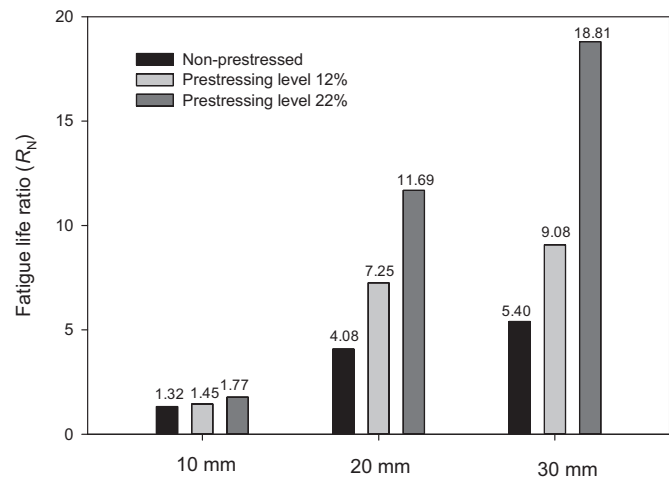


Fig. 13. Increment of fatigue crack propagation life with respect to the CFRP prestressing levels.

parametric study was then performed to evaluate the effect of CFRP configurations on the fatigue crack propagation life of repaired specimens. The results showed that prolonged fatigue crack propagation life could be achieved by increasing the width, the Young's modulus and the prestressing level of CFRP plates. The effect of CFRP prestressing level became more prominent with a wider CFRP plate. These enhancements can be estimated to design future rehabilitation of cracked RHS steel beams with prestressed CFRP plates.

## Acknowledgments

This work was financially supported by NSFC (Grant no. 51678440), the Fundamental Research Funds for the Central Universities and the National Key Technology R & D Program (Grant no. 2014BAD08B01).

## References

- [1] R.E. Koller, I. Stoecklin, S. Valet, G.P. Terrasi, CFRP-strengthening and long-term performance of fatigue critical welds of a steel box girder, *Polymer* 6 (2014) 443–463, <http://dx.doi.org/10.3390/polym6020443>.
- [2] J.M. Ricles, M.F. Hebor, Residual strength and epoxy-based grout repair of corroded offshore tubulars, 1994.
- [3] T.G. Ghazijahani, H. Jiao, D. Holloway, Fatigue tests of damaged tubes under flexural loading, *Steel Compos. Struct.* 19 (2015) 223–236.
- [4] J. Haedir, X.L. Zhao, Design of CFRP-strengthened steel CHS tubular beams, *J. Constr. Steel Res.* 72 (2012) 203–218, <http://dx.doi.org/10.1016/j.jcsr.2011.12.004>.
- [5] J. Wardenier, J. a. Packer, X.L. Zhao, G.J. Van der Vegt, *Hollow Sections in Structural Applications*, Bouwen met Staal, Zoetermeer, The Netherlands, 2010.
- [6] X.L. Zhao, L. Zhang, State-of-the-art review on FRP strengthened steel structures, *Eng. Struct.* 29 (2007) 1808–1823, <http://dx.doi.org/10.1016/j.engstruct.2006.10.006>.
- [7] J.G. Teng, T. Yu, D. Fernando, Strengthening of steel structures with fiber-reinforced polymer composites, *J. Constr. Steel Res.* 78 (2012) 131–143, <http://dx.doi.org/10.1016/j.jcsr.2012.06.011>.
- [8] J. Haedir, M.R. Bambach, X.L. Zhao, R.H. Grzebieta, Strength of circular hollow sections (CHS) tubular beams externally reinforced by carbon FRP sheets in pure bending, *Thin-Walled Struct.* 47 (2009) 1136–1147, <http://dx.doi.org/10.1016/j.tws.2008.10.017>.
- [9] A.W. Al Zand, W.H.W. Badaruzzaman, A.A. Mutalib, S.J. Hilo, Rehabilitation and strengthening of high-strength rectangular CFST beams using a partial wrapping scheme of CFRP sheets: experimental and numerical study, *Thin-Walled Struct.* 114 (2017) 80–91, <http://dx.doi.org/10.1016/j.tws.2017.01.028>.
- [10] Q.Q. Yu, T. Chen, X.L. Gu, X.L. Zhao, Z.G. Xiao, Fatigue behaviour of CFRP strengthened steel plates with different degrees of damage, *Thin-Walled Struct.* 69 (2013) 10–17, <http://dx.doi.org/10.1016/j.tws.2013.03.012>.
- [11] P. Feng, L. Hu, X.L. Zhao, L. Cheng, S. Xu, Study on thermal effects on fatigue behavior of cracked steel plates strengthened by CFRP sheets, *Thin-Walled Struct.* 82 (2014) 311–320, <http://dx.doi.org/10.1016/j.tws.2014.04.015>.
- [12] R. Emdad, R. Al-mahaidi, Effect of prestressed CFRP patches on crack growth of centre-notched steel plates, *Compos. Struct.* 123 (2015) 109–122, <http://dx.doi.org/10.1016/j.compositstruct.2014.12.007>.
- [13] Y. Huawen, C. König, T. Ummenhofer, Q. Shizhong, R. Plum, Fatigue performance of tension steel plates strengthened with prestressed CFRP laminates, *J. Compos. Constr.* 14 (2010) 609–615, [http://dx.doi.org/10.1061/\(ASCE\)CC.1943-5614.000111](http://dx.doi.org/10.1061/(ASCE)CC.1943-5614.000111).
- [14] P. Colombi, A. Bassetti, A. Nussbaumer, Crack growth induced delamination on steel members reinforced by prestressed composite patch, *Fatigue Fract. Eng. Mater. Struct.* 26 (2003) 429–437, <http://dx.doi.org/10.1046/j.1460-2695.2003.00642.x>.
- [15] B. Täljsten, C.S. Hansen, J.W. Schmidt, Strengthening of old metallic structures in fatigue with prestressed and non-prestressed CFRP laminates, *Constr. Build. Mater.* 23 (2009) 1665–1677, <http://dx.doi.org/10.1016/j.conbuildmat.2008.08.001>.
- [16] E. Ghafoori, M. Motavalli, J. Botsis, A. Herwig, M. Galli, Fatigue strengthening of damaged metallic beams using prestressed unbonded and bonded CFRP plates, *Int. J. Fatigue* 44 (2012) 303–315, <http://dx.doi.org/10.1016/j.ijfatigue.2012.03.006>.
- [17] P. Colombi, A. Bassetti, A. Nussbaumer, Analysis of cracked steel members reinforced by pre-stress composite patch, *Fatigue Fract. Eng. Mater. Struct.* 26 (2003) 59–66, <http://dx.doi.org/10.1046/j.1460-2695.2003.00598.x>.
- [18] H. Nakamura, Y. Yamamura, H. Ito, F. Lin, K. Maeda, Development of Pre-Tensioning Device for CFRP Strips and Applicability to Repair of Cracked Steel Members, *Adv. Struct. Eng.* 17 (2014) 1705–1718, <http://dx.doi.org/10.1260/1369-4332.17.12.1705>.
- [19] Y.J. Kim, K.A. Harries, Fatigue behavior of damaged steel beams repaired with CFRP strips, *Eng. Struct.* 33 (2011) 1491–1502, <http://dx.doi.org/10.1016/j.engstruct.2011.01.019>.
- [20] J. Deng, M.M.K. Lee, Fatigue performance of metallic beam strengthened with a bonded CFRP plate, *Compos. Struct.* 78 (2007) 222–231, <http://dx.doi.org/10.1016/j.compositstruct.2005.09.003>.
- [21] A. Hmidan, Y.J. Kim, S. Yazdani, CFRP repair of steel beams with various initial crack configurations, *J. Compos. Constr.* 15 (2011) 952–962, [http://dx.doi.org/10.1061/\(ASCE\)CC.1943-5614.0000223](http://dx.doi.org/10.1061/(ASCE)CC.1943-5614.0000223).
- [22] M. Elchalakani, Rehabilitation of corroded steel CHS under combined bending and bearing using CFRP, *J. Constr. Steel Res.* 125 (2016) 26–42, <http://dx.doi.org/10.1016/j.jcsr.2016.06.008>.
- [23] D. Linghoff, M. Al-Emrani, R. Kliger, Performance of steel beams strengthened with CFRP laminate - Part 1: laboratory tests, *Compos. Part B Eng.* 41 (2010) 509–515, <http://dx.doi.org/10.1016/j.compositesb.2009.05.008>.
- [24] D. Linghoff, M. Al-Emrani, Performance of steel beams strengthened with CFRP laminate - Part 2: Fe analyses, *Compos. Part B Eng.* 41 (2010) 516–522, <http://dx.doi.org/10.1016/j.compositesb.2009.07.002>.
- [25] P. Colombi, G. Fava, Experimental study on the fatigue behaviour of cracked steel beams repaired with CFRP plates, *Eng. Fract. Mech.* 145 (2015) 128–142, <http://dx.doi.org/10.1016/j.engfracmech.2015.04.009>.
- [26] H. Jiao, H.B. Phan, X.L. Zhao, Fatigue behaviour of steel elements strengthened with stand CFRP sheets, *Adv. Struct. Eng.* 17 (2014) 1719–1728, <http://dx.doi.org/10.1260/1369-4332.17.12.1719>.
- [27] Q.Q. Yu, Y.F. Wu, Fatigue strengthening of cracked steel beams with different configurations and materials, *J. Compos. Constr.* (2016), [http://dx.doi.org/10.1061/\(ASCE\)CC.1943-5614.0000750](http://dx.doi.org/10.1061/(ASCE)CC.1943-5614.0000750).
- [28] S. Walbridge, K. Soudki, F. Vatandoost, Fatigue retrofitting of welded steel cover plates using Pre-stressed carbon fibre reinforced polymer strips, *Struct. Eng. Int. J. Int. Assoc. Bridg. Struct. Eng.* 21 (2011) 279–284, [http://dx.doi.org/10.2749/101686611\\_x13049248220122](http://dx.doi.org/10.2749/101686611_x13049248220122).
- [29] E. Ghafoori, M. Motavalli, Lateral-torsional buckling of steel I-beams retrofitted by bonded and un-bonded CFRP laminates with different pre-stress levels: experimental and numerical study, *Constr. Build. Mater.* 76 (2015) 194–206, <http://dx.doi.org/10.1016/j.conbuildmat.2014.11.070>.
- [30] M. Elchalakani, CFRP strengthening and rehabilitation of degraded steel welded RHS beams under combined bending and bearing, *Thin-Walled Struct.* 77 (2014) 86–108, <http://dx.doi.org/10.1016/j.tws.2013.12.002>.
- [31] M. Elchalakani, Plastic collapse analysis of CFRP strengthened and rehabilitated degraded steel welded RHS beams subjected to combined bending and bearing, *Thin-Walled Struct.* 82 (2014) 278–295, <http://dx.doi.org/10.1016/j.tws.2014.05.002>.
- [32] Z.G. Xiao, X.L. Zhao, Cfrp repaired welded thin-walled cross-beam connections subject to in-plane fatigue loading, *Int. J. Struct. Stab. Dyn.* 12 (2012) 195–211, <http://dx.doi.org/10.1142/S0219455412004653>.
- [33] R.E. Koller, I. Stoecklin, S. Valet, G.P. Terrasi, CFRP-strengthening and long-term performance of fatigue critical welds of a steel box girder, *Polymer* 6 (2014) 443–463, <http://dx.doi.org/10.3390/polym6020443>.
- [34] P. Paris, F. Erdogan, A critical analysis of crack propagation laws, *J. Basic Eng.* 85 (1963) 528–533, <http://dx.doi.org/10.1115/1.3656900>.
- [35] R.G. Forman, S.R. Mettu, Behavior of surface and corner cracks subjected to tensile and bending loads in a Ti-6Al-4V alloy (1990).
- [36] J.C. Newman, A crack opening stress equation for fatigue crack growth, *Int. J. Fract.* 24 (1984) R131–R135, <http://dx.doi.org/10.1007/BF00020751>.
- [37] BEASY Ltd, BEASY 10.14, Ashurst, Southampton SO40 7AA, United Kingdom: Ashurst Lodge. (2016).
- [38] W. Ren, L.H. Sneed, Y. Yang, R. He, Numerical simulation of prestressed precast concrete bridge deck panels using damage plasticity model, *Int. J. Concr. Struct. Mater.* 9 (2015) 45–54, <http://dx.doi.org/10.1007/s40069-014-0091-2>.
- [39] H.B. Liu, X.L. Zhao, R. Al-Mahaidi, Effect of fatigue loading on bond strength between CFRP sheets and steel plates, *Int. J. Struct. Stab. Dyn.* 10 (2010) 1–20, <http://dx.doi.org/10.1142/S0219455410003348>.
- [40] British Standards Institution, Guide to Methods for Assessing the Acceptability of Flaws in Metallic Structures, British Standards Institution, London, 2005.



## Fatigue strength of repaired cracks in base material of high strength steels



A. Akyel <sup>a,b,\*</sup>, M.H. Kolstein <sup>b</sup>, F.S.K. Bijlaard <sup>b</sup>

<sup>a</sup> Materials Innovation Institute (M2i), Delft, Netherlands

<sup>b</sup> Delft University of Technology, Delft, Netherlands

### ARTICLE INFO

#### Article history:

Received 6 October 2016

Received in revised form 27 September 2017

Accepted 4 October 2017

Available online 10 October 2017

#### Keywords:

Very high strength steels

Repair weld

Base material

Artificial crack

Fatigue

### ABSTRACT

Fatigue crack formation is an inevitable issue for welded steel structures subjected to cyclic loading. Accordingly, repair of the fatigue crack in welded steel structures is unavoidable to prolong fatigue life. However, there is limited knowledge available about the procedure to be adopted for the repair and the life extension to be expected after the repair. The current paper is focused on the effects of the repaired artificial crack in the base material of S690 and S890 high strength rolled steels on the fatigue strength of the material. An artificial crack was created in the middle of the plate test specimens by spark machining and subsequently, the crack was repaired by using the FCAW (flux-cored arc welding) process. The repaired specimens were tested in a four point bending test rig with a constant amplitude loading for creating a uniform bending moment at the weld region such that the weld cap to be exposed to tensile stresses. The test results show that most of the fatigue cracks initiated at the start-stop points of the weld cap and the fatigue crack initiation life of the specimens occupy approximately 45% of the total fatigue life. The statistical analysis of the test results revealed that the characteristic fatigue strength of the repaired specimens is very close to the detail category 160 of EN 1993-1-9 [5].

© 2017 Elsevier Ltd. All rights reserved.

## 1. Introduction

Modern steel manufacturing techniques make it possible to produce very high strength steels for various application purposes. The application of very high strength steels has enormously increased in the automotive industry in the course of the last decades. Although very high strength steels with good weldability, toughness and yield strength up to 1300 MPa are available for structural application purposes, the use of very high strength steels in the civil engineering structures is rather limited due to lack of knowledge about consequences of manufacturing process and limited available experimental evidence of the structural behaviour of the material.

The use of very high strength steels results in slender members with reduced wall thicknesses which lead to low self-weight and volume of structures. This results in cost savings in production, transportation and erection. In case of welded connections, the slender member with thin wall thicknesses will allow for the smaller weld volumes hence, decrease in weld consumables and lower energy consumption to make the welded connections. Nevertheless, low self-weight of very high strength steel structure causes a high stress variation under live load. Consequently, the fatigue strength of very high strength steel structures is one of the main design criteria for the effective application.

Gurney [1] determined that the fatigue strength of the material becomes more sensitive to the entity of notches and to the surface condition with the enhancement of the material yield strength. In accordance with this, the fatigue sensitivity can be reduced with the reduction of stress concentrations. With the disregarding surface condition of the material, the fatigue strength increases with the higher yield strength of the material. Maddox [2] concluded that the fatigue strength of welded connections is independent of the material yield strength. This was based on the assumption that the welding application leads to micro-cracks which are likely to give rise to fatigue cracks. Accordingly, the fatigue crack propagation life is determinant for the fatigue life of welded connections and depends on the stress ranges, being independent of yield strength. The determination of the fatigue strength of the base material and welded connections made of very high strength steels has become one of the main research topics in the last decade. Demofonti et al. [3] performed fatigue tests on the butt welded specimens with 10 mm thickness and made of S355 up to S960. The results showed that no significant fatigue strength difference exists under constant amplitude loading condition while the beneficial effects of S960 steel investigated under variable amplitude loading condition. In addition, the advantage of very high strength steels on the fatigue strength was determined with reduction of the notch factor which was achieved by machining of the welds. In the framework of a research program of ECSC, Puthli et al. [4] carried out fatigue tests on various butt welded specimens with a thickness of 6–8 mm made of S690, S960 and S1100. The characteristic fatigue strength for all steel

\* Corresponding author at: Materials Innovation Institute (M2i), Delft, Netherlands.

E-mail address: [a.akyel@tudelft.nl](mailto:a.akyel@tudelft.nl) (A. Akyel).

**Table 1**

Chemical compositions of test materials [%wt].

Grade	C %	Si %	Mn %	P %	S %	Cr %	Mo %	Ni %
S690	0.16	0.19	0.87	0.012	0.002	0.33	0.22	0.06
S890	0.168	0.281	0.98	0.012	0.0008	0.494	0.511	0.98
Grade	V %	Nb %	Al %	Cu %	N %	B %		
S690		0.026	0.085		0.0038	0.002		
S890		0.041	0.011	0.074	0.024		0.0022	

**Table 2**

Mechanical properties of test materials.

Grade	R <sub>p,0.2</sub> [MPa]	R <sub>m</sub> [MPa]	A5 %	KVC	
				−40 °C [J]	−20 °C [J]
S690	800	830	17		251
S890	985	1051	14.3	36	

grades was found to be above of the recommended design values of EN 1993-1-9 [5]. The test results of the specimens made of S1100 showed the tendency for the decrease of the free slope to  $m = -5$ . Pijpers et al. [6] concluded from the fatigue tests on the base material and transverse butt welded specimens made of S690 and S1100 that the fatigue crack initiation life of very high strength steels is longer than mild strength steels. Kuhlmann et al. [7] showed that the post weld impact treatments are very effective for improving the fatigue strength of welded connections made of very high strength steels. The effectiveness of post weld impact treatments on fatigue strength of very high strength steels is already standardised in IIW recommendations [8]. Berg et al. [17] concluded that the fatigue strength of high frequency hammer peening treated welded connections made of S960, S1100 and S1300 is at least twice the fatigue strength of the as-welded condition.

As concluded by Gurney [1] and Pijpers [9], the fatigue strength of very high strength steels is susceptible to the surface conditions and the presence of notches. Therefore, the base material with high surface roughness might cause the fatigue crack initiation in the structural elements or even in the base material of welded connections made of very high strength steels. Once the cracks are detected the repair of the base material becomes essential for fatigue life extension.

Yamasaki, et al. [10] focused on the effects of the repair weld on the fatigue crack growth behaviour in the base material of JIS SM50A steel plates with the yield strength of 323 MPa. Fatigue cracks with certain length were created in the pre-notched specimens. The created fatigue cracks were repaired by X-shape welding under three conditions: with applying an axial tensile stress, without external stress and open cracks condition to induce compressive stress with releasing open state after the repair. The results showed that the fatigue crack growth rate in the repaired specimens is higher than the growth rate in the base material and the artificially induced compressive stresses

improved the crack growth behaviour of the repaired specimens. Kudryavtsev et al. [11] investigated the effectiveness of various repairs and retrofit methods for the fatigue cracks in the base material of low alloyed steel with the yield strength of 367 MPa. The hole drilled plate test specimens were subjected to fatigue load to create fatigue cracks at the edge of the hole. The crack propagation was permitted until certain size and the fatigue crack were repaired/retrofitted by the following techniques: drilling a hole at the crack tips with and without cold working, drilling a hole at the crack tips with installation of high strength bolts, overloading of the section, local explosive treatment, local heat treatment, repair by welding with and without ultrasonic peening of the weld toes. The repair by welding with ultrasonic peening provided the longest fatigue life after the repair. According to the test results, the repair by welding without ultrasonic peening was the second effective method for the fatigue cracks repair.

The state of art shows that the fatigue strength of the base material improves with the increase of the yield strength of the material. Nevertheless, the surface conditions can influence of the fatigue strength of the material and lead to fatigue crack initiation in the base material. For fatigue life extension, the repair of the base material cracks becomes essential. However, limited knowledge is available for the fatigue cracks repair procedure, consequences of the repair on the base material of very high strength steels and possible fatigue life extension after the repair of the cracks. This paper presents the repair process of artificially created cracks in the base material of S690 and S890 rolled steels and the fatigue test results of the repaired specimens.

## 2. Plate material properties

Table 1 gives the chemical compositions and Table 2 the mechanical properties of the test materials. The values of the mechanical properties and the chemical compositions are taken from the material certificates.

## 3. Test specimens

The test specimens were cut from S690 and S890 plates by water cutting and have a length of 990 mm and a width of 160 mm. In the middle, the width of the specimens was reduced to 150 mm (see Fig. 1).

For performing the repair procedure, a crack is artificially created in the middle of the specimens. The predefined crack shape and crack size ensure a controllable material removal process and a repair weld with similar length and depth in all specimens. Consequently, this allows the appropriate evaluation for the test results straightforward without the influences of variation due to manufacturing process. The artificial cracks were created by electrical discharge machining (EDM) process.

In practice, the fitness for purposes analysis is carried out to determine the time period for fatigue crack propagation from the detected crack size to the allowable critical crack size. Accordingly, the inspection and repair intervals are specified based on this time period. For simplification of the analysis, half the thickness of the section is assumed to be the allowable critical crack depth unless any other restrictions are defined. With the same approach, the depth of the artificial crack is

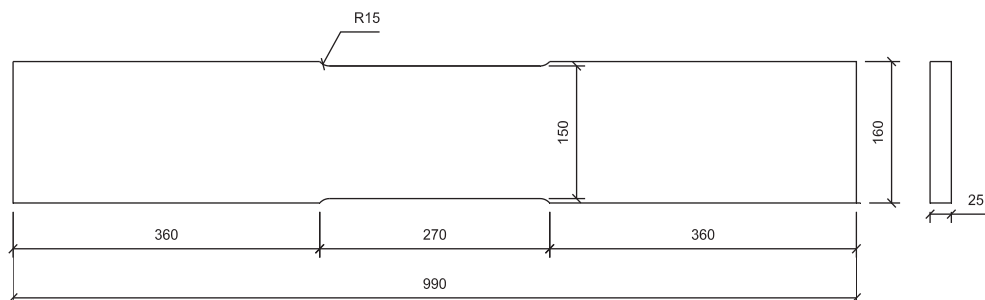
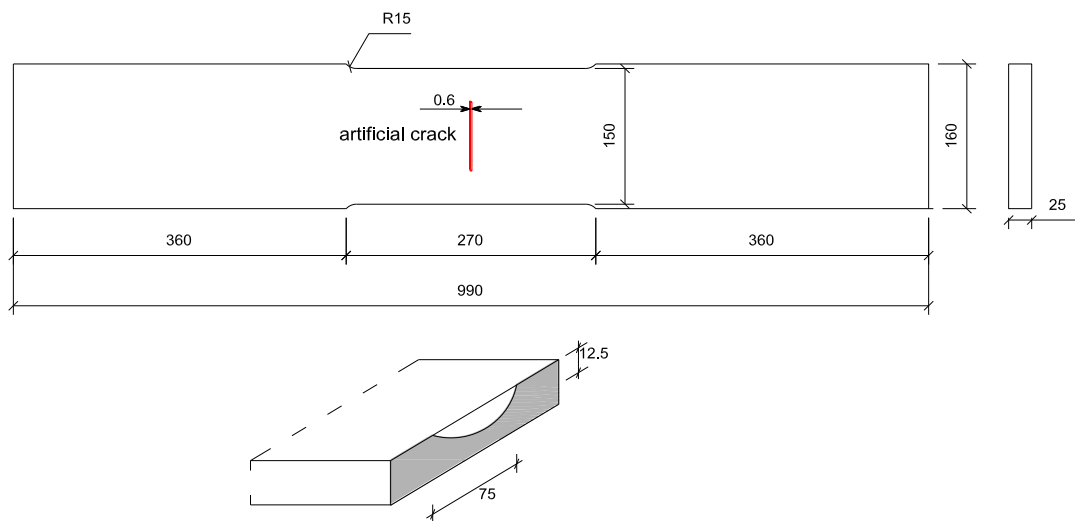
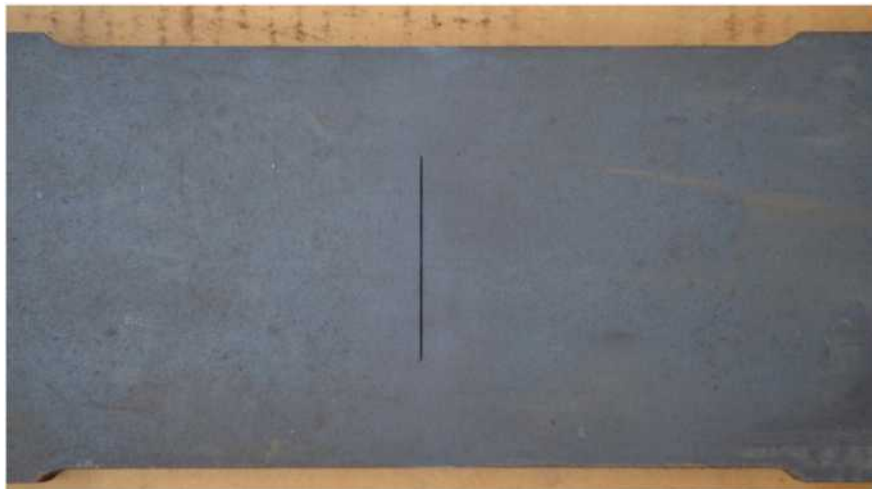


Fig. 1. Dimensions of the test specimens.



**Fig. 2.** Geometry of specimens and detail of artificial crack.



**Fig. 3.** Test specimen with artificial crack.

defined as half the thickness of the test plates; 12.5 mm. Since the fatigue induced cracks forms in a semi elliptical shape after the initiation, the artificial cracks were created with a semi elliptical shape to be more representative for real fatigue cracks. In this context, the crack length is defined as half the width of the plate which is 75 mm. Material removal process, the feasibility of welding and workability for the welder is taken into account for the determination of the crack length. Furthermore, the artificial crack width was kept as narrow as possible for more reflection a real fatigue crack and it is approximately equal to 0.6 mm. According to this description, the test specimen with an artificial crack is schematised in Fig. 2 and Fig. 3 shows the artificial crack in a test specimen.

For each steel grade, 9 test specimens were prepared and the specimens made of S690 steel grade are encoded as BR69x while BR89x encoding is used for the specimens made of S890 steel grade. Consequently, the experimental program consists of two test series.

#### 4. Repairing artificial crack

The measurements took place on the length and the depth of the artificial crack in all specimens. The size of the crack was identical to the drawing in Fig. 2 while the shape of the crack showed some deviation

from the semi elliptical shape. Subsequently, border lines were drawn at the end of the crack length to specify the boundaries for the crack removal process herewith to avoid unnecessary material removal and



**Fig. 4.** Magnetic particle inspection after the crack removal process.

**Table 3**  
Welding parameters for BR series.

Specimens	BR69x	BR89x
Rolled steel grade	S690	S890
Thickness [mm]	25	25
Length [mm]	990	990
Width [mm]	150	150
Preheat temperature °C (min)	100	125
Interpass temperature °C (max)	165	165
Weld metal	Megafill 742 M	Megafill 1100 M
Weld process	FCAW	FCAW
Heat input [kJ/mm]	1.2–1.8	1.2–1.8



Fig. 5. Reshaping start-stop points at the weld cap.

longer weld grooves. The crack removal process was executed with a disc grinder and burr grinder where the disc grinder was used at the initial stage to remove a small amount of the material and the further removal process was continued by the burr grinder.

One of the important requirements of fatigue cracks repair is to ensure complete crack removal as well as to prevent unnecessary material removal. In practice, the crack removal process is usually executed gradually with regular inspection of a non-destructive testing (NDT). However, for the test specimens, the depth of the cracks was known in advance and therefore, the execution of the crack removal proceeded until visually estimated that the prepared weld groove is reached to the

depth of the artificial crack. Subsequent to a magnetic particle inspection on the prepared weld groove to ensure the complete crack removal (see Fig. 4), the groove was filled by welding which was executed by the flux-core arc welding (FCAW) process. Megafill 742 M and Megafill 1100 M filler materials were used for the welding of the specimens made of S690 and S890 respectively. Table 3 summarises the geometry of the specimens and the welding procedure of the repair weld.

In the repair of fatigue cracks, care should be taken that the method used must not cause an additional possible fatigue crack initiation locations and reasons for the deterioration of fatigue strength. Especially in the case of welding application, imperfections might be formed such as cracks, inclusions, undercut etc. and these imperfections can have significant effects on the fatigue strength of welded connections. Therefore, the repair welds in the specimens were examined by magnetic particle and ultrasonic inspection. The repair weld satisfied the quality requirements of EN-ISO 5817 [12].

Furthermore, start and stop points of weld layers usually show different geometrical shapes where a bulge occurs at the start point and cavity at the stop point and as a result, these geometrical features induce a high stress concentration. In addition, these locations usually contain weld defects, therefore, the start-stop points of each weld pass are usually ground for the elimination of these defects. According to Zhang, et al. [13], the start-stop point of the weld also causes high residual stresses compared to other location of the weld layers. As it is known, all these issues negatively affect the fatigue strength of welded connections. For avoiding the occurrence of the start-stop points are therefore preferable; however, it is not possible in the most of the cases. For multi pass welding, start-stop points of the weld layers should be distributed along the weld length to avoid concentrated start-stop point at a location with undesirable effects of them. Since the artificial cracks were placed in the middle of the test specimens, it was difficult to execute the welding process without start-stop points and the length of the repair weld is too short for distributing the start-stop points along the weld length. On the other hand, the stress concentration effects at the start-stop of the weld toe can be reduced by reshaping the start-stop points. In accordance with this, the start-stop points at the weld cap of the specimens were reshaped by a grinding process (see Fig. 5).

## 5. Fatigue test rig

The fatigue tests were carried out in the Stevin II Laboratory of the Delft University of Technology. The fatigue tests were executed with a four point bending test rig. (see Fig. 6). The specimens were loaded cyclically to initiate fatigue cracks in the repair welds and the growth

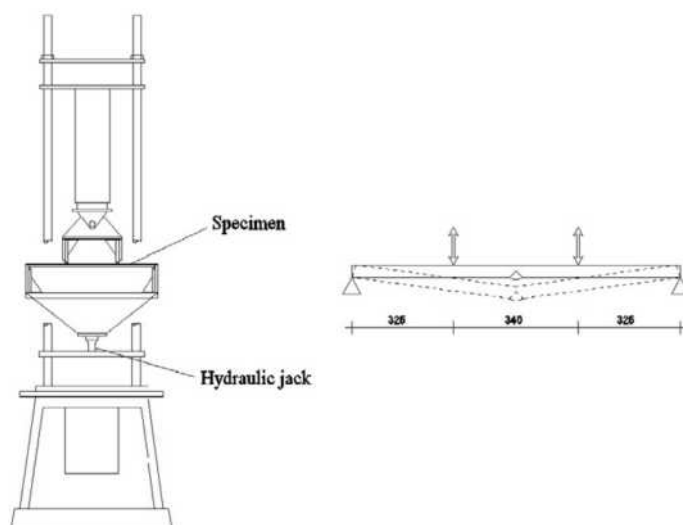
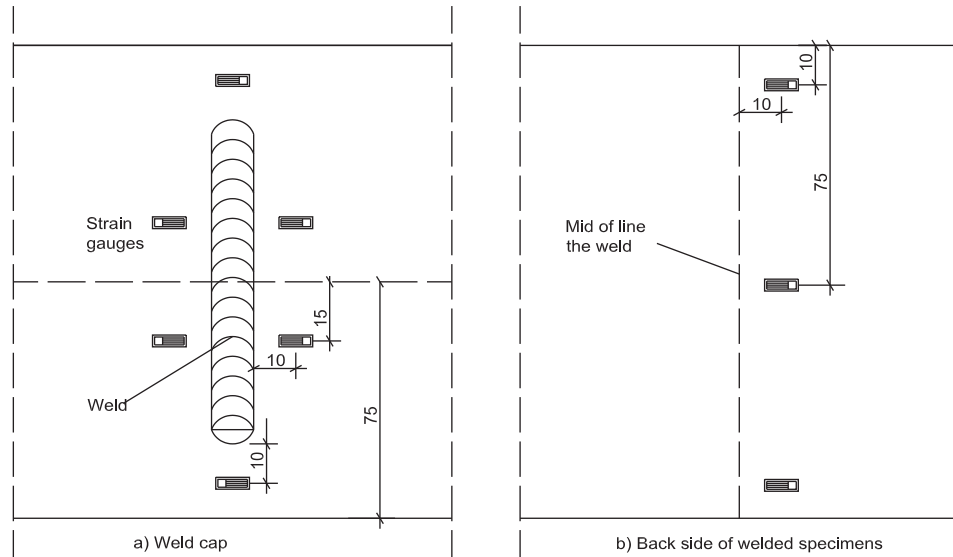


Fig. 6. Four point bending test rig.



**Fig. 7.** Position of strain gauges on specimens.

of the cracks is monitored until failure which was defined such that the specimens broken into two pieces. The specimens were tested with force controlled loading, which means that the force range was constant during the test, even in the case of loss of stiffness when the cracks were growing.

By the use of the four point bending test setup, a uniform bending moment was created in the weld area, resulting in a compression and a tension zone over the thickness. The cap of the repair welds was in the tension zone and the tests were performed with stress ratio  $R = 0.1$ .

## 6. Crack monitoring

Strain gauges are attached to the specimens to measure the strain distribution at the surround of the repair weld and to monitor fatigue cracks development. The strain gauges were placed at 10 mm from the weld toe with a position relatively close to the expected locations of the fatigue crack initiation. At the both sides of the weld toe, two strain gauges were attached. In addition, one strain gauge was applied at 10 mm from both sides of the weld end, for detecting the crack

initiation at the end of start-stop points of the weld cap (see Fig. 7(a)). Moreover, three strain gauges were attached to the back side of the weld area to monitor crack propagation from the weld root which can be the case due to the remained crack tip in the test specimens during the crack removal process (see Fig. 7(b)). The average and range values of the measured forces, displacements and strains were digitally stored during the fatigue tests. The average values of the strain ranges were converted by the uniaxial Hook's law to determine the nominal stress range of each strain gauge and the nominal stress range from the strain gauge at the crack initiation location was used for the analysis.

In the initial stage of the fatigue tests, the range values of the strain gauges are approximately constant, straight line and the crack initiation is visible with the increase or decrease of the strain gauge range from the initial values. Increase or decrease of the values depends on the location of the strain gauges with the respect to the crack and the crack could lead to increase of tension, compression or release of the strain. Fig. 8 shows the strain ranges plots against the number of cycles of a fatigue specimen and the strain values start to deviate from its regular shapes at about 190,000 cycles which specify the fatigue crack initiation

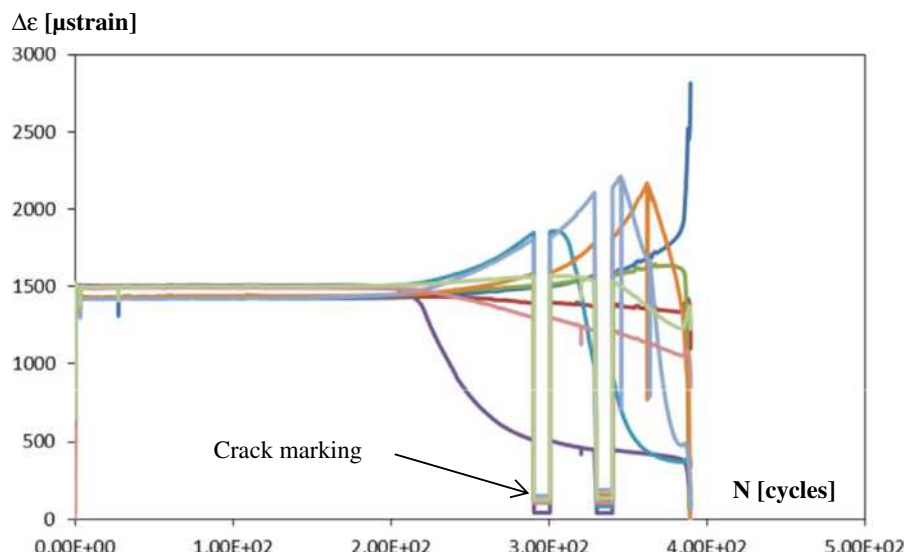


**Fig. 8.** Measured strain range versus the number of cycles.



**Fig. 9.** Beach marking on the fracture surface as result of crack marking procedure.

life of the specimen. An alarm system was used for the determination of the fatigue crack initiation life. The alarm system immediately shuts down the test rig in case of 0.0035 mm deviation in the displacement range which is the result of a decrease in the stiffness of the specimen due to the crack initiation. Thereafter, the fatigue cracks development was monitored by visual inspection.

The crack growth through the specimen thickness was monitored by the crack marking procedure. In this procedure, the lower stress level in the specimen rose to 90% of the upper stress level in the specimens while the upper level of the stress is kept identical and the test was executed for a limited number of cycles. Due to the alteration of the stress range, beach markings were created at the crack boundary and the beach marks became visible on the fracture surface after the failure of the specimens. Accordingly, the crack depth can be measured from the fracture surface and the crack size at the certain number of cycles can be specified. Fig. 9 presents the fracture surface of a specimen with the beach markings. Due to a low stress range during the crack marking procedure, the contribution of the crack marking cycles to the crack propagation is expected to be negligible and these cycles were excluded from the number of cycles at failure during the analysis.

## 7. Fatigue test results

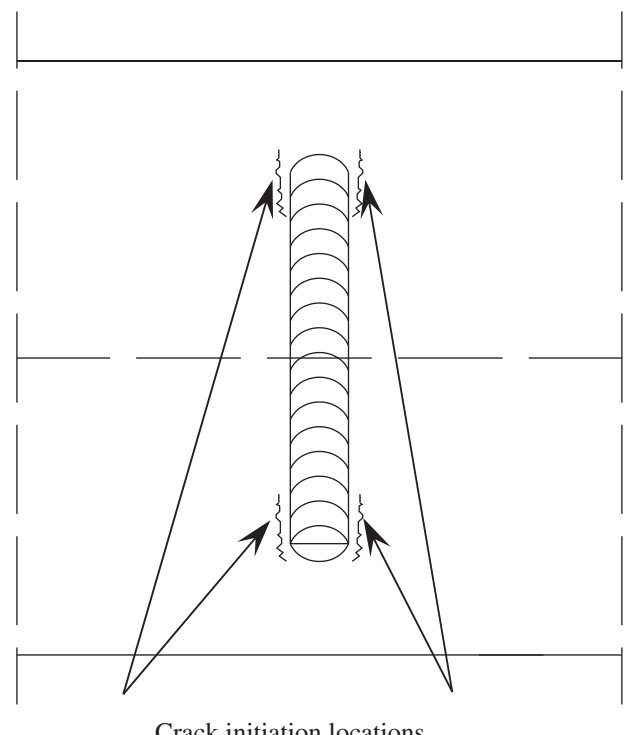
In all specimens, the crack initiation and propagation were observed at the weld toe, as expected. Although the surfaces of the start-stop points were ground to reduce stress concentration effect of these locations, the cracks were initiated at the start-stop points of the weld cap of the specimens made of S690 rolled steel plates. Fig. 10 indicates a schematic view of the fatigue crack initiation locations at the repair. After testing few specimens made of S890 steel plates, it was realised that the crack initiation also took place at the start-stop points of the repair weld. This can be explained by two features of start-stop points; high stress concentration because of the geometrical discontinuity and high residual tensile stresses. For further reduction of stress concentration effect, an additional grinding process was performed at the start-stop points of the welds to obtain a homogeneous weld shape and a smooth transition between the base material and the weld material (see Fig. 11). It was aimed to shift the crack initiation locations from the start-stop points of the weld to the middle of the weld toe. This additional grinding process resulted in a little shifting of the crack initiation points to the middle of the weld toe but not as desired. In one specimen of this series, no any crack initiation was observed after 3 million cycles and it is indicated as runout (Table 4).

Table 4 shows the applied nominal stress ranges to the specimens,  $\Delta\sigma_n$ , the number of cycles at the crack initiation,  $N_i$ , the fatigue crack propagation life,  $N_p$  and the number of cycles at failure,  $N_f$  of the specimens. In average, 45% of the fatigue life was occupied by the fatigue crack initiation life.

## 8. Evaluation of test results

The evaluation of the test results was made using the reference situation with the details presented in EN 1993-1-9 [5]. For the current specimens, it is difficult to make a comparison with a specific detail category of EN 1993-1-9 [5]. The specimens could not be assumed as base material since they contain the weld in the middle of them. In order to classify as a welded connection, the weld needs to be executed along the whole width and through the thickness of the specimens. Accordingly, the comparison was made with the detail categories of both situations; namely, the detail categories of the base material and V-shape welded connection. Fig. 12 shows the detail categories from EN 1993-1-9 [5] for the base material, V-shape welded connection and the applicable conditions of these detail categories.

The fatigue strength curves of EN 1993-1-9 [5] are categorised based on the characteristic stress range,  $\Delta\sigma_c$ , values at 2 million cycles. The characteristic stress range at 2 million cycles,  $\Delta\sigma_c$ , is calculated for a



**Fig. 10.** Schema of the crack initiation locations in the test specimens.

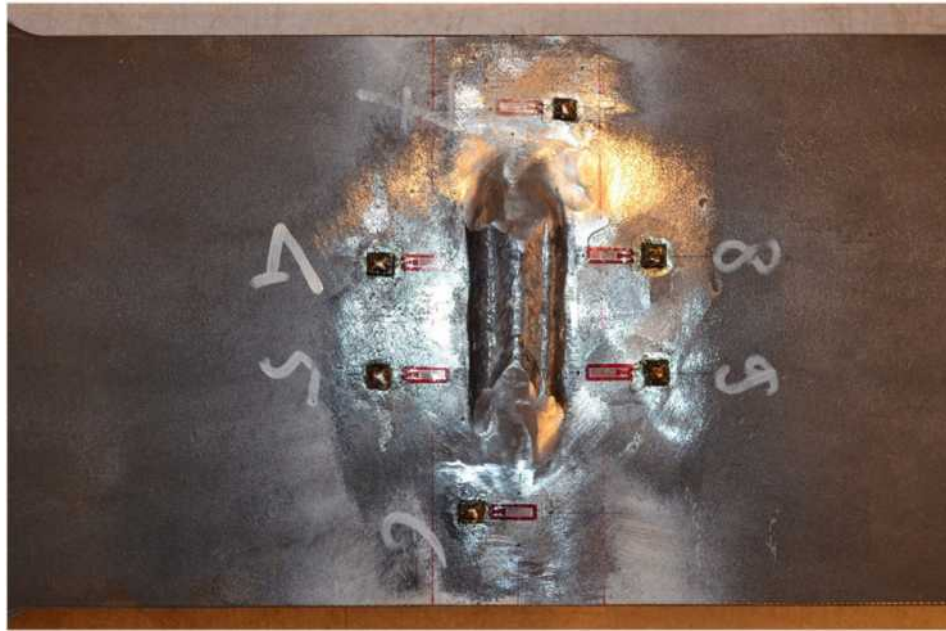


**Fig. 11.** A smooth transition between weld and base material of test specimen of BR89x series.

95% survival probability on a two-sided confidence level of 75% of the mean, parallel to the mean. Fatigue strength curve is represented by a log-log linear relationship between the nominal stress range,  $\Delta\sigma_n$  and the number of cycles up to failure,  $N_f$ .

The statistical analysis was carried out on the test data according to Brozzetti et al. [14] and this analysis procedure is also utilised for the establishing fatigue strength curves of EN 1993-1-9 [5]. The fatigue strength curves of the test data were determined for a fixed slope  $-3$  and a free slope which is calculated by the regression analysis. The fixed slope  $-3$  is recommended by Brozzetti et al. [14] for the analysis and it is also convenient for the comparison with the detail categories of EN 1993-1-9 [5] which are calculated with the fixed slope  $-3$  as well. The fatigue strength curves of the test data were determined for the mean, lower bound and upper bound of the data scatter. The lower bound curve of the data scatter was compared to the fatigue strength curves of EN 1993-1-9 [5]. The run-out test data were excluded from the calculation of the fatigue strength curves with the

fixed slope,  $-3$  and included for the calculation of the fatigue strength curves with the free (calculated) slope.

**Table 5** presents the statistical analysis results on the fatigue tests data of the repaired an artificial crack in the base material specimens made of S690 and S890.

**Fig. 13** shows the lower bound of the data scatter of BR69x series, compared to the detail category 71, 125 and 160 of EN 1993-1-9 [5]. The calculated slope,  $m = -3.05$  is very close to the fixed slope  $m = -3$  which is used for the fatigue strength curves of EN 1993-1-9 [5]. For both slopes, the determined fatigue strength of the repaired base material is very close to the values of the detail category 160 of EN 1993-1-9 [5]. With  $m = -3.05$ ,  $\Delta\sigma_{mean} = 179$  MPa,  $\Delta\sigma_c = 154$  MPa; with  $m = -3$ ,  $\Delta\sigma_{mean} = 178$  MPa,  $\Delta\sigma_c = 154$  MPa.

**Fig. 14** presents the lower bound of the data scatter of BR89x series, compared to the detail category 71, 125 and 160 of EN 1993-1-9 [5]. The calculated slope results in  $m = -5.46$  which is much smaller than  $m = -3$  the slope of the fatigue strength curves given in EN 1993-1-9 [5]. The fatigue strength curve of the test data with the fixed slope  $m = -3$  is reasonably close to the detail category 160 of EN 1993-1-9 [5]. With  $m = -5.46$ ,  $\Delta\sigma_{mean} = 225$  MPa,  $\Delta\sigma_c = 191$  MPa; with  $m = -3$ ,  $\Delta\sigma_{mean} = 173$  MPa,  $\Delta\sigma_c = 151$  MPa.

The fatigue test results of the both series fall in the same scatter range. Since the fatigue strength curves of EN 1993-1-9 [5] are independent on the yield strength of steel, the test results of both series were combined and the statistical analysis was performed on the entire test data. In this way, the amount of test data was increased to perform a more reliable statistical analysis.

**Fig. 15** shows the fatigue strength of the BR series with the lower band of the data scatter compared to the detail category 71, 125 and 160 of EN 1993-1-9 [5]. The slope according to the regression analysis

**Table 4**  
Fatigue test results of both series.

Specimen	$\Delta\sigma_n$ [MPa]	$N_i$ [cycles]	$N_p$ [cycles]	$N_r$ [cycles]	Percentage of $N_i$
BR691	253	169,423	276,599	446,022	37.99
BR692	287	248,143	252,253	500,396	49.59
BR693	257	400,383	354,425	754,808	53.04
BR694	224	578,058	381,769	959,827	60.23
BR695	307	189,479	180,001	369,480	51.28
BR696	273	208,737	217,981	426,718	48.92
BR697	298	278,974	243,503	522,477	53.29
BR698	192	861,753	1,094,883	1,956,636	44.04
BR699	290	265,024	301,861	566,885	46.75
BR891	312	131,804	166,390	298,194	44.20
BR892	257	260,297	283,195	543,492	47.89
BR893	292	193,805	218,760	412,565	46.98
BR894	309	242,539	208,949	451,488	53.72
BR895 <sup>a</sup>	308	188,651	334,304	522,955	36.07
BR896 <sup>a</sup>	307	165,550	154,271	319,821	51.76
BR897 <sup>a</sup>	236	0	3,234,243	3,234,243	run out
BR898 <sup>a</sup>	268	239,380	177,139	416,519	57.47
BR899 <sup>a</sup>	324	152,946	165,078	318,024	48.09

<sup>a</sup> Additional grinding process executed at the start-stop points of the weld cap.

**Table 5**  
Statistical analysis results on the repaired base material.

Steel type	S690	S890		
$m$	-3.05	-3	-5.46	-3
$\Delta\sigma_{mean,2-10}$	179	178	225	173
$\Delta\sigma_c$	154	154	191	151
Specimens	9	9	9	8

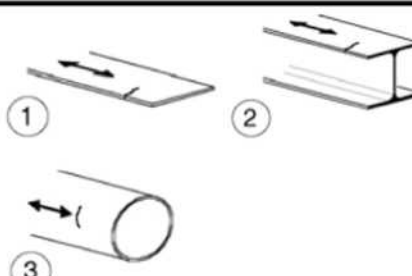
Detail category	Construction details	Description	Requirements
160		1) Plates and flats 2) Rolled sections 3) Seamless hollow sections either rectangular and circular	Sharp edges, surface and rolling flaws to be improved by grinding until removed and smooth transition achieved.
125		Material with machine gas cut edges having shallow and regular drag lines or manual gas cut material subsequently dressed to remove all edge discontinuities. Machine gas cut with cut quality according to EN 1090	Re-entrant corners to be improved by grinding (slope ≤ 1/4) or evaluated using the appropriate stress concentration factors. No repair by weld refill.
71	Size effect for t>25 mm: $k_s = (25/t)^{0.2}$	With backing strip; transverse splice 	Filled welds attaching the backing strip to terminate ≥ 10 mm from the edges of the stressed plates. Track weld inside of the shape of butt welds.

Fig. 12. Detail category of base material and V welded connection according to Table 8.1 and Table 8.3 of EN 1993-1-9 [5].

$m = -3.62$  is close to the slope,  $m = -3$  of the fatigue strength curve of EN 1993-1-9 [5]. There was one run-out specimen and it was also included in the regression analysis to determine the fatigue strength curves for the free slope. Since the slope of the fatigue strength curves of EN 1993-1-9 [5] is  $m = -3$ , an appropriate comparison between the fatigue strength curve of test data and the detail categories of EN 1993-1-9 [5] can be made for the fixed slope  $m = -3$ . The lower band of the scatter of the BR series with  $m = -3$  is laid just below the detail category 160 of EN 1993-1-9 [5] which is representing the fatigue strength of the base material without any weld. With  $m = -3.62$ ,  $\Delta\sigma_{\text{mean}} = 194 \text{ MPa}$ ,  $\Delta\sigma_c = 161 \text{ MPa}$ ; with  $m = -3$ ,  $\Delta\sigma_{\text{mean}} = 176 \text{ MPa}$ ,  $\Delta\sigma_c = 155 \text{ MPa}$ .

Pijpers et al. [15] performed fatigue tests on the base materials of S690 and S1100 steel grades and the thickness of the test specimens was 12 mm and 10 mm respectively. The specimens were tested under axial load with a tensile test rig. The fatigue test data of both series were combined and a statistical analysis performed for this data set. To establish the influence of the repair weld, the test results of BR

series were compared to the results from fatigue tests on the base material. Pusch and Hübner [16] concluded that fatigue strength curves of very high strength steels show a tendency for lower slope,  $m = -5$ . Determining the fatigue strength with fixed slope  $m = -3$  for this kind of data will cause the lower correlation between the curve and the data. Therefore, the comparison between the base material data and the repaired base material data was made according to the calculated slope from the regression analysis.

Fig. 16 presents the fatigue strength curve of the BR series with the lower band of the data scatter compared to the lower band of the data scatter of the base material tests. There is a large difference between the slopes of the curves. The slope of the fatigue strength curve of the repaired base material becomes closer to  $-3$  which is expected for fatigue strength curves of welded connections. In high cycle region, the base material shows higher fatigue strength than the fatigue strength of the repaired base material. With  $m = -3.62$ ,  $\Delta\sigma_{\text{mean}} = 194 \text{ MPa}$ ,  $\Delta\sigma_c = 161 \text{ MPa}$  for BR series; with  $m = -6.11$ ,  $\Delta\sigma_{\text{mean}} = 333 \text{ MPa}$ ,  $\Delta\sigma_c = 243 \text{ MPa}$  for the test data of the base material.

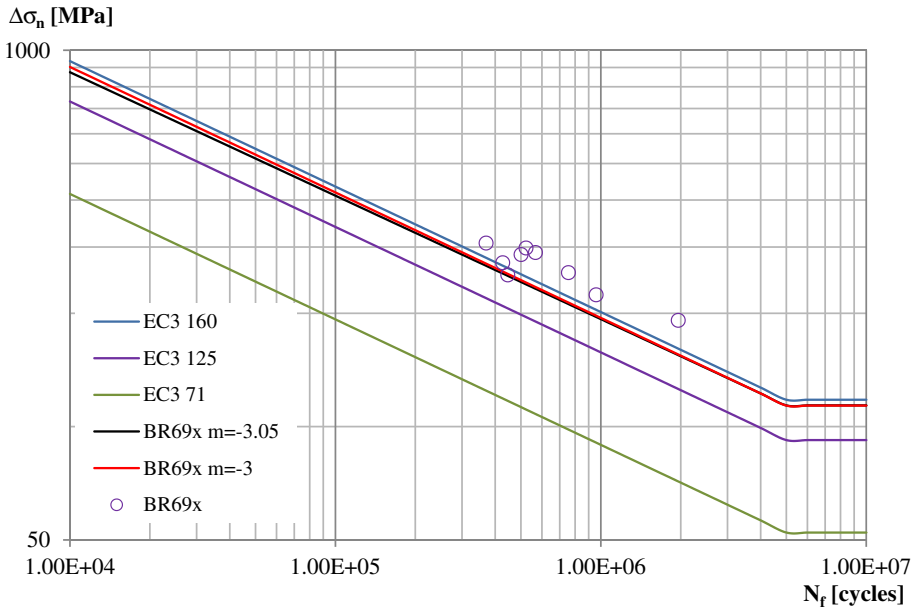


**Fig. 13.** Fatigue results of BR69x series, with the lower bound of the data scatter compared to the detail category 71,125 and 160 of EN 1993-1-9 [5].

## 9. Conclusions

In this study, artificially created crack in the base material of S690 and S890 steel plates were repaired and the repaired specimens were tested for the fatigue strength determination. The test results were compared to the detail categories of EN 1993-1-9 [5] and to the test results of the fatigue tests on the base material of S690 and S1100.

The fatigue strength of the repaired base material,  $\Delta\sigma_c = 155$  MPa, is almost equal to fatigue strength of the detail category 160 of EN 1993-1-9 [5] which represents the fatigue strength of the base material. Consequently, it can be concluded that the repair weld has limited

negative influence on the fatigue strength of the material. This can be explained as follows;

- The welding application is not executed along the whole width of the specimens. It means that the residual tensile stresses due to the welding are locally available and the residual stresses will only influence the fatigue crack initiation and propagation at the location of the weld. The non-welded ligament of the specimens can contribute to the retardation of fatigue crack propagation in the specimens.
- In design curves of EN 1993-1-9 [5], fatigue cracks in base material are indicated at the edge of the specimens while the fatigue cracks were

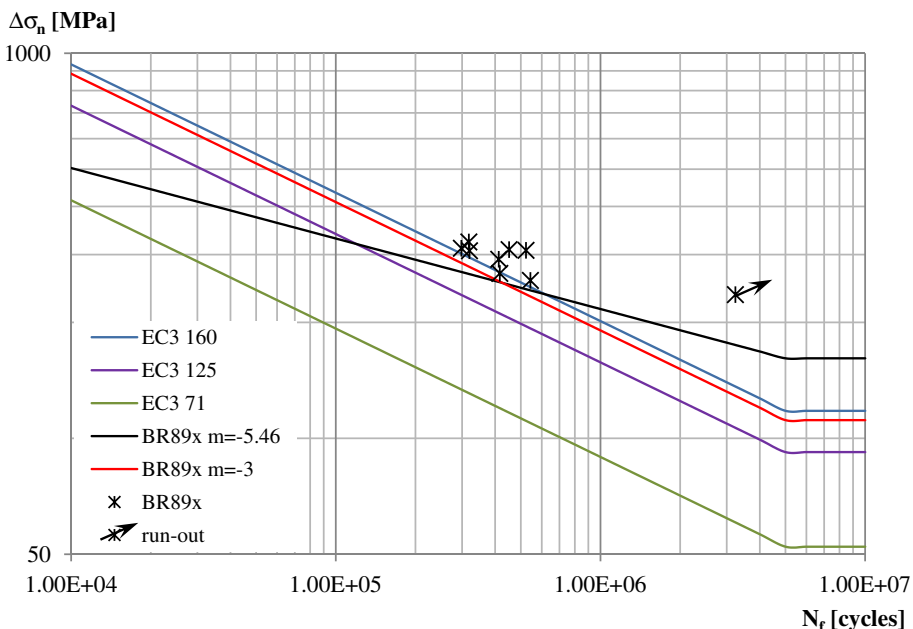


**Fig. 14.** Fatigue results of BR89x series, with the lower bound of the data scatter compared to the detail category 71,125 and 160 of EN 1993-1-9 [5].

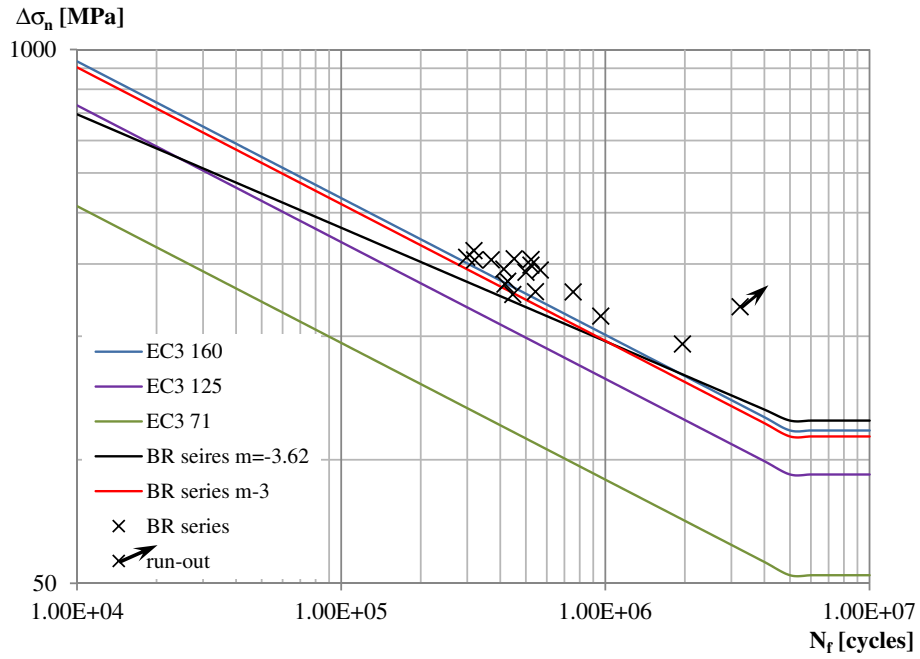


Fig. 15. Fatigue results of BR series with the lower band of the scatter compared to the detail category 71,125 and 160 of EN 1993-1-9 [5].

initiated and propagated in the middle of the current test specimens. The edge cracks have shorter fatigue crack propagation life than semi-elliptical cracks. This influence might have compensated the negative influence of the weld on fatigue strength of the base material.

- Pijpers [9] concluded that the fatigue crack initiation life in the welded connections made of very high strength steel is longer than the welded connections made of mild strength steels. This property of very high strength steels might have a contribution to such high fatigue strength of the current test specimens.

Comparison with the fatigue strength curve of the base material shows that the slope of the fatigue strength curve of the repaired specimens becomes higher than the slope of the fatigue strength curve of the base material. It confirms the commonly known phenomena that the slope of the fatigue strength curves of the base material of high strength steels decreases to  $-5$  while it increases to  $-3$  for the welded connections. The tendency of the increasing slope can be seen from the results of the repaired base material. For the high cycle regime, the characteristic fatigue strength of the base material was located at above the

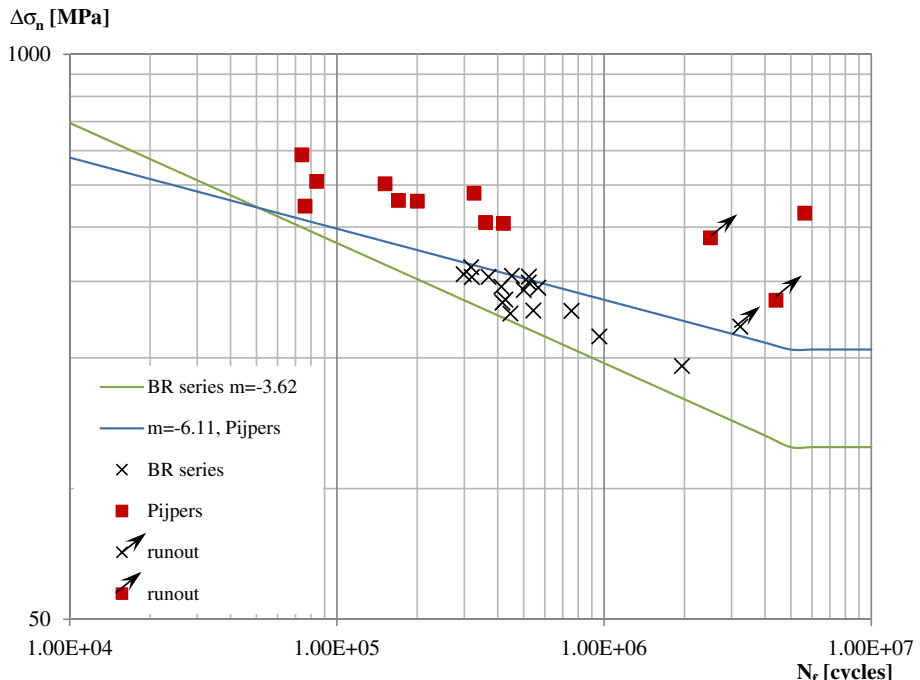


Fig. 16. Comparison between fatigue strength curve of BR series and fatigue strength curve of the base materials.

characteristic value of the repaired base material, mainly because of a large difference between the slopes of the curves.

Regarding the crack initiation and propagation phase, the crack initiation life and crack propagation life of the specimens are almost similar. Approximately, 45% of the fatigue life is occupied by the fatigue crack initiation life which is quite high compared to welded connections made of mild steels. Additional grinding on the start-stop points of some specimens BR89x series provides a little improvement for the crack initiation location. After the grinding process, the crack initiation points were shifted little in the direction of the middle of the weld.

## Acknowledgement

This research was carried out under project number M82.8.12460 in the framework of the Research Program of the Materials Innovation Institute M2i ([www.m2i.nl](http://www.m2i.nl)).

## References

- [1] T.R. Gurney, Fatigue of Welded Structures, 1979 (Cambridge, UK).
- [2] S.J. Maddox, Fatigue design rules for welded structures, *Prog. Struct. Eng. Mater.* 2 (1) (2000) 102–109.
- [3] G. Demofonti, S. Riscuifuli, C.M. Sonsino, H. Kaufmann, G. Sedlacek, C. Müller, F. Hanus, H.G. Wegmann, High strength steels in welded state for lightweight constructions under high and variable stress peaks, Final Report EUR 19989, Luxembourg, 2001.
- [4] R. Puthli, S. Herion, J. Bergers, Untersuchungen zum Ermüdungsverhalten von hochfesten Stählen im Rahmen von LIFTHIGH, *Stahlbau* 11 (75) (2006) 916–924.
- [5] EN 1993-1-9, Design of Steel Structures - General- Part 1.9: Fatigue Strength of Steel Structure, European Committee for Standardization, Brussels, 2006.
- [6] R.J.M. Pijpers, M.H. Kolstein, A. Romeijn, F.S.K. Bijlaard, Fatigue experiments on very high strength steel base material and transverse butt welds, *Adv. Steel Constr.* 5 (1) (2009) 14–22.
- [7] U. Kuhlmann, A. Dürr, H.P. Günther, Verbesserung der ermüdungsfestigkeit höherfester baustähle durch anwendung der UIT nachbehandlung, *Stahlbau* 11 (75) (2006) 930–938.
- [8] G.B. Marquis, Z. Barsoom, IIW recommendations for the HFMI treatment for improving the fatigue strength of welded joints, IIW Collection, Springer, 2016.
- [9] R. Pijpers, Fatigue strength of welded connections made of very high strength cast and rolled teels, Doctoral Dissertation, Delft University of Technology, Delft, Netherlands, 2011.
- [10] T. Yamasaki, Y. Kawai, Y. Maeda, Fatigue life of welded and bolted repair parts, *J. Struct. Eng.* 110 (1984) 2499–2512.
- [11] Y. Kudryavtsev, J. Kleiman, V. Knysh, Fatigue strength of structural elements with crack repaired by welding, International Institute of Welding, IIW Document XIII-2236-08, 2008.
- [12] EN-ISO 5817, Welding – fusion welded joints in steel, nickel, titanium and their alloys beam welding excluded-Quality levels for imperfections, ISO Copyright Office, Geneva, 2007.
- [13] Y.H. Zhang, S. Smith, L. Wei, C. Johnston, Residual stress measurements and modeling, Health and Safety Executive, RP938, Cambridge, UK, 2012.
- [14] J. Brozzetti, M.A. Hirt, I. Ryan, G. Sedlacek, I.F.C. Smith, in: Eurocode Editorial Group (Ed.), Background Information on Fatigue Design Rules - Statistical Evaluation - Chapter 9 - Document 9.01, 1989.
- [15] R.J.M. Pijpers, M.H. Kolstein, A. Romeijn, F.S.K. Bijlaard, The fatigue strength of base material and butt welds made of S690 and S1100, 5th International Conference on Advances in Steel Structures, Singapore, 2007.
- [16] G. Pusch, P. Hübner, Bruchverhalten des Stahles StE 960 und seiner Schweißverbindung bei statischer und zyklischer Belastung, Final Report, EUR 17880 DE, Luxemburg, 1994.
- [17] J. Berg, N. Stranghoener, Fatigue strength of welded ultra high strength steels improved by high frequency hammer peening, *Procedia Material Science* 3 (2014) 71–76.



# Local approaches and XFEM used to estimate life of CFRP repaired cracked welded joints under fatigue loading

Zhiyu Jie\*, Wujun Wang, Chao Chen, Kainan Wang

*Department of Civil Engineering, Ningbo University, Ningbo 315211, China*



## ARTICLE INFO

**Keywords:**

Welded joints  
CFRP  
Local approach  
XFEM  
Fatigue life assessment

## ABSTRACT

Three different local approaches, the Theory of Critical Distances (TCD), the Notch Stress Intensity Factor (NSIF) and the Strain Energy Density (SED), and the Extended Finite Element Method (XFEM) were applied to estimate the fatigue life of unrepairs and CFRP patches repaired cracked welded joints. The effects of CFRP modulus and thickness on the fatigue life of welded joints with different initial crack depths were investigated. The fatigue damage evolution equation using the loading frequency as a new damage variable was used to describe the degradation process. Fatigue life assessment results and crack growth paths compared with experimental results using these methods. The results show that the fatigue life and fatigue strength decrease as the increase of the initial crack depth. Three different fatigue failure modes can be observed from experimental results. The TCD, NSIF, and SED can reliably predict the fatigue life of welded joints without CFRP patches, but it needs to further investigate the values of estimation parameters of welded joints with CFRP patches for the NSIF and the SED. Fatigue crack growth paths and lives predicted by the XFEM and actual results are in good agreement, and the accuracy and reliability are validated by test data.

## 1. Introduction

The welding as an important connection way is widely used in steel bridges, such as cruciform joints and T joints, etc. These welded joints under cyclic loading are very easy to produce fatigue cracks in view of the stress raiser and the welding residual stress. In order to improve the fatigue performance, some effective strengthening methods are devoted to reduce the stress at the crack tips. One of the most popular approaches is that carbon fiber reinforced polymer (CFRP) with the benefits of high strength, light weight, and anti-corrosion is employed to repair the damage regions. This new repairing method can greatly enhance the fatigue life of cracked components [1–3]. In this paper, we focus on that the quantitative variation of the fatigue life for cracked welded joints strengthened by CFRP patches and the use of different fatigue assessment methods. The nominal stress and hot spot stress approaches are commonly applied to the fatigue assessment of welded structures [4]. The nominal stress approach is suitable for the design of those simple weld geometries and loading conditions based on the reference S-N curves. The hot spot stress approach is more appropriate for complex welded structures when the nominal stress is not easy to determine. However, for cracked welded joints retrofitted with CFRP patches, these two methods are not able to charac-

terize the stress field and directly assess the fatigue life. Therefore, local approaches mainly including the Theory of Critical Distances (TCD) [5], the Notch Stress Intensity Factor (NSIF) [6], and the Strain Energy Density (SED) [7] are proposed for the fatigue assessment.

Recently, many researchers apply the TCD to the fatigue evaluation of notched components. This method considers the effect of stress concentrations and loading types via a simple finite element analysis. It avoids the S-N curve classification and requires less computational effort. Zhou et al. [8] predicted the fatigue crack initiation life of cope hole details in orthotropic steel deck via the TCD, and it agreed excellent with experimental values. Nie et al. [9] assessed the fatigue limits of notched components by using the TCD in very high cycle regime. Jie and Susmel [10] reanalyzed the literature data of corroded high strength steel wires and evaluated the fatigue life via the TCD. Besides, the use of the TCD has been extended to welded joints [11–13]. Karakas et al. [12] utilized the TCD to estimate the fatigue behavior of magnesium welded joints with different weld geometries and stress ratios. Baumgartner et al. [14] estimated the fatigue strength of TIG-dressed joints via the TCD, and fatigue details and critical distances were suggested. Al Zamzami et al. [15] assessed the fatigue strength of inclined steel joints in combination with the TCD and the Modified Wöhler Curve Method (MWCM). Gorouhi [16] investigated the fatigue

\* Corresponding author.

E-mail address: [jiezhiyu@nbu.edu.cn](mailto:jiezhiyu@nbu.edu.cn) (Z. Jie).

## Nomenclature

TCD	the Theory of Critical Distances	$a_i$	the extra degree of freedom to model the jump across crack faces
NSIF	The Notch Stress Intensity Factor	$H(x)$	the jump function
SED	the Strain Energy Density	$F_a(x)$	the enrich function
XFEM	the Extended Finite Element Method	$b_i^a$	the added degree of freedom associated with $F_a(x)$
$\Delta\sigma_{\text{eff}}$	effective stress range	$x$	an arbitrary point near the crack face
$\Delta\sigma_1$	the maximum principal stress range	$x^*$	the closest point to $x$ located on the crack face
$r, \theta$	the local polar coordinate	$t, s$	the local coordinate at the crack tip
$L$	the critical distance	$C, m$	fatigue crack growth material parameters
$L_T$	the threshold critical distance	$a, a_i$	the crack depth and the initial crack depth
$\Delta K_{\text{th}}$	the threshold stress intensity factor range	$\Delta K$	the stress intensity factor range
$\Delta\sigma_A$	the fatigue limit of a plain specimen	$c_3, c_4$	material parameters based on the energy release rate
$N$	fatigue life	$\Delta G$	the energy release rate range
$A, B$	parameters related materials and stress ratios	$G_{\text{thresh}}, G_{\text{pl}}$	the threshold value and the upper limit value of energy release rate, respectively
$L_s$	the critical distance under static loading	$c_1, c_2$	material parameters of fatigue crack initiation
$K_{\text{Ic}}$	the fracture toughness	$\Delta K_{\text{I}}, \Delta K_{\text{II}}, \Delta K_{\text{III}}$	mode I, II, and III stress intensity factors
$\sigma_b$	the tensile strength	$P_{\max}, P_{\min}$	fatigue loading with the maximum and minimum values, respectively
$\sigma_s$	the strength under static loading	$t$	adhesive thickness
$m$	the negative inverse slope for the S-N curve	$D$	the damage variable
$\sigma_{\theta\theta}, \tau_{r\theta}$	stress components	$f$	the loading frequency
$\lambda_1, \lambda_2$	Williams' eigenvalues	$f_0, f_f$	are initial and final values of loading frequencies, respectively
$2\alpha$	the notch opening angle	$\sigma_m, \Delta\sigma, n, N$	the mean stress, stress range, fatigue cycles, and fatigue life
$K_1, K_2$	Mode I and II NSIFs	$\alpha, \beta, b, M_0$	fatigue damage material parameters determined by test data
$\Delta K_1, \Delta K_2$	Mode I and II NSIF ranges		
$C_1, p$	material parameters determined by the $\Delta K_1$ - $N$ curve		
$\Delta W$	the elastic averaged SED range		
$R_0$	the control volume radius		
$e_1, e_2$	shape functions depending on $2\alpha$ and Poisson's ratio $\nu$		
$V, E$	Poisson's ratio and elastic modulus		
$\Delta K_{1A}$	the reference value of the NSIF range of notched members		
$N_i$	the shape function		
$u_i$	the degree of freedom		

performance of riveted bridge details by using both the TCD and the S-N curve method. Fang et al. [17] employed the TCD to the fatigue assessment of a welded beam-to-column connection by the finite element analysis.

The NSIF approach is successfully proposed to the fatigue strength estimation of welded joints [18,19]. This method is based on William's solutions for V-notches with a zero radius. The use of NSIF generally required a very fine mesh, but Meneghetti et al. [20–22] tried to use coarse meshes to rapidly calculate it. Due to the fatigue assessment needing different curves for different opening angles, Lazzarin and Zambardi [23] applied the SED averaged over a control volume depending on different materials to the fatigue evaluation. The main benefits of the SED did not rely upon the opening angle and only needed a very coarse mesh for the finite element simulation [24]. Berto et al. [25,26] analyzed the fatigue estimation of different types of welded joints by the SED, and all the results were within the scatter band. Song et al. [27,28] extended the range of previous analytical solutions to estimate the averaged SED both at the weld toe and root in load-carrying cruciform welded joints and predicted different failure modes. Foti et al. [29] investigated the effects of geometrical parameters on the fatigue strength of different welded details using the SED and compared with Eurocode 3, but it resulted in a non-conservative estimation according to Eurocode 3. Luo et al. [30] studied the accuracy and feasibility of the SED used to the fatigue estimation of rib-to-deck welded joints in orthotropic steel deck, and the effect of the weld geometry on the fatigue strength was performed. Fischer et al. [31] reviewed the NSIF and SED approaches considering misalignment effects.

These local approaches cannot consider the crack propagation behavior, and fatigue assessment parameters are relatively single.

Comparing to traditional linear elastic fracture mechanics, the Extended Finite Element Method (XFEM) is another useful approach to study the crack growth and life prediction. There is no need to remesh for the crack growth simulation and define the crack tip with singular elements. Kraedegh [32] considered the effect of crack growth on the fatigue life of unstiffened and stiffened structures via the XFEM. Bergara et al. [33] validated the accuracy of the XFEM by simulating the fatigue crack propagation for a semielliptical crack in a beam under four-point bending. Nikfam et al. [34] reported that the XFEM was used to simulate the fatigue crack growth of welded T-joints, and prediction results agreed well with experiments. Wang et al. [35] investigated the fatigue crack propagation behavior in steel bridge web gaps, and multi-scale numerical analysis models were established using fracture mechanics and the XFEM. Other scholars focused on the use of the XFEM to crack propagation of components retrofitted by composite materials. Zarrinzadeh et al. [36] employed the XFEM to model fatigue crack growth of a cylindrical cracked aluminium pipe repaired with glass/epoxy composite patch. Valadi et al. [37] used the XFEM to investigate crack propagation of thin-walled steel pipes strengthened by fiber reinforced polymer composite. Lesiuk et al. [38] adopted the XFEM to analyze the fracture behavior of fiber-reinforced polymer reinforced beams.

According to the aforementioned analysis, there are few studies on the fatigue assessment of CFRP patches strengthening cracked welded joints by using the TCD, the NSIF, the SED, and the XFEM. In this paper, these methods are used to evaluate the fatigue life of unretrofitted and CFRP patches retrofitted cracked welded joints. Different CFRP modulus and thickness are constructed to investigate their effects on the fatigue life of welded joints with different crack depth based on fatigue tests and numerical simulations. The information

on fatigue life versus stress range is obtained, and different fatigue failure modes can be observed. The fatigue damage evolution equation using the loading frequency as a new damage variable is determined. Finite element analyses are performed using the software ABAQUS. Fatigue life predictions using the TCD, the NSIF, the SED, and the XFEM compare with experimental results. Fatigue crack propagation paths of welded joints retrofitted without and with CFRP patches are predicted by the XFEM. A comparison between simulation paths and actual paths is made. Finally, the accuracy and reliability of local approaches and the XFEM are validated.

## 2. Theoretical knowledge

### 2.1. Local approaches

#### 2.1.1. Theory of critical Distances (TCD)

The TCD assumes that an effective stress range  $\Delta\sigma_{\text{eff}}$  is adopted to conduct the fatigue assessment of notched specimens. First, a critical distance as a material property value can be obtained from standard experiments at the same conditions. Then, the TCD is characterized in three forms: the point method (PM), the line method (LM), and the area method (AM), as shown in Fig. 1 [39]. The PM assumes that  $\Delta\sigma_{\text{eff}}$  is calculated at a certain distance from the maximum principal stress point (Fig. 1b). The LM postulates that  $\Delta\sigma_{\text{eff}}$  is assessed by the maximum principal stress averaged over a line (Fig. 1c). The AM supposes that  $\Delta\sigma_{\text{eff}}$  is determined by the maximum principal stress averaged over an area (Fig. 1d). Thus, the effective stress ranges based on the PM, the LM, and the AM can be expressed as, respectively:

$$\Delta\sigma_{\text{eff}} = \Delta\sigma_1 \left( \theta = 0, r = \frac{L}{2} \right) \quad (\text{Point Method}) \quad (1)$$

$$\Delta\sigma_{\text{eff}} = \frac{1}{2L} \int_0^{2L} \Delta\sigma_1(\theta = 0, r) \cdot dr \quad (\text{Line Method}) \quad (2)$$

$$\Delta\sigma_{\text{eff}} = \frac{4}{\pi L^2} \int_0^{\pi/2} \int_0^L \Delta\sigma_1(\theta, r) \cdot r \cdot dr \cdot d\theta \quad (\text{Area Method}) \quad (3)$$

where  $\Delta\sigma_1$  is the maximum principal stress range,  $r$  and  $\theta$  are the local polar coordinate, and  $L$  is the critical distance.

In Eqs. (1)–(3), the critical distance  $L_T$  can be obtained by the threshold stress intensity factor range  $\Delta K_{\text{th}}$  and the fatigue limit of a plain specimen  $\Delta\sigma_A$  as follows [40]:

$$L_T = \frac{1}{\pi} \left( \frac{\Delta K_{\text{th}}}{\Delta\sigma_A} \right)^2 \quad (4)$$

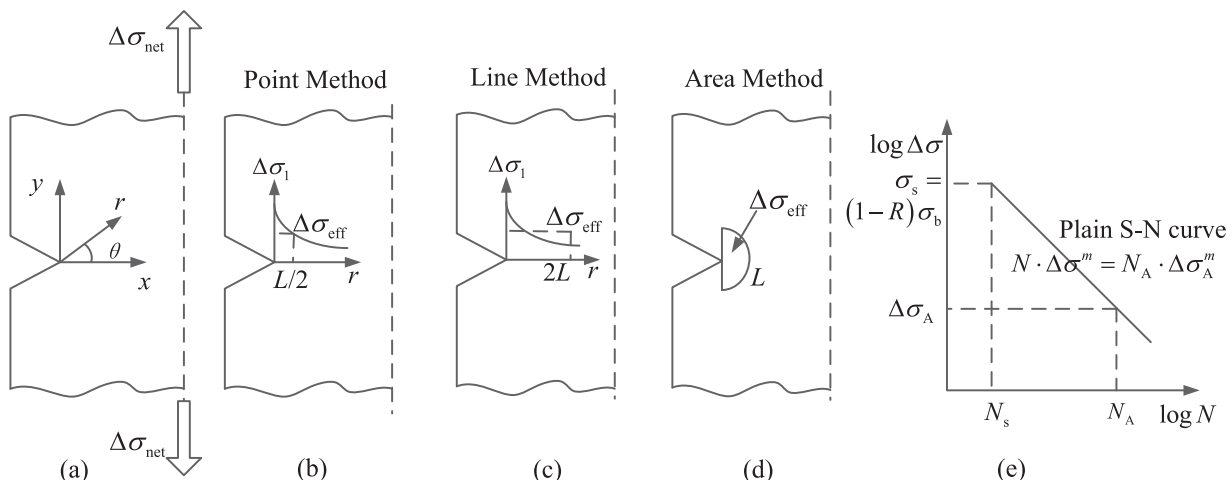


**Fig. 1.** Local coordinate system (a); the Point Method (b); the Line Method (c); the Area Method (d); plain S-N curve (e).

The values of  $\Delta K_{\text{th}}$  and  $\Delta\sigma_A$  should be determined via fatigue tests under the same loading conditions.

The linear-elastic TCD has been successfully to predict the fatigue life of notched specimens in the medium and high-cycle fatigue region. The critical distance  $L$  as a function of the fatigue life  $N$  can be expressed as the following equation [41]:

$$L(N) = A \cdot N^B \quad \text{for } N \leq 5 \times 10^6 \text{ cycles} \quad (5)$$

where  $A$  and  $B$  related to materials and stress ratios are determined by fatigue tests. The critical distance under static loading  $L_s$  is expressed as follows:

$$L_s = \frac{1}{\pi} \left( \frac{K_{\text{lc}}}{\sigma_b} \right)^2 \quad (6)$$

where  $K_{\text{lc}}$  is the fracture toughness, and  $\sigma_b$  is the tensile strength. According to Fig. 1e and Eqs. (4) and (6), parameters  $A$  and  $B$  can be calculated by the following equations:

$$L_T(N_A) = A \cdot N_A^B = \frac{1}{\pi} \left( \frac{\Delta K_{\text{th}}}{\Delta\sigma_A} \right)^2 \quad (7)$$

$$L_s \left( N_s = \frac{N_A \cdot \Delta\sigma_A^m}{\sigma_s^m} \right) = A \cdot N_s^B = \frac{1}{\pi} \left( \frac{\Delta K_{\text{lc}}}{\sigma_b} \right)^2 \quad (8)$$

where  $\sigma_s$  is the strength under static loading at  $N_s$  cycles,  $m$  and  $\Delta\sigma_A$  are the negative inverse slope and the reference stress range of plain specimens at  $N_A$  cycles, respectively. If an initial value of the fatigue life  $N_i$  is assumed, the corresponding critical distance can be obtained:

$$L(N_i) = A \cdot N_i^B \quad (9)$$

The effective stress range  $\Delta\sigma_{\text{eff}}$  is determined by the numerical analysis. According to the S-N curve of the plain specimens,  $\Delta\sigma_{\text{eff}}$  is used to recalculate the fatigue life  $N_j$  as follows:

$$N_j = N_A \left( \frac{\Delta\sigma_A}{\Delta\sigma_{\text{eff}}} \right)^m \quad (10)$$

If  $N_j$  is different from the initial value  $N_i$ , then the whole calculation had to be carried out again by imposing  $N_i = N_j$  until convergence.

#### 2.1.2. Notch stress intensity factor (NSIF)

A considerable research effort focuses on the use of the NSIF approach to fatigue assessment for notched components. According to Ref. [19], mode I and II NSIFs are defined as the following:

$$K_1 = \sqrt{2\pi} \lim_{r \rightarrow 0^+} r^{1-\lambda_1} \sigma_{\theta\theta}(r, \theta = 0) \quad (11)$$

$$K_2 = \sqrt{2\pi} \lim_{r \rightarrow 0^+} r^{1-\lambda_2} \tau_{r\theta}(r, \theta = 0) \quad (12)$$

where  $\sigma_{\theta\theta}$  and  $\tau_{r\theta}$  are stress components,  $\lambda_1$  and  $\lambda_2$  are Williams' eigenvalues related to the notch opening angle  $2\alpha$ , and  $K_1$  and  $K_2$  are Mode I and II NSIFs, respectively. For the same opening angle, the relationship between NSIF range and fatigue life can be written as:

$$\Delta K_1^p \cdot N = C_1 \quad \text{for } N \leq 5 \times 10^6 \text{ cycles} \quad (13)$$

where  $\Delta K_1$  is the Mode I NSIF rang,  $C_1$  and  $p$  are material parameters determined by the  $\Delta K_1 - N$  curve.

### 2.1.3. Strain energy density (SED)

The elastic averaged SED range over a defined volume embracing a sharp notch tip is expressed as [23]:

$$\bar{\Delta W} = \frac{1}{E} \left[ e_1 \cdot \frac{\Delta K_1^2}{R_0^{2(1-\lambda_1)}} + e_2 \cdot \frac{\Delta K_2^2}{R_0^{2(1-\lambda_2)}} \right] \quad (14)$$

where  $\Delta K_2$  is the Mode II NSIF rang,  $R_0$  is the control volume radius, and  $e_1$  and  $e_2$  are shape functions depending on  $2\alpha$  and Poisson's ratio  $\nu$ . The rapid calculation equations for  $e_1$  and  $e_2$  are expressed as the following ( $\nu = 0.3$ ):

$$e_1 = -5.373 \times 10^{-6} (2\alpha)^2 + 6.151 \times 10^{-4} (2\alpha) + 0.1330 \quad (15)$$

$$e_2 = 4.809 \times 10^{-6} (2\alpha)^2 - 2.346 \times 10^{-4} (2\alpha) + 0.3400 \quad (16)$$

According to Eq. (14), the control radius  $R_0$  can be expressed as the following under mode I loading [23]:

$$R_0 = \left( \frac{\sqrt{2}e_1 \Delta K_{1A}}{\Delta \sigma_A} \right)^{\frac{1}{1-\lambda_1}} \quad (17)$$

where  $\Delta K_{1A}$  is the reference value of the NSIF range of notched members. Ref. [42] suggests that the control radius  $R_0$  is 0.28 mm for steel welded joints. The SED range as a function of the fatigue life takes on the following form:

$$\bar{\Delta W}^q \cdot N = C_2 \quad \text{for } N \leq 5 \times 10^6 \text{ cycles} \quad (18)$$

where  $C_2$  and  $q$  are material parameters determined by the  $\bar{\Delta W} - N$  curve.

## 2.2. Extended finite element method (XFEM)

Comparing to the traditional finite element analysis, the XFEM employs additional enrichment functions to describe the crack discontinuity. A near-tip asymptotic field function is used to deal with the crack tip singularity. A Heaviside discontinuous function is utilized to simulate the jump in the displacement field across crack faces. The displacement field considering the existence of a crack is given as follows [43]:

$$u = \sum_{i=1}^m N_i(x) \left[ u_i + H(x)a_i + \sum_{\alpha=1}^4 F_\alpha(x)b_i^\alpha \right] \quad (19)$$

where  $N_i$  is the shape function,  $u_i$  is the degree of freedom,  $a_i$  is the extra degree of freedom to model the jump across crack faces,  $H(x)$  is the jump function,  $F_\alpha(x)$  is the enrich function, and  $b_i^\alpha$  is the added degree of freedom associated with  $F_\alpha(x)$ . The jump function can be written as the following:

$$H(x) = \begin{cases} 1 & \text{if } (x - x^*)n \geq 0 \\ -1 & \text{otherwise} \end{cases} \quad (20)$$

where  $x$  is an arbitrary point near the crack face,  $x^*$  is the closest point to  $x$  located on the crack face, and  $t$  and  $s$  are the local coordinate

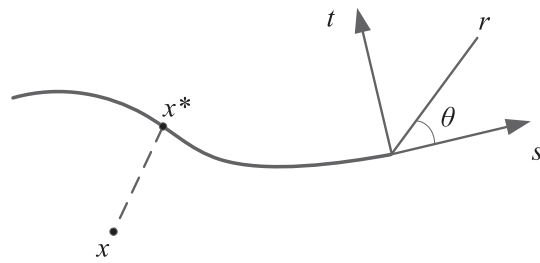


Fig. 2. Definition of  $x$  and  $x^*$  points. [44]

at the crack tip (Fig. 2). The crack tip enrichment function is taken as follows:

$$F_\alpha(x) = \left[ \sqrt{r} \sin\left(\frac{\theta}{2}\right), \sqrt{r} \cos\left(\frac{\theta}{2}\right), \sqrt{r} \sin(\theta) \sin\left(\frac{\theta}{2}\right), \sqrt{r} \sin(\theta) \cos\left(\frac{\theta}{2}\right) \right] \quad (21)$$

The energy release rate at the crack tip is employed for the fatigue analysis in ABAQUS software. The fatigue crack growth life is calculated using the Paris equation, which is presented as follows:

$$\frac{da}{dN} = C \cdot \Delta K^m \quad (22)$$

where  $C$  and  $m$  are fatigue crack growth material parameters,  $a$  is the crack depth, and  $\Delta K$  is the stress intensity factor range. When  $G_{\text{thresh}} < \Delta G < G_{\text{pl}}$ , Eq. (22) in the form of the energy release rate is rewritten as:

$$\frac{da}{dN} = c_3 \cdot \Delta G^{c_4} \quad (23)$$

where  $c_3$  and  $c_4$  are material parameters based on the energy release rate,  $\Delta G$  is the energy release rate range,  $G_{\text{thresh}}$  and  $G_{\text{pl}}$  are the threshold value and the upper limit value of the energy release rate, respectively. The initiation criterion of fatigue crack growth is given as:

$$f = \frac{N}{c_1 \Delta G^{c_2}} \geq 1 \quad (24)$$

where  $c_1$  and  $c_2$  are material parameters of the fatigue crack initiation. Due to the ABAQUS software only taking  $\Delta G$  to investigate the fatigue crack growth, the relationship between  $\Delta G$  and  $\Delta K$  can be written as follows for plane strain conditions:

$$\Delta G = \frac{1 - \nu^2}{E} (\Delta K_I^2 + \Delta K_{II}^2) + \frac{1 + \nu}{E} \Delta K_{III}^2 \quad (25)$$

where  $\Delta K_I$ ,  $\Delta K_{II}$ , and  $\Delta K_{III}$  are mode I, II, and III stress intensity factor ranges.

## 3. Experimental program

### 3.1. Configuration of specimens

Cruciform welded joints were fabricated by using Q345qC steel plate [45]. The formation of welds used carbon dioxide gas shielded welding technology. In order to simulate the actual fatigue cracking, an artificial initial crack through the plate width at the weld toe was manufactured. The configuration of cracked cruciform joints is illustrated in Fig. 3. The full penetration weld was an isosceles right triangle with 8 mm sides. The curvature radius at weld toe was assumed to be zero. The numerical analysis did not consider the influence of very small misalignments. Fig. 4 plots the repairing situations of CFRP patches. The adhesive layer between steel plate and CFRP patches adopted epoxy resin. Fatigue loading conditions of cruciform joints with three different initial crack depths unstrengthened and strengthened by three different CFRP patches are shown in Table 1. All speci-

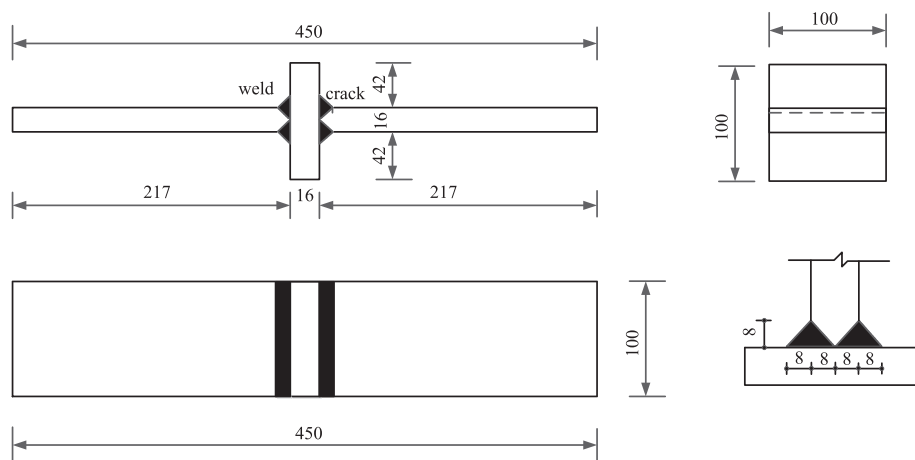


**Fig. 3.** Configuration of a cracked cruciform joint.

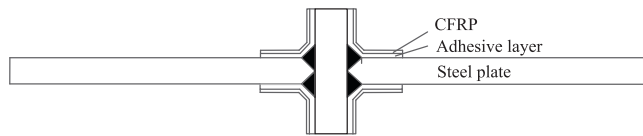


**Fig. 4.** CFRP patches repairing situation.

mens in as-welded are tested subjected to constant amplitude tensile fatigue loading with the maximum and minimum values of  $P_{\max} = 248.9$  kN and  $P_{\min} = 24.9$  kN, respectively, as shown in Fig. 5. These loads were applied at the gross section of the long plate end, and the loading frequency was about 120 Hz. The applied stress has been checked by strain gauges in order to ensure the accuracy of fatigue loading.

### 3.2. Test results

The fatigue life is generally defined when the initial crack depth reaches half the plate thickness [46]. The relationship of nominal stress range versus fatigue life for cracked cruciform joints is shown in Fig. 6. It can be seen that CFRP retrofiting can improve the fatigue life, and the maximum increase in the fatigue life for welded joints strengthened with CFRP patches reaches to 66%. For repairing specimens, fatigue strengths increase from FAT50 (a stress range of 50 MPa at 2 million cycles with a survival probability of  $P_s = 97.7\%$ ), FAT40, and FAT36 to FAT63, FAT50, and FAT40 for  $a_i = 1$  mm, 2 mm, and 3 mm, respectively. When  $a_i = 3$  mm, the fatigue strength is only about one half of undamaged cruciform joints at 2

million cycles. The remaining fatigue life and fatigue strength decrease as the increase of initial crack depth. The strengthening effect for the same CFRP patches is more discrete. The possible reasons are that (1) if the interface between steel plate and CFRP is not smooth, it will affect the reinforcement effect; (2) there are about 5–10% errors in the initial crack manufacturing process.

It can observe three fatigue failure modes for all the specimens: (a) fatigue failure at initial pre-cracks or accompanying the destruction of the adhesive layer, (b) fatigue failure at welds, and (c) fatigue failure both at initial cracks and welds, as shown in Fig. 7. It may occasionally produce the destruction of the adhesive layer when fatigue crack enters the rapid growth stage. The main reason is that the cross-sectional area decreases as the increase of the crack depth, and the adhesive layer and CFRP are subjected to higher stresses. In the fatigue life estimation analysis, it is assumed that there is a good bonding performance between CFRP and steel plate, not considering the effect of adhesive layer debonding. Only a few specimens fail at welds or both at initial cracks and welds. The poor weld quality and the fabrication error may result in these phenomena.

### 3.3. Fatigue damage evolution

Fatigue damage is a continuous degradation process for materials under external loads. Damage variables are used to reflect the decrease in material stiffness. So far, a variety of methods for defining and measuring damage variables have been proposed. Different damage variables have different measurement methods, which are divided into the direct measurement and the indirect measurement. The cross-sectional area is usually used as the direct measurement damage vari-

**Table 1**  
Types and fatigue loading conditions of specimens.

Initial Crack depth $a_i$	Specimen Number	CFRP type	Nominal Stress range (MPa)	Stress ratio	$P_{\max}$ (kN)	$P_{\min}$ (kN)
1 mm	D1C0	Without CFRP	140	0.1	248.9	24.9
	D1C1	$E = 2.4 \times 10^5$ MPa, $t = 0.167$ mm				
	D1C2	$E = 1.8 \times 10^5$ MPa, $t = 0.111$ mm				
	D1C3	$E = 2.4 \times 10^5$ MPa, $t = 0.111$ mm				
2 mm	D2C0	Without CFRP	140	0.1	248.9	24.9
	D2C1	$E = 2.4 \times 10^5$ MPa, $t = 0.167$ mm				
	D2C2	$E = 1.8 \times 10^5$ MPa, $t = 0.111$ mm				
	D2C3	$E = 2.4 \times 10^5$ MPa, $t = 0.111$ mm				
3 mm	D3C0	Without CFRP	140	0.1	248.9	24.9
	D3C1	$E = 2.4 \times 10^5$ MPa, $t = 0.167$ mm				
	D3C2	$E = 1.8 \times 10^5$ MPa, $t = 0.111$ mm				
	D3C3	$E = 2.4 \times 10^5$ MPa, $t = 0.111$ mm				

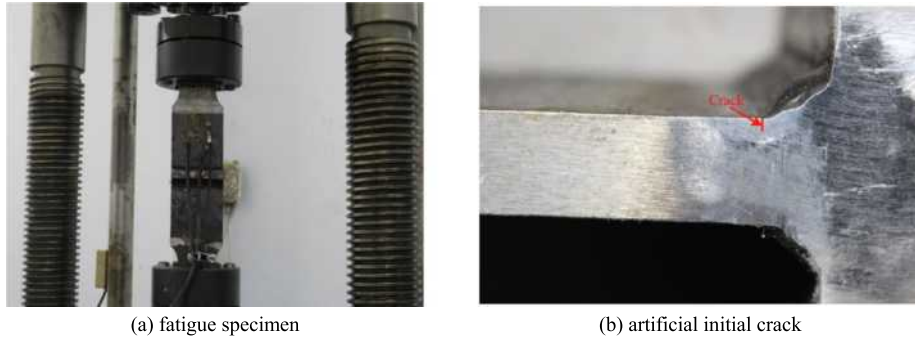


Fig. 5. Fatigue test.

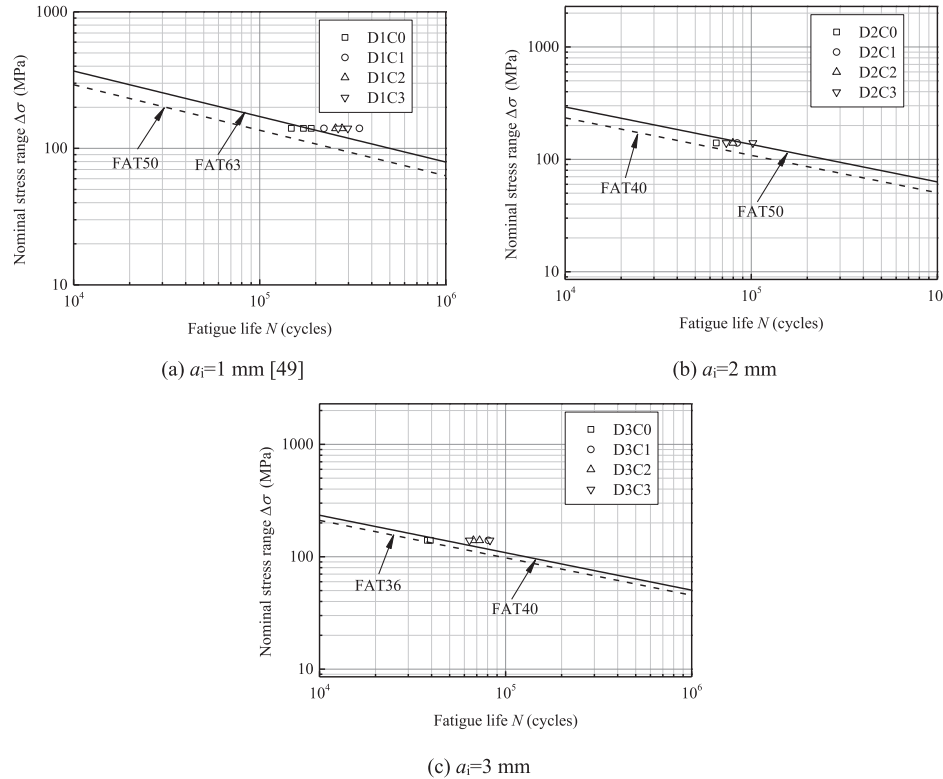


Fig. 6. The relationship of nominal stress range versus fatigue life.

able, but it is difficult to operate in actual conditions. Therefore, it is necessary to use the indirect measurement damage variable. There are many damage variables measured indirectly, such as the elastic modulus, the electric potential (the cross section and the electric resistance changing with the crack growth), and the stress range. It is found that the loading frequency varies with the fatigue crack propagation during the fatigue process. It means that the loading frequency correlates with fatigue damage. Thus, the loading frequency is used to reflect the degradation of the stiffness. The loading frequency decreases with an increase of crack depth due to the cross section not resisting external fatigue loads. The damage variable  $D$  is defined as:

$$D = 1 - \frac{f - f_f}{f_0 - f_f} \quad (26)$$

where  $f$  is the loading frequency,  $f_0$  and  $f_f$  are initial and final values of loading frequencies, respectively.

A nonlinear cumulative fatigue damage model has been proposed to characterize the degradation of materials, and the expression is given as [48]:

$$\frac{dD}{dn} = \left[ 1 - (1 - D)^{1+\beta} \right]^\alpha \left[ \frac{\Delta\sigma}{M_0(1 - b\sigma_m)(1 - D)} \right]^\beta \quad (27)$$

where  $\sigma_m$  is the mean stress,  $n$  is the loading cycles, and  $\alpha$ ,  $\beta$ ,  $b$ , and  $M_0$  are the fatigue damage material parameters determined by test data. Integrating from  $D = 0$  to 1, Eq. (27) gives the relationship between  $N$  and  $\Delta\sigma$ :

$$N = \frac{1}{1 - \alpha} \frac{1}{1 + \beta} \left[ \frac{M_0(1 - b\sigma_m)}{\Delta\sigma} \right]^\beta \quad (28)$$

The damage variable  $D$  is rewritten as the form of  $n/N$ :

$$D = 1 - \left[ 1 - \left( \frac{n}{N} \right)^{1/(1-\alpha)} \right]^{1/(1-\beta)} \quad (29)$$

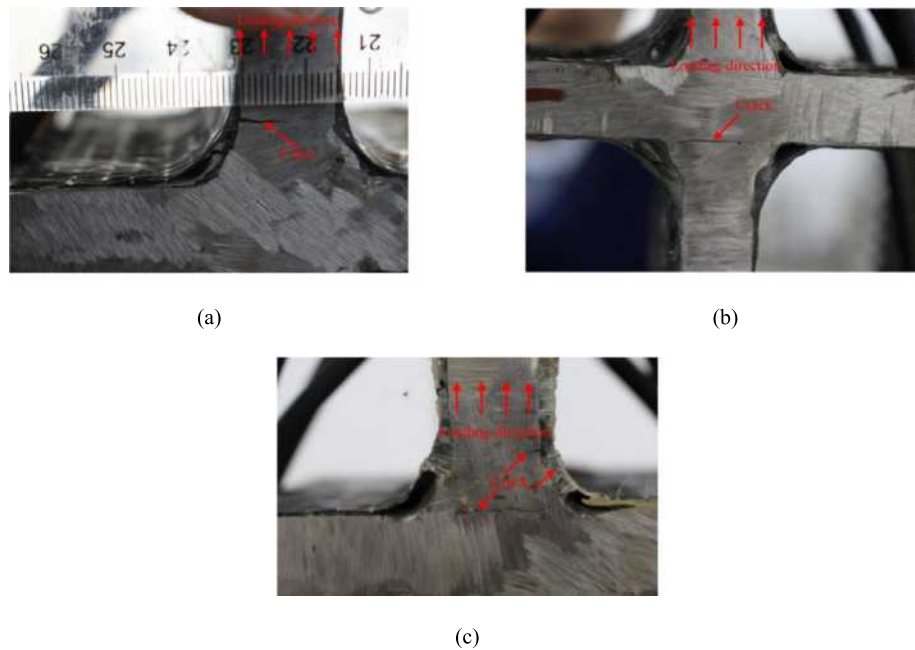


**Fig. 7.** Fatigue failure modes.

According to loading frequency results, damage variables for unpaired and CFRP repaired specimens can be determined by Eq. (26). The relationship between  $D$  and  $n/N$  is plotted in Fig. 8. Then, Eq. (29) is applied to fit these test data via the least squares method, and the regression equations for cruciform joints without and with CFRP patches are expressed as:

$$D_0 = 1 - \left[ 1 - \left( \frac{n}{N} \right)^{5.6497} \right]^{0.5201} \quad \text{C0} \quad (30)$$

$$D_1 = 1 - \left[ 1 - \left( \frac{n}{N} \right)^{14.2248} \right]^{0.4405} \quad \text{C1} \quad (31)$$

$$D_2 = 1 - \left[ 1 - \left( \frac{n}{N} \right)^{8.7566} \right]^{0.5968} \quad \text{C2} \quad (32)$$

$$D_3 = 1 - \left[ 1 - \left( \frac{n}{N} \right)^{8.9847} \right]^{0.5551} \quad \text{C3} \quad (33)$$

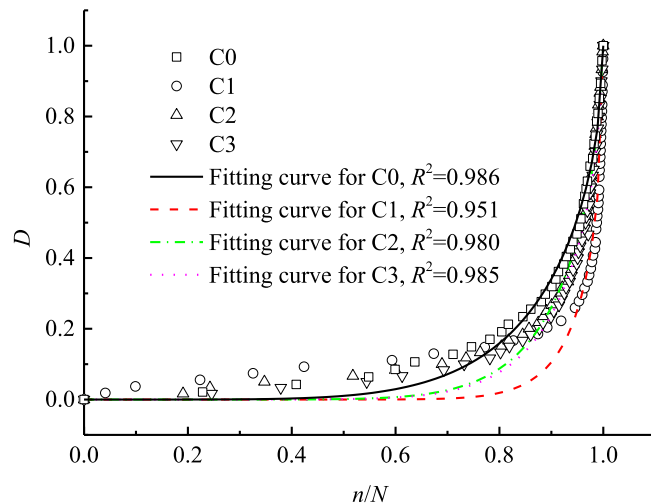


**Fig. 8.**  $D$  versus  $n/N$  based on the Chaboche model.

It is evident that the Chaboche model can be effective to simulate the fatigue damage degradation due to the good correlation. CFRP patches can effectively delay the fatigue damage degradation process. When  $n/N$  is equal to 0.8, welded joints are in the rapid growth stage. Thus, the loading frequency is an important parameter to indirectly reflect the fatigue crack propagation. It is beneficial for understanding the fatigue crack initiation and growth mechanism.

#### 4. Fatigue life estimation

##### 4.1. Local approaches

###### 4.1.1. TCD

An 8-node plane strain element (CPE8) was used to model the steel plate, the adhesive layer, and CFRP patches by using ABAQUS. A finite element model of a cracked welded joint with CFRP patches is plotted in Fig. 9. The global mesh size was about 1 mm according to the size of specimens. The mesh convergence analysis was conducted for a large number of finite element models, and it suggested that the mesh size in the vicinity of the crack was around 0.1 mm to obtain sufficiently accurate effective stresses. Total number of nodes and elements were 315,698 and 104,672, respectively. A fixed constraint was imposed at one end of steel plate, and a uniform tensile stress 140 MPa was applied at the other end according to the fatigue test machine. Material properties of steel, adhesive, and CFRP patches (C1, C2, and C3) are listed in Table 2.

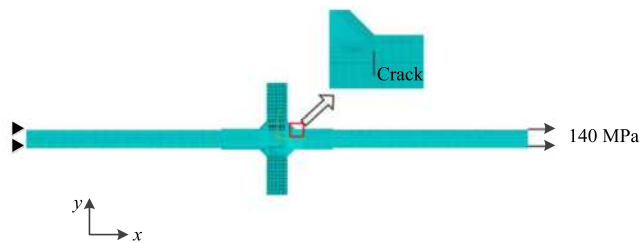


**Fig. 9.** Finite element model of a cracked welded joint with CFRP patches.

**Table 2**  
Material properties of steel, adhesive, and CFRP patches.

Material type	Yield strength (MPa)	Ultimate strength (MPa)	Poisson's ratio	Elastic modulus (MPa)
Steel	345	490	0.3	$2.1 \times 10^5$
Adhesive	–	–		1000
C1	–	3870		$2.4 \times 10^5$
C2	–	3216		$1.8 \times 10^5$
C3	–	3325		$2.4 \times 10^5$

According to Ref. [49], a recommended constant critical distance value of 0.5 mm can be used for steel welded joints in view of simplicity. Thus, Eq. (10) is directly employed to evaluate the fatigue life of cracked specimens using the PM. The fatigue strength of plain specimens  $\Delta\sigma_A$  is 160 MPa at  $N_A = 2$  million cycles, and the negative inverse slope  $m$  is 3 [50]. Based on the finite element calculated results, the relationship between effective stress range and crack depth under different strengthening CFRP patches is shown in Fig. 10. The effective stress range increases with the increase of the crack depth. The effect of different types of CFRP patches on the effective stress range is nearly the same. Fig. 11 shows that fatigue life predictions

compare with test data via the TCD approach. Most estimated data are within an error band of 3. The TCD can be successfully utilized to estimate the fatigue life of cracked welded joints repaired without and with CFRP patches.

#### 4.1.2. NSIF

When  $2\alpha = 0$ , the value of  $\Delta K_{IA}$  was set to 180 MPa mm<sup>0.5</sup> at 5 million cycles, and the inverse slope  $p$  was -3 [42]. According to Eq. (11), Fig. 12 plots the NSIF range varies with  $r$  for D1 specimens. The NSIF range is determined based on the averaged value. Similarly, Fig. 13 plots the all calculated results of NSIF ranges in the same way. The NSIF range increases with the increase of the crack depth. The effect of different types of CFRP patches on the NSIF range is nearly the same. Fig. 14 shows that fatigue life predictions compare with test data via the NSIF approach. Only half estimated data are within an error band of 3. All unstrengthened cruciform joints agree excellent with test results, but there is a relative large error for cruciform joints strengthened with CFRP patches. Existing assessment parameters for the NSIF method are needed to further in-depth study based on fatigue test results.

#### 4.1.3. SED

For fatigue cracks initiate at the weld toe or root, the control radius  $R_0 = 0.28$  mm was usually applied to evaluate the fatigue strength of steel welded joints considering the practical application [42]. The mean value of the SED range at 2 million cycles was 0.105 MJ/m<sup>3</sup>, and the negative inverse slope  $q$  of the  $\Delta W$ - $N$  curve on a log-log scale was 1.5 [42]. Thus, the fatigue life can be conveniently and easily obtained. Fig. 15 shows that fatigue life predictions compare with test results via the SED approach. Only half estimated data are within an error band of 3. Assessment data of all unstrengthened specimens agree excellent with experimental results, but there is a relative large error for cruciform joints strengthened with CFRP patches. Existing assessment parameters for the NSIF method are needed to further in-depth study based on fatigue test results.

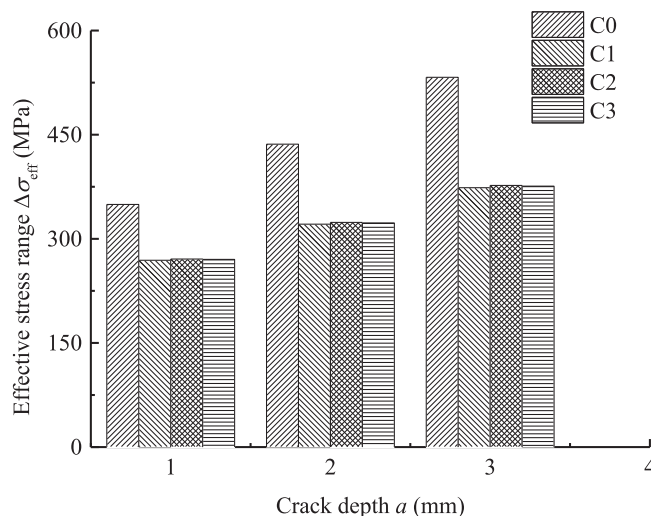


Fig. 10. Effective stress range versus crack depth.

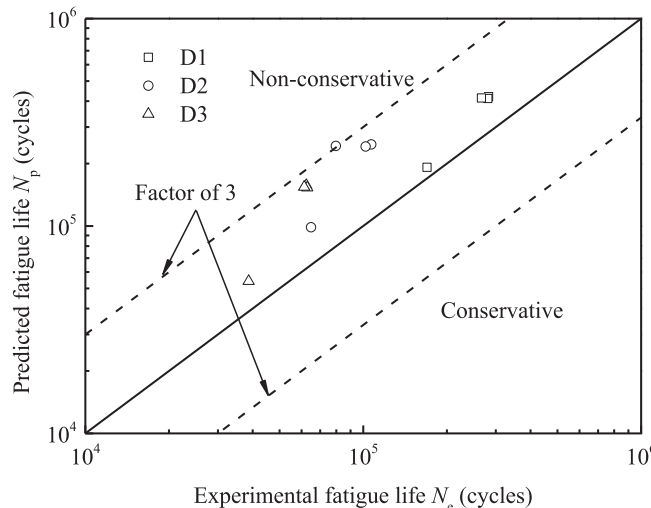


Fig. 11. Fatigue life predictions compare with test data via the TCD approach.

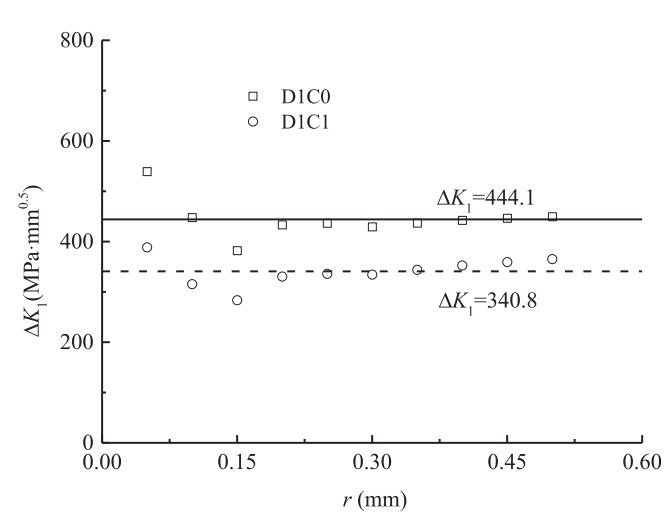


Fig. 12. The relationship between NSIF range and  $r$ .

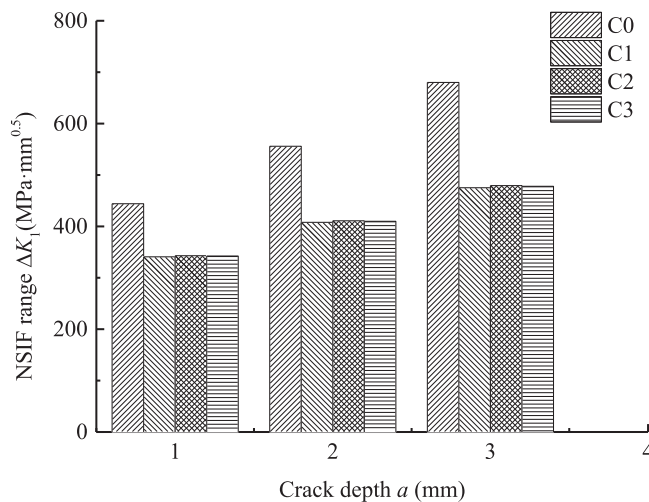


Fig. 13. The relationship between NSIF range and crack depth.

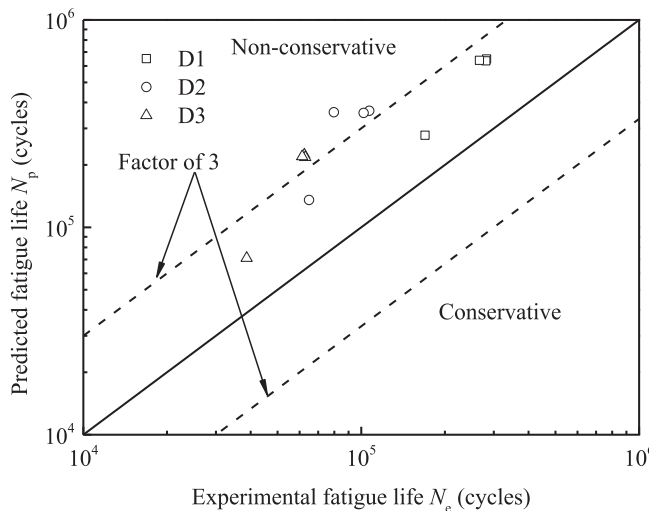


Fig. 14. Fatigue life predictions compare with test data via the NSIF approach.

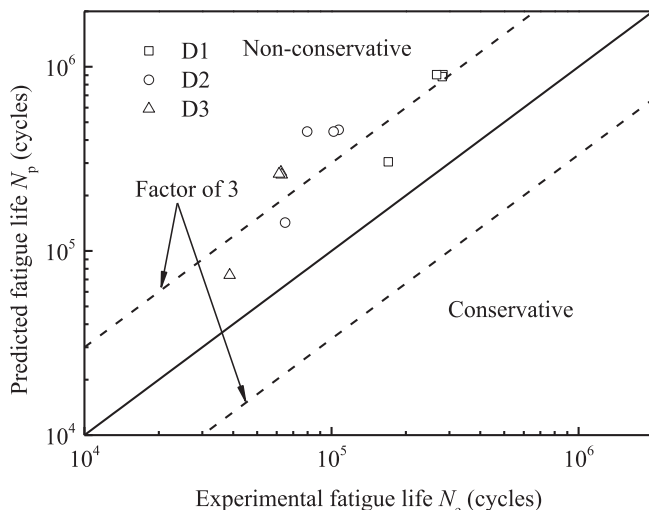


Fig. 15. Fatigue life predictions compare with test data via the SED approach.

to Section 4.1.1, it is found that fatigue life predicted results using the SED are generally larger than those using the TCD. More accurate results are obtained by the TCD. It needs to study suitable assessment parameters for the SED method.

#### 4.2. XFEM

For unreinforced specimens, material constants  $C$  and  $m$  are recommended to be  $3.98 \times 10^{-13}$  and  $2.88$  [51], respectively. For CFRP strengthening specimens, the crack tip stress significantly reduces, and CFRP patches restrict the crack opening. Thus, material constants  $C$  and  $m$  are taken from the values of  $6.03 \times 10^{-15}$  and  $3.639$  [52], respectively. Eq. (25) is inserted into Eq. (22) only considering the effect of  $\Delta K_I$ . Fatigue crack propagation equations of cracked cruciform welded joints repairing without and with CFRP patches in the form of  $\Delta G$  can be expressed as:

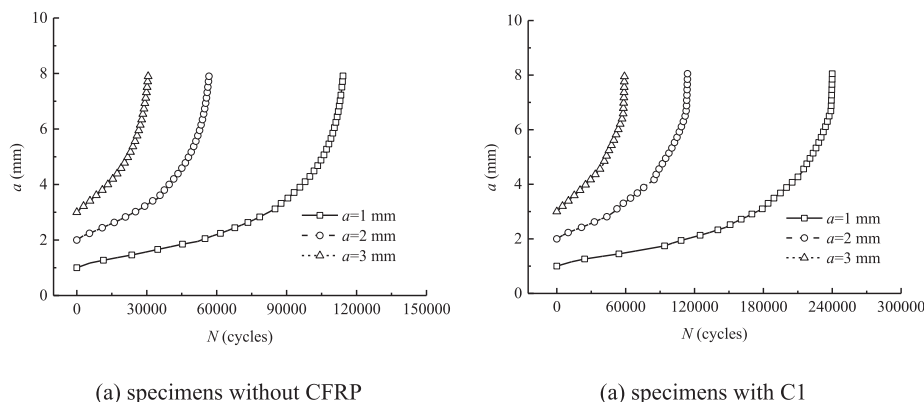
$$\frac{da}{dN} = \begin{cases} 2.10 \times 10^5 (\Delta G)^{1.44} & \text{for without CFRP} \\ 3.46 \times 10^5 (\Delta G)^{1.82} & \text{for with CFRP} \end{cases} \quad (34)$$

Fatigue crack growth can be simulated by the direct cycle in ABAQUS. In order to assure the fatigue crack propagation, material parameters  $c_1$  and  $c_2$  are set to 0.001 and 0, respectively [53]. The relationship between  $a$  and  $N$  obtained from numerical simulations is plotted in Fig. 16. Figs. 17 and 18 show fatigue crack growth simulation paths of unrepaired and CFRP repaired welded joints at different time. Fatigue crack growth actual paths are illustrated in Fig. 19. It is obvious that 80% of the fatigue life is in a slow and stable crack growth stage, and there is an agreement with the variation of the loading frequency. A small deflection angle at the beginning stage of the fatigue crack growth is generated, and then it grows linearly. The main reason is that mode II energy release rates decrease as the increase of crack depth. It agrees reasonably with actual paths. Fig. 20 plots that fatigue life predictions compare with test data using the XFEM. All results are within an error band of 2. The XFEM used to predict the fatigue life is verified by experimental data.

#### 5. Conclusions

Based on the above numerical simulation and fatigue test analyses, the conclusions can be drawn.

- (1) CFRP patches can effectively improve the fatigue life of cruciform welded joints with initial cracks. But there is little difference in strengthening effects between different CFRP patches. The remaining fatigue life and fatigue strength decrease as the increase of initial crack depth. Fatigue strength of welded joints with initial crack depth equal to 3 mm is only about one half of undamaged welded joints at 2 million cycles. There is a large scatter on the fatigue life increase for the same CFRP patches. Three fatigue failure modes can be obtained from the fatigue crack growth. Fatigue damage evolution equations of cruciform joints strengthened without and with CFRP patches are regressed using the fatigue test data.
- (2) The TCD, NSIF, and SED can be successfully used to predict the fatigue life of cruciform joints without CFRP patches. However, it needs to further investigate the values of corresponding estimation parameters for cruciform joints with CFRP patches for the NSIF approach and the SED approach. The XFEM is effective and convenient to estimate the fatigue life of cracked cruciform welded joints repaired without and with CFRP patches. Fatigue crack growth paths and lives simulated agree well with actual results. The accuracy and reliability are validated by fatigue test results.



(a) specimens without CFRP

(a) specimens with C1

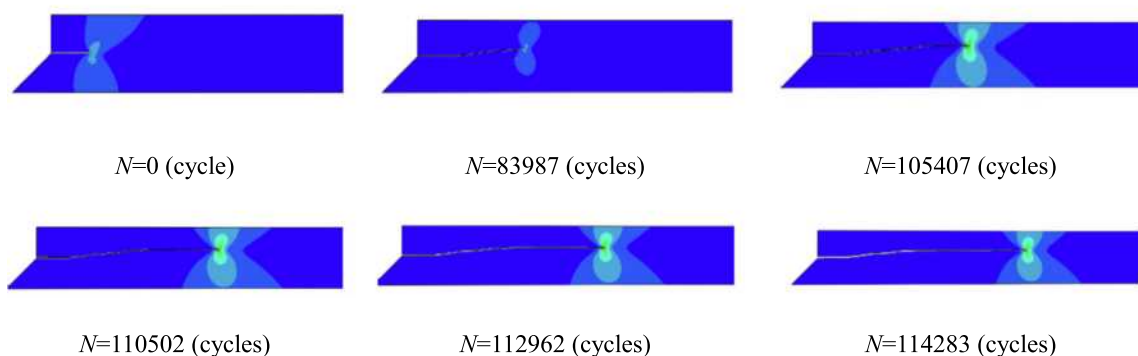
Fig. 16. Crack depth  $a$  versus the number of cycles to failure  $N$ .

Fig. 17. Fatigue crack growth simulation path for D1C0 specimen.

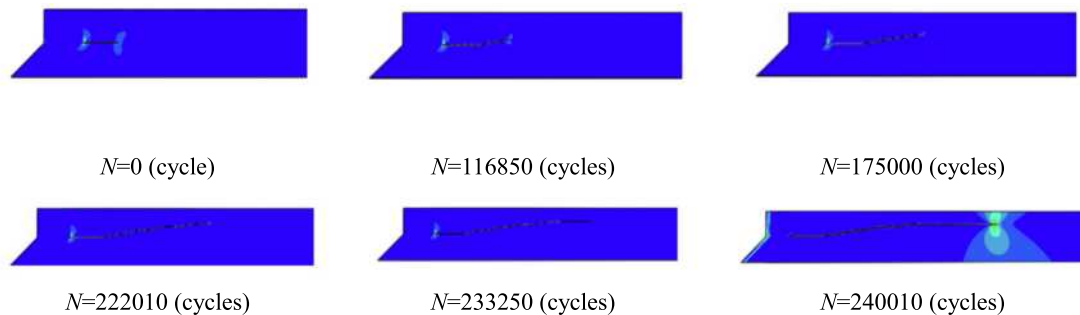
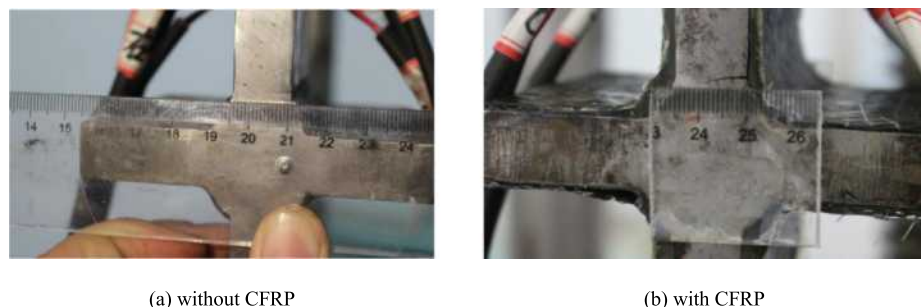


Fig. 18. Fatigue crack growth simulation path for D1C1 specimen.



(a) without CFRP

(b) with CFRP

Fig. 19. Fatigue crack growth actual path.

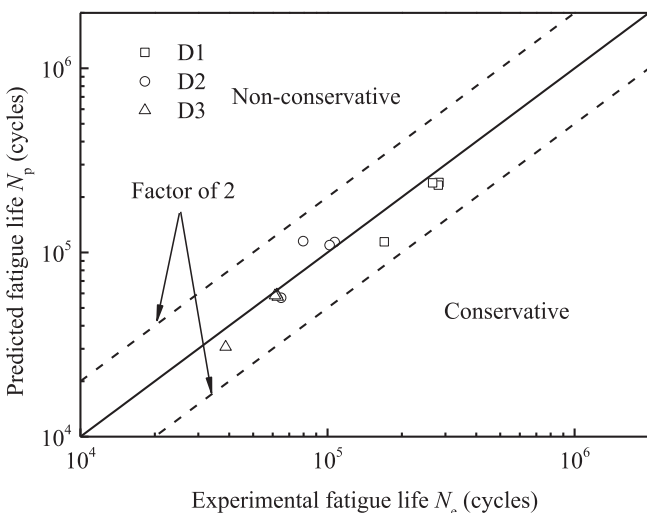


**Fig. 20.** Fatigue life predictions compare with test data via the XFEM.

#### CRediT authorship contribution statement

**Zhiyu Jie:** Conceptualization, Methodology, Investigation. **Wujun Wang:** Software, Validation. **Chao Chen:** Data curation, Formal analysis. **Kainan Wang:** Investigation.

#### Declaration of Competing Interest

The authors declare that they have no known competing financial interests or personal relationships that could have appeared to influence the work reported in this paper.

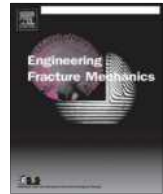
#### Acknowledgements

This work is sponsored by National Natural Science Foundation of China (51708305), Zhejiang Provincial Natural Science Foundation of China (LQ17E080005) and K. C. Wong Magna Fund in Ningbo University.

#### References

- [1] Hassan NK, Ahmed YF, Sayed TH. Fatigue life of cruciform welded joint strengthened with CFRP. *World Appl Sci J* 2015;33(5):823–30.
- [2] Wang Z, Wang Q, Li L, Zhang N. Fatigue behaviour of CFRP strengthened open-hole steel plates. *Thin Wall Struct* 2017;115:176–87.
- [3] Wang H, Wu G. Crack propagation prediction of double-edged cracked steel beams strengthened with FRP plates. *Thin Wall Struct* 2018;127:459–68.
- [4] Radaj D, Sonsino CM, Fricke W. Recent developments in local concepts of fatigue assessment of welded joints. *Int J Fatigue* 2009;31(1):2–11.
- [5] Taylor D. The theory of critical distances. *Eng Fract Mech* 2008;75(7):1696–705.
- [6] Pluvinage G. Fatigue and fracture emanating from notch; the use of the notch stress intensity factor. *Nucl Eng Des* 1998;185:173–84.
- [7] Lazzarin P, Livieri P, Berto F, Zappalorto M. Local strain energy density and fatigue strength of welded joints under uniaxial and multiaxial loading. *Eng Fract Mech* 2008;75(7):1875–89.
- [8] Zhou H, Wen J, Wang Z, Zhang Y, Du X. Fatigue crack initiation prediction of cope hole details in orthotropic steel deck using the theory of critical distances. *Fatigue Fract Eng M* 2016;39(9):1051–66.
- [9] Nie B, Chen D, Zhao Z, Zhang J, Meng Y, Gao G. Notch effect on the fatigue behavior of a TC21 titanium alloy in very high cycle regime. *Appl Sci* 2018;8(9):1614.
- [10] Jie Z, Susmel L. High-strength steel wires containing corrosion pits: stress analysis and critical distance based fatigue life estimation. *Fatigue Fract Eng M* 2020;43(8):1611–29.
- [11] Al Zamzami I, Susmel L. On the accuracy of nominal, structural, and local stress based approaches in designing aluminium welded joints against fatigue. *Int J Fatigue* 2017;101:137–58.
- [12] Karakaş Ö, Zhang G, Sonsino CM. Critical distance approach for the fatigue strength assessment of magnesium welded joints in contrast to Neuber's effective stress method. *Int J Fatigue* 2018;112:21–35.
- [13] Al Zamzami I, Davison B, Susmel L. Nominal and local stress quantities to design aluminium-to-steel thin welded joints against fatigue. *Int J Fatigue* 2019;123:279–95.
- [14] Baumgartner J, Yildirim HC, Barsoum Z. Fatigue strength assessment of TIG-dressed welded steel joints by local approaches. *Int J Fatigue* 2019;126:72–8.
- [15] Zamzami IA, Susmel L. On the use of hot-spot stresses, effective notch stresses and the Point Method to estimate lifetime of notched welds subjected to uniaxial fatigue loading. *Int J Fatigue* 2018;117:432–49.
- [16] Gorouhi H. Novel fatigue analysis of old metallic bridges through the theory of critical distances (TCD). Guildford, UK: University of Surrey; 2017.
- [17] Fang Z, Li A, Ding Y, Li W. Wind-induced fatigue assessment of welded connections in steel tall buildings using the theory of critical distances. *Eur J Environ Civ Eng* 2018;1:26.
- [18] Lazzarin P, Tovo R. A unified approach to the evaluation of linear elastic stress fields in the neighborhood of cracks and notches. *Int J Fracture* 1996;78(1):3–19.
- [19] Lazzarin P, Tovo R. A notch intensity factor approach to the stress analysis of welds. *Fatigue Fract Eng M* 1998;21(9):1089–103.
- [20] Meneghetti G, Campagnolo A. State-of-the-art review of peak stress method for fatigue strength assessment of welded joints. *Int J Fatigue* 2020;105705.
- [21] Campagnolo A, Vormwald M, Shams E, Meneghetti G. Multiaxial fatigue assessment of tube-tube steel joints with weld ends using the peak stress method. *Int J Fatigue* 2020;135:105495.
- [22] Campagnolo A, Zuin S, Meneghetti G. Averaged strain energy density estimated rapidly from nodal displacements by coarse FE analyses: Cracks under mixed mode loadings. *Fatigue Fract Eng M* 2020;43(8):1658–85.
- [23] Lazzarin P, Zambardi R. A finite-volume-energy based approach to predict the static and fatigue behavior of components with sharp V-shaped notches. *Int J Fracture* 2001;112(3):275–98.
- [24] Leonardi A. Advanced local approach for the fatigue assessment of aluminium weldments. Trondheim, Norway: Norwegian University of Science and Technology; 2018.
- [25] Berto F, Vinogradov A, Filippi S. Application of the strain energy density approach in comparing different design solutions for improving the fatigue strength of load carrying shear welded joints. *Int J Fatigue* 2017;101:371–84.
- [26] Berto F, Campagnolo A, Chebat F, Cincera M, Santini M. Fatigue strength of steel rollers with failure occurring at the weld root based on the local strain energy values: Modelling and fatigue assessment. *Int J Fatigue* 2016;82:643–57.
- [27] Song W, Liu X, Berto F, Wang P, Xu J, Fang H. Strain energy density based fatigue cracking assessment of load-carrying cruciform welded joints. *Theor Appl Fract Mec* 2017;90:142–53.
- [28] Song W, Liu X, Razavi SMJ. Fatigue assessment of steel load-carrying cruciform welded joints by means of local approaches. *Fatigue Fract Eng M* 2018;41(12):2598–613.
- [29] Foti P, Berto F, Filippi S. Fatigue assessment of welded joints by means of the Strain Energy Density method: Numerical predictions and comparison with Eurocode 3. *Frattura ed Integrità Strutturale* 2019;13(47):104–25.
- [30] Luo P, Zhang Q, Bao Y, Zhou A. Fatigue evaluation of rib-to-deck welded joint using averaged strain energy density method. *Eng Struct* 2018;177:682–94.
- [31] Fischer C, Fricke W, Rizzo CM. Review of the fatigue strength of welded joints based on the notch stress intensity factor and SED approaches. *Int J Fatigue* 2016;84:59–66.
- [32] Kraedeh AMA. Fatigue crack growth in T welded joint of aluminium alloy. Belgrade, Serbia: University of Belgrade; 2018.
- [33] Bergara A, Dorado JI, Martin-Meizoso A, Martínez-Esnaola JM. Fatigue crack propagation in complex stress fields: Experiments and numerical simulations using the Extended Finite Element Method (XFEM). *Int J Fatigue* 2017;103:112–21.
- [34] Nikfam MR, Zeinoddini M, Aghebati F, Arghaei AA. Experimental and XFEM modelling of high cycle fatigue crack growth in steel welded T-joints. *Int J Mech Sci* 2019;153:178–93.
- [35] Wang C, Wang Y, Cui B, Duan L, Ma N, Feng J. Numerical simulation of distortion-induced fatigue crack growth using extended finite element method. *Struct Infrastruct E* 2020;16(1):106–22.
- [36] Zarrinzadeh H, Kabir MZ, Deylami A. Experimental and numerical fatigue crack growth of an aluminium pipe repaired by composite patch. *Eng Struct* 2017;133:24–32.
- [37] Valadi Z, Bayesteh H, Mohammadi S. XFEM fracture analysis of cracked pipeline with and without FRP composite repairs. *Mech Adv Mater Struc* 2018;23:1–12.
- [38] Lesiuk G, Katkowski M, Correia J, de Jesus AM, Blazewski W. Fatigue crack growth rate in CFRP reinforced constructional old steel. *Int J Struct Integr* 2018;9(3):381–95.
- [39] Louks R, Susmel L. The linear-elastic Theory of Critical Distances to estimate high-cycle fatigue strength of notched metallic materials at elevated temperatures. *Fatigue Fract Eng M* 2015;38(6):629–40.
- [40] El Haddad MH, Smith KN, Topper TH. Fatigue crack propagation of short cracks. *J Eng Mater Technol* 1979;101(1):42–6.
- [41] Susmel L, Taylor D. A novel formulation of the theory of critical distances to estimate lifetime of notched components in the medium-cycle fatigue regime. *Fatigue Fract Eng M* 2007;30(7):567–81.
- [42] Livieri P, Lazzarin P. Fatigue strength of steel and aluminium welded joints based on generalised stress intensity factors and local strain energy values. *Int J Fracture* 2005;133(3):247–76.
- [43] Mohammadi S. Extended finite element method: for fracture analysis of structures. Oxford, UK: John Wiley & Sons; 2008.
- [44] Amiri Rad A, Forouzan MR, Sadeghi DA. Three-dimensional fatigue crack growth modelling in a helical gear using extended finite element method. *Fatigue Fract Eng M* 2014;37(6):581–91.

- [45] GB/T 714-2015. Structural steel for bridge. China, 2015. (in Chinese)
- [46] Fricke W. IIW guideline for the assessment of weld root fatigue. Weld World 2013;57(6):753–91.
- [47] Jie Z, Wang W, Fang R, Zhuge P, Ding Y. Stress intensity factor and fatigue analysis of cracked cruciform welded joints strengthened by CFRP sheets considering the welding residual stress. Thin Wall Struct 2020;154:106818.
- [48] Jie Z, Li Y, Wei X, Zhuge P. Fatigue life prediction of welded joints with artificial corrosion pits based on continuum damage mechanics. J Constr Steel Res 2018;148:542–50.
- [49] Susmel L. Modified Wöhler curve method, theory of critical distances and Eurocode 3: A novel engineering procedure to predict the lifetime of steel welded joints subjected to both uniaxial and multiaxial fatigue loading. Int J Fatigue 2008;30(5):888–907.
- [50] EN 1993-1-9. Eurocode 3: Design of Steel Structures Part 1-9: Fatigue. 2005.
- [51] BS 7910. Guide to methods for assessing the acceptability of flaws in metallic structures. British Standards Institution, 2013.
- [52] Wang H. Study on the fatigue behavior of CFRP plate strengthened steel structures and its design method. Nanjing, China: Southeast University; 2016 (in Chinese).
- [53] Gupta RS. Prediction of Fatigue Crack Propagation in Orthotropic Steel Decks using XFEM based on LEFM and VCCT. Delft, Netherlands: Delft University of Technology; 2019.



## Verification of the repair effect for fatigue cracks in members of steel bridges based on thermoelastic stress measurement



Takahide Sakagami <sup>a,\*</sup>, Yoshiaki Mizokami <sup>b</sup>, Daiki Shiozawa <sup>a</sup>, Taisei Fujimoto <sup>a</sup>, Yui Izumi <sup>c</sup>,  
Taku Hanai <sup>b</sup>, Akira Moriyama <sup>b</sup>

<sup>a</sup> Department of Mechanical Engineering, Kobe University, 1-1 Rokkodai-cho, Nada-ku, Kobe 657-8501, Japan

<sup>b</sup> Honshu-Shikoku Bridge Expressway Company Limited, 4-1-22 Onoe-dori, Chuo-ku, Kobe 651-0088, Japan

<sup>c</sup> Department of Mechanical Systems Engineering, University of Shiga Prefecture, 2500 Hassaka-cho, Hikone 522-0057, Japan

### ARTICLE INFO

*Article history:*

Received 15 January 2017

Received in revised form 15 May 2017

Accepted 17 May 2017

Available online 27 May 2017

*Keywords:*

Nondestructive evaluation

Thermoelasticity

Infrared thermography

Fatigue cracks

Steel bridges

### ABSTRACT

Ageing steel bridges suffer fatigue cracks thereby necessitating immediate inspection, structural integrity evaluation or repair in the life cycle of steel bridges. We propose non-destructive evaluation techniques employing infrared thermography enabling us to remotely inspect the fatigue cracks in steel bridges and evaluate the structural integrity on the basis of thermoelastic stress measurement. This study presents a structural integrity assessment of steel bridges using remote measurement of the stress field around the fatigue cracks. We focus upon experimental results confirming reduction in the severity of the stress distribution around the fatigue cracks after the repair or reinforcement of members in steel bridges.

© 2017 Elsevier Ltd. All rights reserved.

## 1. Introduction

Propagation of fatigue cracks from welded joints in steel bridges is one of the most serious problems associated with the deterioration of ageing infrastructure. Inspection of the deterioration such as fatigue damage or corrosion is necessary for ensuring safety and estimating the remaining strength of the steel bridges. In this respect, nondestructive testing (NDT) and nondestructive evaluation (NDE) techniques play important roles. Conventional NDT techniques for steel bridges include visual testing, eddy-current testing, magnetic-particle testing and ultrasonic testing. However, these are time- and labor-intensive techniques that require special equipment for inspection such as scaffoldings or vehicles for high-lift work. The Japan Ministry of Land, Infrastructure, Transport and Tourism has reported that there are over 0.7 million bridges requiring inspection [1]. This means that it is not realistically possible to employ conventional NDT techniques for ageing bridges; hence, a high-performance NDT method is essential for their effective maintenance. In addition, structural integrity evaluation is considered essential for the fitness for service evaluation of ageing steel bridges. For an accurate structural integrity evaluation, the actual applied-stress distribution around a fatigue crack and its history owing to the moving wheel load caused by vehicles on the bridge needs to be obtained. Conventional stress- and strain-measurement techniques are insufficient for these requirements.

Thermoelastic stress analysis (TSA) using infrared thermography has come into widespread use in the industry as an effective, experimental, full-field stress measurement technique [2–5]. Especially innovative research works on the TSA

\* Corresponding author.

E-mail address: [sakagami@mech.kobe-u.ac.jp](mailto:sakagami@mech.kobe-u.ac.jp) (T. Sakagami).

technique are found in structural integrity evaluations for steel structures as well as composite structures related with fracture mechanics evaluations and/or fatigue damage analyses. As for steel structural members, evaluation schemes of the fracture mechanics parameters have been investigated taking advantages of the TSA technique [6]. The fracture mechanics parameters such as stress intensity factor or  $J$ -integral were determined from the directly measured stress distribution around crack tips in objective structures [7–10]. These techniques have been successfully applied on the fatigue life assessment. Tomlinson et al. [11] investigated fatigue crack propagation under the mixed mode loading. Diaz et al. [12] applied their improved TSA technique for evaluating stress intensity factors in the fatigue test of weld specimen demonstrating the potential of TSA for crack growth analysis influenced by crack closure or residual stress field. Ummenhofer et al. [13] also investigated the applicability of the TSA technique for fatigue damage evaluation in welded joints. The TSA technique has been also employed as a powerful tool for evaluating impact or fatigue damages in composite materials and structures [14–17]. Emery et al. [18] showed the feasibility of the TSA for evaluating fiber breakage, matrix cracking and delamination damage in composites. Fruehmann et al. [19] applied the TSA technique for the assessment of fatigue damage evolution in woven composite materials. Paynter and Dutton [20] applied the TSA technique to wind turbine blade composite structure, in which successful results were obtained in damage evaluation using second harmonic signal correlation. Jones and Molent [21] showed the applicability of the TSA technique for in situ measurement during redesign, reinforcement or repair in aircraft structures.

These literatures showed the strong advantages of the TSA technique for the remote, noncontact, nondestructive and full-field stress measurement, as well as its applicability for various types of structural damages. Therefore, a useful and powerful technique for evaluating structural integrity related with fatigue damage evolution can be developed based on the TSA technique for the maintenance of ageing steel bridges.

This study focuses on the TSA-based in situ evaluation technique for stress reduction and restoration of structural integrity after repair or reinforcement. Fatigue cracks were found in the structural members of the Seto-Ohashi Bridges connecting the Honshu and Shikoku islands in Japan during their 21st-year inspection. Several repair methods have been investigated by experimental studies at the site. The stress distributions around the fatigue cracks were measured by employing the TSA technique when live loading acted on the bridge and the effectiveness of the severity reduction using these repair methods was investigated.

## 2. Fatigue crack evaluation in the life of steel bridges

The present authors [22] developed remote NDT- and NDE-techniques using infrared thermography for the maintenance of ageing steel structures. Fig. 1 shows a schematic of the proposed life cycle NDT- and NDE-techniques for steel bridges using infrared thermography. The first sign of deterioration in ageing steel bridges is the initiation of fatigue cracks. It would be beneficial to predict the occurrence and location of fatigue crack initiation. The feasibility of dissipated energy measurement was investigated for predicting the fatigue-crack initiation [23]. After the initiation of fatigue cracks, detection of these cracks is required for the maintenance of the steel bridges. The present authors [24] developed a relatively simple but useful

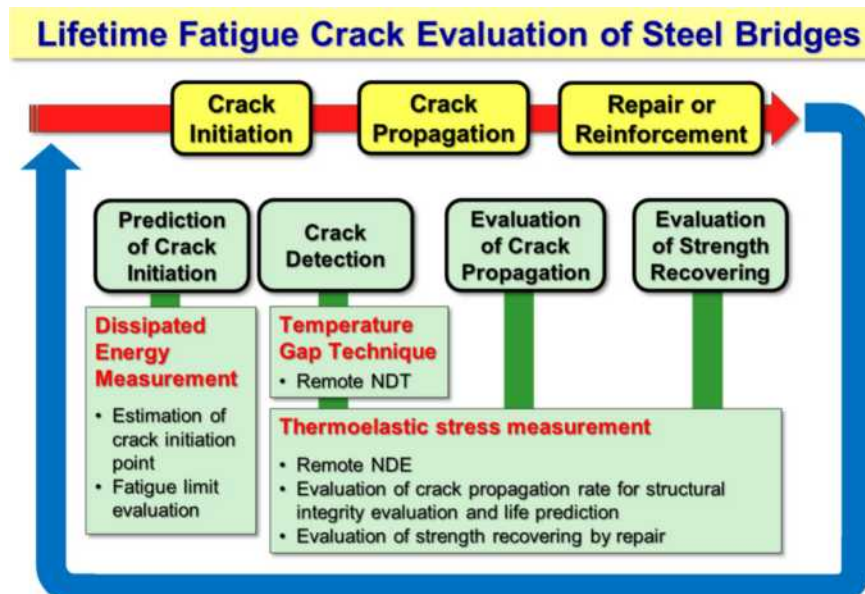


**Fig. 1.** Development of the NDT- and NDE-techniques using infrared thermography for fatigue cracks in steel bridges.

NDT technique for fatigue-crack detection on the basis of the temperature gap that appears on the surfaces of the structural members because of the thermal-insulation effect of the cracks. Fatigue cracks can be also detected on the basis of the stress distribution around the crack tips measured by the TSA technique using infrared thermography. Sakagami et al. [25] developed a self-reference lock-in thermography technique for the signal-noise ratio (S/N) improvement that requires no external reference signals and can be employed even under irregular-waveform loading. Once a fatigue crack is initiated, it is necessary to evaluate its size and propagation rate, and fracture-mechanics analysis needs to be conducted to evaluate the bridge's remaining strength. The TSA technique was effectively applied for a full-field stress-distribution measurement around the crack tips, followed by a fracture-mechanics evaluation using the stress intensity factor [22].

Finally after an ample crack propagation, steel bridges require repair or reinforcement to prolong their life. Various repair-and reinforce-methods have been investigated for fatigue damages in welded steel structures. Matsumoto et al. [26] compared the fatigue-life extension effects among three different types of repairs, namely, crack removal by grinder treatment, impact crack-closure retrofit (ICR) treatment and stop-hole technique. Yuan Zhou et al. [27] also investigated the effect of ICR treatment on welded joints using strain gauges and finite element method (FEM) analyses. Aoki et al. [28] examined the stiffener-bonding repair technique for through-thickness fatigue cracks at the vertical stiffener end in an orthotropic steel deck.

In almost all previous studies, the effect of stress-severity reduction by repair work was investigated only by strain measurement using strain gauges or FEM analyses. The authors consider it is essential to experimentally confirm the severity reduction of the stress distribution around the damaged portion after the repair or reinforcement of the structural members in steel bridges. Therefore, the TSA-based in situ evaluation technique for stress reduction and restoration of structural integrity after repair or reinforcement was developed.

### 3. Thermoelastic stress measurement

Dynamic stress change causes a very small temperature change under adiabatic conditions in a solid. This phenomenon is known as the thermoelastic effect and is described by Lord Kelvin's equation [29], which relates the temperature change ( $\Delta T$ ) to the sum of the changes in the principal stresses ( $\Delta\sigma$ ) under cyclic variable loading as follows.

$$\Delta T = -\frac{\alpha}{\rho C_p} T \Delta\sigma \quad (1)$$

here,  $\alpha$  is the coefficient of thermal expansion,  $\rho$  is the mass density,  $C_p$  is the specific heat at constant pressure and  $T$  is the absolute temperature. The sum of the changes in the principal stresses ( $\Delta\sigma$ ) is obtained by measuring the temperature change ( $\Delta T$ ) using high-performance infrared thermography.

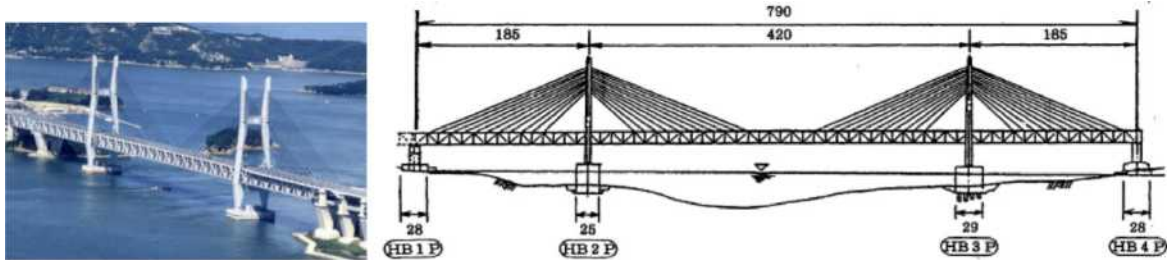
As thermoelastic temperature changes are very small and sometimes hidden by the thermal noise of the infrared camera, lock-in infrared thermography using reference signals synchronized with the stress changes is commonly employed to improve the accuracy of stress measurements. The conventional TSA technique requires a lock-in algorithm with a reference-loading signal extracted from the load cell or strain gauge to improve the signal-noise ratio. However, it is difficult to obtain a reference signal from steel bridges that are in service. Furthermore, the observed load signal contains an irregular waveform because of the wheel loading by vehicles on the bridge. These problems cause difficulties for the conventional lock-in infrared thermography to be employed for on-site thermoelastic stress measurements.

The present authors [25] solved these problems by developing a self-reference lock-in thermography technique that does not require any external reference signals and can be employed even under irregular-waveform loading. In this technique, a reference signal is constructed from a reference region that is arbitrarily set to the same sequential infrared images as those showing thermoelastic temperature changes. The distribution of the relative intensity of the thermoelastic temperature change against that in the reference region can then be obtained using the least-squares approach developed by Lesniak et al. [30], even under irregular-waveform loading, provided that the temperature change in the reference region has a similar and an in-phase waveform as that in the objective area under measurement. As a result of the self-reference lock-in data processing, stress-distribution images with improved S/N can be obtained.

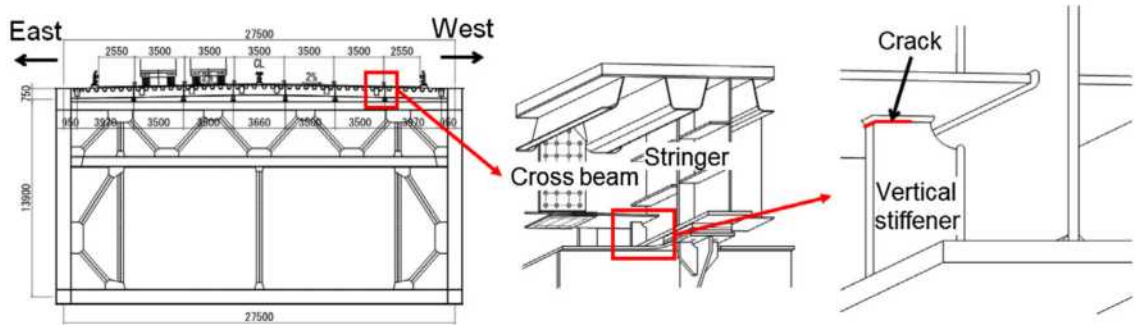
### 4. Objective steel members for evaluating the severity reduction of stress distribution by repair

Objective members for evaluating the reduction in the severity of the stress distribution after repair are the vertical stiffeners at the supports of steel decks where stringers intersect with cross beams in cable-stayed bridges in the part of the Seto-Ohashi Bridges as shown in Fig. 2. Fatigue cracks were detected at the upper weld part of the vertical stiffeners.

Fig. 3 shows the three different repair methods, i.e., (b) circular-arc cutout method, (c) stiffening-plate method (type I) and (d) improved stiffening-plate method (type II), examined in this study. All the repair methods were intended to mitigate the high stress concentration in the weld part located at the top of the stiffeners by transferring the high stress to the arc cutout or the stiffening plate. In areas where the above repair methods were applied, fatigue cracks were found to propagate in the eastern vertical stiffeners along the boxing-welding sections, as shown in Fig. 2. The results of magnetic-particle testing showed that the detected fatigue cracks varied in surface length from 20 mm to 40 mm.



(a) Hitsuishijima bridge in the part of the Seto-Ohashi Bridges



(b) Cross-section of bridge and details of objective member

**Fig. 2.** Objective member for evaluating the reduction in the severity of the stress distribution after repair in Hitsuishijima bridge in the part of the Seto-Ohashi Bridges.

The repair works and the thermoelastic-stress measurements were performed through the following stages: First, thermoelastic stress measurements around the fatigue cracks were conducted before repair. Second, each repair method was applied to the vertical stiffeners, while the cracks themselves were left as they were. Then, thermoelastic stress measurement was conducted to investigate the stress-reduction effect of the applied repair methods. Finally, the fatigue cracks were removed using the grinder treatment and the thermoelastic stress measurement was conducted again. For several vertical stiffeners additional re-welding treatment was applied followed by thermoelastic stress measurement.

## 5. In situ thermoelastic stress measurement under wheel loading

The stress distributions on the vertical stiffeners were measured before the repair and after each repair stage, as described at the end of Section 3. For each measurement, the objective structure was loaded with a vehicle driving on the traffic lane of the bridge at a constant speed of 80 km an hour. A sprinkler truck with three axles as shown in Fig. 4 was employed as a loading vehicle. The total vehicle load and each axle load were measured by the axle-load meter after filling up the water tank. The results were shown in Fig. 4. The thermoelastic temperature measurements were conducted more than 8 times at each experimental study under the same condition, and it was confirmed that reproducibility of the measurement is sufficient.

The thermoelastic stress measurement was conducted using a high-performance infrared camera with a QVGA InSb array detector (temperature resolution 20 mK), as shown in Fig. 5. The integration time and framing rate of the infrared camera were set to 1292 μs and 157 Hz, respectively. The dominant frequency of the thermoelastic temperature change was estimated to be more than 5 Hz. This value was estimated from measured waveform of the thermoelastic temperature change, vehicle speed and the distance between front and center of rear tandem axles. Therefore the adiabatic condition required for the TSA was satisfied in this experimental study. From the temperature change observed by the infrared camera, the change in the sum of the principal stresses was calculated using Eq. (1), material properties of the structural steel (JIS SS400:  $\alpha = 11.8 \times 10^{-6}/\text{K}$ ,  $\rho = 7.86 \times 10^3 \text{ kg/m}^3$ ,  $C_p = 473 \text{ J/kg} \cdot \text{K}$ ) and the ambient temperature. In this study the obtained sequential infrared data were processed using the self-reference lock-in technique to obtain S/N improved stress distribution images.

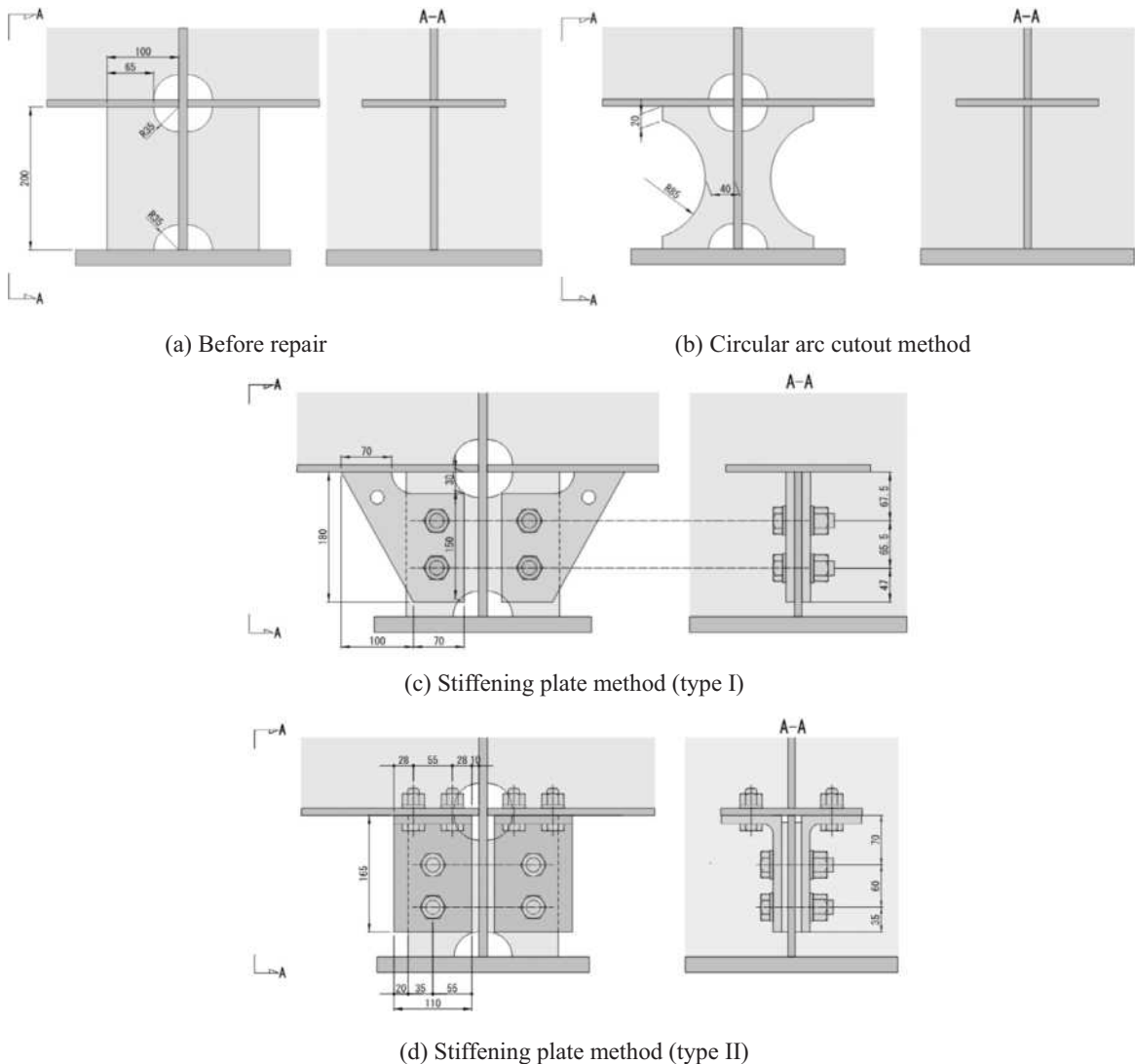


**Fig. 3.** Illustrations of vertical stiffener and employed repair methods.

## 6. Experimental results obtained for the circular-arc cutout repair method

Retrofitting measures applied to the weld of the vertical stiffeners by semicircular cutout treatment have been employed for effective repair of orthotropic steel decks [31]. The aim of this retrofitting measure is to reduce the stress concentration at the weld part and transfer the stress concentration point from that weld to the edge of the semicircular arc, which has a higher fatigue resistance.

The size of the circular cutout was determined by FEM analyses conducted prior to the on-site repair work. FEM analysis results are shown in Fig. 6. It is found that the high-stress concentration points are located in the upper weld regions of the original vertical stiffeners. In contrast, after the circular-arc cutout repair, the stress concentration areas are transferred from the weld part to the edges of the circular arc. The determined radius of the circular cutout was 85 mm.

Experimental thermoelastic stress measurement results obtained for the circular-arc cutout repair method are shown in Fig. 7. It is found from Fig. 7(a) that a high stress concentration can be observed at the crack tip before the repair. In contrast Fig. 7(b) shows that the stress concentration is observed at the edge of circular arc after the circular-arc cutout repair. The change in the sum of the principal stresses at the maximum stress concentration point was reduced by 50% after the circular-arc cutout repair. This experimental result is consistent with that of the FEM analysis, as shown in Fig. 6. From Fig. 7(c), it can be seen that the stress distribution obtained after re-welding did not change much. This experimental study clarified that this method can successfully transfer the high stress concentration from the weld part at the top of the stiffener to the edge of the circular arc where the fatigue resistance is higher. In this experimental study, stress values were simultaneously

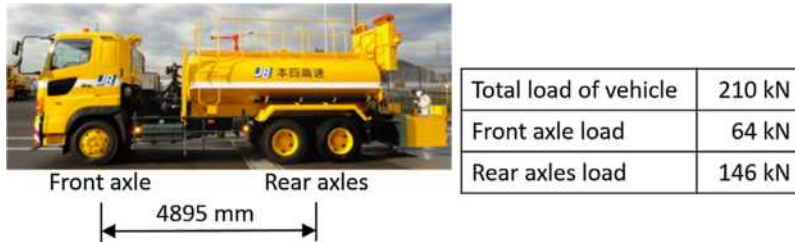


**Fig. 4.** Employed loading vehicle and axle load.

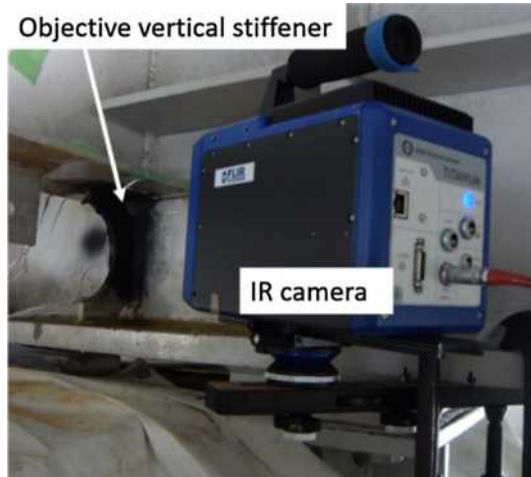


**Fig. 5.** Thermoelastic temperature measurement using infrared cameras.

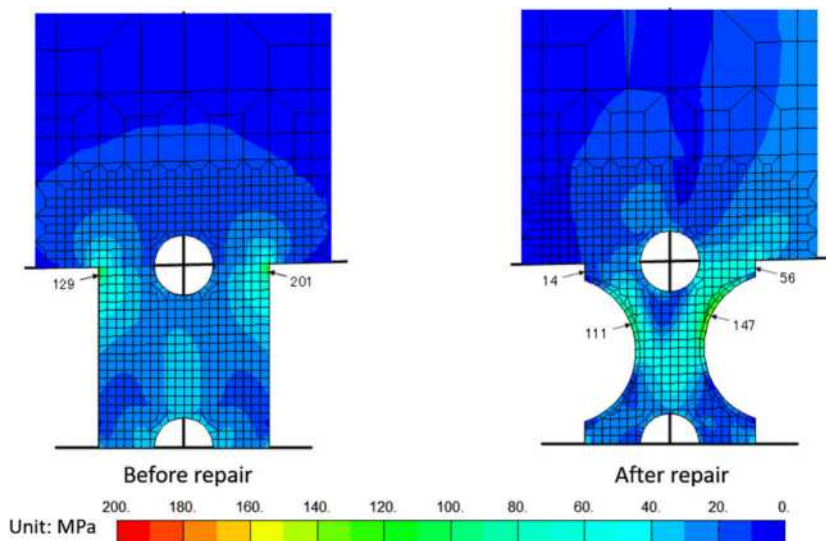


**Fig. 6.** Results of FEM analyses indicating the principal stress distributions before and after repair.

measured by strain gauges at several points on the vertical stiffener. Locations of the strain gauges and measured stress values are shown in Fig. 8. The results of stress reduction by the repair work show the same trend as that shown by the TSA results.

It is worth noting that the circular-arc cutout repair method was applied again to another vertical stiffener for which the radius of the circular cutout was reduced to 75 mm. The procedures of this repair work is compared with that for a circular

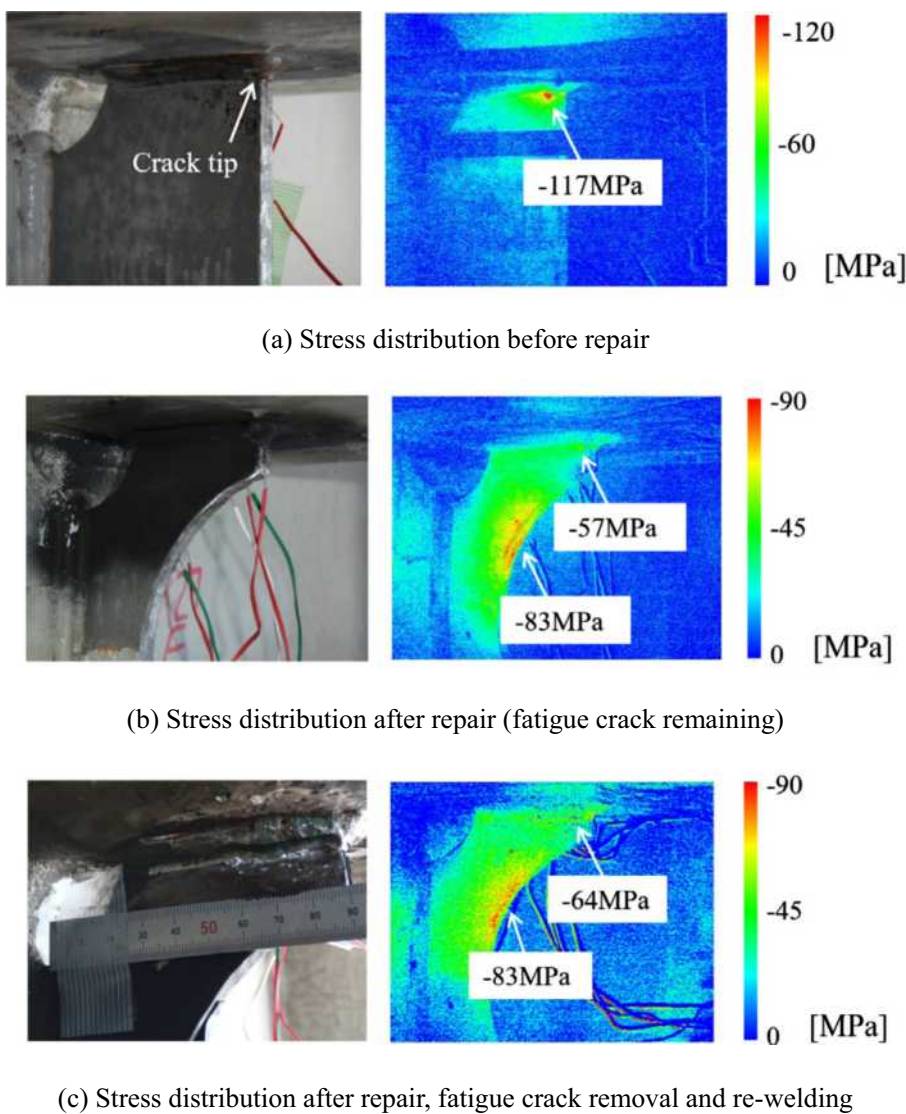


**Fig. 7.** Results of the thermoelastic stress distribution measurement for the circular-arc cutout repair method.

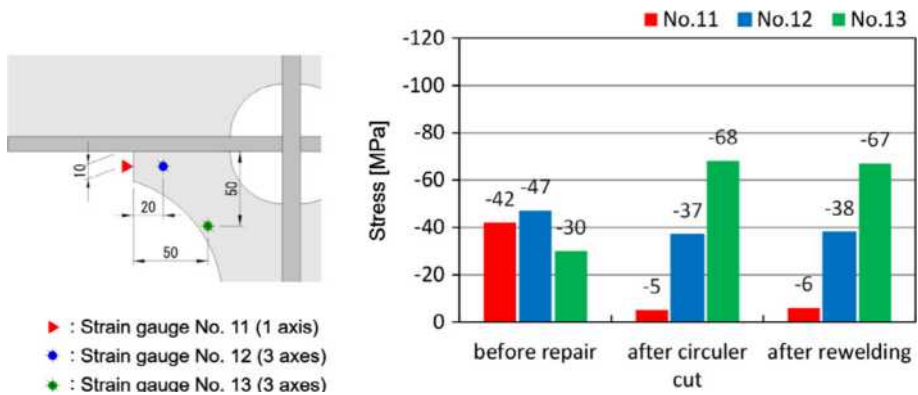


**Fig. 8.** Results of stress measurement by strain gauges obtained for the circular-arc cutout repair method.

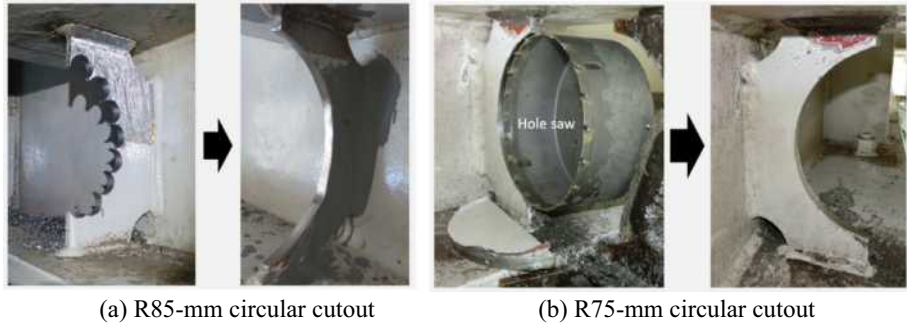


**Fig. 9.** Comparison of the machining processes used in semi-circular arc cutout repair.

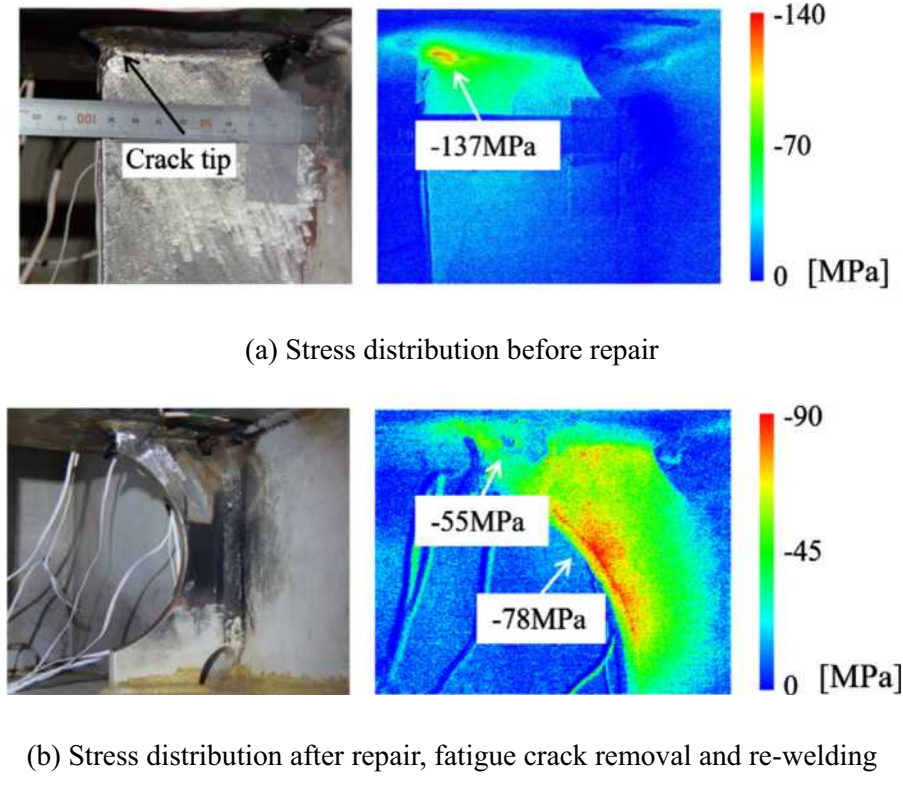


**Fig. 10.** Results of the thermoelastic stress distribution measurement for R75-mm circular arc cutout repair.

cutout with a radius of 85 mm, as shown in Fig. 9. It is found that the machining process of the R75-mm cutout is much simpler and less time consuming than that of the R85-mm cutout. The experimental results of the stress reduction effect are shown in Fig. 10. It was found that a comparable stress reduction effect was achieved in the case of a smaller cutout radius. R75-mm cutout repair is more beneficial for on-site repair work in terms of the effectiveness of stress reduction as well as the machining efficiency.

## **7. Experimental results obtained from the stiffening-plate repair method**

Stiffening-plate repair is a well-known retrofitting measure for the structural members of orthotropic steel decks [32]. The aim of this repair technique is to reduce the high stress concentration in the weld part by sharing the loading paths among the vertical stiffener and stiffening plates. In this study, the stress mitigation effects of two different types of stiffening-plate repair techniques (as shown in Fig. 3(c) and (d)) were examined.

The experimental results of the thermoelastic stress measurement obtained for the type I stiffening-plate repair method are shown in Fig. 11. It is found from the figures that the high stress concentration at the crack tip was not mitigated even after the repair work was conducted. It seemed that the stiffening plates did not share the loading paths, thus the high stress

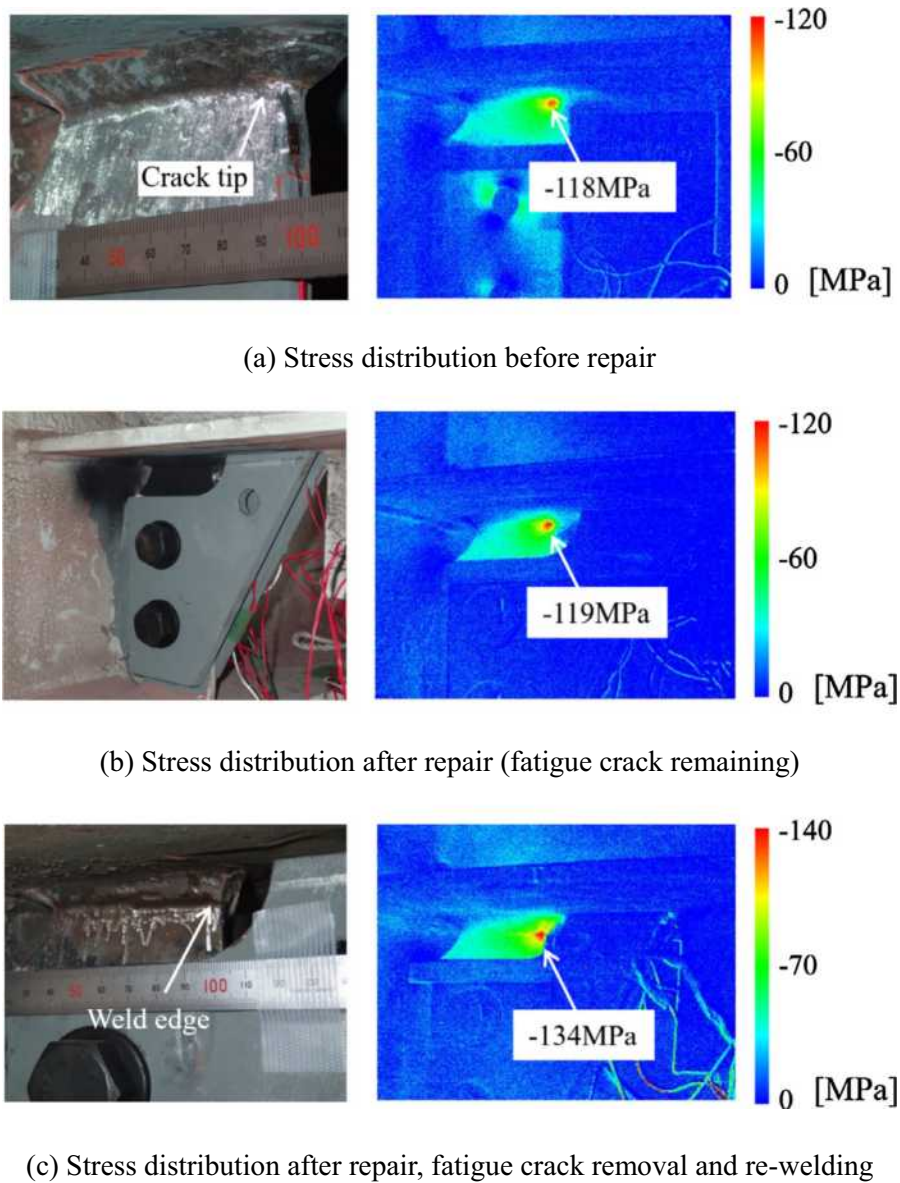


**Fig. 11.** Results of thermoelastic stress distribution measurements for type I stiffening-plate repair.

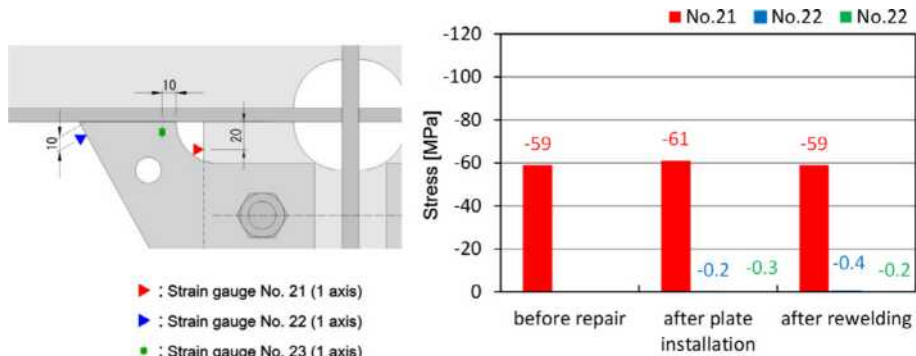


**Fig. 12.** Results of stress measurement by strain gauges obtained for type I stiffening-plate repair.

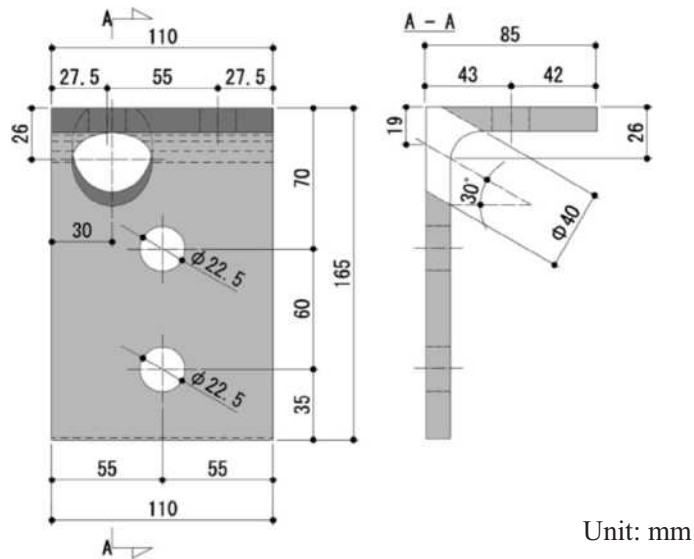


**Fig. 13.** Observation window in angle stiffener plate for infrared measurement.

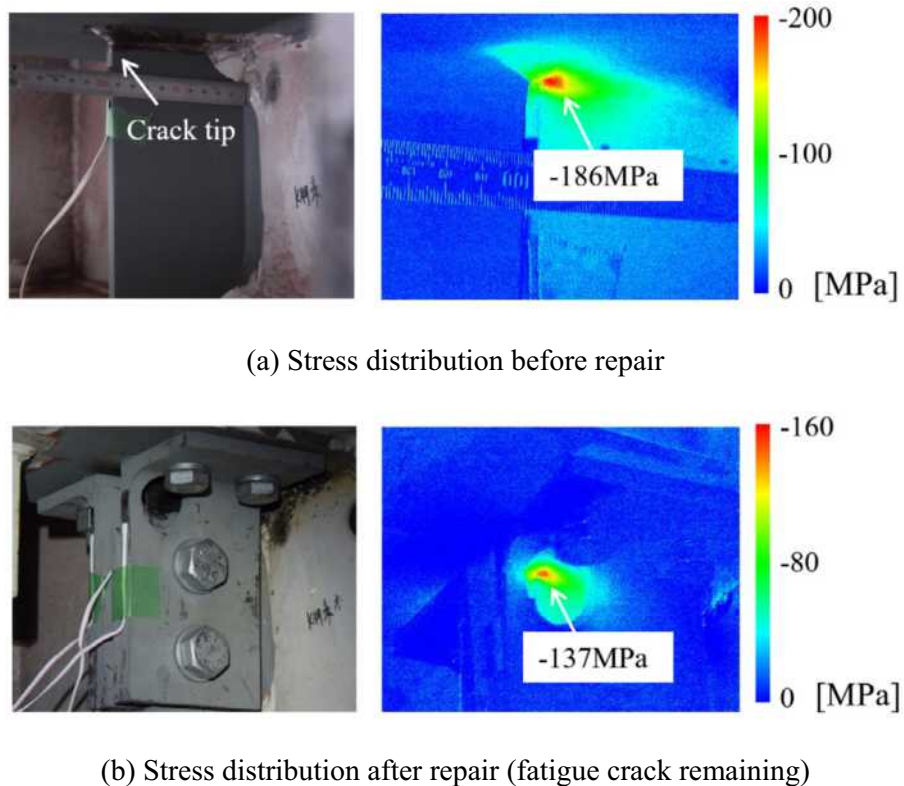


**Fig. 14.** Results of the thermoelectric stress distribution measurement for the type II stiffening-plate repair.

concentration in the weld part at top of the stiffener did not transfer to the stiffening plate. One possible cause is the incomplete contact of the upper edges of the stiffening plates with the lower surface of the cross-beam flange because of the incomplete finishing of the contact surfaces. This study clearly shows the benefit and importance of the in situ evaluation of the actual stress distribution achieved by the TSA technique. Stress values measured using the strain gauges are shown

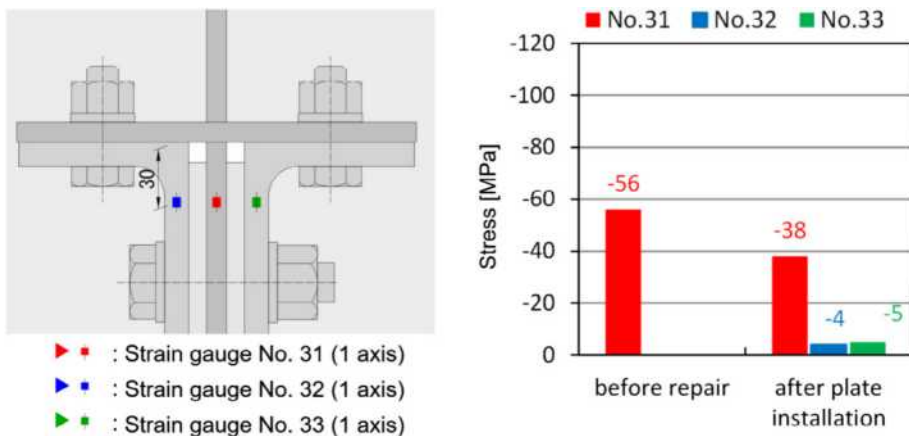


**Fig. 15.** Results of stress measurement by strain gauges obtained for type II stiffening-plate repair.

in Fig. 12. It is found that the high stress concentration near the crack tip was not mitigated after the repair work, and the stiffening plates did not share the loading.

In response to the unsuccessful stress reduction result of the type I stiffening-plate repair, the improved type II stiffening-plate repair method was examined. In this technique, four angle-stiffener plates were fastened to the vertical stiffeners and the lower cross beam flange using fastening bolts to better integrate the stiffeners and structural members. To avoid the problem of the infrared-measurement area being hidden by the angle-stiffener plate, an observation window was made in one of the plates, as shown in Fig. 13.

The experimental results of the thermoelastic stress measurement obtained for the improved type II stiffening-plate repair method are shown in Fig. 14. It is found from Fig. 14(b) that the stress concentration at the weld edge is observed even after stiffening-plate repair work. However in comparison to the stress value shown in Fig. 14(a), the maximum stress value in the vicinity of the crack tip is drastically decreased after the repair work. This result demonstrates that the improved type II stiffening-plate repair was successfully applied for stress mitigation at the crack tip by sharing the loading paths. Stress values measured using the strain gauges are shown in Fig. 15. It is found that the stress value on the edge surface was mitigated after the repair work since the stiffening plates shared the loading. Details of the fatigue life prolonging effect by stress mitigation will be investigated in future fracture mechanics studies by the present authors.

## 8. Conclusions

This study focused on repair techniques for the members of steel bridges with fatigue cracks as well as confirmation of the reduction in the severity of the stress distribution around the repaired portions using the TSA technique. Three different repair methods were investigated by in situ experiments and the following results were obtained.

- (1) It was found from experimental results of the circular-arc cutout repair method that the stress concentration around the fatigue crack tip at the top of stiffener was mitigated, and the high stress concentration area was successfully transferred from the weld part at the top of the stiffener to the edge of the circular arc, where the fatigue resistance is higher.
- (2) Experimental studies using two different types of stiffening-plate repair techniques showed that type I stiffening-plate repair did not effectively mitigate the stress because of the incomplete sharing of the loading paths caused by the incomplete contact between the upper edges of the stiffening plates and the lower surface of the cross-beam flange. In contrast, the improved type II stiffening-plate repair was successfully applied for stress mitigation at the crack tip.

This study clearly showed the benefit and importance of in situ evaluation of the actual stress distribution using TSA techniques. Thermoelastic stress measurement is effective for confirming the effectiveness of the repair works in bridge maintenance.

## Acknowledgements

The authors would like to acknowledge that the research works shown in this paper were partly supported by a Grant-in-Aid for Scientific Research from the Japan Society for the Promotion of Science (B: 26289009) and Casio Science Foundation. The authors also would like to thank T. Higashi, Y. Terauchi and R. Ichihashi for their technical assistance with the experiments and data processing.

## References

- [1] The Road Committee of the Panel on Infrastructure Development, The Japan Ministry of Land, Infrastructure, Transport and Tourism. Recommendations for Full-scale Maintenance of Aging Roads, [http://www.mlit.go.jp/road/road\\_e/pdf/recommendation.pdf](http://www.mlit.go.jp/road/road_e/pdf/recommendation.pdf); 2014 [accessed 17.01.14].
- [2] Greene RJ, Patterson EA, Rowlands RE. Thermoelastic stress analysis. In: Springer handbook of experimental solid mechanics. LLC New York: Springer Science + Business Media; 2008. p. 743–67.
- [3] Dulieu-Barton JM, Stanley P. Development and applications of thermoelastic stress analysis. *J. Strain Anal Eng Des* 1998;33:93–104.
- [4] Dulieu-Barton JM. Introduction to thermoelastic stress analysis. *Strain* 1999;35:35–9.
- [5] Pitarresi G, Patterson EA. A review of the general theory of thermoelastic stress analysis. *J. Strain Anal Eng Des* 2003;38:405–17.
- [6] Tomlinson RA, Olden EA. Thermoelasticity for the analysis of crack tip stress fields – a review. *Strain* 1999;35:49–55.
- [7] Ju SH, Lesniak JR, Sandor BI. Numerical simulation of stress intensity factors via the thermoelastic technique. *Exp Mech* 1997;37:278–84.
- [8] Tomlinson RA, Nurse AD, Patterson EA. On determining stress intensity factors for mixed mode cracks from thermoelastic data. *Fatigue Fract Eng Mater Struct* 1997;20:217–26.
- [9] Diaz FA, Patterson EA, Tomlinson RA, Yates JR. Measuring stress intensity factors during fatigue crack growth using thermoelasticity. *Fatigue Fract Eng Mater Struct* 2004;27:571–83.
- [10] He KY, Rowlands RE. Determining stress intensity factors in orthotropic composites from far-field measured temperatures. *Exp Mech* 2004;44:555–61.
- [11] Tomlinson RA, Marsavina L. Thermoelastic investigations for fatigue life assessment. *Exp Mech* 2004;44:487–94.
- [12] Diaz FA, Yates JR, Patterson EA. Some improvements in the analysis of fatigue cracks using thermoelasticity. *Int J Fatigue* 2004;26:365–76.
- [13] Ummenhofer T, Medgenberg J. On the use of infrared thermography for the analysis of fatigue damage processes in welded joints. *Int J Fatigue* 2009;31:130–7.
- [14] Zhang D, Sandor BI. Thermographic analysis of stress concentrations in a composite. *Exp Mech* 1989;29:121–5.
- [15] Jones R, Heller M, Sparrow JG, Ryall TG. A new approach to structural optimization. *Compos Struct* 1990;16:1–32.
- [16] Zhang D, Enke NF, Sandor BI. Thermographic stress analysis of composite materials. *Exp Mech* 1990;30:68–73.
- [17] Emery TR, Dulieu-Barton JM, Earl JS, Cunningham PR. A generalized approach to the calibration of orthotropic materials for thermoelastic stress analysis. *Compos Sci Technol* 2008;68:743–52.
- [18] Emery TR, Dulieu-Barton JM. Thermoelastic stress analysis of damage mechanisms in composite materials. *Composites: Part A* 2010;41:1729–42.
- [19] Fruehmann RK, Dulieu-Barton JM, Quinn S. Assessment of fatigue damage evolution in woven composite materials using infra-red techniques. *Compos Sci Technol* 2010;70:937–46.
- [20] Paynter RJH, Dutton AG. The use of a second harmonic correlation to detect damage in composite structures using thermoelastic stress measurements. *Strain* 2003;39:73–8.
- [21] Jones R, Molent L. Application of constitutive modeling and advanced repair technology to F111C aircraft. *Compos Struct* 2004;66:145–57.
- [22] Sakagami T. Remote nondestructive evaluation technique using infrared thermography for fatigue cracks in steel bridges. *Fatigue Fract Eng Mater Struct* 2015;38:755–79.
- [23] Shiozawa D, Inaba K, Akai A, Sakagami T. Experimental study of relationship between energy dissipation and fatigue damage from observation of slip band by atomic force microscope. *Adv Mater Res* 2014;891:606–11.
- [24] Sakagami T, Izumi Y, Kobayashi Y, Mizokami Y, Kawabata S. Applications of infrared thermography for nondestructive testing of fatigue cracks in steel bridges. *Proc. SPIE* 2014; 9105: 0S-1–8.
- [25] Sakagami T, Nishimura T, Kubo S. Development of a self-reference lock-in thermography and its application to crack monitoring. *Proc SPIE* 2005;5782:379–87.
- [26] Matsumoto R, Ishikawa T, Tsukamoto S, Awazu Y, Kawano H. Comparison of repair methods for fatigue crack initiated at welded toe between steel deck plate and vertical stiffener. *J Japan Soc Civil Eng, Ser. A1 (Struct Eng Earthq Eng (SE/EE))* 2016; 72(1): 192–205.
- [27] YuanZhou Z, Ji B, Fu Z, Ge H. Local stress variation in welded joints by ICR treatment. *J. Constr Steel Res* 2016;120:45–51.
- [28] Aoki Y, Ishikawa T, Matsumoto R, Kawano H, Adachi Y. Patch bonding repair of through-thickness crack in orthotropic steel deck at vertical stiffener end. *J Struct Eng A* 2015;61A:408–15.
- [29] Thomson W. (Lord Kelvin) On the dynamical theory of heat. *Trans R Soc* 1853;20:261–83.
- [30] Lesniak J, Boyce B, Howenwater G. Thermoelastic measurement under random loading. In: Proc. SEM Spring Conf. Soc. Exp. Mech. 1998. p. 504–507.
- [31] Takada Y, Kawakami Y, Sakai Y, Sakano M. Study on retrofit measures in weld of vertical stiffener cutting treating of the semicircle in orthotropic steel deck. *JSSC Steel Constr Eng* 2009;16(62):35–46.
- [32] Cheng X, Duan L, Najjar WS. Rehabilitation and strengthening of highway bridge superstructures. In: Chen W, Duan L, editors. Bridge engineering handbook. CRC Press: Boca Raton; 2013. p. 465–70.